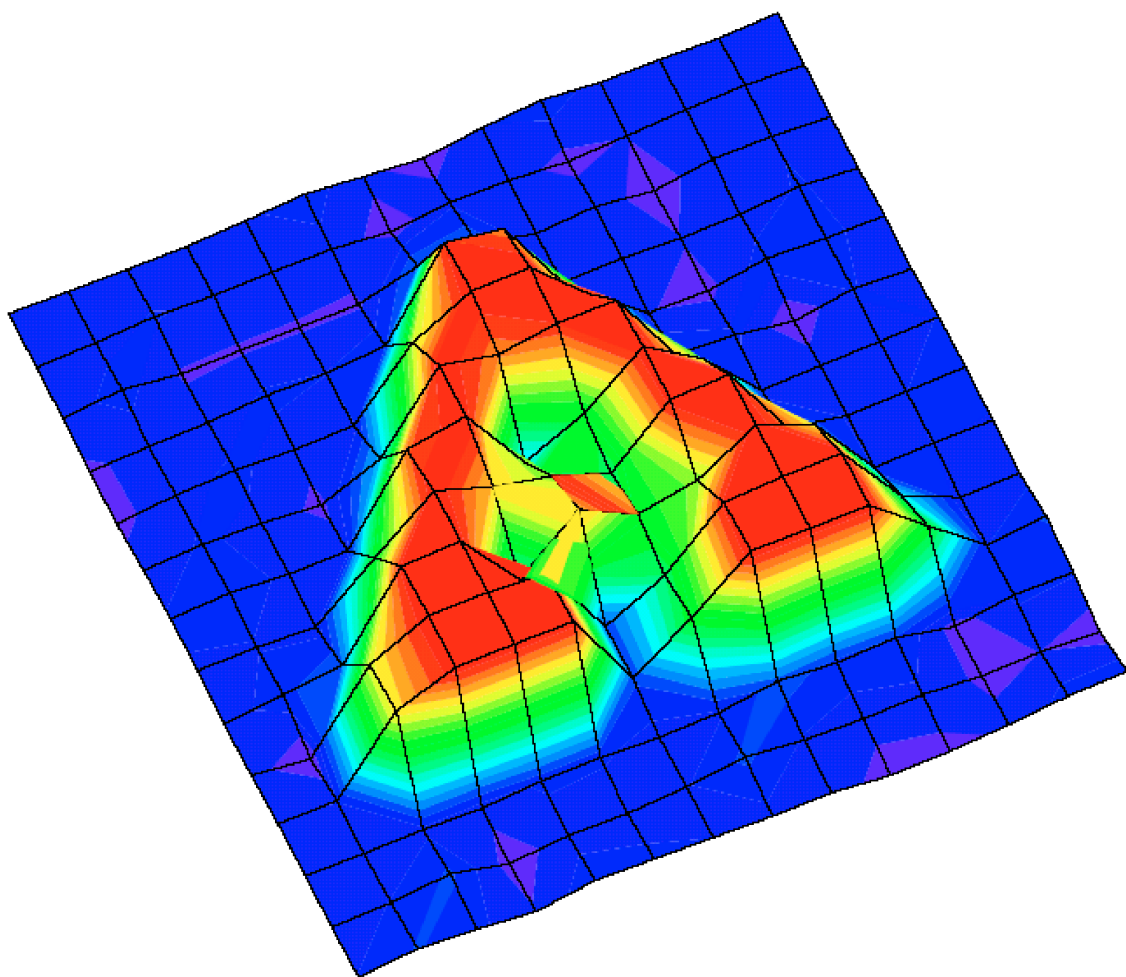


Physics Division Annual Report 2004



About the Cover

An image of the Argonne Logo illuminated by 88 keV X-rays. The image was made using a two dimensionally position sensitive germanium detector developed by Argonne in collaboration with EG&G Ortec. Position sensitive germanium counters have many potential appreciations in nuclear science, space science, medical imaging and in homeland security.

About Argonne National Laboratory

Argonne is a U.S. Department of Energy laboratory managed by The University of Chicago under contract W-31-109-Eng-38. The Laboratory's main facility is outside Chicago, at 9700 South Cass Avenue, Argonne, Illinois 60439. For information about Argonne, see www.anl.gov.

Availability of This Report

This report is available, at no cost, at <http://www.osti.gov/bridge>. It is also available on paper to the U.S. Department of Energy and its contractors, for a processing fee, from:

U.S. Department of Energy
Office of Scientific and Technical Information
P.O. Box 62
Oak Ridge, TN 37831-0062
phone (865) 576-8401
fax (865) 576-5728
reports@adonis.osti.gov

Disclaimer

This report was prepared as an account of work sponsored by an agency of the United States Government. Neither the United States Government nor any agency thereof, nor The University of Chicago, nor any of their employees or officers, makes any warranty, express or implied, or assumes any legal liability or responsibility for the accuracy, completeness, or usefulness of any information, apparatus, product, or process disclosed, or represents that its use would not infringe privately owned rights. Reference herein to any specific commercial product, process, or service by trade name, trademark, manufacturer, or otherwise, does not necessarily constitute or imply its endorsement, recommendation, or favoring by the United States Government or any agency thereof. The views and opinions of document authors expressed herein do not necessarily state or reflect those of the United States Government or any agency thereof, Argonne National Laboratory, or The University of Chicago.

ANL-05/61

ARGONNE NATIONAL LABORATORY
9700 S. Cass Avenue
Argonne, Illinois 60439-4801

**PHYSICS DIVISION ANNUAL REPORT
2004**

Donald F. Geesaman
Director

December 2005

Preceding Annual Reports

ANL-02/15 2001

ANL-03/23 2002

ANL-04/22 2003

Edited by Jeannie Glover

FOREWORD

This report highlights the research performed in 2004 in the Physics Division of Argonne National Laboratory. The Division's programs include operation of ATLAS as a national user facility, nuclear structure and reaction research, nuclear theory, medium energy nuclear research and accelerator research and development. The intellectual challenges of this research represent some of the most fundamental challenges in modern science, shaping our understanding of both tiny objects at the center of the atom and some of the largest structures in the universe. A great strength of these efforts is the critical interplay of theory and experiment.

Notable results in research at ATLAS include a measurement of the charge radius of He-6 in an atom trap and its explanation in ab-initio calculations of nuclear structure. Precise mass measurements on critical waiting point nuclei in the rapid-proton-capture process set the time scale for this important path in nucleosynthesis. An abrupt fall-off was identified in the sub-barrier fusion of several heavy-ion systems. ATLAS operated for 5559 hours of research in FY2004 while achieving 96% efficiency of beam delivery for experiments.

In Medium Energy Physics, substantial progress was made on a long-term experiment to search for the violation of time-reversal invariance using trapped Ra atoms. New results from HERMES reveal the influence of quark angular momentum. Experiments at JLAB search for evidence of color transparency in rho-meson production and study the EMC effect in helium isotopes.

New theoretical results include a Poincare covariant description of baryons as composites of confined quarks and non-point-like diquarks. Green's function Monte Carlo techniques give accurate descriptions of the excited states of light nuclei and these techniques been extended to scattering states for astrophysics studies. A theoretical description of the phenomena of proton radioactivity has been extended to triaxial nuclei.

Argonne continues to lead in the development and exploitation of the new technical concepts that will truly make RIA, in the words of NSAC, "the world-leading facility for research in nuclear structure and nuclear astrophysics." The performance standards for new classes of superconducting cavities continue to increase. Driver linac transients and faults have been analyzed to understand reliability issues and failure modes. Liquid-lithium targets were shown to successfully survive the full-power deposition of a RIA beam. Our science and our technology continue to point the way to this major advance. It is a tremendously exciting time in science for RIA holds the keys to unlocking important secrets of nature. The work described here shows how far we have come and makes it clear we know the path to meet these intellectual challenges.

The great progress that has been made in meeting the exciting intellectual challenges of modern nuclear physics reflects the talents and dedication of the Physics Division staff and the visitors, guests and students who bring so much to the research.

Donald F. Geesaman, Director, Physics Division

TABLE OF CONTENTS

Page

I.	HEAVY-ION NUCLEAR PHYSICS RESEARCH	1
A.	REACTIONS OF ASTROPHYSICAL IMPORTANCE	3
a.1.	Measurement of the E1 Component of the Low-Energy $^{12}\text{C}(\alpha,\gamma)^{16}\text{O}$ Cross Section	3
a.2.	Results from the First ^{16}N Decay Experiment	4
a.3.	$^{18}\text{Ne}(\alpha,p)^{21}\text{Na}$, a Possible Breakout Reaction from the Hot CNO Cycle to the rp Process	6
a.4.	Level Structure and Mass of ^{22}Mg	8
a.5.	In-Beam Spectroscopy Above the Proton Threshold in ^{27}Si and the Production of ^{26}Al in Novae	8
a.6.	Re-Evaluation of the $^{30}\text{P}(p,\gamma)^{31}\text{S}$ Astrophysical Reaction Rate in Novae	9
a.7.	Measurement of ^{44}Ti Half-Life	10
a.8.	The $^{40}\text{Ca}(\alpha,\gamma)^{44}\text{Ti}$ Reaction at Astrophysical Energies	10
a.9.	New Half-life Measurement of ^{182}Hf : An Improved Chronometer for the Early Solar System	11
B.	PHYSICS OF TRAPPED IONS	13
b.1.	Ordering and Temperature in Ions Trapped in Radiofrequency Fields	13
b.2.	Q Value of the Superaligned β -Decay of ^{22}Mg and the Calibration of the $^{21}\text{Na}(p,\gamma)$ Reaction	14
b.3.	Q Value of the Superaligned Decay of ^{46}V and the Unitarity of the CKM Matrix	18
b.4.	Precise Mass Measurement of Light Fission Fragments from ^{252}Cf Source	22
b.5.	The RFQ Decay Trap Component of the Advanced Penning Trap System	23
C.	SPECTROSCOPY OF VERY HEAVY ELEMENTS	27
c.1.	Strength of Octupole Correlations in the Actinides: Contrasting Behavior in the Isotones ^{239}Pu and ^{237}U	27
c.2.	Behavior of ^{240}Pu at the Highest Spins	29
c.3.	Proton Single-Particle States in ^{249}Bk ($Z = 97$)	30
c.4.	Properties of the Lightest Nobelium Isotopes	31
c.5.	Structure of ^{253}No	31
c.6.	Electrons from a 0.3s Isomer in $^{254}\text{No}^*$	33
c.7.	Gamma Decay from a 0.3s Isomer in ^{254}No	34
c.8.	Limiting Angular Momentum in ^{254}No	35

D.	STRUCTURE OF NUCLEI FAR FROM STABILITY	37
d.1.	Neutron-Rich Nuclei	37
d.1.1.	High Spin Structure in Neutron-Rich Ti and Cr Isotopes: Possible N = 32 and 34 Shell Gaps and the Onset of Deformation	37
d.1.2.	Search for $^{82}\text{Ge}_{50}$ Using Deep Inelastic Reactions.....	41
d.1.3.	The $\nu 9/2[404]$ Orbital and the Deformation in the A ~ 100 Region	42
d.2.	Proton-Rich Nuclei	43
d.2.1.	The A = 31 Mirror Nuclei ^{31}P and ^{31}S Used to Investigate the Charge- Symmetry-Breaking “Electromagnetic Spin Orbit” Interaction V_{eso}	43
d.2.2.	High Spin States of T = 3/2 ^{37}Ca and ^{37}Cl	43
d.2.3.	High Spin States in the N = Z - 3 Nucleus ^{49}Fe : Coulomb Effects at Large Proton Excess	44
d.2.4.	Shape Co-Existence in ^{71}Br and the Question of the Groundstate Spin of ^{71}Kr	48
d.2.5.	Fast Alpha Decays Above ^{100}Sn	49
d.2.6.	Discovery of the Deformed Proton Emitter ^{121}Pr	50
d.2.7.	Recoil-Decay Tagging Study of ^{146}Tm	51
d.2.8.	Multi-Particle Configurations in N = 84 Isotones Located at the Proton Drip-Line.....	52
d.2.9.	Alpha Decay of ^{181}Pb	53
d.2.10.	Level Structure of ^{181}Tl	53
E.	OTHER NUCLEAR STRUCTURE RESEARCH	55
e.1.	Investigation of $^{12}\text{C}(^{12}\text{C},\gamma)^{24}\text{Mg}$ Radiative Capture	55
e.2.	Variation with Mass of B(E3; $0^+ \rightarrow 3^-$) Transition Rates in A = 124-134 Even-Mass Xenon Nuclei	56
e.3.	Rotational Damping, Ridges and the Quasicontinuum of γ Rays in ^{152}Dy	57
e.4.	Study of Multi-Quasiparticle Isomers in the A ~ 180 Region Using Deep- Inelastic and Multi-Nucleon Transfer Reactions	60
e.5.	Pair Gaps in the Normal- and Super-Deformed Wells of ^{191}Hg	62
e.6.	Temperature and Spin Dependence of the Giant Dipole Resonance Width in $^{117,118}\text{Sn}$	62
e.7.	Observation of the Hot GDR in Neutron-Deficient Thorium Evaporation Residues	63
F.	THE PHOBOS EXPERIMENT AT RHIC	65
f.1.	The Phobos Experiment at RHIC	65
G.	REACTION MECHANISM STUDIES	73
g.1.	Study of ^7He Using the $d(^6\text{He},p)^7\text{He}$ Reaction.....	73
g.2.	Neutron Spectroscopic Factors in ^9Li from the $d(^8\text{Li},p)^9\text{Li}$ Reaction.....	74
g.3.	Is the Nuclear Spin-Orbit Interaction Changing with Neutron Excess?.....	76

g.4.	Hindrance of Heavy-Ion Fusion at Extreme Sub-Barrier Energies in Open-Shell Colliding Systems	76
g.5.	$^{58}\text{Ni} + ^{89}\text{Y}$ Fusion Hindrance at Extreme Sub-Barrier Energies	81
g.6.	Hindrance of Heavy-Ion Fusion at Extreme Sub-Barrier Energies for a Small Q-Value System $^{28}\text{Si} + ^{64}\text{Ni}$	88
H.	DEVELOPMENT OF NEW EXPERIMENTAL EQUIPMENT	91
h.1.	Target Laboratory Developments	91
h.2.	New Control System Hardware and Software for the FMA.....	92
h.3.	The Isobar Separator Ion Trap for the APT and CPT Trapping Systems.....	92
h.4.	A Solenoid Spectrometer for Reactions in Inverse Kinematics.....	93
h.5.	A New Focal-Plane Detector System at the Argonne Fragment Mass Analyzer for Low Fusion-Evaporation Cross Section Measurements.....	94
h.6.	Performance of a Compton Camera Using Digital Pulse Processing.....	104
h.7.	Ambiguity in Gamma Ray Tracking of “Two Interaction” Events	105
h.8.	A Bragg Scattering Method to Search for the Neutron Electric Dipole Moment.....	105
h.9.	Heavy Element Scattering Chamber Upgrade	106
h.10.	The MUSIC Detector	107
h.11.	Digital Bragg Curve Spectroscopy	108
h.12.	The New Focal Plane Detector for the Notre Dame Spectrometer.....	108
h.13.	Deployment of a Centrally Managed Windows Cluster.....	110
h.14.	Status of the SCARLET Data Acquisition System.....	111
h.15.	Progress on the New Gammasphere Data Acquisition	112
h.16.	Gammasphere Operations.....	112
h.17.	Gammasphere Move	113
h.18.	X-Array Developments.....	113
h.19.	Degradation of the ^{16}N Beam to Very Low Energy.....	115
h.20.	Improvement of the Experimental Setup for the Study of the ^{16}N β Delayed α Decay.....	117
h.21.	The Twin Ionization Chambers	118
h.22.	Backgrounds and Sensitivity to Beta Particles	120
h.23.	Simulation of the Detector Response in the ^{16}N β -Delayed α Decay Experiment.....	122
I.	HIGH-PRECISION AND HIGH-SENSITIVITY EXPERIMENTS	123
i.1.	Search for X-Ray Induced Decay of the 31-y Isomer of ^{178}Hf	123
J.	ATLAS USER PROGRAM	125
a.	Experiments Involving Outside Users	126
b.	Outside Users of ATLAS During the Period October 1, 2003 - September 30, 2004	130

II. OPERATION AND DEVELOPMENT OF ATLAS	133
A. OPERATION OF THE ACCELERATOR	135
a.1. Operations Summary	135
B. DEVELOPMENTS RELATED TO ATLAS	139
b.1. Status of the ECR Ion Sources.....	139
b.1.1. Hexapole and Plasma Chamber Re-Design	139
b.1.2. Special Helium Source for AMS	139
b.1.3. Plasma Potential Measurements and Ion Lifetime.....	139
b.1.4. Other ECR Source Improvements	140
b.2. ECR Source High-Voltage Monitoring and Control	141
b.3. An Improved Pneumatic Frequency Control for Superconducting Cavities	141
b.4. New Harmonic Buncher RF Control System.....	142
b.4.1. RF Power Amplifier.....	143
b.4.2. Harmonic Buncher RF Control Chassis.....	144
b.5. ATLAS Control System.....	148
b.6. ATLAS Cryogenic System	149
b.6.1. Valve Automation Project.....	149
III. R&D RELATED TO A FUTURE RARE ISOTOPE ACCELERATOR FACILITY	151
A. SUPERCONDUCTING RF	153
a.1. Spoke Cavity Development for RIA.....	153
a.2. Superconducting Cavity Surface Processing Facilities.....	154
a.3. Tuners and Couplers for the RIA Cavities.....	154
a.4. Cavities and Prototype Cryomodule for RIA and the ATLAS Upgrade	155
B. BEAM DYNAMICS AND INJECTORS	157
b.1. Design and Construction of a One-Segment Prototype of the RIA Driver RFQ.....	157
b.2. Alternating-Phase Focusing in Low-Velocity Heavy-Ion Superconducting Linac	158
b.3. Design Update of the Injector Section of the RIA Post-Accelerator	160
b.4. Progress with the 2Q-LEBT Prototype	162
b.5. Modifications and rf Tests of the 12 MHz RFQ for Acceleration of a $^{240}\text{U}^{1+}$ Beam	163
b.6. Error Simulations and Beam Loss Studies in the RIA Driver Linac	164
b.7. Longitudinal Fine-Tuning of a Multiple-Charge-State Heavy-Ion Beam	166
b.8. Front End Design of a Multi-GeV H-Minus Linac.....	167

b.9.	Reliability and Availability Studies in the RIA Driver Linac.....	169
b.10.	Optimization of Steering Elements in the RIA Driver Linac	170
C.	RARE ISOTOPE PRODUCTION AND SEPARATION	173
c.1.	Characterization Studies of Prototype ISOL Target Material for RIA.....	173
c.2.	Development of a Windowless Liquid Lithium Stripper for RIA	174
IV.	MEDIUM-ENERGY NUCLEAR PHYSICS	
	RESEARCH.....	191
A.	HADRON PROPERTIES.....	195
a.1.	New Measurement of (G_E/G_M) for the Proton	195
a.2.	High-Resolution Search for the Θ^+ Pentaquark at JLab	196
a.3.	Search for Additional Pentaquark States at JLab.....	197
a.4.	$N \rightarrow \Delta$ Transition Form Factors	197
a.5.	The Charged Pion Form Factor.....	198
a.6.	Separated and Unseparated Structure Functions in the Nucleon Resonance Region.....	198
B.	HADRONS IN THE NUCLEAR MEDIUM.....	201
b.1.	Search for the Onset of Color Transparency: JLab E02-110 Experiment	201
b.2.	Measurement of High Momentum Nucleons in Nuclei and Short Range Correlations.....	203
b.3.	Measurement of the EMC Effect in Very Light Nuclei.....	205
b.4.	Proton Polarization Angular Distribution in Deuteron Photo Disintegration.....	205
b.5.	Measurement of the Nuclear Dependence of $R = \sigma_L/\sigma_T$ at Low Q^2	206
b.6.	Electroproduction of Kaons and Light Hypernuclei.....	206
C.	QUARK STRUCTURE OF MATTER.....	209
c.1.	The Structure of the Pion	209
c.2.	Studies of Nucleon Spin Structure and Related Measurements of Deep- Inelastic Scattering at HERA	209
c.2.1.	Polarization of the Strange Quark Sea in the Proton from Semi-Inclusive Deep-Inelastic Scattering on the Deuteron	210
c.2.2.	Azimuthal Asymmetries and Transversity.....	211
c.2.3.	New Results for Collins and Sivers Asymmetries with a Transversely Polarized Target.....	212
c.2.4.	The Deuteron Tensor Polarized Structure Function b_1	214
c.2.5.	Measurements of Deeply-Virtual Compton Scattering at HERMES	215
c.2.6.	Quark Fragmentation to Pions, Kaons, and Nucleons in the Nuclear Environment.....	216

c.2.7.	Extraction of Hadron Multiplicities from Deep-Inelastic Scattering Data	217
c.2.8.	Search for an Exotic $S = -2, Q = -2$ Baryon Resonance with Mass Near 1862 MeV	218
c.2.9.	Study of Factorization and Flavor Content of the Nucleon in Unpolarized Semi Inclusive Deep Inelastic Scattering at HERMES	219
c.3.	Measurement of the Absolute Drell-Yan Cross Section on Hydrogen and Deuterium	220
c.4.	Drell-Yan Measurements with 120 GeV Protons, FNAL E906	221
D.	ATOMIC TRAP TRACE ANALYSIS	223
d.1.	Laser Spectroscopic Determination of the Nuclear Charge Radius of ${}^6\text{He}$	223
d.2.	Fine Structure of the $1s3p\ {}^3P_J$ Level in Atomic ${}^4\text{He}$: Theory and Experiment	225
d.3.	Atmospheric ${}^{81}\text{Kr}$ as an Integrator of Cosmic Ray Flux Over the Past $\sim 3 \times 10^5$ Years	225
E.	FUNDAMENTAL SYMMETRIES IN NUCLEI	227
e.1.	Probing the Intercombination Transition $7s^2\ {}^1S_0 - 7p\ {}^3P_1$ in ${}^{225}\text{Ra}$ Atoms for an EDM Measurement	227
e.2.	Measurement of $\sin^2\theta_w$ Through Parity Violation in Deep Inelastic Scattering (PV DIS) on Deuterium	228
e.3.	Feasibility Study for a Charge Symmetry Violating Quark Distribution Measurement	230
V.	THEORETICAL PHYSICS	233
A.	NUCLEAR DYNAMICS WITH SUBNUCLEONIC DEGREES OF FREEDOM	235
a.1.	Aspects and Consequences of a Dressed-Quark-Gluon Vertex	236
a.2.	Pseudoscalar Meson Radial Excitations	236
a.3.	Nucleon Electromagnetic Form Factors	237
a.4.	Electromagnetic Properties of Ground and Excited State Pseudoscalar Mesons	239
a.5.	Charge Form Factors of Quark-Model Pions	241
a.6.	Axial Transition Form Factors and Pion Decay of Baryon Resonances	242
a.7.	Quark-Hadron Duality and Parity Violating Asymmetry of Electroweak Reactions in the Δ Region	242
a.8.	Dynamical Coupled-Channel Model of Electromagnetic Meson Production Reactions	245
a.9.	Study of N Resonances with Kaon Photoproduction Reactions	246
a.10.	Medium Effects on the Electromagnetic ρ Meson Production on Nuclei	247
a.11.	Pentaquark $\theta^+(1540)$ Production in $\gamma N \rightarrow K \bar{K} N$ Reactions	247

B.	NUCLEAR FORCES AND NUCLEAR SYSTEMS	249
b.1.	Quantum Monte Carlo Calculations of Light Nuclei Energies	250
b.2.	Scattering Methods for Quantum Monte Carlo Calculations	251
b.3.	Spectroscopic Factors and Cluster Form Factors of Light Nuclei	252
C.	NUCLEAR ASTROPHYSICS	255
c.1.	Moments Methods for Response Functions with Momentum Transfer Dependence	256
c.2.	Short-Lived Nuclei in the Early Solar System and AGB Stars	258
D.	NUCLEAR STRUCTURE AND HEAVY-ION REACTIONS	259
d.1.	Coupled-Channels Calculations of Heavy-Ion Fusion Reactions	260
d.2.	Modeling the Quadrupole Mode in ^{100}Mo	262
d.3.	Constraints on the $^7\text{Be}(p,\gamma)^8\text{Be}$ Reaction from Charge Symmetry	264
d.4.	Model Dependence of the $^7\text{Be}(p,\gamma)^8\text{Be}$ Reaction Rate	265
d.5.	Reconciling Coulomb Dissociation and Radiative Capture Measurements	266
d.6.	Mean Field and Many Body Wave Functions	268
d.7.	Neutron-Proton Pairing	269
d.8.	Energy Levels of the Heavy Elements	271
d.9.	Self-Consistent Beyond-Mean-Field Calculations in Exotic Heavy Nuclei	272
d.10.	A New Microscopic Pairing Force for Self-Consistent Mean-Field Calculations	273
d.11.	Configuration Mixing of Particle-Number and Angular-Momentum Projected Cranked HFB States	273
d.12.	Collective States in the $20 < Z < 28$ and $28 < N < 40$ Region	273
d.13.	Systematics of Ground-State Correlations in Even-Even Nuclei	274
d.14.	QRPA of Spherical Nuclei with Skyrme Interactions	274
E.	ATOMIC THEORY AND FUNDAMENTAL QUANTUM MECHANICS	275
e.1.	Interactions of Photons with Matter	275
e.2.	Interactions of Charged Particles with Matter	276
e.3.	Photon Beam Polarization and Non-Dipolar Angular Distributions	276
e.4.	The Theory Experiment Connection: R_n Space and Inflationary Cosmology	276
F.	OTHER ACTIVITIES	279
f.1.	Hadron Physics: Modern Methods for Modern Challenges	279
f.2.	17 th Annual Midwest Nuclear Theory Get-Together	279

VI. OTHER EDUCATIONAL AND COMMUNITY OUTREACH ACTIVITIES	281
a. Minority Program.....	281
b. Third RIA Summer School.....	282
c. Homeland Security Activities - Scientific Support of the Radiological Assistance Program.....	283
d. Repair and Refurbishment of Germanium Detectors.....	284
Staff List.....	285
Publications.....	297

I. HEAVY-ION NUCLEAR PHYSICS RESEARCH

OVERVIEW

This research involves investigating the structure, stability, reactions and decays of nuclei. This information is crucial for understanding the evolution of the universe, the workings of stars and the abundances of the elements that form the world around us. The forefront area of research is investigating the properties of nuclei which lie very far from stability, and which are critical in understanding nucleosynthesis. Most of our research is based at the Argonne Tandem-Linac Accelerator (ATLAS), a national heavy-ion user facility. During this year programs were also mounted at the Relativistic Heavy Ion Collider (RHIC), at Michigan State University, at Yale University, and at other forefront facilities. The major thrusts of the program are: a) studying the reactions that are important in the cataclysmic events in the cosmos which lead to the synthesis of the chemical elements, b) deepening and generalizing our understanding of nuclear structure to allow a reliable description of all bound nuclear systems, and c) testing the limits of the Standard Model, the fundamental theory that currently best represents our understanding of the laws and fundamental symmetries of nature.

The specific research topics we are pursuing include the measurements of reactions that are important in astrophysics. Many approaches are used, including the production and acceleration of short-lived nuclei in order to measure key reaction rates, and the use of Gammasphere to investigate the properties of states in the "Gamow window". Our program of nuclear physics measurements on trapped atoms and ions has become very productive. An "online" atom trap now complements the existing CPT Penning ion trap and there is rapid development of a new "open-geometry" trap for weak interaction studies. Gammasphere operating on two beamlines offers world-unique opportunities for gamma-spectroscopy and a wide range of experiments are being carried out on both neutron-rich and neutron poor nuclei. The key thrust of spectroscopic studies is to investigate the modification of residual interactions in nuclei far from stability. In addition, there are complimentary efforts in the use of Accelerator Mass Spectrometry (AMS) for environmental research and in the investigation of nuclear matter at relativistic energies. The ATLAS-based research exploits the unique capabilities of the accelerator, both in the stable beam program, and in production of accelerated beams of short-lived isotopes. The experiments employ state-of-the-art research equipment, including the national gamma ray facility, Gammasphere, the Fragment Mass Analyzer (FMA), a large solid angle silicon array, "Ludwig", and the Canadian Penning Trap, (CPT) all of which are operating at ATLAS. Several new detector initiatives are being pursued including refining the "in-flight" radioactive beam facility and its detector systems, constructing the Advanced Penning Trap (APT), and refinement of the online

atom trap (ATTA). Effort continues in developing the next generation gamma ray detectors in the GRETINA project, and development of a compact and efficient array for decay studies (the X-Array). Participation in the PHOBOS experiment at Brookhaven has continued. Some of the specific goals of the program can be summarized as follows:

- Develop and utilize beams of short-lived nuclei, ${}^6\text{He}$, ${}^8\text{Li}$, ${}^8\text{B}$, ${}^{11}\text{C}$, ${}^{14}\text{O}$, ${}^{16}\text{N}$, ${}^{17,18}\text{F}$, ${}^{20,21}\text{Na}$, ${}^{25}\text{Al}$, ${}^{37}\text{K}$, ${}^{44}\text{Ti}$, ${}^{56}\text{Ni}$, and others, to improve the understanding of reactions of astrophysical importance. Emphasis focused on “in-flight” production of short-lived ion-species using kinematically inverse reactions on light gaseous targets. Considerable scope still remains for further improving the intensity and quality of these beams in the future, and the beamline is being continually upgraded.
- Make high-precision measurements of nuclear masses with the CPT, particularly the masses of $N = Z$ nuclei which are of astrophysical interest and are important for testing CVC theory, and measuring the masses of neutron fission fragments that lie close to the anticipated r-process path. Improve the efficiency for production, separation, cooling, transportation, and trap loading of ions to increase sensitivity. Develop the open geometry “Advanced Penning Trap”, the APT.
- Study the structure of neutron-rich nuclei in order to understand the modification of shell gaps and the apparent changes in spin-orbit splitting. Study transfer reactions on spherical tin isotopes, the decay and Coulomb excitation of exotic nuclei produced in fragmentation, and the most neutron rich nuclei that can be reached by multi-nucleon transfer and heavy-ion fusion.
- Investigate the collisions and deconfinement of nucleons in nuclear matter at very high temperatures and densities that are achieved in relativistic heavy-ion collisions of gold nuclei at 200 GeV/u. Our participation is using the PHOBOS detector at the RHIC accelerator at Brookhaven National Laboratory.
- Studying the properties of very heavy nuclei through “in-beam”, “isomer”, and “decay” spectroscopy. The measurements reveal information on the single particle sequence, shell gaps, pairing strength, and fission barriers of very heavy systems. These properties govern the mass limits of nuclear existence.
- Study the shapes, stability and decay modes of nuclei along the proton dripline in order to improve understanding of partially bound nuclei. Study proton tunneling through deformed barriers, in order to increase the spectroscopic information obtained through proton radioactive decay rates. Study the influence of vibrations and coupling to other nucleons in odd-odd systems to generalize the understanding of proton radioactivity. Study excited states in these nuclei using the RDT technique to trigger Gammasphere.
- Perform detailed R&D studies for the Rare Isotope Accelerator (RIA) and participate in all efforts to refine the designs for the accelerators, target stations, post accelerator, and experimental equipment. Intense effort is being directed to development of the “gas catcher” technology for cooling primary beams.
- Developing position-sensitive germanium detectors, for “tracking” gamma rays in order to allow the imaging of the source of radiation. The ANL focus is on developing planar germanium wafer technologies, in parallel with involvement in the GRETINA project to construct a 1π germanium tracking detector.

A. REACTIONS OF ASTROPHYSICAL IMPORTANCE

Research into nuclear reactions that are relevant to astrophysical processes is at the core of our science, and is part of our strategic plan. A wide variety of techniques are currently used, exploiting almost all of our equipment, including experiments with radioactive beams, studies with Gammasphere, measurements with the Canadian Penning Trap (CPT), and the use of Accelerator Mass Spectrometry (AMS) for trace element analysis.

a.1. Measurement of the E1 Component of the Low-Energy $^{12}\text{C}(\alpha,\gamma)^{16}\text{O}$ Cross Section

(X. D. Tang, K. E. Rehm, I. Ahmad, J. Greene, A. Hecht, D. Henderson, R. V. F. Janssens, C. L. Jiang, E. F. Moore, M. Notani, R. C. Pardo, G. Savard, J. P. Schiffer, S. Sinha, M. Paul,* L. Jisonna,† R. E. Segel,‡ A. Champagne,‡ and A. Wuosmaa§)

The radiative capture of α particles on ^{12}C , *i.e.* $^{12}\text{C}(\alpha,\gamma)^{16}\text{O}$, is an important reaction in stellar nucleosynthesis. It not only influences the ratio of the important elements carbon and oxygen, but it also determines the evolution of massive stars. Since there is no resonant level in ^{16}O located in the Gamow window, the astrophysical reaction rate is determined by the contributions from several neighboring states, with the most important ones coming from two sub-threshold states with $J^\pi = 1^-$ and 2^+ . Because of the small cross sections ($\sim 10^{-18}$ b) at stellar temperatures, a direct measurement of the reaction rate at temperatures typical of red giant stars is not possible and one has to rely on indirect methods. Two multiplicities (E1 and E2) contribute to the transition and, thus, several different measurements are required to determine the total reaction rate. To determine these parameters, measurements of the beta-delayed alpha decay of ^{16}N , angular distributions of E1 and E2 alpha capture and of elastic alpha scattering on ^{12}C are needed. In several measurements of the beta-delayed alpha decay of ^{16}N the low-energy alpha particles from the decay of alpha-unstable levels in ^{16}O were detected in thin Si-surface barrier detectors.¹⁻⁴ The small alpha/beta branching ratio in this decay ($\sim 10^{-5}$) results in a very high beta-background that can influence the low-energy part of the alpha spectrum from which the E1 reaction rate, $S(\text{E}1)$, is obtained.

In the present experiment we have used a somewhat different approach to measure the ^{16}N decay. To produce the ^{16}N activity we used the in-flight method, which eliminates the $^{17,18}\text{N}$ contamination of one of the earlier measurements. To reduce the sensitivity to beta particles we have developed an array of high-acceptance ionization chambers of minimal

thickness, to be used for the detection of ^{12}C and alpha particles in coincidence, but which are rather insensitive to β -decays.

A schematic of the experimental setup is shown in Fig. I-1. A ~ 60 MeV ^{16}N ($T_{1/2} = 7.1$ sec) beam is slowed down in a gas-filled attenuator cell and stopped in a $10 \mu\text{g}/\text{cm}^2$ thick carbon foil (foil I) mounted on a rotating wheel which is located in the main part of the detection chamber. The attenuator cell and the main chamber are filled with P10 counting gas at a typical pressure of 150 Torr. After an irradiation period of 15 sec, the foil is rotated (in 60 ms) to be between a pair of twin ionization chambers (pair I) for the coincident detection of $^{12}\text{C} - \alpha$ pairs. The carbon foil is counted in this pair of ionization chambers for 15 sec. During this time a second foil (II), mounted 120° from the first, is irradiated. At the end of the irradiation period foil II is rotated to be between a second pair of ionization chambers (pair II) and counted, while foil I is again irradiated with ^{16}N . Detector pair I is meanwhile counting a non-irradiated foil giving the background in the entire setup. The same foil is also used for measuring the background in detector pair II. A description of the setup and the results of first test measurements have been presented in a previous annual report. In this reporting period several improvements to the setup have been incorporated. They include:

- Installation of a mechanical brake to reduce the electronic noise from the stepping motor,
- Modification of the foil holder,
- Development of a detector simulation program,
- Optimization of the energy attenuator cell,
- Incorporation of the ionization chamber grid signal, which provides information about the emission angles of the particles,
- Measurement of the alpha background,

- Study of the detector response to beta particles.

The results of the different improvements are described in the equipment development chapter

*Hebrew University, Jerusalem, Israel, †Northwestern University, ‡University of North Carolina, §Western Michigan University.

¹L. Buchmann *et al.*, Phys. Rev. Lett. **70**, 726 (1993).

²R. E. Azuma *et al.*, Phys. Rev. C **50**, 1194 (1994).

³Z. Zhao *et al.*, Phys. Rev. Lett. **70**, 2066 (1993).

⁴R. H. France III *et al.*, Nucl. Phys. **A621**, 165c (1997).

(sections h.19.-h.23.). The results from a first "shake-down" run are presented in the following section (a.2.).

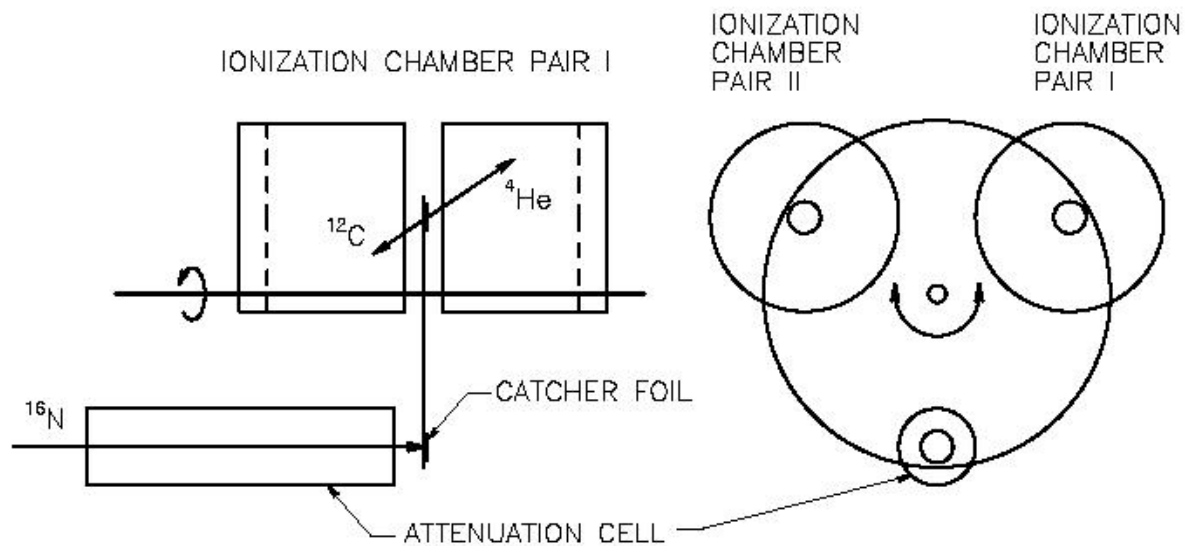


Fig. I-1. Schematic of the experimental setup used to study the beta-delayed alpha decay of ^{16}N .

a.2. Results from the First ^{16}N Decay Experiment (X. D. Tang, K. E. Rehm, I. Ahmad, J. P. Greene, A. Hecht, D. Henderson, R. V. F. Janssens, C. L. Jiang, E. F. Moore, M. Notani, R. C. Pardo, G. Savard, J. P. Schiffer, S. Sinha, M. Paul,* L. Jisonna,† R. E. Segel,‡ A. Champagne,§ and A. Wuosmaa§)

The entire setup for ^{16}N decay studies was tested in a first "shake-down run" at the end of 2004. The statistics that were achieved were determined by a variety of factors. With a beam current of 3×10^6 $^{16}\text{N}/\text{sec}$, from the $d(^{15}\text{N}, ^{16}\text{N})p$ reaction (see section h.20.), a stopping efficiency of the slowed down particles in the $10 \mu\text{g}/\text{cm}^2$ carbon foil of 5%, a counting-efficiency of 0.38 originating from the various delay times during irradiation, α -counting and rotation cycle, and an alpha/beta branching ratio of 1×10^{-5} , we obtain a $\alpha - ^{12}\text{C}$ coincidence rate of the whole array of about 30 counts/minute or $4.5 \times 10^4/\text{day}$. Allowing for the time needed for

$^{10}\text{B}(n,\alpha)^7\text{Li}$ calibration measurements, about 1.6×10^5 coincidences were accumulated in a four day run.

A two-dimensional $^{12}\text{C}-\alpha$ coincidence spectrum of one detector pair is shown in the left part of Fig. I-2. The right part of Fig. I-2 gives the corresponding background spectrum, obtained from a non-irradiated foil. Because of the asymmetry in the foil holder, which influences alpha particles emitted into detector 1 close to the foil, only events emitted at angles larger than $\sim 80^\circ$ with respect to the foil are accepted. The two main peaks correspond to the $^{12}\text{C}-\alpha$ coincidences emitted into the two different detectors, respectively. The background in between the

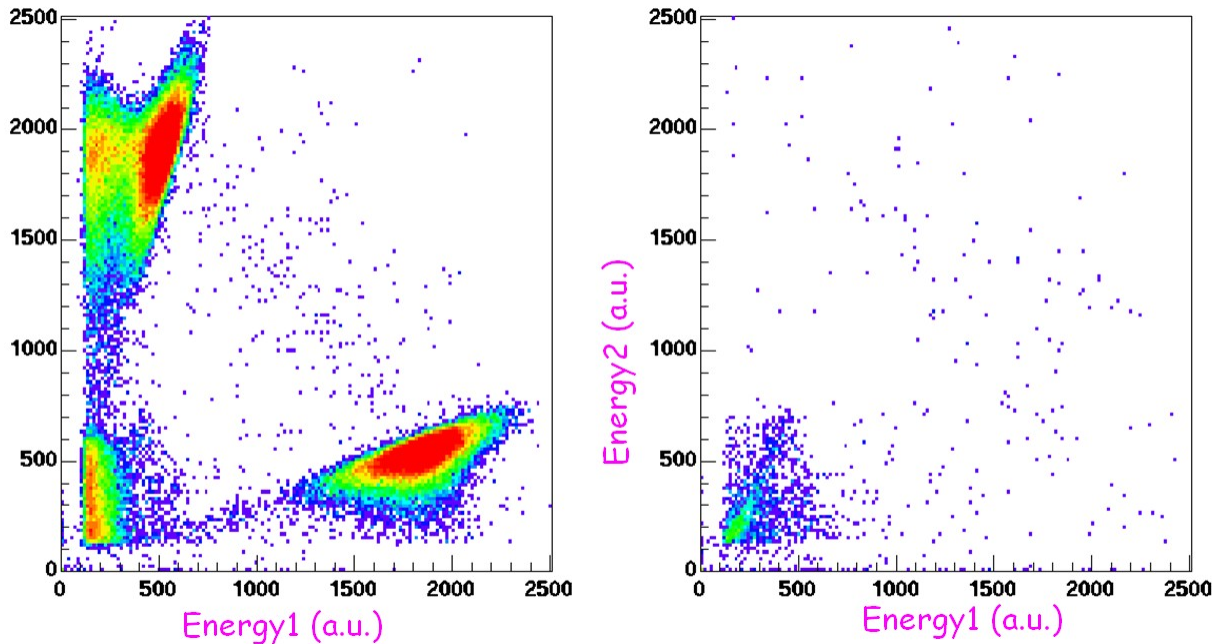


Fig. I-2. Left: ^{12}C - α coincidences measured in one detector pair using a 10 microg/cm^2 thick carbon foil which was bombarded by ^{16}N particles. Right: coincidence spectrum measured in the same detector pair with a non-irradiated carbon foil.

two peaks originates from gaseous ^{16}N diffusing into the detector volume and producing a signal in both detectors whose sum corresponds to the alpha decay energy of ^{16}N . The fact that due to momentum conservation the ^{16}N ^{12}C - α decay events have to show a energy ratio of 3:1 provides an additional restriction to the data.¹ Since pulse height defects in gas counters are smaller than for Si detectors, the pulse height ratio is, on average, about 3.4:1, quite close to the theoretical value of 3.

Selecting events with a pulse height ratio above 3 results in a ^{16}N alpha spectrum from all four detectors, which is shown in the upper part of Fig. I-3 by the open circles. Because of the low detection efficiency for betas, the spectra shown in Figs. I-2a and I-2b extend down to energies of 450 keV. This spectrum has not yet been unfolded for the experimental resolution. Comparisons with earlier results and R-matrix calculations are in progress.

*Hebrew University, Jerusalem, Israel, †Northwestern University, ‡University of North Carolina, §Western Michigan University.

¹R. E. Azuma *et al.*, Phys. Rev. C **50**, 1194 (1994).

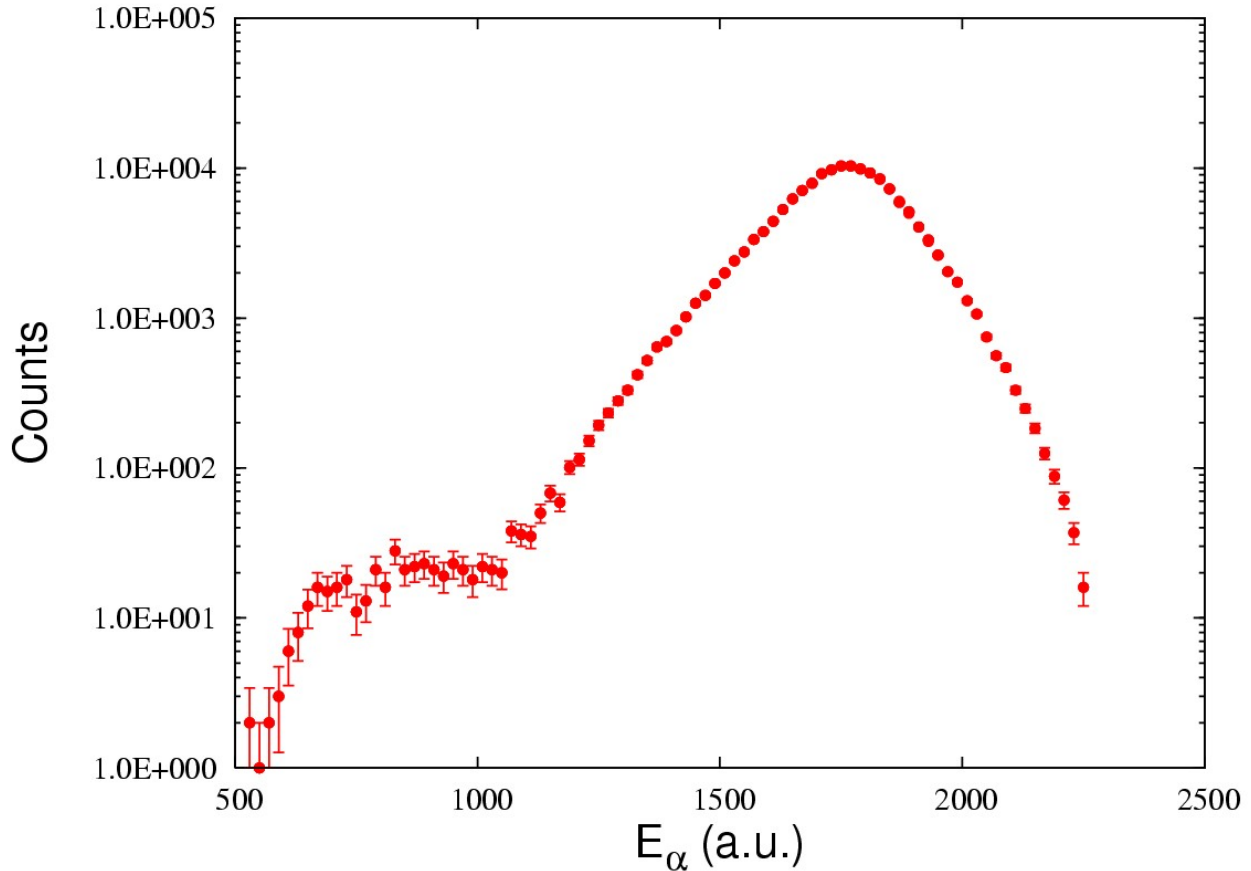


Fig. 1-3. Preliminary beta-delayed alpha spectrum from ^{16}N obtained in a first experiment. This spectrum, taken at a pressure of 150 Torr has not been unfolded for the detector response.

a.3. $^{18}\text{Ne}(\alpha, p)^{21}\text{Na}$, a Possible Breakout Reaction from the Hot CNO Cycle to the rp

Process (S. Sinha, J. P. Greene, D. Henderson, R. V. F. Janssens, C. L. Jiang, E. F. Moore, R. C. Pardo, K. E. Rehm, J. P. Schiffer, X. D. Tang, A. Chen,* R. E. Segel,† L. Jisonna,‡ R. H. Siemssen,‡ and A. H. Wuosmaa§)

At temperatures of 1-2 GK and densities of 10^3 - 10^6 g/cm³, which are typical X-ray bursts conditions, the main route connecting the CNO cycle and the rapid proton capture (rp) process passes through the $^{18}\text{Ne}(\alpha, p)^{21}\text{Na}$ reaction. Earlier direct measurements of this reaction covered an excitation energy range above ~ 10 MeV in the compound nucleus ^{22}Mg , which corresponds from the Gamow window to temperatures above 2 GK. For temperatures of 1-2 GK one has to study the yields at c.m. energies of 1.2-1.8 MeV where, so far, only theoretical cross section estimates exist. Direct measurements of the $^{18}\text{Ne}(\alpha, p)^{21}\text{Na}$ reaction with an active He target are extremely challenging, as shown by the fact that the two earlier measurements^{1,2} differ in their cross sections by up to an order of magnitude.

In an earlier ATLAS experiment we have repeated the cross section measurement of Ref. 2 populating a state in ^{22}Mg at $E_x = 2.51$ MeV with the time-inverse reaction $^{21}\text{Na}(p, \alpha)^{18}\text{Ne}$. The experiment was done with a ^{21}Na beam produced with the "in-flight" technique via the $p(^{21}\text{Ne}, ^{21}\text{Na})n$ reaction, using a ^{21}Ne beam on a cryogenic hydrogen-filled gas cell. Details of the experiment were given in last year's annual report.³ The cross section at this energy was found to be about a factor of 50 smaller than the one given in Ref. 2. The possible reasons for this disagreement are presently being discussed with the Edinburgh group.

In this reporting period we have extended the measurements to the astrophysically important region of $E_x(^{22}\text{Mg}) = 9.3$ -10 MeV. The experiment was again done

via the $^{21}\text{Na}(p,\alpha)^{18}\text{Ne}$ reaction with a ^{21}Na beam bombarding a 370 mg/cm^2 thick CH_2 target. The heavy ions (^{21}Na , ^{18}Ne) were identified in an annular ionization chamber covering the angles $1 - 4.5^\circ$, while the outgoing light particles (protons and alphas) were detected in coincidence, in an array of three annular double-sided Si strip detectors, covering the angular region of $5 - 20^\circ$ (alphas) and $40 - 60^\circ$ (protons). The whole setup was tested with the $^{21}\text{Ne}(p,\alpha)^{18}\text{F}$ reaction which has a similar kinematics. Figure I-4 shows the excitation function of the $^{21}\text{Na}(p,\alpha)^{18}\text{Ne}$ reaction, converted to the $^{18}\text{Ne}(\alpha,p)^{21}\text{Na}$ system and plotted as

function of the excitation energy in ^{22}Mg . Since the inverse $^{21}\text{Na}(p,\alpha)^{18}\text{Ne}$ reaction only connects the ground states of ^{21}Na and ^{18}Ne , the cross sections shown in Fig. I-4 represent a lower limit of the total $^{18}\text{Ne}(\alpha,p)$ yields. A preliminary analysis of the $^{21}\text{Na}(p,p')$ data, obtained in the same experiment, indicates, however, that in this excitation energy region the contributions from excited states in ^{21}Na are, at most, of the same order of magnitude as the ground state, resulting in no more than a factor of 2 increase for the total yields. Calculations of the astrophysical reaction rates are in progress.

*Queen's University, Kingston, Ontario, †Northwestern University, ‡University of Groningen, The Netherlands, §Western Michigan University.

¹W. Bradfield-Smith *et al.*, Phys. Rev. C **59**, 3402 (1999).

²D. Groombridge *et al.*, Phys. Rev. C **66**, 055802 (2002).

³S. Sinha *et al.*, ANL Physics Division Annual Report 04/22, Section a.3.

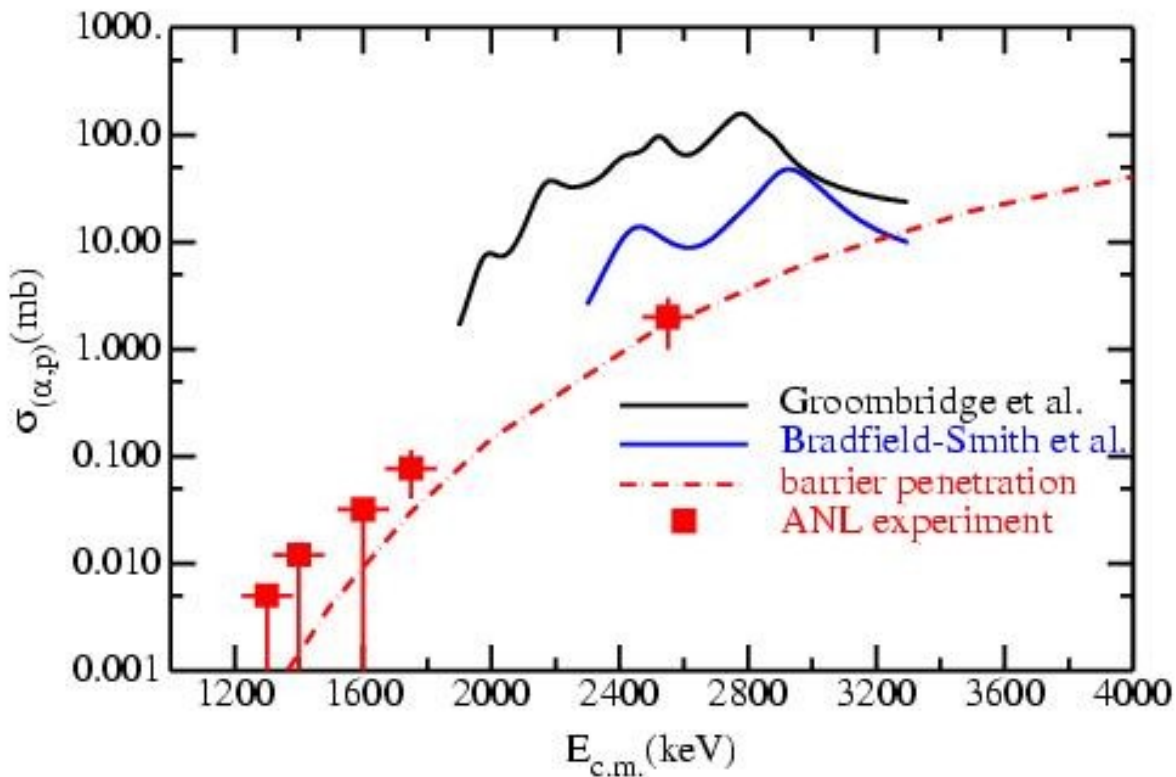


Fig. I-4. Excitation function of $^{18}\text{Ne}(\alpha,p)^{21}\text{Na}$ obtained from a study of the inverse $^{21}\text{Na}(p,\alpha)$ reaction. The solid lines represent the cross sections obtained in Refs. 1 and 2, respectively. The dot-dashed curve is the result of a barrier penetration calculation, normalized to the point at the highest energy.

a.4. Level Structure and Mass of ^{22}Mg (D. Seweryniak, M. P. Carpenter, R. V. F. Janssens, T. Lauritsen, C. J. Lister, S. Sinha, P. J. Woods,* T. Davinson,* D. G. Jenkins,† C. Ruiz,‡ J. Shergur,§ and A. Woehr¶)

The nucleus ^{22}Mg has provoked considerable interest in recent time, both in the astrophysical and weak-interaction communities. A precise and comprehensive knowledge of the states in the region of the proton threshold is essential for determining the $^{21}\text{Na}(p,\gamma)^{22}\text{Mg}$ reaction rate in Oxygen-Neon (ONe) Novae outbursts. This is particularly important since the 1275 keV γ ray associated with the beta decay to ^{22}Na was suggested as an astronomical observable in novae, and its signature has been sought by the COMPTEL satellite mission. The high isotopic abundance of ^{22}Ne in pre-solar grains is indicative of the earlier presence of ^{22}Na material that may have been associated with individual novae outbursts. As a $T_z = -1$ nucleus with a superallowed $0^+ \rightarrow 0^+$ beta decay, a precise

knowledge of the mass of ^{22}Mg is required to improve the precision of tests of the conserved vector current (CVC) hypothesis in the Standard Model.

The level structure of ^{22}Mg has been studied with high-sensitivity γ -ray spectroscopy techniques. A complete level scheme was derived incorporating all sub-threshold states, and all levels in the energy region relevant for novae burning. The excitation energy of the most important astrophysical resonance is measured with improved accuracy and found to differ from previous values. Combining the present result with a recent resonance energy measurement of this state leads to a derived ^{22}Mg mass excess of $-400.5(13)$ keV. The results were published as a Physical Review Letter.¹

*University of Edinburgh, United Kingdom, †University of York, Heslington, United Kingdom, ‡Simon Fraser University, Burnaby, British Columbia, §Argonne National Laboratory and University of Maryland, ¶University of Notre Dame.

¹D. Seweryniak, P. J. Woods *et al.*, Phys. Rev. Lett. **94**, 032501 (2005).

a.5. In-Beam Spectroscopy Above the Proton Threshold in ^{27}Si and the Production of ^{26}Al in Novae (D. Seweryniak, M. P. Carpenter, R. V. F. Janssens, C. J. Lister, S. Zhu, P. J. Woods,* and D. Jenkins†)

The ^{26}Al nucleus is a key astrophysical isotope since its radioactive decay has been observed in space by the detection of a characteristic γ -ray line at 1.809 keV, and its stable daughter ^{26}Mg has been identified in meteorites. An important issue affecting nova outburst production yields for ^{26}Al is the $^{26}\text{Al}^g(p,\gamma)^{27}\text{Si}$ reaction rate.¹ At nova temperatures $\sim 10^8$ K the reaction rate on a single resonance at ~ 188 keV increases the reaction rate by two orders of magnitude.² Consequently this resonance reaction can strongly deplete ^{26}Al in novae explosions.¹ The state was first identified by Vogelaar *et al.*² using the $^{26}\text{Al}(^3\text{He},d)^{27}\text{Si}$ reaction and assigned to be a high spin state since the ground state of ^{26}Al is 5^+ . However, ambiguities in the deuteron angular distributions meant that the proton angular momentum transfer and exact spin could not be determined.

In order to resolve this ambiguity, assign spins and parities to other states above the proton threshold, and search for new resonances in ^{27}Si , excited states in ^{27}Si were populated using the $^{12}\text{C}(^{16}\text{O},n)$ fusion-evaporation reaction. Prompt γ -ray transitions were detected using Gammasphere. The observed γ -ray spectrum was dominated by lines associated with ^{27}Al and ^{24}Mg . The spectrum of γ rays in coincidence with the 2164 keV transition connecting the well know $7/2^+$ state and the $5/2^+$ ground state in ^{27}Si is shown in Fig. I-5. Several transitions visible in Fig. I-5 deexcite known states above the proton threshold in ^{27}Si , including the transition originating from the important resonance at 188 keV. The detailed data analysis of the angular distribution of these transitions and the precise excitation energies of the resonances is in progress.

*University of Edinburgh, United Kingdom, †University of York, Heslington, United Kingdom.

¹R. B. Vogelaar *et al.*, Phys. Rev. C **53**, 1945 (1996).

²J. Jose *et al.*, Astrophys. J. **520**, 347 (1999).

³P. M. Endt, Nucl. Phys. **A521**, 1 (1990).

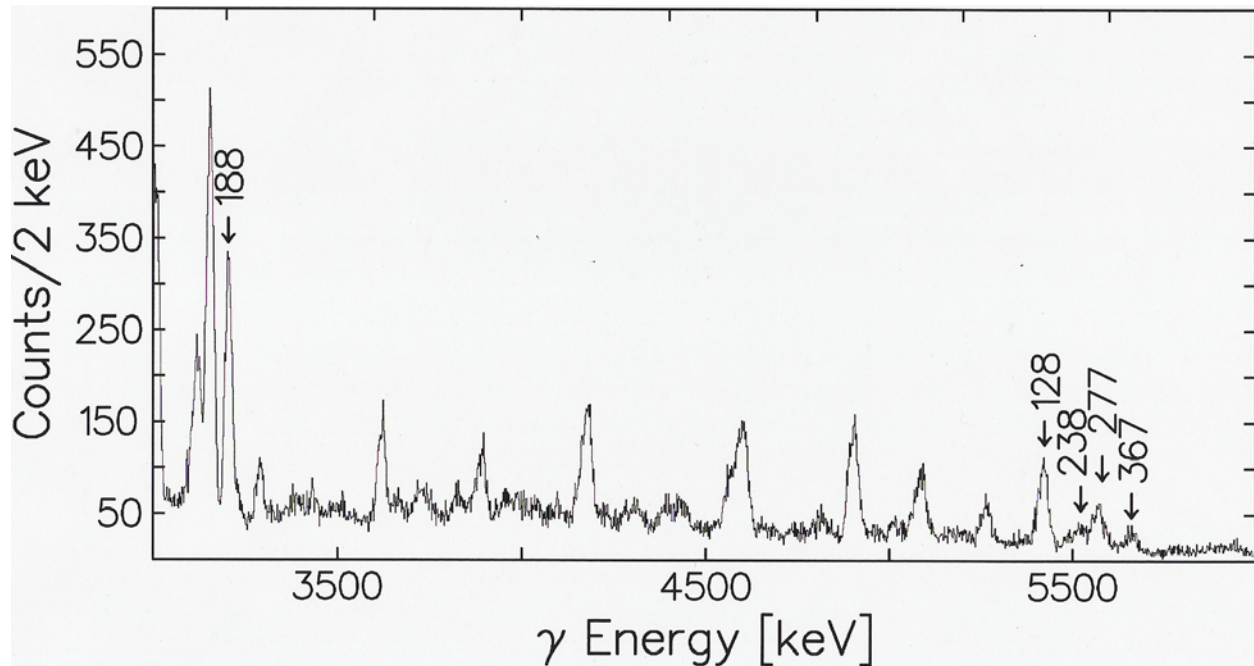


Fig. I-5. Gamma rays in coincidence with the 2164 keV $7/2^+ \rightarrow 5/2^+(gs)$ transition in ^{27}Si . Transitions deexciting states above the proton threshold are labeled with the resonance energies taken from Ref. 3.

a.6. Re-Evaluation of the $^{30}\text{P}(p,\gamma)^{31}\text{S}$ Astrophysical Reaction Rate in Novae (C. J. Lister, M. P. Carpenter, N. J. Hammond, R. V. F. Janssens, T. L. Khoo, T. Lauritsen, D. Seweryniak, E. Rehm, D. G. Jenkins,* A. Medowcroft,* P. Chowdhury,† T. Davinson,‡ P. Woods,‡ A. Jokinen,§ H. Penttila,§ G. Martinez-Pinedo,¶ and J. Jose¶)

The $^{30}\text{P}(p,\gamma)^{31}\text{S}$ reaction rate is believed to be the key determining factor in establishing the end point of the rp-process in Novae. The actual reaction rate is, to date, unmeasured and has been estimated using Hauser-Feshbach methods. We have populated states in the Gamow window of ^{31}S and will use this information to evaluate the true reaction rate.

^{31}S was produced in the $^{12}\text{C}(^{20}\text{Ne},n)^{31}\text{S}$ reaction at 32 MeV. The entry region was preferentially selected by exploiting the properties of the 2-body kinematics and selecting ^{31}S residues of the appropriate velocity at zero-degrees in the FMA. The properties of γ -ray emitting states were deduced by detecting photons in Gammasphere, in coincidence with identified ^{31}S ions at the focal plane.

Online analysis showed this method to be successful, and new states in the appropriate energy range were observed. Some lifetimes (and hence gamma-widths) could be inferred from differential Doppler shift analysis. Angular correlations and branching ratios usually allow determination of the angular momentum of the states. These data have been used to calculate the reaction rate, as a function of temperature. These analyses are in progress and a first draft of a paper is being prepared. It is clear that there are substantial Mirror Energy Differences (MED).

The spectroscopy of the $A = 31$ mirror pair of nuclei, ^{31}S and ^{31}P has been investigated and has led to a separate publication (see section d.2.1.).

*University of York, United Kingdom, †University of Massachusetts-Lowell, ‡University of Edinburgh, United Kingdom, §University of Jyväskylä, Finland, ¶IEEC, Barcelona, Spain.

a.7. Measurement of ^{44}Ti Half-Life (I. Ahmad, J. P. Greene, E. F. Moore, W. Kutschera,* and M. Paul†)

The half-life measurement of ^{44}Ti , which was started in March 1992, has been continued at Argonne and Jerusalem with the aim of reducing statistical and systematic uncertainties. The half-life determined from 5 years decay was published¹ in 1998. The half-life is being determined by measuring spectra of

a mixed source of ^{44}Ti and ^{60}Co with a 25% Ge detector at regular intervals. We have data for 12 years decay and have stopped counting. The data have been analyzed and a paper is under preparation for publication in Phys. Rev. C.

*University of Vienna, Austria, †Hebrew University, Jerusalem, Israel.

¹I. Ahmad *et al.*, Phys. Rev. Lett. **80**, 2550 (1998).

a.8. The $^{40}\text{Ca}(\alpha,\gamma)^{44}\text{Ti}$ Reaction at Astrophysical Energies (I. Ahmad, J. P. Greene, D. Henderson, R. V. F. Janssens, C. L. Jiang, R. C. Pardo, T. Pennington, K. E. Rehm, G. Savard, R. Scott, R. Vondrasek, H. Nassar,* M. Paul,* S. Ghelberg,* N. Trubnikov,* M. Hass,† and B. S. Nara Singh‡)

The radioactive ^{44}Ti nuclide has long been considered an important signature of the conjectured α -rich freezeout regime during the expansion phase of a core-collapse supernova. ^{44}Ti radioactive decay has since been observed¹ from the Cassiopaea A supernova remnant by γ -ray astronomy. Together with the determination of its half-life ($59.2 \pm 0.6 \text{ yr}$)² and the knowledge of the date and distance of the supernova, this observation makes ^{44}Ti one of the very few cases where the absolute total yield of a specific nuclide in a stellar nucleosynthesis event can be quantitatively measured. The relation of this quantity with astrophysical models requires knowledge of nuclear cross sections in the relevant path. We have studied the major reaction for production of ^{44}Ti , namely $^{40}\text{Ca}(\alpha,\gamma)^{44}\text{Ti}$, in the range of energies corresponding to stellar temperatures $T_9 = 0.8 - 3.0$ (where T_9 denotes the temperature in units of 10^9 K), relevant to supernova nucleosynthesis. Preliminary results of our experiment are presented here, showing a significantly stronger yield than observed in previous measurements³ which spanned the range $T_9 = 1.5 - 3.0$.

The experimental method consisted of the bombardment of a He (99.999%) gas target by a ^{40}Ca

beam from the Pelletron Tandem accelerator at the Weizmann Institute and implantation of recoil products in a forward-positioned Cu catcher. ^{44}Ti atoms are chemically extracted together with a ^{nat}Ti carrier by etching the catcher and separated by ion-exchange methods. The $^{44}\text{Ti}/\text{Ti}$ ratio (r_{Ti}) of the order of 10^{-12} is then measured by accelerator mass spectrometry and the yield of ^{44}Ti nuclei produced in the activation is obtained from the relation $Y_{44} = r_{\text{Ti}}n_{\text{Ti}}$ where n_{Ti} denotes the number of atoms of ^{nat}Ti carrier used. The thickness of the ^4He gas target was selected to integrate the reaction yield from $E_{\text{cm}} = 4.2 \text{ MeV}$ down to $E_{\text{cm}} = 1.7 \text{ MeV}$, representing the relevant energy range. The derived ^{44}Ti yield (5.1×10^7 atoms) corresponds to an overall resonance strength of 40 to 60 eV (depending on the energies of contributing resonances), much stronger than that measured by prompt- γ measurements ($\Sigma\omega\gamma = 10 \text{ eV}$). Figure I-6a compares the average cross section measured in this work with recent Hauser-Feshbach calculations. The stronger astrophysical rate (Fig. I-6b) for ^{44}Ti production relative to that currently assumed in stellar calculations, has important consequences regarding the comparison with ^{44}Ti activity of supernova remnants measured by γ -ray astronomy.⁴

†Hebrew University, Jerusalem, Israel, ‡Weizmann Institute, Rehovot, Israel.

¹R. Diehl *et al.*, Astron. Astrophys. **298**, 445 (1995).

²I. Ahmad *et al.*, Phys. Rev. Lett. **80**, 2550 (1998); and to be published.

³E. L. Cooperman, M. H. Shapiro, and H. Winkler, Nucl. Phys. **A284**, 163 (1977).

⁴R. Diehl, N. Prantzos, and P. von Ballmoos, Nucl. Phys. A, in press.

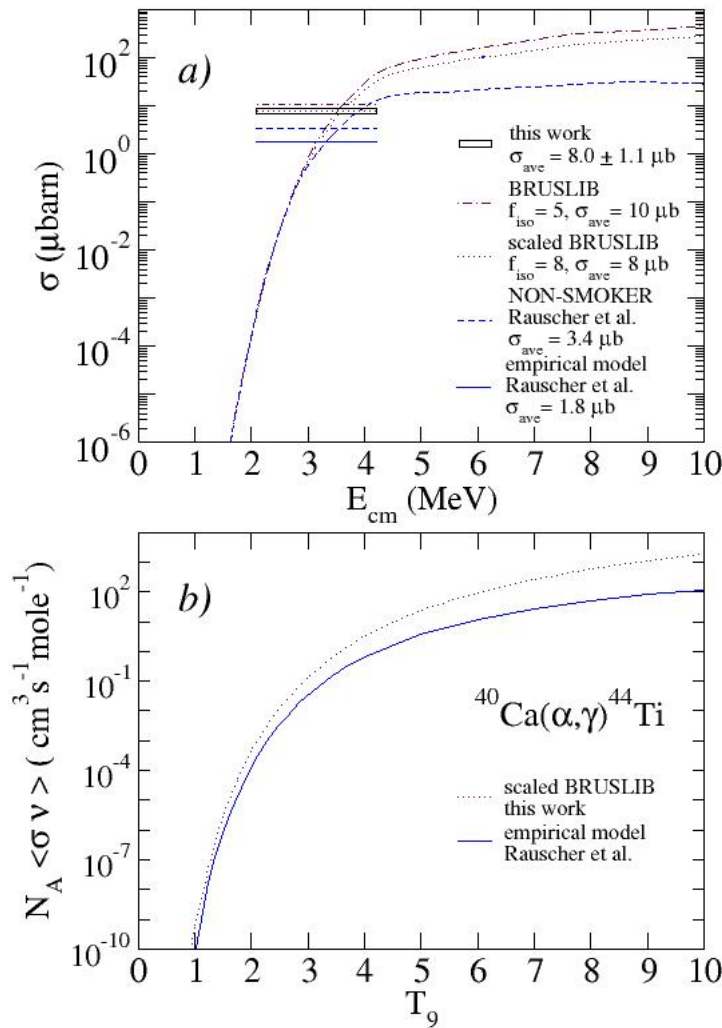


Fig. I-6. a) Comparison of the present experimental average cross section in the range $E_{\text{cm}} = 1.8 - 5$ MeV with recent theoretical estimates and Hauser-Feshbach calculations; b) Astrophysical rate derived from a), showing a strong enhancement of ^{44}Ti production, compared to previous estimates.

a.9. New Half-Life Measurement of ^{182}Hf : An Improved Chronometer for the Early Solar System (I. Ahmad, C. Vockenhuber,* F. Oberli,† M. Bichler,‡ G. Quité,† M. Meier,† A. N. Halliday,† D.-C. Lee,§ W. Kutschera,* P. Steier,* R. J. Gehrke,¶ and R. G. Helmer¶)

The decay of ^{182}Hf , now extinct, into stable ^{182}W has developed into an important chronometer for studying early solar system processes, such as the accretion and differentiation of planetesimals and the formation of Earth and Moon. The only ^{182}Hf half-life measurements were performed 40 years ago and resulted in a rather imprecise value of $(9 \pm 2) \times 10^6$ yr.¹ Because of the importance of the ^{182}Hf - ^{182}W system as a geo-chronometer, we have

remeasured the half-life of ^{182}Hf with the goal of obtaining a more precise value.

Some 35 years ago, a larger quantity of ^{182}Hf was produced by Helmer *et al.*² at Idaho Falls to investigate ^{182}Ta levels populated in decay. We obtained this material and measured the absolute intensities of ^{182}Hf γ rays at Argonne³ and the half-life at Vienna/Zurich. The decay rate of a known mass of the Hf sample was

measured by counting the 270.0-keV γ ray with a Ge detector. The number of ^{182}Hf atoms in the sample was determined by two different methods. In one case, neutron activation technique was applied and in the second case isotopic dilution method was used. The isotopic compositions of the Hf samples were measured at the Department of Earth Sciences, ETH-Zentrum, Zurich/Switzerland using Nu 1700, a new high-resolution multiple-collector inductively

coupled mass spectrometer (MC-ICPMS). The neutron activation-plus-activity measurement method gave a half-life value of 9.034 ± 0.251 yr and the isotope dilution-plus-activity measurement gave a value of 8.896 ± 0.089 yr. The weighted mean of the two values gave a half-life of 8.904 ± 0.088 yr, a twenty times more precise half-life as compared with the original value.¹ The results of this study were published.⁴

*University of Vienna, Austria, †ETH, Zurich, Switzerland, ‡Atominstytut der Osterreichischen Universitaten, Vienna, Austria, §Academia Sinica, Taiwan, Republic of China, ¶Idaho National Engineering & Environmental Laboratory.

¹J. Wing, B. A. Swartz, and J. R. Huizenga, Phys. Rev. **123**, 1354 (1961).

²R. G. Helmer, R. C. Greenwood, and C. W. Reich, Nucl. Phys. **A168**, 449 (1971).

³I. Ahmad *et al.*, Phys. Rev. C **70**, 047301 (2004).

⁴C. Vockenhuber *et al.*, Phys. Rev. Lett. **93**, 172501 (2004).

B. PHYSICS OF TRAPPED IONS

The study of nuclei stored in traps grows in importance for our group. Our theoretical investigation of the dynamics of trapped ions continue. The Canadian Penning Trap (CPT) has now become a rich source of new measurements, both for astrophysics and for weak interaction physics. The Advanced Penning Trap (APT) is under construction, with a goal to studying weak interactions in calendar year 2005. The laser atom trap (ATTA) is online and made its first measurements on radioactive ${}^6\text{He}$ and investigation of a possible measurement of ${}^8\text{He}$ is underway.

b.1. Ordering and Temperature in Ions Trapped in Radiofrequency Fields (J. P. Schiffer)

Some time ago simulations were carried out to better understand the behavior of plasmas confined in radiofrequency traps.¹ In that study it was found that if a plasma was cooled to an ordered state, the kinetic energy in the rf motion, which can be 5-6 orders of magnitude more than the energy corresponding to the temperature, converted into random thermal energy only very slowly – in less than $\sim 10^{12}$ rf periods for a sufficiently cold system.

However, when the ion cloud in the simulation was warmer, this conversion (the coupling of the periodic motion from the confining field into random motion) occurred faster, and this "rf heating" increased quadratically with temperature. The reason for such a T^2 dependence is not understood.

Radiofrequency traps can work with a variety of rf wave forms. In the work of Ref. 1 it was assumed to be sinusoidal. In order to explore whether the

behavior was similar for other wave forms a simulation is carried out where the rf containing field is a square wave rather $\sin(\omega t)$. A cold ordered state was achieved in this system and, as was reported last year, the self-heating (the above coupling of the periodic motion into thermal energy) appears to be much smaller.

The phenomenon has been explored more carefully in the past year. The simulations are extremely time consuming. The very surprising result is that the systems considered (square-wave rf confinement, or "pulsed" rf fields that are applied periodically in opposite directions) the isolated confined systems instead of "self heating" actually seem to be getting slowly "colder" in time as is shown in Fig. I-7. Since the forced oscillations imposed by the confining field provide a large reservoir of energy, no conservation laws or thermodynamic principles are obviously violated. Yet the phenomenon is completely unexpected and counter-intuitive. It is being explored more thoroughly.

¹J. P. Schiffer *et al.*, Proc. Natl. Acad. Sci. **10**, 1073 (2000).

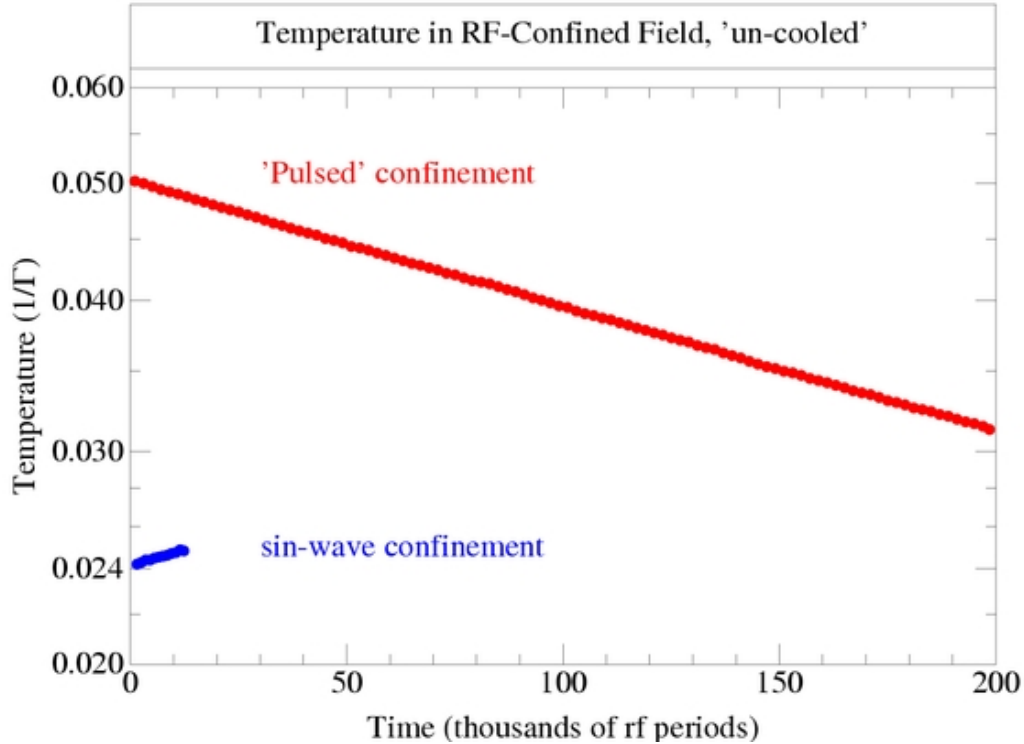


Fig. I-7. The "temperature" (derived from the velocities that are not periodic in the imposed rf confining field) is plotted from the simulation of a confined system of 1000 particles. The simulated confinement is that characteristic of rf quadrupole traps. Temperature is in units of $1/\Gamma$, where $\Gamma = (q^2/a)/kT$, the plasma coupling parameter. The normal transition temperature to an ordered system is $1/\Gamma \approx 0.006$. The blue points represent the behavior of 1000 ions that are confined in a sinusoidally periodic field and allowed to interact with each other through their Coulomb interactions. They show the usual "rf heating" effect. The red points are from a long simulation where the confining field is "pulsed": periodic short pulses of electric field alternating in sign. This system appears to have a gradually lower "temperature".

b.2. Q Value of the Superallowed β -Decay of ^{22}Mg and the Calibration of the $^{21}\text{Na}(p,\gamma)$ Reaction (G. Savard,* J. A. Clark,† A. A. Hecht,‡ A. F. Levand, B. F. Lundgren, N. D. Scielzo, I. Tanihata, W. Trimble, J. C. Wang,† Z. Zhou, F. Buchinger,§ J. E. Crawford,§ S. Gulick,§ J. C. Hardy,¶ V. E. Iacob,¶ J. K. P. Lee,§ K. S. Sharma,|| I. S. Towner,** and Y. Wang||)

Superallowed $0^+ \rightarrow 0^+$ decays play a key role in a number of tests of the electroweak theory. The Ft value for such decays, obtained from measurements of the lifetime, Q value and branching ratio, can be corrected for small radiative and isospin mixing effects to yield a corrected Ft value, which has the simple form

$$Ft \equiv ft(1 + \delta_R')(1 + \delta_{NS} - \delta_C) = \frac{K}{2G_V^2(1 + \Delta_R^V)},$$

with f being the statistical rate function, t the partial half-life, G_V the weak vector coupling constant, and K is a numerical constant. The small correction

terms include δ_C , the isospin symmetry-breaking correction, δ_R' and δ_{NS} , the transition-dependent parts of the radiative correction, and Δ_R^V the transition-independent part. Only δ_C and δ_{NS} depend on nuclear structure.

The Conserved Vector Current (CVC) hypothesis states that the vector current interaction is not modified by the presence of the strongly interacting nuclear system so that exactly the same value of G_V should be obtained from each superallowed decay. The existing set of nine precisely determined transitions confirms this CVC expectation at the 3×10^{-4} level. The resultant average

value of G_V , together with the Fermi coupling constant from the pure-leptonic decay of the muon, yields the most precise available value for V_{ud} , the up-down quark mixing element of the Cabibbo-Kobayashi-Maskawa (CKM) matrix. This matrix is a rotation matrix connecting the weak and mass eigenstates of the quarks and, as such, must be unitary within the standard model. Currently, the most demanding test of CKM unitarity comes from the top-row sum,

$$V_{ud}^2 + V_{us}^2 + V_{ub}^2 = 0.9968 \pm 0.0014,$$

which actually violates unitarity at the 2.3 sigma level. The main contributors to that unitarity test are V_{ud} and V_{us} , which contribute almost equally to the total uncertainty. This discrepancy has attracted considerable attention and both V_{ud} and V_{us} are now under much scrutiny. Recent work indicates that the value of V_{us} might have to be shifted to one yielding a better agreement with unitarity; if this is confirmed it would only further fuel the need for a more precise V_{ud} value.

We report here a Q -value measurement for the ^{22}Mg decay, which complements recent lifetime and branching-ratio measurements¹ to yield a precise Ft value for its superallowed transition. This is the first new superallowed case in a region of well-understood nuclear structure and consequently is the first significant step in testing the validity of the calculated structure-dependent corrections.

The mass measurements were performed at the Canadian Penning Trap (CPT) mass spectrometer located "online" at the ATLAS accelerator. The ^{22}Mg and ^{22}Na activities were created by a 3.5 MeV/u beam of ^{20}Ne passing through a 7 cm long cryogenic target of ^3He gas held at a pressure of 700 mbar and liquid nitrogen temperature. The gas target has 1.3 mg/cm² thick titanium entrance and exit windows. Reaction products recoiling out of the target are carried forward by the kinematics of the reaction. They then proceed through a focusing magnetic quadrupole triplet, a velocity filter to separate the primary beam from the reaction products, and an Enge magnetic spectrograph to make the final selection and focus them on the entrance of a gas catcher system. At that point, the species of interest forms a multi-MeV continuous beam of poor ion-optical quality quite unsuitable for efficient injection into a precision ion trap, which requires a high quality eV-energy pulsed beam. We

achieve the required transformation of beam properties with a gas catcher and injection system.

At the entrance of the gas catcher system, the reaction products lose most of their energy through a thin aluminum foil that can be rotated to adjust the effective thickness and hence the energy lost by the ions. The tunable aluminum degrader is followed by a high-purity 25 cm long helium gas cell. The radioactive ions enter this gas cell through a 1.9 mg/cm² Havar window, losing their remaining energy and then coming to rest in the helium gas, which is pure to the ppb level and is held at roughly 150 mbar pressure. At the final stage of their slowing-down process, the ions, which have been highly charged up to this point, recapture electrons but are unlikely to recapture the final electron since helium has a higher ionization potential than any other species and hence will not give up its electrons to slow ions. The radioactive species are therefore stopped as ions in the high-purity gas and can be manipulated by static and RF electric fields. With the assistance of these electric fields, the ions are extracted from the gas cell in roughly 10 ms as a thermal beam. The ions are then separated from the helium gas extracted with them by being channeled through RF ion guides leading to a linear RF trap, where they are accumulated. The ions in the linear trap are accumulated for 300 ms and transferred in a bunch to a gas-filled Penning trap where mass-selective cooling is applied. The ions are mass selected there with a resolution of 1000 before being transported to the CPT spectrometer itself.

Also present after the gas cell are ions of helium and impurities ionized in the deceleration of the radioactive ions in the helium gas. The helium ions are easily eliminated by the RF ion guide system, but it was found that by focusing on $A = 22$ this experiment incurred a particular difficulty since neon is a common impurity in even the highest purity helium gas. We found that we could not discriminate against the ^{22}Ne isotope, so this isotope saturated the system. The difficulty was overcome by the addition of a cold trap, temperature-regulated at 20 - 30 K, in the helium purification system to remove the neon from the helium gas being fed into the gas cell. With this modification, the mass-22 radioactive ions were collected free of other contamination. The purified radioactive ions with $A = 22$ were transported in bunched mode to the CPT, where the ions were captured in a second linear RF trap and further cooled by buffer-gas collisions before being transferred via a differential pumping section to the precision Penning trap, where the mass measurements take place.

The precision Penning trap is a hyperbolic trap with gold-plated OFHC copper electrodes located in a 6T self-shielded superconducting magnet with high field stability. The trap is in 10^{-10} mbar vacuum section and all material used inside the magnet is non-magnetic, including the vacuum chamber, which is made of molybdenum. This not only avoids perturbations in the homogeneity of the magnetic field but also removes a common source of magnetic-field fluctuations connected to the temperature-dependent magnetic properties of the "non-magnetic" stainless-steel vacuum chamber typically used. In the Penning trap, a mass measurement is performed as a frequency scan. The ions are first loaded into the trap. Remaining contaminant ions (in this case, either mostly ^{22}Na when ^{22}Mg is being measured or the reverse) are removed from the trap by a strong mass-selective RF excitation. The ions of interest are then excited to a finite magnetron orbit by a fixed-frequency dipole RF excitation and are subjected to a quadrupolar RF field, which couples the magnetron and reduced cyclotron motion when the frequency applied corresponds to the true cyclotron frequency. The ions are subsequently ejected and allowed to drift towards a microchannel-plate detector, where a time-of-flight spectrum is recorded. The process is repeated with the injection of another bunch of ions into the trap, repetition of the ion cleaning and preparation, and quadrupolar excitation at the next frequency. This process is continued over the full cyclotron excitation-frequency interval to create a scan, and scans are repeated and summed until sufficient statistics are achieved. At the true cyclotron frequency, the ions will have their magnetron motion converted to reduced cyclotron motion and hence will have higher energy, leading to a reduced time-of-flight to the detector. For these measurements, the excitation time was 0.8 seconds, which yields a mass resolution of $\sim 2.5 \times 10^{-7}$.

Our experiment interleaved measurements of the mass of $^{22}\text{Na}^+$ and $^{22}\text{Mg}^+$ with calibrations of the magnetic field based on molecular ions of $\text{H}_2^{18}\text{OH}^+$ and $\text{H}_2^{16}\text{OH}^+$ and ions of $^{22}\text{Ne}^+$, $^{21}\text{Ne}^+$ and $^{20}\text{Ne}^+$. (Measurements with neon isotopes required our bypassing the 20 K cold trap in the gas purification system.) The results from these calibration

measurements, which were continued over a full week to confirm the stability of the magnetic field, are shown in Fig. I-8. The important features in this figure are the precision, high reproducibility and high stability of the measured masses, which show negligible drift within statistical accuracy over the measurement period. (No correction for field drift is applied in this figure.) The magnetic-field variation was measured to be -1.1 part in 10^{10} per hour. This shift is small at the level of accuracy required since calibration and measurements on radioactive species were interleaved in our case, but all measurements were still corrected for it.

The most insidious source of systematic errors for high-precision measurements on short-lived isotopes in a Penning trap is the possibility that the ions do not probe the same magnetic-field region. No cooling is applied in the measurement trap because of the short time available, and the spatial extent probed by the ions in the trap is determined by the ion preparation and the conditions of injection. The main factor is the timing of the capture pulse applied to let the ions into the measurement trap, which is set by the time-of-flight between the second linear trap, where the cooling is applied, and the measurement trap. For an electrostatic transfer system this time scales as the squared-root of the mass of the transferred ion, but fixed delays in the application of pulses can create small deviations from this simple scaling relation. The capture timing of all measured masses in this experiment was measured precisely and adjusted for the maximum time-of-flight signal of each species. The effectiveness of this procedure is demonstrated in Fig. I-8, which shows that the masses of ^{20}Ne , ^{21}Ne , ^{22}Ne and H_2^{16}OH , all known to better than 2 parts per billion, agree within the accuracy of the measurement, which is typically 1 part in 10^8 . Although the data show that the use of any of these well known isotopes is equivalent within the statistical accuracy, we have opted to be more conservative and have determined all new masses with respect to a well-known mass with the same A value -- ^{22}Ne for the radioactive ions at A = 22 and ^{21}Ne for the H_2^{18}OH molecule -- to eliminate any unforeseen mass-dependent effect. We use the 1 part per 10^8 accuracy demonstrated in the calibration (on mass ratios involving different mass number) as a conservative value for our systematic error for the new mass values obtained below on ratios of same mass number isotopes.

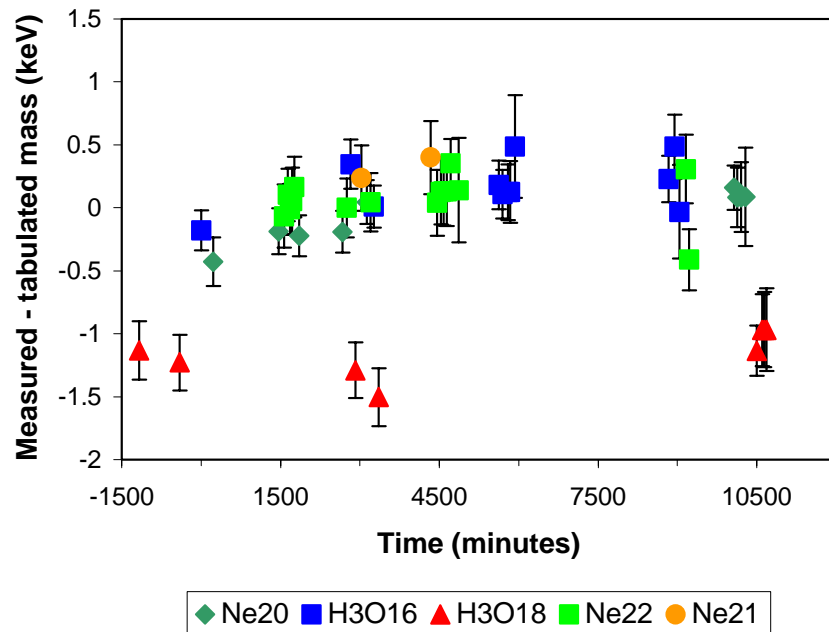


Fig. I-8. Measured mass values (plotted as deviation from the tabulated mass values) for the various isotopes versus time during the run.

Measurements on the stable isotopes and molecules were performed with an average of 1.5 ions detected per cycle; the measurements on ^{22}Mg and ^{22}Na had an average of 0.35 and 0.7 ions per cycle, respectively. Shifts in cyclotron frequency due to ion-ion interactions at these low ion numbers were measured to be 2 ppb per detected ion at the CPT. Corrections to account for the lower ion number obtained with the radioactive species compared with that for the stable calibration isotopes are very small but still adjustments of $0.05 \text{ keV}/c^2$ and $0.04 \text{ keV}/c^2$ were applied to ^{22}Mg and ^{22}Na respectively. Since all measurements on the stable isotopes are made with similar small ion numbers, no adjustments were required among them.

The mass of one of the calibrant molecular ions, $\text{H}_2^{18}\text{OH}^+$, is not known to very high accuracy; the uncertainty in its mass is dominated by the $0.6 \text{ keV}/c^2$ uncertainty in the mass of ^{18}O . We obtained a mass ratio for $\text{H}_2^{18}\text{OH}^+$ versus $^{21}\text{Ne}^+$ of 1.0013712843(65). The ^{18}O mass determined from this value is found to differ by $-1.5 \text{ keV}/c^2$ from the tabulated value and yields, after a minute -0.02 keV correction for molecular binding and electronic ionization energy differences, an improved mass defect for ^{18}O of $-783.06(23) \text{ keV}$, with the quoted error containing the statistical and systematic uncertainties added in

quadrature. This measurement of ^{18}O , via the molecule H_2^{18}OH at mass-21, is consistent with the precisely known calibrations at mass-19, 20, 21 and 22. The previous measurements that have large influence on the tabulated mass² of ^{18}O are inconsistent and are all less precise than the present measurement. Our measurement is compatible with the $^{18}\text{O}(^3\text{He,p})^{20}\text{F}$ reaction result but disagrees with the mass derived from beta endpoint results.

For the $A = 22$ radioactive species, the calibration used was $^{22}\text{Ne}^+$ and the mass ratios observed were 1.000372238(31) and 1.000138820(11) for $^{22}\text{Mg}^+$ versus $^{22}\text{Ne}^+$ and $^{22}\text{Na}^+$ versus $^{22}\text{Ne}^+$ respectively. The final mass defects for the two isotopes of interest, after a -0.01 keV correction for ionization energy differences, are then found to be $\Delta M(^{22}\text{Mg}) = -399.73(67) \text{ keV}$ and $\Delta M(^{22}\text{Na}) = -5181.12(29) \text{ keV}$. They differ by -2.7 keV and $+1.3 \text{ keV}$ respectively from the latest tabulated values, in both cases well outside the tabulated error bars. In the first case, our result for the mass of ^{22}Mg agrees with, but is much more precise than, the value extracted by a recent reevaluation of an older measurement,¹ $-402(3) \text{ keV}$, but is significantly higher than a recent measurement³ of the $^{21}\text{Na}(p,\gamma)^{22}\text{Mg}$ reaction, from which a mass defect of $-403.2(13) \text{ keV}$ was inferred; the latter is, of course, also sensitive to the mass of ^{21}Na and the excitation energy of the state populated in that reaction, both of which now

need to be remeasured. In the case of ^{22}Na , the four previous measurements used to determine the tabulated mass date from 1972 or earlier and the three that disagree with our result were all derived from beta-decay end-point energies.

Our new mass results yield a Q_{EC} value of 4124.39(73) keV for the superallowed decay of ^{22}Mg to the analog 0^+ state at 657.00(14)-keV excitation

energy in ^{22}Na . This corresponds to an f value of 418.33(44). Taking this result, together with the branching ratio, 0.5315(12), and lifetime, 3.8755(12)s, and with the appropriate correction terms, we obtain a corrected Ft value of $Ft = 3081(8)$ s, with the uncertainty now almost entirely due to the uncertainty of the branching ratio measurement. This value agrees with the 3072.2(8) s average Ft value for the nine well-known cases studied so far.

*Argonne National Laboratory and University of Chicago, †Argonne National Laboratory and University of Manitoba, Winnipeg, Manitoba, ‡Argonne National Laboratory and University of Maryland, §McGill University, Montreal, Quebec, ¶Texas A&M University, ||University of Manitoba, Winnipeg, Manitoba, **Queen's University, Kingston, Ontario.

¹J. C. Hardy *et al.*, Phys. Rev. Lett. **91**, 082501 (2003).

²G. Audi *et al.*, Nucl. Phys. **A729**, 337 (2003).

³S. Bishop *et al.*, Phys. Rev. Lett. **90**, 162501 (2003).

b.3. Q Value of the Superallowed Decay of ^{46}V and the Unitarity of the CKM Matrix

(G. Savard, J. A. Clark, A. A. Hecht, A. Levand, N. D. Scielzo, H. Sharma, K. S. Sharma, I. Tanihata, A. C. C. Villari, Y. Wang, F. Buchinger,* J. E. Crawford,* S. Gulick,* J. K. P. Lee,* and J.C. Hardy†)

Superallowed $0^+ \rightarrow 0^+$ decays play a key role in a number of tests of the electroweak theory (see report on the ^{22}Mg Q -value measurement, section b.2.). In particular, they are used to obtain the most precise value of V_{ud} and test the CKM matrix unitarity. The data on the superallowed Fermi decays used to obtain the most precise value of V_{ud} come from over 100 different experiments. They contribute less than 20% of the total uncertainty on V_{ud} , the remainder coming from the small theoretical corrections that must be applied to the data. In particular, the corrections for nuclear structure effects, though not the largest contributors, have a significant impact on the uncertainty. One test of the latter corrections is to examine how precisely they convert the scatter in experimental f_t values to the CVC-predicted constancy of the Ft values. Improved precision for individual transitions sharpen that test. Of the nine most precisely known cases, ^{46}V has the largest uncertainty associated with the Q value. We report here a Q -value measurement for the ^{46}V decay, which yields a more precise Ft value for this superallowed transition. This new Q value disagrees with a previous measurement and uncovers a total of seven inconsistent Q -value measurements from the same reference that should be removed from the previously accepted data set. This leads to a significant change in the average of all Ft values and produces a change

in V_{ud} . It also impacts the derived limits on new physics.

The mass measurements were performed at the Canadian Penning Trap (CPT) mass spectrometer located "online" at the ATLAS accelerator. The ^{46}V and ^{46}Ti isotopes were created by a 3.3 MeV/u beam of ^{36}Ar impinging on a 0.8 mg/cm² rotating target of natural carbon. Reaction products recoiling out of the target are separated from the primary beam and transported to a gas catcher system via a focusing magnetic quadrupole triplet, a velocity filter and an Enge magnetic spectrograph. The gas catcher system thermalizes these fast recoil ions in high-purity helium gas and extracts them as a low-energy doubly charged ion beam, suitable for injection into ion traps. The extracted ions are accumulated for 300 ms in a linear RF trap and transferred in a bunch to a gas-filled Penning trap where mass-selective cooling is applied. The ions are mass selected there with a resolving power of 1000 before being transported to the CPT spectrometer itself. The transport is performed in pulsed mode which allows further selection of the $A/q = 23$ ions by time of flight. At the end of the time-of-flight system, the purified ions with $A = 46$ and $q = +2$ are captured in a second linear RF trap and further cooled by buffer-gas collisions before being transferred via a differential pumping section to the precision Penning trap where the mass measurements take place. The mass measurement takes place in a fashion similar to that described for the recent ^{22}Mg measurement

(see section b.2.) except that the doubly charged ions allow us to reach higher resolution for a given

interaction time. Typical frequency scans obtained for the isotopes $^{46}\text{V}^{2+}$ and $^{46}\text{Ti}^{2+}$ are shown in Fig. I-9.

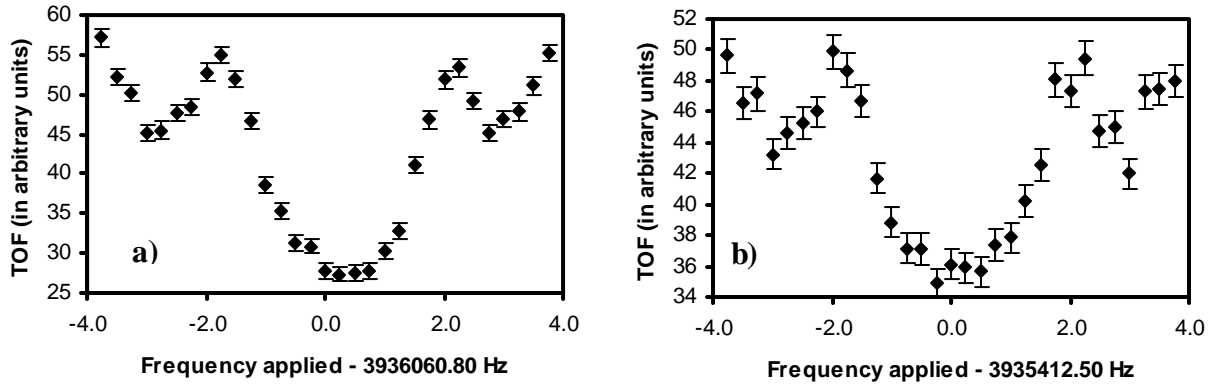


Fig. I-9. Time-of-flight spectra obtained for $^{46}\text{Ti}^{2+}$ (a) and $^{46}\text{V}^{2+}$ (b) using a quadrupole excitation of 500 ms duration. The mass resolution is $\sim 5 \times 10^{-7}$.

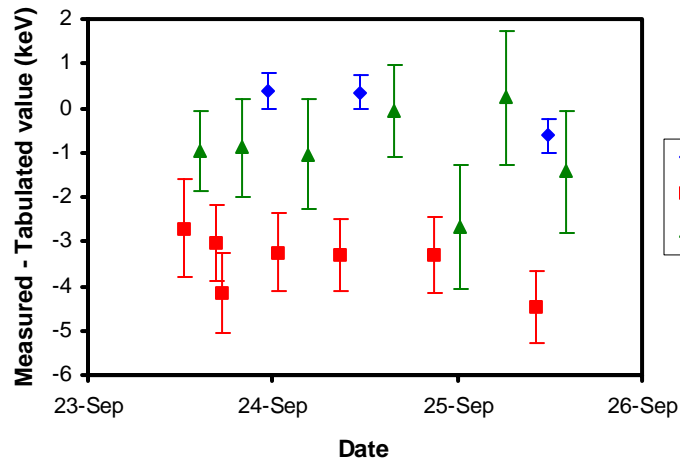


Fig. I-10. Measured mass values (plotted as deviations from the tabulated mass values [10]) for the isotopes of interest versus time during the experiment.

The experiment interleaved measurements of the mass of $^{46}\text{V}^{2+}$ and $^{46}\text{Ti}^{2+}$ with calibrations of the magnetic field via measurements of $^{22}\text{Ne}^+$ (see Fig. I-10). A small magnetic-field drift (about 8×10^{-10} per hour) was observed during the experiment. This shift is negligible at the level of accuracy required since calibration and measurements on radioactive species were interleaved; nevertheless all measure-

ments were corrected for it. The results of the different measurements are then averaged with the proper statistical weights to yield the final values for the cyclotron frequencies and statistical uncertainties. The resulting cyclotron frequency ratios are: $\nu(^{46}\text{V}^{2+})/\nu(^{22}\text{Ne}^{1+}) = 0.956974161(12)$, $\nu(^{46}\text{Ti}^{2+})/\nu(^{22}\text{Ne}^{1+}) = 0.957131846(10)$ and $\nu(^{46}\text{V}^{2+})/\nu(^{46}\text{Ti}^{2+}) = 0.999835252(9)$.

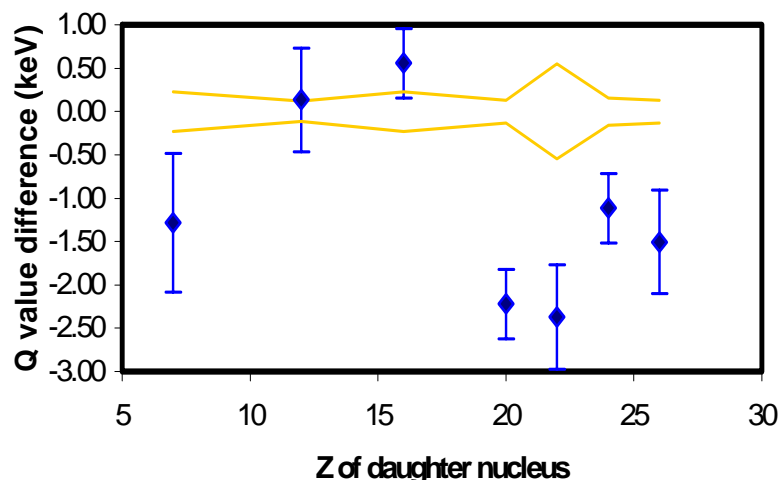


Fig. I-11. Difference between the Q values measured by Vonach et al.,³ (blue diamonds) and the values obtained from all other data. The lines indicate the uncertainty on the relevant Q values from the other existing data.

Measurements on the ^{46}V , ^{46}Ti and ^{22}Ne isotopes were performed with an average of 0.34 ions, 1.02 ions and 1.18 ions detected per cycle respectively. Shifts in cyclotron frequency due to ion-ion interactions for different number of ions in the trap were measured with ^{22}Ne isotopes to be $-1.7(2.7)$ ppb per detected ion, under the conditions used during the experiment. Corrections to the three frequency ratios given above of $1.4(2.3) \times 10^{-9}$, $0.3(4) \times 10^{-9}$ and $1.2(1.8) \times 10^{-9}$ respectively were applied to account for this effect. The spatial extent probed by the ions in the trap is determined by the ion preparation and the conditions of injection. Optimization of the injection conditions to minimize possible systematic errors will be performed following a procedure outlined in section h.3. For measurements of isotopes with different A/q ratios this procedure yields an accuracy better than 10^{-8} ; for species with the same A/q ratio the conditions are identical and no uncertainty is introduced. We use the demonstrated 1 part per 10^8 accuracy as a conservative value for our systematic uncertainty for the new mass values obtained below from ratios of isotopes with different mass number. The masses of the two $A = 46$ isotopes can be obtained from the frequency ratios to the well-known mass of ^{22}Ne , after correction for the missing electron mass (or two electron masses) and the electronic binding energies. This yields mass values of $m(^{46}\text{V}) = 45.96019909(69)$ amu and $m(^{46}\text{Ti}) = 45.95262748(62)$ amu. Our result for ^{46}Ti differs substantially from the value in the 2003 mass tables. It should however be noted that this latter value depends on a 30-year-old unpublished (p, γ) measurement.¹

The Q value for the decay can be obtained more precisely from the ratio of the cyclotron frequencies for ^{46}V and ^{46}Ti directly since most systematic effects (with the exception of the ion number dependency which is corrected for) cancel out for such a close doublet of masses. The measured ratio yields, after corrections, a Q value for the superallowed decay of 7052.90(40) keV, which differs by 2.19 keV from the value determined in the latest compilation² (from the average of two mutually-inconsistent results: 7053.3(1.8) and 7050.41(60) keV). The present measurement agrees with the first of those but is in strong disagreement with the second one,³ which claims smaller error bars. This second result originated from ($^3\text{He,t}$) reaction measurements in a Q3D spectrometer calibrated with a beam whose energy was measured with a time-of-flight system. These measurements actually included results³ on a total of seven high-precision Q values of superallowed emitters and we therefore undertook a reassessment of all seven. In Fig. I-11 we compare the Q values obtained in Ref. 3 to those we obtain using all data from a recent compilation², including our new measurement, but excluding Ref. 3. The deviations average more than 2σ and peaks at 5σ . The probability that the deviations of the results from Ref. 3 are due to statistical fluctuations is below 0.0000001%. Since the energy calibration used in Ref. 3 cannot be traced back and the deviations appear to not only be large but also predominantly in one direction, we have opted to remove these measurements from the high precision data set. The resulting precision data set (Table I-1) yields the Ft value plot shown in Fig. I-12. The agreement amongst the various emitters is still remarkable. The average Ft value for the most precise 12 cases is now shifted to 3073.66(75), one standard deviation above the latest

evaluation, with a reduced χ^2 of 1.12. The increase in the reduced χ^2 is due mainly to the new Ft value for ^{46}V , $Ft(^{46}\text{V}) = 3079.9(23)\text{s}$, with the neighboring decays ^{42}Sc and ^{34}Cl also contributing slightly. This might be a first clear indication of deviations from the calculated isotope-to-isotope variation in nuclear-structure-dependent corrections that we ultimately aim to test. This poorer reduced χ^2 is also reflected in a slightly weaker scalar current limit than that obtained in Ref. 2, the Fierz interference term now being $b_F = 0.0024(28)$. For the ^{46}V decay, the Q value and lifetime measurements now have roughly similar contributions to the total experimental error, both being smaller than the uncertainty in the

nuclear-structure-dependent corrections. The Ft values for both ^{46}V and ^{42}Sc are significantly above the average and in both cases the values were raised with respect to the other emitters by the calculated corrections. An independent calculation of these nuclear structure dependent corrections yields a slightly higher average Ft value but the same general variations from emitter to emitter. A reevaluation of the variations in these calculations may be warranted but at present we follow Ref. 2 and use the mean value for these corrections for the nine most precise cases (for which both calculations are available), assigning a systematic uncertainty equal to half the mean difference. This yields a new average $Ft = 3074.4(12)\text{s}$.

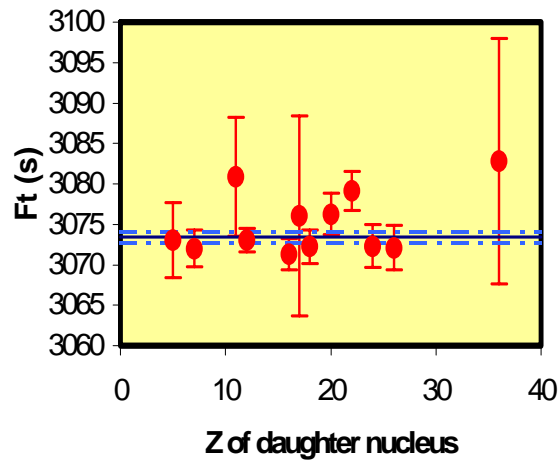


Fig. I-12. Ft values for the most precisely known superallowed beta emitters with the modified data set.

Table I-1. New values for the ft values and corrected Ft values for the 12 most precisely known cases obtained with the modified data set.

Emitter	ft -value	Ft -value
^{10}C	3039.5(47)	3073.0(49)
^{14}O	3043.3(19)	3072.0(26)
^{22}Mg	3052.4(72)	3080.9(74)
$^{26\text{m}}\text{Al}$	3036.8(11)	3073.0(15)
^{34}Cl	3050.0(12)	3071.2(19)
^{34}Ar	3060(12)	3076.6(123)
$^{38\text{m}}\text{K}$	3051.1(10)	3072.2(21)
^{42}Sc	3046.8(12)	3076.4(24)
^{46}V	3050.7(12)	3079.9(23)
^{50}Mn	3045.8(16)	3072.4(27)
^{54}Co	3048.4(11)	3072.2(28)
^{74}Rb	3084.3(80)	3083.3(154)

With the new average Ft value and the transition independent radiative corrections one obtains a new value for the weak vector coupling constant of $G_V/(\hbar c)^3 = 1.1356(5) \times 10^{-5} \text{ GeV}^{-2}$. Combining this

value with the Fermi coupling constant one obtains a new value of $V_{ud} = 0.9736(4)$. This value is lower than that obtained in the latest evaluation of superallowed decay data but is still within the previously quoted uncertainty.

Before proceeding to the unitarity sum of the top row of the CKM matrix, we must first decide on an appropriate value for V_{us} . Recent results from BNL-E865,⁴ KTeV,⁵ NA48,⁶ and KLOE⁷ yield values for $|V_{us}f_+(0)|$ consistently higher than the values quoted by the Particle Data Group.⁸ Various calculations are available for $f_+(0)$ but following most authors we use the value from Czarnecki *et al.*⁹ which yields, with the weighted average of the above experimental results, $V_{us} = 0.2248(19)$. Using this value together with our new value for V_{ud} and the PDG⁸ value for V_{ub} , we obtain

$$V_{ud}^2 + V_{us}^2 + V_{ub}^2 = 0.9985 \pm 0.0012;$$

with equal contributions to the uncertainty coming from V_{ud} and V_{us} . For both elements, the uncertainty is dominated by uncertainty in theoretical calculations ($f_+(0)$ for V_{us} and ΔV_R for V_{ud}).

In conclusion, a high-precision determination of the Q value of the superallowed decay of ^{46}V has resolved a discrepancy in that value and uncovered a set of seven measured Q values that systematically disagree with this and other precise results from the

data set used for the most precise determination of V_{ud} . A new evaluation has been performed with a revised data set that includes the present measurement and excludes the seven faulty values. It yields a lower value for V_{ud} that, when combined with the recently improved value for V_{us} , almost satisfies CKM unitarity in the top-row test (V_{us} has moved towards unitarity while V_{ud} is being moved slightly away by our measurement). The precision of that test is now dominated by theoretical uncertainties in the determination of both V_{ud} and V_{us} . The CVC test connected to the constancy of the Ft values measured in superallowed decays has been worsened slightly by the changes to the data set, as has been the limit on scalar currents.

This measurement marked the first online precision mass measurement on a doubly-charged short-lived isotope in a Penning trap and the gain in resolution yielded a better than 10^{-8} accuracy in the mass ratio, the highest achieved online so far by any system. An extension of these precision measurement techniques to the other superallowed emitters is necessary to shed more light on the current situation and this is ongoing at the CPT at ATLAS.

*McGill University, Montreal, Quebec, †Texas A&M University.

¹G. Guillaume (1971), thesis, Universite de Strasbourg.

²J. C. Hardy and I. S. Towner, Phys. Rev. C **71**, 055501 (2005).

³H. Vonach *et al.*, Nucl. Phys. **A278**, 189 (1977).

⁴A. Sher *et al.*, Phys. Rev. Lett. **91**, 261802 (2003).

⁵T. Alexopoulos *et al.*, Phys. Rev. Lett. **93**, 181802 (2004).

⁶A. Lai *et al.*, Physics Letters **B602**, 41 (2004).

⁷P. Franzini (2004), hep-ex/0408150.

⁸S. Eidelman *et al.*, Phys. Lett. **B592**, 1 (2004).

⁹A. Czarnecki *et al.*, Phys. Rev. D **70**, 093006 (2004).

b.4. Precise Mass Measurement of Light Fission Fragments from ^{252}Cf Source (Y. Wang, H. Sharma, G. Savard, A. Levand, K. S. Sharma, J. Wang, and Z. Zhou)

The injection system of the CPT mass spectrometer is versatile enough to allow radioactive ions produced using various techniques to be injected into the ion trap system effectively. After successful measurements on heavy neutron-rich fission fragments, we have started measurements on the light fragments produced by ^{252}Cf fission. Nine neutron-rich isotopes $^{106,107}\text{Mo}$, $^{107,108}\text{Tc}$, $^{108-111}\text{Ru}$, and ^{111}Rh from the light ^{252}Cf fission fragment peak have been measured with the CPT mass spectrometer to a few tens of keV/ c^2 precision and compared with the most recent atomic mass evaluation (AME 2003). In these

measurements, the gas catcher stops the light fission fragments produced by the ^{252}Cf fission source located just outside the gas cell and guides them to the exit nozzle of the cell by a combination of the 150 Torr pure Helium gas flow, radio frequency (RF) and DC electric fields. The light fission fragments with mass around 110 amu differ from the heavy fragments studied previously in that they are stopped much less efficiently in the gas and are extracted from the gas catcher system mostly as singly-charged particles. After cooling and bunching in the RFQ cooler, the ions are ejected into a mass selective ion trap which purifies them with a mass resolution of about 800

at mass 100 using a recentering RF amplitude of $0.25V_{pp}$. About 400 ms duration time is required in this trap to separate the desired isotopes from the contaminant molecules. About 95% of the contaminant ions can be removed in the mass selective trap. The ions of interest are further selected by time-of-flight technique using a gated $0.1 \mu\text{s}$ deflection pulse that only transmits ion of a single A/q to a gas-filled RFQ linear trap where further cooling takes place before the ions are finally delivered to the Penning trap where the precise mass measurement takes place. A 500 ms excitation time for cyclotron frequency ω_c was employed for all of the light fission fragments measurements and yields a resolving power of about 450000 and a 10^{-7} precision. The CPT measurements of ^{107}Mo , $^{107,108}\text{Tc}$, and $^{108,109,111}\text{Ru}$ have better precision than the AME2003 values. Only ^{108}Tc , $^{108,110}\text{Ru}$, and ^{111}Rh are found to agree with the mass table, within errors, a situation which is not unexpected in a

neutron rich region that has been difficult to access previously. In general, the measured masses are larger than predicted from systematic trends, i.e., the nuclei are less bound than expected (Fig. I-13).

These light fission fragment measurements have benefited from a number of improvements to the CPT system that were implemented in 2004. A $450 \mu\text{Ci}$ ^{252}Cf fission source, which is ten times stronger than the previously used source, was installed in front of the 1.9 mg/cm^2 thickness Havar window of the gas catcher. The activities counted on the silicon detectors increased by about a factor of ten (but so did the observed contaminants). A new cleaning system was installed to provide all the ω_+ cleaning frequencies together in a cosine envelope with 100 ms duration time. The new cleaning system enables us to measure shorter-lived isotopes by saving several hundreds millisecond in the sample preparation in the final Penning trap.

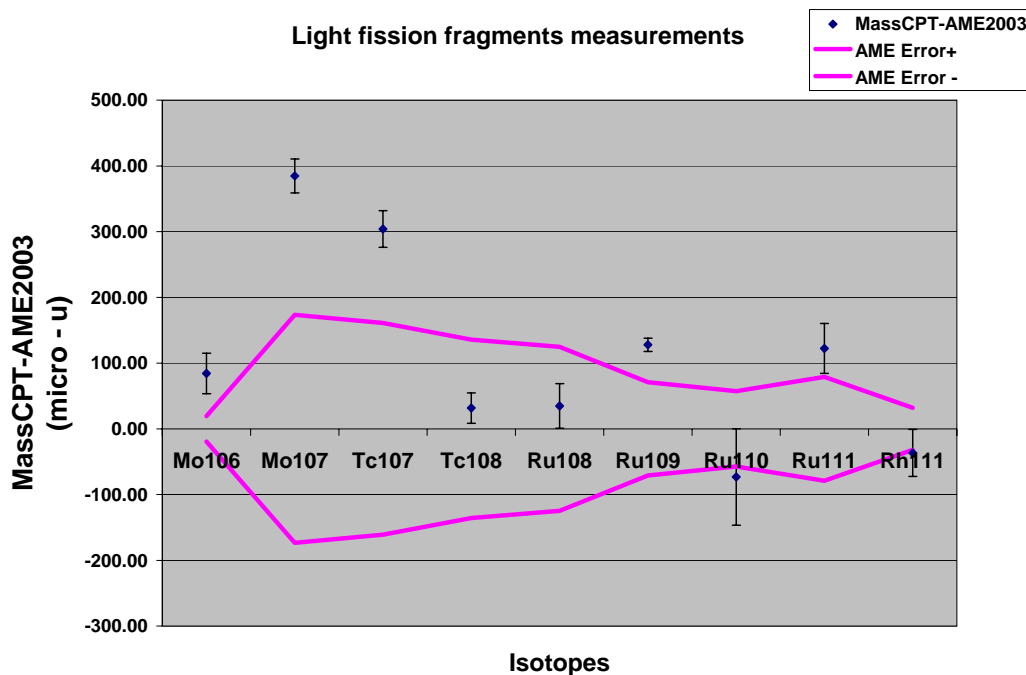


Fig. I-13. Mass comparisons between CPT measured values and the AME2003 values ($1 \mu\text{u} \sim 0.93 \text{ keV}$).

b.5. The RFQ Decay Trap Component of the Advanced Penning Trap System

(N. D. Scielzo, G. Savard, J. A. Clark, S. Gulick, A. A. Hecht, A. Levand, H. Sharma, K. S. Sharma, I. Tanihata, A. Villari, J. Wang, Y. Wang, Z. Zhou, and B. J. Zabransky)

The installation of a RFQ decay trap as part of the Advanced Penning Trap (APT) system is nearing completion in preparation for a first loading with

radioactive ions for precision β -decay measurements. Trapped radioactive ions are a nearly ideal source of activity for measurements of the β - ν correlation

coefficient, a , since scattering of the recoiling daughter nuclei (with energy ~ 100 eV) is essentially eliminated and the neutrino momentum can be inferred from the recoil of the nucleus. Although the tightest constraints on interactions beyond the dominant V - A terms come from measurements of a , contributions from scalar and tensor interactions as large as 10% of the vector and axial-vector terms are not excluded.^{1,2} By detecting β - γ coincidences in the superallowed 0^+ to 0^+ Fermi decay of ^{14}O , the momentum of the recoil nucleus can be inferred from the Doppler shifts of the deexciting 2.313 MeV γ -rays.

The transfer of ions from the isobar separator to the decay trap was simulated using SIMION 7.0 and the

required ion optics elements were constructed. We anticipate nearly 100% efficiency in transfer of ions from the isobar separator trap to the RFQ decay trap. The vacuum chamber to hold the newly constructed RFQ decay trap was built and placed in position in the beamline. Figure I-14 shows the open vacuum chamber with the RFQ trap inside and one HPGe detector held in place. Within the vacuum system, the cabling for the Si detector telescopes, LN₂ and He gas feedthroughs, and thermocouple connections were constructed with UHV-compatible parts to ensure purity of the He buffer gas used to cool the trapped ions. Any impurities in the buffer gas could lead to ion loss from the trap. Decays from untrapped ions would be difficult to distinguish from those of trapped ions and lead to a background that causes a systematic shift in measurements of the β - ν correlation.

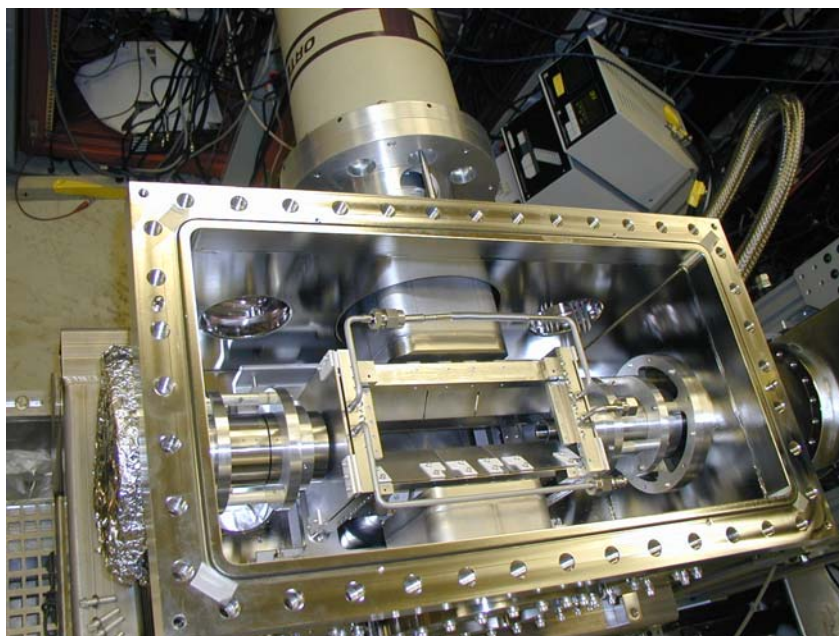


Fig. I-14. Photo of the RFQ vacuum chamber opened to show the RFQ trap. Several pieces of the trap and the Si detectors have been removed to provide a view of the traps interior and electrode plates. One HPGe detector in a re-entrant port is visible. The re-entrant port on the bottom of the chamber is not visible and the fourth one is attached to the chamber lid.

The data acquisition to be used to record β - γ coincidences was tested "offline" with the Si detectors using radioactive sources. RF pick-up (from the trapping fields) on the Si detector telescopes was eliminated by placing a grounded shield around the detectors. The re-entrant ports that enable the HPGe detectors to be brought within 4" of the trapped ion cloud were constructed. The ends of these ports have a 1/16" stainless steel vacuum window to minimize the attenuation of γ -rays. The detector supports attach to the re-entrant port flanges

and allow for precision positioning of the HPGe detectors.

GEANT4 simulations of β -decay of ^{14}O within the trap show that the largest systematic effect in the current geometry is likely to be from positron scattering. The required correction can be reduced to only $\sim 1\%$ by replacing the stainless steel electrodes with beryllium ones and placing beryllium plates on the grounded RF shields. The simulations showed that other potential systematic effects, such as the achievable Si and HPGe

detector positioning (<1 mm) and energy calibration leads to systematic uncertainties of only $\sim 0.2\%$ in a .

The statistical precision required of a competitive measurement of the β - ν correlation coefficient, a , requires a low-energy $^{14}\text{O}^{1+}$ beam with intensities of $\sim 10^5$ ions/sec. Therefore, the ^{14}O produced must be transported through the system with maximum efficiency. An initial production run using the $p(^{14}\text{N}, ^{14}\text{O})n$ reaction demonstrated the ability of the system to transport $^{14}\text{O}^{1+}$ from the gas target to the isobar separator trap. However, the transportation efficiency was a factor 100 less than anticipated. Although the optimal gas catcher settings have been determined for ions of mass $A \sim 100$, the best settings for mass 14 amu are still being determined. New tunable RF feeding circuits were installed on the

cooler of the gas catcher to improve the transmission for light ions. The efficiency for extracting $^{14}\text{O}^{1+}$ from the cone of the gas catcher was also improved as the RF frequency applied to the cone was increased from the normal value for heavy ions of roughly 750 kHz up to about 1.6 MHz. The frequency could however not be increased further due to capacitors within the vacuum system, and as a result the gas catcher had to be operated at a lower than optimal electric field setting. Installing new capacitors will enable us to reach higher frequencies and reach an efficiency of the gas catcher for these light masses similar to what is reached for heavier ions and obtain the required 10^5 cooled ^{14}O ions per second.

It is anticipated that the RFQ trap will be loaded in Fall 2005 for the first β - γ correlation measurements.

¹A. I. Boothroyd, J. Markey, and P. Vogel, Phys. Rev. C **29**, 603 (1984).

²E. G. Adelberger *et al.*, Phys. Rev. Lett. **83**, 1299 (1999).

C. SPECTROSCOPY OF VERY HEAVY ELEMENTS

There has been significant progress in the spectroscopy of heavy nuclei. We have successfully continued our program of decay studies of the very heaviest elements that can be produced in reactors. We have continued to inelastically excite actinide targets with very heavy beams above the Coulomb barrier. Finally, we have continued to use fusion reactions to study entry regions, odd-A nuclei, groundstate α -decays, and isomers. This forefront research on very heavy nuclei continues to be a domain where the ATLAS beams and the Fragment Mass Analyzer (FMA) allow us to make unique contributions. Investment in rotating targets and new focal-plane detectors has been important in keeping this research competitive.

c.1. Strength of Octupole Correlations in the Actinides: Contrasting Behavior in the Isotones ^{239}Pu and ^{237}U (S. Zhu, R. V. F. Janssens, M. P. Carpenter, I. Ahmad, N. Hammond, T. L. Khoo, F. G. Kondev, T. Lauritsen, C. J. Lister, E. F. Moore, D. Seweryniak, G. J. Lane,*† I. Wiedenhöver,‡ A. P. Byrne,* P. Chowdhury,§ D. Cline,¶|| A. Deacon,|| G. D. Dracoulis,* S. J. Freeman,|| G. D. Jones,** A. O. Macchiavelli,† J. F. Smith,|| and C. Y. Wu¶||)

Octupole correlations play an important role in determining the low level structure of nuclei throughout the periodic table. This is the case in the actinide region, where two distinct collective modes have been identified associated with an octupole vibration and the rotation of an octupole deformed

nucleus. A study of high spin states in the odd-neutron isotones ^{239}Pu and ^{237}U was performed at ANL with Gammasphere. Striking differences were found in the properties of rotational bands in these two nuclei. The level schemes for these two isotones deduced from present work are displayed in Figs. I-15 and I-16.

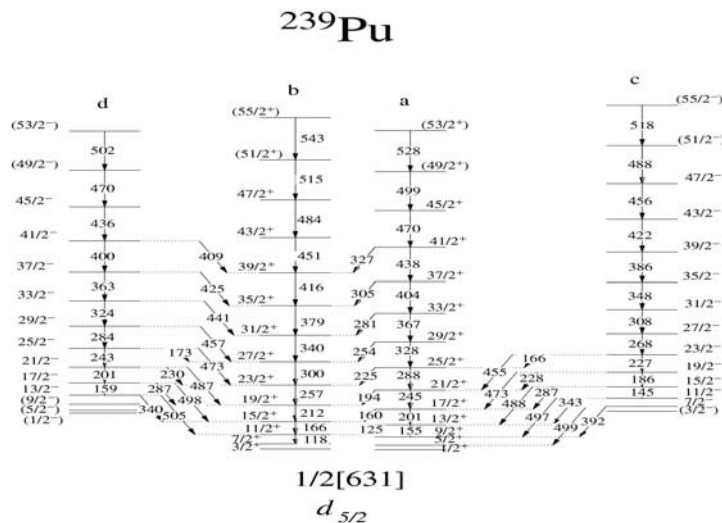


Fig. I-15. Proposed ^{239}Pu level scheme with the transition energies given in keV. Bands c and d are the octupole bands under discussion in this report.

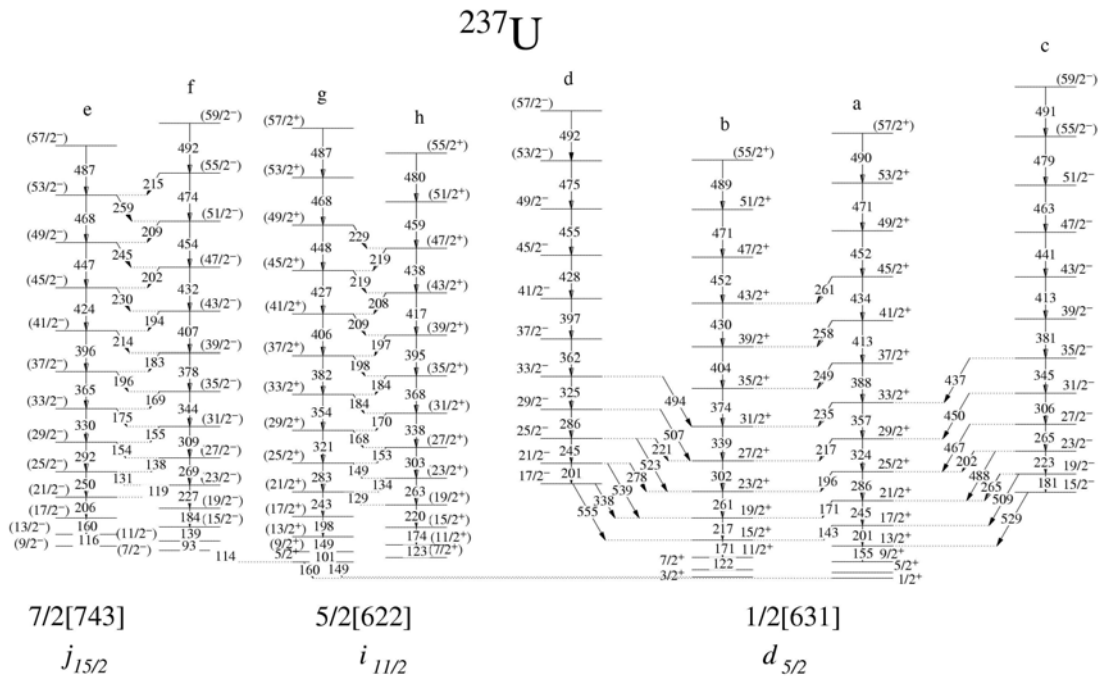


Fig. I-16. Proposed ^{237}U level scheme with the transition energies given in keV. Bands c and d are the octupole bands under discussion in the present report.

A key indicator of strong octupole correlations in odd-mass nuclei is the presence of parity doublets: the stronger the correlations, the smaller the energy difference between quantum states with the same spin and opposite parity. In the ^{237}U and ^{239}Pu isotones, the negative parity bands appear to be associated with an octupole vibration at low spin as the experimental energy difference is ~ 0.5 MeV. However, with increasing angular momentum, the ^{239}Pu levels of same spin and opposite parity come closer and closer in excitation energy: the $45/2^+$ and the $45/2^-$ states are 47 keV apart, the two $49/2$ levels are separated by only 17 keV and the $53/2$ states lie within 8 keV of each other. In contrast, the energy differences at high spin in ^{237}U remain of the order of 200 keV. Furthermore, the staggering factor (which is a measure of the extent to which the sequences of opposite parity are interleaved in spin and can be regarded as a single rotational band of octupole character) in the $^{239,240}\text{Pu}$ isotopes are large at low spin, but become small and comparable to those seen in nuclei with octupole deformation for spins at $I \geq 24 \hbar$. In contrast, in ^{237}U the values of the staggering factor decrease with spin, but start

leveling off at spin $20 \hbar$. Finally, the decoupling parameters are of the same (small) magnitude, but opposite sign in ^{239}Pu , in line with expectations when strong octupole correlations are present. In ^{237}U , the Coriolis effects appear to be negligible in the negative-parity band, illustrating further the contrasting situation between the two isotones. In addition, from the extracted experimental E1/E2 branchings, the D_0 moment of ^{239}Pu is 40% larger than the corresponding quantity in ^{237}U .

All of these differences mirror those observed in the even-even Pu and U immediate neighbors and appear to be related to the assumption that the strength of octupole correlations is larger in ^{239}Pu than in its isotope ^{237}U . It was proposed¹ that the strength of the correlations in the two even $^{238,240}\text{Pu}$ isotopes may be such that a transition from an octupole vibration to a stable octupole deformation occurs at the highest spins, in agreement with the theoretical description by Jolos and von Brentano.^{2,3} The same appears to occur in ^{239}Pu . It is worth noting that, in both odd nuclei under consideration, the octupole excitations are based on the same neutron orbital and the marked difference in behavior then must reflect changes in the respective cores. This in turn points to a significant

role for the additional two protons in Pu in polarizing the nuclear shape. However, these protons cannot be solely responsible for the increase in strength: the neutron number has a significant impact as octupole correlations have been shown to be weaker in both the heavier $^{242,244}\text{Pu}$ ¹ and the lighter ^{236}Pu .⁴ It is believed that strong octupole correlations or stable octupole deformation impact the magnitude of the alignment gain i_x and its evolution with rotational frequency. The Pu yrast bands show a small and gradual alignment of $\sim 2 \hbar$ over the entire frequency range. The negative parity excitations experience the initial (2 - 3) \hbar alignment characteristic of the

octupole phonon and no further increase at higher frequency. In contrast, a strong alignment occurs in every sequence in the two U isotopes, i.e. they all experience a noticeable rise at $\hbar\omega \sim 0.25 \text{ MeV}$. It has been shown that this rise is due to the alignment of a pair of $i_{13/2}$ protons, in agreement with expectations based on cranked shell model calculations.

To summarize, the present work indicates that the striking difference in behavior between the $A = 238, 240$ even Pu isotopes and other actinide nuclei extends to the odd ^{239}Pu nucleus. Further analysis of this data set continues and is focused on ^{238}U in which new bands have been identified.

*Australian National University, Canberra, Australia, †Lawrence Berkeley National Laboratory, ‡Florida State University, §University of Massachusetts, ¶University of Rochester, ||University of Manchester, United Kingdom, **University of Liverpool, United Kingdom.

¹I. Wiedenhöver *et al.*, Phys. Rev. Lett. **83**, 2143 (1999).

²R. V. Jolos and P. von Brentano, Phys. Rev. C **49**, R2301 (1994).

³R. V. Jolos and P. von Brentano, Nucl. Phys. **A587**, 377 (1995).

⁴K. Abu Saleem *et al.*, Phys. Rev. C **70**, 024310 (2004).

c.2. Behavior of ^{240}Pu at the Highest Spins (R. V. F. Janssens, S. Zhu, M. P. Carpenter, I. Ahmad, J. P. Greene, T. L. Khoo, T. Lauritsen, C. J. Lister, D. Seweryniak, X. Wang, § S. Freeman, ¶ F. G. Kondev, * I. Wiedenhöver, † A. Bernstein, † P. Wilson, † E. Diffenderfer, † C. Teal, † A. Larabee, ‡ B. Meredith, ‡ and U. Garg§)

A few years ago,¹ a study of the level structure of ^{240}Pu suggested that this nucleus possibly evolves from an octupole vibrator at low spin to an octupole rotor at high spin, in agreement with theoretical suggestions by Jolos and von Brentano.^{2,3} The evidence was based mostly (a) on the fact that, at the highest spins, the yrast states of spin-parity I^+ become interleaved with the $(I-1)^-$ and $(I+1)^-$ levels of the octupole band and (b) on the strength of the $(I+1)^- \rightarrow I^+$ E1 linking transitions. The purpose of the present experiment was to explore the structure of this nucleus further by (1) identifying the linking E1 transitions between the states of opposite parity at the

highest spins and by (2) searching for additional band structures in this nucleus.

The experiment was carried out with Gammasphere at ATLAS. A ^{208}Pb beam of 1300 MeV bombarded a $350 \mu\text{g}/\text{cm}^2$ ^{240}Pu target evaporated on a thick Au backing. More than 3 billion events with fold 3 or higher were collected.

The analysis is on-going. A number of coincidence cubes and hyper-cubes have been created after the data were transposed into a so-called BLUE data base. It is clear that the available knowledge on ^{240}Pu will be expanded considerably.

*Nuclear Engineering Division, Argonne National Laboratory, †Florida State University, ‡Greenville College, §University of Notre Dame, ¶University of Manchester, United Kingdom.

¹I. Wiedenhöver *et al.*, Phys. Rev. Lett. **83**, 2143(1999).

²R. V. Jolos and P. von Brentano, Phys. Rev. C **49**, R2301 (1994).

³R. V. Jolos and P. von Brentano, Nucl. Phys. **A587**, 377(1995).

c.3. Proton Single-Particle States in ^{249}Bk ($Z = 97$) (I. Ahmad, E. F. Moore, M. P. Carpenter, R. R. Chasman, J. P. Greene, R. V. F. Janssens, T. Lauritsen, C. J. Lister, D. Seweryniak, F. G. Kondev,* R. W. Hoff,† J. E. Evans,† R. W. Loughheed,† C. E. Porter,‡ and L. K. Felker‡)

The heaviest odd-proton nuclide available in a large quantity for spectroscopic measurements is the α decaying ^{253}Es ($T_{1/2} = 20.47$ d). We have studied the level structure of its daughter ^{249}Bk by measuring the γ -ray spectra of an isotopically enriched, chemically pure ^{253}Es sample. Using gamma singles spectra, measured with high-resolution Ge detectors, we were able to identify many weakly populated states that decay by γ rays with intensities as low as $1.0 \times 10^{-6}\%$ per ^{253}Es α decay. A gamma-gamma coincidence experiment was performed with the Gammasphere spectrometer at Argonne in order to determine the decay pattern of high-lying states. The high efficiency and resolving power of Gammasphere allowed us to identify many weak gamma rays that were not observed in the singles spectrum. Information on low spin states of ^{249}Bk was obtained

from γ -ray spectroscopic study following β^- decay of ^{249}Cm at Livermore.

Using the results of the present study and the data available from the previous $^{248}\text{Cm}(\alpha,t)$ investigation, the following single-particle states have been identified in ^{249}Bk : $7/2^+[633]$, 0.0 keV; $3/2^-[521]$, 8.78 keV; $1/2^+[400]$, 377.55 keV; $5/2^+[642]$, 389.17 keV; $1/2^-[530]$, 569.20 keV; $1/2^-[521]$, 643.0 keV; $5/2^-[523]$, 672.9 keV; $9/2^+[624]$, 1075.1 keV. In addition, four vibrational bands were identified at 767.9, 932.2, 1150.7, and 1223.0 keV with tentative assignments of $\{7/2^+[633] \times 1^-\} 9/2^-$, $\{7/2^+[633] \times 0^-\} 7/2^-$, $\{7/2^+[633] 1^-\} 5/2^-$ and $\{7/2^+[633] \times 0^+\} 7/2^+$. The experimental level spacings are in good agreement with the theoretical values, as shown in Fig. I-17. The results of this study were published.¹

*Nuclear Engineering Division, Argonne National Laboratory, †Lawrence Livermore National Laboratory, ‡Oak Ridge National Laboratory.

¹I. Ahmad *et al.*, Phys. Rev. C **71**, 054305 (2005).

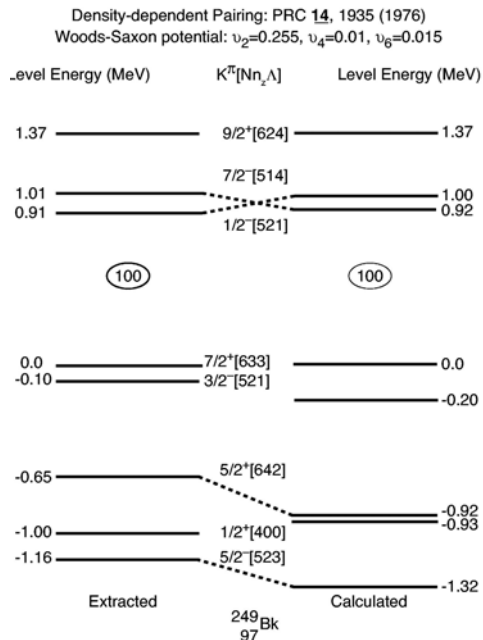


Fig. I-17. A comparison of the measured and calculated level energies in ^{249}Bk . Extracted energies represent the measured energies from which contributions of pairing correlations have been removed. Level energies on the right side represent energies calculated with a Woods-Saxon potential with deformation parameters $v_2 = 0.255$, $v_4 = 0.01$ and $v_6 = 0.015$.

c.4. Properties of the Lightest Nobelium Isotopes (D. Peterson, B. B. Back, M. P. Carpenter, C. Davids, A. Hecht, R. V. F. Janssens, C. L. Jiang, T. L. Khoo, T. Lauritsen, C. J. Lister, D. Seweryniak, X. Wang, S. Zhu, P. Chowdhury,* S. Tandel,* U. Tandel,* and A. Heinz†)

Recent experiments in the synthesis of superheavy elements utilizing beams of ^{48}Ca are both exciting and puzzling. To study systematic trends in the $Z > 100$ region, two separate studies^{1,2} of neutron-deficient nobelium isotopes via the $^{204}\text{Pb}(^{48}\text{Ca},\text{xn})$ reaction were undertaken by groups working in Dubna. Both experiments only observed spontaneous fission (SF) decay, but measured three different lifetimes (60[1], 36[2], and 6[2] μs). Belozarov *et al.*,² attributed the 36 μs lifetime to ^{249}No , but the possibility of an isomeric decay could not be excluded. Those experiments also suffered from limited statistics, and the 3n channel necessary to produce ^{249}No was expected to be very small at the energies used.²

We have conducted a new experiment to clarify these decays. Our goal in the present experiment was to use the Fragment Mass Analyzer (FMA) at Argonne National Laboratory to collect enough statistics to unambiguously determine the masses corresponding to each decay and to unfold the multiple decay components if present. Furthermore, with increased statistics, we hoped to find the previously unobserved α decay to obtain a branching ratio for SF/ α . Finally, the focal plane of the FMA was equipped with three Ge clover detectors to detect γ 's emitted from the decay of an isomer if that was a source of one of the decays.

*University of Massachusetts-Lowell, †Yale University.

¹Oganessian *et al.*, Phys. Rev C **64**, 054606 (2001).

²Belozarov *et al.*, Eur. Phys. J. A **16**, 447-456 (2003).

³D. Peterson *et al.*, section h.9. of this report.

An isotopically pure ^{204}Pb (99.708%) target consisting of four wedges of average thickness 0.540 mg/cm^2 was mounted onto a Gammasphere-style rotating target wheel, which was in turn mounted to a support arm specifically designed to allow the use of this smaller target wheel in the heavy-element scattering chamber.³ The wheel was rotated at speeds of 1100 - 1700 rpm to prevent the target material from melting under intense beam currents. The maximum current delivered to the target was 85 pA ($q = 10^+$), with an average intensity of 55 pA. The beam current was limited by the ion source operation. Future experiments with this setup can certainly take advantage of larger currents. Besides the modified target wheel assembly, another new technique for this experiment was the use of three separate amplifier channels for each strip of the focal plane silicon strip detector (DSSD). In addition to the standard delay-line amplifiers and shaping amplifiers with gains for energy signals in the range of 0-20 MeV (α -equivalent), we also incorporated a low-gain branch range of 0 - 800 MeV to register the expected fission decays without signal saturation.

Analysis is ongoing. We have identified nearly 160 implant-fission coincidences. Proper normalization to obtain absolute cross sections, as well as uncertainties in the χ^2 -space for fitting the decays must be understood. The search for indications of γ -rays from an isomeric level and possible α -decays are also in progress.

c.5. Structure of ^{253}No (T. L. Khoo, I. Ahmad, A. Heinz, T. Lauritsen, C. J. Lister, D. Seweryniak, M. P. Carpenter, C. N. Davids, J. P. Greene, F. Kondev, R. V. F. Janssens, A. A. Sonzogni, I. Wiedenhöver, P. Reiter,* A. Afanasjev,† P. A. Butler,‡ A. J. Chewter,‡ J. A. Cizewski,§ P. T. Greenlees,¶ K. Helariuta,¶ R.-D. Herzberg,‡ G. Jones,‡ R. Julin,¶ H. Kankaanpää,¶ H. Kettunen,¶ W. Korten,§ P. Kuusiniemi,¶ M. Leino,¶ S. Siem,|| and J. Uusitalo¶)

The heaviest nuclei are stabilized by a shell-correction energy, which lowers the ground-state, thereby creating a barrier against fission. The shell-correction energy originates from the clustering of single-particle orbitals. Hence, the single-particle

eigenstates form the basis of the shell stabilization. The most direct data on the orbital energies come from odd-A nuclei, providing our motivation to investigate the odd-N nucleus ^{253}No . The single-particle energies also provide a direct test of nuclear models that predict the properties of

superheavy nuclei. Thus, by testing model predictions¹ against data on the heaviest nuclei that are accessible for spectroscopy, one may judge their reliability for predicting the properties of superheavy elements, e.g. the next spherical shell closures beyond ²⁰⁸Pb.

The production cross section of ²⁰⁷Pb(⁴⁸Ca,2n)²⁵³No reaction was measured as ~0.5 μb at Jyväskylä. In a subsequent experiment at Argonne, the γ rays were detected with Gammasphere, in coincidence with ²⁵³No residues detected in the FMA. The γ-ray spectrum for ²⁵³No has many weak lines, but is dominated by the K X-rays. Heavy odd-A nuclei, such as ²⁵³No, represent the limits of in-beam γ spectroscopy due to overwhelming conversion electron competition in M1 transitions. Of the expected low-lying configurations in ²⁵³No, only the 7/2⁺[624] orbital is expected to have sufficiently small M1 branching ratios to permit detection of intraband E2 γ rays. However, due to the low γ-ray cross sections of 25-50 nb, it was necessary to develop new methods based on (a) quantitative comparisons of results from experiment and from model predictions; (b) enhancement of transitions with high γ multiplicity; and (c) finding evidence for a rotational band in a sparse γγ matrix. Similar methods will be required for in-beam γ spectroscopy of nuclei far from stability, which have diminutive cross sections.

The kinematic and dynamic moments of inertia, $J^{(1)}$ and $J^{(2)}$, of the 7/2⁺[624] band are shown in Fig. I-18,

where they are compared with values from those of the neighboring nuclei ^{252,254}No. The $J^{(1)}$ and $J^{(2)}$ moments of inertia of ²⁵³No are rather well reproduced by the self-consistent cranked relativistic Hartree Bogoliubov (CRHB) theory. In contrast, the theoretical description² of the $J^{(2)}$ moments of inertia of the even-even nuclei ^{252,254}No is not as good. That is probably due to a less-than-perfect description of the quasiparticle energies. On the other hand, the moments of inertia in an odd-even nucleus is sensitively dependent on (and hence characteristic on) the occupied orbital; hence the $J^{(1)}$ and $J^{(2)}$ moments of the 7/2⁺[624] band could be well described.

A bandhead energy of 355 keV was deduced from the data for the 7/2⁺[624] configuration. This energy compares with theoretical predictions of 240, 400 and 1200 keV, which are given by, respectively, a Nilsson model based on the Wood-Saxon potential and by self-consistent mean-field theories using the Skyrme Hartree-Fock or CRHB methods.¹⁻² Of course, a systematic test of theory should encompass a set of quasiparticle states, and has recently been performed for self-consistent mean-field theories.¹⁻² For example, Ref. 1 points out that the relativistic mean-field method is able to describe many single-particle energies, but that several (including the 7/2⁺[624] orbital) that originate from specific spherical orbitals deviate by more than 1 MeV from experimental energies.

A paper on the results has been accepted for publication in Phys. Rev. Lett.

*University of Cologne, Germany †University of Notre Dame, ‡University of Liverpool, United Kingdom, §Rutgers University, ¶University of Jyväskylä, Finland, ||University of Oslo, Norway.

¹A. Afanasjev *et al.*, Phys. Rev. C **67**, 024309 (2003).

²M. Bender *et al.*, Nucl. Phys. **A723**, 354 (2003).

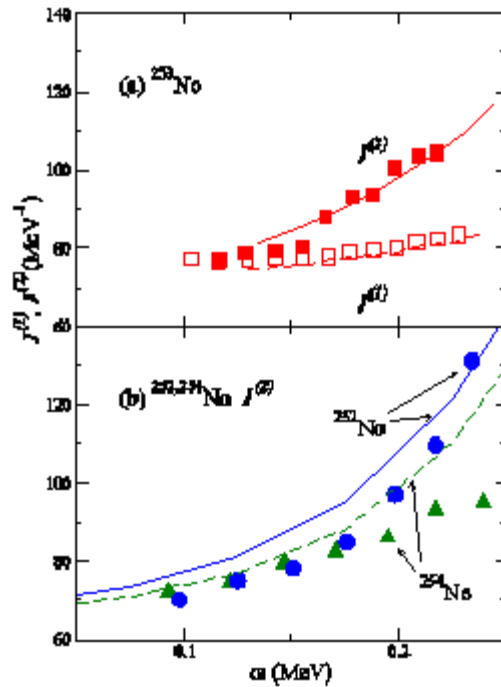


Fig. I-18. (a) The moments of inertia $J^{(1)}$, $J^{(2)}$ for the $7/2^+$ [624] band in ^{253}No . (b) $J^{(2)}$ for $^{252,254}\text{No}$. (a) Experimental data. Results from CRHB theory are shown as solid or dashed lines.

c.6. Electrons from a 0.3s Isomer in $^{254}\text{No}^*$ (T. L. Khoo, R. Blinstrup, D. Seweryniak, I. Ahmad, M. P. Carpenter, C. N. Davids, S. Freeman, J. P. Greene, N. Hammond, R. V. F. Janssens, F. G. Kondev, T. Lauritsen, C. J. Lister, G. Mukherjee,* P. A. Butler,† P. Chowdhury,* J. A. Cizewski,‡ R. Gramer,* R. D. Herzberg,† A. Heinz,§ P. Ikin,† M. Johnson,‡ G. D. Jones,† E. Ngijoi-Yogo,* and P. Reiter¶)

Data on pairing and single-particle energies are essential for reliable predictions of the stability of the superheavy elements. The single-particle energies constitute the basis of the shell-correction energy, which provides the essential bulk of the binding energy, and pairing further lowers the ground-state. The energies and configurations of 2-quasiparticle high-K isomers in heavy shell-stabilized nuclei can provide information on both single-particle energies and the pair gap.

High-K isomers are expected in shell-stabilized nuclei around ^{254}No because there are many high- Ω single-particle orbitals near the Fermi level. An isomer has been identified¹ in ^{254}No ($T_{1/2} = 0.28$ s), but no information on its decays exists. We have observed the electrons accompanying the decay of this isomer in an experiment where nobelium nuclides are produced with the $^{208}\text{Pb}(^{48}\text{Ca}, 2n)$ reaction at ATLAS. The evaporation residues were

transported and identified with the Fragment Mass Analyzer (FMA) and implanted in $1 \times 1 \text{ mm}^2$ pixels of a Si double-sided strip detector. In the *same pixel* where a residue was implanted, electrons from the decay of an isomer were observed in a 1.4 s time interval, followed by α decays from the ground state of ^{254}No within a 120 s interval. (Similar results have recently been obtained² at Jyväskylä.) The source of the electrons was unambiguously characterized by: (i) identification of ^{254}No ; (ii) time and spatial correlations of residue, electron and α ; and (iii) the electron and α decay half-lives. The electron spectrum represents the sum energy from transitions within a rotational band following the isomer decay, either from the ground band or an excited band. In a search for the γ rays depopulating the isomer, two transitions were found at 944 and 842 keV, which were previously identified as prompt ($< \text{few ns}$) emissions in experiments at Argonne and Jyväskylä. This finding implies that the 0.26 s decays to an excited rotational band, which is the source of the isomeric electrons.

*Argonne National Laboratory and University of Massachusetts-Lowell, †University of Liverpool, United Kingdom, ‡Rutgers University, §Yale University, ¶University of Cologne, Germany.

¹A. Ghiorso *et al.*, Phys. Rev. C **7**, 2032 (1973).

²R. Herzberg *et al.*, University of Liverpool, private communication (2004).

c.7. Gamma Decay from a 0.3s Isomer in ²⁵⁴No* (T. L. Khoo, D. Seweryniak, I. Ahmad, M. P. Carpenter, J. Chapman, C. N. Davids, J. P. Greene, R. V. F. Janssens, F. G. Kondev, T. Lauritsen, C. J. Lister, S. Tandel,* P. A. Butler,† P. Chowdhury,* P. Greenlees, R. D. Herzberg,† A. Heinz,§ P. Ikin,† G. D. Jones,† G. Mukherjee,* P. Reiter,¶ and U. Tandel*)

Reliable calculations of the stability of the superheavy elements require accurate single-particle energies. Gaps in the single-particle energies give rise to the quantum-mechanical shell-correction energy. Data on the single-particle energies come not only from odd-A nuclei, but also from the energies of 2-quasiparticle states in even-even nuclei. In addition, the latter provide valuable constraints on the pair gap.

Evidence of a high-K isomer in ²⁵⁴No ($T_{1/2} = 0.28$ s) has been found from the electron sum-energy spectrum (see section c.6.). In order to establish the energy and quantum numbers of the isomer, we have recently succeeded in detecting the γ rays which accompany the decay of the isomer. Residues of ²⁵⁴No were produced with the ²⁰⁸Pb(⁴⁸Ca,2n) reaction at ATLAS, using beams of up to 100 pnA intensity. The residues were transported and mass-identified with the Fragment Mass Analyzer (FMA). Gamma rays coincident with isomeric electrons were detected in an interval of ~ 1 s following implantation of a

²⁵⁴No nucleus. High-energy transitions at 842 and 944 keV were observed. These two γ rays have previously been observed as prompt emissions with Gammasphere at ATLAS, as well as in experiments at Jyväskylä. Hence, these transitions cannot directly deexcite the 0.28 s isomer, but instead decay from a short-lived (\sim ns) two-quasiparticle state. We deduce that the isomer decays, probably via a 53-keV transition, to a rotational band built on a $K = 3^+$ two-quasiparticle state at 988 keV. Decays within the bands proceed predominantly through emission of electrons. The electron sum energy spectrum was previously detected (see section c.6.). A preliminary level scheme for the isomer is shown in Fig. I-19. In addition, a new shorter-lived isomer (~ 200 μ s) has been found, which is established to decay into the 0.28 s isomer.

The $K = 3^+$ two-quasiparticle state has a proposed proton $1/2^- [521] \times 7/2^- [514]$ configuration. Its low energy (988 keV) puts tight constraints on the individual quasiparticle excitation energies and also sets a lower bound of 0.5 MeV on the proton pair gap.

*Argonne National Laboratory and University of Massachusetts-Lowell, †University of Liverpool, United Kingdom, ‡Rutgers University, §Yale University, ¶University of Cologne, Germany.

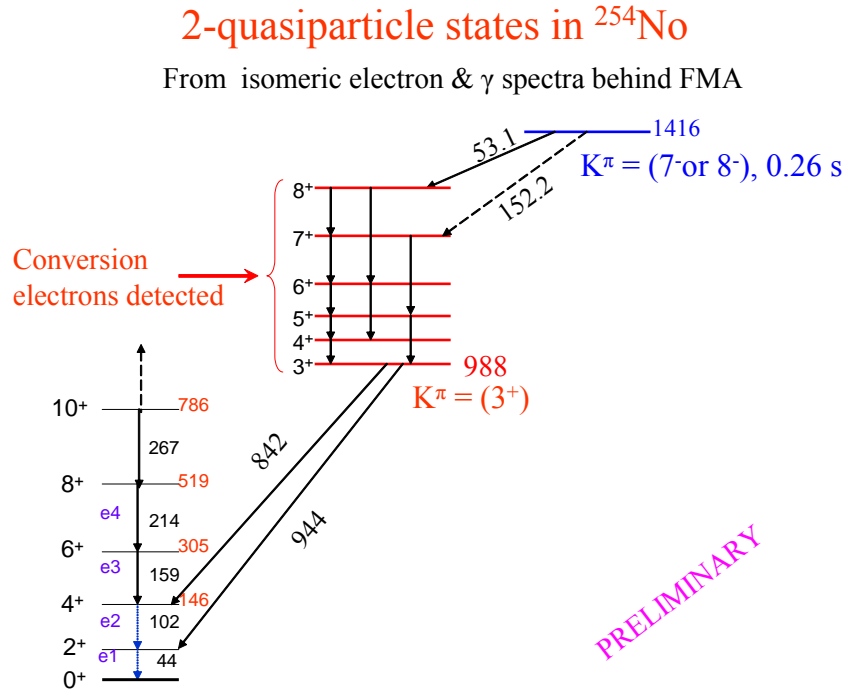


Fig. I-19. Tentative decay scheme for the 0.26 s isomer in ^{254}No .

c.8. Limiting Angular Momentum in ^{254}No (T. L. Khoo, D. Seweryniak, I. Ahmad, M. P. Carpenter, C. N. Davids, S. Freeman, J. Greene, N. Hammond, R. V. F. Janssens, F. G. Kondev, T. Lauritsen, C. J. Lister, P. A. Butler, ‡ P. Chowdhury, † J. A. Cizewski, § R. Gramer, † R. D. Herzberg, ‡ A. Heinz, ¶ P. Ikin, ‡ M. Johnson, § G. D. Jones, ‡ G. Mukherjee, * † E. Ngijoi-Yogo, † and P. Reiter ||)

Our investigations of the shell-stabilized nobelium nuclei have shown that they, perhaps surprisingly, survive up to high angular momentum and that the fission barrier is >5 MeV for spins larger than $10 \hbar$. In other words, shell-stabilized nuclei are quite robust at high spin. Stimulated by these experiments, several self-consistent mean-field theory calculations have found that the fission barrier that the barrier remains sizeable at high spin. The HFB predictions of Egido and Robledo¹ suggest that ^{254}No should survive up to spin 30 - 35 \hbar . Self-consistent mean-field theories, with interactions determined from properties of lighter nuclei, provide a promising method for predicting the properties of superheavy nuclei, particularly since they do not employ parameters tailored to different mass regions. However, the reliability of these predictions needs to be tested by comparison to data of shell-stabilized nuclei and also by expanding the small database for this comparison.

To determine how much angular momentum a ^{254}No nucleus can sustain before it is torn apart by fission, we have conducted an experiment with Gammasphere operated in coincidence with the FMA. This combination provides a capability, which is unique in the world for reactions with sub- μb cross sections, namely the ability to detect γ rays with both high resolution and with 4- π calorimetric capability. We attempted to measure the two-dimensional entry distribution, i.e. the initial spin-energy distribution of the nucleus. However, a technical problem with Gammasphere precluded measurements of the BGO energy and, hence, of the sum energy in the reaction. The multiplicity information remained intact. The maximum input angular momentum was increased from ~ 20 to $\sim 33 \hbar$ by using a higher beam energy than in our previous experiment² -- from 219 to 223 MeV. The measured fold distribution clearly demonstrated an increase of the maximum spin from 22 to 28 \hbar . Although ^{254}No is loosely bound, it is quite stable against rotation;³

its fission barrier remains large enough at high angular momentum for it to survive to a spin of almost $30 \hbar$.

*Argonne National Laboratory and University of Massachusetts-Lowell, †University of Massachusetts-Lowell, ‡University of Liverpool, United Kingdom, §Rutgers University, ¶Yale University, ||University of Cologne, Germany.

¹L. Egido and L. Robledo, Phys. Rev. Lett. **85**, 1198 (2000).

²P. Reiter *et al.*, Phys. Rev. Lett. **84**, 3542 (2000).

³A. Afanasjev *et al.*, Phys. Rev. C **67**, 024309 (2003).

D. STRUCTURE OF NUCLEI FAR FROM STABILITY

A core issue in nuclear structure research concerns the evolution of nuclear behavior as one moves away from stability by varying the neutron-to-proton ratio. Traditional shell gaps are shown to disappear and new gaps arise. The exact origins of these phenomena still have to be fully understood, though modification of the spin-orbit effect and other residual interactions appears likely. We continue to probe nuclei along the proton dripline from light masses to heavy. In addition, our efforts to reach neutron-rich nuclei have grown, through fragmentation experiments, traditional fusion of very neutron-rich species, and using multi-nucleon transfer.

d.1. Neutron-Rich Nuclei

d.1.1. High Spin Structure in Neutron-Rich Ti and Cr Isotopes: Possible N = 32 and 34

Shell Gaps and the Onset of Deformation (R. V. F. Janssens, S. Zhu, M. P. Carpenter, F. G. Kondev, C. J. Lister, N. J. Hammond, T. Lauritsen, D. Seweryniak, P. Chowdhury, ‡ D.-C. Dinca,* A. Gade,* D. Bazin,* C. M. Campbell,* J. M. Cook,* T. Glasmacher,* J.-L. Lecouey,* S. N. Liddick,* P. F. Mantica,* W. F. Mueller,* H. Olliver,* J. R. Terry,* B. A. Tomlin,* K. Yoneda,* S. J. Freeman, § A. Deacon, § J. F. Smith, § B. J. Varley, § R. Broda, † and B. Fornal †)

Over the last few years, our collaboration has initiated a program to investigate the properties of neutron-rich nuclei above doubly-magic ^{48}Ca . At the onset, the primary motivation for these studies was the expectation that substantial modifications can occur to the intrinsic shell structure of nuclei with a sizable neutron excess.¹ Alterations to the energy spacings of the orbitals and/or to their ordering can have a considerable impact on global nuclear properties such as the nuclear shape or the type of excitations characterizing the low-energy level spectra.

Our approach has been one where we combine beta decay and intermediate-energy Coulomb excitation measurements performed at the NSCL with deep inelastic reactions or fusion-evaporation with radioactive targets carried out with Gammasphere at ATLAS. Our main results can be summarized as follows:

(1) Following first indications of the onset of a N = 32 sub-shell gap in ^{56}Cr ,² we have demonstrated the power of combining techniques and accelerators by firmly establishing the N = 32 sub-shell in ^{54}Ti .³ This gap manifests itself through the high energy of the first excited 2^+ state and the large energy gap between the lowest 6^+ level and higher spin states (which reflects the high energy cost of promoting

neutrons across the gap). The data were found to be in good agreement with shell model calculations using the recently developed GXPF1 effective interaction which accounts for the N = 32 gap by the combined action of a weakening of the $\pi[1f_{7/2}] - \nu[1f_{5/2}]$ proton-neutron monopole interaction as protons are removed from the $1f_{7/2}$ orbital (filled at Z = 28) and a significant $\nu(2p_{1/2} - 2p_{3/2})$ spin-orbit splitting.

(2) With the same combined techniques, we subsequently studied ^{56}Ti and discovered (a) from beta decay that its first excited 2^+ state is much lower in excitation energy than the corresponding state in ^{54}Ti ,^{4,5} and (b) from deep inelastic reactions⁶ that the higher excitations do not show any indication of a shell gap at N = 34, contrary to predictions based on shell model calculations with the GXPF1 interaction.

(3) To place the interpretation above on firmer ground, the $B(E2; 0^+ \rightarrow 2^+)$ reduced transition probabilities were measured for the $^{52-56}\text{Ti}$ even isotopes.⁷ From Fig. I-20, a clear anti-correlation between two observables can be readily seen: while the 2^+ energies increase significantly at N = 28 and N = 32 the $B(E2)$ strengths are lowest for these two neutron numbers. Furthermore, both these physical quantities also differ markedly from the corresponding values at neutron numbers N = 26, 30 and 34. For ^{50}Ti , the well known shell closure at N = 28 translates into a

small transition probability: with the $B(E2)$ value of Fig. I-20(b), the deexcitation from the 2^+ level to the ground state has a strength of only 5.6 single-particle units. The fact that the excitation energy and the reduced transition probability observed in ^{54}Ti are comparable to those in ^{50}Ti then confirms that the Ti isotope with $N = 32$ is as good a semi-magic nucleus as its $N = 28$ counterpart and, hence, that a substantial sub-shell gap must occur at $N = 32$. Conversely, the fact that the three other Ti isotopes have 2^+ excitation energies lower by several hundreds of

keV and $B(E2)$ values higher by a factor of ~ 2 can be interpreted as an experimental indication for the absence of sub-shell gaps in the neutron single-particle spectrum at $N = 26, 30$ and 34 .

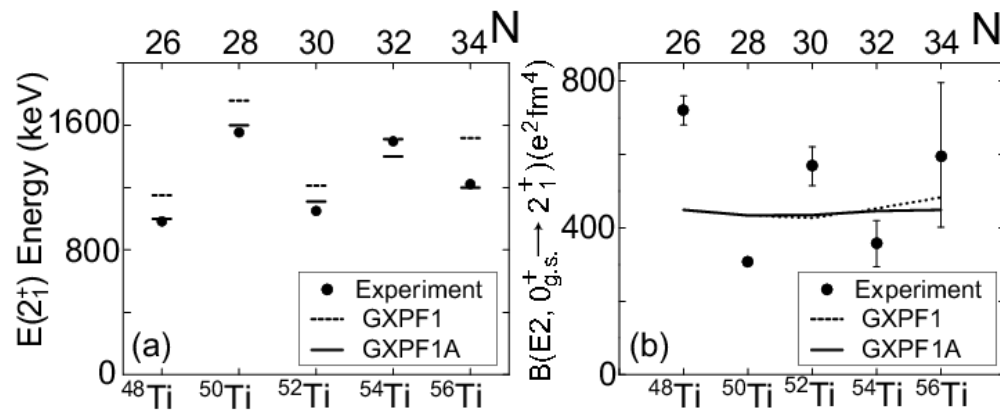


Fig. I-20. 2^+ excitation energies and $B(E2)$ transition probabilities compared to shell model calculations with the GXPF1 and the GXPF1A interactions.

The results summarized above have led to further theoretical work, both in the framework of the shell model and with other approaches. Specifically, our results have led to a modified version of the interaction, labeled GXPF1A, in which the matrix elements of the interaction involving mostly the $p_{1/2}$ orbital have been readjusted. It is worth pointing out that the evaluation of the properties of this orbital from experimental data is particularly challenging since it contributes little angular momentum to any given state. Traces of its impact are often obscured as a result. The solid lines in Fig. I-20(a) indicate that the GXPF1A calculations reproduce the $E(2^+)$ energies. In fact, they provide a satisfactory description of all the known levels in the even Ti nuclei, including those above the 6^+ level in ^{54}Ti which involve neutron excitations across the $N = 32$ shell. They also describe the odd Ti nuclei satisfactorily.⁸ We note that the calculations do not reproduce the $B(E2)$ probabilities very well. This may well be due to the poor knowledge we have at present of the values of the effective charges to be used.

The success of the GXPF1A interaction depends also sensitively on the size of the neutron gap at $N = 40$. A large $N = 40$ gap effectively isolates the low-lying structure from the neutron $g_{9/2}$ state, whereas a weak shell closure facilitates excitations involving this shape-driving orbital. The Cr isotopes lie in the middle of the $\pi f_{7/2}$ shell and could potentially display some of the strongest collective effects.

Our collaboration has been investigating the Cr nuclei of interest as well, and so far, we have carried out a number of investigations of the neutron-rich Cr nuclei. At the NSCL, beta decay into some of the nuclei of interest has been studied.¹ Based on the latter, yrast and near-yrast level structures in ^{56}Cr and ^{58}Cr have been delineated from deep inelastic data measured with Gammasphere following the $^{48}\text{Ca} + ^{208}\text{Pb}$ and $^{48}\text{Ca} + ^{238}\text{U}$ reactions.⁹ To obtain the level structure of ^{60}Cr as well as that of the odd $^{57,59}\text{Cr}$ isotopes, another approach was used at ATLAS with Gammasphere and the Fragment Mass Analyzer (FMA). The $^{14}\text{C}(^{48}\text{Ca}, 2p)^{60}\text{Cr}$ fusion-evaporation reaction with a ^{14}C radioactive target has a very small cross section (neutron-rich compound nuclei are 100-1000 times more likely to evaporate neutrons), but with the

selectivity of the FMA it was possible to identify the relevant transitions with Gammasphere.⁹ From the same experiment, the level scheme of ⁵⁷Cr was obtained as well.¹⁰ The same experimental approach, but with the ¹³C(⁴⁸Ca,2p)⁵⁹Cr reaction, has provided the recently published ⁵⁹Cr level structure.¹¹

The ^{57,59,60}Cr level schemes are given in Fig. I-21, while the 2⁺ excitation energies for the N = 26-38 Cr isotopes are summarized in Fig. I-22. As can be seen from Fig. I-22, the N = 32 shell gap discussed above for the Ti isotopes is present in the Cr nuclei as well, but the effect is less pronounced, as one would expect since two additional protons occupy the f_{7/2} shell and the $\pi[1f_{7/2}] - \nu[1f_{5/2}]$ proton-neutron monopole interaction is correspondingly stronger. In fact, the latest GXPF1A interaction accounts for the level structure of the N = 28-34 nuclei quite well⁹ (not shown). However, from Fig. I-21, it is evident that the situation changes drastically for N = 35, 36. Remarkably, the 2⁺ energy drops considerably at N = 36: to 645 keV from 1007 and 880 keV in ⁵⁶Cr and ⁵⁸Cr, respectively. In addition, the ⁶⁰Cr level structure of Fig. I-21 differs quite markedly from that of the lighter even isotopes (not shown): the transition energies involved are lower and, while the 6⁺→4⁺→2⁺→0⁺ cascade can hardly be characterized as rotational, it nevertheless shows a degree of regularity not seen in the lighter even Cr isotopes with the transition energies increasing with spin. In addition, the ⁶⁰Cr level structure cannot be reproduced by shell model calculations with the GXPF1A interaction. These observations parallel those made when we studied ⁵⁹Cr (Fig. I-21). Here

too, the level structure could not be accounted for with the GXPF1A interaction.¹¹ It is quite possible that deformation needs to be considered in the interpretation of ⁵⁹Cr and ⁶⁰Cr. A striking feature of ⁵⁹Cr level structure is the presence of the long-lived 9/2⁺ level at low excitation energy. This level is associated with the g_{9/2} neutron orbital^{10,11} which is shape driving. It is shown¹¹ that, for oblate deformations $\beta_2 < 0.25$, the g_{9/2} orbital falls dramatically in energy towards the Fermi surface and one can achieve a qualitative understanding of the ⁵⁹Cr level structure. Effects associated with deformation are perhaps even more dramatic in ⁵⁷Cr,¹⁰ where a rotational cascade can be observed on top of a 9/2⁺ level. It is shown¹⁰ that this sequence can be understood in the framework of TRS calculations as a rotational band with prolate deformation induced by the excitation of the odd (N = 33) neutron into the 1/2⁺[440] of g_{9/2} parentage. The calculations reproduced all the observed features, including a strong gain in alignment at high spin. The calculations also account for a similar, but less well developed structure in ⁵⁵Cr.¹⁰

The picture that emerges thus far for the odd Cr isotopes is that the excitation of a g_{9/2} neutron is sufficient to polarize the soft core into a deformed shape. In ^{55,57}Cr, the low-lying negative-parity states appear to be roughly spherical in nature and the vg_{9/2} excitation produces a prolate shape and a decoupled band. In ⁵⁹Cr, a prolate shape is incompatible with the isomeric nature of the 9/2⁺ state and it appears that the excitation of a g_{9/2} neutron drives an already mildly oblate core towards oblate deformation. The latter deformation then also characterizes ⁶⁰Cr.

*Michigan State University, †Niewodniczanski Institute of Nuclear Physics, Krakow, Poland, ‡University of Massachusetts-Lowell, §University of Manchester, United Kingdom.

¹B. A. Brown, Prog. in Part. and Nucl. Phys. **47**, 517 (2001).

²J. I. Prisciandaro *et al.*, Phys. Lett. **B510**, 17 (2001).

³R. V. F. Janssens *et al.*, Phys. Lett. **B546**, 55 (2002).

⁴S. N. Liddick *et al.*, Phys. Rev. Lett. **92**, 072502 (2004).

⁵S. N. Liddick *et al.*, Phys. Rev. C **70**, 064303 (2004).

⁶B. Fornal *et al.*, Phys. Rev. C **70**, 064304 (2004).

⁷D.-C. Dinca *et al.*, Phys. Rev. C **71**, 041302(R) (2005).

⁸B. Fornal *et al.*, Proceedings 8th Spring Seminar on Nuclear Physics, Paestum, Italy, May 2004, to be published.

⁹S. Zhu *et al.*, to be published.

¹⁰A. N. Deacon *et al.*, submitted to Phys. Lett. B.

¹¹S. J. Freeman *et al.*, Phys. Rev. C **69**, 064301 (2004).

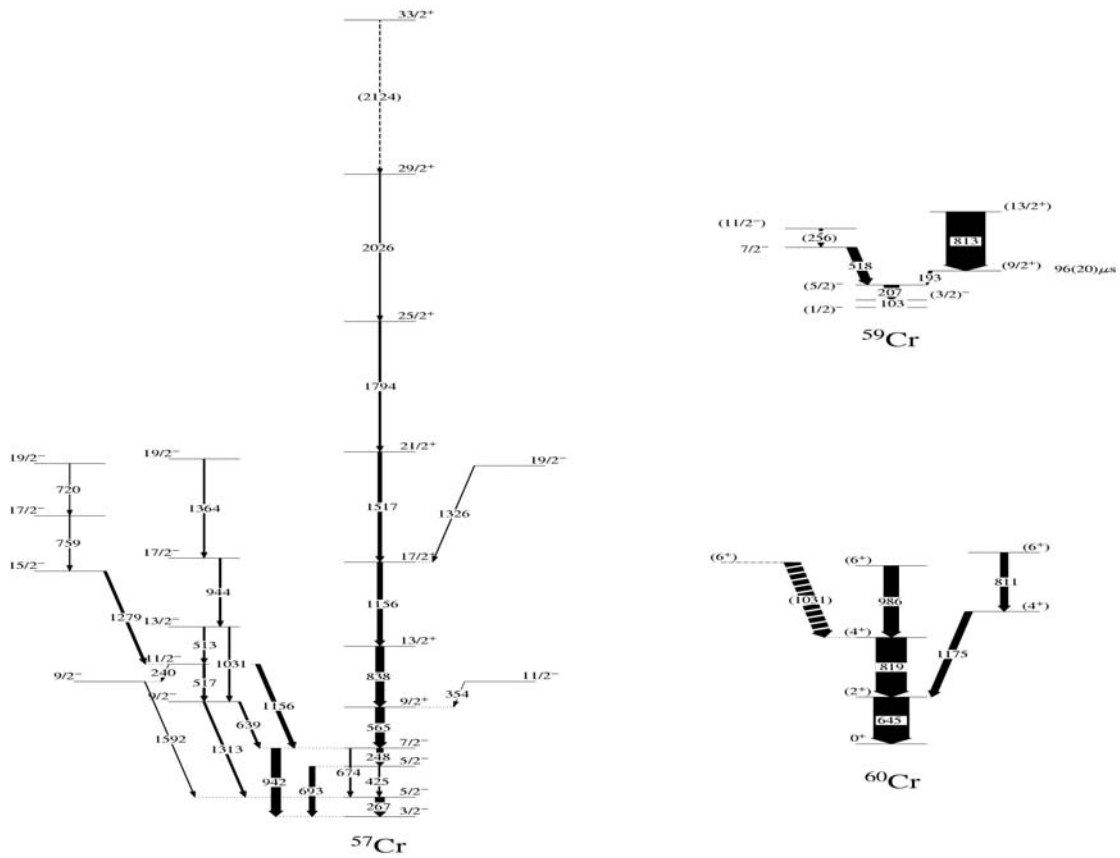


Fig. I-21. Preliminary level schemes for $^{57,59,60}\text{Cr}$ obtained with Gammasphere and the FMA.

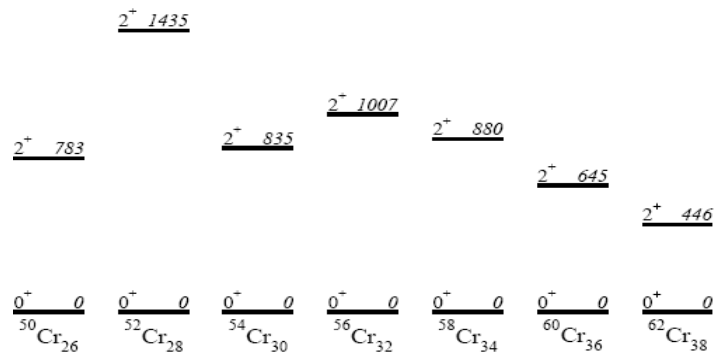


Fig. I-22. Systematics of the 2^+ energies for the Cr isotopes.

d.1.2. Search for $^{82}\text{Ge}_{50}$ Using Deep Inelastic Reactions (M. P. Carpenter, F. G. Kondev, R. V. F. Janssens, T. L. Khoo, T. Lauritsen, C. J. Lister, D. Seweryniak, and S. Zhu)

The study of doubly and semi magic nuclei have historically proven to be important in establishing for example the parameter strengths for the shell model. Until recently, these parameters were set by nuclei lying near the line of beta-stability, however, with the coming online of a number of first and second generation radioactive beam facilities, studies of exotic neutron rich nuclei at and near closed shells have begun. What has motivated many of these measurements from a nuclear structure standpoint is the fact that rearrangements of single-particle energies are observed for neutron rich. Such changes in the single-particle energies have been attributed to the attractive strength of the spin-isospin part of the effective nuclear interaction. As a result, one has observed the disappearance of certain magic numbers and the emergence of new closed shells.

Our collaboration has been actively studying neutron rich nuclei in the Ca-Ti region in order to examine a similar phenomenon. Specifically, we have been investigating Ti and Cr isotopes with $N > 28$. Recent shell model calculations using the GXPF1 Hamiltonian had suggested a new closed shell for $N = 32$ and $Z \leq 24$ and the emergence of a shell gap at $N = 34$ for $Z \leq 22$.¹ Our recent results from Gammasphere using both the $^{48}\text{Ca} + ^{208}\text{Pb}$ and $^{48}\text{Ca} + ^{238}\text{U}$ reactions has confirmed the $N = 32$ gap for ^{54}Ti ($Z = 22$)² and shown that no such gap has developed at $N = 34$ for $Z = 22$ (^{56}Ti).³ Indeed, shell model calculations using the GXPF1 Hamiltonian do an excellent job in reproducing the excitation energy of levels up to $I = 10 \hbar$ in $^{50,52,54}\text{Ti}$ but fail for the ^{56}Ti case. We also note that the study of the high-spin properties of $^{54,56}\text{Ti}$ were made possible by the previous identification of the $2^+ - 0^+$ transition in both these nuclei from β -decay of $^{54,56}\text{Sc}$ produced at the MSU fragmentation facility.^{2,4} In addition, we have recently performed Coulomb excitation experiment

on $^{52,54,56}\text{Ti}$ at MSU in order to measure the $B(E2)$ rates for the $2^+ - 0^+$ transition in each isotope and further quantify the magicity of ^{54}Ti .⁵

With the success of the Gammasphere experiments utilizing a ^{48}Ca beam to explore the yrast sequences in the neutron rich Ti isotopes, we have extended our measurements into the region around $N = 50$ and $Z = 28$ (^{78}Ni). Neutron rich nuclides in this region are of particular interest due to their role in the r-process, and in particular, their contribution to the peak in the solar elemental abundance near $A = 80$. While much is known with regards to the $N = 50$ isotones starting at ^{86}Kr and proceeding up towards ^{100}Sn , very little is known about the isotones approaching and including ^{78}Ni . In the Gammasphere measurement, data were collected using an ^{82}Se beam incident on both thick ^{208}Pb and ^{238}U targets. As a result, all products produced in these reactions are stopped in the target. Data were taken at two different beam energies 525 and 630 MeV. In addition, the time between beam pulses was 400 ns allowing for the identification of isomers with lifetimes as long as several μ sec.

One of the main goals of this measurement was to identify the yrast structures for both $^{84}\text{Se}_{50}$ and $^{82}\text{Ge}_{50}$ to spins up to $\sim 12 \hbar$. In addition, we hoped to develop detailed level structures for ^{81}Se , ^{83}Se , ^{83}As , ^{81}Ge , and possibly ^{83}Ge . Two separate "blue" data bases have been created from the data taken take at 630 MeV which correspond to the ^{208}Pb and ^{238}U targets respectively. Several coincidence cubes have been constructed from these data bases, corresponding to prompt-prompt-prompt, prompt-prompt-delayed and prompt-delayed-delayed transitions. While the analysis is ongoing, current results include a more extensive level scheme for ^{84}Se than previously known as well as new level schemes for ^{81}Se and ^{83}Se . The data is currently under analysis.

¹J. I. Prisciandaro *et al.*, Phys. Lett. **B510**, 17 (2001).

²R. V. F. Janssens *et al.*, Phys. Lett. **B546**, 55 (2002).

³B. Fornal *et al.*, Phys. Rev. C **70**, 064304 (2004).

⁴S. Liddek *et al.*, Phys. Rev. Lett. **92**, 072502 (2004).

⁵D.-C. Dinca *et al.*, Phys. Rev. C **71**, 041302 (2005).

d.1.3. The $\nu 9/2[404]$ Orbital and the Deformation in the $A \sim 100$ Region (I. Ahmad, W. Urban,* J. A. Pinston,† J. Genevey,† T. Rzaca-Urban,* A. Zlomaniec,* G. Simpson,‡ J. L. Durell,§ W. R. Phillips,§ A. G. Smith,§ B. J. Varley,§ and N. Schulz¶)

Levels in ^{101}Zr were investigated by prompt γ -ray spectroscopy of fission fragments produced in the spontaneous fission of ^{248}Cm . The measurements were carried out with the EURO GAM2 array of Compton-suppressed Ge detectors. An isomeric level was identified at 941.8 keV in ^{101}Zr and its half-life was measured to be 16 ± 2 ns. The level is interpreted as a K-isomer corresponding to the $9/2[404]$ neutron-hole excitation. The level scheme of ^{101}Zr is shown in Fig. I-23. Several transitions were identified in the $9/2^+[404]$ rotational band.

Using the cross-over to cascade γ -ray intensities we deduced the g_K-g_R/Q_0 values. Substituting the theoretical value of g_K and $g_R = 0.2$ in the expression, we deduced the quadrupole moment $Q_0 = 3.6(4)$ eb. This quadrupole moment corresponds to a deformation $\beta_2 = 0.38(4)$. Similar deformations are observed in ^{97}Sr and ^{99}Zr . These deformations and shape changes as a function of neutron number are understood in terms of the single-particle states available in this mass region. The results of this study were published.¹

*Warsaw University, Poland, †Institut des Sciences Nucleaires/Universite Josef Fourier, Grenoble, France, ‡Institut Laue-Langevin, Grenoble, France, §University of Manchester, United Kingdom, ¶Institut de Recherches Subatomiques, Strasbourg, France.

¹W. Urban *et al.*, Eur. Phys. J. A **22**, 157 (2004).

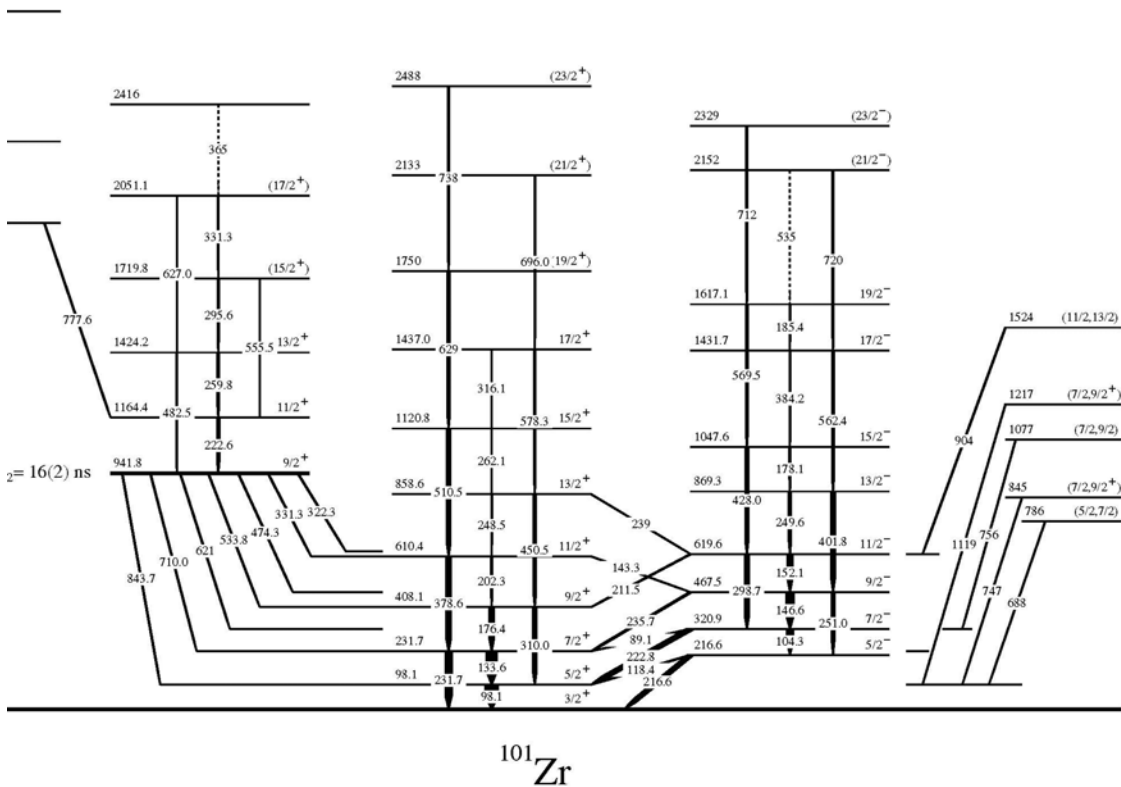


Fig. I-23. A partial level scheme of ^{101}Zr .

d.2. Proton-Rich Nuclei

d.2.1. The $A = 31$ Mirror Nuclei ^{31}P and ^{31}S Used to Investigate the Charge-Symmetry-Breaking “Electromagnetic Spin Orbit” Interaction V_{eso} (C. J. Lister,

M. P. Carpenter, N. J. Hammond, R. V. F. Janssens, T. L. Khoo, T. Lauritsen, D. Seweryniak, D. G. Jenkins,* P. Chowdhury,† T. Davinson,‡ P. Woods,‡ A. Jokinen,§ and H. Penttilä§)

If nuclear forces were charge symmetric and neutrons and protons had equal mass, charge and magnetic moments, then the spectrum of states mirror pairs of nuclei should be identical. In fact, the spectra are indeed similar, and deviations between mirror partners provide a sensitive probe of our knowledge of nuclear structure. If the position of each level relative to its groundstate is compared, then much of the monopole shift, arising from proton and neutron mass difference and the Coulomb displacement, is removed and subtle differences in structure emerge. These differences are called Mirror Energy Differences (MEDs), the difference $\Delta E = \{E(J, T_z = -1/2) - E(J, T_z = +1/2)\}$. In general these MEDs are small, on the order of ~ 50 keV. However, attention has been drawn to some much larger differences. Ekman *et al.* have recently examined the $T = 1/2$ $A=35$ mirror pair ^{35}Ar and $^{35}\text{Cl}^1$ and also reviewed $T = 1/2$ data from $A = 33$ to $A = 39$. Many interesting effects could be investigated, especially arising in very pure, single-amplitude, shell model configurations. Here, MEDs of several hundred keV were found. The interpretation of these relative shifts was through modern large basis shell model calculations which provide an excellent description of the wavefunctions and allow detailed investigation of charge-symmetry-breaking in the interactions. A key observation was that of the “electromagnetic” spin-orbit effect on the uncoupled last nucleon; the effect of the interaction between its magnetic moment and the magnetic field

induced by motion in the Coulomb field of the nucleus. This effect is completely analogous to the spin-orbit interaction felt by atomic electrons. If this interaction conforms to predictions it should be a rather ubiquitous feature in mirror pairs of nuclei. We have made new measurements on ^{31}S which allow the $A = 31$ mirror pair ^{31}S and ^{31}P to be added to this investigation, and reveal effects consistent with those reported in Ref. 1.

^{31}S was produced in the $^{12}\text{C}(^{20}\text{Ne},n)^{31}\text{S}$ reaction at 32 MeV. The FMA was used to identify the reaction channel, and Gammasphere was used to measure the decays from states in ^{31}S . Many new levels were found and their spectroscopic properties could be determined. We found the yrast states of ^{31}S and ^{31}P showed very small MEDs (< 50 keV), but, as for $A = 35$, some stretched configurations showed shifts of the order of ~ 250 keV, consistent with simple expectations of the Electromagnetic Spin orbit Splitting. Our results have been written up in a Rapid Communication to PRC.² We are in the process of examining the overall systematics of this effect in known data, and have written a proposal to seek the effect in heavier nuclei, where the orbital angular momentum is bigger, so the effect more clear. However, we have also become more aware of binding energy effects on the Coulomb energy.³ Quantification of the electromagnetic spin-orbit shifts can only be made after correction for the difference in binding energy of equivalent states in any mirror pair.

*University of York, United Kingdom, †University of Massachusetts-Lowell, ‡University of Edinburgh, United Kingdom, §University of Jyväskylä, Finland.

¹J. Ekman *et al.*, Phys. Rev. Lett. **92**, 132502 (2004).

²D. G. Jenkins *et al.*, submitted to Phys. Rev C (2005).

³J. D. Millener, private communication (2005).

d.2.2. High Spin States of $T = 3/2$ ^{37}Ca and ^{37}Cl (M. P. Carpenter, C. J. Lister, C. N. Davids, S. Williams,* P. H. Regan,* M. A. Bentley,† A. M. Bruce,‡ C. Chandler,† J. Ekman,§ W. Gelletley,† G. Hammond,† D. T. Joss,† D. Rudolph,§ and D. D. Warner¶)

Following the successful investigation of production of ^{49}Fe (see section d.2.3.) a similar “proof-of-principle” experiment was conducted to investigate the possibility of performing gamma-ray spectro-

scopy on $T = -3/2$ ^{37}Ca and testing the Isobaric Mass Multiplet Equation in the sd-shell, where traditional shell modeling is at its most sophisticated. The reaction $^{12}\text{C}(^{28}\text{Si},3n)^{37}\text{Ca}$ was used. Again, absolutely excellent

Z-resolution was achieved, and there is no doubt that sufficient channel selection can be achieved to isolate ^{37}Ca . The FMA could be set to eliminate almost all

scattered beam. Fig. I-24 shows the Z-separation, just from the ion chamber (1a), and with ET^2 selection of $A = 37$ events (1b).

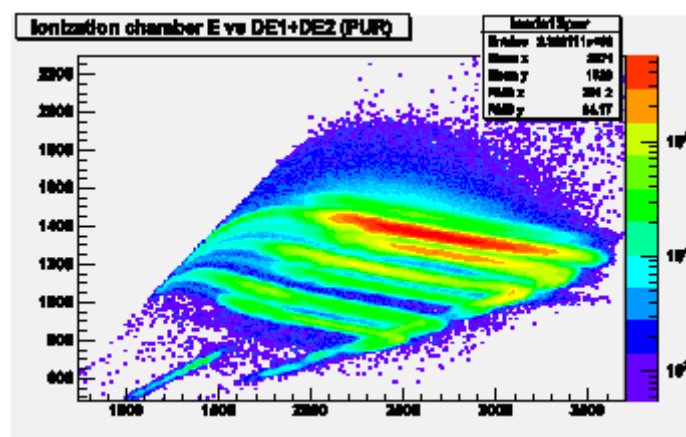


Fig. I-24. Ion Chamber Bragg curves for $A = 37$ ions stopping in isobutane. The excellent Z-resolution is clear, and loci for $A = 37$ Ca, K, Ar, and Cl could be identified.

*University of Surrey, United Kingdom, †Keele University, Staffordshire, United Kingdom, ‡University of Brighton, United Kingdom, §Lund University, Sweden, ¶CLRC Daresbury Laboratory, Warrington, United Kingdom.

d.2.3. High Spin States in the $N = Z - 3$ Nucleus ^{49}Fe : Coulomb Effects at Large Proton Excess (C. J. Lister, M. P. Carpenter, D. Seweryniak, C. Davids, M. A. Bentley,* G. Hammond,* D. D. Warner,† J. Simpson,† R. C. Lemmon,† D. Rudolph,‡ J. Ekman,‡ C. Fahlander,‡ L-L. Andersson,‡ E. Johansson,‡ A. M. Bruce,§ D. Judson,§ M. J. Taylor,§ W. Gelletly,¶ and S. J. Williams¶)

Measuring isobaric mass multiplets and comparing their excited states has had a long history in investigating charge-symmetry breaking effects in nuclear forces. As one moves to heavier nuclei this research continues to raise new issues, especially as the proton dripline is approached. The development of large basis shell models has provided a powerful theoretical tool for this kind of investigation.

^{49}Fe is a $T = -3/2$ nucleus about which little is known. Comparing its excited states with more bound isobars will provide a spin-dependent test of the Isobaric Mass Multiplet Equation. However, it is a cutting-edge challenge to obtain data on this nucleus. A test experiment was performed to investigate if spectroscopy is feasible.

The key issues were (a) Can ^{49}Fe be produced at a rate which allows spectroscopy with Gammasphere? (b) Can sufficiently clean isotope identification be

achieved to produce clean gamma-ray spectra of nuclei produced at the $1/4$ mb level? (c) Can these conditions be achieved given the use of degrader foils, located downstream of the target, which were required due to the very high recoil velocity?

The experiment was performed as an FMA stand-alone experiment, but with one clover gamma-ray detector located at 90 to the beam direction. The FMA focal plane detectors consisted of a micro-channel plate detectors for determination of position ($A = Q$) and a ionization chamber, for Z-identification through measurement of energy loss and total energy of the recoils. A 230 MeV ^{40}Ca beam impinged on a 0.26 mg/cm^2 ^{12}C target. The recoils, which had an energy of around 160 MeV, were slowed down in degrader foils located between 9 and 12 cm downstream of the target. This was necessary in order to reduce the recoil energy into a range that would be deflected by an electric field corresponding to the maximum achievable voltage on the FMA electric

dipoles. The FMA focal plane slits were wound in to select $A = 49$ recoils with $Q = 19$, cutting out $A = 48$ and 50 recoils in the same charge state.

Of critical importance was the production of a clean E/DE spectrum in the ionization chamber with little scattered beam and clean separation in Z of different isobars. The effect of the degrader foil needed to be investigated. Two different degrader foils were used in the test - a 3.1 mg cm^2 Au foil and a 1.71 mg cm^2 Ti foil. In both of these cases, the resulting E/DE spectrum showed very clear separation of isobars of different Z , although the use of the Au foil resulted in more scattered beam than recoils - in a ratio of about 5:1. The use of the Ti foil improved this dramatically, with a beam recoil ratio of about 1:1 in the E/DE spectrum. The results shown in Fig. I-25 correspond only to data taken with the Ti foil degrader. The ionization chamber spectrum is shown

in Fig. I-25(a). The spectrum shows a very clear separation in Z , with the recoils dominated by the expected $A = 49$ isobars of V, Cr and Mn. In addition, the spectrum shows contamination due to charge-state ambiguities (mainly ^{46}Ti), scattered beam and higher- Z recoils generated by reactions in the Ti foil. In order to clean this spectrum, an analysis using calibrated total energy (E) and time-of-flight (T) was undertaken. ET^2 is proportional to mass, and a 2D plot of ET^2 vs. A/Q can be used to separate recoils of the desired mass from charge-state ambiguities and scattered beam. The ET^2 value for $A = 49$ was determined, and a 2D gate placed on the ET^2 vs. A/Q plot. The resulting ionization chamber spectrum is shown in Fig. 1(b). The result of the ET^2 gating is that most of the scattered beam and charge-state ambiguities, and essentially all of the reactions from the Ti foil, have been removed.

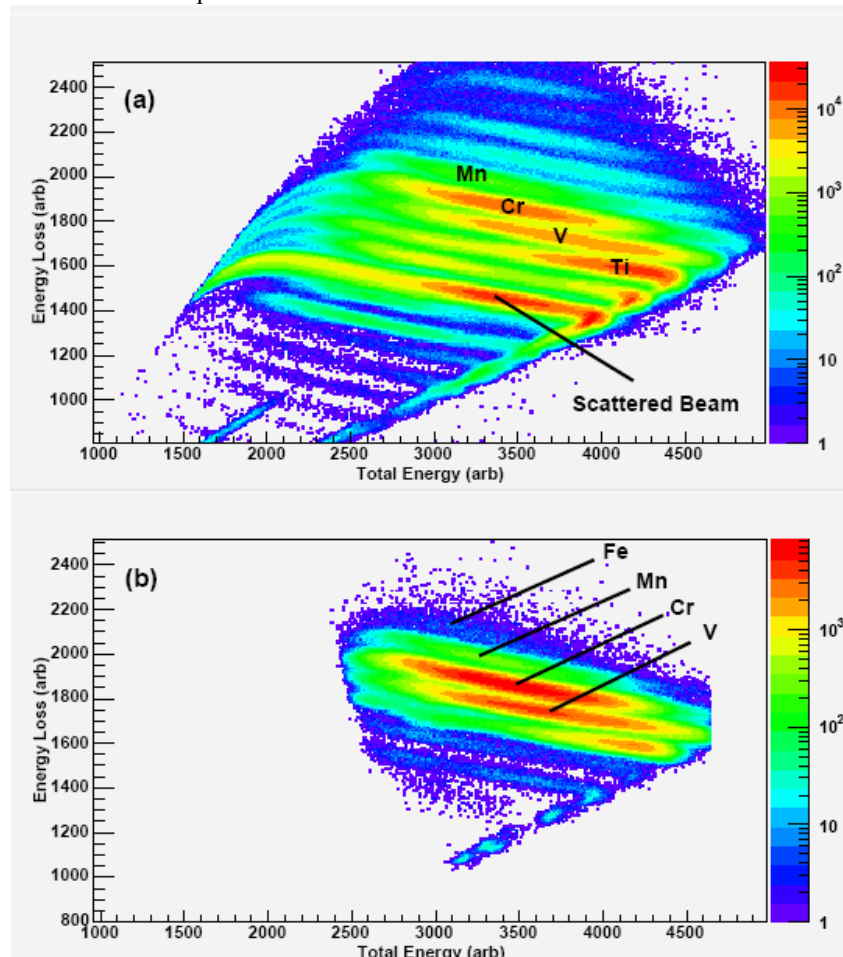


Fig. I-25. E/DE maps from the ionization spectrum, taken from data using the Ti degrader foils. (a) The raw E/DE spectrum, and (b) the E/DE spectrum gated by the ET^2 value corresponding to $A = 49$.

The $A = 49$ isobars now dominate the spectrum, as expected, and a clear region of counts in the expected

position for Fe recoils is now apparent. Thus, we believe that this region corresponds to mostly ^{49}Fe recoils. The

number of counts in this region was determined to be around 3000 in 10 hours of beam time. Using the 250 μb cross-section for ^{49}Fe used in the original proposal, one would expect around 1500 recoils in this time assuming a 10% FMA efficiency. This seems consistent, as one would expect some fraction of the counts in the region of interest to originate from breakthrough from ^{49}Mn and other residual background. Thus we are confident that the cross-section estimate is reasonable.

Gamma-spectra from the clover detector, gated by the different regions of Fig. I-25(b), are shown in Fig. I-26. This combination of 2D gates on E/DE and ET^2 vs. A/Q results in extremely clean spectra of the isobars ^{49}V , ^{49}Cr and ^{49}Mn . All the labeled gamma rays originate from these three isobars, and the

spectra are free from contaminants other than a 511 keV peak. As would be expected, the Fe-gated spectrum has very low statistics, but is also clearly free from contamination. The comparison of the spectra of the mirror pair $^{49}\text{Cr}/^{49}\text{Mn}$ is important, as eventually the ^{49}Fe level scheme will be determined by comparison of the spectrum with that of its mirror-partner, ^{49}V . Comparison of Figs. I-26(b) and (c) shows that ^{49}Mn can be *just* be identified up to $J^\pi = 23/2$ from this clean spectrum. To be confident of establishing the level scheme of ^{49}Fe up to the same spin, we estimate that we need a factor of 2-3 improvement in the statistics in Fig. I-26(b) in an equivalent spectrum generated for ^{49}Fe . We therefore require a factor of around 300 improvement in statistics for a good measurement. This is achievable in a full seven day Gammasphere-FMA experiment.

*Keele University, Staffordshire, United Kingdom, †CLRC Daresbury Laboratory, Warrington, United Kingdom, ‡Lund University, Sweden, §University of Brighton, United Kingdom, ¶University of Surrey, United Kingdom.

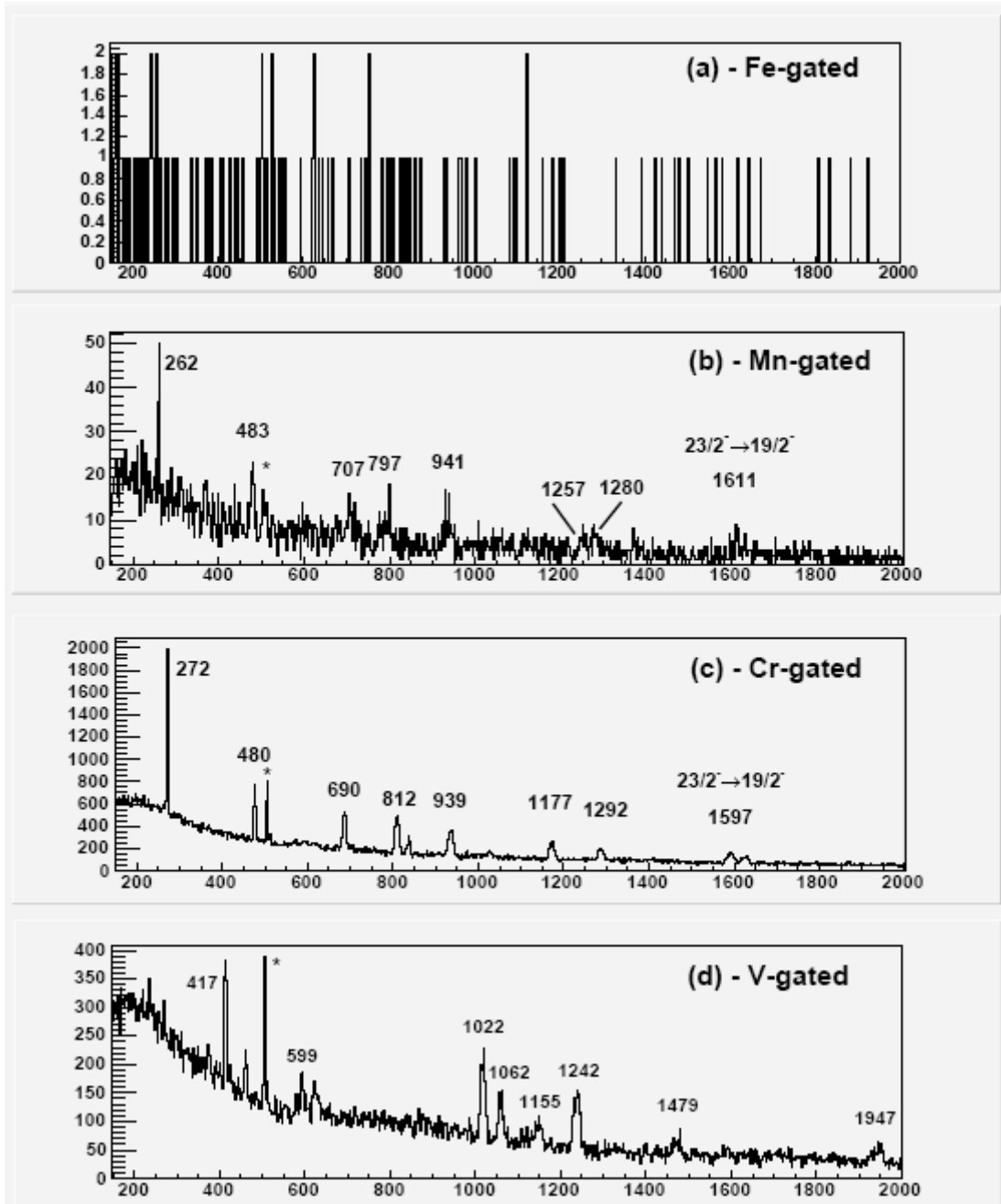


Fig. I-26. Gamma-ray spectra from the single clover detector located at 90 degrees to the beam direction. All the spectra were gated by a 2D region of the ET^2 vs. A/Q plot corresponding to $A = 49$ recoils. The individual spectra are also gated by regions of the E/DE map corresponding to (a) Fe, (b) Mn, (c) Cr and (d) V. The marked transitions are known gamma rays in the relevant $A = 49$ isobars - (b) ^{49}Mn , (c) ^{49}Cr and (d) ^{49}V . The * symbol indicates the 511 keV transition.

d.2.4. Shape Co-Existence in ^{71}Br and the Question of the Groundstate Spin of ^{71}Kr (S. M. Fischer, C. J. Lister, D. P. Balamuth,* P. A. Hausladen,* T. Anderson,† D. Svelnys,† G. Mesoloras,† and D. G. Sarantites‡)

When the $N = Z$ line approaches the proton dripline above ^{56}Ni an increasing distortion of mirror symmetry is expected as the proton rich partner becomes marginally bound. Urkedal and Hamamoto¹ have considered ^{71}Kr and suggest the distortion could lead to a different groundstate spin to its mirror partner ^{71}Br , based on the reinterpretation of a β -decay measurement. This would be a unique situation in $T = 1/2$ nuclei. We have performed a new "inbeam" spectroscopic measurement of ^{71}Br , following the $^{40}\text{Ca}(^{40}\text{Ca}, 2\alpha p)$ reaction at 160 MeV and using Gammasphere. Many new states have been found, with candidates for eight Nilsson bandheads below 1 MeV. Cross-linking decays tightly constrain most of the angular momentum assignments. The ^{71}Kr β -decay data, seen in the light of this new information on ^{71}Br , support the original

groundstate assignment of ^{71}Kr as $J^\pi = 5/2^-$, and as would be normally expected for the mirror partner of $J^\pi = 5/2^-$ ^{71}Br .

This research is now complete and a long paper has been published in Phys. Rev. C.² The investigation revealed the importance of comparing ^{71}Br to its mirror, ^{71}Kr . This $A = 71$ mirror pair is rather special, as an isomer allows ultra-sensitive clean, Doppler free spectroscopy between beam bursts. The ^{71}Br isomer decay is shown in Fig. I-27. Predictions for the analogous isomer in ^{71}Kr show sensitivity to the charge-symmetry-breaking "Electromagnetic-Spin-Orbit" effect, V_{eso} . Estimates indicate the isomer is lowered in ^{71}Kr by ~ 250 keV, close to 500 keV and with a half-life of several hundred ns. A proposal for an optimized experiment has been accepted by the ATLAS PAC.

*Pennsylvania State University, †DePaul University, ‡Washington University.

¹P. Urkedal and I. Hamamoto, Phys. Rev. C **58**, R1889 (1998).

²S. M. Fischer *et al.*, Phys. Rev. C **72**, 024321/1-16 (2005).

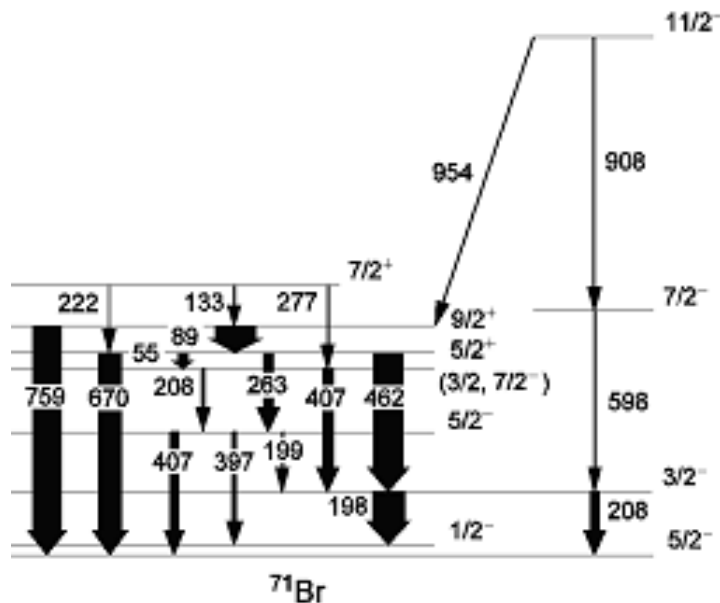


Fig I-27. The low lying levels in ^{71}Br . The $T_{1/2} = 33$ ns isomer allows ultra sensitive Doppler-free spectroscopy. In this case, three doublets of transitions were discovered, leading to a considerably modified sequence of levels. This is a perfect laboratory for testing for violation of Mirror Symmetries.

d.2.5. Fast Alpha Decays Above ^{100}Sn (A. A. Hecht,* C. J. Lister, C. N. Davids, D. Seweryniak, S. Zhu, N. Hoteling,† J. Palombo,† J. Shergur,† W. B. Walters,† P. J. Woods,‡ A. Heinz,§ and C. Mazzocchi¶)

Since the initial discovery of groundstate alpha decays immediately above ^{100}Sn ,¹ in tellurium isotopes, the possibility of enhanced “superallowed” alpha decays has been often discussed. Briefly, the concept is that near the $N = Z$ line the valence particles all occupy the same orbits, so alpha preformation should be enhanced relative to the classic cases of spherical alpha decay beyond ^{208}Pb , for example in ^{212}Po . Consequently, the reduced alpha-decay widths might be very large. Despite these possible large alpha-widths, the decay Q-values are quite modest and the absolute alpha decay rates are not high, so strong competition from β -decay usually occurs which makes experimental measurements difficult. Further, the nuclei lie far from stability, and the most interesting cases, those with $N \sim Z$ lie at or even beyond the proton dripline, so can only be produced with low cross-section reactions. A number of alpha emitters beyond ^{100}Sn have now been found, most recently the decay of ^{114}Ba .^{2,3} The experiments at GSI used an ISOL technique to separate ions and measure the decay modes. This technique is very sensitive, especially when molecular species are extracted from the ion source, but has limitations in extracting very short-lived ions. We have attempted to push close to the $N = Z$ line by using the Argonne Fragment Mass Analyzer (FMA) to separate ions in-flight and enhance sensitivity for decays in the μs and ms half-life ranges.

Two experiments were attempted. First, the $^{58}\text{Ni}(^{58}\text{Ni},3n)^{113}\text{Ba}$ reaction was studied at 250 and 260 MeV. This channel was estimated to have a cross-section ~ 5 nb. Ions were mass separated by the FMA and implanted into a 80×80 strip silicon DSSD. The advantage of this study is the parent is expected to be relatively long (~ 100 ms),^{4,6} but is followed by fast subsequent alpha decays of the daughter (^{109}Xe),⁷ so implant-decay-decay correlations could be used. The disadvantage of this study is the long lifetime implies severe competition from β -decay that steals flux from the interesting

alpha-decay channels. The second experiment was to form ^{109}Xe directly, using the $^{54}\text{Fe}(^{58}\text{Ni},3n)$ reaction at 240 MeV. Here, the expected decay energy is higher, so the half-life is expected to be shorter (~ 10 ms), reducing competition from β -decay. However, the daughter decay, that of ^{105}Te , is expected to be very fast, ~ 1 μs , so may pile-up with the decay of the parent, and suppress implant-decay-decay correlations. This strongly reduces the sensitivity of the experiment.

The experiments ran smoothly and large data sets were collected for both experiments. The former experiment ran for 89 hours with an average beam current of 9 pna. The latter study ran for 24 hours with an average current of 6 pna. Targets were ~ 0.5 mg/cm^2 and the FMA transport efficiency for a single charge state was estimated as 8%. Both reactions produced known alpha emitters in other reaction channels which could be used to verify the correct functioning of the experiment. Data analysis is still in progress. However, no clear candidates for either of the $N = Z + 1$ emitters ^{113}Ba nor ^{109}Xe could be identified, despite the fact that our estimates indicated 10-100s of decays should have been observed. It is possible that at the beam energies these experiments were run at the “3n” evaporation channel was much weaker than predicted by evaporation calculations re-scaled to experimental data. However, it would have to be < 1 nb to provide a satisfactory explanation. Reaching far from stability by multi-neutron evaporation is essential for dripline spectroscopy, especially for studying nuclei immediately around ^{100}Sn , so this reaction mechanism issue needs further investigation. In the case of ^{113}Ba , strong competition from β -decay may have suppressed our observation of decay correlations. In the case of ^{109}Xe decays, searches for implant-decay and implant-summing events were made, but the lack of granddaughter correlations greatly reduced our sensitivity.

This research is continuing with a goal to establishing firm limits on production cross-sections and on possible decay modes.

*Argonne National Laboratory and University of Maryland, †University of Maryland, ‡University of Edinburgh, United Kingdom, §Yale University, ¶Oak Ridge National Laboratory.

¹R. D. McFarlane and A. Siivols, Phys. Rev. Lett. **14**, 14 (1965).

²A. Guglielmetti *et al.*, Phys. Rev. C **56**, R2912 (1997).

³C. Mazzocchi *et al.*, Phys. Lett. **B352**, 29 (2002).

⁴S. Liran and N. Zeldes, At. Data and Nucl. Data Tables **17**, 431 (1976).

⁵P. Moller, J. R. Nix, and K.-L. Kratz, *ibid* **66**, 131 (1997).

⁶J. O. Rasmussen, *Phys. Rev.* **113**, 1593 (1959).

⁷G. Audi *et al.*, *Nucl. Phys.* **A729**, 337 (2003).

d.2.6. Discovery of the Deformed Proton Emitter ^{121}Pr (C. N. Davids, D. Seweryniak, M. P. Carpenter, R. V. F. Janssens, D. Peterson, S. Sinha, S. Zhu, A. P. Robinson,* P. J. Woods,* A. A. Hecht,† J. Shergur,† and W. B. Walters†)

Ground state proton radioactivity has been identified in ^{121}Pr . 240 MeV ^{36}Ar beams were used to bombard a 0.7 mg/cm² thick ^{92}Mo target, and produced ^{121}Pr via the $1p6n$ fusion-evaporation channel. The recoiling nuclei were separated from the primary beam and other contaminants by the FMA, and implanted into a double-sided silicon strip detector (DSSD). Figure I-28 shows the energy spectrum for decay events in the DSSD occurring within 30 ms of an $A = 121$ recoil being implanted into the same quasi-pixel. The protons have an energy of

882(5) keV, and decay with a half-life of 10^{+6}_{-3} ms. The estimated production cross-section is ~ 300 pb. Calculations indicate that the observed decay rate is consistent with the proton occupying either the $K = 3/2^+[422]$ or $K = 3/2^-[541]$ deformed Nilsson orbital. Other nearby orbitals with $K = 1/2^+[420]$ or $K = 9/2^+[404]$ give calculated decay half-lives more than an order of magnitude too short or too long, respectively.

This work has been published as a Physical Review Letter.¹

*University of Edinburgh, United Kingdom, †University of Maryland.

¹A. P. Robinson, P. J. Woods, D. Seweryniak, C. N. Davids, M. P. Carpenter, A. A. Hecht, D. Peterson, S. Sinha, W. B. Walters, and S. Zhu, *Phys. Rev. Lett.* **95**, 032502/1-4 (2005).

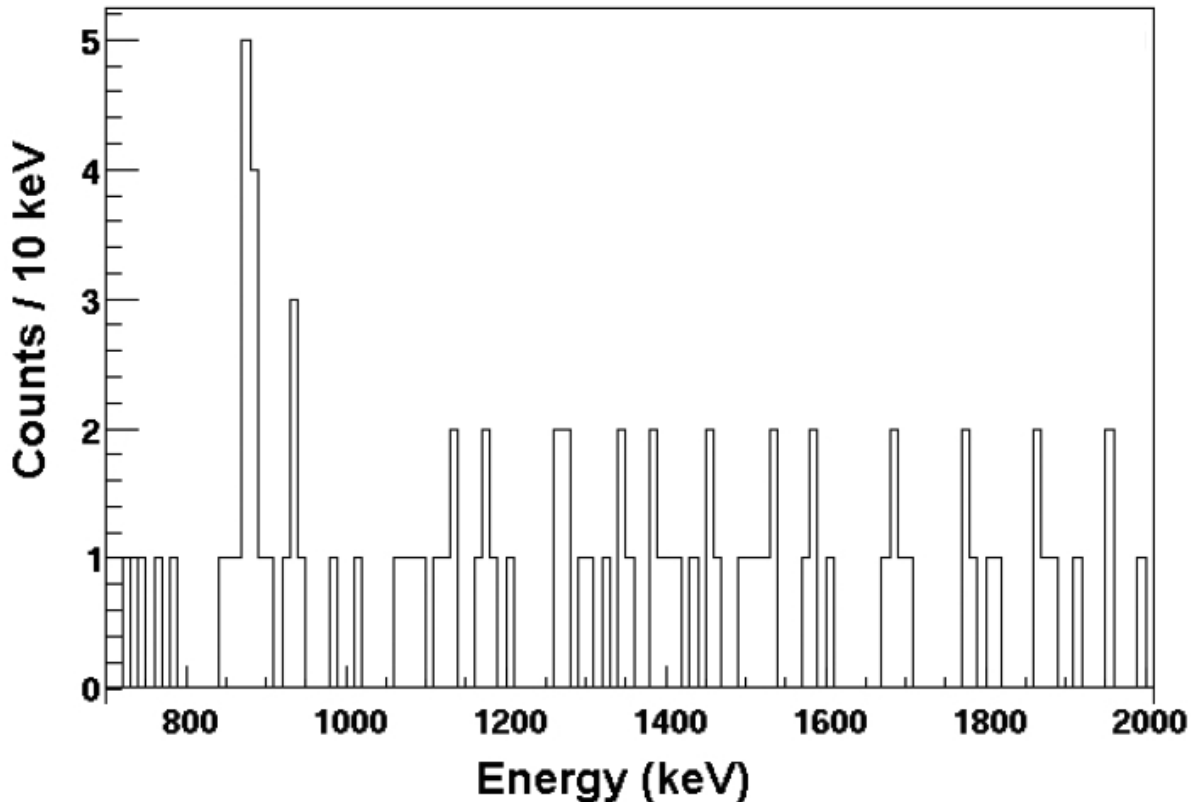


Fig. I-28. Decays in the DSSD produced using a 240 MeV ^{36}Ar beam to bombard a ^{92}Mo target, within 30 ms of implantation into a DSSD quasi-pixel. The ground-state proton decay peak of ^{121}Pr falls at an energy of 882(5) keV.

d.2.7. Recoil-Decay Tagging Study of ^{146}Tm (C. N. Davids, D. Seweryniak, B. Blank, M. P. Carpenter, N. Hammond, R. V. F. Janssens, G. Mukherjee, S. Sinha, A. Robinson,* P. J. Woods,* T. Davinson,* Z. Liu,* S. J. Freeman,† N. Hoteling,‡ J. Shergur,‡ W. B. Walters,‡ A. Woehr,‡ C. Scholey,§ and A. A. Sonzogni¶)

^{146}Tm is an odd-odd proton emitter which lies in the transitional region between predicted deformed and near-spherical shapes. It is potentially a rich source of information regarding the role of the odd neutron in proton decay. The improved statistics in this experiment allow some of the long-standing difficulties with the level scheme of ^{146}Tm to be addressed. A tentative decay scheme is shown in Fig. I-29. The most intense ~ 200 ms 1122 keV transition is assigned as an $l = 5$ transition from a $(10^+, 9^+, 8^+)$ state based on the $\pi h_{11/2} \nu s_{1/2}$ configuration, which agrees with previous work. As in previous work the 1192 keV transition is assigned as an $l = 5$ transition from a $(6^-, 5^-)$ state based on the $\pi h_{11/2} \nu s_{1/2}$ configuration to the ground state of ^{145}Er . From the present half-life measurements it appears that the 937 keV, 1010 keV and 1192 keV transitions occur from the same state, with a half-life of ~ 80 ms. The neighboring $N = 77$ isotones have a number of low lying $3/2^+$ and $5/2^+$ states below the $11/2^-$ state. On the basis of this, and the delayed γ -rays seen in coincidence with the 937 keV and 1010 keV transitions (see Fig. I-30) the 937 keV and 1010 keV transitions are assigned as decays from the $(6^-, 5^-)$ state in ^{146}Tm to low lying $(5/2^+)$ and $3/2^+$ states in

^{145}Er . This is the first example of decay to 3 states in the daughter nucleus from a proton emitter. The placement of the 892 keV transition is more problematic. It has previously been assigned as a decay from the (10^+) isomeric state in ^{146}Tm to a $9/2^-$ state in ^{145}Er , however this assignment would require a significant admixture of the $\pi f_{7/2}$ orbital to the emitter wave function. An alternative assignment could be the $l = 0$ decay of a low lying (1^+) state in ^{146}Tm to the ground state of ^{145}Er . A similar state is seen in neighboring odd-odd isotopes.

The recoil-decay tagged prompt γ -ray spectra (not shown) correlated with the 892 keV and 1122 keV transitions also provide information on the origin of the 892 keV particle group. Despite the low statistics in the 892 keV spectrum, it does not contain the most intense transition correlated with the 1122 keV spectrum. This suggests that the decays occur from two separate states in ^{146}Tm , rather than from the same state as in earlier work. The absence of delayed γ -rays in coincidence with the 892 keV transition suggests that the decay is to the ground state. A comparison of experimental partial proton decay half-lives with detailed theoretical calculations is needed to fully determine the structure of ^{146}Tm .

*University of Edinburgh, United Kingdom, †University of Manchester, United Kingdom, ‡University of Maryland, §University of Jyväskylä, Finland, ¶Brookhaven National Laboratory.

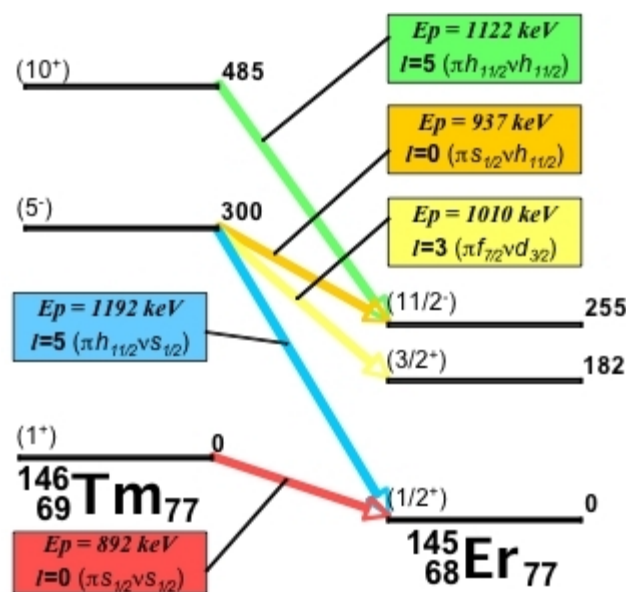


Fig. I-29. Tentative proton decay scheme for ^{146}Tm .

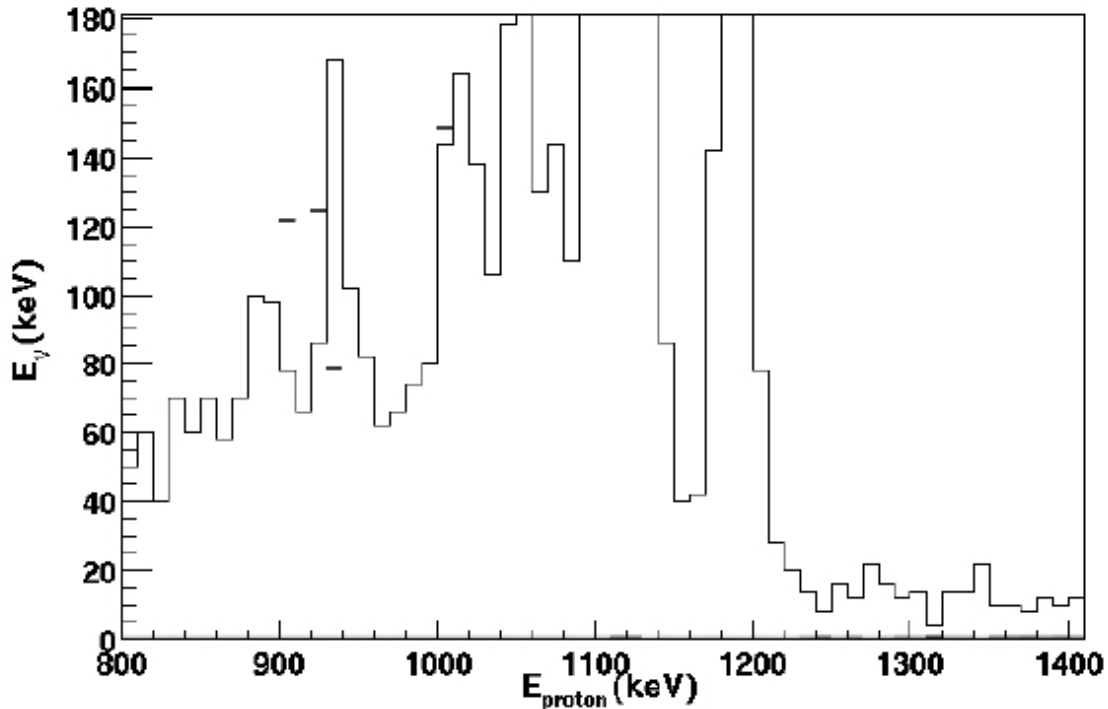


Fig. I-30. Delayed γ -rays in coincidence with particle decays detected at the FMA focal plane. The (4) events detected are shown as horizontal lines. The particle decay spectrum is shown overlaid.

d.2.8. Multi-Particle Configurations in $N = 84$ Isotones Located at the Proton Drip-Line (D. Seweryniak, J. Uusitalo, M. P. Carpenter, C. N. Davids, R. V. F. Janssens, T. Lauritsen, C. J. Lister, D. Nisius, P. Reiter, P. Bhattacharyya,* J. A. Cizewski,† K. Y. Ding,‡ N. Fotiades,§ A. O. Macchiavelli,¶ W. B. Walters,|| and P. J. Woods**)

Excited states in the proton rich $N = 84$ isotones ^{156}Hf , ^{157}Ta , and ^{158}W , were observed using $^{102}\text{Pd}(^{58}\text{Ni}, xp2n)$ reactions at 270 MeV. Gamma rays were detected with the Gammasphere array of Compton suppressed Ge detectors coupled with the Argonne fragment mass analyzer, and were assigned to individual reaction channels using the recoil-decay tagging method. Prompt γ -ray cascades were

associated with the α decay of both the ground state and the 8^+ isomeric state in ^{156}Hf , the $h_{11/2}$ state in ^{157}Ta , and the 8^+ isomeric state in ^{158}W . The level schemes were constructed for ^{156}Hf , ^{157}Ta , and ^{158}W . The details of the data analysis and the comparison between the proposed level schemes with the lighter $N = 84$ isotones and the shell model calculations were published in Ref. 1.

*Purdue University, †Argonne National Laboratory and Rutgers University, ‡Rutgers University (present address: Telecordia Technology, Piscataway, NJ 08854), §Rutgers University (present address: Los Alamos National Laboratory), ¶Lawrence Berkeley National Laboratory, ||University of Maryland, **University of Edinburgh, United Kingdom

¹D. Seweryniak, J. Uusitalo *et al.*, Phys. Rev. C **71**, 054319 (2005).

d.2.9. Alpha Decay of ^{181}Pb (M. P. Carpenter, F. G. Kondev, R. V. F. Janssens, I. Ahmad, C. N. Davids, N. J. Hammond, T. L. Khoo, T. Lauritsen, C. J. Lister, G. Mukherjee, D. Seweryniak, S. Sinha, D. G. Jenkins,* P. Raddon,* R. Wadsworth,* S. J. Freeman,† S. M. Fischer,‡ G. Jones,§ A. J. Larabee,¶ and A. Liechty¶)

With the return of Gammasphere to ATLAS, we have continued our program to look at proton-rich nuclei in the vicinity of the $Z = 82$ closed proton shell. One of recent measurements utilized the $^{90}\text{Zr} + ^{92}\text{Mo}$ reaction to produce ^{181}Tl and ^{181}Pb via the $1p$ and $1n$ channel, respectively. For this measurement, Gammasphere was coupled with the FMA to characterize both the ground and excited states in these two nuclei. At the focal plane of the FMA, the PGAC measured the mass, the DSSD detected the energies of both implants and the α particles emitted from the decay of the implanted ions and associated daughter nuclides. In addition four Ge detectors surrounded the DSSD in order to measure γ rays in coincidence with detected particles.

^{181}Pb with $N = 99$ is the lightest odd-A Pb isotope identified thus far. In our measurement, we observe two α lines at 7015(10) and 7075(10) keV with nearly equal intensity. Both of these decays are correlated with the 6580-keV α decay of ^{177}Hg . Our observations are in contrast to a previous result which reported observing only one α line at 7065 keV.¹ In addition, the 7015 keV α line is in coincidence with a 77 keV γ ray. This γ ray has been identified previously, resulting from the decay of an excited $9/2^-$ state to the $7/2^-$ ground state in ^{177}Hg .² Both α lines have the same half-life, 39.6 ± 0.9 msec, suggesting that both are associated with the decay of the ^{181}Pb ground state. While it is clear that the 7015 keV α feeds the $9/2^-$ state in ^{177}Hg , an α -decay feeding

directly the ground state in ^{177}Hg would have an energy of ~ 7088 keV. In addition, a 78-keV M1 transition is highly converted with a conversion coefficient of around four. Since the K threshold for $Z = 80$ is at 90 keV, the majority of the emitted electrons emanate from the L-shell resulting in electron energies of ~ 60 keV which is the energy difference between the two observed α lines. Factoring all of this information together, it appears that the 7075 keV α results from the sum of the 7015 keV α and the electron emitted during the conversion process. In conclusion, we observe only one α decay coming from the ground state in ^{181}Pb and feeding the lowest $9/2^-$ state in ^{177}Hg . As a result, the ground state of ^{181}Pb must be $9/2^-$ as well. This is in contrast to the heavier odd-A Pb isotopes, where two α -decaying states have been identified and associated with a high-spin ($13/2^+$) isomer state and a low-spin ($3/2^-$) ground state.

This change in the ground state results from the fact that the $p_{1/2}$, $p_{3/2}$, $f_{5/2}$ and $i_{13/2}$ orbitals should be emptied at $N = 100$. Below $N = 100$, one begins to empty either the $h_{9/2}$ or $f_{7/2}$ shell. Our measurements show that at $N = 99$, the $h_{9/2}$ orbital lies above the $f_{7/2}$, which has been experimentally determined for the first time. This can be contrasted to ^{207}Pb where the ordering in energy is reversed. In addition, this result shows that the $7/2^-$ ground states in $^{177}\text{Hg}^2$ ($N = 97$) and $^{179}\text{Hg}^3$ ($N = 99$) are built on weakly deformed prolate shapes as opposed to spherical states where the expected spin/parity would be $9/2^-$ as in ^{181}Pb .

*University of York, United Kingdom, †University of Manchester, United Kingdom, ‡DePaul University,

§University of Liverpool, United Kingdom, ¶Greenville College.

¹K. S. Toth *et al.*, Phys. Rev. C **53**, 2513 (1996).

²A. Melerangi *et al.*, Phys. Rev. C **68**, 041301(R) (2003).

³F. G. Kondev *et al.*, Phys. Lett. **B528**, 221 (2002).

d.2.10. Level Structure of ^{181}Tl (M. P. Carpenter, F. G. Kondev, R. V. F. Janssens, I. Ahmad, C. N. Davids, N. J. Hammond, T. L. Khoo, T. Lauritsen, C. J. Lister, G. Mukherjee, D. Seweryniak, S. Sinha, D. G. Jenkins,* P. Raddon,* R. Wadsworth,* S. J. Freeman,† S. M. Fischer,‡ G. Jones,§ A. J. Larabee,¶ and A. Liechty¶)

With the return of Gammasphere to ATLAS, we have continued our program to look at proton rich nuclei in the vicinity of the $Z = 82$ closed proton shell. One of

our most recent experiments utilized the $^{90}\text{Zr} + ^{92}\text{Mo}$ reaction to produce ^{181}Tl and ^{181}Pb via the $1p$ and $1n$ channel, respectively. For this measurement,

Gammasphere was coupled with the FMA to characterize both the ground and excited states in these two nuclei. At the focal plane of the FMA, the PGAC measured the mass, the DSSD detected the energies of both the implants and the α particles emitted during the decay of the implanted ions. In addition, four Ge detectors surrounded the DSSD in order to measure γ rays in coincidence with detected particles.

The mid-shell Tl isotopes mimic the mid-shell Pb isotopes in that structures built on spherical, oblate and prolate shapes have been established in $^{183,185,187}\text{Tl}$.¹⁻³ A comparison of the excitation energy of single-particle states associated with the different shapes shows that the excitation energy of the $13/2^+$ prolate state continues to decrease as one approaches mid-shell ($N = 102$) while the oblate structure built on the $h_{9/2}$ orbital minimizes in excitation energy at $N = 108$ and rises in energy with decreasing neutron number. In all of these isotopes the ground state remains spherical. It is an open question whether this same trend continues beyond mid-shell.

In the analysis of our Gammasphere experiment, we have followed the de-excitation of the $i_{13/2}$ prolate band in ^{181}Tl down to the 1 msec isomer built on the $9/2^-$ oblate state. Based on our RDT measurements, most of the decay of this isomer precedes via γ emission to the ground state while a small α decaying branch directly feeds an excited $9/2^-$ state in the daughter nucleus, ^{177}Au . Unfortunately, our measurement was not sensitive to the γ decay of the isomer to the spherical ground state. However, in a recent measurement with the FMA and two clover detectors placed at its focal plane, we were able to measure the gamma decay of this isomer and thus establish its excitation energy at 834 keV. A partial level scheme of our results is given in Fig. I-31 showing the gamma decay path starting from the $i_{13/2}$ rotational down to the ground state. These results establish that both the oblate structure and the $i_{13/2}$ prolate band rise in excitation energy when compared to the same states in ^{183}Tl . In the case of the prolate structures, this is the same trend observed for the prolate bands in the even-even Pb and Hg isotopes.

*University of York, United Kingdom, †University of Manchester, United Kingdom, ‡DePaul University, §University of Liverpool, United Kingdom, ¶Greenville College.

¹W. Reviol *et al.*, Phys. Rev. C **61**, 044310 (2000).

²M. Muikku *et al.*, Phys. Rev. C **64**, 044308 (2002).

³G. J. Lane *et al.*, Nucl. Phys. **A586**, 316 (1995).

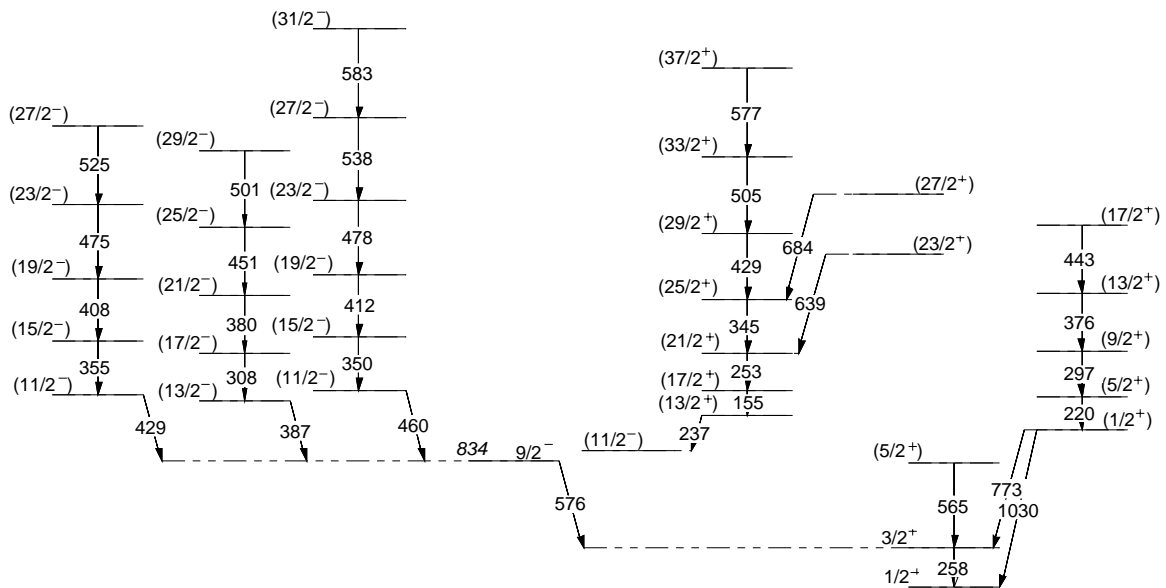


Fig. I-31. Partial level scheme for ^{181}Tl deduced from this work.

E. OTHER NUCLEAR STRUCTURE RESEARCH

Gammasphere at ATLAS allows a full program of gamma-ray spectroscopy to be explored. “Two-beamline” operation has allowed both the FMA and Gammasphere projects to be productive. A wide variety of programs continue at Gammasphere, including studying hot nuclei and studying nuclei at the very highest angular momenta.

e.1. Investigation of $^{12}\text{C}(^{12}\text{C},\gamma)^{24}\text{Mg}$ Radiative Capture (C. J. Lister, N. Hammond, D. Jenkins,[†] P. Chowdhury,[‡] and D. Hutcheon[§])

The $^{12}\text{C} + ^{12}\text{C}$ reaction has a historic role in heavy ion physics, as the strongly resonant scattering and fusion cross-sections offered the promise of exotic new phenomena like “nuclear molecules” and elongated cluster configurations. A great deal of effort was put into measuring and understanding the resonances. One line of investigation, through the energy dependence of radiative capture (the complete fusion of the ions without emission of particles) clearly indicated a direct connection between some of the resonances and states in the fused compound system, ^{24}Mg .^{1,2}

The original radiative capture experiments measured “one-step” decays, emission of ~ 20 MeV photons which cooled the nucleus from the compound nuclear state to the ground (or low-lying) states. The cross-sections were small, $\ll 1 \mu\text{b}$, and attributed to enhanced radiation from part of the giant quadrupole resonance. For twenty years it has remained an open question as to whether this mechanism is the dominant process in radiative capture, and if more information can be learned either about the fusion reaction mechanism or about the structure and shapes of states involved in the fusion and cooling process.

We have conducted a series of experiments using Gammasphere, using the Argonne Fragment Mass Analyzer (FMA) and using the DRAGON separator at the ISAC facility at TRIUMF in Canada. Considerable progress has been made, and a paper

published³ on some of our findings. In short, for the resonances populated near 16 MeV in beam energy, thought to have angular momentum $J \sim 4$.

- The fusion cross-section, inferred from measuring ^{24}Mg residues, is considerably larger than the “1-step” channel observed by Nathan and Sandorfi.² The enhancement is energy dependent, but is usually >5 times stronger.
- The major radiative capture flux passes through a few doorway states at ~ 11 MeV in excitation in ^{24}Mg . These states are only a few of the many that could be populated at this energy. Gamma ray calorimetry confirmed the finding of large radiative capture cross-section, and allowed doorway states to be identified.
- The arrival at low spin is also selective, with population of the $K = 2$ excited band much stronger than the ground-state band.

The experiment at the DRAGON facility concentrated on studying near barrier resonances at energies of 12.0, 13.4 and 15.8 MeV. An array of BGO counters triggered by identified $A = 24$ residues was used to study the gamma-decay. The findings were similar to the higher energy experiment: that the main radiative capture mechanism was dominated by multi-step decays. Online analysis suggested the same doorway states were involved at all beam energies, but this effect is still being studied. These data are undergoing analysis.

[†]University of York, United Kingdom, [‡]University of Massachusetts-Lowell, [§]TRIUMF, Vancouver, British Columbia.

¹A. M. Sandorfi and A. M. Nathan, Phys. Rev. Lett. **40**, 1252 (1978).

²A. M. Sandorfi in *Treatise on Heavy Ion Science*, Vol. 2, Sect. 2, ed. D. A. Bromley (Plenum Press, New York 1984).

³D. G. Jenkins *et al.*, Phys. Rev. C **71**, 041301(R)/1-5 (2005).

e.2. Variation with Mass of $B(E3; 0^+ \rightarrow 3^-)$ Transition Rates in $A = 124-134$ Even-Mass Xenon Nuclei (M. P. Carpenter, D. T. Henderson, R. V. F. Janssens, C. J. Lister, E. F. Moore, T. O. Pennington, W. F. Mueller,* J. A. Church,* D. C. Dinca,* A. Gade,* T. Glasmacher,* Z. Hu,* A. F. Lisetskiy,* H. Olliver,* B. C. Perry,* I. Wiedenhöver,‡ and K. L. Yurkewicz*)

Three years ago, an experiment at ATLAS measured transition matrix elements for even-mass $^{124-134}\text{Xe}$ nuclei using sub-barrier Coulomb excitation in inverse kinematics. These xenon isotopes are located in a transitional region where the dominant structure evolves from a weakly-deformed, gamma-soft rotor to a vibrator. The description of these nuclei represents a stringent test of theoretical models.

Thus far, the analysis has focused on the excitation of the 3^- state. For the determination of the electromagnetic transition matrix elements, the angle-dependent gamma-ray yields were analyzed using the Coulomb excitation code GOSIA, which combines the semi-classical theory of multiple Coulomb excitation and the measured gamma-ray deexcitation patterns with a numerical least-squares analysis to determine the electromagnetic matrix elements from the experimental gamma-ray yields. In addition to the gamma-ray yields determined in the present experiments, gamma-ray branching ratios and multipole mixing ratios found in the literature for relevant transitions were used when ever possible as additional information to constrain the determination of the matrix elements further. The measured $B(E2; 0^+ \rightarrow 2^+)$ and $B(E3; 0^+ \rightarrow 3^-)$ transition rates are presented as a function of mass in Fig. I-32 and a

number of features are readily visible. First, the $B(E2)$ values decrease steadily from the lighter to the heavier Xe isotopes, illustrating a drop in collectivity as the $N = 82$ shell closure is approached. In contrast, the $B(E3)$ rates remain relatively constant for $^{124,126,128}\text{Xe}$, but exhibit a marked drop in strength for the next three isotopes $^{130-134}\text{Xe}$, while a large return in collective octupole strength occurs for ^{136}Xe .

Calculations with the Quasiparticle Phonon Model (QPM)¹ have been carried out in an attempt to understand the data. As can be seen in Fig. I-32, the generally decreasing trend in $B(E2)$ values toward heavier xenon isotopes is reproduced, but the overall strength is overpredicted in the heaviest nuclei. Likewise, the calculated $B(E3)$ values for $^{124,126,128}\text{Xe}$ isotopes are in reasonable agreement with the data, but the dramatic drop in $E3$ strength for $^{130-134}\text{Xe}$ is not accounted for. The model suggests that, as the mass increases, the contributions to the $E3$ strength come increasingly from higher-energy 2-qp configurations, as well as from admixtures of 4-qp configurations, and/or multi-phonon excitations for which the model is rather schematic.

A paper reporting these results has been submitted for publication.²

*Michigan State University, †Florida State University.

¹V. G. Soloviev, *The Theory of Atomic Nuclei: Quasiparticles and Phonons*, Inst. of Phys. Publ., Bristol, 1992.

²W. F. Mueller *et al.*, submitted to *Phys. Rev. C*.

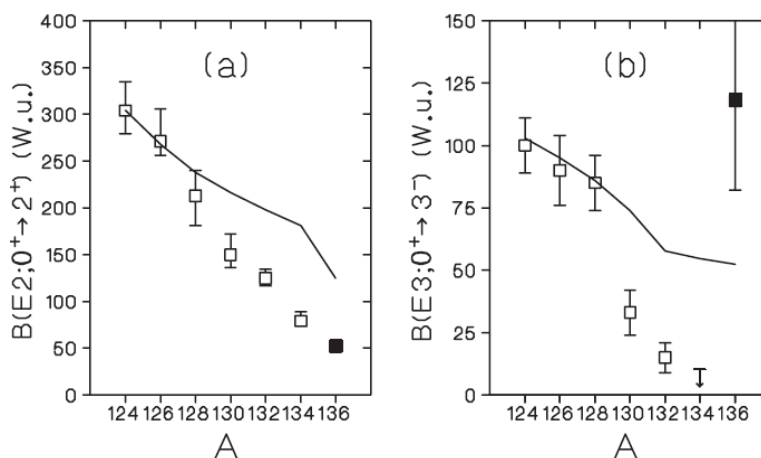


Fig. I-32. Comparison between measured reduced transition probabilities and calculations with the QPM model.

e.3. Rotational Damping, Ridges and the Quasicontinuum of γ Rays in ^{152}Dy

(T. Lauritsen, I. Ahmad, M. P. Carpenter, A. M. Heinz, R. V. F. Janssens, D. G. Jenkins, T. L. Khoo, F. G. Kondev, C. J. Lister, D. Seweryniak, P. Fallon,* A. O. Macchiavelli,* D. Ward,* R. M. Clark,* M. Cromaz,* G. Lane,* B. Herskind,† T. Døssing,† A. Lopez-Martens,‡ A. Korichi,‡ and S. Siem‡)

The effort to [i] understand the feeding and decay of superdeformed band 1 in ^{152}Dy , [ii] measure the ridges and quasicontinuum of gamma rays when gates are placed on discrete normal and superdeformed transitions and [iii] extract the rotational damping in the superdeformed and normal wells of the nucleus has progressed significantly.

We have now measured the entry distribution for the reaction $^{108}\text{Pd}(^{48}\text{Ca},4n)^{152}\text{Dy}$ at ^{194}MeV . The

measured entry distribution was subsequently the starting point for gamma cascades that are followed in Monte Carlo calculations which will attempt to simultaneously reproduce the ND and SD QC and ridge spectra. The calculation of the QC and ridge spectra allows for the extraction the rotational damping widths in the SD and ND wells of ^{152}Dy and will elucidate the feeding and decay of SD bands in the A 150 mass region. The measured total entry distribution is shown in Fig. I-33.

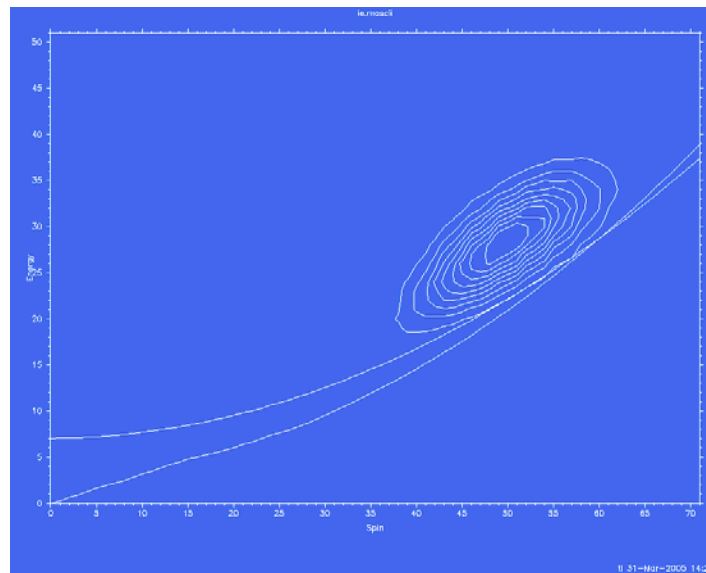


Fig. I-33. Measured (I,E) entry distribution for the gamma cascades that feed ND states above the 17^+ isomer in ^{152}Dy . The two lines are the ND and SD yrast lines used in the MC calculations. The yrast lines have been extrapolated where data was not available.

The Monte Carlo calculations have also been expanded to use more realistic (scaled) functions of the rotational damping parameters Γ_{rot} , Γ_{μ} and the fraction of narrow to wide component, I_{nar} , taken from theoretical models.¹ These distributions are now functions of spin and excitation energy over the yrast lines. Using these functions add known effects such as motional narrowing to the calculations as well as a spin dependence, especially of Γ_{rot} , and the strong dependence on excitation energy for all the rotational damping parameters.

The ridges and quasicontinuum of gamma rays gated on discrete normal and superdeformed transitions can be reproduced as well as when average values were used in the Monte Carlo calculations (see previous annual report). However, it was found that the theoretical functions had to be scaled as shown in Table I-2 in order to reproduce the measured ridge and quasicontinuum spectra. The rotational damping parameter values that are probed by the cooling gamma cascades are shown in Figs. I-34, I-35 and I-36.

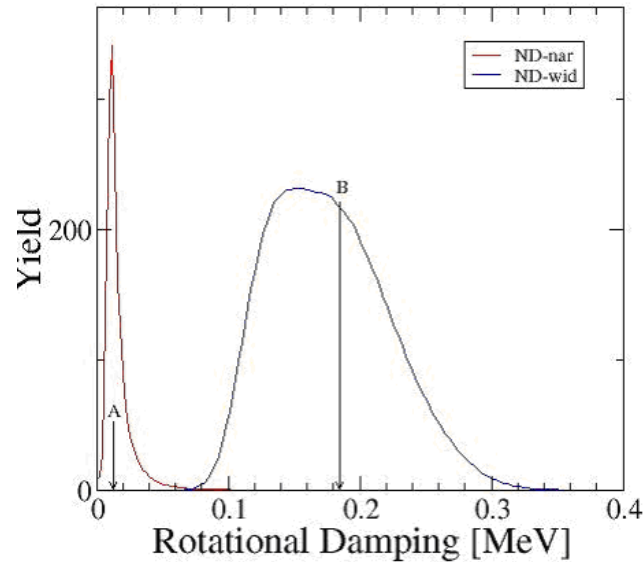


Fig. I-34. Distributions of narrow and wide rotational damping widths, Γ_{μ} and Γ_{rot} that are sampled by the gamma cascades in the ND well when gates are placed on clean combination of discrete ND lines. "A" and "B" marks the associated mean values that were obtained in the first MC1 calculations with average rotational damping parameters.

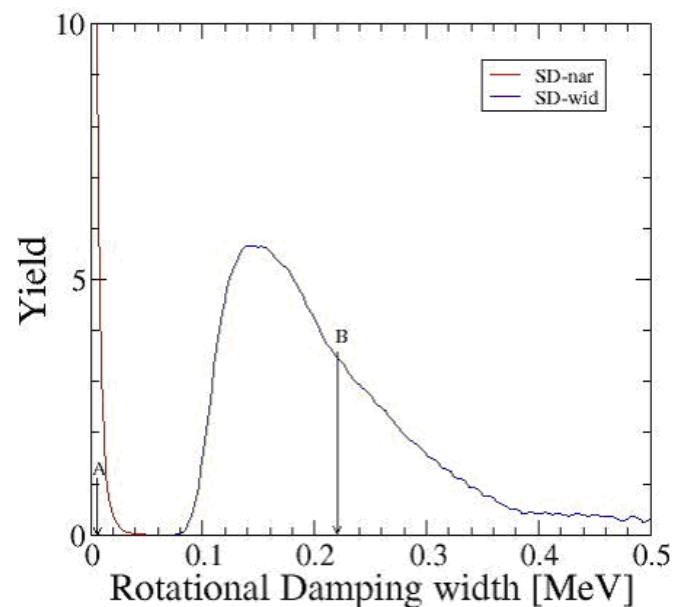


Fig. I-35. Distributions of narrow and wide rotational damping widths, Γ_{μ} and Γ_{rot} that are sampled by the gamma cascades in the SD well when gates are placed on clean combinations of discrete SD lines. The narrow fraction has been down scaled by a factor of 5 with respect to the wide components distribution. "A" and "B" marks the associated mean values that were obtained in the MC1 calculations with average rotational damping parameters.

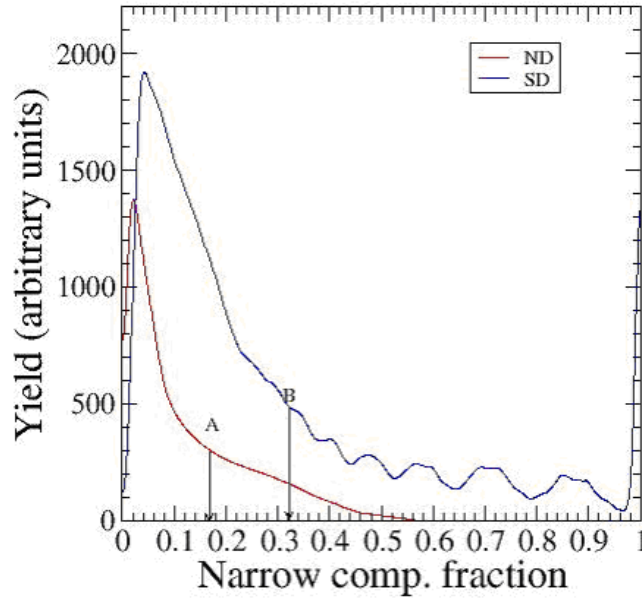


Fig. I-36. Distributions of narrow to wide rotational damping width fractions in the ND and SD wells. "A" and "B" marks the mean values that were obtained in the first MC calculations with average rotational damping parameters.

The SD entry distribution was also measured and is shown in Fig. I-37. Compared to the ND (I,E) entry distribution in Fig. I-33, the SD entry distribution is clearly moved towards higher spins and relative lower excitation energies. To show this effect more clearly a difference spectrum was generated by normalizing the SD and ND 2D spectra in Figs. I-37 and I-33, respectively, to have the same number of counts and subtracting the ND distribution from the SD distribution. The resulting 2D distribution is

shown in Fig. I-38 in a contour plot. Positive channels (solid lines) shows enhanced entry point selection and negative channels (dashed lines) shows areas of the total entry distribution in the (I,E) plane where gamma cascades that feed SD band ~ 1 are unlikely to start from. Obviously, the part of the entry distribution below the lowest of the two yrast lines in Fig. I-37 is unphysical and is attributed to uncertainties in the measurement of the entry distribution. The analysis is nearly complete and a first draft of a Phys. Rev. C article is almost ready.

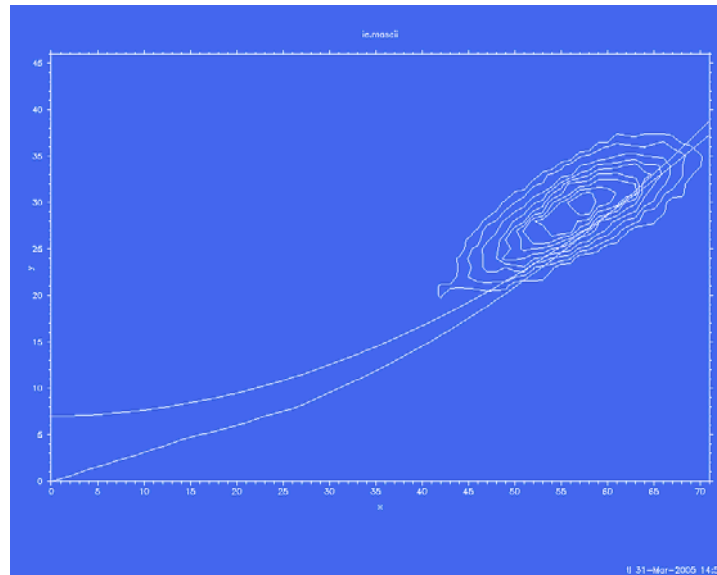


Fig. I-37. Measured (I,E) entry distribution for the gamma cascades that feed SD band 1 in ^{152}Dy . The mean entry spin and energy is $56.3 \hbar$ and 30.2 MeV .

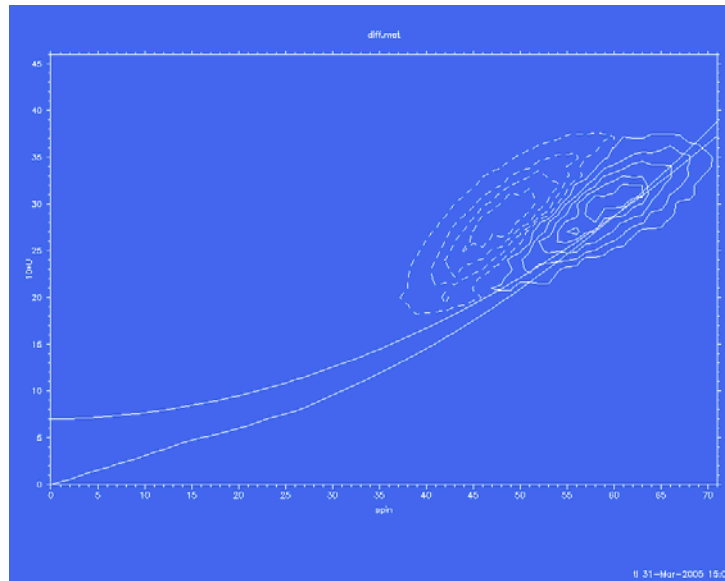


Fig. I-38. Normalized difference between the SD and ND entry distributions in ^{152}Dy .

Table I-2. In order to reproduce the ND and SD QC spectra and ridges in the MC calculation, it was necessary to multiply the theoretical rotational damping widths and narrow fractions with the factors shown in this table. Also shown are the resulting mean values of the distributions of Γ_{μ} , Γ_{rot} and I_{nar} . These are preliminary results, the analysis is still in progress.

Quantity	ND factor	ND mean val	SD factor	SD mean val
Γ_{μ}	0.08	16.8 keV	0.034	5 keV
Γ_{rot}	0.50	176 keV	5.5	220 keV
I_{nar}	40	12%	120	32%

*Lawrence Berkeley National Laboratory, †Niels Bohr Institute, Copenhagen, Denmark, ‡C.S.N.S.M., IN2P3-CNRS, Orsay Campus, France.

¹B. Lauritzen *et al.*, Nucl. Phys. **A457**, 61 (1986).

e.4. Study of Multi-Quasiparticle Isomers in the $A \sim 180$ Region Using Deep-Inelastic and Multi-Nucleon Transfer Reactions (I. Ahmad, M. P. Carpenter, S. J. Freeman, N. J. Hammond, R. V. F. Janssens, T. Lauritsen, C. J. Lister, G. Mukherjee, D. Seweryniak, F. G. Kondev,^{*} G. D. Dracoulis,[†] G. J. Lane,[†] A. P. Byrne,[†] T. Kibedi,[†] P. Nieminen,[†] H. Watanabe,[†] P. Chowdhury,[‡] and S. K. Tandel[‡])

A characteristic feature of many axially symmetric, deformed nuclei near $A \sim 180$ is the dominance of high- Ω orbitals in the vicinity of both the neutron and proton Fermi surfaces. This gives rise to the presence of multi-quasiparticle K-isomers with half-lives ranging from a few nanoseconds to hundreds of years. Most of the studies so far have focused on

neutron deficient structures that are accessible by heavy-ion fusion evaporation reactions. The information for nuclei near the valley of stability or on the neutron-rich side of it is rather scarce, despite the fact that this is the region where the longest lived isomers are known (and predicted) to reside, and hence, there is interest for various applications. The most notable examples include

the $K^\pi = 16^+$, 31-y isomer in ^{178}Hf and the $K^\pi = 23/2^-$, 160-d isomer in ^{177}Lu . Spectroscopic studies in this region provide important nuclear structure information on the limits of existence of high-K isomeric states at the extremes of proton and neutron numbers, and on the seniority dependence of the major residual interactions in deformed nuclei.

We have pursued studies using Gammasphere and 820 MeV pulsed ^{136}Xe beams on natural Lu and enriched ^{176}Lu , and $^{174,176}\text{Yb}$ targets aimed at identifying multi-quasiparticle states in nuclei near ^{176}Lu , and neighboring ytterbium, hafnium, and tantalum isotopes. The targets were approximately 6 mg/cm^2 in thickness backed by 25 mg/cm^2 Au foils. The choice of the beam energy ($\sim 20\%$ above the

Coulomb barrier) resulted in the population of a variety of structures near and beyond the line of stability in these nuclei via so-called multi-nucleon transfer and deep-inelastic reactions. Complementary experiments aimed at measuring the lifetimes of long-lived isomers were also carried out.

Many new high-seniority isomers have been identified and the results on the predicted 5-quasiparticle $K^\pi = 39/2^-$ isomer in ^{177}Lu ,¹ the 7-quasiparticle $K^\pi = 49/2^+$ isomer in ^{179}Ta that exhibits an unusually fast decay² (shown in Fig. I-39) and a suite of multi-quasiparticle isomers in ^{174}Yb ³ have already been published. A number of isomers and corresponding excited structures were also observed in nuclei near ^{176}Lu and ^{176}Yb . For these the data analysis is still in progress.

*Nuclear Engineering Division, Argonne National Laboratory, †Australian National University, Canberra, Australia,

‡University of Massachusetts-Lowell.

¹G. D. Dracoulis *et al.*, Phys. Lett. **B584**, 22 (2004).

²F. G. Kondev *et al.*, Eur. Phys. J. A **22**, 23 (2004).

³G. D. Dracoulis *et al.*, Phys. Rev. C **71**, 044326 (2005).

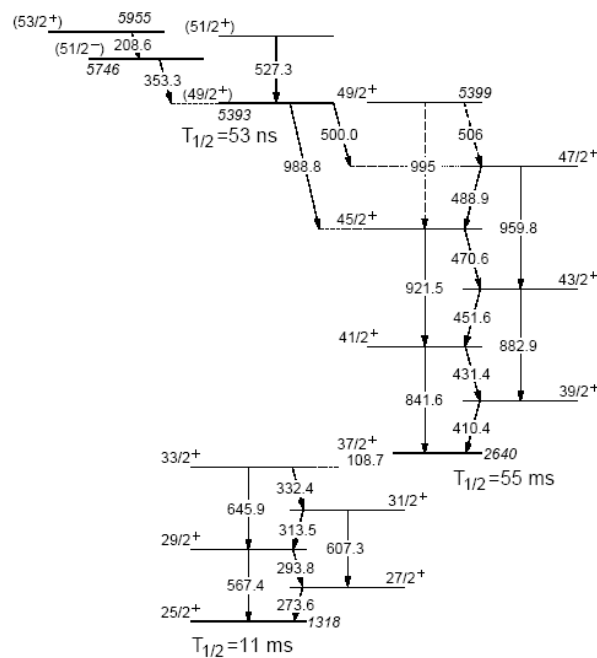


Fig. I-39. Partial level scheme of ^{179}Ta showing the decay of the $K^\pi = 49/2^+$ and previously known $37/2^+$ isomers.²

- e.5. Pair Gaps in the Normal- and Super-Deformed Wells of ^{191}Hg** (T. L. Khoo, T. Lauritsen, M. P. Carpenter, I. Ahmad, I. Calderin, T. Duguet, S. M. Fischer, D. Gassmann, G. Hackman, R. V. F. Janssens, E. F. Moore, D. Nisius, S. Siem,* P. Reiter,†† P.-H. Heenen,† H. Amro,‡ I. T. Døssing,§ U. Garg,¶ F. Hannachi,|| B. Kharraja,¶¶ A. Korichi,|| I.-Y. Lee,** A. Lopez-Martens,|| A. O. Machiavelli,** and C. Schück||)

Although about 250 superdeformed (SD) bands have been found in the $A = 150$ and 190 regions, the energies and quantum numbers have been determined for only a handful of SD bands. The excitation energies and spins of the yrast superdeformed band in ^{191}Hg have been found from two single-step γ transitions and the quasi-continuum spectrum connecting the superdeformed and normal-deformed states. This is the first case where the energies and spins of a SD band have been determined in an odd- A nucleus. The results are compared with those from self-consistent mean-field calculations with different Skyrme interactions. The SLy4 interaction gives better agreement with experiment than other interactions, such as SkP and SkM*.

By comparing the energies of normal-deformed (ND) and SD states in adjacent even-even and odd- A nuclei, we can extract information of the pair correlations in the respective wells. The neutron

separation energy contains information about the Fermi energy λ_N , the neutron pairing gap Δ^{pairing} , as well as a so-called polarization energy E^{pol} arising from occupying a single-particle level: $\Delta^{(2)} = (-1)^N S_n \sim \Delta^{\text{pairing}} + E^{\text{pol}} + (-1)^{N+1} \lambda_N$ where N is the number of valence neutrons. The masses of the normal- and super-deformed “ground-states” at zero rotational frequency in $^{191,192}\text{Hg}$ give $S_n = 9.5$ and $8.6\text{--}8.9$ MeV, for the ND and SD wells, respectively. In other words, it is easier to remove a neutron from the SD well. With λ_N taken from Hartree-Fock-Boglyubov theory with the Skyrme SLy4 interaction, we obtain $\Delta^{\text{pairing}} + E^{\text{pol}} = 1.1$ and $0.7\text{--}1.0$ MeV for ND and SD states. (E^{pol} is expected to be around ± 100 keV.) The latter value establishes that a pair gap exists for SD states, but the uncertainties are too large to determine that its value is smaller than that for ND states.

A paper on this work has been published.¹

*Argonne National Laboratory and University of Oslo, Norway, †Service de Physique Nucleaire Theorique, Brussels and Oak Ridge National Laboratory, ‡Argonne National Laboratory and North Carolina State University, §The Niels Bohr Institute, Copenhagen, Denmark, ¶University of Notre Dame, ||C.S.N.S.M., Orsay, France, **Lawrence Berkeley National Laboratory, ††University of Cologne, Germany.

¹S. Siem *et al.*, Phys. Rev. C **70**, 014303 (2004).

- e.6. Temperature and Spin Dependence of the Giant Dipole Resonance Width in $^{117,118}\text{Sn}$** (B. B. Back, M. P. Carpenter, T. L. Khoo, T. Pennington, D. J. Hofman,* P. Heckman,† T. Baumann,† I. Diószegi,† S. Mitsuoka,† V. Nanal,‡ J. P. Seitz,† M. Thoennesen,† E. Tryggestad,† and R. L. Varner§)

The dependence of the GDR width on temperature and spin was investigated in Sn nuclei, by using the reactions $^{17}\text{O} + ^{100}\text{Mo}$ and $^{18}\text{O} + ^{100}\text{Mo}$ to form ^{117}Sn and ^{118}Sn , respectively. Widths of $\Gamma = 6.9 \pm 0.5$ MeV and $\Gamma = 8.2 \pm 0.5$ MeV were extracted for temperatures of 1.74 and 1.84 MeV, respectively. The large increase of the width over this relatively small temperature range is inconsistent with the thermal shape fluctuation model. However, the spin

dependence of the width is well reproduced by the model. The experiment was performed with the LEPPEX BaF₂ array (from ORNL, MSU and TAMU) at ATLAS. Coincidences with evaporation residues detected in the Fragment Mass Analyzer selected exclusively γ rays following the decay of the compound nuclei $^{117,118}\text{Sn}$ – see Fig. I-40. This work constituted part of the thesis of P. Heckman at MSU.¹

*University of Illinois at Chicago, †Michigan State University, ‡Tata Institute of Fundamental Research, Mumbai, India, §Oak Ridge National Laboratory.

¹P. Heckman *et al.*, Nucl. Phys. A750, 175 (2005).

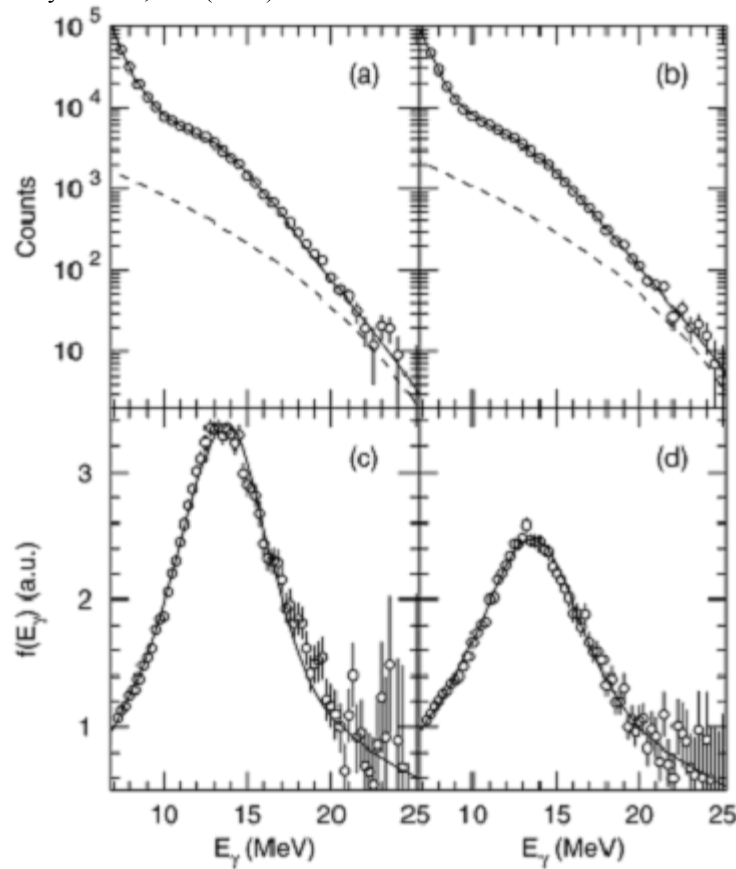


Fig. I-40. The open circles in panels (a) and (b) show the γ -ray decay spectra for the compound nuclei ^{117}Sn and ^{118}Sn , respectively. The open circles in panels (c) and (d) show the divided plots of $f(E_\gamma)$ for ^{117}Sn and ^{118}Sn , respectively. The solid curve in all panels shows the overall fit, while the dashed curve in panels (a) and (b) corresponds to the bremsstrahlung contribution.

e.7. Observation of the Hot GDR in Neutron-Deficient Thorium Evaporation Residues

(B. B. Back, M. P. Carpenter, M. P. Kelly, T. L. Khoo, R. H. Siemssen, T. Pennington, J. P. Seitz,* I. Diószegi,† K. Eisenman,* P. Heckman,* D. J. Hofman,‡ S. Mitsuoka,* V. Nanal,§ M. Thoennessen,* and R. L. Varner¶)

The giant dipole resonance built on excited states was observed in very fissile nuclei in coincidence with evaporation residues - see Fig. I-41. The reaction $^{48}\text{Ca} + ^{176}\text{Yb}$ populated evaporation residues of mass $A = 213 - 220$ with a cross section of $\sim 200 \mu\text{b}$ at 259 MeV. The experiment was performed at ATLAS with the LEPPEX BaF₂ array (from ORNL, MSU and TAMU). Coincidences with evaporation residues detected in the Fragment Mass Analyzer ensured

exclusive selection of only γ rays following the decay of the compound nucleus ^{224}Th . In addition, coincidences with the Argonne-Notre Dame BGO array were recorded to provide multiplicity and sum-energy data. This work constituted part of the thesis of J. Seitz at MSU. The extracted giant dipole resonance parameters are in agreement with theoretical predictions for this mass region.¹

*Michigan State University, †State University of New York-Stony Brook, ‡University of Illinois at Chicago, §Tata Institute of Fundamental Research, Mumbai, India, ¶Oak Ridge National Laboratory.

¹J. P. Seitz *et al.*, Nucl. Phys. **A750**, 245 (2005).

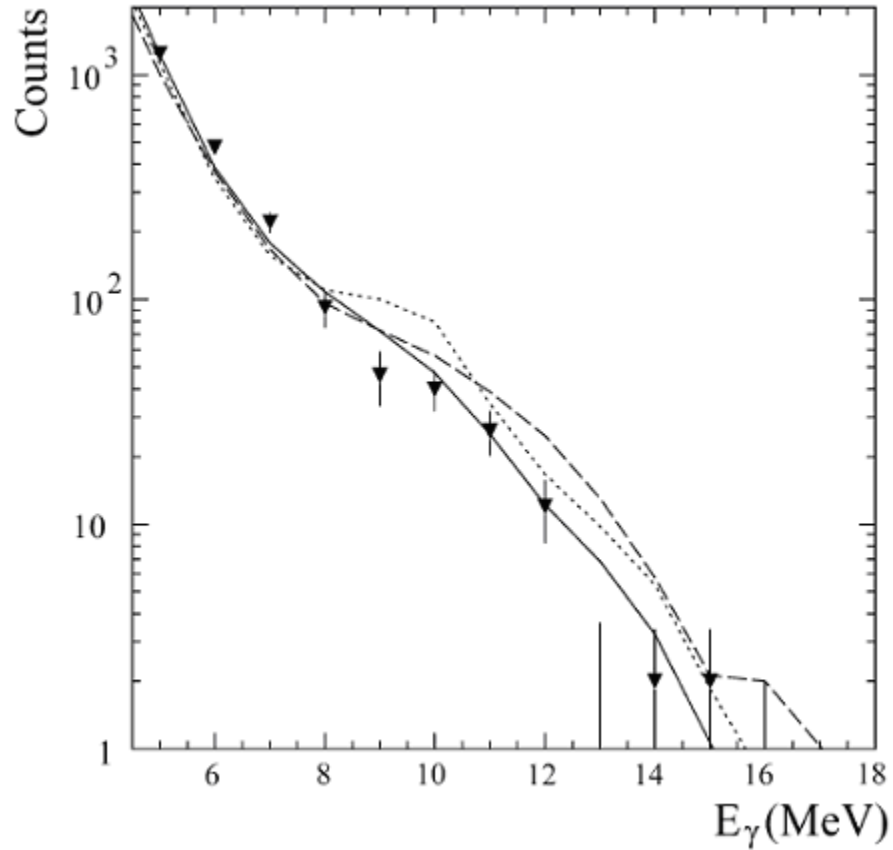


Fig. I-41. High-energy γ -ray spectra in coincidence with evaporation residues compared to results from statistical model calculations assuming different deformations: $\beta = -0.1$ (solid), $\beta = 0.3$ (dashed) and $\beta = 0.56$ (dotted).

F. THE PHOBOS EXPERIMENT AT RHIC

The Phobos experiment has made significant progress over the past year. During the 2004 RHIC running Phobos collected a substantial data set for Au + Au collisions at energies of both $\sqrt{s_{NN}} = 200$ GeV and 62.4 GeV. The latter energy was chosen to be able to compare with pp collisions from CERN. A new large data set was also collected for $\sqrt{s_{NN}} = 200$ pp collisions. An upgrade of the Phobos data acquisition system allowed for substantially increased data rates, taking advantage of large improvements in the RHIC luminosity.

f.1. The Phobos Experiment at RHIC (B. B. Back for the Phobos Collaboration*)

The present status of Phobos physics results has been summarized in a recent white paper,¹ which will be published in Nucl. Phys. A along with similar status papers from the other three RHIC experiments. Based on these white papers there is a general consensus among the experiments that the following discoveries has been made at RHIC:

- 1) A new form of matter, which cannot be described in terms of hadronic degrees of freedom has been produced in head-on Au + Au collisions.
- 2) This matter has an energy density, which substantially exceeds the theoretical threshold for entering the quark-gluon plasma phase.
- 3) The observation of collective flow patterns in the particle emission point to a strongly interacting, essentially ideal fluid description of this matter.
- 4) The disappearance of back-to-back high- p_T particles expected for hard parton scattering indicates that this matter is highly opaque because of a high density of unscreened color charges.

At this point, the RHIC research has thus achieved a rough characterization of this new form of matter. Some of the results are contrary to the naïve expectation that a weakly interacting quark-gluon plasma may be formed. The strongly interacting nature and the opaqueness were surprises. These results are expected to substantially advance our

understanding of the quantum chromodynamics theory of the strong interaction, especially as it relates to the temperature regimes probed in these reactions.

In the following, several new results obtained by the Phobos collaboration will be discussed.

Centrality Dependence of D + Au Multiplicities

The centrality dependence of charged particle emission in 200 GeV d + Au collisions has been studied. Figure I-42 shows the pseudorapidity distributions, $dN/d\eta$, for five centrality bins with the pseudorapidity, η , being measured relative to the deuteron beam direction.² We observe that the distribution for the most central collisions (0-20%) is quite asymmetric relative to $\eta = 0$. This effect is believed to reflect the fact that for these collisions about 13.5 nucleons from the Au nucleus participate in the reaction with the two nucleons in the deuteron. Momentum conservation therefore demands that more particles be emitted in the direction of the incoming Au nucleus. We observe also that this asymmetry subsides for the more peripheral collisions such that an almost symmetric distribution is observed for the 80-100% bin, which involves about 1.6 Au nucleons and 1.1 deuteron nucleons, on average. Guided by the “extended longitudinal scaling” observed in hadronic collisions we are able to obtain the total number of charged particles via an extrapolation into the unmeasured regions.² The consequences of a further analysis of these results are discussed in the following section.

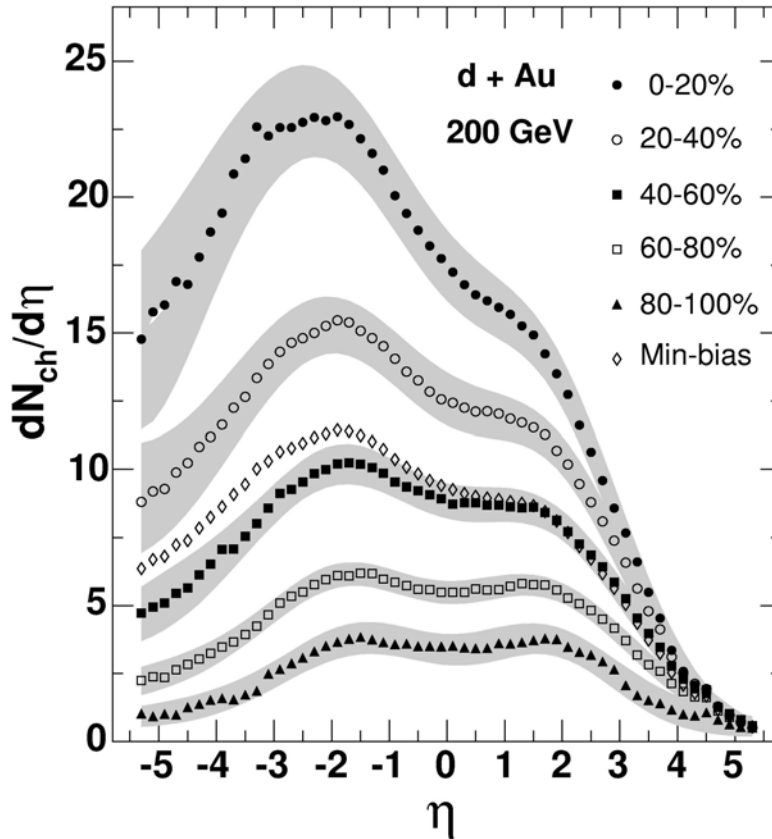


Fig. I-42. Distribution of pseudorapidity densities of charged particles emitted in $d + Au$ collisions at $\sqrt{s_{NN}} = 200$ GeV for five centrality bins.² The positive pseudorapidity direction is that of the deuteron. The centrality is designated by the fraction of the total inelastic cross section, with smaller numbers being more central. Grey bands indicate the systematic uncertainties (90% C.L.).

Scaling in Charged Particle Production

Because the Phobos multiplicity detector covers an angular range from $\theta = 0.5^\circ$ to 179.5° it is possible, with a very small extrapolation, to obtain the total number of charged particles emitted in a collision. By studying Au + Au collisions as a function of centrality, we have found that the total number of charged particles, N_{ch} , scales rather rigorously with the number of participant pairs, $N_{part}/2$, in the collision, such that the ratio $N_{ch}/N_{part}/2$ is essentially constant as a function of centrality as illustrated in Fig. I-43 (solid points).³ This scaling feature also applies to the simpler $d + Au$ collisions (open points), but we note that the charged particle production rate in this case is substantially lower (by about 40%),

which is at the level observed in proton-proton collisions at the same energy⁴ (solid square). The enhanced charged particle production in Au + Au collisions does not appear to be simply a consequence of the number of participants in the collisions because there is no indication of an increased multiplicity even for the most central $d + Au$ collisions. We also note that the multiplicity for e^+e^- collisions⁵ is consistent with the heavy-ion data. A possible explanation for this disparity between nucleon-induced and heavy-ion or lepton induced collisions is the fact that leading particles in nucleon-induced collisions carry away about half of the energy, which is then not available for particle production.⁶ It is surprising, however, that this mechanism is still effective in $d + Au$ collisions, which involve a substantial number of subsequent collisions.

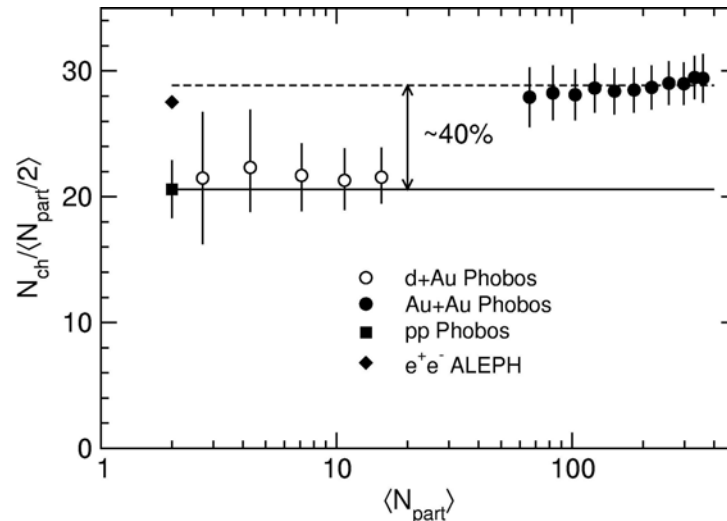


Fig. I-43. $N_{ch}/N_{part}/2$ for $Au + Au^6$ (solid points), $d + Au^1$ (open circles) are shown as a function of N_{part} and compared to values for pp^4 (solid square) and e^+e^- (solid diamonds) collisions. The horizontal dashed line represents the average value for $Au + Au$ collisions, which is $\sim 40\%$ higher than the pp level (solid line).

Multiplicity Scaling in $Au + Au$ Collisions at 19.6 and 200 GeV

At all $Au + Au$ collision energies, we have found that the pseudorapidity density, $dN/d\eta$ at midrapidity, $\eta = 0$, increases with centrality (N_{part}) in a smooth fashion. This increase was attributed to hard collisions (between partons) since such collisions are expected to scale roughly with $N_{part}^{4/3}$ and therefore assume increased importance in central collisions. Furthermore, it was assumed that the hard processes would prevail with increasing collision energy. Recently we have found, however, that the increase

in multiplicity with centrality is the same in $Au + Au$ collisions at 19.6 and 200 GeV as illustrated in Fig. I-44, see Ref. 7. Here the ratio, $dN/d\eta(200)/dN/d\eta(19.6)$ is seen to be flat as a function of centrality indicating that the fraction of hard collisions is constant with collision energy. In fact, since the centrality dependence of $dN/d\eta$ is independent of collision energy there is a straight factorization of $dN/d\eta$, which may be expressed as: $dN/d\eta(s, N_{part}) = f(s) g(N_{part})$.

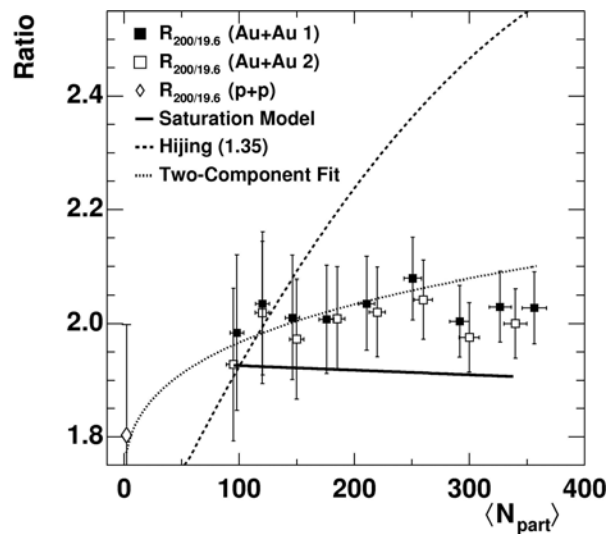


Fig. I-44. The ratio, $R_{200/19.6}$ of the multiplicity density per participant pair at 200 and 19.6 GeV versus $\langle N_{part} \rangle$ binned by fraction of cross section (closed circles) and by matching $\langle N_{part} \rangle$ (open squares).⁷ The ratio of inelastic $p + p$ collision data is given at $N_{part} = 2$ (open diamond). Curves give various calculations. The vertical error bars are combined statistical and systematic $1-\sigma$ uncertainties.

Elliptic Flow

One of the important discoveries at RHIC is that of elliptic flow, *i.e.* the preferential emission of particles at azimuthal angles corresponding to the reaction plane between the two interacting ions. The elliptical flow is measured in terms of the second Fourier coefficient of the particle azimuthal angular distribution $v_2 = \langle \cos[2(\psi - \psi_{\text{reac}})] \rangle$, where $\psi - \psi_{\text{reac}}$ is the azimuthal angle of the emitted particle relative to that of the reaction plane. The average is extended over all particles emitted within a certain pseudorapidity interval in each event. Figure I-45 shows the elliptic flow signal as a function of event centrality, given in terms of N_{part} , (left panel) and

particle transverse momentum (right panel).⁸ The data are in remarkable agreement with the predictions of a hydrodynamic model (solid lines),⁹ which indicates that the matter formed in these collisions behave much like an ideal, non-viscous liquid. This observation, which is in accord with those from the other three RHIC experiments, is contrary to the original naïve expectation that matter in the Quark Gluon Plasma phase behave as a weakly interacting gas. The observation of a strong collective flow signal in heavy-ion collisions at RHIC energies is thus a first, but important, step in the characterization of this new phase of matter.

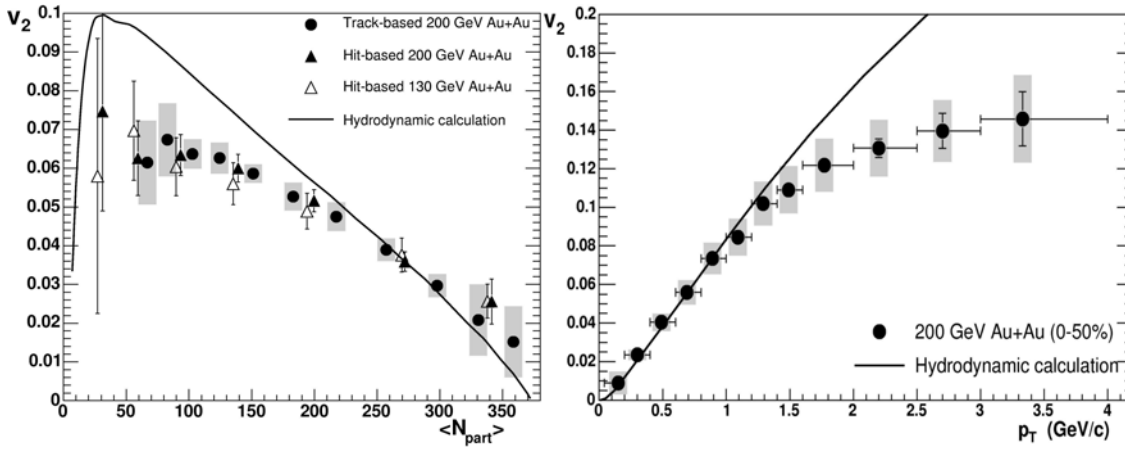


Fig. I-45. Left panel: Elliptic flow ($v_2(|\eta| < 1)$) as a function of $\langle N_{\text{part}} \rangle$ determined by the track-based method (closed circles) and hit-based method (closed triangles) for Au + Au collisions at 200 GeV.⁸ The open triangles are the $v_2(|\eta| < 1)$ as a function of $\langle N_{\text{part}} \rangle$ results from Au + Au collisions at 130 GeV. The line shows a calculation from hydrodynamics⁹ at $\sqrt{s_{\text{NN}}} = 200$ GeV. The grey boxes show systematic uncertainties for the 200 GeV results from the track-based method. Right panel: Elliptic flow as a function of transverse momentum, $v_2(p_T)$, for charged hadrons with $0 < \eta < 1.5$ for the most central 50% of the 200 GeV Au + Au collision cross section.⁷ The grey boxes represent the systematic error. The data points are located at the average p_T position with a p_T bin whose size is given by the horizontal error bars. The curve shows a calculation from hydrodynamics.⁹

The ability of Phobos to measure charged particles over a very wide angular range allows us to also perform unique, complete measurements of the elliptical flow signal. Such results are shown for three centrality bins in Fig. I-46 for Au + Au collisions at 200 GeV. We observe an interesting strong peaking of the v_2 signal at mid-rapidity followed by an immediate fall-off at both positive

and negative values of η . Although the hydro-dynamical models have been quite successful in describing the v_2 signal at mid-rapidity, such models have had difficulties explaining the rapid falloff seen experimentally. Recently, however, it appears that the Buda-Lund version of the hydro-dynamic model is able to reproduce the η -dependence seen in the Phobos results by including the effects of a directed flow (v_1 component).¹⁰

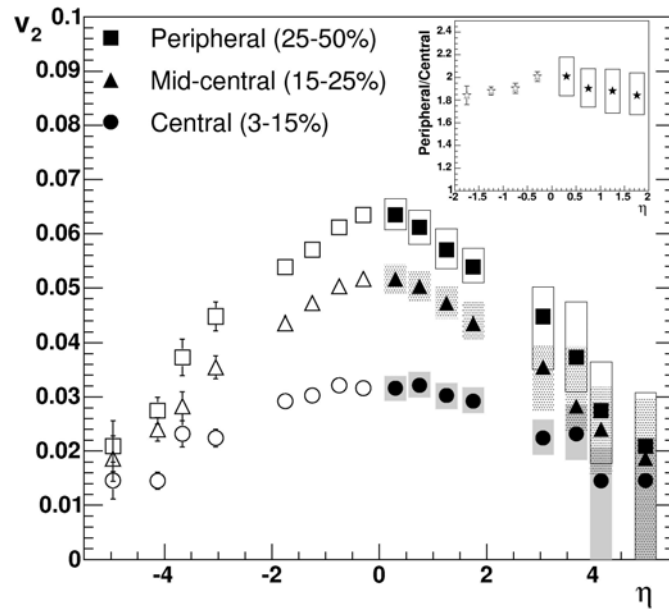


Fig. I-46. Elliptic flow as a function of pseudorapidity, $v_2(\eta)$, for charged hadrons from 200 GeV Au + Au collisions for three different centrality classes.⁸ The data for $\eta > 0$ are determined by reflecting the hit-based results about mid-rapidity and combining them with the track-based results and shown with the systematic errors only. The same data are reflected around $\eta = 0$ and shown as open symbols with statistical errors only. The inset shows the ratio of the peripheral to central combined results where the two methods overlap, with only statistical errors shown for $\eta < 0$ and only systematic errors for $\eta > 0$.

In Fig. I-47 we show the elliptic flow signal, v_2 , for 0-40% central collisions for all four energies studies so far. The data are plotted vs. the parameter $\eta' = |\eta| - y_{\text{beam}}$, where y_{beam} is the beam rapidity. We have previously shown¹¹ that the charged-particle production, $dN/d\eta$ obeys limiting fragmentation scaling i.e. $dN/d\eta$ is independent of collisions energy

in the region near η' . It is now interesting to observe that a similar scaling behavior applies to the elliptical flow signal as demonstrated in Fig. I-47. Because of the universality of this scaling behavior the term ‘extended longitudinal scaling’ has been attached to this feature. No satisfactory theoretical explanation for this scaling has been put forth.

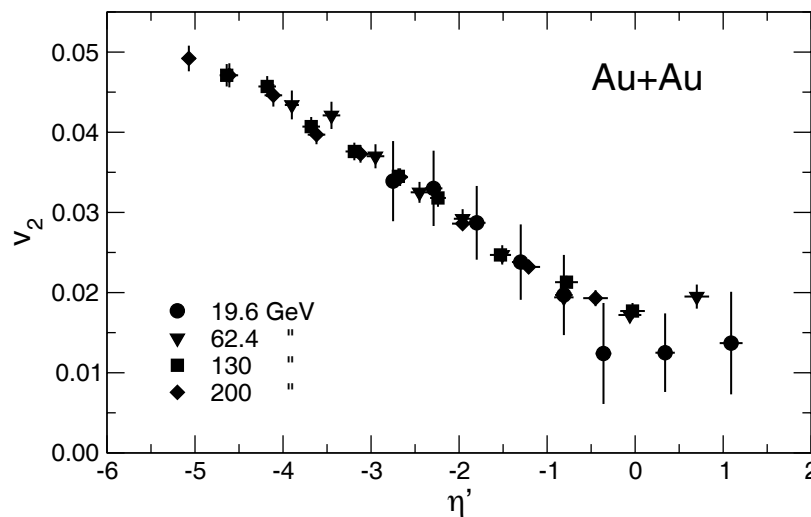


Fig. I-47. Elliptic flow, averaged over centrality (0-40%), as a function of $\eta' = |\eta| - y_{\text{beam}}$ for four collision energies for the Au + Au system.¹² The error bars represent 1σ statistical errors only.

Hanbury-Brown/Twiss Analysis of Two-Particle Correlations

The method of analysis of two-photon correlations from astronomical objects to estimate their radial extent is well established.¹³ This method can also be applied to estimate the spatial extent of the fireball created in heavy-ion collisions at ultra-relativistic energies. In Phobos we have performed such an analysis based on pairs of pions, which are detected and momentum analyzed in the Phobos spectrometer. Experimentally the correlation function is defined as

$$C(\vec{q}) = \frac{P(\vec{p}_1, \vec{p}_2)}{P(\vec{p}_1)P(\vec{p}_2)}$$

where \vec{p}_1 and \vec{p}_2 are the particle four-momenta with relative four-momentum $\vec{q} = \vec{p}_1 - \vec{p}_2$ and $P(\vec{p}_1)$ and $P(\vec{p}_2)$ are single-particle probabilities. The numerator is determined directly from the data, while the denominator is constructed using a standard event-mixing technique. The experimentally determined correlation function $C(\vec{q})$ can be fit to the Bertsch-Pratt¹⁵ parameterization of a Gaussian source in three dimensions

$$C(\vec{q}) = 1 + \lambda e^{-(q_0^2 R_0^2 + q_s^2 R_s^2 + q_l^2 R_l^2 + 2q_0 q_l R_{0l}^2)},$$

where q_l is the component of \vec{q} along the beam direction, q_0 is the component along the pair transverse momentum $k_T = \frac{1}{2}(\vec{p}_{T1} + \vec{p}_{T2})$, and q_s is the component orthogonal to the other two. Results of such an analysis are shown in Fig. I-48 and compared with data from other experiments at RHIC energies, as well as studies at lower collision energies at the CERN SPS and the Brookhaven AGS facilities. First we observe that the results of the Phobos analysis agree well with those from other experiments. Of particular interest is the ratio between the “out” and “side” dimension of the source at freeze-out, R_o/R_s . This ratio is found to be near unity at both energies (left panel), whereas hydrodynamical models of the expansion of the fireball predicts values of the order $R_o/R_s \sim 1.5-2.0$.¹⁹ This discrepancy is observed by all RHIC experiments and has not yet been understood although a recent publication²⁰ suggests that a quantum-mechanical treatment of the opacity and refractive effects in the fireball may partly contribute to this effect.

*Brookhaven National Laboratory, Institute of Nuclear Physics, Krakow, Poland, Massachusetts Institute of Technology, National Central University, Taoyuan, Taiwan, University of Rochester, University of Illinois-Chicago, and University of Maryland.

¹B. B. Back *et al.*, Nucl. Phys. **A757**, 28 (2005).

²B. B. Back *et al.*, Phys. Rev. C **72**, 031901 (2005).

³B. B. Back *et al.*, Intl. J. Mod. Phys. A (2005).

⁴R. Nouicer *et al.*, J. Phys. G **30**, 51133 (2004).

⁵H. Stenzel *et al.*, Eur. Phys. J. C **35**, 457 (2004).

⁶P. Steinberg *et al.*, Nucl. Phys. **A715**, 490c (2003).

⁷B. B. Back *et al.*, Phys. Rev. C **70**, 021902R (2004).

⁸B. B. Back *et al.*, Phys. Rev. C **72**, 051901 (2005).

⁹P. Kolb *et al.*, Phys. Lett. **B500**, 232 (2001).

¹⁰M. Csanad, T. Csorgo, B. Lorstad, and A. Ster, J. Phys. G **30**, 1079 (2004).

¹¹B. B. Back *et al.*, Phys. Rev. Lett. **91**, 052303 (2003).

¹²B. B. Back *et al.*, Phys. Rev. Lett. **94**, 122303 (2005).

¹³R. Hanbury-Brown and R. Q. Twiss, Phil. Mag. Ser. 7, Vol. **45**, No. 366, 663 (1954); Nature **178**, 1046 (1956).

¹⁴B. B. Back *et al.*, accepted for publication in Phys. Rev. C; nucl-ex/0409001.

¹⁵S. Pratt, Phys. Rev. D **33**, 1314 (1986); G. Bertsch, Nucl. Phys. **A498**, 173 (1989).

¹⁶J. Adams *et al.*, Phys. Rev. Lett. **93**, 012301 (2004).

¹⁷S. S. Adler *et al.*, nucl-ex/0401003.

¹⁸C. Adler *et al.*, Phys. Rev. Lett. **87**, 082301 (2001); K. Adcox *et al.*, Phys. Rev. Lett. **88**, 192302 (2002);

L. Ahle *et al.*, Phys. Rev. C **66**, 054906 (2002); D. Adamova *et al.*, Nucl. Phys. **A714**, 124 (2003); M. A. Lisa *et al.*,

Phys. Rev. Lett. **84**, 2798 (2000); I. G. Bearden *et al.*, Phys. Rev. C **58**, 1656 (1998); S. Kniege *et al.*, nucl-

ex/0403034; M. M. Aggarwal *et al.*, Eur. Phys. J. C **16**, 445 (2000).

¹⁹U. W. Heinz and P. F. Kolb, hep-ph/0204061.

²⁰J. G. Cramer, G. A. Miller, J. M. S. Wu, and J. H. Yoon, Phys. Rev. Lett. **94**, 102302 (2005).

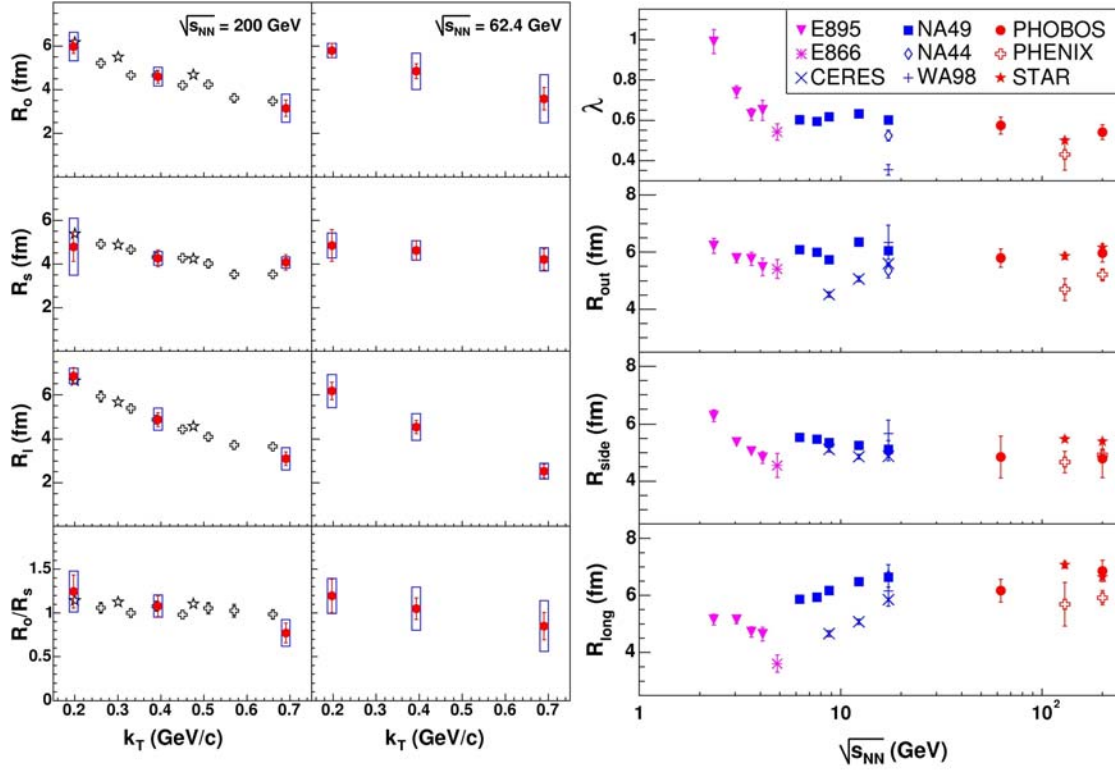


Fig. I-48. Left figure: Bertsch-Pratt parameters R_o , R_s , R_l and the ratio R_o/R_s for $\pi^+\pi^-$ pairs at 200 GeV (left panel) and 62.4 GeV (right panel) Au + Au collisions as a function of $\langle k_T \rangle$.¹⁴ For comparison, data from STAR¹⁶ (open stars) and PHENIX¹⁷ (open crosses) are presented at 200 GeV. Phobos systematic errors (90% C.L.) are shown as boxes; systematic errors from STAR and PHENIX are not shown. Right figure: Bertsch-Pratt parameters λ , R_{out} , R_{side} , R_{long} as a function of $\sqrt{s_{NN}}$ for $\pi^+\pi^-$ pairs. The presented data are near mid-rapidity and represent comparable k_T bins from each experiment.¹⁸ Phobos data are represented by solid circles. Systematic errors are not shown.

G. REACTION MECHANISM STUDIES

Direct Reactions have played a pivotal role in understanding nuclear wavefunctions, residual interactions between nucleons, and collective correlation of particles. Historically, light ion transfers like the (d,p) reaction, were used on stable targets to investigate the structure of states. However, using radioactive beams, reactions in inverse kinematics, and sophisticated detector arrays, the possibility of performing direct reactions on unstable nuclei has emerged. This seems to be a technique with great potential for the future, both at ANL using “in-flight” production of radioactive beams, and at other radioactive beam facilities. In these reactions, and in the studies of far-sub-barrier fusion, improvements in experimental techniques have led to new insights.

g.1. Study of ${}^7\text{He}$ Using the $d({}^6\text{He},p){}^7\text{He}$ Reaction (K. E. Rehm, J. P. Greene, D. J. Henderson, R. V. F. Janssens, C. L. Jiang, E. F. Moore, R. C. Pardo, S. C. Pieper, G. Savard, J. P. Schiffer, D. Peterson, S. Sinha, X. Tang, R. B. Wiringa, A. H. Wuosmaa,* L. Jisonna,† M. Paul,‡ and R. E. Segel†)

We have studied the $d({}^6\text{He},p){}^7\text{He}$ reaction using a ${}^6\text{He}$ beam to study the properties of the exotic, neutron-rich nucleus ${}^7\text{He}$. The nucleus ${}^7\text{He}$, which possesses no particle-bound states, is one of the simplest nuclei for which there remains considerable debate about its structure. The structure of ${}^7\text{He}$ is particularly interesting in light of the current interest in systems containing many loosely bound neutrons. In addition to the well established ground state,¹ several experimental efforts have been made to understand the properties of possible excited states of this system.²⁻⁴ In one of these⁴ it has been suggested that there may exist a low-lying level that possesses significant overlap with ${}^6\text{He}_{\text{g.s.}} + n$, and should thus be populated strongly in the $d({}^6\text{He},p){}^7\text{He}$ reaction.

To examine the properties of possible low-lying excited states in this nucleus, we have studied the inverse-kinematic reaction $d({}^6\text{He},p){}^7\text{He}$ using a radioactive ${}^6\text{He}$ beam produced at the in-flight facility at the ATLAS accelerator at Argonne National Laboratory. The ${}^6\text{He}$ beam was produced using the $d({}^7\text{Li},{}^6\text{He}){}^3\text{He}$ reaction, with a primary ${}^7\text{Li}$ intensity of 50 pA, and primary beam energy of 81 MeV. The resulting ${}^6\text{He}$ secondary beam had an intensity of between 10 and 15×10^4 particles per second and an energy of 69 MeV. The ${}^6\text{He}$ beam bombarded a 540 $\mu\text{g}/\text{cm}^2$ thick CD_2 target.

In inverse kinematics at the present bombarding energies, the protons of interest are emitted at backward angles in the laboratory. These protons were detected using an array of segmented annular silicon detectors, and coincident ${}^4,{}^6\text{He}$ ions were detected and identified using an array of silicon E Δ E telescopes at very forward angles. Figure I-49 shows a representative Q-value spectrum, obtained for p - ${}^6\text{He}$ coincidence events. The ground state is clearly strongly excited, and there also appears a broad distribution of counts that extends to higher excitation energies. The low-lying state reported in⁴ lies at an excitation energy of 0.56 MeV, and would therefore appear almost exactly in the valley between the ground state and this broad distribution. If such a state exists, it is not strongly populated in $d({}^6\text{He},p){}^7\text{He}$, and is likely not to correspond to a $J^\pi = 1/2^-$ state as claimed in Ref. 4.

The angular distribution for the $d({}^6\text{He},p){}^7\text{He}$ ground-state transition appears in Fig. I-50. Also plotted in Fig. I-50 is a curve representing a calculation of that angular distribution using the code PTOLEMY, taking as input the one-neutron spectroscopic overlap taken from Quantum Monte-Carlo methods. The calculated angular distribution is in reasonable agreement with the data, although the calculation over-predicts the data.

These results have been accepted for publication in Physical Review Letters.

*Western Michigan University, †Northwestern University, ‡Hebrew University, Jerusalem, Israel.

¹R. H. Stokes and P. G. Young, Phys. Rev. **178**, 2024 (1969).

²A. A. Koshennikov *et al.*, Phys. Rev. Lett. **82**, 3581 (1999).

³H. G. Bohlen *et al.*, Phys. Rev. C **64**, 024312 (2001).

⁴M. Meister *et al.*, Phys. Rev. Lett. **88**, 102501 (2002).

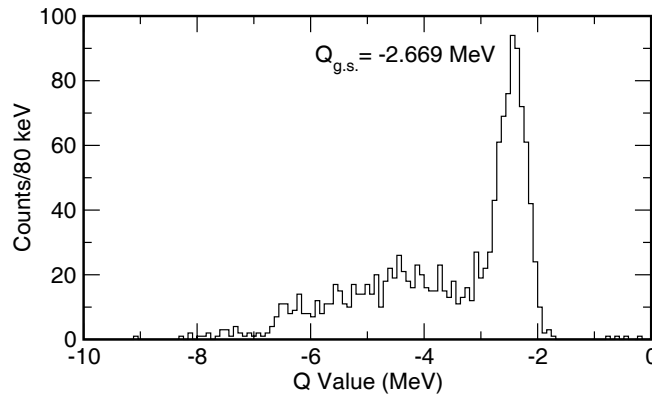


Fig. I-49. Proton Q -Value spectrum from the $d(^6\text{He},p)^7\text{He}$ reaction for $110^\circ \leq \theta_p \leq 160^\circ$.

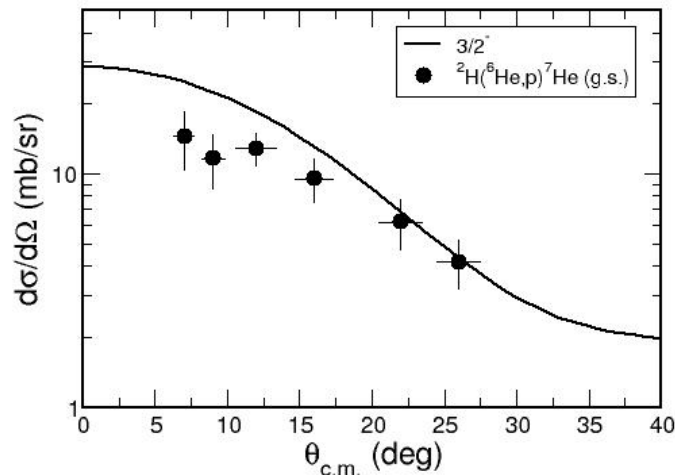


Fig. I-50. Angular distribution for the $d(^6\text{He},p)^7\text{He}$ ground-state transition.

g.2. Neutron Spectroscopic Factors in ^9Li from the $d(^8\text{Li},p)^9\text{Li}$ Reaction (K. E. Rehm, J. P. Greene, D. J. Henderson, R. V. F. Janssens, C. L. Jiang, E. F. Moore, R. C. Pardo, S. Sinha, X. Tang, and R. B. Wiringa, D. Peterson, S. C. Pieper, G. Savard, J. P. Schiffer, A. H. Wuosmaa,* L. Jisonna,† M. Paul,‡ and R. E. Segel†)

Modern computational and theoretical techniques, such as the quantum Monte Carlo method¹ have made significant progress in the understanding of the structure of light nuclei. Many predicted properties are in good agreement with the measured values, however for many light nuclei data are unavailable due to the difficulty of populating these nuclei with the simple, well understood transfer reactions that have been used historically to probe nuclear structure. With unstable beams, it is now possible to carry out so-called “classical” nuclear physics measurements to study properties of light nuclei that

had previously been inaccessible. One experimental property of the wave function of simple nuclear states is the neutron spectroscopic factor, for which the best probe is the (d,p) reaction. The *ab-initio* theoretical methods described¹ can be used to make first-principles predictions of the neutron spectroscopic factor.

We have studied the $d(^8\text{Li},p)^9\text{Li}$ reaction using a radioactive ^8Li beam to determine neutron spectroscopic factors in the nucleus ^9Li . In the p shell, (d,p) reactions have already been used extensively to determine single-

neutron spectroscopic factors for Li isotopes that can be produced with stable targets.²

In ${}^9\text{Li}$, only 5 levels are known, with only the ground state assigned a firm spin-parity value of $3/2^-$.³ To extend the available data for this nucleus, we have studied the inverse-kinematic reaction $d({}^8\text{Li},p){}^9\text{Li}$ using a radioactive ${}^8\text{Li}$ beam produced at the in-flight facility at the ATLAS accelerator at Argonne National Laboratory. The ${}^8\text{Li}$ beam was produced using the $d({}^7\text{Li},p){}^8\text{Li}$ reaction, with a ${}^7\text{Li}$ beam energy of 80 MeV, and an intensity of 50 pA on the D_2 gas-cell production target. Due to the low Z and mass of the ${}^8\text{Li}$ secondary-beam particles, and the large

difference in m/q between primary and secondary beams, the resulting ${}^8\text{Li}$ beam had very good transverse and longitudinal emittance properties and was very pure. This beam bombarded a $540 \mu\text{g}/\text{cm}^2$ CD_2 foil target.

In an inverse kinematic (d,p) reaction, the protons of interest, emitted forward in the center-of-mass system, emerge at backward angles in the laboratory. These backward emitted protons were detected using an array of segmented annular silicon detectors, and the coincident ${}^{7,8,9}\text{Li}$ ions were detected and identified using an array of silicon EAE telescopes at very forward angles. Figure I-51 shows a representative proton Q-value spectrum.⁴

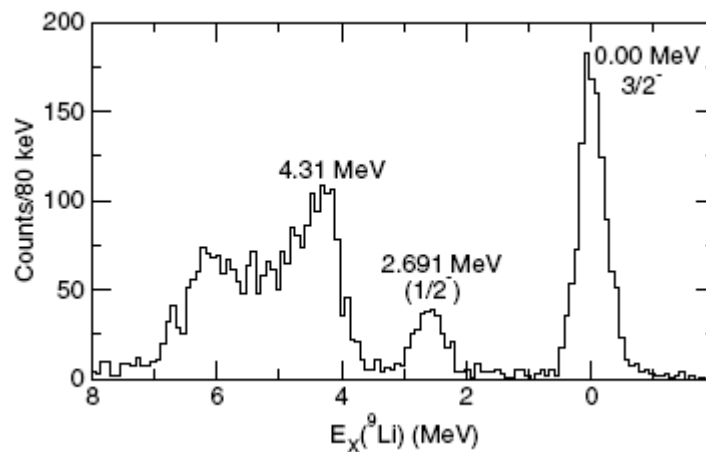


Fig. I-51. Excitation-energy spectrum for the $d({}^8\text{Li},p){}^9\text{Li}$ reaction.

Proton angular distributions for transitions to the ground, first- and second-excited states appear in Fig. I-52.⁴ Also plotted in Fig. I-52 are curves representing the calculations of the transfer angular distribution using the code PTOLEMY which takes as input the calculated neutron spectroscopic factor for the $d({}^8\text{Li},p){}^9\text{Li}$ reaction.

The solid and dashed curves represent the results from two different optical-model potential sets.² The data are in good agreement with the theory and show that the quantum Monte-Carlo calculations of neutron spectroscopic factors are reliable. The results also make it clear that measurements of simple, single-particle transfer reactions such as (d,p) can be carried out at the energies best suited to such measurements, between 6-10 MeV/nucleon.

*Western Michigan University, †Northwestern University, ‡Hebrew University, Jerusalem, Israel.

¹S. C. Pieper and R. B. Wiringa, *Ann. Rev. Nucl. Part. Sci.* **91**, 53 (2001); S. C. Pieper, K. Varga, and R. B. Wiringa, *Phys. Rev. C* **66**, 044310 (2002).

²J. P. Schiffer *et al.*, *Phys. Rev.* **164**, 1274 (1967).

³P. G. Young and R. H. Stokes, *Phys. Rev. C* **4**, 1597 (1971); F. Ajzenberg-Selove *et al.*, *Phys. Rev. C* **17**, 1283 (1978).

⁴A. H. Wuosmaa *et al.*, *Phys. Rev. Lett.* **94**, 082502 (2005).

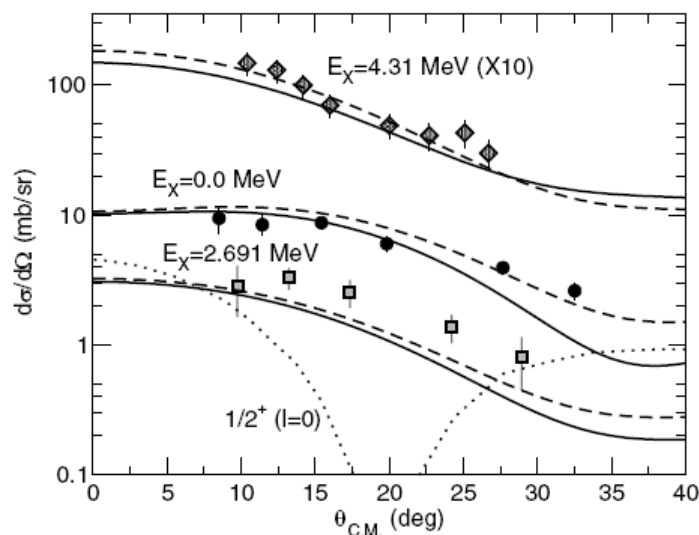


Fig. I-52. Angular distributions for three states in ${}^9\text{Li}$, populated in the $d({}^8\text{Li},p){}^9\text{Li}$ reaction. Calculated angular distributions are discussed in the text.

g.3. Is the Nuclear Spin-Orbit Interaction Changing with Neutron Excess?

(J. P. Schiffer, S. J. Freeman,* C.-L. Jiang, P. D. Parker,† and K. E. Rehm)

The single-particle character of nuclei underlies much of our understanding of nuclear structure. The states formed by a proton outside the closed shell of 50 protons were studied with the (α,t) reaction on all the stable, even Sn isotopes two years ago to demonstrate that the spin-orbit splitting for the proton states was changing with neutron excess.¹ A closely

related experiment, to obtain quantitative information on neutron single-particle states outside $N = 82$ with the $(\alpha,{}^3\text{He})$ reaction, had been proposed, also to be carried out at the Yale ESTU tandem. Unfortunately, He beams were not available at Yale during the past year because of ion source problems and the experiments are planned for later in 2005 after the source has been replaced.

*University of Manchester, United Kingdom, †Yale University.

¹J. P. Schiffer *et al.*, Phys. Rev. Lett. **92**, 162501 (2004).

g.4. Hindrance of Heavy-Ion Fusion at Extreme Sub-Barrier Energies in Open-Shell

Colliding Systems (C. L. Jiang, K. E. Rehm, H. Esbensen, R. V. F. Janssens, B. B. Back, C. N. Davids, J. P. Greene, D. J. Henderson, C. J. Lister, R. C. Pardo, T. Pennington, D. Peterson, D. Seweryniak, B. Shumard, S. Sinha, X. D. Tang, I. Tanihata, S. Zhu, P. Collon,* S. Kurtz,* and M. Paul†)

Heavy-ion induced fusion reactions have been studied extensively for more than forty years, especially since the discovery of the sub-barrier enhancement phenomenon. Coupled-channels descriptions were shown to explain the phenomenon successfully. Recently, evidence was found for a strong hindrance of the fusion process at extreme sub-barrier energies, an effect for which there is no satisfactory explanation in present model calculations.¹⁻³ The aim of the present work is to

further investigate the hindrance phenomenon by measuring fusion evaporation for the open-shell system ${}^{64}\text{Ni} + {}^{100}\text{Mo}$.

The experiment was performed with ${}^{64}\text{Ni}$ beams in the energy range of 196-262 MeV from the superconducting linear accelerator ATLAS at Argonne National Laboratory. The maximum beam current used was ~ 60 pA. The high melting point of the target material, metallic molybdenum evaporated on a $40 \mu\text{g}/\text{cm}^2$ carbon

foil, prevented damage to the target by the relatively high beam current. The target thickness was constant during the experiment, as monitored with Si detectors. Thin targets with thicknesses of 8 or 18 $\mu\text{g}/\text{cm}^2$ were used in order to reduce the correction for target thickness in the energy regime of the steep fall off of the excitation function. The isotopic abundance of ^{100}Mo was 97.42%, with the remainder coming from ^{98}Mo (0.96%), ^{97}Mo (0.28%), ^{96}Mo (0.34%), ^{95}Mo (0.29%), ^{94}Mo (0.18%), and ^{92}Mo (0.53%). The selection of the beam and target combination excluded the possibility of background from fusion reactions coming from beam or target contaminants.¹ Two surface-barrier Si detectors, located at $\pm 43^\circ$ with respect to the beam direction, served as monitors. The absolute cross sections for fusion-evaporation were determined by measuring the elastic scattering in the monitors.

For most settings of the FMA, two charge states of the residues were collected simultaneously. For the energies $E_{\text{lab}} = 260.5, 245.8, 209.1, 207.1$ and 202.2 MeV, full charge state distributions were measured, while for most other energies, two FMA settings, *i.e.* four charge states were recorded. At the four lowest energies, only two charge states were measured. From the full charge state distributions, charge state fractions were determined for extrapolation to all other energies. The energy distributions and angular distributions of evaporation residues were calculated with the statistical code PACE.⁴ Total angular distributions for fusion-evaporation have been measured in Ref. 5 for $^{64}\text{Ni} + ^{100}\text{Mo}$. In order to check the PACE code, calculations were compared with these experimental angular distributions of Ref. 5 and good agreement was found as long as the total calculated angular distributions were taken as a weighted sum of the angular distributions of the different masses from our m/q measurements and folded with multiple scattering. Whereas in Ref. 5 rather thick targets were used, the corrections from multiple scattering are small in the present experiment. The transport efficiencies of the FMA were calculated with these angular distributions together with Monte Carlo simulations, using a modified version of the GIOS Code.⁶ The large momentum acceptance, $\pm 10\%$, and the large angular acceptance, $\theta_{\text{lab}} < 2.3^\circ$, of the FMA result in a high detection efficiency for the residues. The detection of the residues has been described in another report.⁷

The fusion-fission cross sections for $^{64}\text{Ni} + ^{100}\text{Mo}$ have not been measured previously. They were,

however, calculated in Ref. 5 with the code CASCADE.⁸ Similar calculations with the same parameters were performed for the present experiment. Rather large uncertainties were given for the fusion-fission contributions resulting in somewhat larger errors for the total cross sections at the highest beam energies.

The experimental results for the total fusion cross sections, spanning eight orders of magnitude, are presented as a function of laboratory energy in Fig. I-53 (solid circles). The incident energies have been corrected for target thickness and for the steep energy dependence; these corrections are small because rather thin targets were used. For the lowest two energies no evaporation residue was observed. The results are shown as upper limits corresponding to one count in each case. The two earlier measurements^{5,9} are also shown in Fig. I-53 as open circles and open squares, respectively. Statistical errors are smaller than the size of the symbols. The three measurements are generally in good agreement within the quoted uncertainties, except for the lowest energy point of Ref. 9.

Detailed coupled-channels calculations have been carried out. The ion-ion potential was parameterized as a Woods-Saxon well with a depth of $V_0 = -82.9$ MeV, diffuseness $a = 0.686$ fm, and nuclear radius $R_N = 10.19$ fm + ΔR . A value of $\Delta R = 0.21$ fm was needed to reproduce the present data in the cross section region of 1 to 100 μb . The long-dashed curve in Fig. I-53 shows as a reference, the results obtained in a one-dimensional calculation, *i.e.*, without any couplings (with $\Delta R = 0.21$ fm). The coupled-channels calculations exhibit essentially the same energy dependence (slope) as the one-dimensional calculation when the cross sections are small (< 10 μb). The coupled-channels calculations are just shifted to lower energies relative to the one-dimensional calculation. In the present case the shift is about 7 MeV (for the same $\Delta R = 0.21$ fm). This is a general feature of coupled-channels calculations and it is, therefore, very unlikely that any minor adjustment in the coupled-channels calculations would reproduce the steep fall off that the data exhibit at extreme sub-barrier energies. Thus, it appears that the fusion hindrance behavior, which now has been observed for many systems, is also present in the new data for $^{64}\text{Ni} + ^{100}\text{Mo}$. This will be shown more convincingly in the following, where other representations of the fusion cross section are discussed.

The logarithmic derivative, $L(E) = d\ln(\sigma E)/dE$, originally introduced in Ref. 1, is shown in Fig. I-54a for the $^{64}\text{Ni} + ^{100}\text{Mo}$ system. The solid circles were obtained directly from two successive data points, whereas the stars were derived from least-squares fits to three

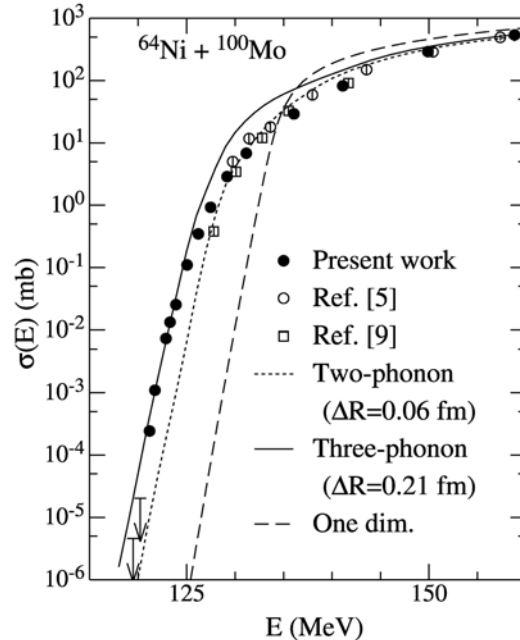


Fig. I-53. Fusion excitation function for $^{64}\text{Ni} + ^{100}\text{Mo}$ compared with several calculations described.

neighboring data points. The lower limit of the logarithmic derivative was derived from the upper limit on the cross section at $E_{cm} = 120.2$ MeV and the data point at $E_{cm} = 121.2$ MeV. The present data are compared to those of Refs. 5 and 9, which are represented by those of open circles and open squares in Fig. I-54a, respectively. Only two-point derivatives are shown for these data. The three-phonon coupled-channels and the one-dimensional barrier penetration calculations are shown as solid and long-dashed curves, respectively, while the thick solid, nearly horizontal line corresponds to the constant S -factor expression derived in Ref. 2. The present experimental results just reach the constant S -factor line, implying that the experimental data have reached a maximum value for the S -factor. The energy, E_s , representing the intersection between the experimental logarithmic derivatives and the constant S -factor line corresponds to a value of $E_s = 120.6$ MeV. The dotted line in Fig. I-54a is an extrapolation obtained under the assumption that the logarithmic derivative is a straight line near the crossing point. This method was first introduced in Ref. 3 in order to obtain the extrapolated values of E_s for the systems $^{58}\text{Ni} + ^{60}\text{Ni}$ and $^{58}\text{Ni} + ^{64}\text{Ni}$. The calculated logarithmic derivatives are seen to saturate around $L = 1.5 - 2$ MeV $^{-1}$ (or start to oscillate) below $E_{cm} = 124$ MeV, whereas the corresponding experimental values continue to grow with

decreasing energies. This saturation behavior has already been noted in Refs. 1-3.

The S -factor representation for the $^{64}\text{Ni} + ^{100}\text{Mo}$ system is presented in Fig. I-54b. As the experimental logarithmic derivatives only just reach the constant S -factor curve, the S -factor maximum is not fully developed. Additional measurements would be required to clearly delineate the maximum in the S -factor. The dotted curve corresponds to the straight line extrapolation of the logarithmic derivative in Fig. I-54a. The two- and three-phonon calculations are shown in Fig. I-54b as dashed and solid curves, respectively. It is evident that coupled-channels calculations overpredict the fusion cross section at extreme sub-barrier energies.

The experimental fusion data involving Ni projectiles and compound nuclei in the $A = 100-200$ region have been summarized. For four systems, namely the $^{58}\text{Ni} + ^{58}\text{Ni}$,¹⁰ $^{64}\text{Ni} + ^{64}\text{Ni}$,³ $^{60}\text{Ni} + ^{89}\text{Y}$ ¹ and the present $^{64}\text{Ni} + ^{100}\text{Mo}$ reactions, the cross sections have been measured to sufficiently low energies to determine the energy, E_s , of the maximum of the S -factor representation. In addition, we have previously obtained the E_s values for the $^{58}\text{Ni} + ^{60}\text{Ni}$ ¹¹ and $^{58}\text{Ni} + ^{64}\text{Ni}$ ¹² systems³ by extrapolation of the logarithmic derivative as explained below. Two additional systems, namely $^{58}\text{Ni} + ^{74}\text{Ge}$ ¹² and $^{64}\text{Ni} + ^{74}\text{Ge}$ ¹² from Ref. 13, have been measured down to levels close to where the S -factor maximum occurs. The

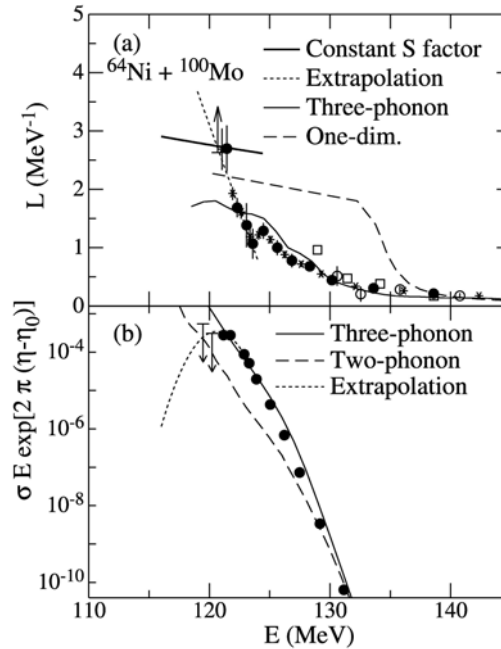


Fig. I-54. (a) Logarithmic derivative representation of the $^{64}\text{Ni} + ^{100}\text{Mo}$ fusion excitation function. The solid circles were obtained from two successive data points and stars were derived from least square fits to three neighboring data points. Included in are also the data from Ref. 5 (open circles) and Ref. 9 (open squares). (b) S -factor representation of the same data. Calculations are shown by curves in both panels. The extrapolation curve (dotted) shown in panel (b) was obtained from a straight line extrapolation of the logarithmic derivative representation in panel (a). A value of $\eta_0 = 105.74$ was used. See text for details.

location of the S -factor maximum was obtained by performing a small extrapolation of the logarithmic derivative to where it crosses the constant S -factor line. Because of the uncertainties inherent in these extrapolations, errors of 2% (~ 2 MeV) were assigned to the extrapolated E_s data, whereas an accuracy of 1% (~ 2 MeV) is obtained for the four systems where a maximum in the S -factor was observed.

The values of E_s are plotted as a function of the parameter $Z_1 Z_2 \mu^{1/2}$ in Fig. I-55 and compared to the empirical formula (solid curve)², which was obtained from a fit to all available fusion data involving stiff nuclei. Obviously, only two systems, $^{58}\text{Ni} + ^{58}\text{Ni}$ and $^{60}\text{Ni} + ^{89}\text{Y}$ follow the systematics; all other systems fall below the curve. Previously, it has been pointed out³ that there is a rather compelling correlation between the stiffness of the interacting nuclei and the location of the S -factor maximum, E_s , relative to the empirical trend. The addition to the systematics of the data points for $^{64}\text{Ni} + ^{100}\text{Mo}$ and for the two Ni + Ge systems, which all involve soft nuclei, appears to corroborate this observation. Thus, for the $^{64}\text{Ni} + ^{100}\text{Mo}$ system, the value of E_s^{ref} predicted from the empirical formula is 134.5 MeV whereas the

measured value of $E_s = 120.6$ MeV is only 90% of this value. The reason for this reduction is presumably that $^{64}\text{Ni} + ^{100}\text{Mo}$ should be viewed as an open-shell colliding system so that strong coupling effects broaden the effective barrier distribution and push the energy where the hindrance behavior occurs down to even lower energies.

The deviation of the measured or extrapolated values of E_s from the expected E_s^{ref} value, seen in Fig. I-55, thus appears to depend on the stiffness of the fusing nuclei. A quantitative relation between the stiffness and the deviation from E_s^{ref} is not yet known. As a first attempt, we associate the stiffness of a nucleus to its proximity to closed proton or neutron shells and define the number of "valence nucleons", N_{ph} , as the sum of particles and holes outside the nearest closed shells. Here, ^{64}Ni is considered to have four holes in the $N = 40$ neutron shell rather than eight particles outside $N = 28$. In Fig. I-56, the ratio E_s/E_s^{ref} is plotted as a function of this parameter. There is a general trend of decreasing values of E_s/E_s^{ref} with increasing values of N_{ph} . We observe that for the other systems not included in Fig. I-56, the data for E_{min} (upper limits) are not in contradiction with Figs. I-55 and I-56. It should be noted that all of the systems shown in Figs. I-55

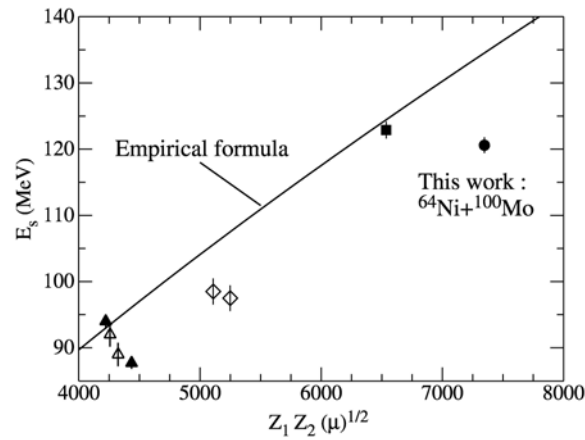


Fig. I-55. Plot of E_s vs. $Z_1 Z_2 \sqrt{\mu}$ for Ni bombarding different targets. Solid symbols correspond to systems for which the S-factor maximum is well determined: $^{64}\text{Ni} + ^{64}\text{Ni}$, $^{60}\text{Ni} + ^{89}\text{Y}$ and $^{64}\text{Ni} + ^{100}\text{Mo}$. Open symbols are associated with the extrapolations for the systems $^{58}\text{Ni} + ^{60}\text{Ni}$, $^{58}\text{Ni} + ^{64}\text{Ni}$, $^{58}\text{Ni} + ^{74}\text{Ge}$ and $^{64}\text{Ni} + ^{74}\text{Ge}$. The triangles represent Ni + Ni, diamonds Ni + Ge, a square $^{60}\text{Ni} + ^{89}\text{Y}$ and a circle $^{64}\text{Ni} + ^{100}\text{Mo}$, respectively.

and I-56 have rather large negative fusion Q-values. One may also compare the E_s -values to the height of the Coulomb barrier V_c (like obtained from the Bass prescription). The ratio E_s/E_s^{ref} exhibit a stronger dependency on the value of N_{ph} than that obtained for the ratio E_s/V_c indicating that the observed effect does not just depend on the change in the Coulomb barrier height with addition of neutrons to the interacting nuclei.

The above observations are all phenomenological in nature as there is at present no satisfactory understanding of the fusion hindrance at extreme sub-barrier energies. The data are most likely still

insufficient to lead to the correct explanation. More precision sub-barrier fusion measurements are required to further explore which modifications in the theoretical models are relevant for a correct description of the phenomenon.

In conclusion, an interesting nuclear structure dependence of the fusion hindrance has been observed. The origin of this effect is still unknown. It occurs at relatively high excitation energies (for systems in Figs. I-55 and I-56, they are around $E_{ex} \sim 30\text{-}40$ MeV), where the natural width of compound levels is larger than their spacing. A lack of available final states thus appears to be ruled out as an explanation.

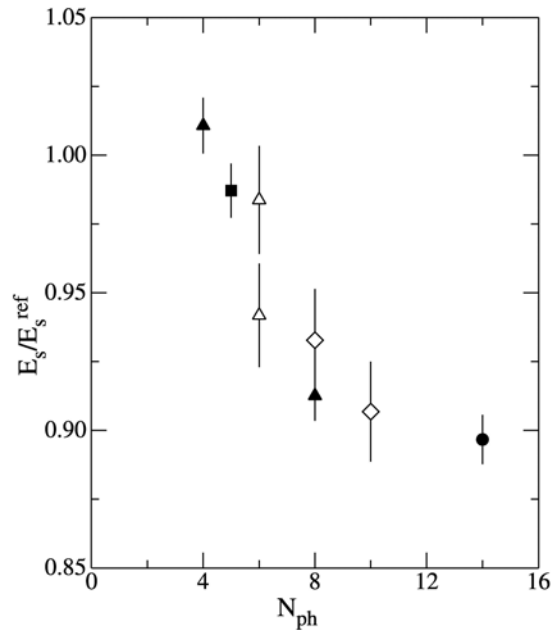


Fig. I-56. Plot of E_s/E_s^{ref} vs. N_{ph} , where N_{ph} is the total number of "valence nucleons" outside closed shells in the entrance channel. Symbols are defined in Fig. I-55.

*University of Notre Dame, †Hebrew University, Jerusalem, Israel.

¹C. L. Jiang *et al.*, Phys. Rev. Lett. **89**, 052701 (2002).

²C. L. Jiang, H. Esbensen, B. B. Back, R. V. F. Janssens, and K. E. Rehm, Phys. Rev. C **69**, 014604 (2004).

³C. L. Jiang *et al.*, Phys. Rev. Lett. **93**, 012701 (2004).

⁴A. Gavron, Phys. Rev. C **21**, 230 (1980).

⁵K. E. Rehm, H. Esbensen, J. Gehring, B. Glagola, D. Henderson, W. Kutschera, M. Paul, F. Soramel, and A. H. Wuosmaa, Phys. Lett. **B317**, 31 (1993).

⁶C. L. Jiang and C. N. Davids, ANL Phys. Div. Annual Report **ANL-95/14**, 74 (1995).

⁷C. L. Jiang *et al.*, submitted to Nucl. Instrum. Methods A.

⁸F. Pühlhofer, Nucl. Phys. **A280**, 267 (1977).

⁹M. L. Halbert, J. R. Beene, D. C. Hensley, K. Honkanen, T. M. Semkow, V. Abenante, D. G. Sarantites, and Z. Li, Phys. Rev. C **40**, 2558 (1989).

¹⁰M. Beckerman, J. Ball, H. Enge, M. Salomaa, A. Sperduto, S. Gazes, A. DiRienzo, and J. D. Molitois, Phys. Rev. C **23**, 1581 (1982).

¹¹A. M. Stefanini *et al.*, Phys. Rev. Lett. **74**, 864 (1995).

¹²M. Beckerman *et al.*, Phys. Rev. C **25**, 837 (1982).

g.5. $^{58}\text{Ni} + ^{89}\text{Y}$ Fusion Hindrance at Extreme Sub-Barrier Energies (C. L. Jiang, K. E. Rehm, H. Esbensen, B. B. Back, R. V. F. Janssens, J. P. Greene, D. J. Henderson, T. O. Pennington, D. Seweryniak, J. A. Caggiano,* P. Collon,† A. M. Heinz,‡ and I. Nishnaka§)

Fusion reactions between heavy ions have been studied extensively for a long time, especially since the discovery of the strong enhancement phenomenon at sub-barrier energies.¹ In most fusion-evaporation experiments carried out thus far, cross

sections have been measured down to the 0.1 to 1 mb level, and coupled-channels calculations have been quite successful in reproducing the general trend of the measured yields.² It was recently found that heavy-ion fusion is often hindered at extreme sub-barrier energies,

where fusion cross sections are very small (say in the μb to nb region).³⁻⁶ This phenomenon has not yet been explained in realistic model calculations.

The present work deals with the experimental results for the system $^{58}\text{Ni} + ^{89}\text{Y}$ and also reports on one of the experiences learned when the measured cross sections are very low; *i.e.* the influence of contaminants, either in the beam or in the target. We have previously measured the fusion evaporation excitation function for the $^{60}\text{Ni} + ^{89}\text{Y}$ system down to the 100 nb level and discussed the fusion hindrance phenomenon for this system in detail.³⁻⁴ The excitation function obtained is reproduced in Fig. I-57 with open circles. It is seen that the cross section in this semi-logarithmic plot falls off increasing steeply as the energy becomes smaller.

The fusion-evaporation excitation function for the system $^{58}\text{Ni} + ^{89}\text{Y}$ was measured using the same technique applied in the $^{60}\text{Ni} + ^{89}\text{Y}$ experiment. The two measurements were performed at the Argonne superconducting linear accelerator ATLAS. The fusion-evaporation residues were identified and measured with the Fragment Mass Analyzer (FMA).⁷ A mono-isotopic target of yttrium was used. More

details can be found in Ref. 3. The measured fusion-evaporation excitation function for $^{58}\text{Ni} + ^{89}\text{Y}$ is shown in Fig. I-57 by solid circles, and the data are listed in Table I-3, together with the data for the $^{60}\text{Ni} + ^{89}\text{Y}$ system.

The lowest cross section measured for $^{58}\text{Ni} + ^{89}\text{Y}$ fusion is 0.070 ± 0.010 mb, much higher than what we obtained for the reaction $^{60}\text{Ni} + ^{89}\text{Y}$, $<7.0 \times 10^{-5}$ mb. This is due to the fact that a small amount of ^{58}Fe contaminant was present in the ^{58}Ni beam. During the experiment, an ECR source was used and the subsequent beam transport system is not sufficient to separate all the isobars completely. For the ^{60}Ni beam, no other stable $A = 60$ isobar exists in nature, so the beam was pure. In contrast, for the ^{58}Ni beam, ^{58}Fe is a stable nucleus, with a natural isotopic abundance of 0.3%. A small amount of ^{58}Fe contamination could be present in the ^{58}Ni beam, and the fusion-evaporation residues from the reaction $^{58}\text{Fe} + ^{89}\text{Y}$ would not be identified as a background and would be counted as "real" products in the experiment. The exact amount of contamination in the beam depends on the operation of the ECR source. During the $^{58}\text{Ni} + ^{89}\text{Y}$ experiment, a component of ^{58}Fe , $<10^{-4}$ was observed in the spectrum of the ECR source output, but the amount could not be determined precisely.

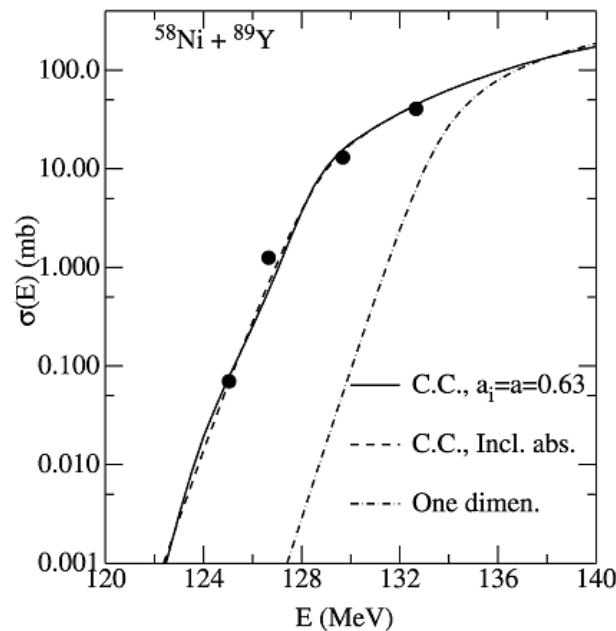


Fig. I-57. Fusion evaporation excitation functions for $^{58}\text{Ni} + ^{89}\text{Y}$ (solid circles) and $^{60}\text{Ni} + ^{89}\text{Y}$ (open squares) as function of the center-of-mass energy. Two open triangles are the measurements in which contributions from ^{58}Fe beam contaminations are not negligible.

Table I-3. Measured fusion evaporation cross sections for the systems $^{58}\text{Ni} + ^{89}\text{Y}$ and $^{60}\text{Ni} + ^{89}\text{Y}$.

$^{58}\text{Ni} + ^{89}\text{Y}$			$^{60}\text{Ni} + ^{89}\text{Y}$		
$E_{c.m.}$ (MeV)	σ (mb)	$\Delta\sigma$ (mb)	$E_{c.m.}$ (MeV)	σ (mb)	$\Delta\sigma$ (mb)
157.4	140.3	21.0	136.3	109.7	16.5
144.6	203.0	30.5	131.2	28.7	4.3
132.7	40.6	6.1	129.7	11.5	1.7
129.7	13.0	2.0	127.9	5.5	0.82
126.7	1.25	0.19	126.4	2.1	0.32
125.0	0.070	.010	125.8	0.71	0.11
			124.9	0.42	.063
			124.2	0.094	.014
			123.5	0.030	.0049
			122.8	.0089	.0014
			122.1	.0016	3.9E-4
121.4	<7.0E-5				

The Coulomb barriers of $^{58}\text{Ni} + ^{89}\text{Y}$ and $^{58}\text{Fe} + ^{89}\text{Y}$ are 137.33 and 126.05 MeV (from the Bass model),⁸ respectively. The sizeable difference in Coulomb barrier between the two systems translates in cross sections differing by orders of magnitude. The ratio of the cross sections for the two reactions is ~ 1000 at $E = 125$ MeV (indicated by the vertical dashed line in Fig. I-57). The contribution from ^{58}Fe induced fusion is much less than the uncertainty for the measurement at $E = 125$ MeV as this data point is in line with expectation (Fig. I-57). When the energy is even lower, however, the cross section for the reaction $^{58}\text{Ni} + ^{89}\text{Y}$ could easily decrease by orders of magnitude, while that for the reaction $^{58}\text{Fe} + ^{89}\text{Y}$, would only decrease modestly. The ratio of the cross sections for the two reactions would, therefore, become greater than 10^4 at the lower energies. Thus, a minute amount of ^{58}Fe contamination in the ^{58}Ni beam could produce a significant contribution to the measured yield of evaporation residues and distort the measured data.

In order to test the above hypothesis, two extra measurements at lower energies than that of Table I-3 were carried out. It was found that the yields measured at these two energies were really abnormal, higher than expected. On the other hand, from PACE calculations⁹ for the reaction $^{58}\text{Ni} + ^{89}\text{Y}$, it is found that the ratio of the $A = 144$ to the $A = 145$ residues should decrease with decreasing energy. During the

measurements, it was observed that this ratio does indeed decrease at the energies listed in Table I-3, but then starts to increase for these two additional energies. For the reaction $^{58}\text{Fe} + ^{89}\text{Y}$, at the corresponding energies, residues of $A = 144$ are more abundant than those of $A = 145$. This observation points to the same conclusion, namely, that the contaminant, $^{58}\text{Fe} + ^{89}\text{Y}$ reaction starts to play a dominant role at energies lower than those of Table I-3. Thus data obtained at these two energies are not included in Table I-3 but included in Fig. I-57 as open triangles and this is the reason that our results for $^{58}\text{Ni} + ^{89}\text{Y}$ are restricted to 0.070 mb.

Our previous studies of the fusion hindrance phenomenon include the systems $^{64}\text{Ni} + ^{64}\text{Ni}$ and $^{64}\text{Ni} + ^{100}\text{Mo}$, where ^{64}Ni was the beam.⁵⁻⁶ It is conceivable that the ^{64}Ni beam was contaminated with ^{64}Zn . Because the element number Z is higher for ^{64}Zn than for ^{64}Ni , the corresponding Coulomb barrier is also higher, and the cross section for the ^{64}Zn induced fusion reactions will be smaller than that for ^{64}Ni induced reactions. The contribution from ^{64}Zn induced fusion reactions will, therefore, be negligible if the contamination of the ^{64}Ni beam is of the order of 10^{-4} or less.

In the following, we will try to estimate the hindrance phenomenon in the $^{58}\text{Ni} + ^{89}\text{Y}$ fusion reaction, although the excitation function was measured only in an energy range higher than the energy, E_s where the hindrance is expected to set in.

Table I-4. Structure input for the low-lying states in ^{58}Ni . The $B(E\lambda)$ -values for the quadrupole transitions are from Ref. 10, and the octupole transitions are from Ref. 11.

Nucleus	λ^π	E_x (MeV)	$B(E\lambda)$ (b^λ)	β_λ^C	β_λ^N
^{58}Ni	2^+	1.454	680	0.181	0.208
	$2\text{ph}(4^+)$	2.908		0.181	0.208
	3^-	4.475	18600 ¹¹	0.204	0.209

We performed detailed coupled-channels calculations (C.C.) for $^{58}\text{Ni} + ^{89}\text{Y}$ fusion. These are similar to those reported for $^{60}\text{Ni} + ^{89}\text{Y}$.⁴ The nuclear structure input for ^{58}Ni is given in Table I-4, while the input for ^{89}Y is the same.⁴ The calculated results are shown in Figs. I-58 and I-59, where they are compared with the data. The solid curve in Fig. I-58 is based on a real ion-ion potential, with the same parameters.⁴ Fusion is simulated by in-going-wave boundary conditions and the fusion cross section is obtained from the in-going flux inside the Coulomb

barrier, near the local minimum of the interaction potential. The dashed curve in Fig. I-58 is based on a similar calculation, but it includes an additional short-ranged imaginary potential. Fusion is then obtained as the sum of the absorbed and in-going fluxes. These two methods produce almost identical excitation functions, but there are some differences which can be seen more clearly in the logarithmic derivative representation discussed below. The dashed-dotted curve shows the results of one-dimensional penetration calculations based on the same ion-ion potential.

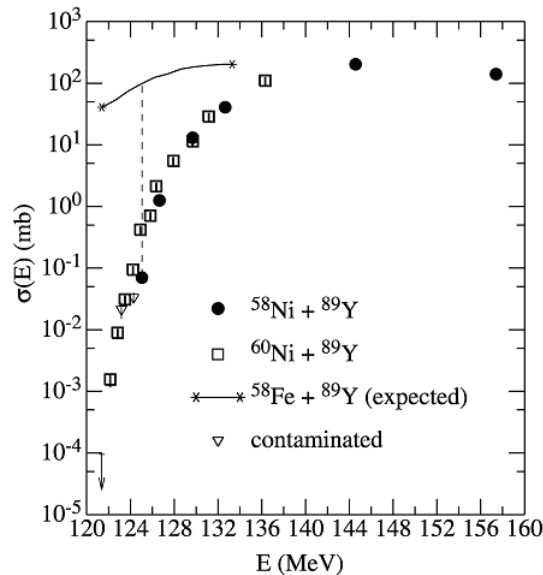


Fig. I-58. Fusion evaporation excitation function for $^{58}\text{Ni} + ^{89}\text{Y}$ (solid circles) and model calculations. The solid curve is the result of C.C. calculations based on a real ion-ion potential. The dashed curve includes also an additional short-ranged imaginary potential. The dashed-dotted curve represents one dimensional penetration calculations.

A new recipe for the ion-ion potential was introduced,⁴ which modifies the ion-interaction for $r < R$ (here r is the distance between ^{58}Ni and ^{89}Y ions, and R , the radius parameter of the potential), with a larger diffuseness a_i , but keeps the interaction unchanged for $r > R$ (with a diffuseness a). The two interactions

match up at $r = R$ with a continuous derivative. Calculations based on this recipe are shown in Fig. I-59 and are compared with the original one (solid curve). The dotted and dashed curves are both from $a_i = 2a$ calculations, but with and without the imaginary potential, respectively. It appears that the $a_i = 2a$

calculations produce better fits to the data than the original $a_i = a$ ones.

The logarithmic derivative, $L(E) = d\ln(E\sigma)/dE$, and the S-factor, $S(E)$ representations for the reaction $^{58}\text{Ni} + ^{89}\text{Y}$ are given in Figs. I-60a and I-60b, respectively. The solid circles and triangles in Fig. I-60a show the values of $L(E)$ obtained from two successive data points and from least square fits to three neighboring data points, respectively.

In the case of $^{60}\text{Ni} + ^{89}\text{Y}$ and other stiff ones, the experimental $L(E)$ data increase with decreasing energy⁴ and pass through the constant S-factor curves. For $^{58}\text{Ni} + ^{89}\text{Y}$, the experimental $L(E)$ curve does not

yet reach the constant S-factor curve.⁴ An extrapolation line (solid line) can be obtained using the method developed.⁵ This line intersects the constant S-factor curve (dashed-dotted line) at 124.1 ± 2 MeV. The energy of this crossing point is the location E_s of the maximum in the S-factor curve. The experimental values of $S(E)$ are presented in Fig. I-60b by the solid circles. The open circles show the values^{3,4} for the reaction $^{60}\text{Ni} + ^{89}\text{Y}$. The solid curve for $^{58}\text{Ni} + ^{89}\text{Y}$ is obtained from the linear extrapolation of $L(E)$ shown in Fig. I-60a. It exhibits a maximum S-factor at the energy $E_s = 124.1 \pm 2$ MeV, as determined above. As references, data from the two contaminated measurements are included in Fig. I-60a by corresponding open symbols.

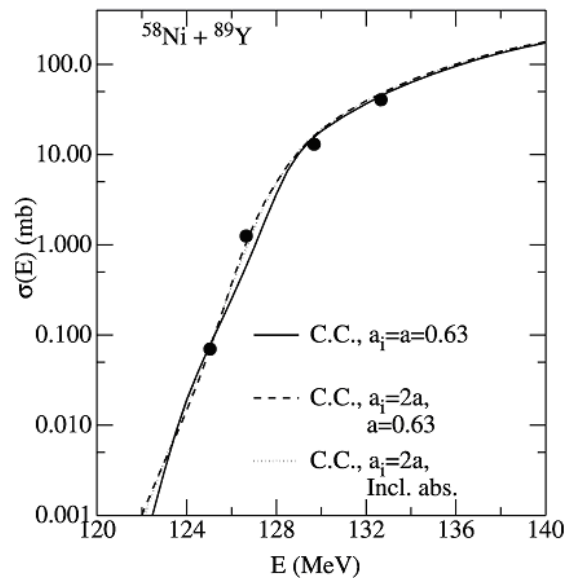


Fig. I-59. Fusion evaporation excitation function for $^{58}\text{Ni} + ^{89}\text{Y}$ (solid circles) and model calculations. The solid curve is the same as in Fig. I-58; the dotted one corresponds to $a_i = 2a$ with an imaginary potential, dashed, $a_i = 2a$ without an imaginary potential. See text for details.

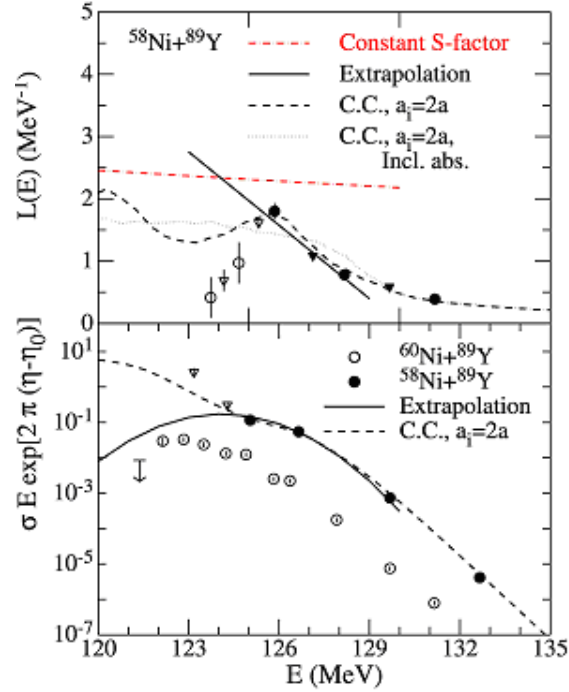


Fig. I-60. Logarithmic derivative representations (a) and S-factor representations (b) for the systems $^{58}\text{Ni} + ^{89}\text{Y}$ and $^{60}\text{Ni} + ^{89}\text{Y}$. Model calculations are included. Open symbols in (a) and open triangles in (b) are data from contaminated measurements. See text for details.

The results from some of the C.C. calculations are also included in Fig. I-60. The calculations for $a_i = 2a$ without the imaginary potential display an oscillatory behavior at the lowest energies (dashed curve), but these amplitude of the oscillations is strongly reduced when an imaginary potential is employed in the calculations (dotted curve). Similar behaviors occur for the two calculations displayed in Fig. I-58. The logarithmic derivatives of the C.C. calculations shown in Fig. I-60a are seen to saturate at values that are below the constant S-factor curve. Consequently, the associated S-factors do not exhibit a maximum.

In the systematic study reported⁴ it was shown that the energy E_s , where the maximum S-factor occurs, can be described rather well for stiff, closed-shell colliding systems by the empirical formula

$$E_s^{\text{ref}} = 0.356 (Z_1 Z_2 \mu^{1/2})^{2/3} \text{ (MeV)}, \quad (1)$$

where $\mu = A_1 A_2 / (A_1 + A_2)$. For softer systems, this formula provides an upper limit for the energy where the S-factor has its maximum. The E_s value for $^{58}\text{Ni} + ^{89}\text{Y}$ obtained above, with an uncertainty of 2 MeV, is compared in Fig. I-61 with the empirical formula of Eq. (1). The agreement between data the

empirical formula is quite satisfactory. This was expected because the system $^{58}\text{Ni} + ^{89}\text{Y}$ belongs to a category of stiff heavy-ion systems. It is, therefore, very plausible that the fusion of $^{58}\text{Ni} + ^{89}\text{Y}$ is actually hindered at low energies.

An abnormal behavior of the fusion cross section may also occur at extreme sub-barrier energies, when heavy isotopic contaminants are present in a target. For isotopic targets, like ^ANi , ^AZr , ^AMo , ^ASm , etc., there are often several other isotopic components, ranging from 0.1% to several percents in any isotopically enriched targets. If one measures the excitation function for a light-isotopic target, the contributions from a heavy-isotopic contamination can become a serious problem at extreme sub-barrier energies *i.e.*, at very low cross sections. The reason is that the center of mass energy is higher for heavier isotopes and fusion cross sections are thus usually larger for the heavier systems at the same beam energy. Hence, even a very small contamination is likely to show up at very low energies. On the other hand, the isotopic contamination of the target would not be such a serious problem if one wants to measure fusion reaction with the heaviest isotope. This is one of the reasons why ^{64}Ni and ^{100}Mo targets were selected in our studies of fusion hindrance at extreme sub-barrier energies.^{5,6}

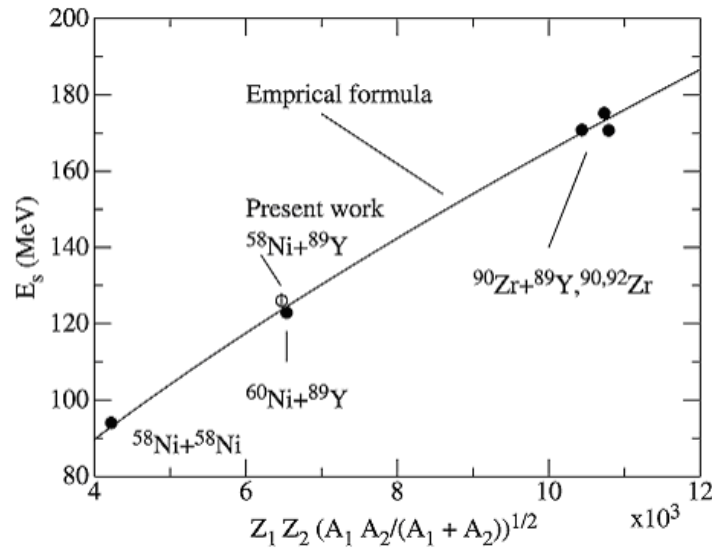


Fig. I-61. Plot of E_s vs. $Z_1Z_2\mu^{1/2}$ for some stiff colliding systems. The open circle is for the present work, $^{58}\text{Ni} + ^{89}\text{Y}$. Solid symbols are for other well determined stiff systems. Solid curve is from Eq. (1).

In the literature, one can find many measurements that use light-isotope targets, and some of the excitation functions do exhibit an abnormal behavior at extreme sub-barrier energies, which could perhaps be caused by the isotopic contamination mechanism discussed above. The abnormal behavior may not be seen so clearly in a plot of the excitation function, but it could probably be seen more clearly in the other representations, *i.e.* in terms of $L(E)$ or $S(E)$.

In summary, the influence of isobaric contamination of the beam, and/or isotopic contamination in the target, may introduce a serious problem in measurements of fusion-evaporation residues at extreme sub-barrier energies. The fusion hindrance at extreme sub-barrier energies was extracted for the reaction $^{58}\text{Ni} + ^{89}\text{Y}$, and it was found to be consistent with the systematics obtained for stiff systems.

*TRIUMF, Vancouver, British Columbia, †University of Notre Dame, ‡Yale University, §JAERI, Japan.

¹M. Beckerman, Physics Report **129**, 145 (1985); M. Beckerman, Rep. Prog. Phys. **51**, 1047 (1988); R. Vandenbosch, Annu. Rev. Nucl. Part. Sci. **42**, 447 (1992); A. B. Balantekin and N. Takigawa, Rev. Mod. Phys. **70**, 77 (1998); M. Dasgupta, D. J. Hinde, N. Rowley, and A. M. Stefanini, Annu. Rev. Nucl. Part. Sci. **48**, 401 (1998).

²K. Hagino and N. Takigawa, Phys. Rev. C **55**, 276 (1997).

³C. L. Jiang *et al.*, Phys. Rev. Lett. **89**, 052701 (2002).

⁴C. L. Jiang, H. Esbensen, B. B. Back, R. V. F. Janssens, and K. E. Rehm, Phys. Rev. C. **69**, 014604 (2004).

⁵C. L. Jiang *et al.*, Phys. Rev. Lett. **93**, 012701 (2004).

⁶C. L. Jiang *et al.*, Phys. Rev. C **71**, 044613 (2005).

⁷C. N. Davids and J. Larson, Nucl. Instrum. Methods **B40/41**, 1224 (1989); **A345**, 528 (1994).

⁸R. Bass, Nucl. Phys. **A231**, 45 (1974).

⁹A. Gavron, Phys. Rev. C **21**, 230 (1980).

¹⁰J. Charbonneau *et al.*, Bull. Am. Phys. Soc. (1971).

¹¹M. A. Duguay *et al.*, Phys. Rev. **12**, 1677 (1967).

g.6. Hindrance of Heavy-Ion Fusion at Extreme Sub-Barrier Energies for a Small Q-Value System $^{28}\text{Si} + ^{64}\text{Ni}$ (C. L. Jiang, K. E. Rehm, B. B. Back, H. Esbensen, R. V. F. Janssens, C. N. Davids, J. P. Greene, D. J. Henderson, L. Jisonna, C. J. Lister, M. Notani, R. Pardo, D. Peterson, D. Seweryniak, B. Shumard, X. D. Tang, I. Tanihata, X. F. Wang, S. F. Zhu, P. Collon,* S. Kurtz,* and M. Paul†)

An unexpected hindrance of heavy-ion fusion at extreme sub-barrier energies has been observed in experiments performed at ATLAS.¹⁻⁴ It was observed that the excitation functions of some heavy-ion fusion reactions exhibit an abrupt decrease in cross section at extreme sub-barrier energies. This decrease cannot be described by present model calculations.

In all measurements of the hindrance phenomenon investigated thus far, the Q -value for heavy-ion fusion is rather negative, $Q < -36$ MeV. As a result it is inevitable that the S -factor must reach a maximum at sufficiently low beam energies as the final state phase space disappears as the centre-of-mass energy, E approaches $-Q$ (see Ref. 2 for a detailed discussion). This behavior is different from that seen in light-ion or light heavy-ion fusion reactions, *e.g.*, $^{16}\text{O} + ^{16}\text{O}$,⁵ where $S(E)$ is a rather flat function at very low energies.

In order to further explore this issue, we have measured the fusion-evaporation excitation function for the system $^{28}\text{Si} + ^{64}\text{Ni}$ down to 30 nb. This system has a rather small negative fusion Q -value ($Q = -1.78$ MeV). The experiment was performed with ^{28}Si beams in the energy range of 63 - 95 MeV from the superconducting linear accelerator ATLAS at Argonne National Laboratory. The maximum beam current used was ~ 100 pA. The high melting point of the target material, metallic Nickel evaporated on a $40 \mu\text{g}/\text{cm}^2$ carbon foil, prevented damage to the target by the relatively high beam current. Thin targets with thicknesses of about $15 \mu\text{g}/\text{cm}^2$ were used in order to reduce the correction for target thickness in the energy regime of steep fall off of the excitation function. The isotopic abundance of ^{64}Ni was 98.02%, with the remainder coming from ^{58}Ni (0.97%), ^{60}Ni (0.57%), ^{61}Ni (0.05%) and ^{62}Ni (0.39%). The selection of the beam and target combination excluded the possibility of background from fusion reactions coming from beam or target contaminants.¹ Two surface-barrier Si detectors, located at $\pm 43^\circ$ with respect to the beam direction, served as monitors. The absolute cross sections for fusion-evaporation were determined by using elastic scattering measured with the monitors.

The evaporation residues were analyzed with the Fragment Mass Analyzer (FMA)⁶ at 0° , which has been

upgraded with the installation of a split-anode in the first electric-dipole.⁷ The background, originating mostly from scattered beam, was greatly suppressed after this upgrade. The evaporation residues were detected and identified with a focal-plane detector with the configuration PGAC-TIC-PGAC-TIC-PGAC-IC.⁸ Here, the symbols PGAC stand for x - y position sensitive parallel grid avalanche counters, TIC for transmission ionization chambers and IC for a large volume multi-anode ionization chamber. The first PGAC was mounted at the horizontal (x -direction) focal-plane of the FMA. Only one charge state can be measured at each FMA setting. Full charge state distributions were measured at five energies. Three to five charge states were measured at five intermediate energies and one charge state was measured for the lowest six energies. These data are sufficient to determine with the desired accuracy the charge state fractions of the detected evaporation residues.

The angular distributions of evaporation residues were obtained by measuring their velocity distributions. This method was developed previously at Argonne.⁹ Assuming an isotropic emission of particles from the fused system, which is a rather good assumption at low energies, the velocity-distribution of the evaporation residues is also isotropic in the center-of-mass system. A measurement of the velocity distribution in the laboratory system at zero degree therefore yields the complete information about the velocity distribution, also in the transverse direction, which is required to compute the angular distribution and the evaporation residue cross sections.

Because the quantity

$$\frac{1}{v^2} \frac{d^2\sigma}{d\Omega dv} \quad (1)$$

is invariant under the transformation between the laboratory system and the center-of-mass system, one obtains

$$\frac{d^2\sigma}{d\Omega_{cm} dv_{cm}} (\theta_{cm} = 0^\circ) = \frac{v_{cm}^2}{v_{lab}^2} \frac{d^2\sigma}{d\Omega_{lab} dv_{lab}} (\theta_{lab} = 0^\circ). \quad (2)$$

Since $d^2\sigma/d\Omega_{cm}dv_{cm}$ is independent on the angle we obtain the total cross section σ_{total} following

$$\sigma_{total} = \int \int \frac{d^2\sigma}{d\Omega_{cm}dv_{cm}} d\Omega_{cm} dv_{cm} = 4\pi \int \frac{d\sigma}{dv_{cm}} dv_{cm}, \quad (3)$$

where v_{lab} and v_{cm} are the velocity magnitudes of the evaporation residues in the laboratory and centre-of-mass systems, respectively, and $v_{lab} = v_{cm} + v_0$ at 0° (v_0 is the centroid of the velocity distribution of the center of mass in the laboratory system).

Moreover one can get the angular distribution in the laboratory system also by using the following equations:

$$\frac{d^2\sigma}{d\Omega_{lab}dv_{lab}}(\theta_{lab}) = \frac{v_{lab}^2}{v_{cm}^2} \frac{d^2\sigma}{d\Omega_{cm}dv_{cm}}(\theta_{cm} = 0^\circ) = \quad (4)$$

$$\frac{v_{lab}^2}{v_{lab}^2 + v_0^2} \frac{1}{2v_{lab}v_0 \cos(\theta_{lab})} \frac{d^2\sigma}{d\Omega_{cm}} dv_{cm}(\theta_{cm} = 0^\circ).$$

$$\frac{d\sigma}{d\Omega_{lab}} = \int \frac{d^2\sigma}{d\Omega_{lab}dv_{lab}}(\theta_{lab}) d\Omega_{lab}, \quad (5)$$

where $\vec{v}_{lab} = \vec{v}_{cm} - \vec{v}_0$.

Two methods have been used to measure the velocity spectra, the flight time from the target to the PGAC₁, or the flight time between PGAC₁ and PGAC₃. The FMA efficiency was calculated by using these deduced angular distributions.

The primary experimental result of the excitation function (down to about 30 nb) is show in Fig. I-62. This system has been measured previously by the Legnaro group¹⁰ down to a cross section of 41 μb . In the near barrier region the two measurements agree well within experimental uncertainties. There is an energy shift, $\Delta E_{lab} \sim 1.2$ MeV between these two experiments. This situation is rather similar to experiments for the fusion system $^{64}\text{Ni} + ^{64}\text{Ni}$, where an energy shift, $\Delta E_{lab} \sim 1.5$ MeV was observed between Argonne's measurement and Ref. 11.

Coupled channel calculations fitted to the Legnaro data¹² are plotted in Fig. I-62 by the solid line (with an energy shift of 0.8 MeV). Obviously, they over predict the present cross sections at extreme sub-barrier energies.

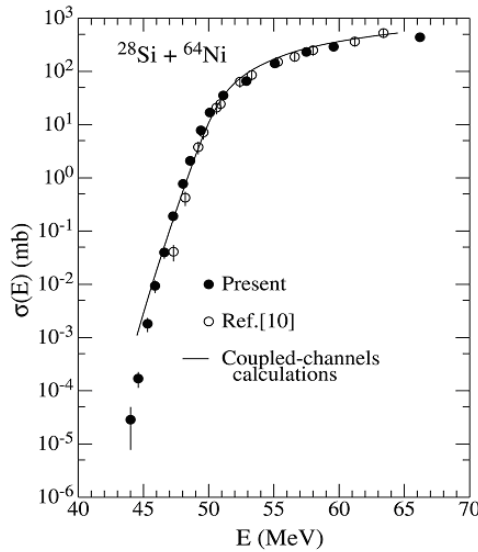


Fig. I-62. Excitation function for $^{28}\text{Si} + ^{64}\text{Ni}$. Solid circles are our preliminary results. Open circles are taken from Ref. 10.

The deduced logarithmic derivatives $L(E)$ and the S -factor are shown in Fig. I-63. In Fig. I-63a the solid line is the constant S -factor expression that was derived in Ref. 2. The dotted line is a linear fit to the low-

energy experimental $L(E)$ data. The crossing point of these two lines determines the location of the maximum of S -factor. There is a clear maximum in the S -factor (see Fig. I-63b), which cannot be reproduced by the

coupled-channels calculations (long-dashed curve, shifted by 0.8 MeV). It thus seems that the fusion hindrance behavior also exists for the system

$^{28}\text{Si} + ^{64}\text{Ni}$. The dotted curve in Fig. I-63b was obtained from the extrapolation line in Fig. I-63a. Data analysis is still in progress.

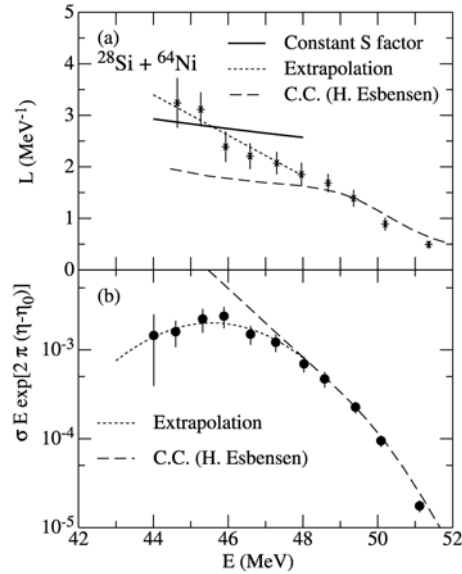


Fig. I-63. (a) The logarithmic derivative $L(E) = d(\ln \sigma E)/dE$, plotted as the function of center-of-mass energy E for $^{28}\text{Si} + ^{64}\text{Ni}$. Stars are obtained from least-squares fits to three data points. (b) The S-factor $S(E) = \sigma E \exp(2\pi\eta)$, plotted as function of center-of-mass energy E . Solid circles are experimental results. The solid curve corresponds to a constant S-factor.² Long-dashed curves are coupled-channels calculations and dotted curves are extrapolation results.

*University of Notre Dame, †Hebrew University, Jerusalem, Israel.

¹C. L. Jiang *et al.*, Phys. Rev. Lett. **89**, 052701 (2002).

²C. L. Jiang *et al.*, Phys. Rev. C **69**, 014604 (2004).

³C. L. Jiang *et al.*, Phys. Rev. Lett. **93**, 012701 (2004).

⁴C. L. Jiang *et al.*, Phys. Rev. C **71**, 044613 (2005).

⁵R. G. Stokstadt *et al.*, Phys. Rev. Lett. **37**, 888 (1976).

⁶C. N. Davids and J. D. Larson, Nucl. Instrum. Methods **B40/41**, 1224 (1989); C. N. Davids, B. B. Back, K. Bindra, D. J. Henderson, W. Kutschera, T. Lauritsen, Y. Nagame, P. Sugathan, A. V. Ramayya, and W. B. Walters, Nucl. Instrum. Methods **B70**, 358 (1992).

⁷C. N. Davids, ANL Phys. Div. Annual Report **ANL-03/23**, 104 (2003).

⁸C. L. Jiang *et al.*, submitted to Nucl. Instrum. Methods A.

⁹C. L. Jiang *et al.*, ANL Phys. Div. Annual Report **ANL-97/14**, 55 (1997).

¹⁰A. M. Stefanini *et al.*, Nucl. Phys. **456**, 509 (1986).

¹¹D. Ackermann *et al.*, Nucl. Phys. **A609**, 91 (1996).

¹²H. Esbensen, private communication.

H. DEVELOPMENT OF NEW EXPERIMENTAL EQUIPMENT

New techniques and new approaches drive the field of nuclear physics forward. It is encouraging that the current year has been very rich in equipment developments. In almost all our experimental areas new projects are emerging that offer unparalleled opportunities for the future.

h.1. Target Laboratory Developments (J. P. Greene)

The target development laboratory is a key component of our research that produces targets and foils of various thicknesses and substrates, depending on the requirements, for experiments performed at ATLAS. The targets are prepared from both naturally occurring materials and stable isotopes that are supplied either in pure, elemental form or as stable compounds. In addition to ATLAS experiments, targets and foils are provided for all staff members whether working within the Physics Division or undertaking experiments at other facilities, for instance, the Advance Photon Source (APS). Also, wherever possible, support is provided to other ANL Divisions, and in particular to requests from researchers at the University of Chicago. Numerous collaborations have grown out of efforts between the Physics Division and target laboratory staff with outside groups in order to provide targets.

In the past year, numerous targets were fabricated either as self-supporting foils, on various substrates or as "sandwich" targets. Targets produced included Ag, Al, Au, ^{10}B , BN, ^{12}C , ^{40}Ca , ^{106}Cd , ^{141}Ce , ^{50}Cr , ^{54}Fe , Havar, ^{180}Hf , $^{92,94,100}\text{Mo}$, Mylar, Nd_2O_3 , ^{58}Ni , ^{208}Pb , $^{108,110}\text{Pd}$, Polycarbonate, Pt, ^{28}Si , ^{112}Sn , Ta, $^{128,130}\text{Te}$, Teflon, Th, ThF_4 , ^{46}Ti , ^{234}U , UC_2 , UF_4 , Valine, Y, and ^{176}Yb . Many of these target foils have been fabricated via mechanical rolling using our small rolling mill. During 2004, approximately 528 targets were prepared for various experiments.

Efficient Gammasphere operation has prompted an increase in demand for various targets and sources prepared by the target laboratory. For the past calendar year, 237 targets were prepared for experiments using Gammasphere.

Beyond target development, the production of thin plastic films and foils for use in various detector systems and energy degraders needed for the CPT and for astrophysics research continues.

As part of ATLAS accelerator support, the target lab routinely produces carbon stripper foils of $2\ \mu\text{g}/\text{cm}^2$ for use in the Tandem Van de Graff as well as other thickness for additional stripping throughout the accelerator. Over 233 carbon stripper and gold foils of various types were prepared for ATLAS during this past year. There continues to be an increase in the preparation of various dilutions of isotopic source material into a form and shape suitable for introduction into the ion sources for the production of enriched beams at ATLAS. These have included ^{64}Ni , $^{34,36}\text{S}$ and ^{50}Ti .

The target development laboratory includes state-of-the-art equipment used for thin-film fabrication. The addition of a new, multi-purpose, computer-controlled vacuum evaporation system extends our capabilities and provides a stable platform for the continued production of accelerator targets. The available techniques consist of multiple resistive heating, focused ion beam sputtering, ion assisted deposition, electron beam and electron bombardment evaporation, carbon arc evaporation, electrodeposition and mechanical rolling. The evaporators are maintained under high vacuum and each vessel contains a quartz-crystal film-thickness monitor with deposition rate indicators. Also included are movable shutters, quartz-lamp substrate heaters and thermocouple temperature sensors, allowing for complete process monitoring during target deposition.

Other auxiliary equipment used for target development includes electrodeposition apparatus, a small rolling mill, an alpha particle counting chamber, inert atmosphere glove box, laminar flow clean bench, pellet press, a reduction furnace, and a variety of precision balances. A turbo-pumped target storage facility is in operation for maintaining, under high vacuum, those targets that readily oxidize in air. This system utilizes computer-controlled circuitry to prevent targets from exposure to atmosphere during power interruptions. A second storage system employing a bank of vacuum desiccators and connected to a mechanically pumped manifold is available for use by individual experimenters. An additional set-up,

consisting of two large glass desiccators evacuated using a small turbo-pump system, is in operation for long-term material storage. This allows a separation of material storage from target storage, hence eliminating repeated exposure when transferring and retrieving targets.

A low-level radioactive source and target preparation laboratory exists at a separate location within the Division that is dedicated to the production of these sources and targets. Available preparation techniques include multiple resistive heating, employing a diffusion-pumped vacuum evaporator. A second, smaller evaporator system was constructed for close proximity evaporations of higher activity materials, to be used as targets as well as radioactive sources. The small size of this system allows for installation within a hood. Preparation and handling of ^{14}C targets as well as fission sources (mainly ^{252}Cf) by electrodeposition has been done in this lab for experimental studies at ATLAS as well as routine

rolling of natural U and Th foils.

Another area of increased research effort has been toward development of radioactive beams for the RIA proposal and involves neutron producing targets which in turn induce fission in uranium or a uranium compound production target. Toward this end, direct measurements of the thermal conductivity of uranium carbide have been made using the method of electron beam heating provided by a 10 kV mortar source in vacuum with the temperature measured as a function of beam current using a two-color pyrometer. Sample uranium carbide material of small grain size is being prepared in-house in collaboration with the ES Division in Building 212. This work is still in progress.

In August, the Physics Division hosted a RIA Summer School, which included a “hands-on” Accelerator Targets Session which gave students access to the target facility and target making techniques.

h.2. New Control System Hardware and Software for the FMA (C. N. Davids)

When the FMA was first put into operation in 1991, a control system using an Apple Macintosh II was written in Borland’s Turbo Pascal, taking advantage of the Macintosh graphical user interface. Communication between the computer and the FMA ion-optical devices, power supplies, and vacuum sensors was accomplished via an RS-232 serial link. However, after several years, Turbo Pascal for the Macintosh was discontinued, thus freezing the development environment. Many surplus Macintosh II computers were stockpiled for replacement parts,

but as aging and obsolete hardware began to cause reliability problems, replacement of the control software and hardware finally became a necessity. New software for the FMA control system has been written using REALbasic, an object-oriented program development environment for Macintosh, Microsoft Windows, and Linux. The program utilizes the existing serial communication link, and the user interface was made identical to the Pascal version. The new program is now in regular use, with backups and development being done on a separate identical computer.

h.3. The Isobar Separator Ion Trap for the APT and CPT Trapping Systems (G. Savard, N. D. Scielzo, J. A. Clark, J. Fallis, J. Guest, S. Gulick, A. A. Hecht, A. Levand, B. Lundgren, B. Nardi, H. Sharma, K. S. Sharma, M. Sternberg, I. Tanihata, A. Villari, J. Wang, Y. Wang, Z. Zhou, and B. J. Zabransky)

The Advanced Penning Trap (APT) System consists of two newly constructed ion traps – a Penning Trap “Isobar Separator” for the purification of ion samples and an RFQ “Decay Trap” that will be used to study radioactive decays. These new traps will expand the ion trapping capabilities on the Canadian Penning Trap (CPT) mass spectrometer beamline.

The Isobar Separator will deliver extremely pure samples of radioactive ions to the RFQ Decay Trap

for decay studies or to the CPT mass spectrometer to extend its reach to even more weakly-produced and short-lived species. With a magnetic field of 6.83 T, the Isobar Separator will ultimately be able to obtain mass resolutions ($\Delta m/m$) of 10^{-5} and will allow removal of unwanted isobars from ion samples by applying weak RF electric fields at the appropriate cyclotron frequencies.¹ In 2004, the superconducting magnet was shimmed and the titanium vacuum tube used to host the trap installed and lined up on the magnetic field axis using collimated

electron beams. The trap was installed together with the gas feeding system. The ion optics elements used to transfer ions from the existing CPT ion injection

system to the Isobar Separator were designed, constructed, and assembled in the Triangular Room (see Fig. I-64).

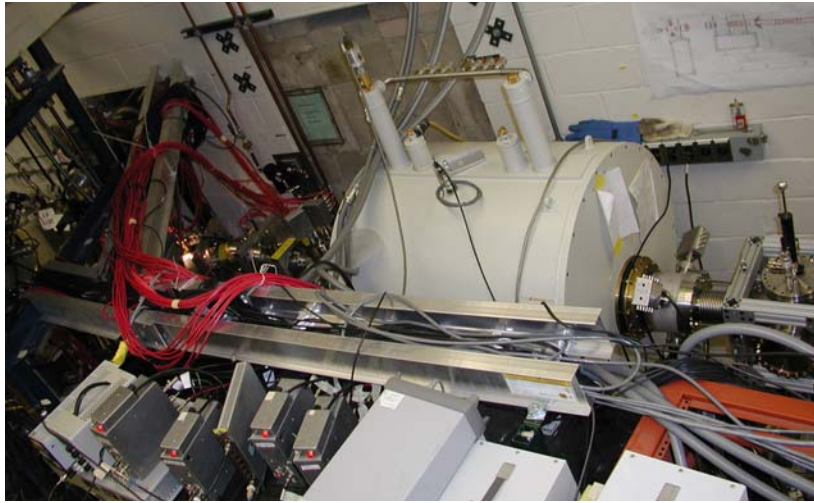


Fig. I-64. Photo of the isobar separator ion trap magnet in location in the triangular room and of the transfer lines feeding ions into and out of it. After cooling and mass separation, the purified- ion sample can either be sent back towards the CPT mass precision trap or be transported (to the right on the figure) to the APT decay trap.

While loading ions into the RFQ Trap should be straight-forward, directing ions back to the CPT requires ejecting ions from the Isobar Separator in the direction from which they entered. The electronics needed for the required rapid control of the beamline flow is nearly completed. In addition, the MCP and Silicon detector diagnostics used to optimize ion transport have been designed to accommodate the bi-direction ion flow. The diagnostic detectors are located off-axis at 90° from the ion flow direction.

By applying the appropriate electric potentials to a quadrupole deflector, the ion beam can be directed to either detector while moving either towards the isobar separator or coming back from it. Using these diagnostics, ions were loaded into the isobar separator, and with the injection of He gas into the trap, the cooling and centering frequencies for various contaminants have been determined. Optimization of the mass resolution and efficiency in the isobar separator ion trap is ongoing.

¹G. Savard *et al.*, Phys. Lett. **A158**, 247 (1991).

h.4. A Solenoid Spectrometer for Reactions in Inverse Kinematics (B. B. Back, C. J. Lister, K. E. Rehm, J. P. Schiffer, S. J. Freeman,* and A. H. Wuosmaa†)

The study of the structure of short-lived nuclei can often be studied only with reactions in inverse kinematics, such as transfer reactions. This poses severe experimental problems that are difficult to overcome. A magnetic device has been discussed (see ANL Physics Division Annual Report, 2003 p. 96) that would overcome many of the difficulties encountered by the large arrays of Si detector telescopes that are used at present.

During the last year the technical and operating aspects of the device have been investigated. A

construction site was chosen in the general purpose area, which can receive both stable and radioactive beams. A cost and effort breakdown has been made. In early 2005 a formal proposal was submitted to the DOE Office of Nuclear Physics for the construction of such a device.

In developing the science case for such an instrument a workshop was conducted and several scientists made contributions to the proposal, in addition to the names on this report. They included: Dr. L. Ahle (LLNL), Dr. K. L. Jones (Rutgers), Dr. A. O. Macchiavelli (LBNL), and Professor A. Champagne (North Carolina).

A more detailed design is being carried out and options for conducting a set of test measurements in a “demonstrator” project have been investigated.

*University of Manchester, United Kingdom, †Western Michigan University.

h.5. A New Focal-Plane Detector System at the Argonne Fragment Mass Analyzer for Low Fusion-Evaporation Cross Section Measurements (C. L. Jiang, D. J. Henderson, D. Seweryniak, I. Tanihata, K. E. Rehm, C. N. Davids, D. Peterson, B. B. Back, J. P. Greene, R. V. F. Janssens, C. J. Lister, R. C. Pardo, T. O. Pennington, B. Shumard, S. Sinha, X. D. Tang, S. Zhu, P. Collon,* S. Kurtz,* and M. Paul†)

A recent program at the ATLAS facility has begun to study and characterize a new hindrance phenomenon at extreme sub-barrier energies for heavy-ion fusion reactions.¹⁻³ In order to study this behavior to very low cross sections, a new focal-plane detector system has been designed and constructed with the Fragment Mass Analyzer (FMA).

The new detector system has a modular structure configured as:

PGAC-TIC-PGAC-TIC-PGAC-IC,

where PGAC stands for an x - y position-sensitive parallel grid avalanche counter⁴, TIC for a transmission ionization chamber⁵ and IC for a large volume multi-anode ionization chamber.⁶ The first PGAC is mounted at the x focal-plane of the FMA. The three PGACs measure the position sets (x_1, y_1) , (x_2, y_2) , and (x_3, y_3) . Time-of-flight (TOF) measurements, t_2 and t_3 , between PGAC₁-PGAC₂ and PGAC₁-PGAC₃, are also recorded. The ionization chambers provide seven ΔE signals: ΔE_1 - ΔE_4 from the two TICs (two each), and ΔE_5 - ΔE_7 from the IC. Another TOF signal, t_{rf} , measures the time difference between the accelerator radio frequency (RF) and the first PGAC. Each of the three PGACs also provides a ΔE signal. These measurements provide a rich data set from which excellent separation of desired signals over background has been obtained. The three PGACs and the two TICs share a common gas volume and are operated at a pressure of 3 Torr of isobutane. The last ionization chamber had an adjustable pressure of 22-30 Torr of isobutane. The gas pressures in both volumes were regulated to better than 0.05 Torr. A mylar foil of 0.12 mg/cm² served as the entrance window to the first PGAC. A second mylar foil of 0.22 mg/cm² thickness separated the third PGAC from the last ionization chamber.

At low energies, the fusion evaporation residues often concentrate into only one or two masses and the element separation is generally unimportant. Full tracking of each event, using all of the signals measured in the detector system, is a good way to identify residues, but this can be rather tedious. A simpler method is desirable. In most cases a single, appropriate two-dimensional plot allows for the identification of evaporation residues at moderately low cross sections. Full tracking is required only at the lowest cross sections, where there are very few events.

Previous excitation function measurements at the FMA have found that pile-up from the E or ΔE signals is often the main background, even when pile-up rejection electronic circuits are used, because the counting rates are often very high in these low level cross sections experiments with most events originating from scattered beam. On the other hand, the pile-up behavior of the time-of-flight signal is different; it does not result in "peak summing". A rather successful residue-background separation method often employed was a two-dimensional plot of ΔE (or E) versus TOF. On that basis, the new design incorporates more TOF signals, longer flight paths, and tracking capability. Some performances of the present detector in an experiment $^{64}\text{Ni} + ^{100}\text{Mo}$ will be described. The experimental results of the excitation function are published in Ref. 7.

A set of x_i spectra at PGAC₁, PGAC₂ and PGAC₃ from a measurement at $E_{lab} = 245.8$ MeV, gated on only two masses, $m = 160$ and $m = 161$, are shown in Fig. I-65. The FMA was set for $q_0 = 25.5$ and $m_0 = 160$. Thus two charge states, $q = 25$ and 26 , were measured simultaneously. The PGAC₁ (m/q) spectrum is shown in (a), PGAC₂ spectra for $q = 25$ and $q = 26$ are shown in (b) and (d), and PGAC₃ spectra for $q = 25$ and $q = 26$ are shown in (c) and (e), respectively.

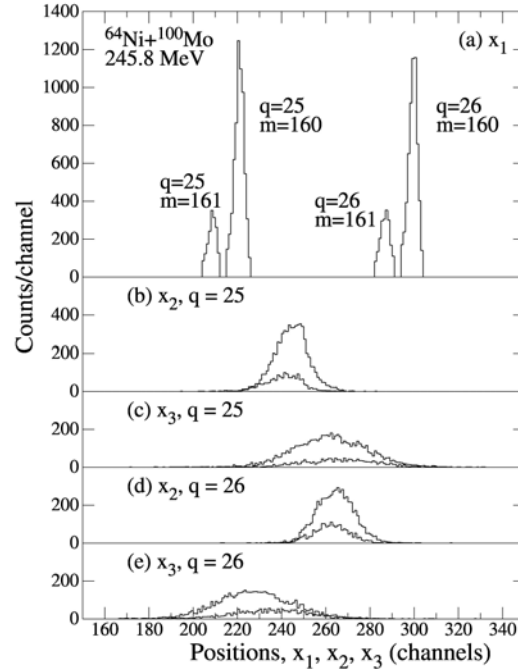


Fig. I-65. Measured x -tracking for the case mentioned in the text. x_1 , x_2 , and x_3 are measured at the three PGACs. Two masses and two charge states are shown for x_1 (a). Also shown is the evolution to x_2 and x_3 for the low charge state peaks ((b) and (c)) and high charge state peaks ((d) and (e)). Higher yield lines are for mass 160, and lower yield lines for mass 161, respectively. See text for details.

These position signals, at the three PGACs, constitute one kind of position-tracking for the present detector system. Another way to illustrate the position tracking behavior is with an x_1 - x_2 - x_3 plot. For each event, the measured values x_1 , x_2 and x_3 are used as ordinates and the values 100, 200 and 300 are respectively assigned to x_i along the abscissa. The three points of each event are then connected by

lines. An example is presented in Fig. I-66. In this figure, only 100 events with mass, $m = 161$, and two charge states, $q = 23$ and 24 , are shown. Good residue events are shown as dashed lines. Also shown in this figure are some dark, solid lines from background events that can be easily discriminated. It should be noted that this measurement corresponds to a low cross section level of ~ 300 nb.

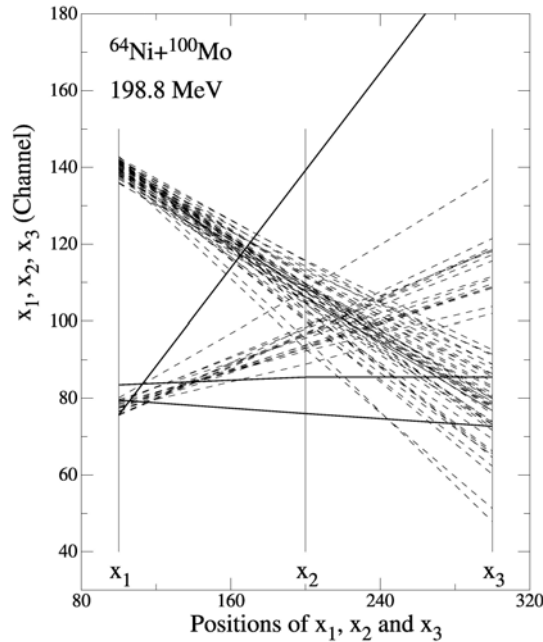


Fig. I-66. An x_1 - x_2 - x_3 tracking plot for $E_{lab} = 198.8$ MeV. The dashed lines are tracks due to evaporation residues: $m = 161$, $q = 23$ (smaller x_1) and 24 (larger x_1), respectively. The three dark solid lines are due to background events.

In order to show the resolution of the x_i determinations, a one dimensional plot dx is shown in Fig. I-67 for the same measurement at $E_{lab} = 245.8$ MeV. The quantity dx is defined as $x_2 - (x_1 + x_3)/2$, since the distances from PGAC₁ to PGAC₂ and PGAC₂ to PGAC₃ are the same. For clarity, only the group $m = 160$ and $q = 26$ is given. The FWHM of

the dx spectrum is 5.3 channels that corresponds to a x_2 peak centered at channel 265.8, with a x_i resolution of about $\pm 1\%$.

The y -tracking behavior is similar to the x -tracking and can be used as an auxiliary tool, though the y_i resolutions are poorer than the x_i resolutions.

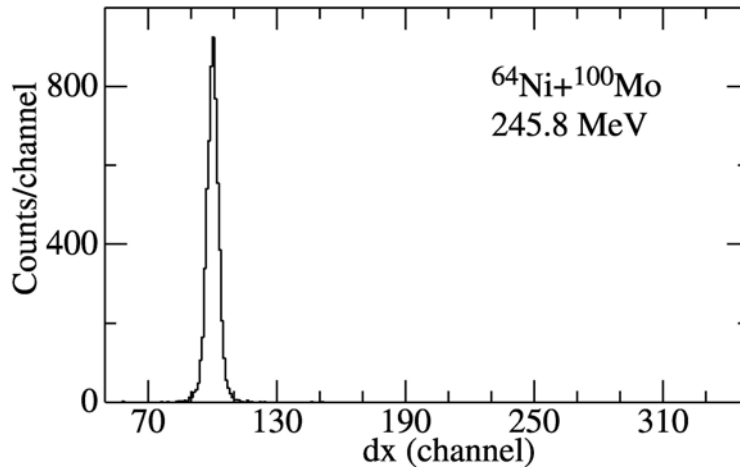


Fig. I-67. Illustration of x -tracking resolution for $q = 26$ and $m = 160$ in a measurement for $E_{lab} = 245.8$ MeV. The abscissa is defined as $dx = x_2 - (x_1 + x_3)/2$.

For our detector system each of the seven ΔE signals, $\Delta E_1 - \Delta E_7$ and their combinations (sums), together

with each of the two time-of-flight signals, t_2 and t_3 , can form a two-dimensional ΔE - t spectrum. In Fig. I-68, six

$\Delta E_i - t_3$ spectra are compared from a measurement at $E_{lab} = 211.8$ MeV. The ΔE_7 versus t_3 plot is not shown because, in this measurement, the gas pressure in the last ionization chamber was too high (30 Torr) and many residues produced only small signals in the ΔE_7 region. In each plot of Fig. I-68 there is a region originating from the evaporation-residues, which is indicated in Fig. I-68d as an example. The other

events are due to background. Obviously, as different particles pass from the focal-plane (PGAC₁) downstream to the last IC chamber, their ΔE_i behavior is different. In this case, ΔE_i signals from the background decreased more rapidly than the corresponding signals for residues as they moved away from the focal-plane. The separation between the residues and the background is best in the $\Delta E_6 - t_3$ spectrum.

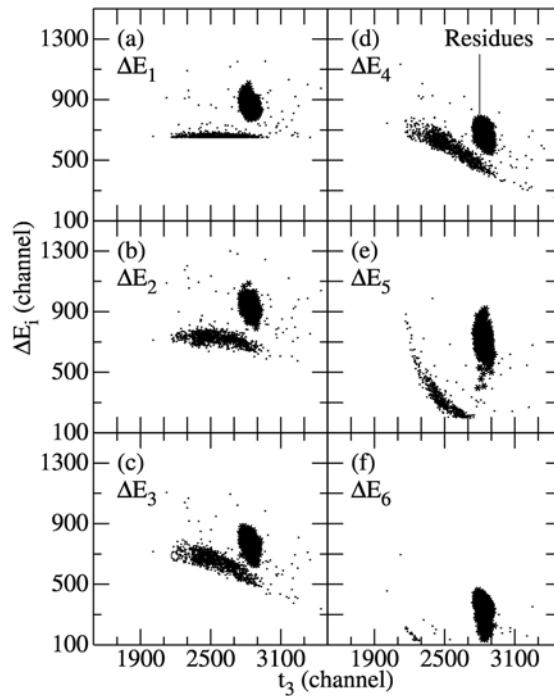


Fig. I-68. Two-dimensional ΔE_i vs. t_3 spectra, measured at $E_{lab} = 211.8$ MeV. The gas pressure in the IC was 30 Torr. The region in the right part of each plot is due to evaporation residues, which is marked in (d). All other events are background. In (a), only part of the background events are shown (a ΔE_1 cut appears).

In Fig. I-69, three plots of ΔE_i vs. t_2 and ΔE_i vs. t_3 are compared for a measurement at $E_{lab} = 205.1$ MeV (the gas pressure in IC was 22 Torr). There is good

separation of residues from background in all spectra, with $\Delta E_6 - t_3$ being the best choice, when using a single two-dimensional spectrum for residue identification.

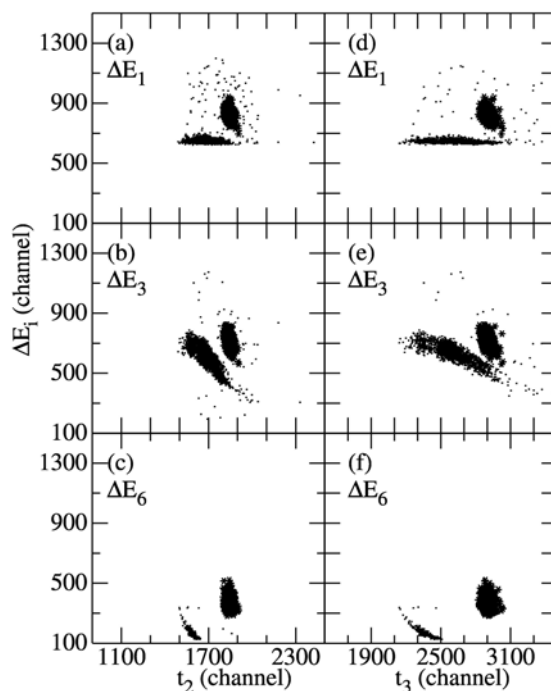


Fig. I-69. Comparisons of two kinds of two-dimensional spectra, $\Delta E_i - t_2$ and $\Delta E_i - t_3$, measured at $E_{lab} = 205.1$ MeV. The gas pressure in the IC was 22 Torr. The separations between evaporation residues and background are better with signal t_3 than with signal t_2 . Just as in Fig. I-68, ΔE_1 cuts were applied in Figs. I-68a and I-68b.

The seven ΔE_i signals (measured by the TIC or IC) effectively measure the Bragg curve of the particles. Figure I-70 illustrates such a curve obtained from a 245.8 MeV bombardment. The y-axis is the ΔE_i energy-loss per unit length and unit pressure ($\Delta E_i/\text{cm/Torr}$), and the x-axis follows the seven ΔE sections. The 100 dotted lines are due to the evaporation-residues and the 50 dashed ones originate from background. It can be seen that residue events and background events stop in different anode regions. In fact, Figs. I-68a-f display a similar behavior in the $\Delta E_i - t_3$ spectra. The circles inside the residue trajectories in Fig. I-70 are energy-loss calculations of the central tracks, normalized to

the measured data. Because residues stopped in the region of ΔE_7 , rendering the quantity $\Delta E_7/\text{cm/Torr}$ is meaningless, and the simulations are only shown for ΔE_1 to ΔE_6 . In this experiment, all residue energies are lower than the maximum of the Bragg curve so that the Bragg peak is not visible. Thus, the dE/dx measurements only show the increasing part of the Bragg curve. Background events from pile-up signals may have similar amplitudes for some ΔE_i signals, but it is highly unlikely that all of their ΔE_i signals would be similar to the residues. This provides yet another important tracking method that can be used to suppress background contaminations. Other two-dimensional plots, such as t_2 versus t_3 and ΔE_i versus E , can also be helpful in identifying the background.

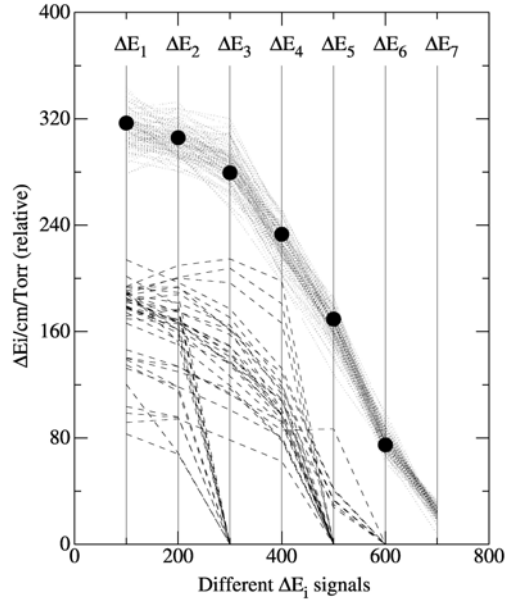


Fig. I-70. A Bragg curve spectrum obtained from seven ΔE_i signals. The y-axis is the energy lost per unit length and unit pressure ($\Delta E_i/\text{cm/Torr}$); the x-axis tracks the ΔE sections. The dotted lines indicate evaporation residues and the dashed lines indicate background. The filled circles are from calculations for the energy loss of an evaporation residue normalized to the measurement.

As mentioned above, the TOF from the longer flight distance, t_3 , combined with a ΔE signal measured far away from the focal-plane, (e.g. ΔE_6), yields the best separation between evaporation residues and background. The conditions during the commissioning experiment were chosen by assuming that some background particles would have longer ranges compared with the residues and enter the third anode region of the IC, while the residues stop in the second anode region of the IC. The third anode signal (ΔE_7) would then be used as a veto. During the experiment, however, it was found that the ranges of most background particles were less than the range of the residues. Thus, the pressure of this last IC was decreased to stop the residues in the last anode

region. Four plots of ΔE_6 versus t_3 , from measurements at different beam energies, are shown in Fig. I-71. The measured fusion-evaporation cross sections are 1.1 mb, 242 nb, <20 nb, and <4.6 nb, respectively. As in Figs. I-68 and I-69, the bands to the left in Fig. I-71 originate from background, most of which comes from multiply-scattered beam particles from the FMA beamline entrance or the beamstop in the first split-anode region. The events inside the windows of Figs. I-71a and I-71b are from residues. There are no events inside the window of Fig. I-71c. Further analysis reveals that the events inside the window of Fig. I-71d are due to background rather than evaporation residues. This will be discussed below, after a preliminary discussion of the background.

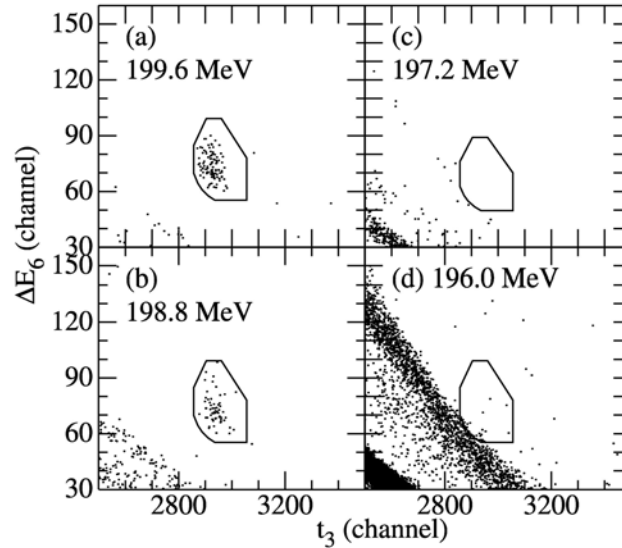


Fig. I-71. Two-dimensional plots of ΔE_6 versus t_3 obtained at incident energies of 199.6 MeV (a), 198.8 MeV (b), 197.2 MeV (c) and 196.0 MeV (d), respectively. The events inside the windows of (a) and (b) originate from evaporation residues. Other events are background.

The spectra in Figs. I-71a and I-71b represent about 5 and 12 hours of data, respectively, with an average beam current of 60 pA on target. The background is minimal. The m/q spectra in Figs. I-72b and I-72c were obtained by gating with a window around the respective residues in the ΔE_6 versus t_3 plots of Fig. I-71. Peaks at channels 103 and 146 are for $m = 162$ and $q = 23$ and 24, respectively. The m/q spectrum of Fig. I-72a, which was taken at a higher incident energy with larger cross sections, is included for comparison. The spectrum in Fig. I-71c represents 3 hours of data only, shorter than Fig. I-71b (12 hours), but the background is higher. Figure I-71d, a 15

hours run, exhibits even more intense background. The sources of this background are still uncertain. It is not simply proportional to the beam current or the integrated dose. The only differences between the data of Figs. I-71b, c and d are the beam energies and the E_0 setting of the FMA. The incident energies, E_{lab} , were 198.8, 197.2 and 196.0 MeV, and the FMA was set for $E_0 = 71.8$, 71.0 and 71.0 MeV, respectively. This means that small differences in these energies or slightly different beam-tuning settings resulted in scattering from more "sensitive" regions of the FMA. This background will be examined in more detail in future studies.

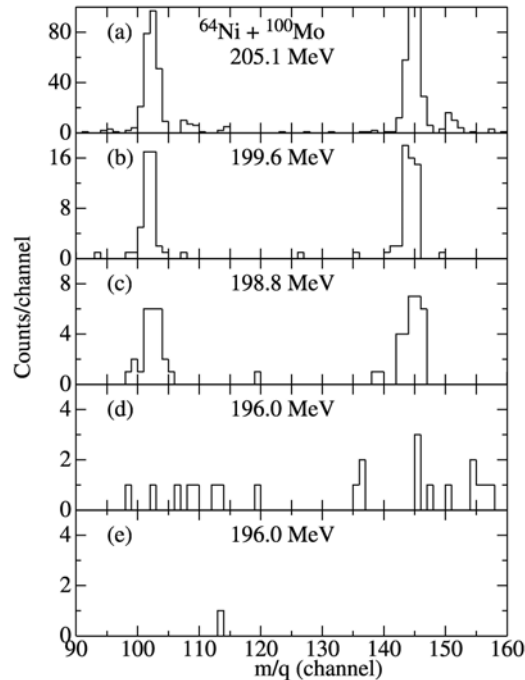


Fig. I-72. Position (m/q) spectra obtained at the various indicated energies of 205.1 MeV (a), 199.6 MeV (b), 198.8 MeV (c), 196.0 MeV (d) and 196.0 MeV (e), respectively. The events correspond to counts inside the respective windows of Fig. I-71, but for (e), the additional window (Fig. I-74) is applied as well. See text for details.

Despite the increased background of Figs. I-71c and I-71d, the residue separation is still rather clean. For both of these runs, a rather large window in the ΔE_6 versus t_3 spectrum was used. For clarity, Figs. I-71b and I-71d are reproduced in Fig. I-73, with open circles representing the events inside the windows. Each event inside the window was then fully tracked to check whether it corresponded to a real evaporation residue event or to a background event. For example, there are 23 events inside the window of expected residues in Fig. I-71d. Their respective m/q spectra are shown in Fig. I-72d. These 23 events are rather random in m/q , with residue-candidates around channel 103 and 146. Examining the plots of ΔE_5 versus t_3 shown in Fig. I-74b reveals that 22 of these 23 events fall outside the indicated window for

the location of the expected residues. Figure I-74a is the same ΔE_5 versus t_3 plot corresponding to the measurement of Fig. I-73a, where the open circles are residue events inside the ΔE_6 versus t_3 window. There is one event inside the expected window in Fig. I-73b. Its m/q value, shown in Fig. I-72e, lies outside the expected m/q peaks around channels 103 or 146. Even though several background events are located inside the ΔE_5 versus t_3 window in Fig. I-74a, they are outside the ΔE_6 versus t_3 window in Figs. I-73a or I-71b. Further checks utilizing all of the other signals and tracking methods mentioned above clearly reveal that for the last two energies, these "candidate" events were all associated with background. Hence, only upper limits for the measured cross sections could be determined.

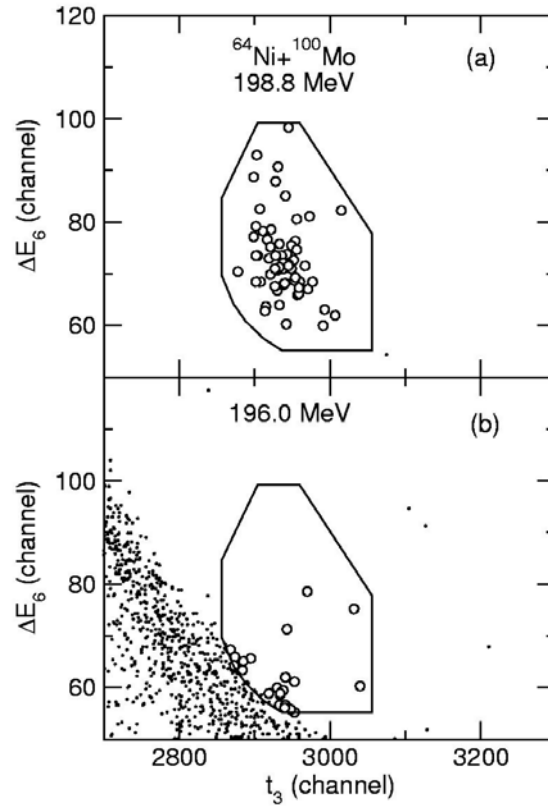


Fig. I-73. Enlarged views of Figs. I-71b and I-71d, respectively. The isolated group in (a) (open circles) originates from evaporation residues, whereas the other events are caused by background. At $E = 196.0 \text{ MeV}$ (b), 23 events (open circles) fall inside the acceptance window for evaporation residues. Further analysis (Figs. I-72 and I-74) shows that these events are background, as discussed in detail in the text.

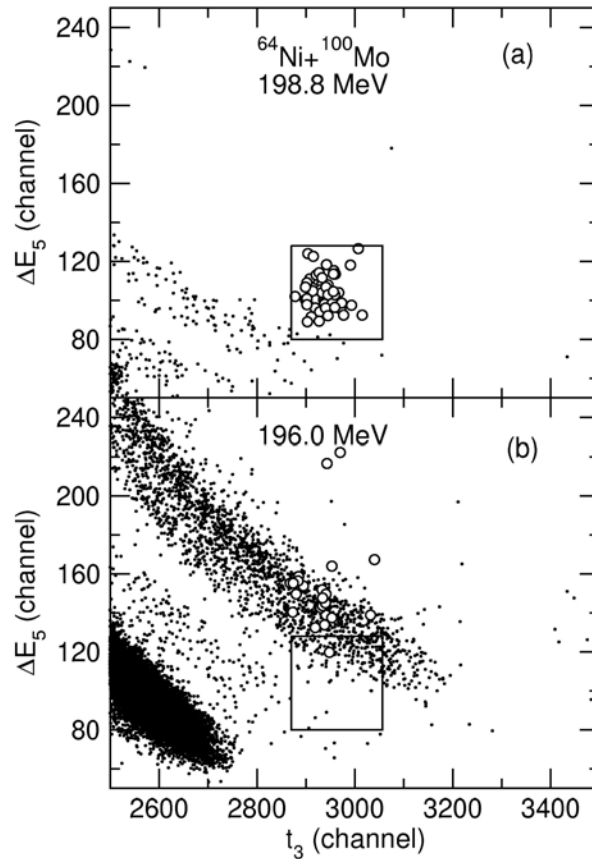


Fig. I-74. Two-dimensional plots of ΔE_5 vs. t_3 obtained at incident energies of 198.8 MeV (a) and 196.0 MeV (b). Open circles are the events inside the ΔE_6 versus t_3 windows in Figs. I-73a and I-73b, respectively. See text for details.

It was found that, with the upgraded FMA and the present detector system, a beam suppression factor of about 4×10^{-17} can be achieved for the Ni + Mo system. The experimental result for the $^{64}\text{Ni} + ^{100}\text{Mo}$ and other related details of the experiment can be found in Ref. 7.

Five main conclusions can be drawn from the present work are as follows: 1) Even for a rather low energy heavy-ion fusion experiment, full tracking of the evaporation residues is possible and important, especially for low cross section measurements where background suppression is crucial. For this purpose a new detector system has been built and successfully deployed. 2) For the new focal plane detector system of the FMA, the longer flight path and the ΔE signals near the end of the track give the most useful

information for the separation of residues from background. 3) A rather clean separation between evaporation residues and background events can be achieved by using a two-dimensional $\Delta E_6 - t_3$ spectrum, resulting in cross sections down to the ~ 300 nb level for the $^{64}\text{Ni} + ^{100}\text{Mo}$ system. For even lower incident energies, full tracking is necessary to identify the good events. The new detector system also avoids the detector damage problem frequently experienced with Si solid-state detectors at the FMA focal plane. 4) With the upgraded FMA and the new detector system, a beam suppression factor of about 4×10^{-17} has been demonstrated. 5) The sources of some of the background events are still unknown. The new detector system will allow us to study the background in more detail, thereby enabling the measurement of even smaller cross sections.

*University of Notre Dame, †Hebrew University, Jerusalem, Israel.

¹C. L. Jiang *et al.*, Phys. Rev. Lett. **89**, 052701 (2002).

²C. L. Jiang *et al.*, Phys. Rev. C **69**, 014604 (2004).

³C. L. Jiang *et al.*, Phys. Rev. Lett. **93**, 012701 (2004).

⁴D. G. Kovar, D. J. Henderson, and B. B. Back, ANL Phys. Div. Annual Report **ANL-90/18**, 108 (1990).

⁵T. O. Pennington *et al.*, ANL Phys. Div. Annual Report **ANL-03/23**, 105 (2003).

⁶A. N. James *et al.*, Nucl. Instrum. Methods **A267**, 144 (1988).

⁷C. L. Jiang *et al.*, Phys. Rev. C **71**, 044613 (2005).

h.6. Performance of a Compton Camera Using Digital Pulse Processing (C. J. Lister, E. F. Moore, F. G. Kondev,* B. Philips,† and E. Wulf†)

Position sensitive hyperpure germanium wafers have considerable potential in many areas of imaging as well as in nuclear physics research. We have been working on an LDRD project to construct a Compton Camera capable of seeking and imaging sensitive materials. The camera has position sensitivity on two levels, “strip level” using analog electronics gives position resolution of ± 2.5 mm and “digital interpolation” level of ~ 1 mm. During this year we set up a fully digital Compton Camera at the Naval Research Laboratory in Washington, DC, and made our first measurements. These results were reported and have been published in the IEEE proceedings

from the Rome conference on advanced imaging techniques.¹ Good 3-D information was obtained, using rise time information to establish the depth of each interaction, and induced signals on neighbor strips to improve lateral location.

We also have established a procedure for the loan of sensitive materials from within ANL to test our detector system. We arranged the loan of a set of plutonium foils and mounted them in Gammasphere in order to establish methods for determining the provenance of the material. Analysis of these data is in progress (Fig. 1).

*Nuclear Engineering Division, Argonne National Laboratory, †Naval Research Lab, Washington, D.C.

¹E. A. Wulf, B. F. Philips, W. N. Johnson, J. D. Kurfess, E. I. Novikova, C. J. Lister, and F. G. Kondev, Proceedings of the IEEE Nuclear Science Symposium and Medical Imaging Conference (NSS/MIC), Rome, Italy, October 16-22, 2004, to be published (2005).

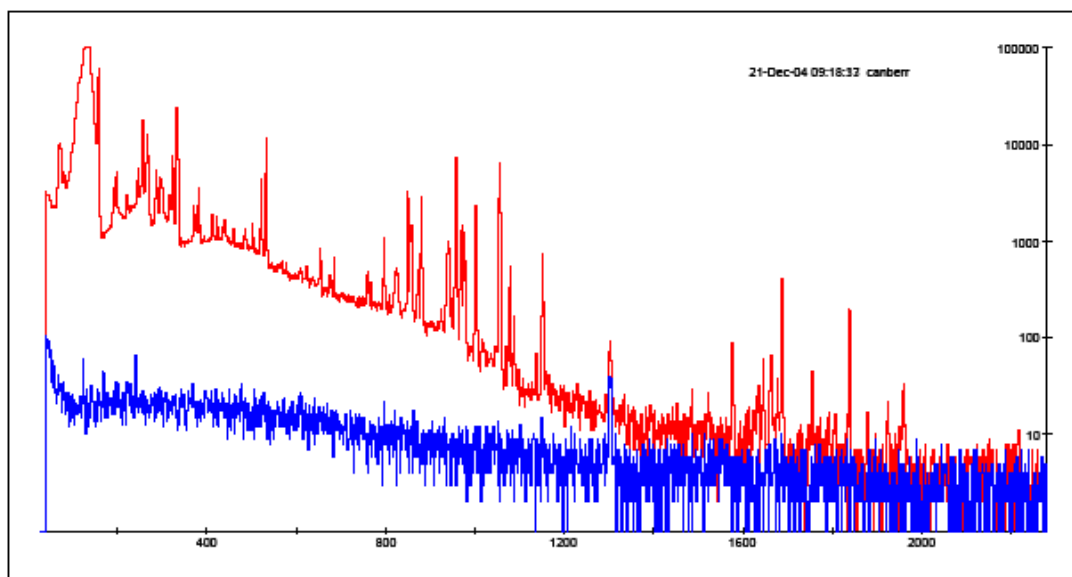


Fig. I-75. Gamma ray spectrum from a plutonium sample assayed with Gammasphere. The intensity of various lines can be used to establish the exact isotopic makeup of the sample and hence its provenance.

h.7. Ambiguity in Gamma Ray Tracking of “Two Interaction” Events (N. J. Hammond, T. Duguet, and C. J. Lister)

Tracking of gamma-rays in germanium detectors can allow the full reconstruction of interactions, a feature that is useful in many applications. Scrutiny of the kinematics and geometry of gamma rays which are Compton scattered only once prior to full absorption reveals that there are special cases where even perfect spatial and energy resolution cannot resolve the true interaction sequence and consequently the gamma-ray tracks cannot be unambiguously reconstructed. The photon energy range where this ambiguity exists is from 255 keV to about 700 keV. This is an energy

region of importance for nuclear structure research and a domain where two-point interactions are probable.

We have made a careful analysis of this ambiguity and produced analytical formulae to identify the regions of difficulty. Figure I-76 shows an illustration of an event that cannot be properly reconstructed, even in a detector with perfect spatial and energy resolution. This research has been accepted for publication in *Nuclear Instruments and Methods*.¹

¹N. J. Hammond, T. Duguet, and C. J. Lister, *Nucl. Instrum. Methods* **A547**, 535-540 (2005).

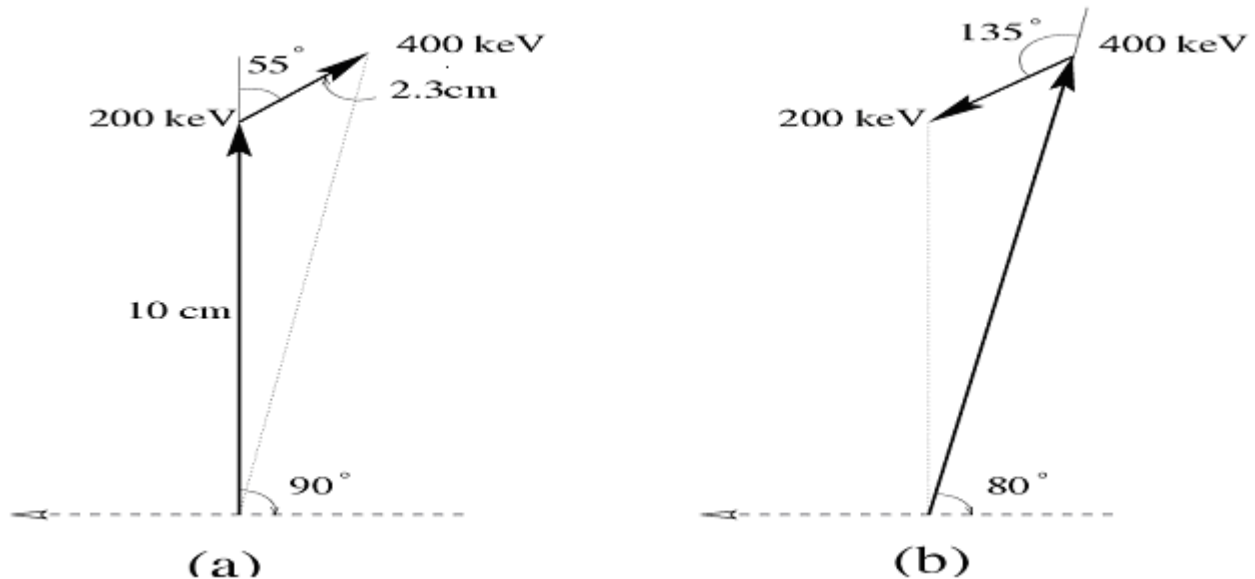


Fig. I-76. An example of an ambiguous event in which the energy deposition and the location of interaction points can be exchanged, so the true sequence of events is not resolvable.

h.8. A Bragg Scattering Method to Search for the Neutron Electric Dipole Moment

(M. Peshkin, G. R. Ringo, T. W. Dombeck,* D. S. Hussey,¶ D. L. Jacobson,¶ H. Kaiser,† D. D. Koetke,‡ T. D. S. Stanislaus,‡ R. K. Smither,§ and S. A. Werner¶)

The goal of this project is to measure the neutron EDM by observing the precession of the neutron spin in the crystalline electric field when the neutron undergoes several thousand Bragg reflections from a perfect silicon crystal. A preliminary experiment carried out at the Missouri University Research Reactor showed that the reflectivity coefficient of one of our crystals is greater than 0.9999, with 95%

confidence. In the past year we completed construction of a table to hold and orientate the crystal within the solenoid and we moved the experiment to the NIST reactor. Also, two NIST physicists, Daniel S. Hussey and David L. Jacobson, have joined the collaboration. In spring 2005, we will repeat the reflectivity measurement at NIST and plan to achieve an uncertainty in the reflectivity of 2×10^{-5} . The reflectivity measurement will

be followed in fall 2005 by a proof-of-principle experiment to measure the neutron's magnetic dipole

moment by the same method and in the same electric fields as in the EDM measurement.

*University of Hawaii, †University of Indiana, ‡Valparaiso University, §APS User Program, Argonne National Laboratory, ¶National Institute of Standards and Technology.

h.9. Heavy Element Scattering Chamber Upgrade (D. Peterson and J. Falout)

The heavy element scattering chamber¹ was designed to accommodate large-diameter rotating wheel targets necessary to withstand high beam currents. A recent experiment² performed at ATLAS required highly-enriched (>99%) ²⁰⁴Pb target material, the cost of which prohibited fabrication of a large target wheel. The chamber was therefore modified to accommodate a smaller target wheel designed for use with Gammasphere experiments since one could expect to produce two or three such wheels from a modest amount of target material. The primary modification required the translation of the rotation axis from the chamber center to only a few cm below the beam. Figure I-77 shows the solution. An aluminum mounting bracket attaches to the main shaft bearing housing via a C-clamp mechanism. A

wheel (below) directly mounted to the main axis drives the target wheel (top) with a nylon belt which is kept taut via an adjustable idler wheel assembly (left). The translation is a two-piece design so that the top wheel can be moved up or down relative to the bottom wheel in order to properly align with the beam axis. The idler shaft is also adjustable to maintain proper tension regardless of the spacing between the two main gears. The target wheel mounts directly to the top gear, which has openings to match the target frames. All gears are one-to-one, ensuring consistent rotational velocity relationships regardless of target wheel geometry. This assembly was successfully used in a 6-day run, rotating at velocities between 1100 and 1700 rpm with beam intensities up to 85 pnA. The Pb targets showed no effects of melting or unusual stress indicating the success of this design.

¹A. Heinz *et al.*, ANL 2001 Annual Report, ANL-02/15 (2002).

²D. Peterson *et al.*, section c.4. of this report.

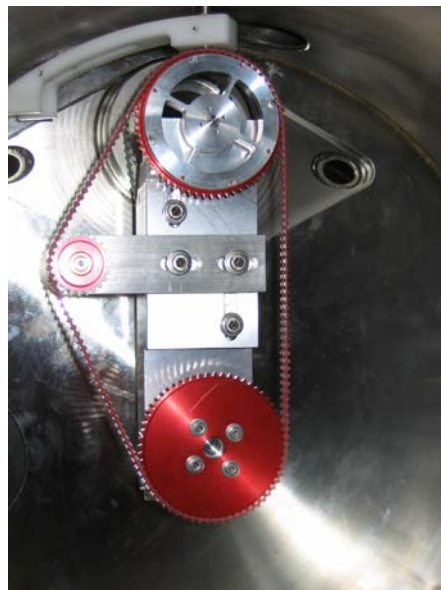


Fig. I-77. Photo of the new rotating target wheel assembly in place with a blank target wheel attached. See text for details.

h.10. The MUSIC Detector (B. Shumard)

A Multiple Sampling Ionization Chamber (MUSIC) was developed for use in conjunction with the ATLAS Scattering Chamber (ATSCAT). This chamber was developed to study the (α, p) reaction in stable and radioactive beams. We will use the counter gas of an ionization chamber as a target (either CH_4 for hydrogen) or He and detect both particles in the outgoing channel ($p + \text{beam particles}$ for elastic scattering or $p + \text{residual nucleus}$ for (α, p) reactions). The MUSIC detector will be followed by a Si detector to provide a trigger for anode events. The anode events will be gated by a gating grid so that only (α, p) reactions where the proton reaches the Si detector will show a signal on any one of the anode pads.

The MUSIC detector works as a segmented Ionization Chamber. The active area of the chamber is 11.95 in. and is divided into 16 equal anode segments (3.5 in. \times 0.70 in. with 0.3 in spacing between pads). The dead area of the chamber was reduced by the addition of a Delrin snout that extends 0.875 in. into the chamber from the front face. The snout is fitted with a reinforced mylar window capable of withstanding 300 torr of internal pressure. 0.5 in. above the anode is a Frisch Grid that is held at ground potential. 0.5 in. about the Frisch grid is a gating grid. The gating grid functions as a filter, stopping the drift of electrons to the anode,

effectively halting the gathering of signals. This is accomplished by setting two alternating sets of wires at differing potentials. This creates a lateral electric field which effectively traps the drift electrons rather than allowing them to pass on to the anode. The gate can be opened by removing the voltage gradient between the alternating wires (*i.e.* setting both sets of wires at equal potential). The chamber also has a reinforced mylar exit window which allows a Si detector to be placed at the end of the chamber in vacuum. This allows for protons from the (α, p) reaction to be detected. The detection of those protons will trigger the gating grid to the open state to allow the drift electrons released from the ionizing gas during the (α, p) reaction to reach the anode segment below the reaction. The segmentation of the anode allows a reaction vertex to be determined. Figure I-78 shows a photograph of the detector.

In a first test we plan to measure the use of the MUSIC for a measurement of elastic proton scattering on ^{10}B at an incident energy of 3 MeV/u. We then plan to bring the incident energy up to 6 MeV/u and proceed to a measurement of the $^{10}\text{B}(p, \alpha)^7\text{Be}$ reaction. The high energy branch of the alpha's ($E > 40 \text{ MeV}$) will be a clear signature for a (p, α) reaction. (To stop all the recoiled ^7Be within MUSIC, we have to scarifify the low energy alpha branch.). In a third run, we then plan to bring the energy down to 3.0 MeV/u again to study the $^{10}\text{B}(\alpha, p)^{13}\text{N}$ reaction by adding ^4He to the counter gas.

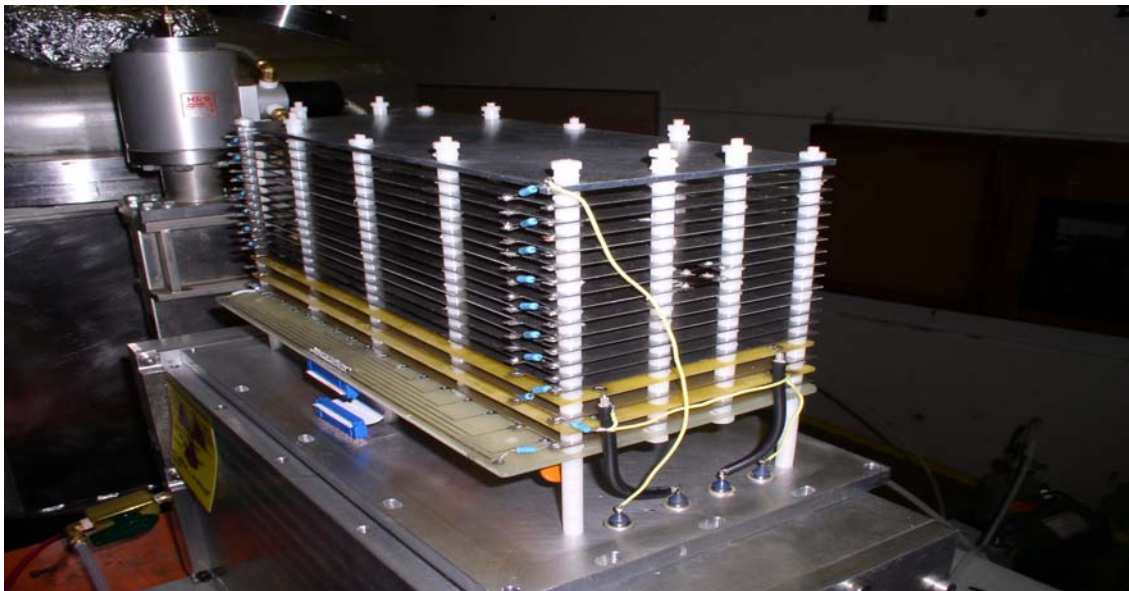


Fig. I-78. The Multiple Sampling Ionization Chamber. The photograph is of the electrode structure of the detector standing on top of the vacuum chamber in which it operates.

h.11. Digital Bragg Curve Spectroscopy (X. Tang, K. E. Rehm, and R. C. Pardo)

Digital Signal Processing (DSP) has been widely used in many aspects of nuclear physics. The detail information from the detectors, captured by a high-speed waveform recorder, provides more possibilities and flexibilities to the nuclear physicists compared to traditional analog modules. In the past year, we studied the waveforms captured from our Bragg detector,¹ located at the focal plane of the Enge spectrograph, with a mixed ^{12}C , ^{15}N , ^{18}O beam with an energy of 40 for ^{12}C , 50 MeV for ^{15}N and 60 MeV for ^{18}O . The signal from the charge sensitive pre-amplifier was feed into a wide-band amplifier (Phillips 778) to match the input range of the digitizer. The amplified signal is then digitized with a LR2262 waveform recorder. The waveform recorder was working in post-trigger mode with a trigger coming from the PPAC detector. The signal

was sampling at a speed of 80 MHz with a resolution of 1024 bits. The digitized spectrum after a triangle filter is shown in Fig. I-79. In this figure, ^{12}C , ^{15}N , ^{18}O , ^{24}Mg and ^{27}Al are clearly identified without the use of any algorithm. Meanwhile, the signal was also feed into analog modules for comparison. The energy from the DSP is obtained with a trapezoid filter.² The range is measured by the timing between the PPAC and the Leading Edge Discriminator (red line in Fig. I-79). The results from digital signal processing are comparable with those from analog signal processing. To demonstrate the advantage of DSP, we will try to identify some heavier isotopes, which are difficult to resolve for analog technique. The authors would like to thank I.-Y. Lee of LBNL for providing DSP programs and encouraging discussions.

¹K. E. Rehm and F. L. H. Wolfs, Nucl. Instrum. Methods **A273**, 262 (1988).

²V. T. Jordanov and G. F. Knoll, Nucl. Instrum. Methods **A345**, 337 (1994).

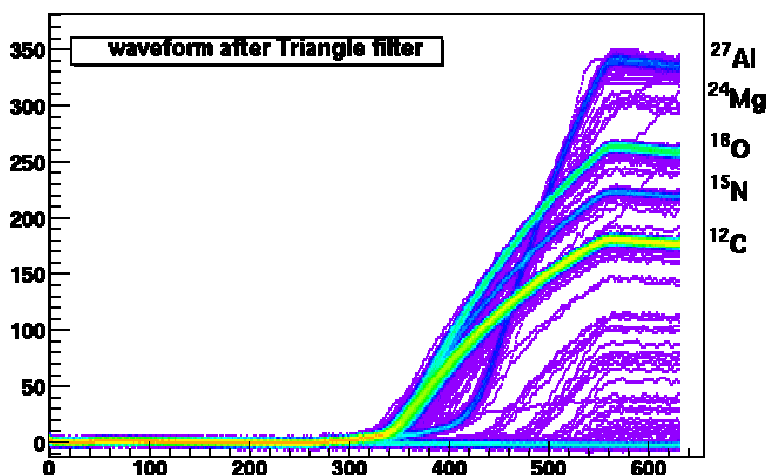


Fig. I-79. The digitized signal from the charge-sensitive preamplifier. The ^{12}C , ^{15}N , ^{18}O , ^{24}Mg and ^{27}Al are clearly separated.

h.12. The New Focal Plane Detector for the Notre Dame Spectrometer (P. Collon)

The study of reactions induced by stable and radioactive beams requires powerful detection techniques. One of these techniques is the use of a magnetic field to separate the reaction products from the initial beam as well as any beam-induced background. We are currently developing the gas-filled magnet isobar separation technique using the Brown-Buechner vertical spectrograph at the Nuclear

Structure Laboratory of the University of Notre Dame. The interest for having a gas-filled magnet both for Accelerator Mass Spectrometry (AMS) as well as for the study of nuclear reactions with low cross sections stems from its basic property of physically separating the trajectories of ions of different elements. This is of particular interest for nuclear astrophysics where the identification of specific reaction products requires their

separation from other interfering reactions as well as machine background that are often several orders of magnitude higher in intensity than the isotope of interest. This technique has already successfully been applied to the detection of such isotopes as ^{39}Ar , ^{44}Ti , ^{63}Ni and ^{182}Hf .

The ND Brown-Buechner spectrograph is currently being upgraded with new vacuum control and pumping systems, new LabView controls, beam optics and in particular a new focal plane detector. The original photo-plate detection system at the focal plane is being replaced by a new multi-wire position sensitive proportional counter and ionization chamber that was built with the help of a Notre Dame undergraduate student (S. Kurtz) in collaboration with Argonne National Laboratory (D. Henderson and B. Shumard). This detector with an active window of 470×114 mm will also be fitted with an ionization chamber following the position sensitive

counter (see Figs. I-80a and I-80b). Both chambers of the detector have independent gas handling systems that were developed in parallel to the detectors. Thin mylar windows ($350 \mu\text{g}/\text{cm}^2$) will both provide the entrance windows and enable to run both chambers at independent pressures while providing minimal energy loss for the particles. This project, which started in the Summer of 2004 and has been running through 2004 and 2005 provided an incredible research and development opportunity for a Notre Dame undergraduate student by giving him the possibility of working with experts in the field of gas filled detectors from Argonne National Laboratory during his undergraduate time, as well as providing the Nuclear Structure Laboratory with fantastic technical support for the construction of a new detector that will be used for highly sensitive and cutting edge measurements in the field of nuclear astrophysics. Continual support during the year has made it possible to test and calibrate the system with maximum efficiency.

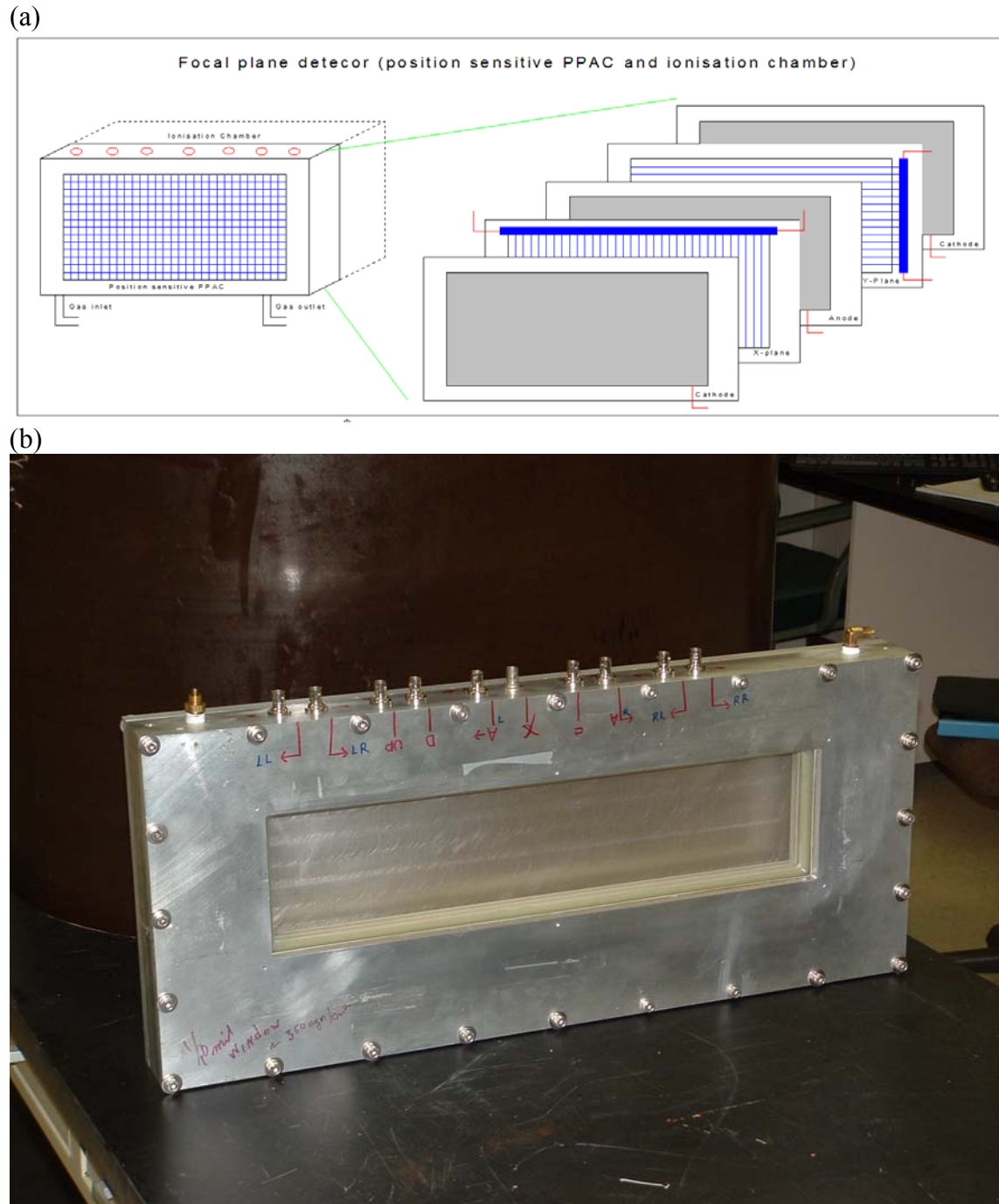


Fig. I-80. (a) illustrates the different planes of the position sensitive proportional counter that will constitute the front part of the new ND focal plane detector. (b) A picture of the actual detector. The active window is 470×114 mm.

h.13. Deployment of a Centrally Managed Windows Cluster (C. Stuart)

Within the past year the Division's infrastructure has undergone many changes.

Originally, the system management was decentralized and the PCs were intermittently updated for cybersecurity.

All desktop computers were standalone. There was no easy way of sharing data. There were very few shared resources available to users who had Windows desktops.

Today, all systems are members of a centralized Windows domain (about 140 desktops). There are many resources and benefits available now that were not in the past. Everyone can now use a single username and password to access systems and resources. Before, everyone had to have a different username and password. There are now many network resources available. There is now a central file server. Users can now store their data on the server and access it from anywhere, on and off-site. This makes sharing data between colleagues a lot easier. There is a central print server. Users connect to printers through this server. Any changes, or updates, made to the printer settings are automatically set for everyone connected. There is a

new e-mail solution, as well. It has a very intuitive web interface as well as a slew of very useful features, such as online calendaring and a Global Address List which contains all of the contact information for everyone working at the Laboratory.

This centralization of resources has also improved the Division's security stance. There is now a centralized antivirus service which forces updates down to the clients. There is now a two-front patch management system forcing updates to each of the clients. By improving the security of the systems we can more confidently guarantee the integrity of our data.

Each server is backed up regularly. If a user accidentally deletes a file from the file server, it can be restored. Just as important, if a server fails, it can be restored in a minimal amount of time. Migrating all the users to the new e-mail system is in progress.

h.14. Status of the SCARLET Data Acquisition System (K. Teh)

There are presently four single-CAMAC-crate SCARLET systems that have been assembled and deployed. One system has been used for "online" experiments at the FMA and the Enge Spectrograph. A second system is located at the Argonne Penning Trap. The third system is used for "offline" development of the Germanium strip detectors while the most recent system is used by members of the Chemistry Division at the APS.

All of the systems use a commercial Wiener CC32 CAMAC-PCI interface for crate control. A programmable CAEN interface takes the experimenters event trigger and initiates readout, and also returns an "end-of-event" signal for generation of a "readout-busy" signal. The acquisition systems comprises of two rack-mounted PCs, one to drive the CAMAC interface (ROC1) and one to build events and deliver them to the ethernet link. One (or more) further PCs can be used to control the acquisition, archive the data to disk, and visualize the data, using the CERN "Root" sorting package. Progress towards a multi-crate system has been slow, with several options being explored, but each showing shortcomings. It is hoped that a commercial module can be found that

will offer a simple and cost-effective solution to trigger and busy legislation and keeping the data from multiple crates synchronized.

A new data acquisition infrastructure will be set up this year to fully support the SCARLET deployments. Issues of the architecture of this infrastructure were discussed at length with staff scientists and representatives from the ATLAS Users Group. It was decided that the infrastructure should include a "farm" of computers for data analysis, a large disk array to store data, and an assortment of tape drives. An earlier idea to support remote retrieval of data via anonymous FTP was deemed inadvisable and has been shelved for the moment. The hardware for the analysis farm and the disk array have been procured and work is underway to set them up. Finally, work is also underway to develop monitoring software based on CERN's ROOT system. It was decided that the ROOT system, while extremely powerful and flexible, was too unwieldy for the kinds of data analyses performed at ATLAS. A plan to develop a more specific DAPHNE-like interface to ROOT was discussed and it is expected this software will be deployed together with the new infrastructure in the data room.

h.15. Progress on the New Gammasphere Data Acquisition (T. Lauritsen)

The commissioning of the new Gammasphere Data acquisition (DAQ), which was built at LBNL, has continued. This new DAQ will replace the old DAQ with the Motorola "event filter formatters" (EFFs). Among other things, a 'watchdog' function was implemented that monitors various errors in the data assembled by the eventbuilder VME module. If this monitor senses that the eventbuilder is producing invalid data, it will reset the eventbuilder. Thus, the DAQ will now recover and the DAQ will continue after a momentary interruption. Such a function is also necessary in the current DAQ. Numerous other functions needed to control the new DAQ have been

implemented as well. A thorough documentation of the new DAQ has been written and placed on the WWW along with the current "online" documentation for Gammasphere.

The new DAQ now appears quite stable, running for days with just sources in the array. On two occasions the new DAQ has been used "online" for short periods with in-beam data. In both cases the DAQ performed well. More tests will be performed during a variety of upcoming experiments, to thoroughly test the new DAQ before it is deployed. The infrastructure for writing all the data to disk, as opposed to tape, is being developed.

h.16. Gammasphere Operations (M. P. Carpenter, C. J. Lister, R. V. F. Janssens, T. L. Khoo, T. Lauritsen, J. Rohrer, E. F. Moore, D. Seweryniak, P. Wilt, S. Zhu, P. Chowdhury,* and F. G. Kondev†)

In the fall of 2002, Gammasphere was successfully relocated from Berkeley National Laboratory to the ATLAS facility at Argonne. All Ge detectors were annealed and all BGO bases repaired. Gammasphere was reassembled in area IV on the FMA beamline during January 2003.

In 2004, twenty-one PAC approved experiments were completed using Gammasphere. This can be compared to thirty experiments performed the previous year. The decrease in the number of experiments can be attributed to (i) the move of Gammasphere from the FMA beamline to the stand alone beamline and (ii) a decrease from 7-day operations to 5-day operations at ATLAS. With regards to the move of Gammasphere, the device was out of operations for two and half months.

By the end of 2004, Gammasphere had been operating at ATLAS for nearly two years, and it appears that the device will operate at our facility for the foreseeable future. In 1997, 2000 and 2002, Gammasphere was moved after approximately two years of operation at the host facility. In each instance, all Ge detectors were annealed and optimum energy resolution was restored to the array. Since Gammasphere is not scheduled to move from

Argonne, we have undertaken a policy to anneal a detector once its resolution has degraded beyond 3 keV at 1.33 MeV. As a result, we are annealing on average five detectors a month, and we anticipate this number to stay constant in the future. The three new Ge detectors ordered from ORTEC have been delivered. Two were accepted and are operating in Gammasphere. The third was returned to the vender to fix a mechanical problem.

As reported in the last annual report, due to failures of the resistors along the bias chain, we continue to see breakdowns on the BGO PMT bases. This results in a non-responsive channel. The PMT can be repaired by locating the failed resistor and replacing it, however, this is a very time consuming operation. While it is our plan to replace all of these bases with new components in the long run, we still are repairing the bases as they fail and as the schedule allows.

Several upgrade paths are being pursued. A replacement for the dual crate VME acquisition system has been developed and debugged. VME readout capabilities are finalized and in the testing stage. Finally, a move of Gammasphere from the FMA beamline to the old APEX beamline occurred in May, 2004. Details of the move can be found in separate contribution to the annual report.

*University of Massachusetts-Lowell, †Nuclear Engineering Division, Argonne National Laboratory.

h.17. Gammasphere Move (C. J. Lister, M. P. Carpenter, R. V. F. Janssens, T. Lauritsen, J. Rohrer, B. Zabransky, B. Nardi, P. Wilt, S. Zhu, and P. Chowdhury*)

To maximize the physics potential of both Gammasphere and the FMA, we have made Gammasphere “portable” allowing it to operate with the FMA (as it did during the 1997-2000 campaign), or in “standalone” mode (as it was operated during the 1995-1997 and 2000-2002 Berkeley campaigns). Preparation for the move was performed in 2003 and moving Gammasphere was performed for the first time in 2004. The new location of Gammasphere is about 4 meters from the FMA at the former APEX beamline.

Before the move could take place, many issues needed to be resolved. We investigated movement by crane, airpads and rollers. Rollers were finally selected on the grounds of cost. The floor and trench areas needed stiffening to permit the move of the device. A test move of the Gammasphere platform was successfully conducted using a test load of 15 tons of shielding blocks in 2003. Detailed plans for the re-routing of LN2 and signal cables were also completed in 2003.

The move itself was done in June of 2004. The biggest challenge was the maintenance of the signal infrastructure. The detectors need to be kept cold and the amount of time the detectors are not-biased

minimized. Both requirements were necessary in order to prevent a need to disassemble the array and anneal all 101 Ge detectors. This also demands that the physical transition must be completed in less than 8 hours.

The move was carried out in May 2004. First, all the grey cables were disconnected and taken down from the cable trays and the LN fill system disconnected. The Gammasphere frame was then jacked up and placed on the rollers. Finally the device was slowly rolled from the FMA beamline to the new beamline. Approximately fifteen people assisted in pushing and pulling Gammasphere across the floor and the whole process took half a day. The grey cables and LN system were then reconnected before the next scheduled fill sequence, thus completing the move in under 8 hours. After bias was reapplied to the Ge detectors, no appreciable degradation in energy resolution was observed and the move was deemed a success.

While the physical move of Gammasphere took only a day, pre-move preparation and permanent installation afterwards requires significant effort, in excess of 1 FTE. As a result, we do not anticipate moving the device more than once a year. The move back to the FMA is scheduled for late 2005, approximately 18 months after the initial move.

*Sabbatical visitor from the University of Massachusetts-Lowell.

h.18. X-Array Developments (C. J. Lister, T. L. Khoo, R. V. F. Janssens, M. P. Carpenter, and S. Zhu)

The X-Array is designed to enhance gamma ray detection for many kinds of offline spectroscopy, such as α - γ , p - γ , β - γ coincidences, or isomer decays, that may be measured at the FMA focal plane or at the open geometry APT. The concept is to construct a flexible and compact box detector with modest segmentation but very high efficiency. We have procured three large “clover” detectors that are now frequently used in a variety of experiments, most significantly in a campaign at the FMA focal plane (Fig. I-81) which were critical in investigating isomers in ^{254}No (for example, see section c.7. in this report). Further procurement of two more large clover detectors, to complete the box, has been delayed by the sharp rise in the Euro/Dollar exchange rate.

An opportunity for significant enhancement of our offline system has come from a decommissioned gamma-array owned by the DOE remote sensing laboratory. Fourteen large (100% relative efficiency) germanium crystals were transferred to ANL under an agreement that called for refurbishment, followed by a long-term loan for research. The refurbishment called for remounting the crystals in liquid nitrogen cooled cryostats. These counters will enhance our capabilities for “offline” counting and will be used in the X-Array. Figure I-82 shows some of the detectors delivered to ANL with their “Joule-Thompson” cooling system, prior to return to ORTEC for refurbishment.

The construction of a new FMA focal plane vacuum envelope has been hampered by shortage of resources. A

cost-effective partial rebuild of the chamber to allow the mounting of three clover elements (Fig. I-81) was implemented, which has provided much useful guidance for the full rebuild. In the light of this experience, the design of the new focal plane is being revisited, and construction should be finished in calendar year 2005.

To date, the electronics we have used for the X-Array have been culled from the former ANL-ND BGO Array. This has been quite successful, but many modules are >20 years old, and shown some unreliability, so some refurbishment with more modern modules is needed for optimum use. A dedicated setup is being established to facilitate use of the array. This investment will start in calendar year 2005.

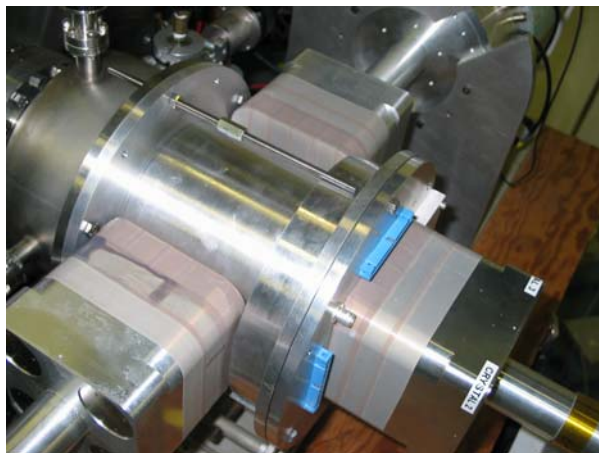


Fig. I-81. The three clover arrangement used in the spectroscopy of ^{254}No isomers. The mass-separated residues arrive across the FMA focal plane (top left) and are implanted in a silicon DSSD mounted at the center of the cylindrical spool. Gamma rays are detected in a clover detector mounted behind the DSSD (bottom right), and two further counters mounted on either side of the chamber.



Fig. I-82. Six of the large germanium detectors obtained from the DOE Remote Sensing Laboratory for refurbishment. The crystals are being remounted in liquid-nitrogen cooled cryostats for laboratory use.

h.19. Degradation of the ^{16}N Beam to Very Low Energy (M. Notani, R. C. Pardo, K. E. Rehm, X. D. Tang, J. P. Greene, A. Hecht, D. Henderson, R. V. F. Janssens, C. L. Jiang, E. F. Moore, J. P. Schiffer, S. Sinha, M. Paul,* R. E. Segel,† L. Jisonna,‡ and A. Wuosmaa‡)

In the ANL experiment, the ^{16}N beam is produced by bombarding a deuterium-filled cryogenic gas cell with a 82 MeV beam of ^{15}N . $^{16}\text{N}^{7+}$ ions produced via the $d(^{15}\text{N}, ^{16}\text{N})p$ reaction are then focused with a superconducting solenoid, located immediately behind the production cell, and are subsequently separated from the primary beam with a 22° bending magnet. A superconducting debunching resonator

improved the energy width of the secondary beam to about 61.3 ± 0.3 MeV. The secondary particles were identified with respect to mass and Z in the focal plane of the split pole spectrograph. Figure I-83 shows a plot of particle range vs. energy indicating the purity (80%) and the observed beam contaminants. All of the contaminants are stable isotopes and, therefore, do not result in any heavy-ion – alpha coincidences.

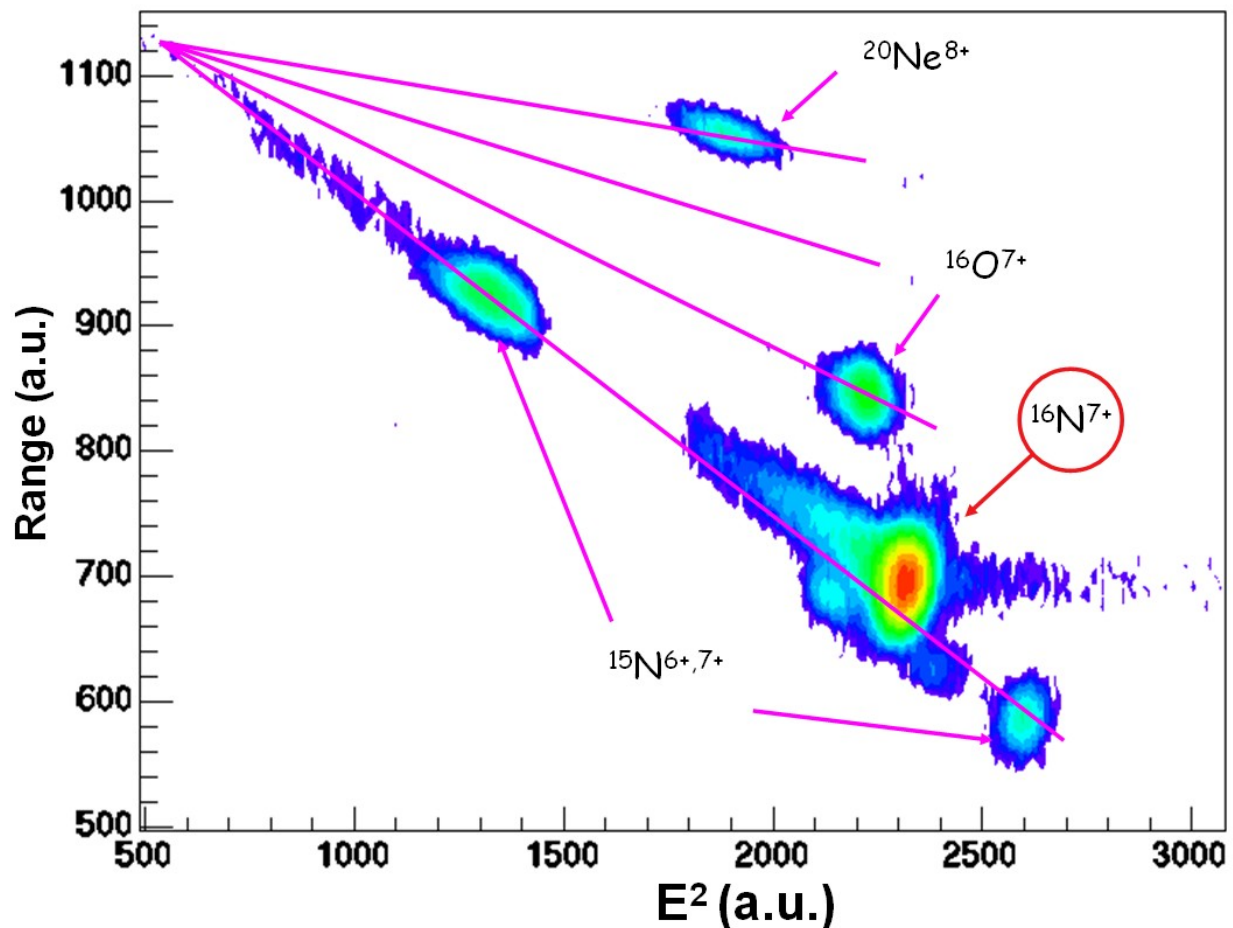


Fig. I-83. Particle identification spectrum measured in the focal plane of the magnetic spectrograph. The various particle groups are identified in the figure.

The 60 MeV ^{16}N ions are first slowed down in the 16-cm long attenuation cell filled with P10 gas, with 1.3 mg/cm^2 thick Ti foils as entrance and exit windows. An additional Al absorber, installed after the attenuation cell, reduces the energy of ^{16}N ions to about 250 keV. The Al absorber replaced a similar Mylar foil, which in an earlier test experiment was

damaged when it was hit by an intense ^{15}N beam during the beam tuning procedure. The gas pressure in the attenuation cell can be adjusted independent of the pressure in the ionization chamber volume, in order to maximize the number of ^{16}N particles stopped in the $10 \text{ }\mu\text{g/cm}^2$ thick carbon catcher foils (see Fig. I-84a).

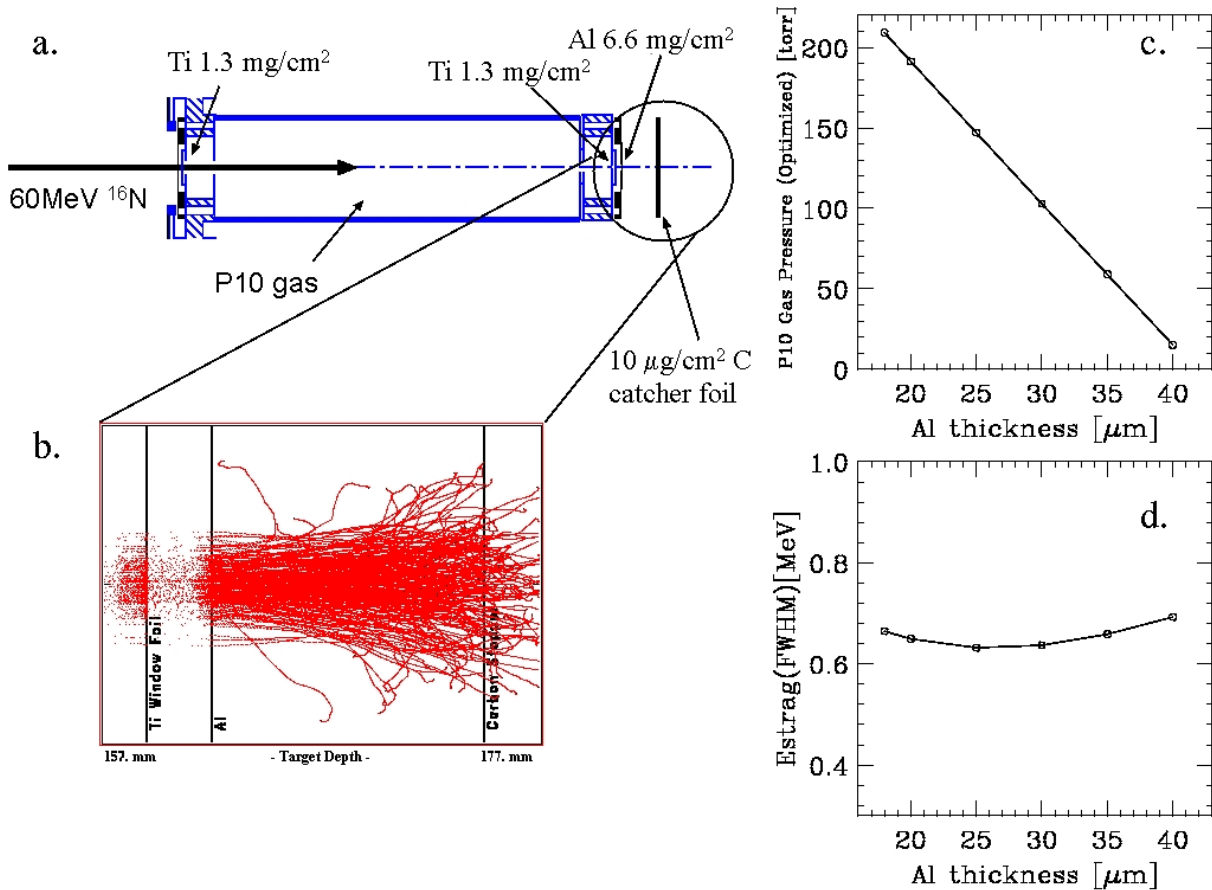


Fig. I-84. (a) Layout of the experimental setup to attenuate the ^{16}N particles for measuring the beta-delayed alpha decay of ^{16}N ; (b) Particle trajectories of ^{16}N calculated with the program SRIM¹ in the vicinity of the carbon stopping foil; (c) Gas pressure (P10) in the attenuation cell needed to stop the ^{16}N particles in the carbon catcher foil as function of the Al absorber thickness; (d) Energy spread of ^{16}N particles at the C catcher foil as function of the Al absorber thickness.

The thickness of the Al absorber and the pressure in the attenuation cell were chosen to minimize the energy straggling of the ^{16}N beam at the catcher foil location. In Fig. I-84d, the calculated energy spread of the ^{16}N at the foil is shown as a function of the Al absorber thickness. Figure I-84c shows the P10 gas pressure needed to stop the ^{16}N particles in the C foil as a function of the Al thickness. Based on these simulations a 25 μm thick Al absorber was chosen for the experiment. Figure I-84b shows the results of a

TRIM calculation of the particle trajectories in the vicinity of the carbon stopping foil.

To determine the optimum pressure in the attenuation cell the percentage of ^{16}N particles stopped in the C catcher was measured with a Si surface barrier detector. The results are shown in Fig. I-85. The optimized pressure was found to be 146 Torr, in very good agreement with the calculated values. At the optimum pressure 5.5% of the ^{16}N were stopped in the foil.

*Hebrew University, Jerusalem, Israel, †Northwestern University, ‡Western Michigan University.

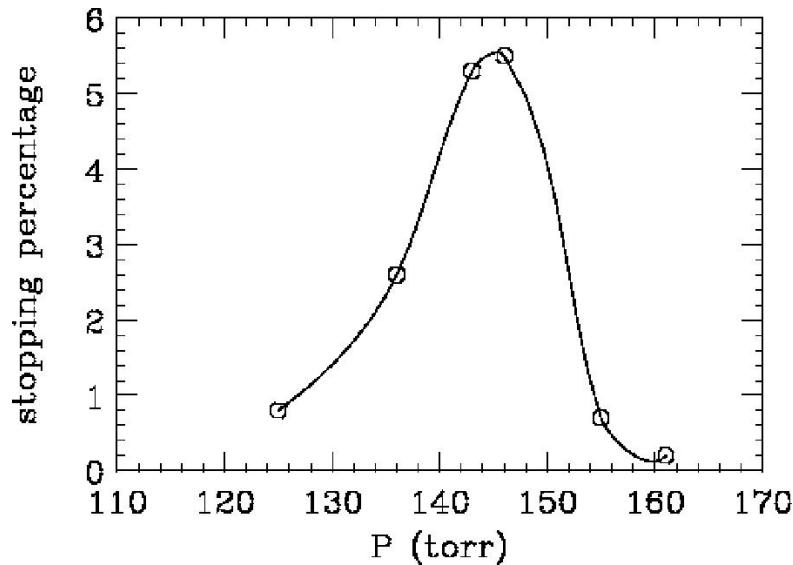


Fig. I-85. Measured stopping percentage of ^{16}N particles at the C catcher as a function of P10 pressure in the attenuation cell.

h.20. Improvement of the Experimental Setup for the Study of the ^{16}N β Delayed α Decay (B. Zabransky, B. Nardi, S. Gerbick, X. D. Tang, K. E. Rehm, and J. P. Schiffer)

For the measurement of the beta-delayed α decay of ^{16}N , a dedicated vacuum chamber containing two pairs of ionization chambers has been developed. Details are given in previous annual reports. In this reporting period, two major modifications have been implemented. The need to detect particles with very low energies (~ 100 keV) forced us to eliminate all possible sources of electronic interference. One of them originates from the stepping motor, which rotates the target wheel by 120° within 60 ms from the irradiation position into one pair of the twin ionization chambers. While the irradiated foil is being counted, the stepping motor keeps the sample in place using a small pulsed holding current. This current was found to induce a noise signal in the

amplifiers. To eliminate this interference, a mechanical brake was installed, which was activated once the wheel was in its proper position. With this brake the stepping motor could be switched off completely during the counting period.

The shape of the ^{16}N spectra was sensitive to the detailed geometry around the beam spot. ^{12}C or alpha particles emitted close to the plane of the foil and stopped in the target frame or the holding screws, produced signals that could distort a critical part of the spectrum. To eliminate these effects, larger asymmetric frames were designed with all crews located outside the ionization chamber. The geometry was optimized based on simulations that are described in section h.22.

h.21. The Twin Ionization Chambers (X. D. Tang, D. Henderson, K. E. Rehm, I. Ahmad, J. P. Greene, A. Hecht, R. V. F. Janssens, C. L. Jiang, E. F. Moore, M. Notani, R. C. Pardo, G. Savard, J. P. Schiffer, S. Sinha, M. Paul,* L. Jisonna,† R. E. Segel,† A. Champagne,‡ and A. Wuosmaa§)

Ionization chambers have several advantages over Si detectors for the measurement of the beta-delayed alpha decay of ^{16}N :

- Beta particles experience a very small energy loss (~ 3 keV in this experiment),
- They can be built with very high acceptances,
- They can be built with the required thickness and are very homogenous,
- They don't have any dead-layers,
- They don't experience radiation damage in long experiments.

For our measurement of the beta-delayed α decay of ^{16}N , we have built two pairs of gridded ionization chambers for the detection of α - ^{12}C coincidences.¹

Figure I-86 shows a photograph of the full setup. The two ion chambers (diameter 10 cm, depth 6.5 cm) share a common cathode, which also acts as a target wheel. The ionization chambers provide the standard energy signal from the anodes, and, in addition, information about the angle of emission with respect to the plane of the cathode, from the Frisch grids. The ionization chambers have been tested and calibrated with α sources (^{228}Th and ^{148}Gd) as well as with α - ^7Li coincidences obtained from the $^{10}\text{B}(n,\alpha)^7\text{Li}$ reaction using a PuBe neutron source. The neutron source was located outside the ionization chamber and two ^{10}B foils ($10 \mu\text{g}/\text{cm}^2$ evaporated on $10 \mu\text{g}/\text{cm}^2$ C) were mounted on the target wheel. The neutrons were thermalized in a 5 cm thick layer of high-density polyethylene.

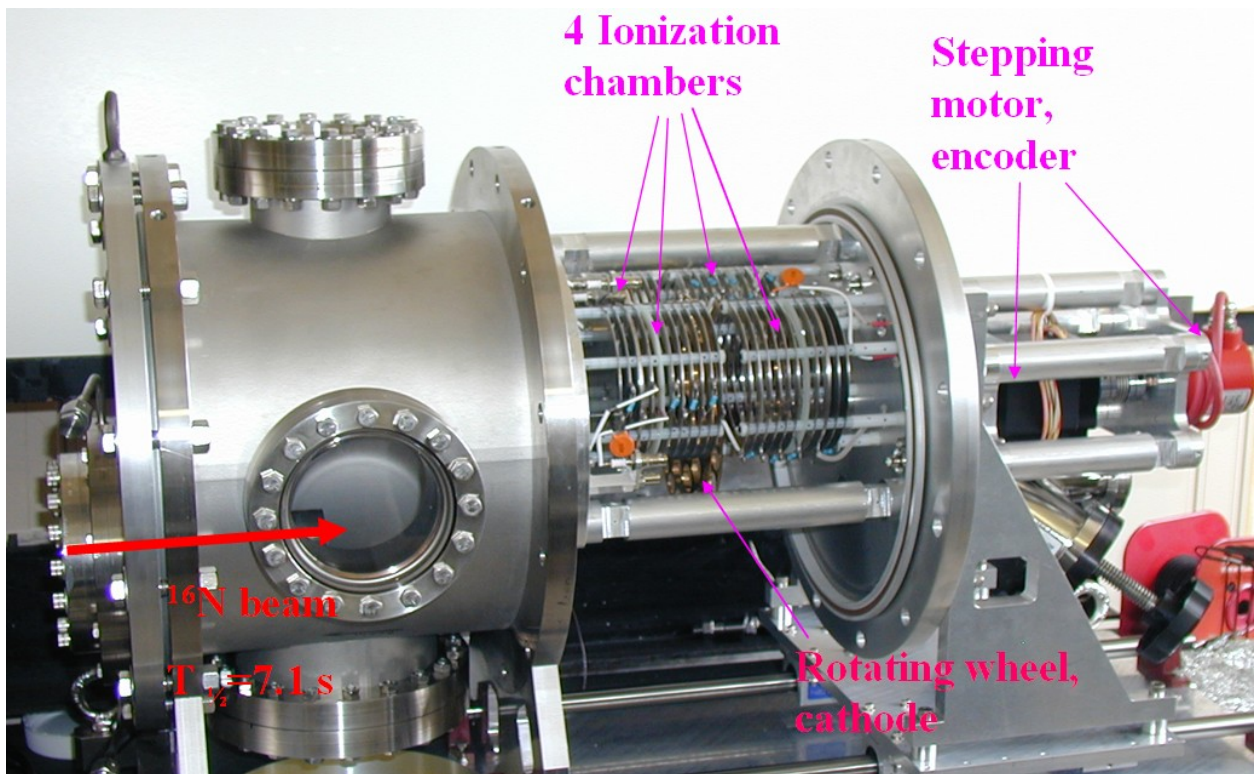


Fig. I-86. Photograph of the experimental setup for measuring the beta-delayed alpha decay of ^{16}N .

Alpha particles emitted perpendicular to the cathode produce a small signal on the Frisch grid, while alphas emitted along the foil's surface result in a

larger grid signal. A two-dimensional spectrum of grid vs. anode signal is given in Fig. I-87. The two vertical lines are due to the 1.483 and 1.789 MeV alpha particles,

produced in the $^{10}\text{B}(n,\alpha)^7\text{Li}$ reaction and emitted at different angles with respect to the foil, while the two lower-energy groups are caused by the coincident ^7Li particles, which have a smaller range in the ion chamber and are all stopped in the vicinity of the

target wheel. The energy resolution obtained from the 1.485 MeV line is 40 keV, sufficient to notice the difference in the energies of the alphas passing through the carbon backing.

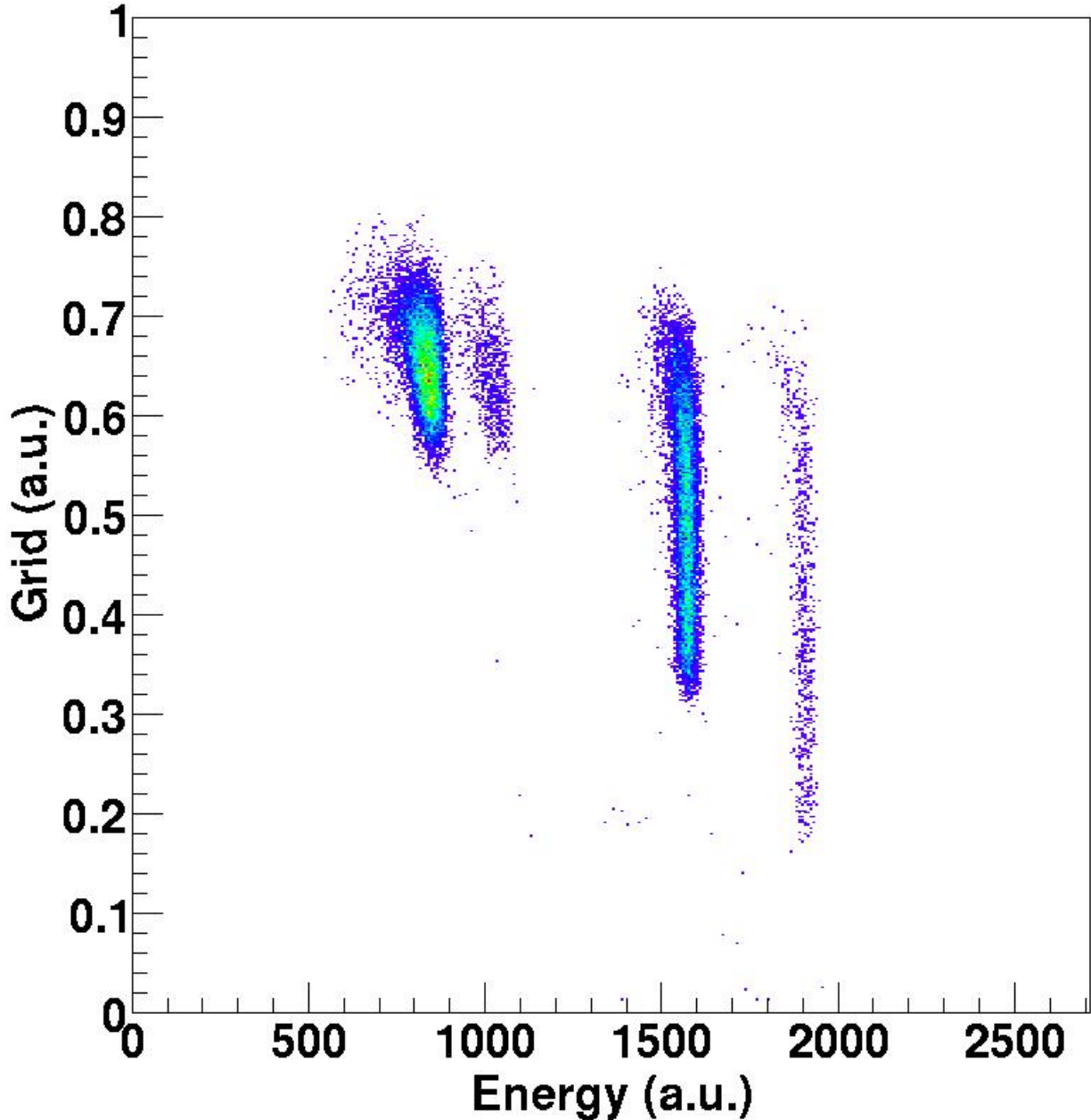


Fig. I-87. Spectrum of grid vs. anode signals measured in one of the twin-ionization chambers for ^7Li -alpha coincidences obtained from the $^{10}\text{B}(n,\alpha)^7\text{Li}$ reaction.

In order to use the kinematically calculated alpha energies one has to make sure that the reaction is induced by thermal neutrons. This was shown by repeating the measurement with an additional 1 mm thick Cd foil positioned behind the polyethylene. Under this condition the α - ^7Li coincidence rate is

reduced by more than a factor of 15, very close to the calculated value.

The stability of the detectors was measured over a period of 10 days. For three of the detectors, the stability was found to be better than 3×10^{-3} , while the fourth detector

showed a (temperature dependent) drift of about 40 keV. The electronics for this branch will be replaced. Altogether, the detector system proved to

be well suited for the new measurement of the beta-delayed α decay of ^{16}N .

*Hebrew University, Jerusalem, Israel, †Northwestern University, ‡University of North Carolina, §Western Michigan University.

¹C. Budtz-Jorgenson *et al.*, Nucl. Instrum. Methods **A258**, 209 (1987).

h.22. Backgrounds and Sensitivity to Beta Particles (X. D. Tang, M. Notani, K. E. Rehm, I. Ahmad, J. Greene, A. Hecht, D. Henderson, R. V. F. Janssens, C. L. Jiang, E. F. Moore, R. C. Pardo, G. Savard, J. P. Schiffer, S. Sinha, M. Paul,* L. Jisonna,† R. E. Segel,† A. Champagne,‡ and A. Wuosmaa§)

Because of the low count rates expected for the so-called interference peak in the ^{12}C - α coincidences in (typically 3 events/hour) the background in the twin-ionization chamber needs to be well understood. This was tested in a series of "offline" tests. In order

to stop α particles up to about 5 MeV, the pressure in the ionization chambers was raised to 760 Torr. The singles spectra measured in the four detectors are given in Fig. I-88.

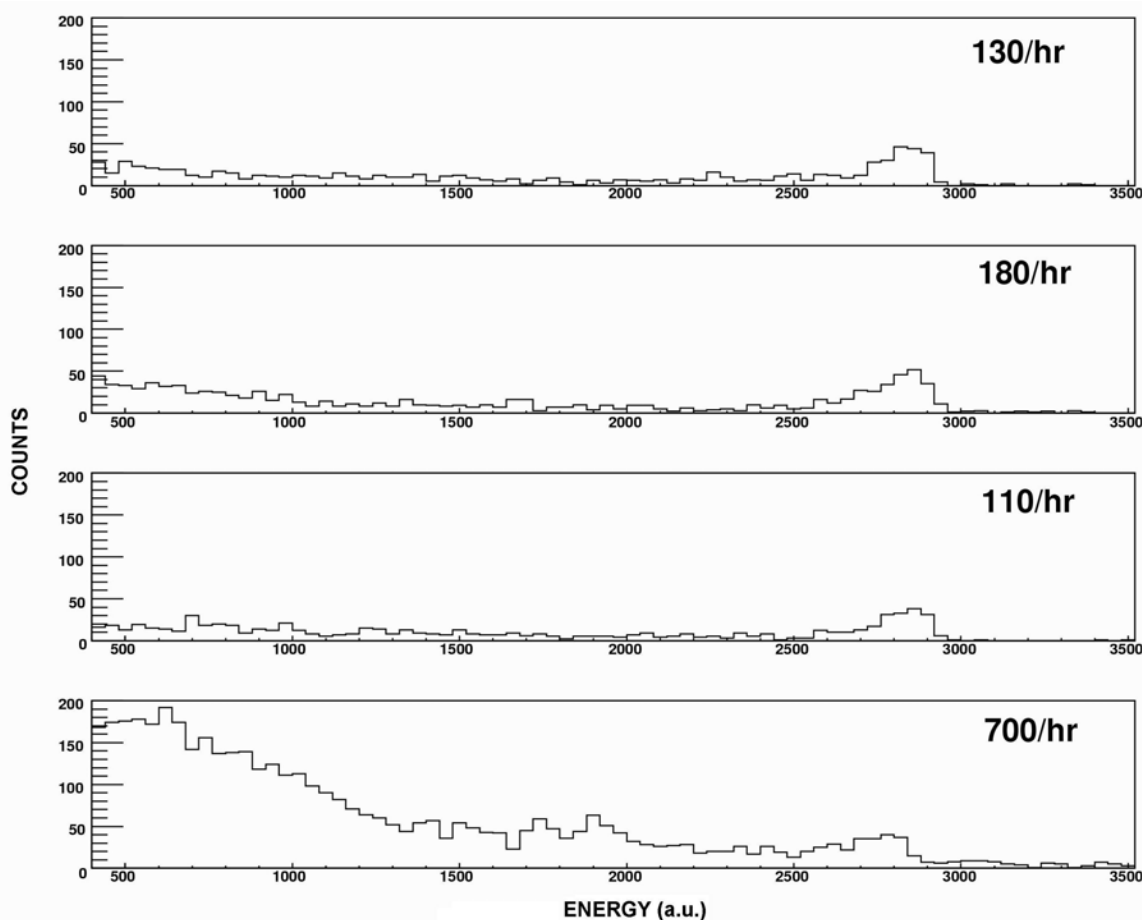


Fig. I-88. Background spectra measured in the four ionization chambers. The peak in the spectra originates from the alpha decay of ^{210}Po in the solder material. The pressure in the ionization chambers during these measurements was 760 Torr.

As can be seen from these results, the rates above the threshold of ~ 100 keV are about 150 particles/hour for three of the detectors, while the rate of the fourth detector is about five times this value. From the energy of the peak (5.2 MeV) and the higher count rate for detector 4, the origin of the background could be traced back to ^{210}Po which is produced via beta decay from ^{210}Pb present in the solder material used for the Frisch grid. This background is known from other low-count rate experiments which experienced an alpha background with a half life of 138 days. Since the Frisch grid of detector 4 had been re-ordered shortly before this measurement, a higher background was observed for this detector. The rate has since decreased by more than a factor of four and the background rates of the four detectors now approach 1-2 counts/minute. Another source of background originated from ^{16}N diffusing from the

irradiation region into the ion chambers. To eliminate this contribution all detectors have been surrounded with a thin layer of Teflon.

To test the sensitivity of the ionization chambers to beta particles, a ^{22}Na β^+ source with a strength of about 10^5 decays/s was mounted on the target wheel and positioned in front of detector 3. The energy spectra measured for the four detectors are shown in Fig. I-89. The count rates of these spectra, taken about 4 months after the ones shown in Fig. I-88 exhibit a decrease of the count rate in detector 4 by the expected factor of two. Detector 3, which faces a β source emitting about 5×10^4 into its active volume, only shows an increase in count rate of 60 counts/hr above the threshold of 100 keV. For a coincidence measurement this background rate is negligible.

*Hebrew University, Jerusalem, Israel, †Northwestern University, ‡University of North Carolina, §Western Michigan University.

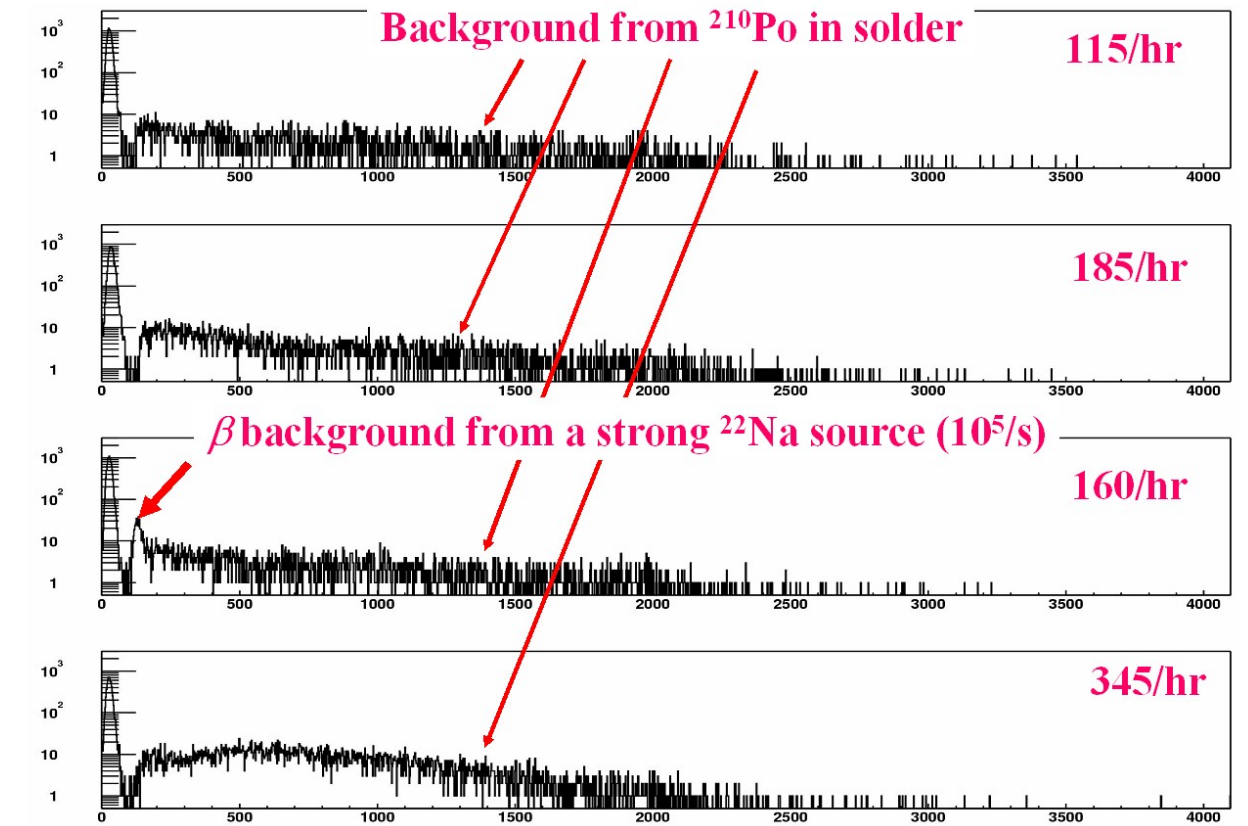


Fig. I-89. Test of the response of the ionization chambers to beta particles. A strong ^{22}Na source was facing detector 3. The main background (typically 200 counts/hour) is caused by the alpha decay of ^{210}Po . The pressure in the ionization chamber during these measurements was 150 Torr.

h.23. Simulation of the Detector Response in the ^{16}N β -Delayed α Decay Experiment (X. D. Tang, K. E. Rehm, and J. P. Schiffer)

In the study of the ^{16}N β -delayed α decay there are three effects that need to be investigated carefully:

- Alpha particles with energies down to 0.6 MeV have to be detected in coincidence with ^{12}C ions of even lower energies (~ 0.2 MeV). Any significant energy loss of the outgoing particles in the absorber foil will deform the shape of the spectrum. It is, therefore, crucial to minimize the energy loss and to reduce the electronic noise so that even the low-energy ^{12}C particles can be clearly identified.
- If a particle, emitted from the foil is stopped in the support frame, only a part of the energy is deposited in the gas. Such an event must be clearly separated from the good coincidences.
- The detection efficiency must be constant over the important alpha energy range from 0.6 MeV to 2 MeV.

A detailed Monte Carlo simulation program has been developed to investigate these effects. In the simulations, the theoretical alpha spectrum from

Ref. 1 was used to sample the decay. An example of a simulation in comparison with real events from a test run is shown in Fig. I-90. The ionization chamber was filled with P10 gas at a pressure of 150 Torr and the thickness of the absorber foil was $15 \mu\text{g}/\text{cm}^2$. The two main groups correspond to ^{12}C - α coincidences identified in detector 1-2 or 2-1, respectively. The third group, located in the vicinity of the origin, results from alpha particles that hit the target wheel and deposited only part of their energy in the P10 gas. Events between the two main peaks originate from gaseous ^{16}N particles that diffuse into the ionization chamber and deposit their energy in both detectors.

After varying the various geometrical parameters, the best experimental configuration was determined. For a beam spot with a diameter of 5 mm, we chose a $10 \mu\text{g}/\text{cm}^2$ thick carbon catcher foil mounted on a target frame with a thickness of 1.75 mm and a 10 mm diameter hole. In order to reduce the background from the diffusion of ^{16}N , the ion chambers were wrapped with Teflon foil. The simulations also provide an important input for a better understanding of the energy-angle relation obtained from the Frisch-grid and anode signals of the twin-ionization chamber and for the pressure dependence of the device.

¹R. E. Azuma *et al.*, Phys. Rev. C **50**, 1194 (1994).

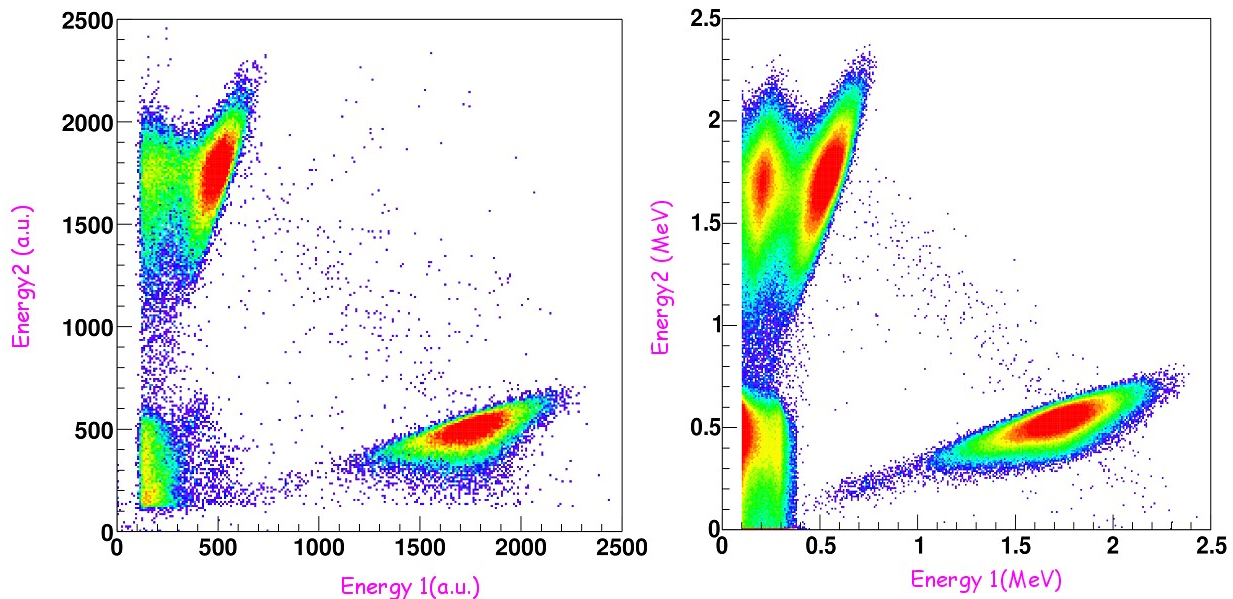


Fig. I-90. Left: Two-dimensional spectrum of ^{12}C -alpha coincidences measured in one of the twin-ionization chambers using a $10 \mu\text{g}/\text{cm}^2$ carbon foil that was irradiated with ^{16}N particles. Right: Monte Carlo simulation of the detector response using the actual geometry of the detectors.

I. HIGH-PRECISION AND HIGH-SENSITIVITY EXPERIMENTS

The powerful and sensitive techniques of nuclear physics can be turned to many fields. Frequently, important results can emerge. This is the case using the Advanced Photon Source at Argonne to investigate, and debunk, claims for “enhanced” decay from hafnium isomers. The ability to reliably perform such measurements remains at the heart of our program.

i.1. Search for X-Ray Induced Decay of the 31-y Isomer of ^{178}Hf (I. Ahmad, D. S. Gemmell, E. F. Moore, J. P. Schiffer, J. C. Banar,* J. A. Becker,† T. A. Bredeweg,* J. R. Cooper,† A. Kraemer,† A. Mashayekhi,‡ D. P. McNabb,† G. G. Miller,* P. Palmer,* L. N. Pangault,* R. S. Rundberg,* S. D. Shastri,‡ T.-F. Wang,† and J. B. Wilhelmy*)

In recent years considerable attention has focused on the published claims¹ that the 31-year isomer of ^{178}Hf can be “triggered” by subjecting it to x-rays. This possibility has been widely publicized in the media (Hf-powered aircraft,² and Hf-based explosives)³ and DARPA has explored the possibility of large-scale production of the isomer. We carried out an experiment to confirm the published claims using the intense x-ray beams of the Advanced Photon Source. In the last year, the refined final analysis of these results was completed and a final paper was published.⁴ This refined analysis was necessary

because the original results,¹ where an enhanced decay rate was reported in the 20 - 40 keV x-ray region, was followed by reports of triggering, first at lower x-ray energies around 10 keV,⁵ and by reports of new gamma-ray lines in the decay.⁶ No evidence of triggering was found in any of these regions – with limits some 4 - 5 orders of magnitude below the published claims. Limits were set both for prompt triggering and for triggering that would populate a lower, 4-s, isomer as is shown in Fig. I-91. No new line was seen at a level lower than the reported value by over two orders of magnitude. This work has now been published.

*Los Alamos National Laboratory, †Lawrence Livermore National Laboratory, ‡Advanced Photon Source, Argonne National Laboratory.

¹C. B. Collins *et al.*, Phys. Rev. Lett. **82**, 695 (1999).

²Popular Mechanics, May 2004, p. 98.

³New Scientist, August 16, 2003, p. 4.

⁴I. Ahmad *et al.*, Phys. Rev. C **71** 024311 (2005).

⁵C. B. Collins *et al.*, Laser Phys. **14**, 154-165 (2004).

⁶C. B. Collins *et al.*, Hyperfine Int. **135**, 51 (2001).

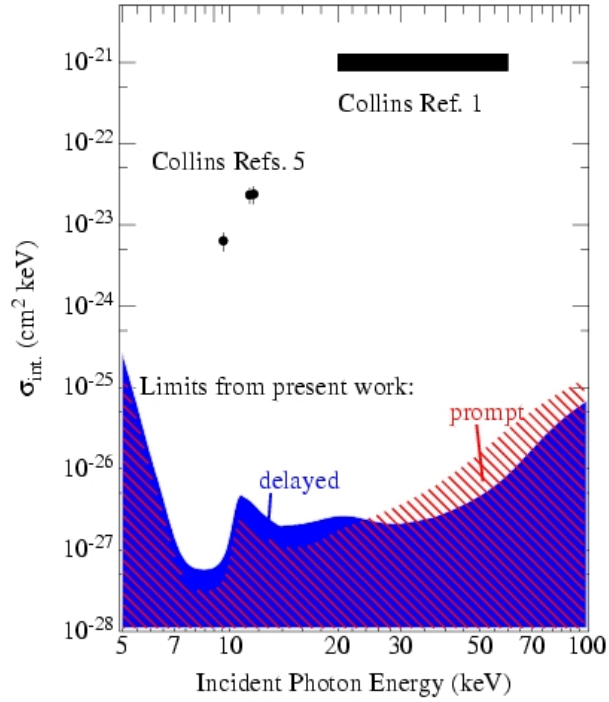


Fig. I-91. Limiting Cross sections (99% confidence limit, including systematic errors) for cross sections for enhancing the decay of the Hf isomer by x-rays. The area above the hatched regions is excluded for prompt or delayed signals, as indicated in the figure. The values corresponding to the reported levels from Refs. 1 and 5 are indicated in the figure.

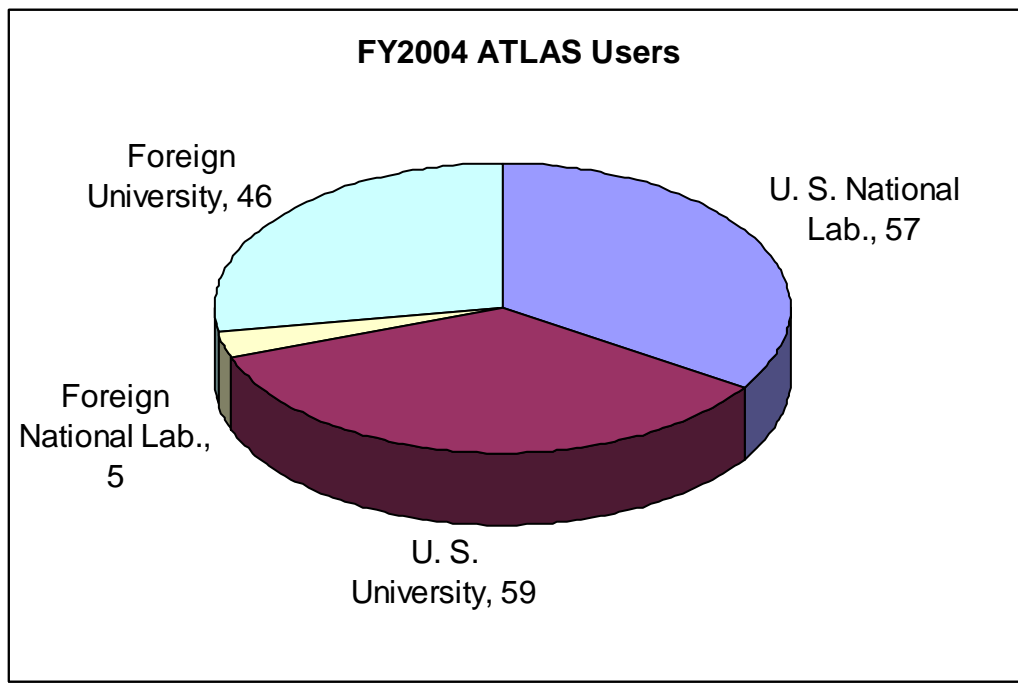
J. ATLAS USER PROGRAM (E. F. Moore)

During the fiscal year 2004, ATLAS hosted strong "campaigns" involving radioactive beams, the CPT, and, of course, Gammasphere. During the first half of the FY, Gammasphere was coupled to the FMA. In May 2004, Gammasphere was moved over to the old APEX beam line. ATLAS was down for approximately one month during the move. Following the move, Gammasphere was operated in "stand alone" mode, allowing campaigns using CHICO and the Microball. It is anticipated that Gammasphere will return to the FMA in the fall of 2005.

Many of the experimental programs were driven by outside Users, and in all programs, there was considerable outside User involvement. Over 95% of all experiments performed in fiscal year 2004 included one or more outside Users and roughly 50% of the approved experiments had an outside User as the Principal Investigator. Frank Moore continued to be available in a user liaison capacity to handle the

scheduling of ATLAS experiments, provide assistance in experiment proposal submission matters, and help facilitate the effective performance of research at ATLAS by outside scientists. In addition, a large portion of the Heavy-Ion in-house scientific staff and members of the technical support staff spent substantial amounts of their time in experiment setup, preparation and assistance for the many different experiments performed at ATLAS.

A total of 167 Users from 48 different institutions were present at ATLAS for experiments in FY 2004. The pie chart below shows the distribution of the institutions represented by ATLAS Users and the number of Users of each type. Of the 57 Users from U.S. National Laboratories, 48 are from Argonne (47 from the Physics Division, including 7 summer students and 3 long-term visitors). There were 52 students at ATLAS for experiments this FY, of which 11 were based at Argonne long-term. The names and institutions of all outside Users who were present at ATLAS in FY 2004 are listed below in section (b).



The program advisory committee met once during the 2004 fiscal year, on June 4-5, 2004 to recommend

experiments for beam time allocation at ATLAS. In FY 2004 the Program Advisory Committee members were:

June 4-5, 2004

Birger Back
Art Champagne
Augusto Macchiavelli

Argonne National Laboratory
University of North Carolina, Chapel Hill
Lawrence Berkeley National Laboratory

David Morrissey
 David Radford (*Chair*)
 Piet Van Duppen
 Alan Wuosmaa

Michigan State University
 Oak Ridge National Laboratory
 University of Leuven, Belgium
 Western Michigan University

The PAC reviewed 47 proposals for 236 days of requested running time. Due to the large demand for Gammasphere beam time, the PAC was asked to prioritize experiments into two categories; those that must be run at any cost (*priority I*), and those that should be granted beam time if at all possible (*priority II*). Of the submitted proposals, the Program Advisory Committee recommended priority I acceptance of 28 proposals for a total of 138 days of running time, and priority II acceptance of 2 proposals for 16 additional days of beam time.

Immediately following the Conference on "Nuclei at the Limits" held at ANL from July 26-30, 2004, the ATLAS User Community held a workshop on July 31-August 1, 2004 at the ANL Physics Division. Approximately 80 ATLAS Users attended the workshop and the presentations included future plans for ATLAS and experimental equipment, and a summary of the results of a "User Satisfaction" survey by Susan Fischer. Input from the Workshop attendees was incorporated into the Strategic Plan for the future of ATLAS.

The fall meeting of the American Physical Society, Division of Nuclear Physics was held in Chicago, IL, from October 27-30, 2004. The US national nuclear laboratories with low-energy heavy-ion facilities; ATLAS at Argonne, HRIBF at Oak Ridge, and the NSCL at Michigan States University held a joint User Meeting. In addition, the Gammasphere and RIA User groups meetings were also held during the same session. The Chair of the ATLAS User Group Executive Committee, Prof. Alan Wuosmaa (W. Michigan Univ.) introduced the ATLAS user program, Frank Moore presented a summary of the ATLAS User Program and announced the upcoming election for the ATLAS User Group Executive Committee, and Robert Janssens discussed the results of the User Workshop and the ATLAS Strategic Plan. Mike Carpenter discussed the status of Gammasphere at ATLAS during the Gammasphere Users group session. There were approximately 100 scientists in attendance at the meeting.

In FY 2004, the ATLAS User Group Executive Committee consisted of Alan Wuosmaa (Chair, Western Michigan University), Jolie Cizewski (Rutgers University), Susan Fischer (De Paul University), and Walter Reviol (Washington University).

a. Experiments Involving Outside Users

All experiments in which outside users directly participated during FY 2004 are listed below. The spokesperson for each experiment is given in square

brackets after the title, and the collaborators who were present for the experiment are given below each entry.

1. Measuring the Charge Radius of ${}^6\text{He}$ [Lu]
 Z.-t. Lu, K. E. Rehm, R. C. Pardo, L.-B. Wang, P. Mueller, K. Bailey, T. P. O'Connor, D. Henderson, T. O. Pennington, J. P. Schiffer, R. J. Holt, and R. V. F. Janssens
2. The Proton Decay of the $T_z = -1/2$ "Waiting Point" Nucleus ${}^{69}\text{Br}$ [Seweryniak]
 D. Seweryniak, G. Mukherjee, B. Blank, C. N. Davids, N. Hammond, M. P. Carpenter, S. Sinha, T. O. Pennington, D. G. Sarantites, D. Rudolph, R. V. F. Janssens, C. J. Chiara, C. H. Fahlander, P. J. Woods, T. Davinson, and S. Zhu
3. Spins of Excited States in ${}^9\text{Li}$ and the Nuclear Three-Body Force [Wuosmaa]
 K. E. Rehm, R. C. Pardo, J. P. Greene, S. Sinha, A. H. Wuosmaa, A. M. Heinz, D. Henderson, E. F. Moore, R. V. F. Janssens, X. Tang, D. A. Peterson, J. P. Schiffer, G. Savard, C. Jiang, R. E. Segel, and L. Jisonna
4. Continuation of the Precision Measurement of the Q-Value of the Superallowed Decay of ${}^{22}\text{Mg}$ with the CPT Mass Spectrometer [Savard]
 G. Savard, J. Clark, K. S. Sharma, J. C. Hardy, Z. Zhou, J. Wang, A. Levand, W. L. Trimble, N. Scielzo, V. E. Iacob, and A. A. Hecht

5. Electromagnetic Decay Properties of the $T_z = \sim 1/2$ $A = 67$ Mirror Pair: Isospin Symmetry From E1 Amplitudes [De Angelis]
G. De Angelis, D. V. Tonev, D. R. Napoli, S. Lunardi, E. Farnea, C. A. Ur, D. G. Sarantites, C. J. Chiara, W. Reviol, O. Pechenaya, M. P. Carpenter, C. J. Lister, G. Mukherjee, and N. Hammond
6. High-Resolution Particle-Gamma Coincidence Spectroscopy [Rudolph]
D. Rudolph, L.-L. Andersson, J. Ekman, C. H. Fahlander, E. K. Johansson, R. K. G. du Rietz, R. J. Charity, C. J. Chiara, O. Pechenaya, W. Reviol, D. G. Sarantites, L. G. Sobotka, C. Andreou, D. A. Torres Galindo, C. J. Lister, D. Seweryniak, and S. Zhu
7. Measurement of the Beta-Delayed Alpha Spectrum of ^{16}N With a New Technique [Rehm]
K. E. Rehm, A. H. Wuosmaa, C. Jiang, S. Sinha, G. Mukherjee, J. P. Schiffer, R. C. Pardo, E. F. Moore, R. E. Segel, L. Jisonna, X. Tang, G. Savard, J. P. Greene, and D. Henderson
8. Finding the Oblate Excited States in ^{72}Kr [Fischer]
S. M. Fischer, C. J. Lister, S. J. Freeman, N. Hammond, G. Mukherjee, S. Sinha, T. O. Pennington, D. Henderson, R. V. F. Janssens, M. P. Carpenter, D. Seweryniak, D. P. Balamuth, P. A. Hausladen, and E. F. Moore
9. Neutron-Proton Correlations and the Wavefunction Purity of Low-Lying $T = 0$ and $T = 1$ States in the $N = Z$ Odd-Odd Nucleus ^{74}Rb [Lister]
C. J. Lister, S. M. Fischer, M. P. Carpenter, E. F. Moore, N. Hammond, R. V. F. Janssens, T. L. Khoo, T. Lauritsen, and S. Sinha
10. Radiative Capture and Fusion Dynamics in Cold Fusion $^{90}\text{Zr} + ^{89}\text{Y}$ Reaction [Kondev]
F. G. Kondev, A. Bracco, F. Camera, O. Wieland, M. P. Carpenter, T. L. Khoo, R. V. F. Janssens, C. J. Lister, I. Ahmad, C. N. Davids, S. J. Freeman, N. Hammond, T. Lauritsen, G. Mukherjee, D. Seweryniak, D. J. Hartley, T. Goon, P. Chowdhury, U. Garg, S. Zhu, and E. F. Moore
11. Possible Improvements in ^{39}Ar AMS at ATLAS [Collon]
P. Collon, K. E. Rehm, C. Jiang, R. Golser, R. Vondrasek, R. C. Pardo, R. H. Scott, M. Paul, and G. Zinkann
12. Quadrupole Moments of Wobbling Bands in ^{167}Lu [Amro]
H. Amro, G. B. Hagemann, P. J. Bringel, A. Neusser, C. Engelhardt, C. R. Hansen, B. Herskind, D. J. Hartley, G. Gurdal, Y. Zhang, W. C. Ma, D. G. Roux, R. B. Yadav, D. A. Meyer
13. Measurement of ^3He to ^4He Ratios in Isotopically Purified Helium [Doyle]
R. C. Pardo, K. E. Rehm, P. R. Huffman, S. Dzhosyuk, C. Jiang, J. P. Schiffer, P. Collon, R. Vondrasek, R. H. Scott, S. Sinha, X. Tang, and L. Yang
14. Proton Decay of ^{121}Pr [Davids]
C. N. Davids, D. Seweryniak, W. B. Walters, P. J. Woods, A. P. Robinson, A. A. Hecht, R. V. F. Janssens, M. P. Carpenter, S. Sinha, and S. Zhu
15. Study of the $^{18}\text{Ne}(\alpha, p)^{21}\text{Na}$ Reaction in Inverse Kinematics [Sinha]
S. Sinha, J. P. Greene, A. H. Wuosmaa, D. Henderson, R. V. F. Janssens, C. Jiang, L. Jisonna, R. C. Pardo, D. A. Peterson, K. E. Rehm, J. P. Schiffer, R. E. Segel, R. H. Siemssen, E. F. Moore, X. Tang, A. A. Chen, and P. D. Parker
16. Is There Octupole Deformation at High Spin in ^{240}Pu ? [Wiedenhöver]
I. Wiedenhöver, A. P. Bernstein, E. S. Diffenderfer, C. Teal, Jr., P. C. Wilson, A. Larabee, B. A. Meredith, I. Ahmad, J. P. Greene, T. L. Khoo, E. F. Moore, R. V. F. Janssens, S. Zhu, T. Lauritsen, G. Mukherjee, C. J. Lister, D. Seweryniak, M. P. Carpenter, and A. A. Hecht

17. Study of Excited States in ${}^7\text{He}$ - Update [Wuosmaa]
A. H. Wuosmaa, K. E. Rehm, J. P. Greene, J. P. Schiffer, R. E. Segel, L. Jisonna, S. Sinha, E. F. Moore, X. Tang, R. C. Pardo, C. Jiang, G. Savard, and D. A. Peterson
18. Search for Hyperdeformation in ${}^{126}\text{Xe}$ [Hübel]
H. K. Hübel, P. J. C. Bringel, C. Engelhardt, A. Neusser, B. Herskind, G. B. Hagemann, G. Sletten, C. R. Hansen, P. Fallon, R. M. Clark, A. Bracco, G. Benzoni, F. Camera, S. W. Ødegård, M. P. Carpenter, T. L. Khoo, T. Lauritsen, R. V. F. Janssens, P. Chowdhury, and J. Roccas
19. Measurement of the β -Delayed α Spectrum of ${}^{16}\text{N}$ With a New Technique-2 [Rehm]
C. Jiang, G. Savard, J. P. Schiffer, X. Tang, S. Sinha, R. C. Pardo, E. F. Moore, R. V. F. Janssens, R. E. Segel, L. Jisonna, D. Henderson, J. P. Greene, T. O. Pennington, K. E. Rehm, and M. Paul
20. Shape Transitions at High Spin in Neutron-Rich ${}^{180,182}\text{Hf}$ Nuclei [Chowdhury]
P. Chowdhury, S. K. Tandel, U. S. Tandel, S. P. Sheppard, D. Cline, C.-Y. Wu, D. Seweryniak, S. Zhu, R. V. F. Janssens, M. P. Carpenter, F. G. Kondev, T. L. Khoo, and T. Lauritsen
21. How Does the $j_{15/2}$ Neutron Pair Align in Actinide Nuclei? [Wu]
D. Cline, A. Hayes, M. A. Riley, C.-Y. Wu, A. O. Macchiavelli, E. Rodriguez-Vieitez, R. V. F. Janssens, M. P. Carpenter, S. Zhu, I. Ahmad, and J. P. Greene
22. Search for Triaxial Superdeformation and Wobbling Mode in Even-Even ${}^{172}\text{Hf}$ [Ma]
W. C. Ma, D. G. Roux, R. B. Yadav, S. W. Ødegård, S. Rigby, D. M. Cullen, D. J. Hartley, J. A. Winger, Y. Zhang, T. Lauritsen, M. P. Carpenter, E. F. Moore, R. V. F. Janssens, T. L. Khoo, S. Zhu, and D. T. Scholes
23. Determination of P_{cn} for Cold Fusion [Loveland]
W. Loveland, D. A. Peterson, P. H. Sprunger, C. J. Lister, P. Chowdhury, C. Jiang, S. Zhu, X. Tang, S. Sinha, and R. S. Naik
24. Measurement of ${}^{64}\text{Ni}$ Induced Fusion on the Transitional Nucleus ${}^{100}\text{Mo}$ at Extreme Sub-Barrier Energies [Jiang]
C. Jiang, K. E. Rehm, R. V. F. Janssens, X. Tang, S. Sinha, D. A. Peterson, S. Zhu, P. Collon, I. Tanihata, A. H. Wuosmaa, D. Seweryniak, and C. N. Davids
25. Shapes and the Shell Model at $A = 60$ [Freeman]
S. J. Freeman, R. V. F. Janssens, J. F. Smith, B. J. Varley, A. N. Deacon, S. L. Tabor, I. J. Calderin, D. Seweryniak, T. Lauritsen, S. Zhu, and N. Hammond
26. Determining the End-Point for Nova Nucleosynthesis: Evaluating the ${}^{30}\text{P}$ (p,γ) Reaction Rate [Jenkins]
D. G. Jenkins, C. J. Lister, M. P. Carpenter, D. Seweryniak, P. Chowdhury, N. Hammond, S. Sinha, K. E. Rehm, A. S. Jokinen, and H. T. Penttilä
27. Search for Wobbling Excitations in Odd-Odd ${}^{164}\text{Lu}$ [Ødegård]
S. W. Ødegård, P. J. C. Bringel, A. Neusser, C. Engelhardt, H. K. Hübel, C. R. Hansen, B. Herskind, G. Sletten, D. G. Roux, M. P. Carpenter, T. L. Khoo, F. G. Kondev, T. Lauritsen, and W. C. Ma
28. Entry Distribution for SD Bands in ${}^{152}\text{Dy}$ [Lauritsen]
T. Lauritsen, R. V. F. Janssens, P. Fallon, C. J. Lister, M. P. Carpenter, A. J. Larabee, S. Zhu, E. F. Moore, T. L. Khoo, I. Ahmad, F. G. Kondev, D. Seweryniak, A. A. Hecht, N. Hammond, and P. Chowdhury

29. Mass Measurements on Refractory Isotopes Around the rp-Process Waiting Point Nuclei ^{80}Zr , ^{84}Mo , and ^{92}Pd [Savard]
G. Savard, J. Clark, J. Wang, Z. Zhou, A. Levand, N. Scielzo, K. S. Sharma, A. A. Hecht, S. Sinha, and N. Scielzo
30. Structure of Threshold States in the $^{21}\text{Na}(p,\gamma)^{22}\text{Mg}$ Reaction [Woods]
P. M. Davidson, P. J. Woods, D. Seweryniak, C. N. Davids, J. M. Shergur, S. Sinha, M. P. Carpenter, T. Lauritsen, R. V. F. Janssens, and D. G. Jenkins
31. In-Beam γ Spectroscopy of the Proton Emitter ^{117}La [Seweryniak]
D. Seweryniak, P. J. Woods, Z. Liu, A. P. Robinson, C. N. Davids, T. Davinson, R. V. F. Janssens, M. P. Carpenter, X. Tang, and S. Zhu
32. Reflection Asymmetry in the Actinides [Hammond]
N. Hammond, M. P. Carpenter, R. V. F. Janssens, D. Seweryniak, E. F. Moore, T. Lauritsen, F. G. Kondev, S. Zhu, T. L. Khoo, J. F. Smith, S. J. Freeman, A. N. Deacon, G. D. Jones, and P. Chowdhury
33. Studies of Excited States in ^{101}Sn . Phase I: Search for ^{101}Sn β -Delayed Protons [Seweryniak]
D. Seweryniak, S. Zhu, R. V. F. Janssens, C. J. Lister, M. P. Carpenter, N. Hammond, D. Henderson, A. A. Hecht, W. B. Walters, and D. A. Peterson
34. $T = 0$ Pairing in the Even-Even $N = Z$ Nucleus ^{92}Pd [Chiara]
C. J. Chiara, D. G. Sarantites, W. Reviol, O. Pechenaya, L.-L. I. S. Andersson, E. K. Johansson, D. Rudolph, D. Seweryniak, A. O. Macchiavelli, and S. Zhu
35. Studies of the Breakout Reaction $^{18}\text{Ne}(p,\alpha)^{21}\text{Na}$ in Inverse Kinematics [Sinha]
A. H. Wuosmaa, K. E. Rehm, X. Tang, S. Sinha, L. Jisonna, C. Jiang, J. P. Schiffer, R. C. Pardo, J. P. Greene, D. Henderson, R. E. Segel, R. V. F. Janssens, E. F. Moore, M. M. Notani, and N. Goodman
36. Search for TSD Bands and Wobbling Excitations in ^{171}Ta [Hartley]
D. J. Hartley, J. R. Vanhoy, W. H. Mohr, M. A. Riley, A. L. Aguilar, C. Teal, Jr., L. L. Riedinger, M. T. Danchev, M. K. Djongolov, S. W. Ødegård, R. V. F. Janssens, F. G. Kondev, M. P. Carpenter, T. Lauritsen, P. Chowdhury, S. K. Tandel, and E. F. Moore
37. Continuation of the Mass Measurement Program on Refractory Isotopes around the rp-Process Waiting Point Nuclei ^{80}Zr , ^{84}Mo , and ^{92}Pd [Savard]
G. Savard, J. Clark, Z. Zhou, J. Wang, Y. Wang, B. Lundgren, A. Levand, A. A. Hecht, N. Scielzo, I. Tanihata, A. C. Villari, H. Sharma, J. Fallis, S. Russell, and M. Scholte-van de Vorst
38. Test of the Upgraded Area II Enge Spectrograph in Gas-Filled Mode [Savard]
G. Savard, J. Clark, K. S. Sharma, B. Lundgren, I. Tanihata, N. Scielzo, Y. Wang, W. L. Trimble, A. Levand, A. A. Hecht, M. Sternberg, M. Scholte-van de Vorst, S. Russell, J. Fallis, and I. M. Percher
39. The Structure of Neutron-Rich sdf-Shell Nuclei using Multi-Nucleon Transfer Reaction Studies at Gammasphere [Fallon]
P. Fallon, I.-Y. Lee, E. Rodriguez-Vieitez, M. Descovich, C.-Y. Wu, D. Cline, S. Zhu, D. Seweryniak, M. P. Carpenter, and R. V. F. Janssens

b. Outside Users of ATLAS During the Period October 1, 2003 - September 30, 2004

This list includes all outside Users who were an experiment spokesperson (a), alternate spokesperson (b), student (s), or collaborator actually present at ATLAS for an experiment. An additional 30 Users

listed as collaborators on the various experiment proposals were not at ATLAS in person, and thus are not represented in the list below.

1. Clark University
G. Gurdal (s)
2. CSNSM
J. Roccaz (s)
3. De Paul University
S. M. Fischer (a)
4. Florida State University
A. L. Aguilar (s)
A. P. Bernstein (s)
I. J. Calderin (s)
E. S. Diffenderfer (s)
M. A. Riley (b)
S. L. Tabor
C. Teal, Jr. (s)
I. Wiedenhöver (a)
P. C. Wilson (s)
5. GANIL
A. C. Villari
6. Greenville College
A. J. Larabee
B. A. Meredith (s)
7. Harvard University
J. M. Doyle (a)
L. Yang (s)
S. Dzhosyuk
8. Hebrew University of Jerusalem
M. Paul (b)
9. Lab. Nazionali di Legnaro
G. De Angelis (a)
D. R. Napoli
D. V. Tonev
10. Lawrence Berkeley National Lab.
R. M. Clark
M. Descovich
P. Fallon (a)
I.-Y. Lee
A. O. Macchiavelli (b)
E. Rodriguez-Vieitez (s)
11. Lawrence Livermore National Lab.
C.-Y. Wu (a)
12. Louisiana State University
T. Goon
13. Lund University
L. S. Andersson (s)
R. K. G. du Rietz (s)
J. Ekman (s)
C. H. Fahlander
E. K. Johansson (s)
D. Rudolph (a)
14. McMaster University
A. A. Chen
15. Mississippi State University
W. C. Ma (a)
D. G. Roux (b)
J. A. Winger
R. B. Yadav (s)
Y. Zhang (s)
16. National Institutes of Standards and Technology
P. R. Huffman (b)
17. Northwestern University
L. Jisonna (s)
R. E. Segel (b)
18. Oak Ridge National Laboratory
P. A. Hausladen
19. Oregon State University
W. Loveland (a)
P. H. Sprunger (s)
20. Saha Institute of Nuclear Physics
G. Mukherjee
21. Texas A & M University
J. C. Hardy
V. E. Iacob
22. United States Naval Academy
D. J. Hartley (a)
W. H. Mohr (s)
J. R. Vanhoy

23. Universidad Nacional de Colombia
D. A. Torres Galindo (s)
24. Universität Bonn
P. J. C. Bringel (s)
C. Engelhardt (s)
H. K. Hübel (a)
A. Neusser (s)
25. Universität Wien
R. Golser
26. Università degli Studi di Milano
G. Benzoni (s)
A. Bracco
F. Camera
O. Wieland
27. University of Chicago
W. L. Trimble (s)
28. University of Copenhagen
G. B. Hagemann (b)
C. R. Hansen (s)
B. Herskind (b)
G. Sletten
29. University of Edinburgh
T. Davinson
A. P. Robinson (s)
P. J. Woods (a)
30. University of Groningen
R. H. Siemssen
31. University of Guelph
C. Andreoiu
32. University of Jyväskylä
A. S. P. Jokinen
H. T. Penttilä
33. University of Liverpool
G. D. Jones (b)
34. University of Manchester
D. M. Cullen
A. N. Deacon (s)
S. J. Freeman (a)
S. Rigby (s)
D. T. Scholes (s)
J. F. Smith
B. J. Varley
35. University of Manitoba
J. Clark (b)(s)
36. University of Maryland
K. S. Sharma
J. M. Shergur (s)
W. B. Walters
A. A. Hecht (s)
37. University of Massachusetts, Lowell
P. Chowdhury (a)
S. P. Sheppard (s)
S. K. Tandel
U. Tandel (s)
38. University of Notre Dame
Ph. Collon (a)
U. Garg
S. Zhu
39. University of Oslo
S. W. Ødegäard (a)
40. University of Padova
E. Farnea
S. Lunardi
C. A. Ur
41. University of Pennsylvania
D. P. Balamuth
42. University of Rochester
D. Cline
A. Hayes (s)
43. University of Surrey
Z. Liu
S. Williams
44. University of Tennessee
M. T. Danchev
M. K. Djongolov (s)
L. L. Riedinger
45. University of York
D. G. Jenkins (a)
R. Wadsworth
46. Washington University
R. J. Charity
C. J. Chiara (a)
O. Pechenaya (s)
W. Reviol
D. G. Sarantites (b)
L. G. Sobotka
47. Western Michigan University
N. Goodman (s)
A. H. Wuosmaa (a)(b)

- 48. Yale University
 - H. Amro (a)
 - D. A. Meyer (s)
 - P. D. Parker

II. OPERATION AND DEVELOPMENT OF ATLAS

OVERVIEW

Highlights of the operation of the Argonne Tandem Linear Accelerator System (ATLAS), a DOE national user facility, and related accelerator physics R&D projects are described in this chapter. ATLAS is funded to provide heavy-ion beams for basic research in nuclear physics but also serves other areas of research and development, including material science. In addition ATLAS has a rich program in developing the tools of accelerator mass spectroscopy (AMS) applied to wide ranging research programs such as oceanography, nuclear physics, astrophysics and geology. Over half of the beam time is allocated to experiments for which the spokesperson is an outside user. Recent ATLAS operating performance and related development projects are described in the next section. ATLAS personnel are also involved in developing technology in support of a future advanced facility, based on ATLAS technologies, for beams of short-lived nuclei. Projects related to the Rare Isotope Accelerator (RIA) Facility are described in the third section below.

For the first half of Fiscal Year 2004, ATLAS operated at maximum efficiency: running 7-days per week, 24-hours a day. But in May 2004 ATLAS was required to returned to 5.3 day operation with some limited 7-day operation in the summer. This schedule was initially precipitated by operator resignations, and the need to train new operators, but has now been continued to the present and immediate future due to significant budget constraints. For Fiscal Year 2004 ATLAS provided 28 beams of different isotopes to users. A total of 5559 hours of beam time was provided for the research program; that total rises to 6202 hours when setup time is included.

Since Fiscal Year 1995, ATLAS has made beams of short-lived rare isotopes (RIBs) available for nuclear physics research. A total of 15 different radioactive beams have been developed to date and are generally available for use. Further development of RIBs is planned as required by the nuclear physics and nuclear astrophysics programs at ATLAS. During Fiscal Year 2004, beams of ${}^6\text{He}$, ${}^8\text{Li}$, ${}^{16}\text{N}$, and ${}^{21}\text{Na}$ were provided. Construction of a new cryostat and resonators for a major energy upgrade of the facility, that will increase the overall voltage of ATLAS by 25%, continues. First "offline" tests, with two prototype resonators, are expected by the end of the 2005 calendar year. The final six resonators are

now under construction. This project is made possible by AIP funds provided in Fiscal Year 2001 – 2005.

A new Cf-fission source project that will allow ATLAS to provide unique neutron-rich radioactive beams for research has been proposed and is undergoing review by DOE. A three-year funding profile is proposed. The detailed proposal was submitted to DOE in February 2005.

Gammasphere has operated on its own dedicated beamline since late May 2004. This has allowed the FMA to undertake experiments requiring higher beam currents and more intense radiation fields than would have been possible with Gammasphere surrounding the FMA target.



Table II-1. Summary of ATLAS experiments and user statistics.

	<u>FY2004</u> (actual)	<u>FY2005</u> (actual)	<u>FY2006</u> (pred.)	<u>FY2007</u> (pred.)
<u>Beam Use for Research (hr)</u>				
Nuclear Physics	5402	4570	3610	4550
Accelerator R & D (RIA & ATLAS)	47	92	70	100
Accelerator Mass Spectroscopy	110	0	150	150
Other	<u>0</u>	<u>24</u>	<u>50</u>	<u>100</u>
Total	5559	4686	3880	4900
Number of Experiments Receiving Beam	47	43	40	48
Number of Scientists Participating in Research	169	187	170	200
<u>Institutions Represented</u>				
Universities (U.S.A.)	20	25	25	26
DOE National Laboratories	3	4	5	5
Other	25	18	25	27
<u>Usage of Beam Time (%)</u>				
In-House Staff	43	45	45	35
Universities (U.S.A.)	36	35	35	35
Other DOE National Laboratories	3	5	5	15
Other Institutions	<u>18</u>	<u>15</u>	<u>15</u>	<u>15</u>
Total	100	100	100	100

A. OPERATION OF THE ACCELERATOR

a.1. Operations Summary (R. C. Pardo, D. Barnett, J. Bogaty, L. Carlquist, A. Deriy, G. Devane, G. Gribbon, R. Jenkins, A. Krupa, E. Lindert, A. McCormick, S. McDonald, F. H. Munson, Jr., D. R. Phillips, M. Power, D. Quock, A. Ruthenberg, R. H. Scott, S. Sharamentov, J. R. Specht, P. Strickhorn, R. C. Vondrasek, L. Weber, and G. P. Zinkann)

ATLAS provided a total of 28 different isotopes for research in Fiscal Year 2004. The distribution of species is shown in Fig. II-1. The calcium isotopes were, again, the most popular beams for Fiscal Year 2004 and only 13% of all beam time was for isotopes heavier than the nickel isotopes.

The replacement of the corona voltage distribution system with a resistor voltage-divider system in the tandem injector was undertaken last year. The first experiments with the rebuilt accelerator were conducted this year and the tandem performed very well. Conditioning to 8.8 MV terminal voltage went

well and experiments were run with terminal voltages as high as 8.3 MV. The tandem was used for a variety of experiments this year, providing beams for approximately 27% of the total beam time. The new tandem terminal communication process installed last year was improved with the addition of software that provides a history of tandem terminal stripping foil usage. The operator can now enter the type of foil and "time stamp" the time of insertion into the beam path. The hours of usage can then be tracked for each foil.

In addition to the tandem repair, improvements at the tandem ion source system were also undertaken. As part

of those studies, the transmission from the source to the tandem was improved significantly. Approximately a factor of two improvement in transmission was realized by realignment and by the removal of a HV vertical steering element that was found to be causing significant degradation to the beam emittance. This improvement is most important for the long-lived radioactive beam program and for tandem-based AMS experiments.

The switching magnet that delivers beam to the FMA or stand-alone Gammasphere beamlines was replaced this year with a magnet able to bend beams of much higher rigidity. This was required because of the improved performance of the ECR sources for the heaviest beams eliminating the need to strip the beam at an intermediate point to achieve Coulomb-barrier energies. By eliminating this stripping, approximately a factor of 5 higher beam intensities are available but the increased beam rigidity requires a more robust magnet. The magnet installed was obtained from the decommissioned nuclear structure laboratory at the University of Rochester. Extensive modification to the support structure and vacuum chamber was required for use at ATLAS.

The program to high-pressure water rinse resonators in ATLAS in order to restore their performance

continued this year with four resonators in the first Booster linac cryostat rinsed. The technique continues to show significant gains in resonator performance, but the cryostat design which employs a common vacuum for the beam and resonator interior with the thermal isolation vacuum means that fields deteriorate over time as dirt re-deposits on resonator surfaces. Even so, the technique has produced significant gains in field performance.

ATLAS has for many years relied on a time-of-flight (TOF) resonant pick-up system that continuously monitors the beam energy delivered to experiments. A new software application has been developed that runs continuously, logging the TOF (Time Of Flight) energy measurement data into a permanent file identified by date, beam type and accelerator parameters sufficient for unique identification. Energy measurements are made every 30 seconds and the results are archived in these permanent files. This application is capable of storing trend type data files where the file name consists of the ion source and injector being used, the atomic number and mass, and the date the file was created, thereby associating a trend file with an experiment. These files can be made available to the user, upon their request. After selecting the archived trend file, the user can view the plotted data "online" using a Vsystem utility, or export the data to a non-Vsystem utility such as MS Excel.

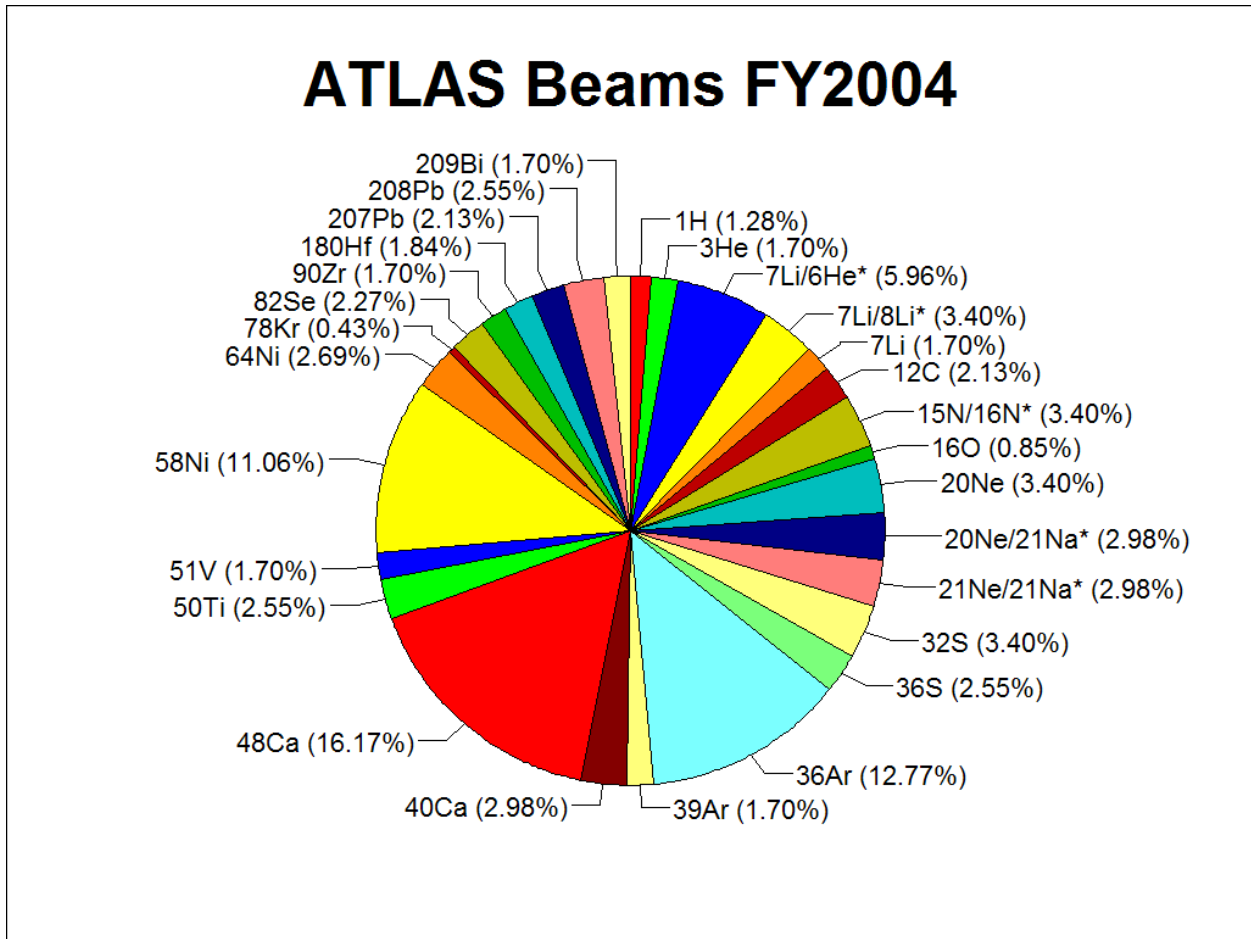


Fig. II-1. Distribution of beam time by isotope provided by ATLAS in Fiscal Year 2004. A total of 28 different isotopes were provided to the research program. Radioactive beams (indicated by an asterisk) comprised 18.7% (1040 hours) of all beam time in Fiscal Year 2004.

B. DEVELOPMENTS RELATED TO ATLAS

b.1. Status of the ECR Ion Sources (R. C. Vondrasek and R. H. Scott)

b.1.1. Hexapole and Plasma Chamber Re-Design

The ECR2 hexapole design was modified in 2003 resulting in significantly improved source performance. However, the cooling of the permanent magnet hexapole continued to be an issue with damage occurring to three of the hexapole bars. A new hexapole chamber design was adopted which directs the cooling water along the hexapole pole tips, where the majority of the heat from the plasma is deposited, rather than along the sides of the magnets as in the previous design. This change also allowed an increase in the number of radial ports (from three

to six) available for solid material introduction and improved pumping to the central region of the plasma chamber (Fig. II-2).

The magnet bars which showed damage due to excessive heating were repaired and then encased in stainless steel cans to prevent corrosion of the permanent magnet material. The cans were fabricated on site and then laser welded once the magnet bars were in place. The source is presently being reassembled and operations will resume in early 2005.

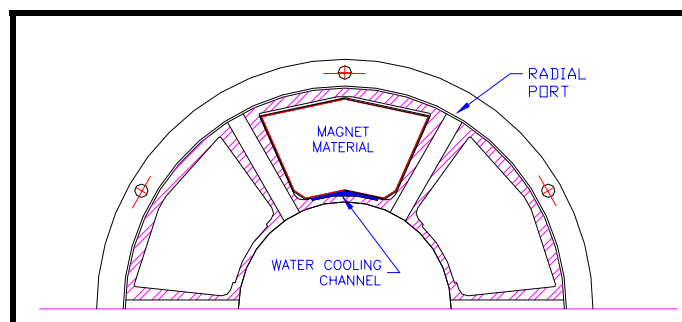


Fig. II-2. ECR2 hexapole showing half of the hexapole and the aluminum plasma chamber. The pole tip cooling channel is highlighted and one of the six radial ports is indicated.

b.1.2. Special Helium Source for AMS

Accelerator Mass Spectroscopy (AMS) continues to be an active area for ECR development. The techniques used to measure ^3He concentrations in ultra-pure ^4He samples have been refined. The performance of the mini-quartz source used for these studies was improved by a modification to the internal waveguide configuration. Instead of

broadcasting the RF into the full plasma chamber and allowing the waves to propagate to the quartz source, the waveguide was extended within the source chamber and the launching point was established next to the quartz. This has greatly simplified source operation and has improved the source performance.

b.1.3. Plasma Potential Measurements and Ion Lifetime

In collaboration with the University of Jyväskylä ECR group, a device was constructed to measure the source plasma potential. The device was installed on ECR2 and a series of measurements were performed in both single and two-frequency heating modes. In addition the production times of various charge states

of lead were monitored using a fast pulsed sputter sample.

The injection microwave power using two frequencies creates two concentric ECR surfaces for electron heating which leads to an increased electron density and population thereby extending the ion confinement time.

The ECR surfaces must be closed to produce stable electron heating, and the choice of a large frequency separation creates discrete ECR surfaces (i.e. - 11 and 14 GHz). An electrostatic potential structure is established via the confinement and loss mechanisms of the electrons and ions within the plasma. The structure consists of a central plasma potential ($\sim 4\text{-}10\text{ V}$) with a central dip of a smaller magnitude which serves to confine the ions (Fig. II-3).

Observed increases in the beam intensities and decreases in the production times of lead charge states indicate that the electron density and population are increasing when two frequency heating is used. The peak of the charge state distribution (CSD) also shifts higher when in two frequency mode indicating a longer confinement time within the plasma. However, measurements with O^{7+} showed that while the beam intensity increased (31 μA to 68 μA) with two frequency heating, the

plasma potential remained constant at 4.6 V. Additional tests which involved altering the magnitude of the gap between the two frequencies showed that while a larger gap favored higher charge state production and decreased the production times, the overall beam output decreased. This would indicate a decrease in the electron population, while at the same time the electron density and the confinement time are increasing in order to produce the higher charge states.

To provide a consistent model for these opposing observations, a multiple potential structure for two-frequency heating has been proposed (Fig. II-3). A “core plasma” defined by the inner resonance is created by the superposition of the two electrostatic potential structures. The core plasma maintains a higher density than the surrounding plasma and is responsible for the production of the highly charged ions by deepening the electrostatic potential well. The outer resonance supplies “warm” electrons and ions to the inner resonance.

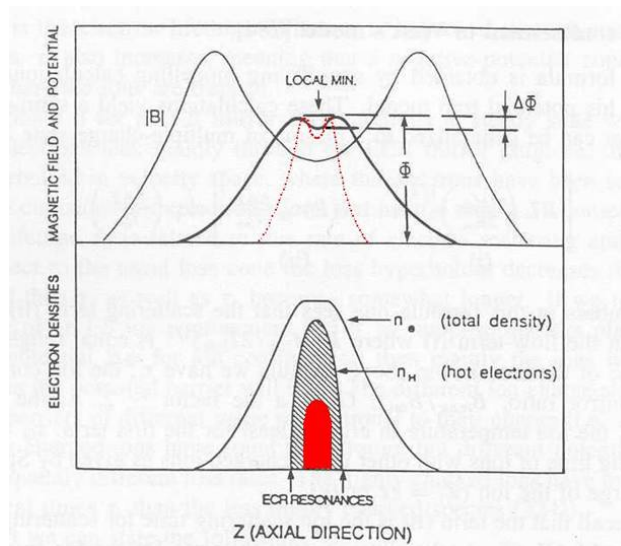


Fig. II-3. The proposed plasma potential structure for two frequency heating. The main plasma potential ($\sim 4\text{-}10\text{ V}$) regulates the electron loss term while the inner potential dip regulates the ion loss term. The potential structure of the second resonance, in red in the upper frame, is within the primary potential structure and has a higher electron density, denoted in red in the lower frame.

b.1.4. Other ECR Source Improvements

Several small but significant improvements in equipment were made on the sources. The 14 GHz transmitter which was purchased in 2003 was installed on ECR1. This enables ECR1 to operate in two-frequency mode and provides more of an overlap between ECR1 and ECR2 in beam production capabilities. New high frequency switching power

supplies were installed on one coil of ECR1. This allows for higher magnetic field levels and hence improved source performance. And the oil pumps on ECR1 were eliminated and replaced with dry pumps. This has eliminated a major source of carbon contamination and has improved source performance.

b.2. ECR Source High-Voltage Monitoring and Control (J. M. Bogaty)

ATLAS ion sources ECR-I and ECR-II now have precision monitoring of platform and extractor voltage levels. New, carefully characterized, high voltage divider stacks were installed at both ion sources. Voltage coefficients of the divider stack resistors were measured from which first order correction equations were determined. Resistor voltage coefficients contribute most of the error when accurate measurements are desired over a large range

of voltages. Temperature effects can contribute significant errors but this is being controlled through design considerations. Each ECR has a correction equation that allows mutual calibration with the other ECR's platform voltage as well as restoration of past operating voltages to high precision. One ECR can be shutdown and the other ECR's platform voltage set for the same value. Computerized correction will insure that the transfer error will be within 40 ppm.

b.3. An Improved Pneumatic Frequency Control for Superconducting Cavities (G. P. Zinkann and S. Sharamentov)

The ATLAS (Argonne Tandem Linear Accelerator System) superconducting cavities use a pneumatic system to maintain the average cavity eigenfrequency at the master oscillator frequency. The present pneumatic slow tuner control has a limitation in the tuning slew rates. In some cases, the frequency slew rate is as low as 30 Hz/sec. The total tuning range for ATLAS cavities varies from 60 kHz to as high as 450 kHz depending on the cavity type. With the

present system, if a cavity is at the extreme end of its tuning range, it may take an unacceptable length of time to reach the master oscillator frequency. We have designed a new slow tuner control system that increases the frequency slew rates by a factor of three hundred in the most extreme case. This improved system is directly applicable for use on the RIA (Rare Isotope Accelerator) cavities (see Fig. II-4 for plots of the old and new slew rates).

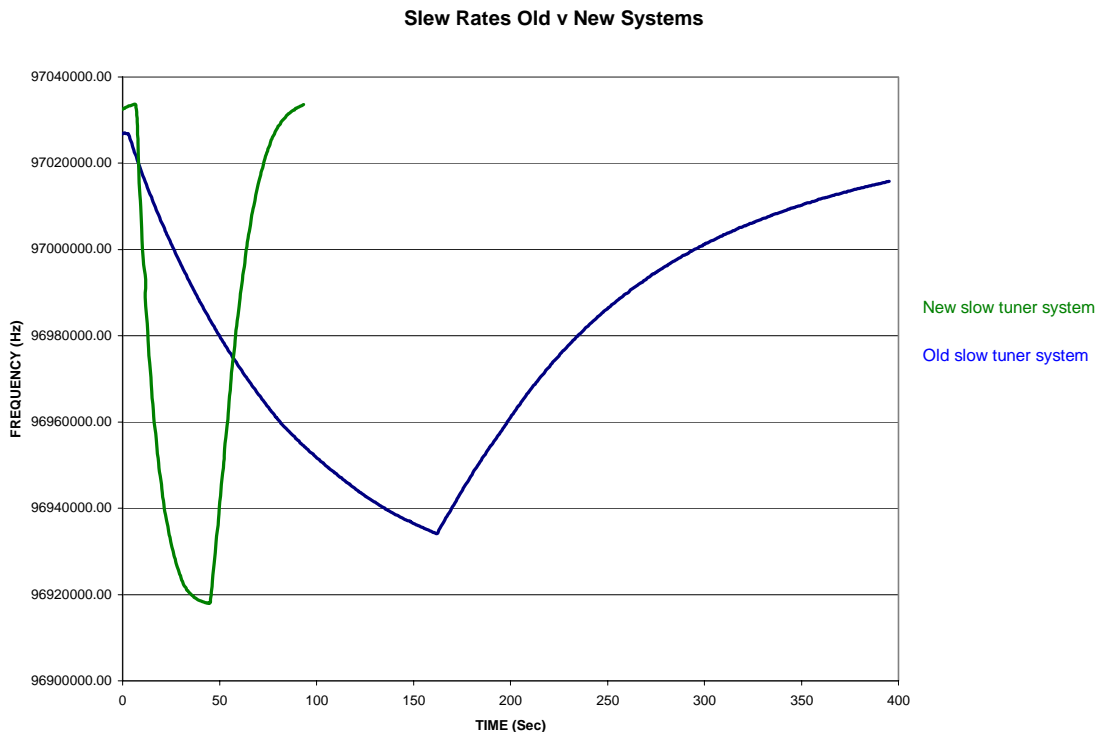


Fig. II-4. A comparison of the slew rates between the old resonator slow tuner system and the new system.

b.4. New Harmonic Buncher RF Control System (S. I. Sharamentov)

The block diagram of the PII harmonic buncher RF control system is shown in Fig. II-5 and the photograph of the electronic rack is shown in Fig. II-6. The system includes a four-harmonic resonant structure, two-channel RF power amplifier, RF

amplifier power supply, new harmonic buncher RF control chassis and the original phase shifter, located in the master oscillator rack. Power supply, RF amplifier and RF control chassis are mounted in the RR214 rack close to the four-harmonic resonant structure.

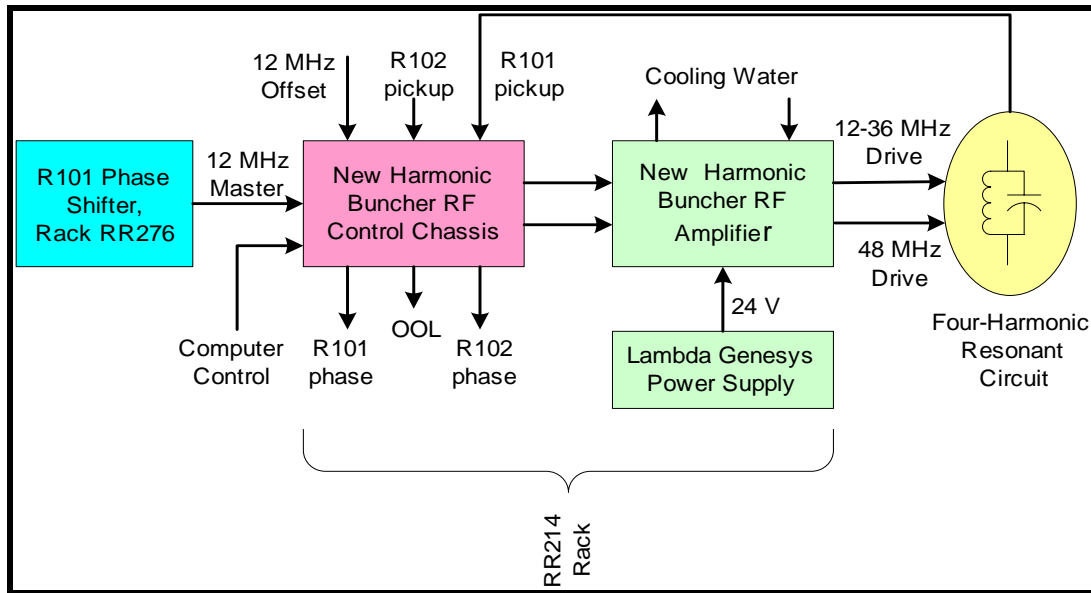


Fig. II-5. R101 Harmonic Buncher RF Control System Block Diagram.



Fig. II-6. RR214 rack view showing the harmonic buncher control chassis and associated power supplies.

b.4.1. RF Power Amplifier

The two-channel RF power amplifier block diagram is shown in Fig. II-7 and the photograph of the front and rear panels is shown in Fig. II-8. In addition to adding a 48-MHz channel, the amplifier has a feature which is new for the ATLAS RF amplifiers. It is a built-in protection and metering board, which provides measurement and indication of the output

RF power for forward/and reflected waves, as well as measurement of 12-36 MHz RF amplifier module supply current. The board also protects the RF module against temperature overload, supply current overload, water flow trip and VSWR trip. All the trips can be reset by the reset button on the amplifier front panel.

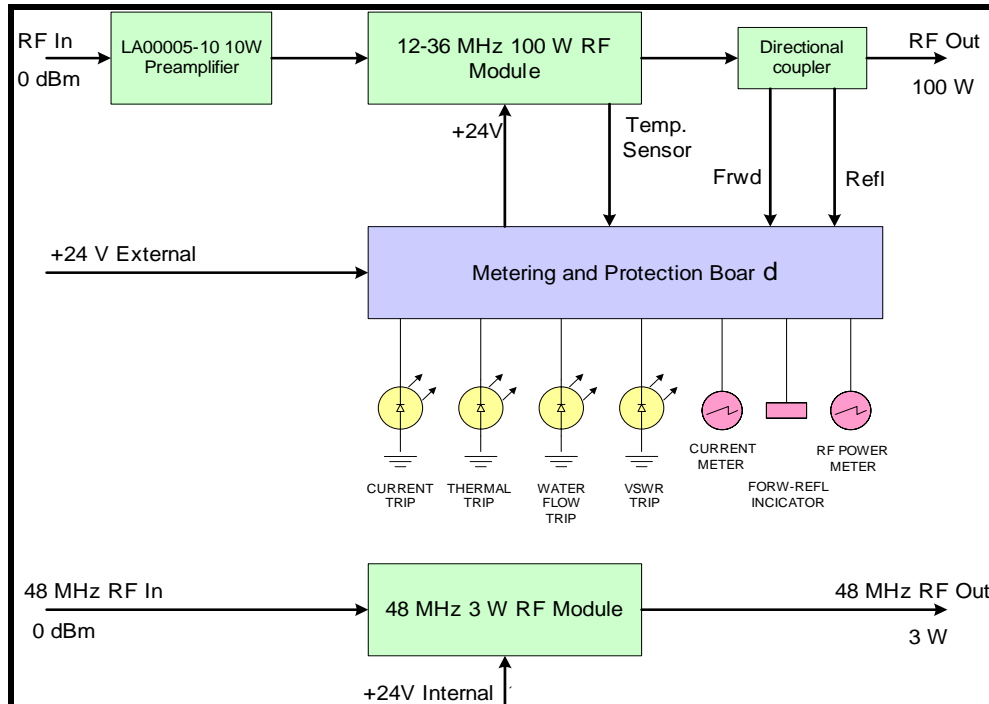


Fig. II-7. Two-channel RF power amplifier block diagram.



Fig. II-8. Front panel and rear panel amplifier view.

b.4.2. Harmonic Buncher RF Control Chassis

The new harmonic buncher RF control chassis is a four-channel **I** and **Q** type RF feedback controller. Each channel controls a single harmonic of a composite four-harmonic RF field in the buncher grid space, at the fundamental frequency of 12.125 MHz.

RF feedback control systems of **I** and **Q** type are becoming more and more popular these days. Unlike conventional systems which represent an RF vector in a polar system of coordinate, i.e. with phase and amplitude, **I** and **Q** system does that in rectangular system of coordinate, i.e. by **I**-phase (or sine) and **Q**uadrature (or cosine) components.

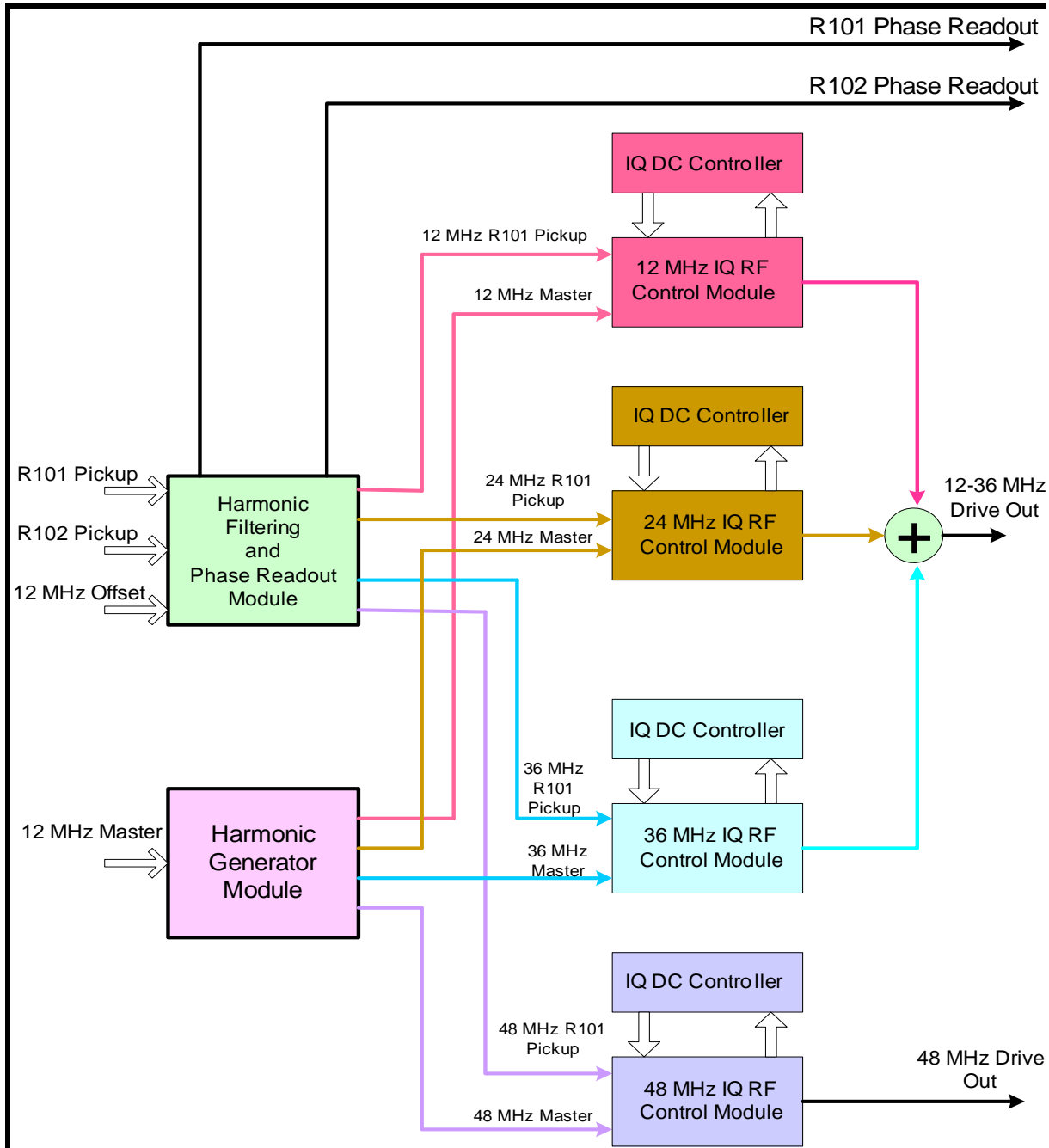


Fig. II-9. Block diagram of the new harmonic buncher RF control chassis.

A block diagram of the **I** and **Q** chassis is shown in Fig. II-9. A harmonic filtering and phase readout module filters and splits buncher composite pickup signal into four 12, 24, 36 and 48 MHz single frequency channels. It also provides phase readout outputs for the R101 harmonic buncher and R102 traveling wave chopper. The harmonic generator module uses the 12.125 MHz master oscillator signal

for generation of the 24, 36 and 48 MHz master signals.

Each frequency channel is built with two modules (boards): a **I** and **Q** RF control module and a **I** and **Q** dc feedback controller. Each **I** and **Q** RF control module performs sine-cosine demodulation of the RF feedback signal and sine-cosine modulation of the RF power amplifier drive signal, as shown in Fig. II-10.

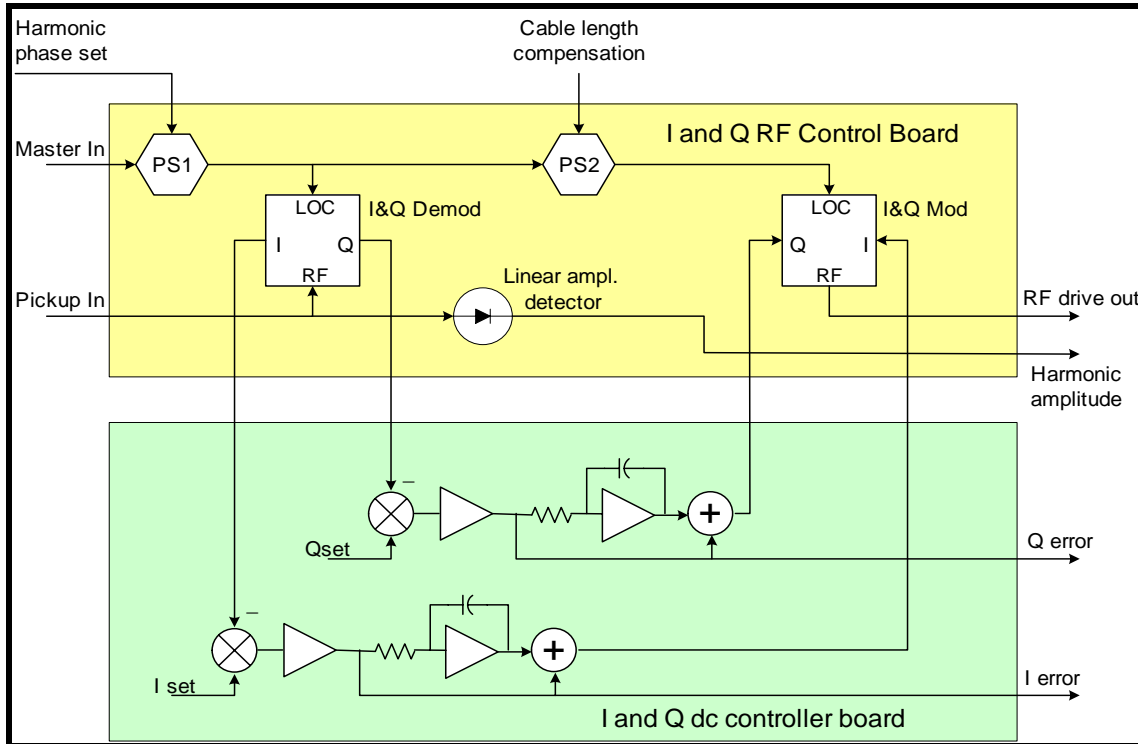


Fig. II-10. Simplified block diagram of the single frequency control channel.

Analog phase shifters, PS1 and PS2, on the RF control board allow setting of individual harmonic phase and provide cable length compensation. Each RF control board also has a linear RF amplitude detector, which is used to display harmonic amplitude on a front panel indicator. A DC **I** and **Q** controller board does the proportional-integral regulation of the **I** and **Q** error signals and performs interlocking and some auxiliary functions.

The harmonics phase and amplitude control diagram is shown in Fig. II-11 and photographs of the electronic racks are shown in Figs. II-12 and II-13. Unlike the old control system, the new system can be fully operated in local mode, i.e. master amplitude and each harmonic phase and amplitude can be manually set by means of the front panel controls. Moreover, the local mode of harmonics phase and amplitude control (except for the master amplitude set) is considered as a primary and main control mode.

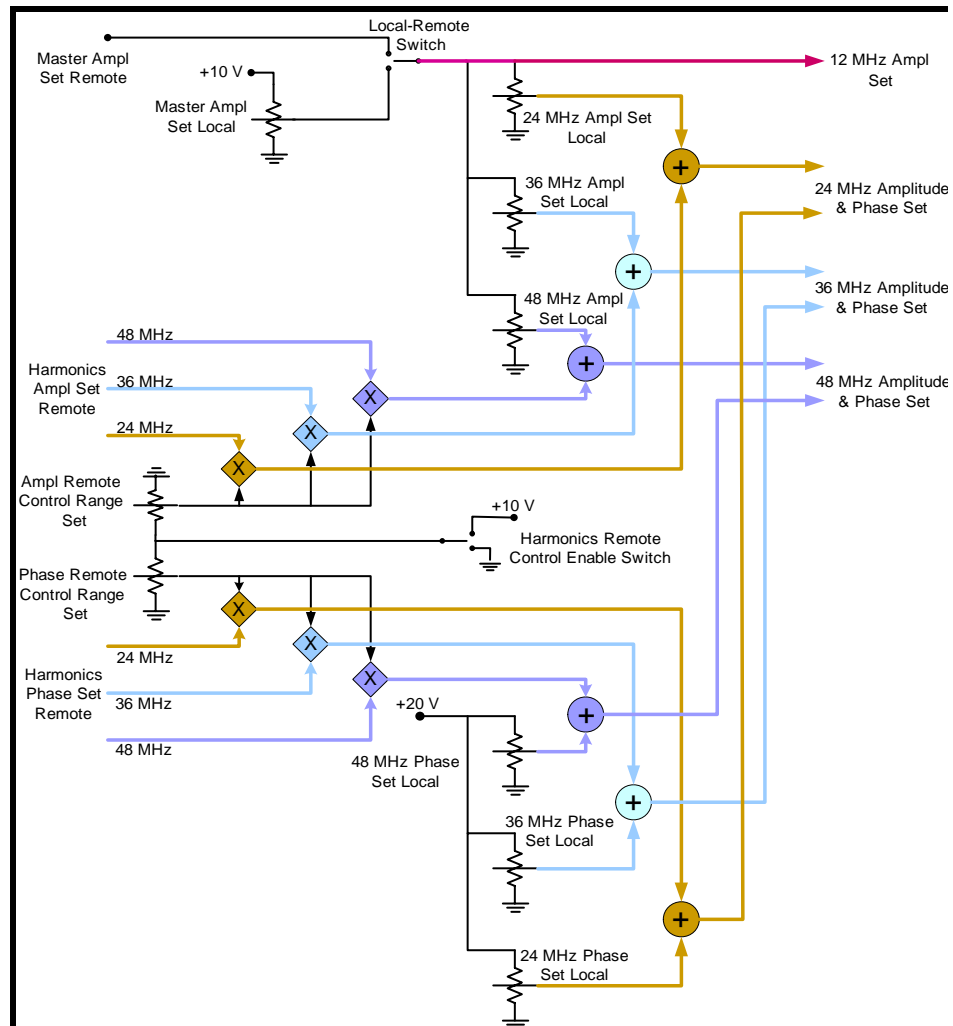


Fig. II-11. Local and Remote harmonics control diagram.

It means that the relationships between each harmonic phase and amplitude required to achieve an optimal saw-tooth waveform in four-harmonic representation (see Fig. II-14), is set locally by using the chassis front panel trim potentiometers. It is assumed that for the future routine buncher operation, normally there is no need to change these relationships.

But, if in some cases the necessity to control each

harmonic amplitude and phase remotely would arise, it can be done by means of the Harmonic Remote Enable Switch (see control diagram in Fig. II-11). The range (or relative value) of the remote phase and amplitude control can be locally set with the trim potentiometers inside the chassis. It is done by multiplying each frequency remote control voltage to a constant voltage, the value of which can be set by the trim potentiometer, separately for the harmonic's amplitude and phase.



Fig. II-12. Front and rear panel of the harmonic buncher RF control chassis.



Fig. II-13. Detailed view of the individual harmonic and master amplitude controls.

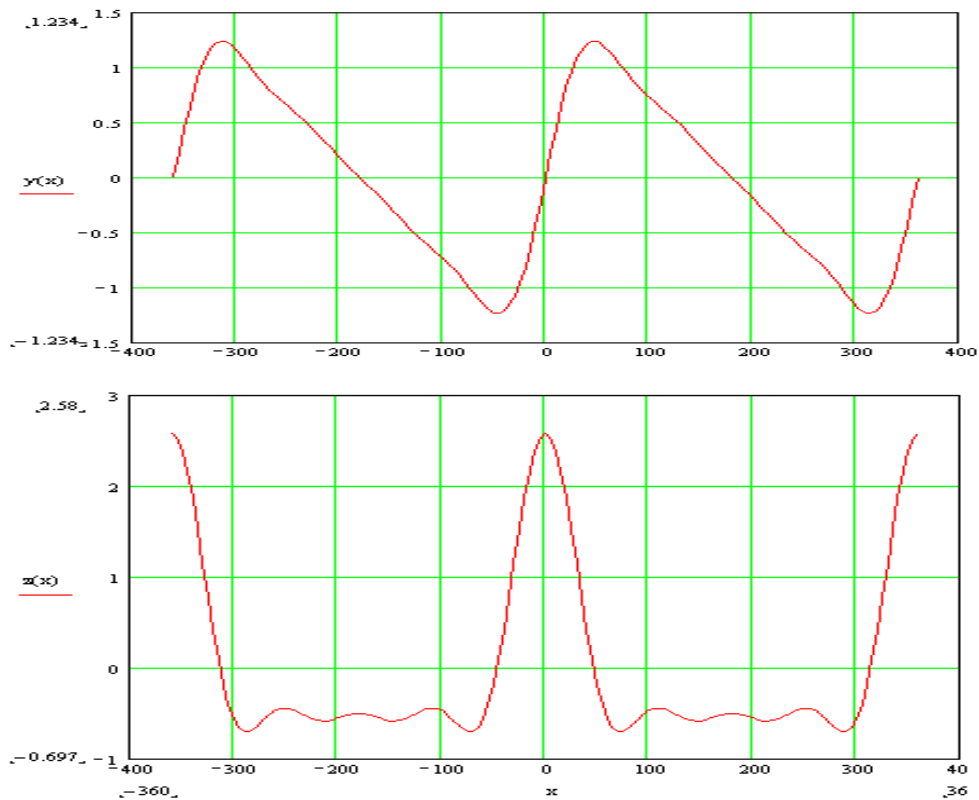


Fig. II-14. $Y(x)$ is a four-harmonic saw-tooth waveform representation, $z(x)$ is a waveform of the buncher pickup signal – the first derivative of the waveform.

b.5. ATLAS Control System (F. H. Munson, M. Power, D. Quock, and R. Carrier)

The ATLAS control system comprises three database management systems. Two of these systems are of a relational database design, and are used more for process initialization and data archiving. The third database is a real-time database providing a user interface for controlling accelerator associated devices, and providing moment to moment device monitoring. This real-time database system is a commercial product called Vsystem. When Vsystem was first installed as part of the control system it was only available for use on the OpenVMS operating system. More recently, this product has been made available on MS Windows, Linux, Unix, and other operating systems. It has been decided to reduce the control system's reliance on the OpenVMS operating system. Therefore, having already acquired the necessary licenses to run Vsystem on Linux, most recently licenses have been acquired to run Vsystem

on MS Windows. Vsystem now runs on OpenVMS, Linux, and MS Windows platforms at ATLAS.

There has been a growing interest at ATLAS in another commercial product called LabVIEW. This product provides non-software engineers tools to develop control and data acquisition systems. Two licenses and the distribution media for this product were acquired, and the software was successfully installed on two control-system-associated PCs for initial development.

Using the software described previously, prototype software was developed that provides an interface between LabVIEW applications and the ATLAS main control system running Vsystem. This was accomplished by developing a LabVIEW application on a PC running MS Windows that also had Vsystem software installed. The LabVIEW application was able to control and monitor CAMAC (Computer Automated Measurement

And Control) connected devices that are part of the main control system via a Vsystem network connection. Two visiting researchers used this prototype software to further demonstrate the LabVIEW – Vsystem connection by successfully developing two software applications that were related to ion source projects.

The two network domains maintained by the ATLAS control system group consist of two PDCs (Primary Domain Controllers) and two BDCs (Backup Domain Controllers). The operating system software for these systems has been upgraded from MS Win 2000 Server to the latest version of this operating system, MS Win Server 2003.

Other projects include a new software application that runs continuously, and for trending purposes, logs TOF (Time Of Flight) energy measurement data. This application is capable of storing trend type data

files where the file name consists of the ion source and injector being used, the atomic number and mass, and the date the file was created, thereby associating a trend file with an experiment. If any of the previously named parameters are changed, a new experiment is assumed, the current file is closed, and a new file is opened. After selecting the archived trend file, the user can view the plotted data "online" using a Vsystem utility, or export the data to a non-Vsystem utility such as MS Excel.

Another new software application that has been added provides the operator with the ability to log "online" a history of Tandem terminal foil usage. Options provided by this new application allow the operator to "time stamp" the installation date of all of the foils, and log the time when a foil is placed into service (inserted into the beam path). Additional information that is logged when a foil is time stamped is the atomic number of the beam in use and the number of hours used.

b.6. ATLAS Cryogenic System (S. W. MacDonald and R. C. Jenkins)

b.6.1. Valve Automation Project

The current means of adjusting the manual cryogenic valves located in the various ATLAS radiation areas requires the experiment to be stopped. Automation of these valves would be desirable; however the traditional means would require a redesign of the valves along with a lengthy cryogenic system shutdown. To avoid these complications, a retrofit actuator and single controller were designed, built and successfully tested on the helium supply valve to PII. A 6 valve controller was subsequently designed and built and enough parts were procured to automate 6 strategic valves in the Booster and ATLAS areas (see Fig. II-15).

With the exception of the resonator thermometry, the cryogenic display system was successfully separated

from the CAMAC serial highway. This separation will provide the ability to monitor critical cryogenic parameters during the accelerator control system software maintenance and emergencies.

The cryogenic alarm system was chosen to be upgraded as a starting point for the eventual automation of critical cryogenic processes. LabVIEW real time was chosen for its ease of programming, expandability, and ability to interface with a broad range of devices. A system architecture was designed and enough hardware was acquired to double the number of alarms and allow for a redesign of the current dewar level control system. This system will also enable the remote operation of the new alarm system along with future cryogenic control processes.



Fig. II-15. A cryogenic valve control chassis to be used to control six helium distribution valves in the ATLAS and Booster accelerating sections.

III. R & D RELATED TO A FUTURE RARE ISOTOPE ACCELERATOR FACILITY

OVERVIEW

The Rare Isotope Accelerator (RIA), a next-generation facility for basic research in nuclear physics, continues to be a high priority for construction in the United States by the Department of Energy Office of Science. In late 2003 RIA was ranked a very high priority in the Office of Science 20-year plan. The CD-0 milestone for RIA was passed early in 2004. To prepare for RIA design and construction it is essential to continue a vigorous R&D program for RIA.

This section is a progress report on the RIA R&D efforts at Argonne during 2004. The RIA R&D topics addressed at Argonne during the year 2004 are covered in three main sub-sections of this chapter: (A) Superconducting RF, (B) Beam Dynamics and Injectors, and (C) Rare Isotope Production and Separation. We continued to develop and improve the baseline design for the RIA proposal.

Highlights of developments during 2004 include:

- Completion of the design and significant progress on the construction of a prototype RIA drift-tube cryomodule that will also be used for the ATLAS Energy Upgrade Accelerator Improvement Project.
- Successful operation of a fully dressed prototype triple-spoke beta = 0.5 superconducting drift-tube resonator.
- Continued development of the beam dynamics for an alternative RIA Driver Linac option based on a 345-MHz triple-spoke resonator including studies to quantify the effects of misalignment and RF setting errors, and the development of algorithms for optimization of the longitudinal tuning of multiple-charge-state beams.
- Application of a failure modes and effects analysis (FMEA) to the RIA driver linac design.
- Update of the design of the low q/m injector of the RIA RIB Post Accelerator.

- Significant progress towards to the construction of a full power prototype module of the RIA Driver RFQ.
 - Preliminary development and design of a prototype system to demonstrate a thin film liquid lithium stripper for the RIA driver linac.
 - Characterization of a full-scale RIA prototype fast gas catcher at the RIA beam energies at the GSI Fragment Separator.
- 

A. SUPERCONDUCTING RF

a.1. Spoke Cavity Development for RIA (Z. Conway, J. Fuerst, M. Kedzie, M. Kelly, and K. W. Shepard)

A prototype 345 MHz, $\beta = 0.5$ triple-spoke cavity has been completed, the niobium cavity shell being enclosed in an integral stainless-steel helium jacket. The prototype has been tested at 4.2 K and 2 K, and could be operated cw at accelerating gradients exceeding 10 MV/m, as is detailed in Fig. III-1. With

an active length of 65 cm, at the gradients achieved, the cavity produces more than 6 MV of accelerating potential. The prototype shows good mechanical properties. The Lorenz de-tuning was measured to be 7 Hz per $(\text{MV/m})^2$ and microphonics were measured while operating at 9.5 MV/m at 4.2 K to be less than 2 Hz RMS.

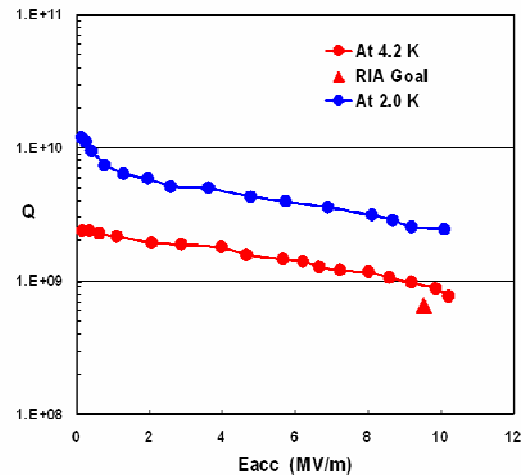
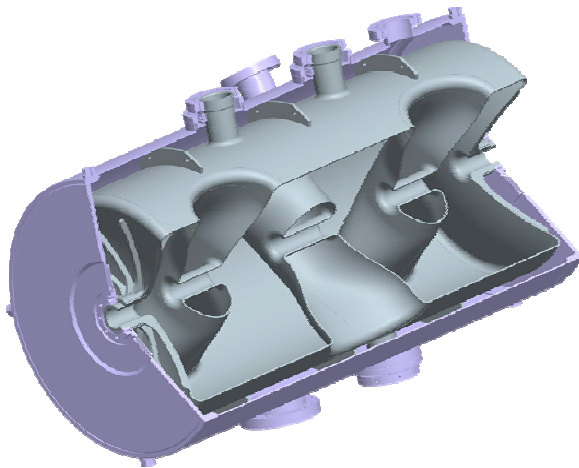


Fig. III-1. **Left:** cut-away view of the prototype 345 MHz, $\beta = 0.5$ triple-spoke cavity showing the niobium shell contained within the integral stainless-steel helium jacket. **Right:** Cavity Q at 4.2 K and 2 K. The cavity operated cw at accelerating gradients of more than 10 MV/m.

A prototype 345 MHz, $\beta = 0.62$ triple-spoke cavity has been completed, and the cavity is being readied for cold tests. Figure III-2 shows the 82 cm long

niobium shell just prior to attachment of the end-faces by electron beam welding



Fig. III-2. Niobium elements of the prototype $\beta = 0.64$ triple-spoke cavity after electropolishing and before the final closure welds.

a.2. Superconducting Cavity Surface Processing Facilities (M. Kedzie, M. Kelly, and K. Shepard)

The Physics Division is coordinating construction of a surface processing facility for superconducting cavities at Argonne in a collaborative project with

Fermi National Accelerator Laboratory. Two chemical processing rooms and a 2500 CFM air-scrubber have been completed, as shown in Fig. III-3.



Fig. III-3. Chemical-processing rooms and a 2500 CFM air-scrubber, installed as part of a surface processing facility for superconducting cavities.

Installation of a class-100 clean area is underway, and is expected to be completed in 2005. The multi-partitioned clean area will have a latticed floor with an underlying drainage system which will facilitate a variety of configurations for ultra-pure, high-pressure water rinse-cleaning of superconducting components.

The completed facility will enable development of superconducting cavities and surface processing techniques for a variety of applications such as RIA, the 8 GeV proton driver, ILC, fourth-generation light-source, etc.

a.3. Tuners and Couplers for the RIA Cavities (Z. Conway, J. Fuerst, M. Kedzie, M. Kelly, and K. W. Shepard)

We are developing tuners and couplers to control the amplitude and phase of RF fields in the superconducting cavities to the level of precision

required for RIA. Figure III-4 shows a photograph of a prototype tuner installed on a spoke-cavity assembly and a microphonics response curve for the system.

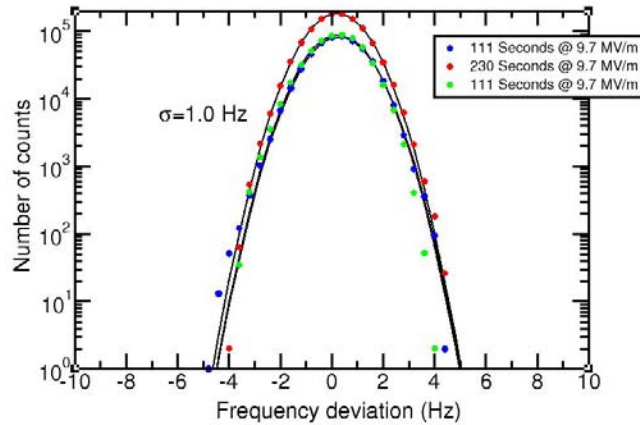
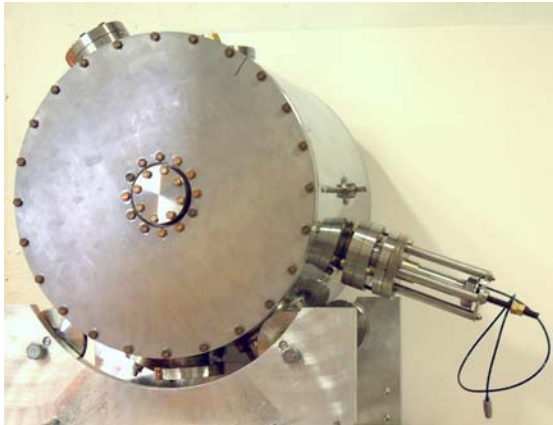


Fig. III-4. A prototype piezo-electric fast tuner that can rapidly tune the rf frequency of the spoke-loaded cavity to which it is attached by 800 Hz. This tuning bandwidth is much more than needed to control the observed microphonic detuning, which is typically 1 Hz.

a.4. Cavities and Prototype Cryomodule for RIA and the ATLAS Upgrade (Z. Conway, J. Fuerst, M. Kedzie, M. Kelly, and K. W. Shepard)

Six 109 MHz QWR cavities are being constructed to complete the eight-resonator string for a cryomodule which will add more than 16 MV of accelerating

potential to the ATLAS heavy-ion linac. Figure III-5 shows the prototype QWR cavity being assembled with the required ancillary tuning and rf coupler systems.

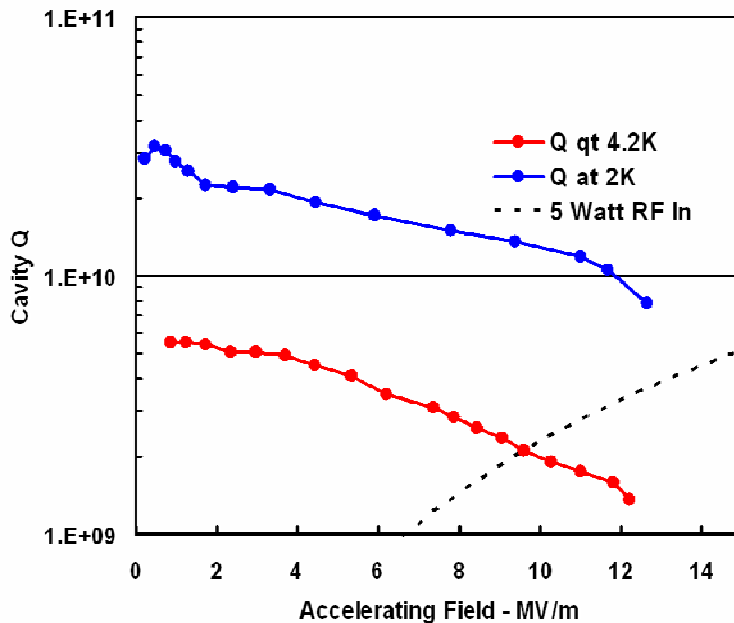


Fig. III-5. Prototype 109 MHz quarter-wave cavity for the ATLAS upgrade and for the RIA driver linac. The cavity is shown with the RF power coupler and slow-tuner yoke assembled for cold-testing. In initial cold-tests the prototype cavity could provide as much as 3 MV of accelerating potential in cw operation at 4.2 K.

Nearly all elements of the cryostat have been fabricated and are in the assembly process.

Cryomodule assembly will include clean-assembly of the cavity string.

B. BEAM DYNAMICS AND INJECTORS

b.1. Design and Construction of a One-Segment Prototype of the RIA Driver RFQ

(P. N. Ostroumov, A. Barcikowski, F. DePaola, B. Rusthoven, S. Sharma, V. E. Vinogradov, D. Schrage,* and J. Rathke†)

We continue development of fabrication techniques for the 57.5 MHz driver linac RFQ. Successful tests of the RFQ prototype over a wide range of power levels (by a factor of 70) will demonstrate the feasibility of acceleration of masses from protons up to uranium in a single RFQ. The ANL infrastructure is being used for the preliminary machining, first-stage brazing, mechanical, vacuum and rf tests of the RFQ prototype. The work in 2004 has been concentrated on the fabrication of the resonator parts and preparation to the final machining, assembly and brazing. A full set of construction drawings has been completed. Significant contributions have been made by LANL and AES engineers to provide state-of-the-art fabrication technology for the OFE copper resonator.

Figure III-6 shows a general view of the RFQ when completed. The right picture of Fig. III-6 presents an exploded view of major RFQ resonator parts that will be brazed together in a large high-temperature furnace in a hydrogen atmosphere using Cusil alloy

(^{72}Ag - ^{28}Cu). To verify the correct engineering choice of the brazing seams and alloy we have performed a braze test for OFE copper pieces. The tests have confirmed the particular design of grooves for the alloy and overall brazing procedure. The brazed seams have been tested for vacuum and structural stability and have shown the expected performance. After the purchase of OFE copper for the vanes, quadrants and flanges, the material samples were sent for chemical analysis in terms of oxygen content. In some samples the oxygen content exceeded standard limitations and we have done ‘blister’ test of the material samples at ANL central shops. These tests have shown that the purchased OFE copper material is suitable to proceed with the high-temperature brazing. The OFE copper has been used for machining of all quadrants, vanes, flanges and end caps of the resonator. After preliminary machining of quadrants and vanes the water plugs and stainless steel insertions have been brazed. Figure III-7 shows a quadrant and a vane after the first-step brazing at ANL CMS. All manufacturing steps are completed except final machining and the following assembly of the resonator.

*Los Alamos National Laboratory, †Advanced Energy Systems.

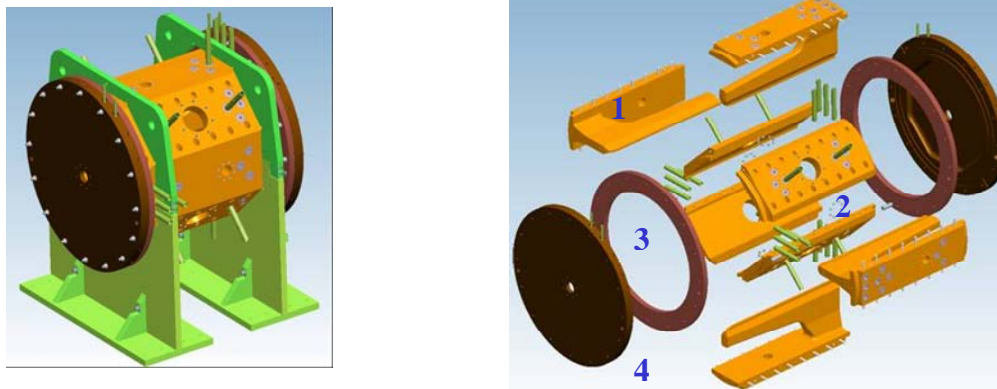


Fig. III-6. Engineering 3-D model of the one-segment RFQ assembly (on the left) and exploded view (on the right).
1) vanes; 2) quadrant plates; 3) main flanges; 4) end caps.

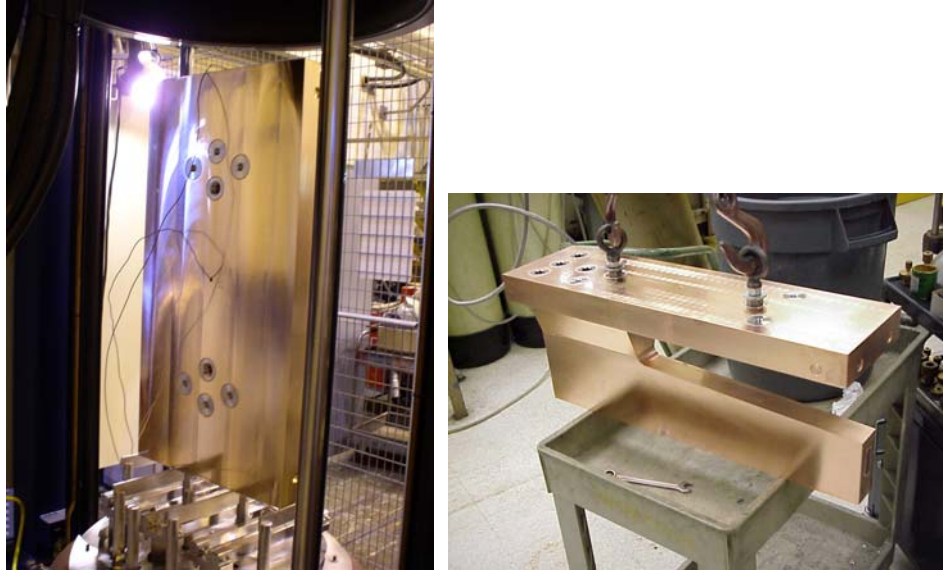


Fig. III-7. Quadrant (on the left) and vane (on the right) after first-step brazing.

b.2. Alternating-Phase Focusing in a Low-Velocity Heavy-Ion Superconducting Linac (P. N. Ostroumov, K. W. Shepard, A. A. Kolomiets,* and E. S. Masunov†)

The low-charge-state radioactive ion beam (RIB) accelerator requires strong transverse focusing, particularly at low velocities. For the charge-to-mass ratios considered here ($q/A > 1/66$) the proper focusing can be reached by using strong SC solenoid lenses with a field of up to ~ 15 T. Both the number of the solenoids and field can be reduced applying Alternating Phase Focusing (APF). A method to set the rf field phases has been developed and studied both analytically and with the help of the three-dimensional ray tracing code TRACK.^{1,2} As a reference design of the RIB linac we consider the focusing by high-field SC solenoids alternating with SC resonators. For the acceleration of heavy ions with $q/A = 1/66$ from 75 keV/u to 1.0 MeV/u with effective phase angle -20° , the RIB linac requires a

total of 63 resonators of four different types. The constant average beam radius along the linac can be provided with average focusing field 14.7 T. The cavities and solenoids will be distributed in seven cryostats with ~ 7 m length each. There is a drift space between the cryostats which is ~ 50 cm. Appropriate beam matching in both transverse and longitudinal phase space can be provided without any additional accelerating or focusing elements. However, careful tuning of the solenoids and resonator phases at each cryostat interface is required.

Beam dynamics simulations in the reference design of the RIB linac performed with the code TRACK have shown that there is minor emittance growth along the structure as is seen in Fig. III-8.

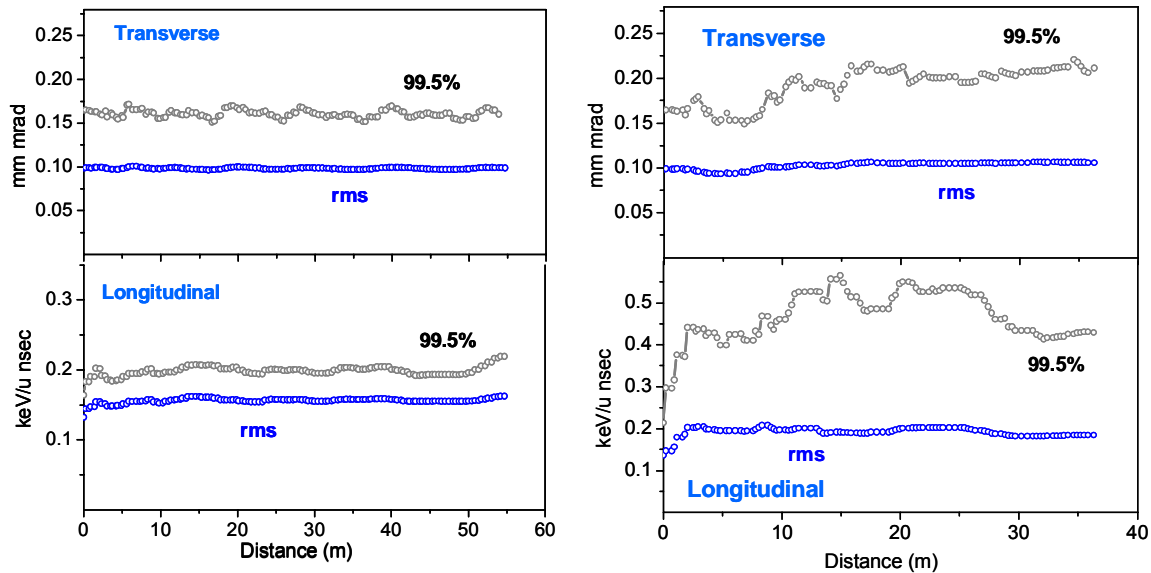


Figure III-8. Emittance evolution along the baseline (on the left) and CFS (on the right) designs of the RIB linac simulated by the TRACK code.

The reference design completely meets the specifications for the RIB linac. However, it is achieved with a significant number of solenoids and the linac is long. As a result the accelerating gradient real-estate is $\sim 30\%$ of the gradient provided by the SC cavities. Also, very high-field SC solenoids are required due to the high value of the defocusing factor in the SC resonators. The strong defocusing can be converted to focusing by applying an alternating phase focusing (APF). As a result, the accelerating gradient real-estate can be increased. To create the APF, the effective ‘synchronous’ phase angle φ_e must be alternated between positive and negative values. The analytical estimate has shown,¹ that the simultaneous stability of the transverse and longitudinal motion can be achieved despite significant phase slippage of up to 100° in an individual cavity. However to create a sufficient stability area, large values of the effective phase angles $|\varphi_e|$ in the cavities are required. The area of stability can be extended even for lower values of $|\varphi_e|$ by adding a solenoid into the focusing period that will also allow separate control of transverse and longitudinal beam dynamics. The combined focusing

structure (CFS) includes both SC solenoid and APF in every focusing period. We have designed an accelerator section from 75 keV/u to 1.0 MeV/u using CFS concept. Figure III-8 shows an evolution of transverse and longitudinal emittances in the CFS. As in the reference design there is no transverse emittance growth while the longitudinal rms emittance growth is 35% and emittance containing 99.5% of particles increases even more. The longitudinal emittance growth is a consequence of the electric field dependence from the radial coordinate in the low-velocity accelerating structures. This effect takes place in the first several resonators and can be minimized by lowering accelerating gradients or re-arranging the focusing period. Some additional studies are required to minimize the longitudinal emittance growth in the CFS. The CFS allows reduction of the number of solenoids more than 50% and reduces the real-estate length of the linac. In addition the required solenoid fields are lower. A significant saving in the total cost of the accelerator is expected. The disadvantage of the CFS is in strong coupling of the transverse and longitudinal degrees of ion motion and higher growth in longitudinal emittance. The combined focusing structure can be effectively used in many other applications of heavy ion accelerators.

*On leave from Institute of Theoretical and Experimental Physics, Moscow, Russia, †Moscow Physical Engineering Institute, Moscow, Russia.

¹E. S. Masunov, D. A. Efimov, and P. N. Ostroumov, RF Focusing of Low-Charge-to-Mass-Ratio Heavy-Ions in a Superconducting Linac, Proc. of the EPAC-2004, Lucerne, Switzerland, p. 1405.

²P. N. Ostroumov, K. W. Shepard, A. A. Kolomiets, and E. S. Masunov. Alternating Phase Focusing in Low-Velocity Heavy-Ion Superconducting Linac, Proc. of the LINAC-2004, Lubeck, Germany, p. 374.

b.3. Design Update of the Injector Section of the RIA Post-Accelerator (P. N. Ostroumov, A. A. Kolomiets, and V. N. Aseev)

The original design of the injector section of the post-accelerator included a 380 kV open-air variable-voltage platform that consist of a multi-harmonic buncher, first two sections of 12 MHz RFQ, and both helium gas stripper cells. Our objective of the front end design modifications was to reduce the potential of the HV deck significantly while keeping capabilities to form high quality beams. Main features of the updated design of the RIB injector are:

- Beam energy of ions entering RFQ is significantly reduced down to 0.4 keV/u which allows us to lower the bias potential of the HV deck;
- Ion source voltage can be reduced down to 60 kV;
- Use an external buncher and additional bunching inside the RFQ;
- Use a separate beamline for acceleration of ions with mass numbers below 66. The beamline #2 may be necessary if the main beamline #1 is not stable at very low rf power level tuned for acceleration of light ions.

The simplified layout of the RIB injector section without focusing elements is shown in Fig. III-9. Ions with charge-to-mass ratio in the range $1/240 \leq q/A \leq 1/66$ are accelerated in line #1 that consists of conventional RFQ and Hybrid RFQ (HRFQ). Both structures are operated at 12.125 MHz. Energies of the beam exiting RFQ (7.4 keV/u) and HRFQ (24.4 keV/u) have been chosen to optimize efficiency of the gas stripping.

To adjust energies of different ions extracted from ion source at constant voltage 60 keV, the RFQ is placed on open-air HV deck, potential of which should be adjusted within $-26 \text{ kV} \leq U \leq 44 \text{ kV}$ to obtain the required velocity for different ions.

The accelerating structures on beamline #1 require very low rf power for acceleration of light ions that can be unstable due to multipacting, for example. Beamline #2 can be constructed specifically for the acceleration of light ions. The RFQ on beamline #2 operates at 24.25 MHz and requires an injection energy of 1.6 keV/u. The latter requires a voltage adjustment of the HV deck in the range $-46 \text{ kV} \leq U \leq 52 \text{ kV}$. Note, the bunching frequency is 12.125 MHz which is the fundamental frequency in the post-accelerator. Due to the fact that RFQ focusing is scaled as

$$\frac{A}{q} \lambda^2,$$

where λ is the rf wavelength, the RFQs on both beamlines can be designed with the same average radius R_0 and inter-electrode voltage. Beams from both lines enter the second HRFQ operating at 24.25 MHz and are accelerated up to 92.7 keV/u which is sufficient to inject into the SC linac.

The longitudinal emittance of heavy-ion beam is formed using a two-stage bunching process. The TRACK simulations have been performed using full 3D fields. The results obtained for $2 \cdot 10^5$ simulated particles with charge-to-mass ratio $q/A = 240$ in beamline #1 are shown in Fig. III-10. Longitudinal emittance evolution along the front-end structures is shown in Fig. III-11. Table III-1 lists emittance values along the elements of the RIB injector.

¹P. N. Ostroumov, M. P. Kelly, A. A. Kolomiets, J. A. Nolen, M. Portillo, and K. W. Shepard, A Post Accelerator for the U.S. Rare Isotope Accelerator Facility, Nucl. Instrum. Methods **B204**, 433 (2003).

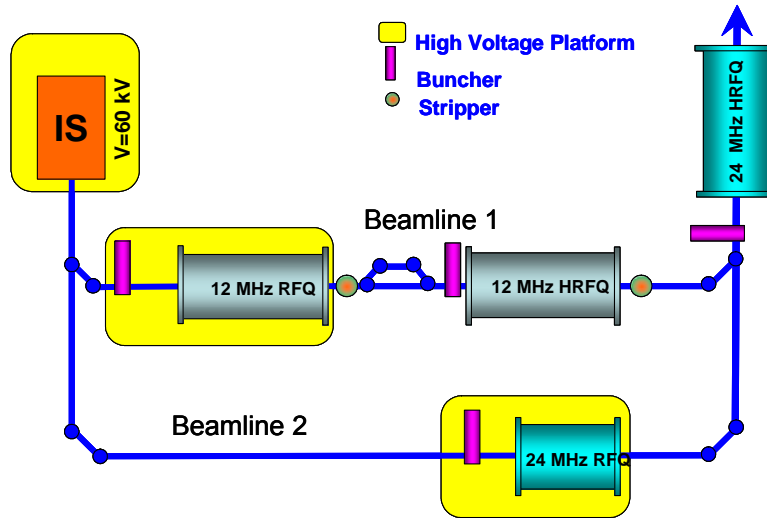


Fig. III-9. Schematic layout of upgraded front end of the RIA post-accelerator.

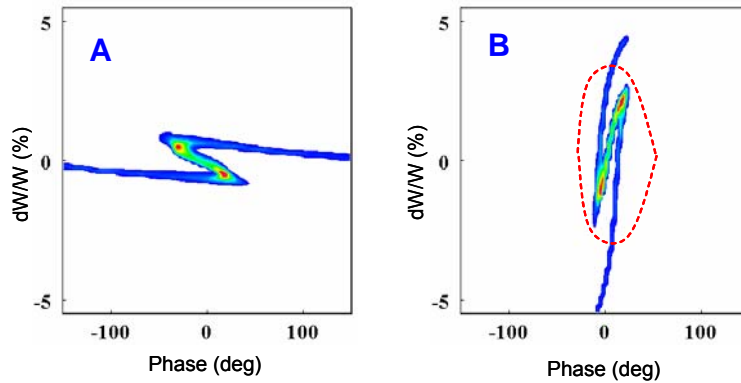


Fig. III-10. Beam longitudinal phase space plots after the external buncher (A) and RFQ internal buncher (B). The red dashed line represents the RFQ separatrix.

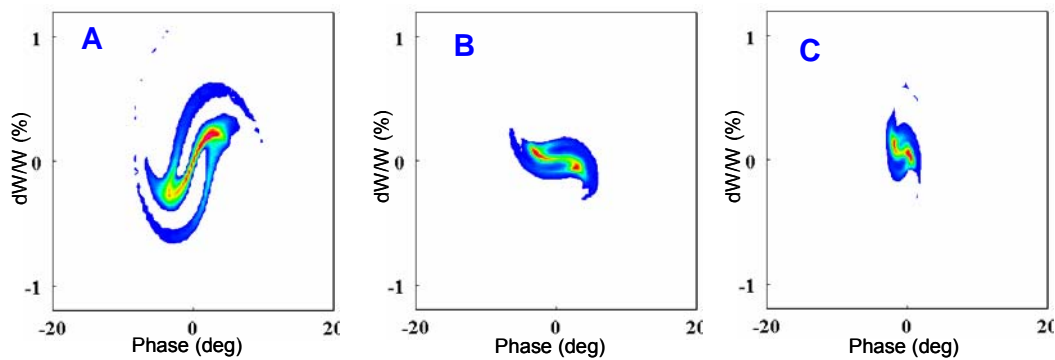


Fig. III-11. Beam longitudinal phase space plots after the RFQ (A), Hybrid RFQ (B) and second Hybrid RFQ (C).

Table III-1. Beam parameters along the injector elements of beamline #1.

	RFQ	HRFQ 1	HRFQ 2
Beam energy (keV/u)	7.4	24.4	92.7
Long. emittance (4 rms, keV/u-nsec)	0.057	0.059	0.065
Long. emittance (95%, keV/u-nsec)	0.082	0.098	0.103
Trans. emittance (4 rms, π mm-mrad)	0.035	0.036	0.039
Trans. emittance (95%, π mm-mrad)	0.041	0.043	0.051

b.4. Progress with the 2Q-LEBT Prototype (N. E. Vinogradov, P. N. Ostroumov, R. Pardo, and R. Scott)

A prototype injector of the RIA Driver Linac is being developed at the high bay area of the Physics Division Dynamitron. On the final stage of the project, the prototype called 2Q-LEBT will include an ECR ion source installed on 100 kV high voltage platform, an achromatic bending system consisting of two 60° bending magnets, a gridless multi-harmonic buncher and 57.5 MHz RFQ segment. At the present moment, the 2Q-LEBT facility consists of BIE-100 ECR ion source, 60° bending magnet and beam diagnostic system. A number of modifications were implemented to increase beam production performance of the original source. A new Einzel lens, a puller, a high voltage insulator between source body and main beamline have been fabricated. Additionally, we have redesigned the injection assembly and heating oven, and equipped the facility with a new interlock system. A dipole magnet has been installed in the beamline downstream of the Einzel lens for vertical steering of the beam. In some cases, adjustment of the beam position in vertical direction allows us to increase output current up to

30%. For careful studies of the output beam the emittance measurement station based on a combination of slit and scanning wire have been designed and built. A fully automatic LabVIEW control system provides user with an on-line data treatment. At present, comprehensive measurements of various beams are being carried out. Figure III-12 represents an example of Argon beam spectrum measured at relatively low level of the rf power. Three typical patterns of measured beam emittances are shown in Fig. III-13. In the concept of simultaneous acceleration of two charge states developed for the RIA, it is assumed that the ECR source forms a beam with similar phase space distributions of the neighboring charge states. Typical values of different charge state intensities along with corresponding normalized emittances and Twiss parameters are listed in Table III-2. As is seen in the table, Twiss parameters of different charge states generated by BIE-100 are very close to each other. Installation of the HV platform and related equipment including isolation transformer is planned to complete in 2005.

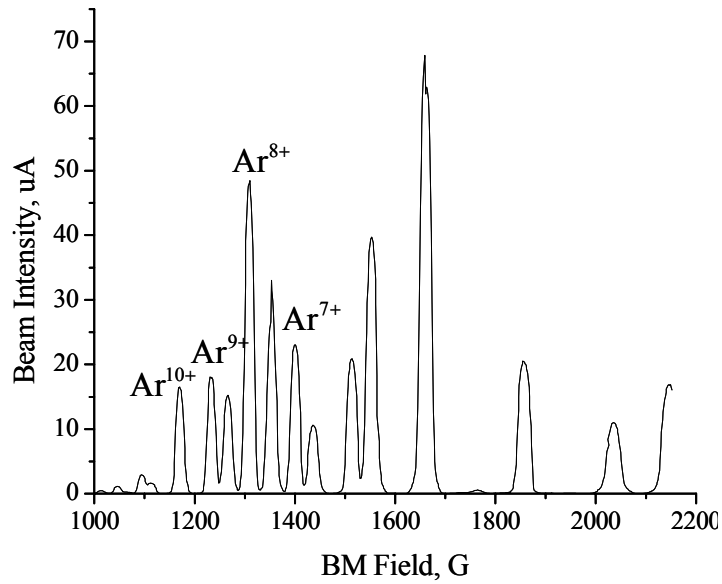


Fig. III-12. Argon charge state distribution at 250 W rf power and 20 kV source bias.

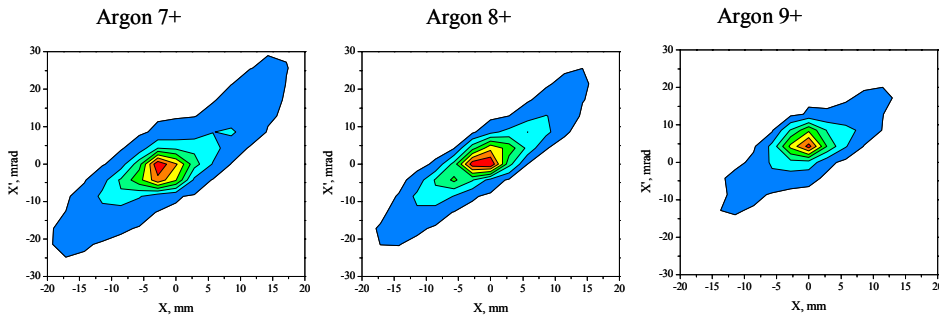


Fig. III-13. Typical emittance patterns for Argon beam.

Table III-2. Beam intensities, normalized emittances and Twiss parameters for sample Argon and Xenon beams.

Charge State	Intensity, μA	Normalized RMS emittance, $\pi \cdot \text{mm} \cdot \text{mrad}$	α	β , mm/mrad
Ar^{7+}	22	0.07	-2.08	1.23
Ar^{8+}	49	0.07	-1.9	1.28
Ar^{9+}	19	0.05	-2.3	1.18
Xe^{13+}	20	0.10	-1.1	0.83
Xe^{14+}	17	0.10	-1.3	0.97
Xe^{15+}	14	0.11	-1.34	0.91

b.5. Modifications and rf Tests of the 12 MHz RFQ for Acceleration of a $^{240}\text{U}^{1+}$ Beam
(P. N. Ostroumov, A. A. Kolomiets, and N. E. Vinogradov)

A proper choice of the peak surface field E_p is extremely important for reliable cw operation of accelerating structures. In the case of RFQ, E_p is

defined by breakdown voltage between adjacent electrodes which depends on vane tip width, average aperture and electrodes modulation. The available

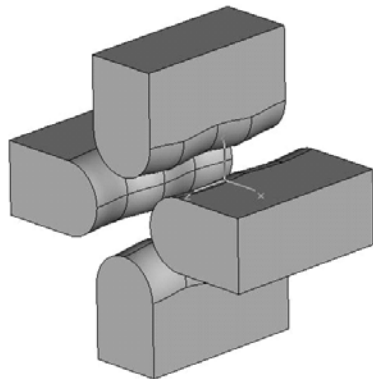
experimental data can not be directly extended to any type of RFQ structure due to strong dependence of the breakdown limit on operating frequency, shape and material of electrodes, manufacture and assembly procedures, conditioning and other features of the specific design. A full power prototype of the 12 MHz split-coaxial RFQ structure for the RIA post-accelerator has been designed and tested for acceleration of Xe^{1+} beam.¹ It has demonstrated a high performance enabling one to achieve ~ 130 MV/m peak surface field at 90 kV inter-vane voltage and mean bore radius of 10 mm. At the same time, a resonator detuning and reduction of the quality factor have been observed at ~ 90 kV due to over-heating of vane tips which are not directly water cooled.¹ We propose to modify the split-coaxial electrodes for acceleration of $^{240}\text{U}^{1+}$ beam and include appropriate water cooling of vanes. The design value of the peak surface field for the new RFQ vanes is based on operational experience of the 12 MHz RFQ

prototype¹ and ISAC 35 MHz RFQ.² The computer simulations by the code CST EM Studio have been performed to define E_p for the existing and proposed geometries of modulated vanes (see Fig. III-14). The simulation results are consistent with the reported experimental data within less than 10%. According to this model, the 12 MHz RFQ for acceleration of a $^{240}\text{U}^{1+}$ beam can be designed with 6.8 mm average aperture radius and 2.6 mm vane tips curvature radius. The required inter-vane voltage is 68 kV and corresponds to $E_p = 135$ kV/cm, which is slightly lower than in the ISAC RFQ. To verify the breakdown voltage we propose to carry out high power rf test using the existing 12 MHz RFQ tank. The RFQ tank is being prepared for this test. Currently, we are modifying the vacuum system of the tank to use one turbo pump in combination with oil-free scroll backing pump and one or two 500 l/s Perkin Elmer ions pumps for continuous operation. A special fixture table equipped with alignment mechanism is being designed and fabricated to replace the vanes of the RFQ.

¹M. P. Kelly *et al.*, Proc. of the 2001 PAC Accel. Conf., Chicago, p. 506, 2001.

²R. L. Poirier *et al.*, Proc. of the 2000 Linac Conf., Monterey, CA, p. 1023.

CST Model of an RFQ Electrodes



Electric Field Distribution

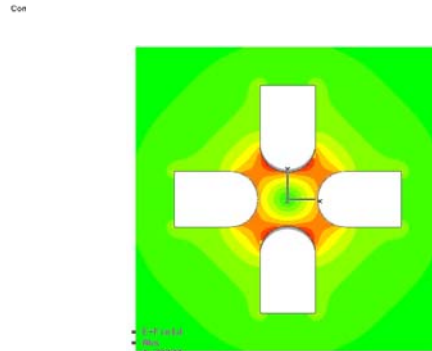


Fig. III-14. Modulated RFQ vanes in the CST EM Studio model.

b.6. Error Simulations and Beam Loss Studies in the RIA Driver Linac (B. Mustapha, P. N. Ostroumov, and V. A. Aseev)

The RIA Facility includes a high-intensity 1.4 GeV driver linac. To avoid problems from beam-induced radio-activation, beam losses must be limited to low values, particularly in the high-energy section of the linac, where the fractional beam loss must be less than 10^{-4} . Beam dynamics studies including all sources of error are necessary in order to identify the possible sources of beam halo formation that could lead to excessive beam losses. The study of beam

losses to the level of 10^{-4} - 10^{-5} requires the simulation of large number of particles which calls for the use of parallel computing. The code TRACK was then parallelized and simulations performed on the computer cluster JAZZ at Argonne. End-to-end (from the ECR ion source to the target) simulations including all possible sources of error were performed in order to study the effect of the different errors and identify the most critical ones. The simulations were performed for a multi-

component uranium beam: 2 charge states (28^+ , 29^+) in the injector and the low energy section, 5 charge states (74^+ , 75^+ , 76^+ , 77^+ , 78^+) after the first stripper and 5 charge states (87^+ , 88^+ , 89^+ , 90^+ , 91^+) after the second stripper. It was found¹ that the RF field errors (phase and amplitude) and the stripper thickness fluctuations are the most critical errors significantly affecting the longitudinal emittance of the beam and eventually producing beam losses.

In order to study eventual beam losses, high-statistics simulations were performed for 6 different combinations of most critical errors (see Table III-3) and for both the baseline and the Triple-spoke designs of the driver linac. The two designs differ mainly by the type of cavities used in the high-energy section of the linac. In the Triple-spoke design, the recently developed triple-spoke cavities replace the elliptical-cell cavities used in the original baseline design.

The results show that the baseline design is in general more sensitive to these errors and to the overall tuning of the linac. Beam losses were observed in the high-energy section for the baseline design whereas no losses for the Triple-spoke design even for the highest error amplitudes (see Table III-3). To quantify these losses, Fig. III-15 shows the losses in

Watts/m along the linac for each error combination and both designs. The horizontal red line is the 1 Watts/m limit required for hands-on maintenance of the linac. The first two peaks in all plots correspond to the losses at the two strippers. The losses at the strippers are controlled because they will be stopped in specifically designed collimators. The uncontrolled losses observed in the high-energy section of the baseline design are small for combinations 1&2, about 1 Watts/m for combinations 3&4 and about 10 Watts/m for combinations 5&6. No uncontrolled losses for the Triple-spoke design. It is clear that to keep uncontrolled losses below the 1 Watts/m limit for the baseline design, the RF field errors should not exceeds 0.5° for the phase and 0.5% for the amplitude and the stripper thickness fluctuation should be about 5%. However, the Triple-spoke design may tolerate higher errors. The preliminary conclusion of these studies is that due to its larger longitudinal acceptance the Triple-spoke design is more tolerant of errors without producing uncontrolled beam losses. The study also showed that the losses in the baseline design are extremely sensitive to the longitudinal tuning in the linac. A careful tuning in terms of phase setting to produce the lowest possible effective emittance at the location of the strippers, especially in the medium-energy section, was proven to reduce the losses in the subsequent high-energy section.

Table III-3: Uncontrolled beam losses for 6 combinations of most critical errors and for both the baseline and the Triple-spoke designs.

Combination	RF errors	Stripper Thickness fluctuation	Baseline design	Triple-spoke design
1	Field: 0.3%, Phase: 0.3 deg	5% FWHM	$3.0 \cdot 10^{-8}$	0.0
2	Field: 0.3%, Phase: 0.3 deg	10% FWHM	$8.2 \cdot 10^{-7}$	0.0
3	Field: 0.5%, Phase: 0.5 deg	5% FWHM	$5.5 \cdot 10^{-5}$	0.0
4	Field: 0.5%, Phase: 0.5 deg	10% FWHM	$2.7 \cdot 10^{-4}$	0.0
5	Field: 0.7%, Phase: 0.7 deg	5% FWHM	$1.4 \cdot 10^{-3}$	0.0
6	Field: 0.7%, Phase: 0.7 deg	10% FWHM	$2.6 \cdot 10^{-3}$	0.0

¹P. N. Ostroumov, V. N. Aseev, and B. Mustapha, Phys. Rev. ST. Accel. Beams **7**, 090101 (2004).

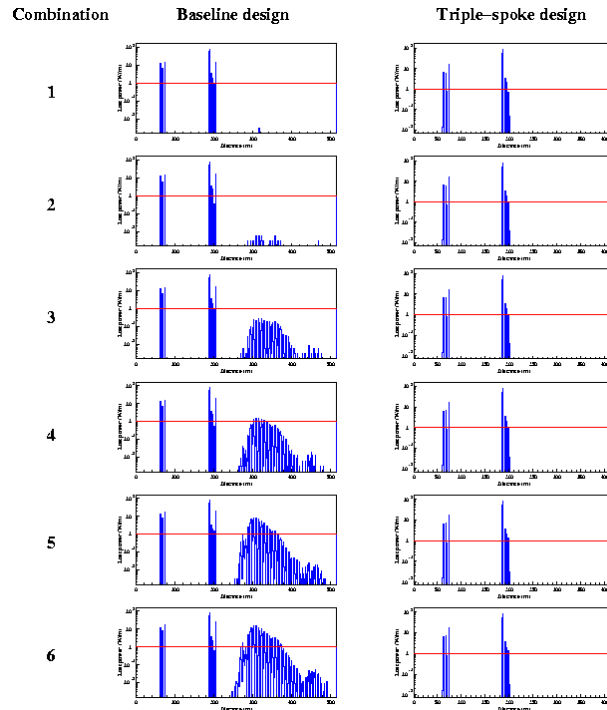


Fig. III-15. Beam losses in Watts/m along the linac for 6 combinations of most critical errors and both the baseline and the Triple-spoke designs. Explanations are given in the text.

b.7. Longitudinal Fine-Tuning of a Multiple-Charge-State Heavy-Ion Beam (B. Mustapha and P. N. Ostroumov)

In a recent study¹ we reported the results of large scale simulations for two design options of the RIA driver linac. The two design options are the original baseline design and the alternative triple-spoke design. They differ mainly by the type of cavities used in the high-energy section of the linac. In the triple-spoke design, the recently developed triple-spoke cavities replace the elliptical-cell cavities used in the baseline design. The simulations for both designs were performed for a multiple-charge-state uranium beam using the recently developed beam dynamics code TRACK. The simulations included all sources of error such as elements misalignment, rf field errors and stripper thickness fluctuations. A thorough beam loss analysis has been performed showing that the baseline design is less tolerant to rf field errors and to fluctuations in the stripper thickness. Beam losses were observed in the high-energy section of the baseline design while no losses were observed in the triple-spoke design even for the highest error amplitudes. The study also showed that the losses in the baseline design are extremely sensitive to the longitudinal tuning in the linac. A

careful tuning in terms of phase setting to produce the lowest possible effective emittance at the location of the strippers, especially in the medium-energy section, has proven to reduce the losses in the subsequent high-energy section. We here focus on the baseline design and attempt to develop tunes that significantly reduce beam losses.

For a fast and reliable way to longitudinally fine tune a multiple-charge-state heavy-ion beam we started developing an automatic procedure to replace the slow and often less than optimal manual procedure. But prior to implementing the automatic tuning procedure we investigated few simple and efficient ways of doing it manually. Among these methods, and of particular interest from beam dynamics standpoint, we tried to bring the reference phases of individual charge state beams to their corresponding synchronous phases. For this we considered a design option where a single cavity type (single frequency) is used in the medium-energy section of the RIA driver. Figure III-16(a) shows the evolution of beam phase and energy centroid

deviations of the individual charge states throughout the whole section. In this case and for simplicity, all cavity phases were set to -30° . We clearly notice that the reference phase and energy of the five charge states (74^+ , 75^+ , 76^+ , 77^+ , 78^+) oscillate around those of the reference charge state (76^+) corresponding to the horizontal lines. By setting the phases of two particular cavities at the beginning of the section to -90° , converting them into bunchers, we were able to suppress or significantly reduce the phase and energy

oscillations of individual charge state beams about those of the reference charge state, see Fig. III-16(b). We clearly see that the oscillations around the reference charge state are either absent or significantly reduced which usually results in more stable beam dynamics along the linac. However, to bring the centers of individual beams together at the end of the section we had to use 4 cavities and set them to -90° with 15% increase in their field levels.

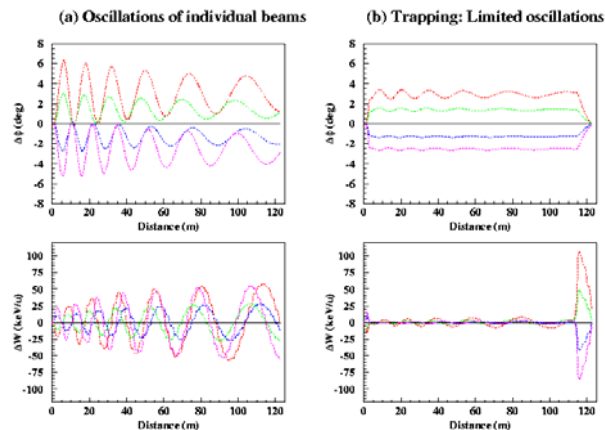


Fig. III-16. Beam phase and energy centroid deviations for the five charge states (dashed curves) with respect to the reference charge state (solid line) plotted as function of distance along the single frequency option of the medium-energy section of the RIA driver linac. (a) Case where all cavity phases are set to -30° showing the oscillations of individual charge state beams. (b) Case where few cavities are used to bring the reference phases of individual charge state beams to their corresponding synchronous phases in order to limit beam oscillations and produce more stable beam dynamics.

Bringing the reference phases of the individual charge state beams to their corresponding synchronous phases has the advantage of producing a much more stable beam dynamics by significantly reducing beam oscillations at the cost of few additional cavities. However, this method is more useful for a single frequency lattice and will be hard to apply in our case where two different cavity types

with different frequencies are used in the medium-energy section of the linac. It also does not necessarily match the Twiss parameters of the different charge state beams, which is required to produce a minimal overall beam emittance. For these reasons we are developing a fully automatic longitudinal beam tuning procedure for multiple-charge-state heavy-ion beams.

¹P. N. Ostroumov, V. N. Aseev, and B. Mustapha, Phys. Rev. ST. Accel. Beams **7**, 090101 (2004).

b.8. Front End Design of a Multi-GeV H-Minus Linac (P. N. Ostroumov, K. W. Shepard, G. W. Foster,* I. V. Gonin,* and G. V. Romanov*)

The proposed 8-GeV driver at FNAL is based on 422 independently phased SC resonators. Significant cost saving is expected by using an rf power fan out from high-power klystrons to multiple cavities. Successful development of superconducting (SC) multi-spoke resonators operating at ~ 345 - 350 MHz provides a strong basis for their application in the front end of

multi-GeV linear accelerators. Such a front-end operating at 325 MHz would enable direct transition to high-gradient 1300 MHz SC TESLA-style cavities at ~ 400 MeV. The proposed front end consists of 5 sections: a conventional RFQ, room-temperature (RT) triple-spoke resonators, single-, double- and triple-spoke super-conducting resonators. There is a large advantage

in using independently phased RT TSRs between the RFQ and SC sections in the energy range 3-15 MeV. These resonators (see Fig. III-17) operate on π -mode and provide extremely high shunt impedance which

changes from 160 M Ω /m to 80 M Ω /m for given energy range 3-15 MeV. The compact RT-TSRs will be alternated with SC focusing solenoids providing strong focusing.

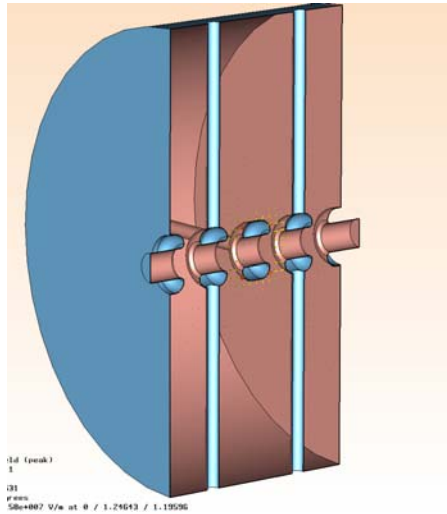


Fig. III-17. Cut-out view of the RT-TSR.

Beam dynamics studies show that the proposed front end can provide high quality beams and its tune does not depend from the current. Figure III-18 shows 30 mA beam rms and total envelopes in the front end

from 65 keV to 410 MeV. About 2 mA of the beam injected into the RFQ is not accelerated and lost primarily on the collimators in the Medium Energy Beam Transport (MEBT).

*Fermi National Accelerator Laboratory.

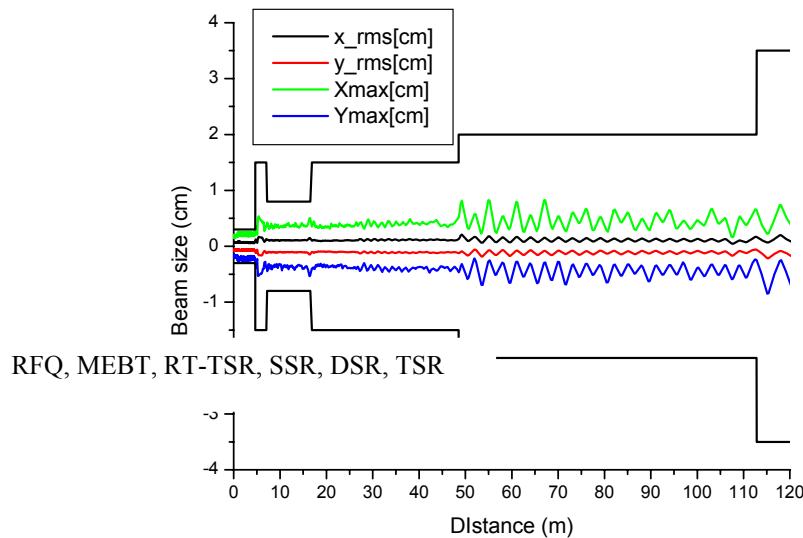


Fig. III-18. Beam envelopes of 30 mA H⁻ beam in the front end of the 8-GeV linac. The black solid line shows the aperture.

b.9. Reliability and Availability Studies in the RIA Driver Linac (E. S. Lessner and P. N. Ostroumov)

The Rare Isotope Accelerator (RIA) facility will include various complex systems and must provide radioactive beams to many users simultaneously. The availability of radioactive beams for most experiments at the fully-commissioned facility should be as high as possible within design cost limitations. To make a realistic estimate of the achievable reliability a detailed analysis is required. The RIA driver linac is a complex machine containing a large number of superconducting (SC) resonators and capable of accelerating multiple-charge-state beams. At the pre-CDR stage of the design it is essential to identify critical facility subsystem failures that can prevent the driver linac from operating. The reliability and availability of the driver linac were studied using expert information and data from operating machines such as ATLAS, APS, JLab, and LANL. Availability studies are performed with a Monte-Carlo simulation code previously applied to availability assessments of the NLC facility and the results used to identify subsystem failures that most affect the availability and reliability of the RIA driver, and guide design iterations and component specifications to address identified problems.

Analysis of the RIA SC linac driver availability is based on simulations using a code developed at SLAC to assess the impact of various technologies or configuration choices in the Next Linear Collider (NLC) performance. The code emulates failures in a Monte-Carlo process that uses real-time as the independent variable. It calculates the machine average availability based on:

- i. given Mean Time Between Failures (MTBF) and Mean Time To Repair (MTTR) values for each component,
- ii. degradation of parameter affected by component failure,
- iii. redundancy of components,
- iv. number of repair people available for tunnel access,
- v. recovery and tuning time, and
- vi. total number of people available for repairs.

A detailed list of machine components, and, for each component, its number, MTBF and MTTR are required. Availability data for individual components were based on data from different accelerator facilities, namely ATLAS, APS, JLab, LANL, and

from reports of planned machines such as NLC and APT. Also required is an estimate of the degradation in the appropriate machine parameter caused by a component failure. For instance, we can tune around a failed resonator and degrade the beam energy by the resonator's accelerating field integrated over its length. Access requirements are divided in three categories: a) component failure brings the accelerator down but does not require access to repair, b) repair/replacement of the component requires access to the accelerator tunnel, or c) the component can be repaired while the accelerator is running ("hot repair"). Included in the category of "broken but no access needed" are failures of single resonators that require rephasing of neighboring resonators (retuning) and may degrade the beam energy, but repair can wait until a long access is required. The calculations take into account the constraints imposed by the number of people available for repair during an access.

For the availability analysis of the SC driver linac we imposed that a minimum beam power at the target be maintained, while, at this stage of the machine design, making assumptions about component failure effects. These assumptions were based on the performance of existing accelerators and experienced operators, and need to be validated with detailed Failure Modes and Effects Analysis (FMEA) studies. Listed below are some of the requirements and assumptions made.

- Some parameters have a minimum value that, when reached, cause the accelerator to be declared broken. The meaningful parameter for RIA is the beam power on the target, which will be specified as a percentage of the user requested beam power. As an initial assumption, the minimum acceptable beam power is set to 60% of the user requested power. Since beam power is proportional to its energy and intensity, both energy and current are used as "budget" parameters according to the criteria given below.
- Some component failures cause the machine to go down, such as failure of the Machine Protection System, and require immediate tunnel access to repair; others cause the machine to go down, but the machine can be retuned without tunnel access.
- Each time a component breaks the intensity is decreased by the specified amount, and the component is scheduled for repair, immediately if it can be fixed hot, or at the next downtime. When the minimum allowed operational energy or intensity is

- reached the accelerator is declared broken, and many accumulated repairs are done.
- Downtime planning: after a budget parameter reaches its allowable limit, the code computes the time necessary to fix the components affecting the parameter. An additional time can be added to the downtime to repair other components.
- Except for the first cryostat in the low-energy section, where failures cause the beam to be lost, failure of a whole cryostat can be recovered by retuning.
- Amplifiers and other RF power equipment are situated in a separate utility building and can be replaced quickly, if there is sufficient redundancy.
- Solenoid failure increases beam losses by 10%. Beam can be retuned, with a MTTR of 4 hours. The driver is declared broken if losses are higher than twice the initial nominal setting.

- Quadrupoles are warm. Failure increases beam losses by 10%.
- Power supplies, water pumps, etc, are located in the support building and can be repaired hot.

For the current design, with values based on the historical data and engineering expertise from many accelerator groups the SC linac availability is 96%. The high availability comes from assuming an “universal spare” cold cryostat that can be used to replace a broken unit in eight hours, SC magnets run in persistent mode, high redundancy of power supply elements for the warm magnets and redundant amplifiers and klystrons. By assuming a support building, where power supply and controllers, and RF power sources are located, the number of tunnel accesses is reduced significantly. Figure III-19 shows the preliminary results for estimates of downtime based on this analysis

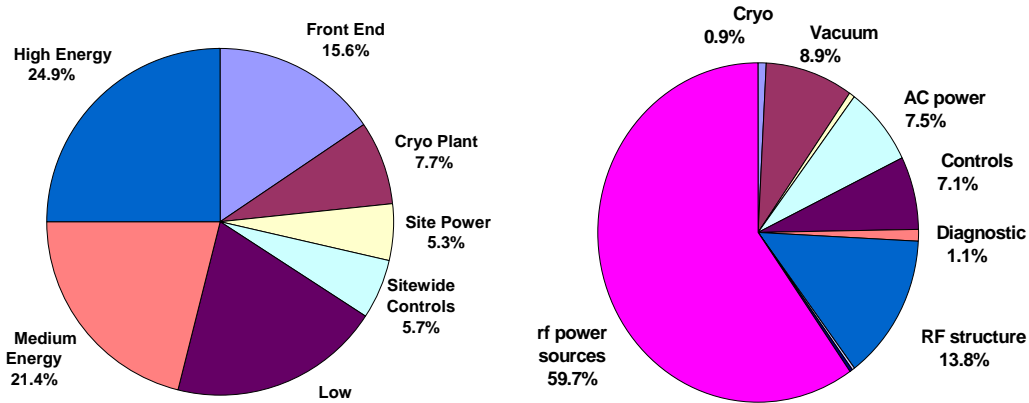


Fig. III-19. The distribution of downtime per region is shown on the left. Distribution due to systems contributing more than 0.4% of the SC linac downtime is shown on the right.

b.10. Optimization of Steering Elements in the RIA Driver Linac (E. S. Lessner, V. S. Aseev, and P. N. Ostroumov)

The driver linac of the projected RIA facility is a versatile accelerator, a 1.4-GV, CW superconducting (SC) linac designed to simultaneously accelerate several heavy-ion charge states, providing beams from proton to uranium at 400 MeV/u at power levels at a minimum of 100 kW and up to 400 kW for most beams. Acceleration of multiple-charge-state uranium beams places stringent requirements on the linac design. A steering algorithm was derived that fulfilled the driver’s real estate requirements, such as placement of steering dipole coils on SC solenoids and of beam position

monitors outside cryostats, and beam-dynamics requirements, such as coupling effects induced by the focusing solenoids. The algorithm has been fully integrated into the tracking code TRACK and it is used to study and optimize the number and position of steering elements that minimize the multiple-beam centroid oscillations and preserve the beam emittance under misalignments of accelerating and transverse focusing elements in the driver linac (see Table III-4 for a listing of the elements used in this analysis).

A correction algorithm applied to the driver must comply with real-estate limitations of very tight drift spaces and coupling introduced by solenoidal focusing elements was derived previously. In this paper, we present the algorithm as fully implemented in the code TRACK, a multi-purpose tracking simulation code specially suited to simulations of acceleration of heavy-ions in SC linacs. The algorithm has been rewritten for computational efficiency, and has additional features such as the assignment of accuracy and precision errors to each monitor. We present the algorithm in its new implementation and preliminary studies to optimize the number and location of steering elements in the SC driver linac.

The algorithm can be implemented in “correction sections”, whereby N correctors and M monitors are related by:

$$(R + \Delta R) F = - (X + \Delta X), \tag{2}$$

where R and X represent the transport matrix and monitor vector coordinates for the ideal lattice, respectively. ΔR denotes the matrix deviations due to lattice errors (misalignments and field errors), and ΔX are errors in the monitor-coordinates vector introduced by monitor inaccuracies. The corrector strengths are then determined by minimizing the function Ω given in Eq. 3. Ω includes statistical weights, w_i , useful in evaluating the correction scheme effectiveness. The minimization must obey constraints imposed by realistic limits, C, on the corrector strengths:

$$\Omega(F) = \sum_{i=1}^{2M} \left(\frac{\sum_{k=1}^{N_x+N_y} (R_{ik} + \Delta R_{ik}) F_k + X_i + \Delta X_i}{w_i} \right)^2, |F_k| \leq C_k. \tag{3}$$

Figure III-20 displays a possible scheme for a correction section.

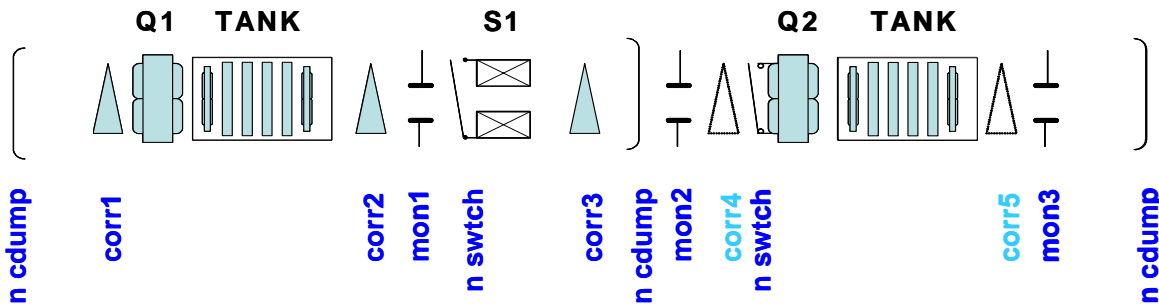


Fig. III-20. A possible correction section showing focusing, steering elements, and tanks, or cryostats, containing accelerating elements. The correctors in light blue correspond to correctors not used in the depicted correction section.

Table III-4. Steering elements distribution in the three SC driver sections. Accelerating and focusing components are also shown.

Element	Low Energy	Medium Energy	High Energy
Resonator	83	184	172
Solenoid	40	45	0
Quadrupole	0	0	84
Corrector	13	19	22
Monitor	7	18	41

Figures III-21 and III-22 show the corrected horizontal beam envelope for 60 seeds, and the

corresponding vertical (top) and horizontal (bottom) corrector strength distributions, respectively.

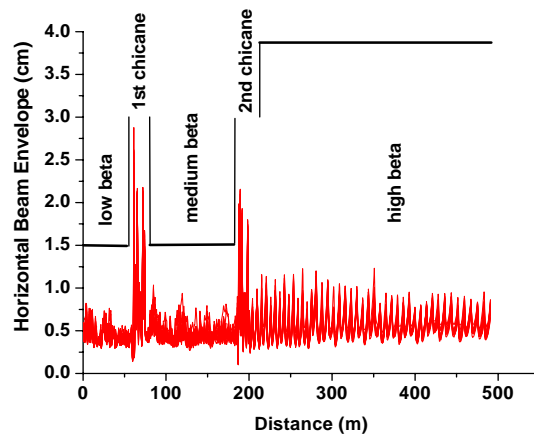


Fig. III-21. Corrected horizontal envelope, where the aperture radius is indicated for 60 seeds.

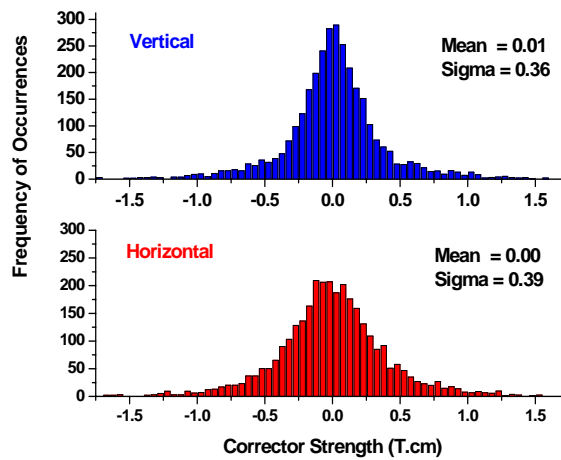


Fig. III-22. Vertical (top) and horizontal (bottom), corrector strength distributions over 60 seeds.

Simulations were carried for random-uniform resonator misalignments of 0.05-cm, solenoid misalignments varying from 0.015 for the shortest solenoids up to 0.05-cm for the longest solenoids, and quadrupole misalignments of 0.02 cm. Monitor precision errors were set at 100 μm .

A 4D minimization algorithm tailored to multiple-beam steering can correct position and angle and

account for solenoid-induced couplings. It is a beam-based algorithm and amenable to be implemented experimentally. It has been optimized for computational efficiency in its full integration in TRACK. It is being used to optimize the number and position of correcting elements in the RIA driver linac. Additional features will include a realization of correction by dipole coils mounted on solenoids and automatic evaluation of correction scheme effectiveness.

C. RARE ISOTOPE PRODUCTION AND SEPARATION

c.1. Characterization Studies of Prototype ISOL Target Material for RIA

(John P. Greene, Janelle Neubauer, Jerry A. Nolen, Tatiana Burtseva,*
Antonio C. C. Villari,† and Itacil C. Gomes‡)

One option as a high power isotope separator on-line (ISOL) production target proposed for the Rare Isotope Accelerator (RIA) will be one based on fission from uranium or a compound of uranium to produce ion species far from stability.¹ The two-step target design employs neutrons first generated in a cooled, refractory, primary target which then induce fission in a surrounding assembly of uranium carbide.

The prototype target design was done by TechSource, Inc.² with the fine-grained, high thermal conductivity UC₂ target material to be supplied by Argonne National Laboratory (ANL). The primary target will be a liquid cooled tungsten cylinder, irradiated by the RIA driver beam. The small energy deposition rate in the surrounding UC₂ secondary target material is not sufficient to heat the target to the desired operating conditions (1600 to 2100 C) necessary to promote effective release of fission products. Thermal conductivities on the order of 2 W/m-K (or greater) over the operating temperature range are required for a viable secondary target design.

A second spallation target approach involves exposing a tilted target slab to the full power primary beam but at an oblique angle, thereby dispersing the energy deposited over a large area.³ The use of fissionable target material would allow for a broad range of interesting isotopes to be produced. The target would possess a high thermal conductivity along its planar dimensions and yet be thin enough to allow rapid diffusion of fission products out of the target surface. The simple design would also allow for near term testing in high power beams while work progresses on the two-stage target.

As the original material used for this research is no longer commercially available, an effort was immediately mounted for manufacture. Preparation in-house has begun on this uranium carbide material by the method of arc melting.⁴

As grain size may prove to play an important role in ultimate densities, thermal conductivities and release properties achieved, this prepared material is

characterized using sieves for selecting the fine-grain material. The initial runs produced 20 g of powder (-325 mesh), grain size 44 μm. Investigations are now underway employing samples prepared with this material.

The thermal conductivity measurement sample disks are prepared in a laboratory hood by first weighing out UC₂ powder together with carbon (ratio of 8:1) in the form of high-purity synthetic graphite powder which is necessary to hold the refractory material in the form of a pellet. The mixture, with albumin added as a binder, is poured into a 13 mm compaction die and pressed to 5 tons (10,000 psi) using a laboratory press. Densities of 5 g/cc and greater have been achieved, meeting design specifications.

These thin sample pellets then have their thermal conductivity measured using the recently developed method of electron bombardment.⁵ The sample is heated on the bottom face by a vertical electron beam source installed within a vacuum evaporator. After achieving thermal equilibrium, the temperature of both faces of the sample was measured with the aid of a two-color pyrometer. Thermal conductivities for these UC₂ samples exhibit improved properties, comparable to values found in the literature.

When heated, changes may occur in the density, thermal conductivity and the microscopic structure of the uranium carbide pressed powder samples and are being investigated for long-term stability at elevated temperatures (2000 C). Access to a high-temperature graphite heated vacuum furnace with a sufficiently large hot zone for acceptance of the actual production target disks is of paramount importance.

Duplicate samples were forwarded to the Thermophysical Properties Users Center at ORNL for independent Laser Flash Thermal Diffusivity determinations. In this method, a short pulse of heat is applied to the front face of the pellet using a laser, with the temperature change of the rear face measured with an infrared detector. To determine the specific heat, a Differential Scanning Calorimeter is used to measure the thermal response of the UC₂ pellet as compared to a standard while heating uniformly at a constant rate. These measurements taken

together are then used for the determination of thermal conductivity.

The desired release of the fission products produced under sample irradiation is also being explored as a function of density/grain size. The target/ion source of the University Isotope Separator at Oak Ridge (UNISOR) facility is being used for characterization of the secondary target material release properties. We are working closely with Dan Stracener and Ken Carter at ORNL and sets of UC₂ pellets have been shipped there for these measurements. Experimental studies of the release properties of radioactive ions from the newer, smaller grain size ANL material are

to be performed soon after completion of the modifications to the UNISOR beam line.

With verification of the thermal properties coupled with new data from ORNL on the release properties of the fine-grain (-325 mesh) material, we hope to move towards fabricating actual secondary target disks using custom designed dies and a large area press. It is believed that the densities and thermal conductivity achieved for these UC₂ samples are sufficient for a prototype high-power RIA target to be built and tested under experimental conditions. Slabs of this uranium carbide material may also be fabricated for use in a tilted target design for testing under high power beams.

*Energy Technology Division, Argonne National Laboratory, †Argonne National Laboratory and GANIL, Caen, France., ‡I. C. Gomes Consulting and Investment, Inc.

¹Report to ATLAS Users Facility, ANL-ATLAS-99-1, March (1999).

²W. Talbert *et al.*, TechSource, Inc. (SBIR Grant).

³I. C. Gomes *et al.*, "Progress Towards a Uranium Carbide Tilted Target Design for RIA," February, 2004.

⁴J. Crane, F. B. Litton, and H. S. Kalish, *Arc Skull Melting and Casting of Uranium Carbide*, ASM Trans. Quarterly **56**, 176 (1963).

⁵J. P. Greene *et al.*, Sixth International Meeting on Nuclear Applications of Accelerator Technology (AccApp'03), San Diego, CA, June 1-5, 2003.

c.2. Development of a Windowless Liquid Lithium Stripper for RIA (J. A. Nolen, J. R. Specht, C. B. Reed,* V. J. Novick,* and Y. Momozaki*)

Introduction

The RIA driver linac requires two strippers to increase the charge states of the heavy ion beams. The development of a uniform and stable high velocity thin liquid lithium film stripper would increase the reliability and beam quality of the RIA driver. The alternative, a rotating wheel of carbon foils, is a much less desirable solution. Results from measurements performed to determine the best materials and optimum thicknesses for stripper films at the two energies required for the RIA driver linac indicate that lithium is an excellent choice for the lower energy (first) stripper and that the optimum thickness is about 6 microns.¹ Higher energy tests, for the second stripper, showed that lithium is not optimum for that case.

To provide consistent stripping characteristics, the thickness of the film must remain constant. In addition,

Jet Stability

It has been shown that a liquid jet is inherently unstable, meaning that a slight disturbance in the jet

to avoid excessive vaporization of the liquid, the mass flow rate of the jet must be high enough (≥ 50 m/s) to remove the thermal energy deposited in the film from the beam without a significant temperature rise. Therefore, producing a very thin, stable, film jet with a high flow rate in a vacuum environment is a key element in the development of a liquid stripper. Our primary objective is to demonstrate that the required parameters can be achieved in lithium, however, since neither the required film thickness nor the required film speed are known with great confidence at this time, a secondary objective is to establish the film thickness vs. velocity operating window, in the neighborhood of these nominal values, which can be reliably attained in the presence of a hard vacuum at roughly 230°C.

is spontaneously amplified and the jet eventually breaks up into small droplets by capillary pinching.³ Figure III-

23 shows two different modes of instabilities: (a) absolute instability, and (b) convective instability. In general, as the jet velocity, U , increases, the instability mode shifts from absolute to convective.⁵

Absolute instability occurs when the surface tension of the fluid dominates over its inertial force. This is the case that the fluid velocity is small. A disturbance propagates both in space as well as in time. Thus, the liquid does not form a stable jet, but forms droplets as soon as it exits from the nozzle as shown in Fig. III-23a. Obviously, it is not possible to operate the liquid stripper in this regime. As the jet velocity increases, the inertia becomes dominant and the instability shifts to the convective mode, in which a disturbance propagates and grows only in the downstream direction. Because the disturbance does not grow in time, as the liquid exits from the nozzle, a continuous jet is formed that extends to a point at which the spatially growing disturbance in the jet eventually breaks up the jet as shown in Fig. III-23b. When the amplitude of the disturbance imposed on the jet grows large enough, capillary pinching due to the surface tension of the fluid causes the breakup of the jet. In Fig. III-23b, L_j represents the length of

the continuous portion of the jet, which is called intact length.³ The intact length, L_j is schematically presented as a function of the jet velocity, U in the bottom of Fig. III-23. In higher jet velocity ranges (dashed line in the bottom of Fig. III-23), no experimental measurements in vacuum have been reported, and thus, the intact length of the jet is not known. However, experiments in air show that the intact length of the circular jet decreases as the liquid in the jet becomes turbulent (Debler and Yu, 1988). Therefore, it is reasonable to assume that as the velocity of the jet further increases in a vacuum environment, turbulence in the jet prevents the intact length from extending indefinitely. Since jet instability phenomena in a vacuum involve only the surface tension, viscous force, and inertial force, the intact length is expected to be a function of these three parameters and characteristics of the applied disturbances. For this reason, it is possible to draw a stability diagram in a 2-D space that consists of the Weber number, We , and the Reynolds number, Re , as parameters. The Weber number and the Reynolds number are the ratios of the inertia force to the surface tension force and of the inertia force to the viscous force, respectively and expressed as,⁴

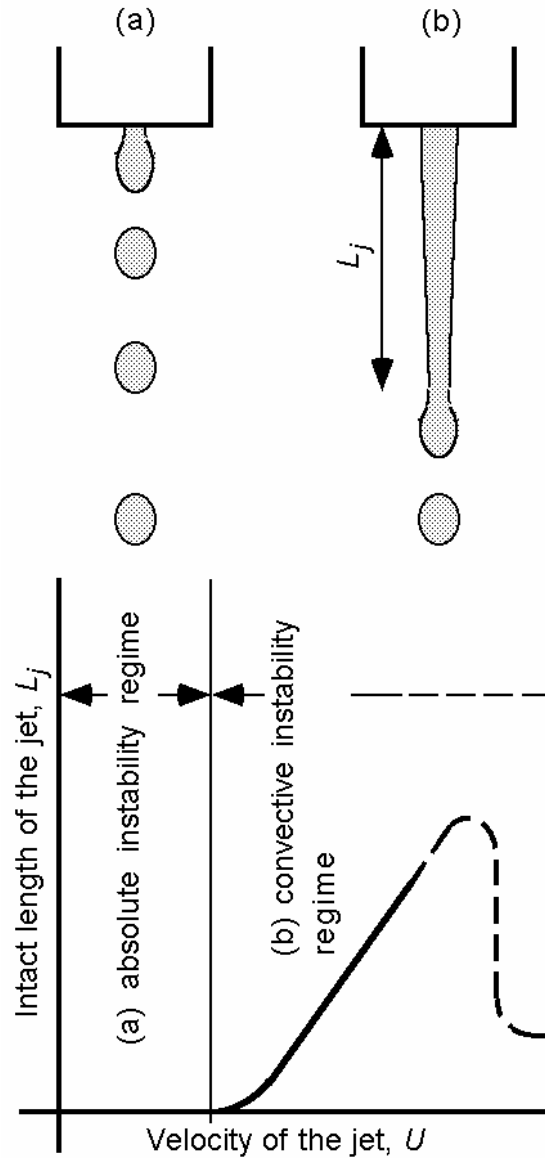


Fig. III-23. Evolution of circular jet in vacuum.

$$We = \frac{\rho U^2 R_h}{\sigma}, \text{ and } Re = \frac{\rho U R_h}{\mu}, \quad (1)$$

where ρ is the liquid density, U is the average jet velocity, R_h is the hydraulic radius of the nozzle, σ is the surface tension of the liquid, and μ is the liquid dynamic viscosity. This fact suggests that any liquid jets in vacuum would behave similarly and the diagram should be universal and applicable to any liquids as long as both We and Re are matched. This fact allows the use of Li simulants for the experiment instead of using liquid Li as a working fluid,

significantly reducing complexity, difficulty, and cost of performing experiments.

The intact length of the jet strongly depends on the amplitude of the initial disturbance and the size of the liquid jet, in other words, it depends on the physical dimensions of the nozzle, the surface finish of the nozzle interior, externally induced pressure fluctuations in the fluid, and other mechanical vibrations, etc. Especially, the quantities such as surface finish, pressure fluctuation, and vibration in the real system are extremely hard to determine. Therefore, it is not reasonable to attempt to theoretically estimate the maximum intact length with a

high degree of accuracy. Thus, to determine the intact length of the jet for the present purpose, an experimental measurement is absolutely necessary.

An example of a typical stability diagram is presented in Fig. III-24. This figure shows that in the region where $We > We_{CR}$, one has a convective instability and where $We < We_{CR}$, one has an absolute instability. We_{CR} the critical Weber number and is expressed as a function of Reynolds number.² Also in this figure, the region where $Re < Re_{CR}$ indicates that the liquid flow in the nozzle remains laminar at

the exit of the nozzle, spouting out smoothly without any internal disturbances forming the jet with constant shape, whereas the region of $Re > Re_{CR}$ is where the liquid in the nozzle becomes turbulent and the liquid jet at the exit of the nozzle is expected to be wavy, shortening the intact length; this would not be suitable for stripper operation. Smooth jet formation with a finite length is expected only in the shaded area in Fig. III-24. Conducting experiments to measure the intact length to assess the feasibility of the liquid stripper is, therefore, necessary only in this shaded area.

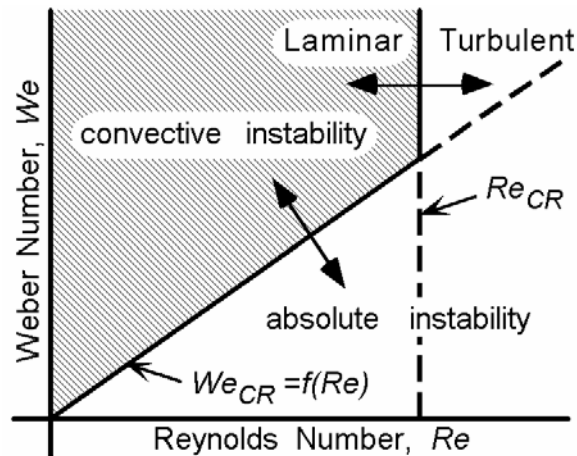


Fig. III-24. Schematic representation of stability diagram for the jet in vacuum.

The ultimate goal of this project is to develop a liquid lithium 1st stripper that can effectively strip heavy beams including uranium at ~ 10 MeV/u. The main objective of current work is to produce a very thin, hydrodynamically stable liquid lithium film with a high flow rate in a vacuum environment. Because of the extreme technical difficulty in conducting developmental work with liquid lithium, tasks are divided into three steps: (1) experimentally develop

a liquid thin film formation scheme, (2) experimental development of the film stability diagram for the film production scheme using simulants. This diagram will provide the range of design parameters such as nozzle width and the film velocity, that are potentially capable of producing a stable, smooth liquid lithium film, and (3) experimentally demonstrate the thin film liquid lithium jet and confirm that the intact length of the film is sufficient to be used as a stripper.

Development of a Liquid Thin Film Formation Scheme

The most straightforward method to produce a liquid film would be a direct method, using a slit nozzle whose dimensions match the required film dimensions. For the 1st stripper, however, since the film thickness required from nuclear physical consideration is only on the order of a micrometer and the width of the film must be on the order of a centimeter, it appears extremely difficult to fabricate and manage such a high aspect-ratio nozzle with a very narrow opening.

Another method is to produce a film indirectly. In one proposed method, liquid issues from a round nozzle, forming a round jet, which subsequently impacts on a deflector on which the round jet transforms into a thin film. Preliminary experiment shows that a nice thin water jet can be produced using a round nozzle and a metal deflector (Fig. III-25). In this method, it is expected that the velocity of the thin film is similar to, but slightly less than that of the round jet, thus requiring a relatively large driving pressure.

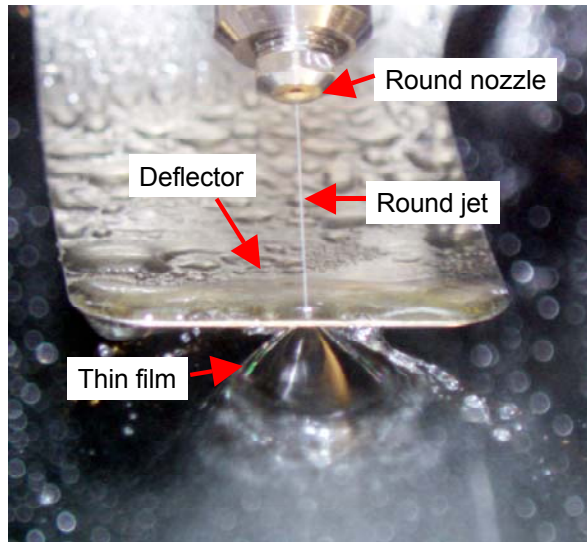


Fig. III-25. Thin film formation after impact on deflector.

To reduce the driving pressure, two methods were considered: (1) use of a rotating deflector, and (2) use of a notched deflector. In the rotating deflector design, the deflector is a rotating round disk. The flow direction of the round jet is parallel to the circumferential direction of the rotating disk. As the jet impacts on the disk, the rotation of the disk is expected to accelerate the jet. As a result, the film velocity is expected to be higher than that of the

initial jet velocity before impact. However, preliminary experiments show that the rotating disk disturbs liquid significantly and the thin film does not appear smooth (Fig. III-26). Since the film needs to be steady and fluctuation in the film thickness needs to be much smaller than the order of film thickness ($\sim 10 \mu\text{m}$), the film produced by this method is not the primary candidate for the stripper.

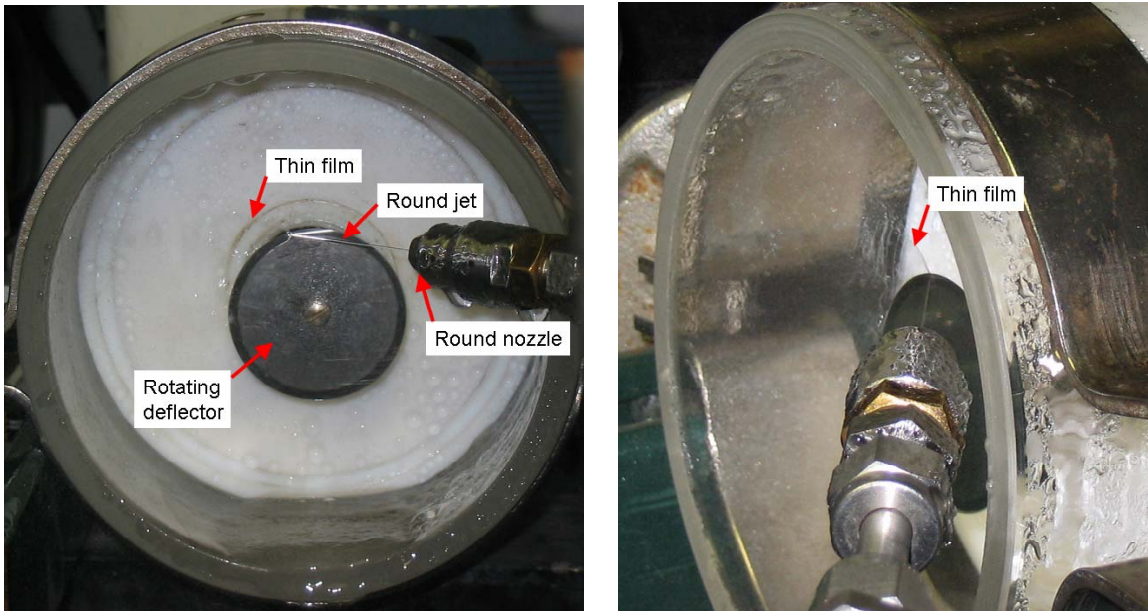


Fig. III-26. Thin film formation using rotating disk.

In the notched deflector design, the deflector has two cuts on it and they form a notch. The round jet hits at the base of the notch and the film is formed within the notch. As the film is formed, both sides of the film are expected to attach to the deflector, enhancing the stability of the film at low jet velocity. However,

preliminary experiments show that since most of the film edge is attached to the deflector, the quality of the film is significantly more affected by microscopic imperfections on the deflector, resulting in the formation of a poor quality film (Fig. III-27).

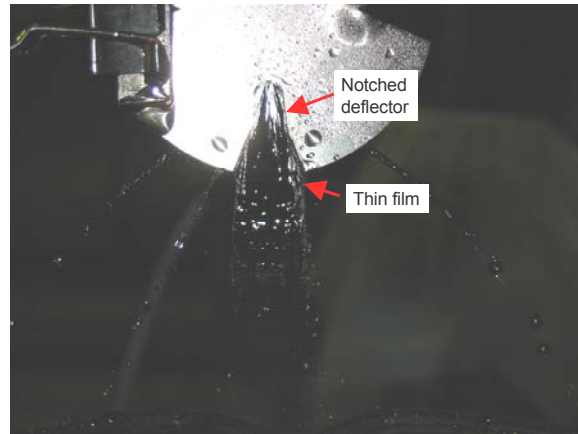


Fig. III-27. Thin film formation using notched deflector.

In conclusion, the indirect method using a stationary deflector appears to be the best film-forming scheme, in which a round jet from a round nozzle impacts on

a deflector on which the round jet transforms into a thin film.

Experimental Development of the Film Stability Diagram using Li Simulants

After analyzing various potential Li simulants, water and 3M’s FC-3283 were selected not only because of their inert and non-hazardous characteristics, which significantly reduce complexity, difficulty, and cost of performing experiments, but also, as shown in Table III-5, the difference between physical properties of FC-3283 and those of water for the same combination of Re and We is similar to that

between water and lithium. Therefore, comparing the results obtained for FC-3283 and water is expected to allow direct extrapolation of these thin film stability experimental results to lithium. Using Re-We scaling, a Li film at 10 μm thick, 473 K, and 50 m/s is equivalent of a water film at 58 μm thick, 303 K, and 6.4 m/s and of a FC-3283 film at 420 μm thick, 303 K, and 0.83 m/s. For all these 3 films, Re = 450, We = 33.

Table III-5. Various physical properties of Lithium and ratio of FC 3283 and water to Lithium.

	Lithium		FC-3283	Water	Lithium
Temperature [K]	473.15	Temperature (K)	R.T.	298.15	473.15
Density [kg/m ³]	514.9849	Density ratio	3.53	1.94	1
Surface tension [N/m]	0.392075	Surface tension ratio	0.0408	0.1835	1
Viscosity [Pa-s]	0.000572	Viscosity ratio	2.45	1.59	1

Prior to designing and fabricating the Li thin film stripper loop, several series of hydrodynamic stability experiments were performed using Li simulants to determine the range of stable jet formation and to investigate the film behaviors. Objectives of the experiments included investigating:

1. Effects of surrounding air on film breakup.

2. Effects of driving pressure (thus jet velocity), nozzle size, angle of the impinging jet relative to the deflector plate, distance between the nozzle exit and the deflector, and jet to deflector edge distance on film formation.
3. Effects of orifice finish. A sapphire orifice in the nozzle has better physical definition and surface

finish than a stainless steel orifice does, however, chemical compatibility of sapphire with liquid lithium is not known.

4. Velocity measurement of the droplets after film breakup using Phase Doppler Particle Analysis (PDPA) to estimate actual velocity of the water film.
5. Whether the stability diagram represented by Re and We numbers is universal for other working fluids with different physical properties as the linear stability theory suggests. This can be done by plotting the stability diagram for water and FC-3283 on the same graph in Re and We space. They should form the same stability diagram.
6. The nozzle sizes of 0.1 mm (4 mils) – 1 mm (40 mils), jet velocity range between 10 – 30 m/s

for water and 2.1 – 5.3 m/s for FC-3283, and nozzle angles between 15 – 60 degrees were tested. It must be noted that jet velocities for water and FC-3283 corresponding to a 10 μm thick, 50 m/s Li film (6.4 m/s for water and 0.83 m/s for FC-3283) were not achievable, since no films at those velocities were formed due to absolute instability, suggesting that the minimum film velocity is not set by the thermal requirement, but by the hydrodynamic requirement.

In summary, these experiments have shown that:

1. Water experiments at reduced pressure (~9 kPa) indicated that the effects of ambient air around the jet on break-up phenomena are negligible at the velocity range of interest (< ~15 m/s, see Fig. III-28, Fig. III-29, and Fig. III-30).

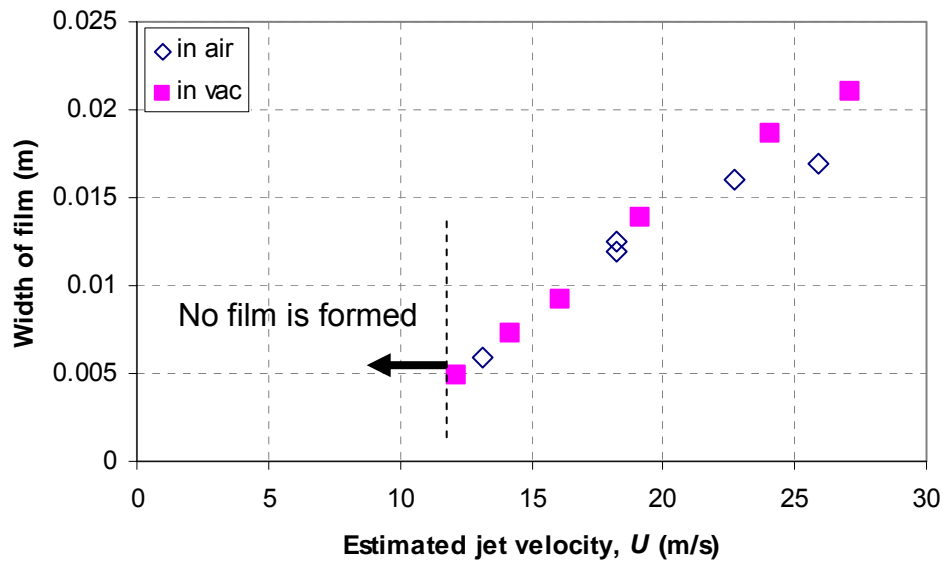


Fig. III-28. Effect of surrounding air on film width.

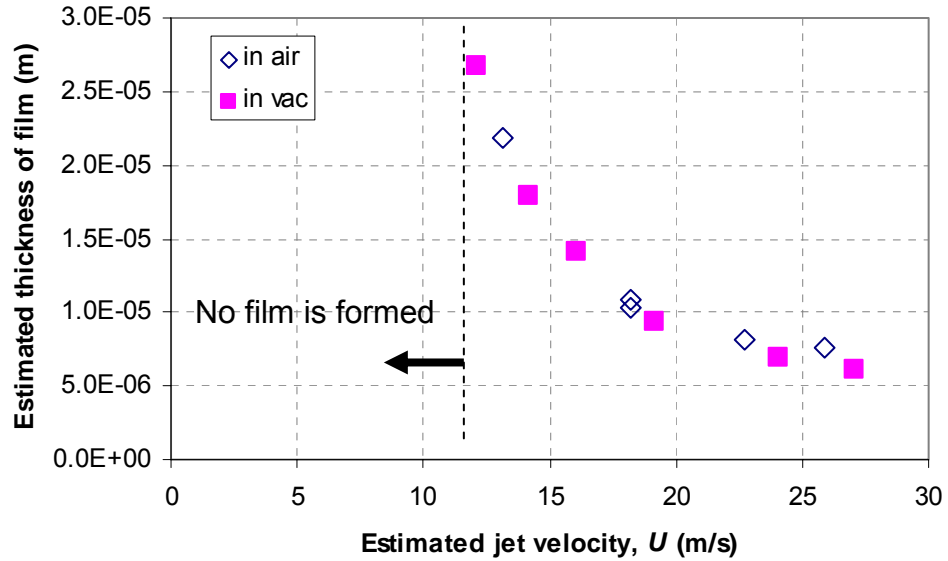


Fig. III-29. Effect of surrounding air on film thickness.

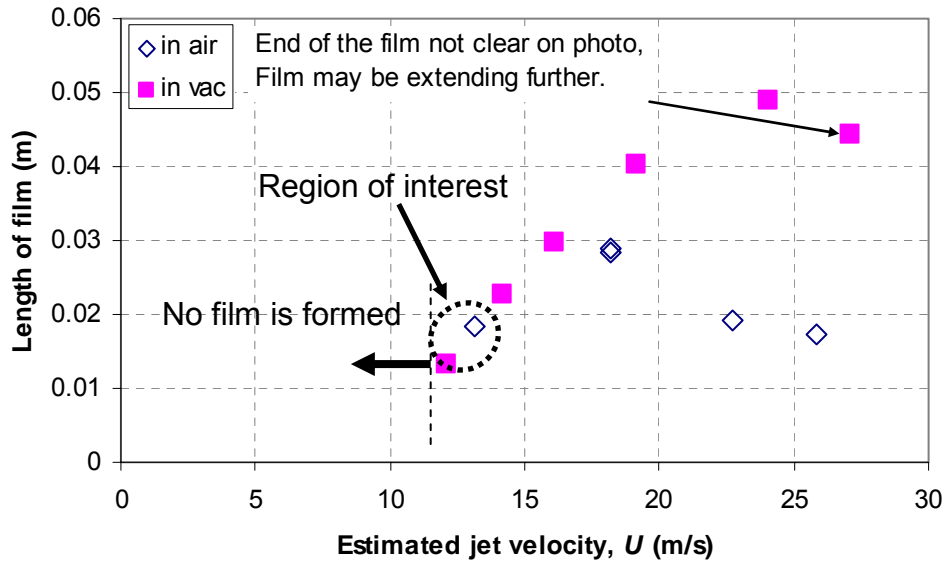


Fig. III-30. Effect of surrounding air on film length.

2. The jet at the smallest pressure high enough to produce a film appears to form the film (0.4 – 1.0 MPa for water) with the highest quality (see Fig. III-31). When the pressure is

too low, the jet did not form a film due to absolute instability (at 0.34 MPa). On the other hand, when the pressure is high (at ≥ 1 MPa), the film became wavy.

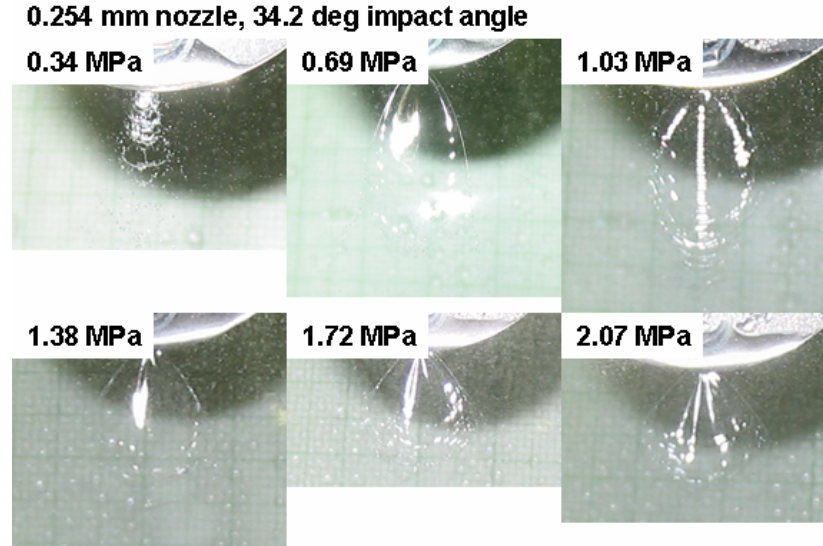


Fig. III-31. Effect of drive pressure on film formation.

3. Distance between the impact point on the deflector and the edge of the deflector is critical. If too short, the jet is not completely deflected and the film is not uniform and flat. If too long, friction on the deflector surface slows down the film velocity. The value of the distance is ~ 1 mm in the range of present experiments and depends on the nozzle size and jet velocity, however, this distance should be adjusted within an accuracy of 0.1 mm.
4. The distance between the nozzle exit and the deflector must be smaller than the intact length for the round jet to form high quality films (less than ~ 2.5 cm for water). If this distance is too long, the round jet develops large waves, disturbing the flow pattern. The smaller the distance between the nozzle exit and the deflector, the higher the quality of the thin film.
5. A jet angle of between 30-45 degrees and a nozzle diameter of 0.25 mm (10 mils) – 0.5 mm (20 mils) appear to be the most suitable range to produce the best looking stable film for both water and FC-3283 (see Fig. III-32). A film produced using the 0.5 mm nozzle showed that the variation in film thickness within the expected beam diameter of 5 mm on the film is $< 1 \mu\text{m}$ (see Figs. III-33 and III-34). A film produced by a jet issuing from the large diameter nozzle (1.0 mm = 40 mils) appears wavy at almost all conditions and is not suitable for the stripper.

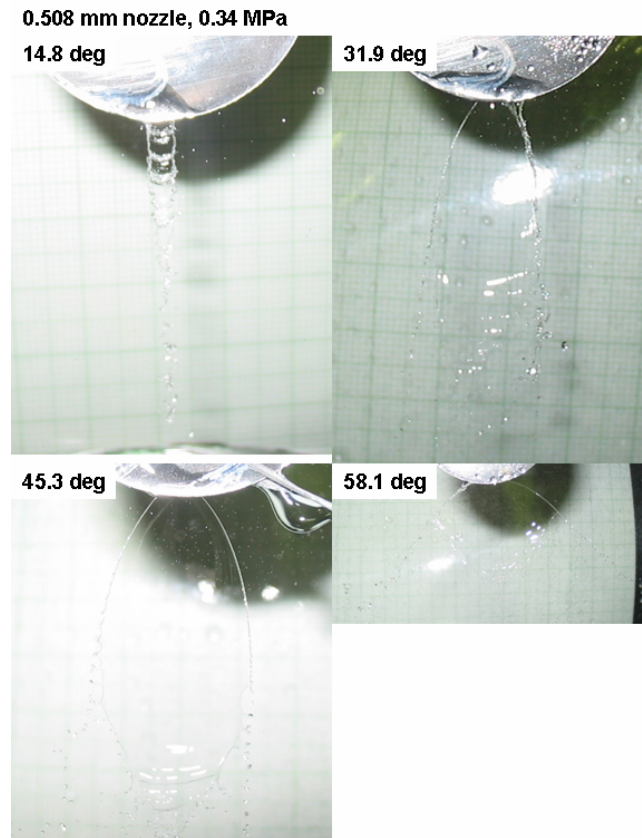


Fig. III-32. Effect of impact angle on film formation.

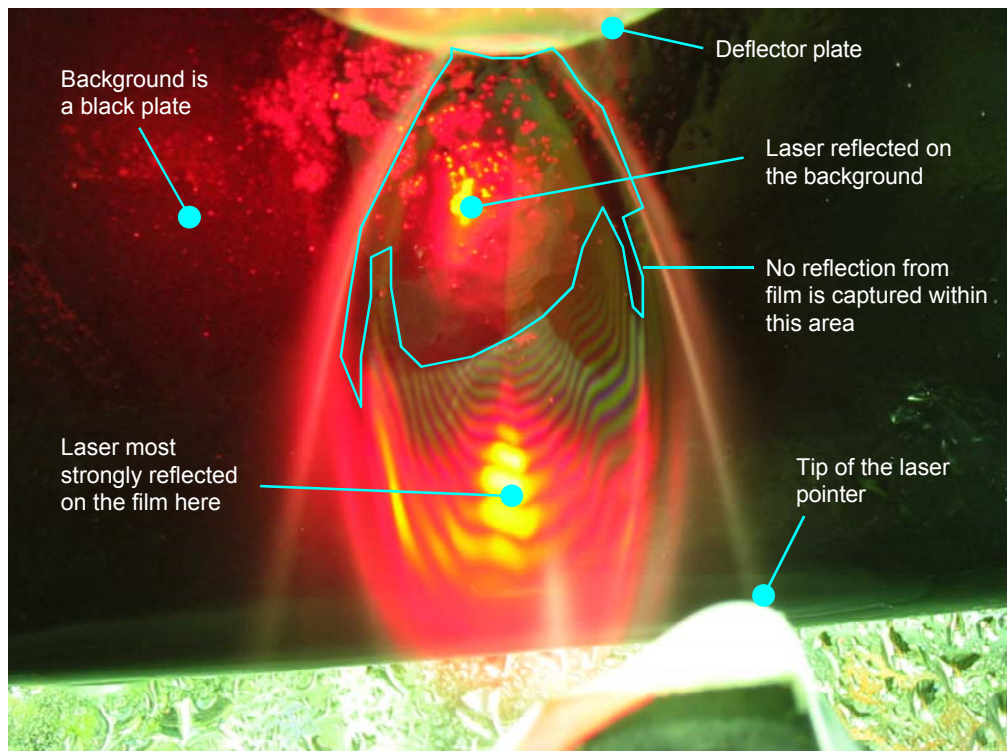


Fig. III-33. Measurement of film thickness variation using a laser.

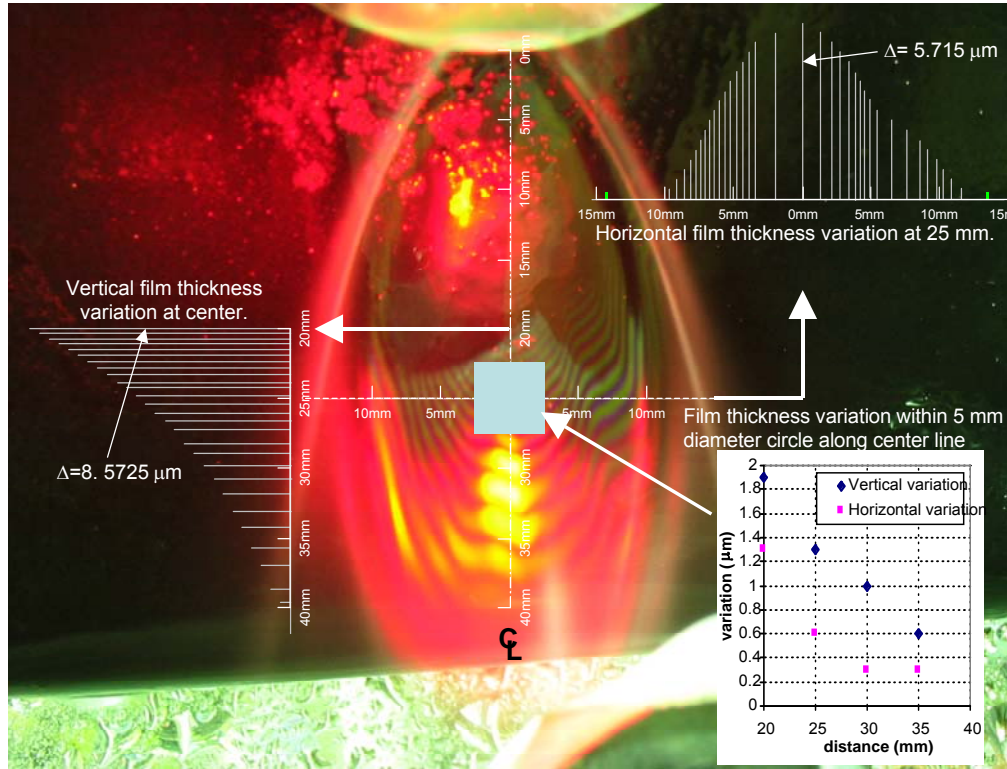


Fig. III-34. Measured film thickness variation using a laser.

6. A nozzle with a sapphire orifice produced better quality film than that with a stainless steel orifice did (Fig. III-35).
7. The film velocity seems to be somewhat slower than the initial jet velocity. Although no direct measurement was possible, it appears that jet

velocity can be interpolated from the droplet velocity after break-up measured by PDPA and initial jet velocity (see Fig. III-36 for a picture of the PDPA measurement and Fig. III-37 for the analysis).

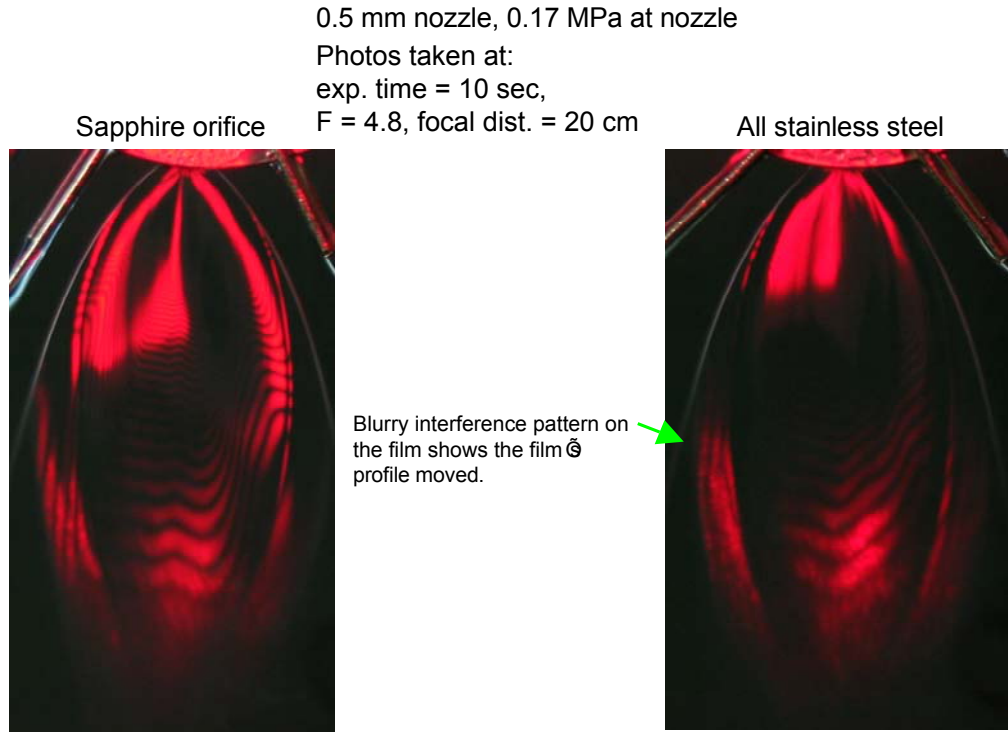


Fig. III-35. Interference patterns on films produced by a sapphire orifice and all stainless steel nozzles.

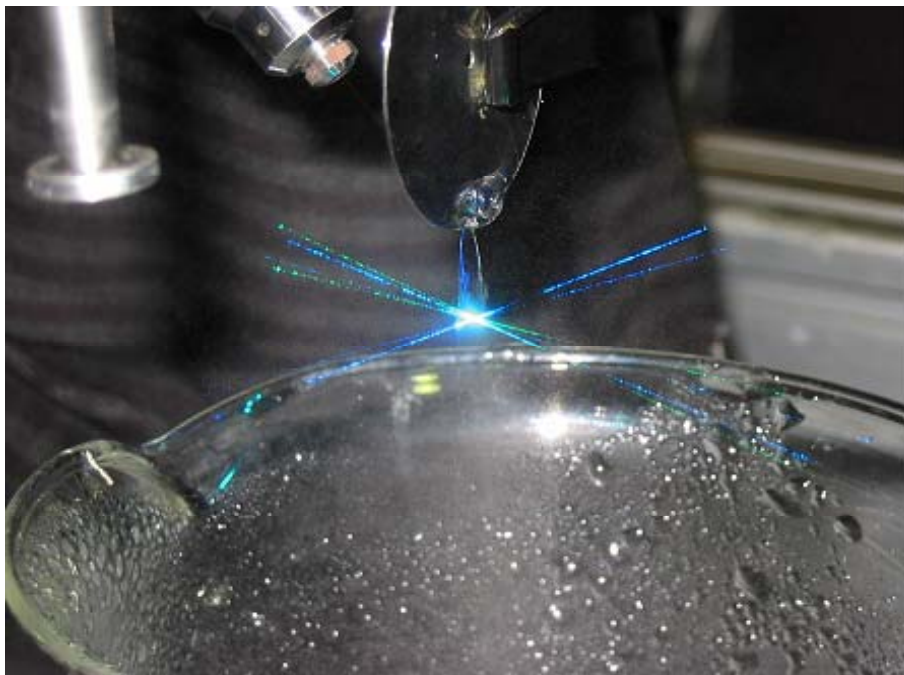


Fig. III-36. Velocity measurement using PDPA.

8. The stability diagrams represented as a function of Re and We numbers for water

and FC-3283 seem to be very similar, indicating its universal nature (Fig. III-38).

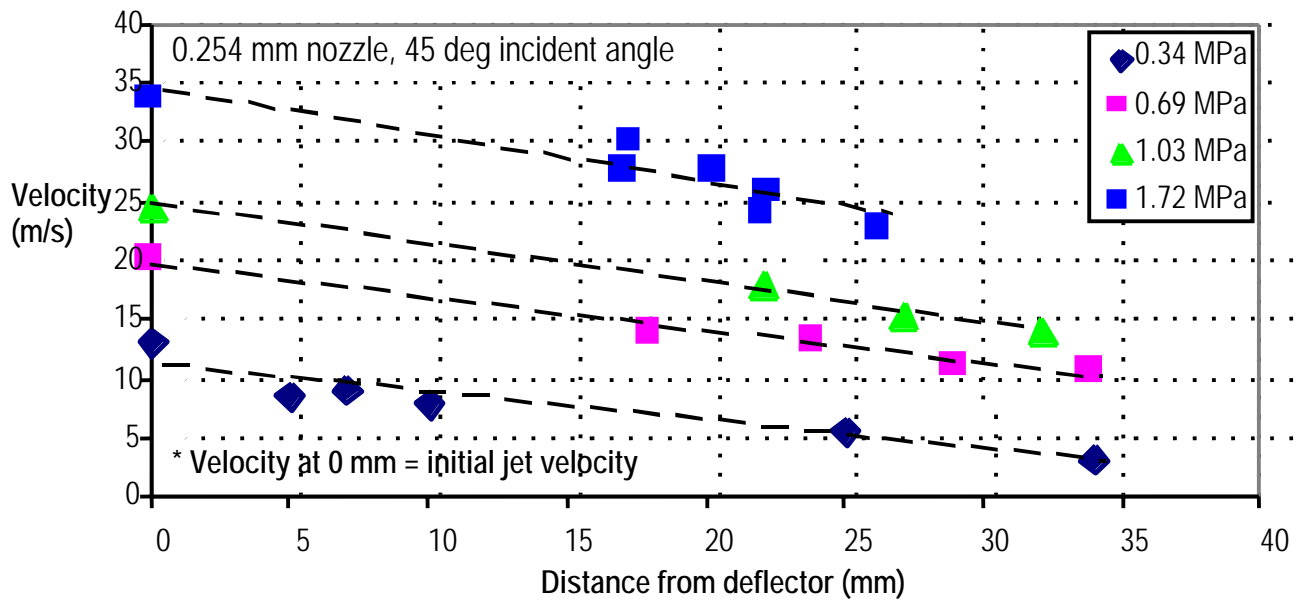


Fig. III-37. Measured droplets velocity after break-up.

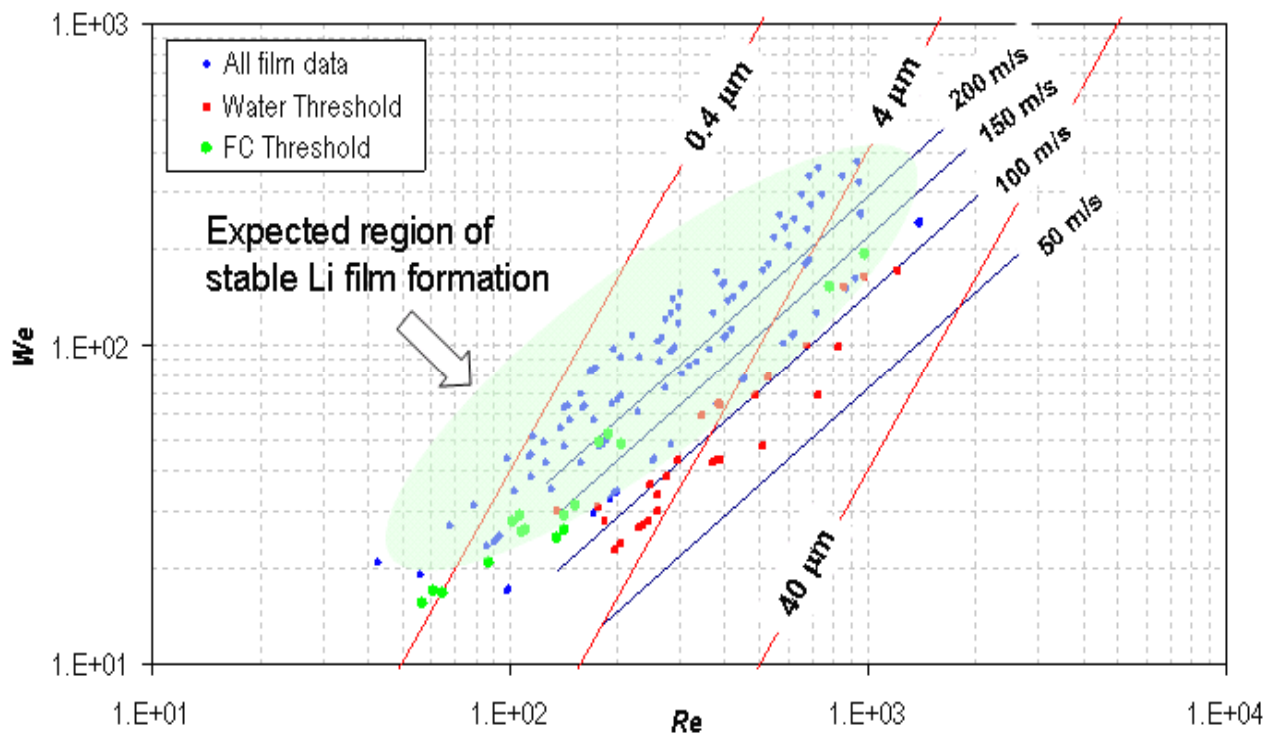


Fig. III-38. Experimentally developed stability diagram.

Figure III-38 shows that threshold data (velocity below which no film formation was observed) for both water and FC-3283 form a single, relatively narrow band in Re-We space, indicating the stability

boundary above which film formation is expected (green shaded region in Fig. III-38) and this stability boundary appears to be universal. Values for velocity and thickness in Fig. III-38 are for Li. This figure suggests that a Li

film of $\sim 4 \mu\text{m}$ thick at $\geq 100 - 150 \text{ m/s}$ would be stable. The same data presented in Fig. III-38 are also plotted in the film velocity-film thickness space (Fig. III-39). This figure shows that for the same set of Re and We , the difference in physical parameters for FC-3283 and water is approximately the same as

that for water and lithium. For the same Re and We , no apparent differences in film behavior were observed between FC-3283 and water films, suggesting insignificant difference in film behavior between water and Li films is expected, if any.

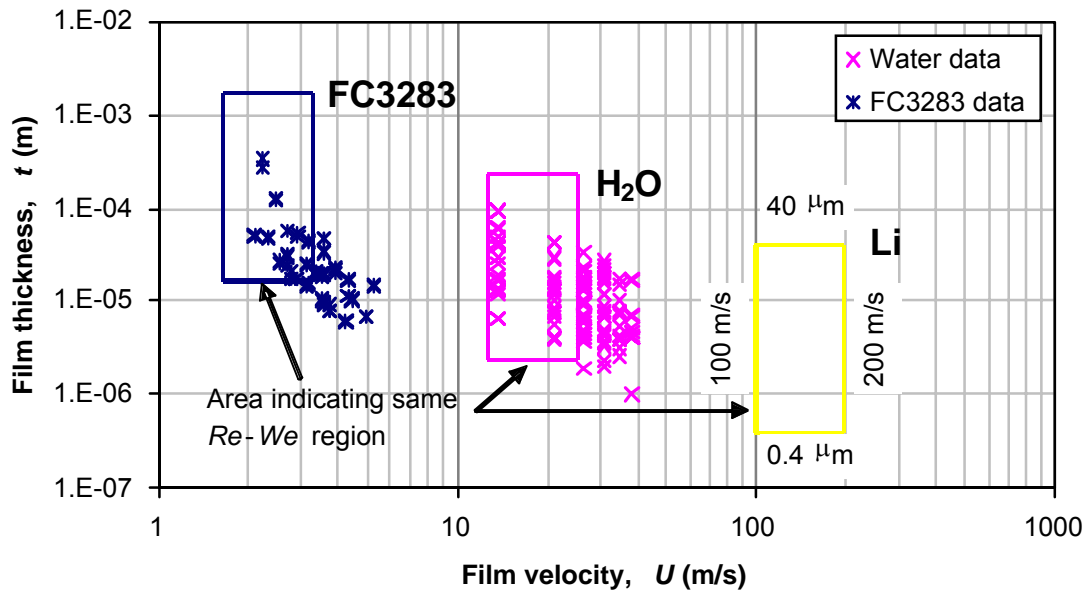


Fig. III-39. Thickness of various demonstrated thin films as a function of film velocity.

To summarize this phase of study, as the linear stability theory suggests, the films of different fluids appear to behave in a similar manner when their Re and We are kept the same. Although larger nozzle size is better to avoid potential plugging, it was found that a nozzle diameter of $\sim 0.5 \text{ mm}$ may be the largest size to form a nice film. Also to form a stable Li thin

film, a Li jet needs to be issued at $\geq 100 - 150 \text{ m/s}$ (corresponding a driving pressure of $3 - 6 \text{ MPa}$). The angle of incidence should be between $30 - 45$ degrees and the relative position of the nozzle to the deflector must be adjustable with a resolution of $\sim 0.1 \text{ mm}$ (Fig. III-40).

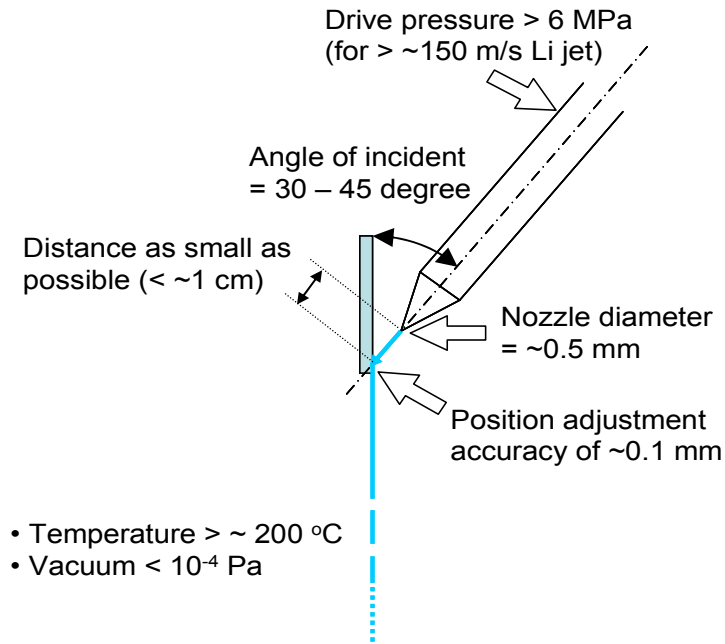


Fig. III-40. Summary of critical design parameters.

Experimental Demonstration of Thin Li Film Formation

To experimentally demonstrate the formation of a thin Li jet that has the correct physical dimensions to be used as a 1st stripper for RIA, an experimental Li stripper film system has been designed based on the results presented in this report. Experiments are planned in 2005. See Fig. III-41 for a CAD model of the concept.

The system will be a once-through type and Li will be driven by compressed Ar gas. The maximum design

drive pressure is 13.8 MPa (2000 psig). Experiment run time is longer than a few minutes with a Li inventory of ~ 20 liters. Initially a nozzle diameter of 0.5 mm will be used, but the nozzle piece will be changeable. The Li jet will issue into the vacuum chamber in which the pressure will be maintained at $\leq 10^{-4}$ Pa (~ 10^{-6} Torr). The nozzle assembly will be movable such that fine adjustment can be accomplished.

Summary and Conclusions

A series of experiments for development of the 1st stripper using liquid lithium for RIA was conducted. For the film production, the indirect method using a stationary deflector appears to be the best scheme, in which a round jet from a round nozzle impacts on a deflector on which the round jet transforms into a thin film. It was experimentally shown that films of different fluids appear to behave in a similar manner when their Re and We are kept the same. This fact suggests that results obtained using Li simulants are directly applicable to estimate the behavior of the Li film. After conducting various preliminary

experiments using water and FC-3283, several critical design parameters for successfully forming a good quality Li film were determined:

- The nozzle diameter of ~0.5 mm,
- Li jet velocity > ~100 - 150 m/s (corresponding drive pressure of 3 – 6 MPa),
- The angle of incidence should be between 30 – 45 degrees,
- The relative position of the nozzle to the deflector should be adjustable with a resolution of ~ 0.1 mm.

*Nuclear Engineering Division, Argonne National Laboratory.

¹W. Debler and D. Yu, *The Break-Up of Laminar Liquid Jets*, Proc. R. Soc. London **A415**, 107-119 (1988).

- ²S. J. Leib and M. E. Goldstein, *Convective and Absolute Instability of a Viscous Liquid Jet*, Phys. Fluids **29**(4), 952-954 (1986).
- ³S. P. Lin and R. D. Reitz, *Drop and Spray Formation from a Liquid Jet*, Annual Review of Fluid Mechanics **30**, 85-105 (1998).
- ⁴S. P. Lin, M. Hudman, and J. N. Chen, *Absolute and Convective Instability of a Liquid Jet*, Proceedings of the Fourth Microgravity Fluid Physics & Transport Phenomena Conference, August 12-14, 1998, Cleveland, OH, pp. 534-538, (1999).
- ⁵Y. Momozaki, *Development of an Electron Stripper Using Thin Liquid Lithium Film for Rare Isotope Accelerator*, unpublished (2004).

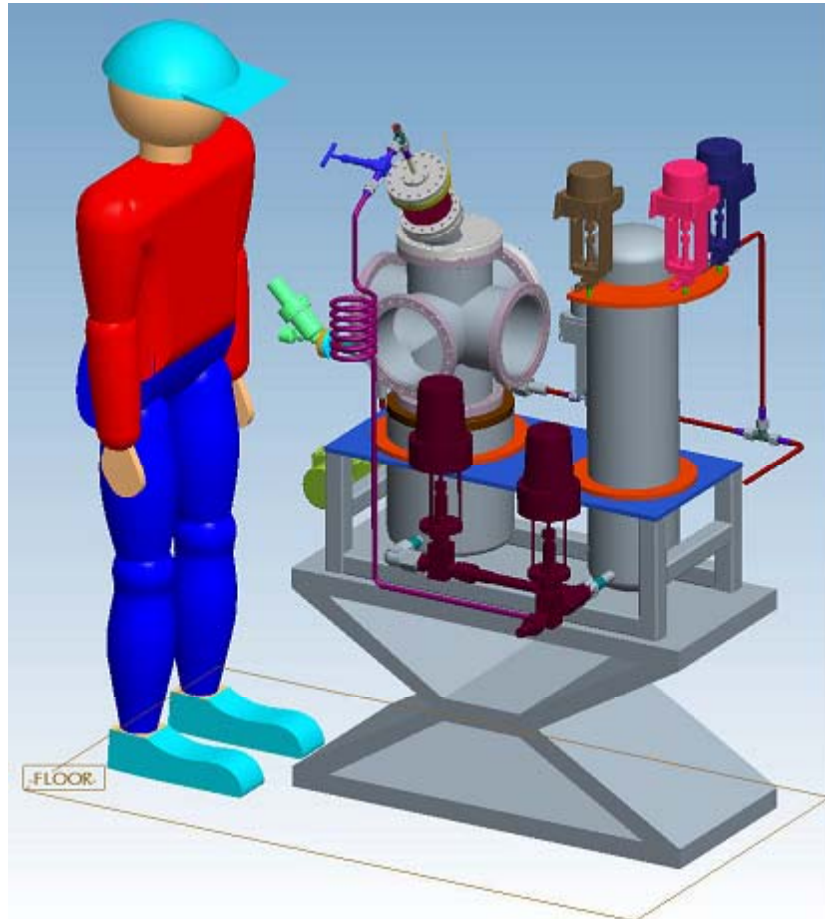


Fig. III-41. CAD model of the thin lithium jet apparatus concept.

IV. MEDIUM-ENERGY NUCLEAR PHYSICS RESEARCH

OVERVIEW

The overall goals of the Medium-Energy Physics research program in the Argonne Physics Division are to test our understanding of the structure of hadrons and the structure of nuclei, and to develop and exploit new technologies for high-impact applications in nuclear physics as well as other national priorities. In order to test our understanding of the structure of hadrons and the structure of nuclei within the framework of quantum chromodynamics, the medium-energy research program emphasizes the study of nucleons and nuclei on a relatively short distance scale. Because the electromagnetic interaction provides an accurate, well-understood probe of these phenomena, primary emphasis is placed on experiments involving electron scattering, real photons and Drell-Yan processes. The electron beams of the Thomas Jefferson National Accelerator Facility (JLab) are ideally suited for studies of nuclei at hadronic scales and represent one center of the experimental program. Staff members led in the construction of experimental facilities, served as spokespersons or co-spokespersons for 20 experiments and were actively involved in others. The group constructed the general-purpose Short Orbit Spectrometer (SOS) which forms half of the coincidence spectrometer pair that is the base experimental equipment in Hall C. Last year, Argonne had a major role in re-establishing the SOS in Hall C for a series of five experiments. Argonne led the first experiment to be carried out at JLab in Fiscal Year 1996 and has completed 15 other experiments.

Recently, staff members have focused increasingly on studies of the nucleon and the search for exotic phenomena. In Fiscal Year 2004 the analysis was completed for the ratio of the electromagnetic elastic form factors of the proton using a modified Rosenbluth method. These results agree with data recorded previously with the traditional Rosenbluth method, but strongly disagree with the polarization transfer data. A new initiative to search for color transparency in ρ production in nuclei was completed last year in Hall B at JLab. This work represents an important extension of Argonne's earlier ρ electro-production studies at HERMES. A new experiment to search for partners of the Θ^+ pentaquark was completed last year in Hall A. Finally, two experiments, a study of the EMC effect in light nuclei and $x > 1$ studies in nuclei, were completed last year in Hall C. Three new proposals – a high-resolution search for the

Θ^+ pentaquark, a search for two-photon exchange effects in elastic electron-proton scattering, and parity-violating deep inelastic scattering from the deuteron – were approved this year by the JLab PAC.

The HERMES collaboration is studying the spin structure of the nucleon using internal polarized targets in the HERA storage ring at DESY. Deep inelastic scattering has been measured with polarized electrons on polarized hydrogen, deuterium and ^3He . Argonne has concentrated on the hadron particle identification of HERMES, a unique capability compared to other spin structure experiments. In 1999 and under Argonne leadership, the dual-radiator ring imaging Cerenkov counter (RICH) was brought into operation at the design specifications to provide complete hadron identification in the experiment. The RICH has been operating routinely since its installation. This has allowed HERMES to make decisive measurements of the flavor dependence of the spin distributions. Last year, HERMES met one of its principal objectives by publishing a five-component decomposition of the proton's spin structure function and the first measurement of the x-dependence of the strange sea polarization. During 2001, HERMES installed a transversely polarized target. Measurements with this target will continue through 2005. These results are expected to provide significant information on the quark's transverse motion. Finally, HERMES will continue the investigation of quark propagation in nuclear matter.

Measurements of high mass virtual photon production in high-energy proton-induced reactions have determined the flavor dependence of the sea of antiquarks in the nucleon. These measurements gave insight into the origin of the nucleon sea. In the same experiment, the high-x absolute Drell-Yan cross sections were measured. In Fiscal Year 2001, a new initiative was approved by the FNAL PAC to continue these measurements with much higher luminosity at the FNAL Main Injector. These Drell-Yan experiments not only provide the best means to measure anti-quark distributions in the nucleon and nuclei, but represent an outstanding opportunity to perform these measurements at an ideal proton beam energy of 120 GeV. Plans are underway to prepare this experiment at FNAL.

The technology of laser atom traps provides a unique environment for the study of nuclear and atomic systems and represents a powerful new method that is opening up exciting new opportunities in a variety of fields, including nuclear physics. In particular, the group has developed a high-efficiency, high-sensitivity magneto-optical trap for rare, unstable isotopes of krypton. Last year, the group demonstrated the power of this novel method by dating ancient Sarahan ground water. A highlight during this year was the optical trapping of single atoms of ^6He and performing precision laser spectroscopy on the individual ^6He atoms. The nuclear charge radius of ^6He was determined for the first time.

A new initiative to search for an electric dipole moment (EDM) of ^{225}Ra is in progress. The ultimate goal is to search for a non-zero EDM for ^{225}Ra and

improve the sensitivity for nuclear EDM searches by approximately two orders of magnitude. This test of time-reversal symmetry represents an outstanding opportunity to search for new physics beyond the Standard Model. Laser spectroscopy was performed for the ^{225}Ra beam from the oven system. A Zeeman slower and optical trap for ^{225}Ra are being developed.

A new experiment to measure parity violation in deep inelastic scattering from the deuteron was approved by the JLab PAC. The ultimate goal of this experiment is to provide the best possible measurement for the neutral current axial vector coupling to the quarks. Finally, as a test of one of the main assumptions underlying the NuTeV anomaly, a feasibility study is underway for a possible charge symmetry violation experiment at the partonic level.



A. HADRON PROPERTIES

a.1. New Measurement of (G_E/G_M) for the Proton (J. Arrington, R. Beams, K. Hafidi, R. J. Holt, I. A. Qattan, E. C. Schulte, K. Wijesooriya, X. Zheng, B. Zeidman, and the JLab E01-001 Collaboration)

The discrepancy between Rosenbluth and polarization transfer measurements of the proton electromagnetic form factors led to significant questions about our level of understanding of the proton. Experiment E01-001 was designed to provide a Rosenbluth measurement with both significantly improved sensitivity and greatly reduced systematic uncertainties than previous Rosenbluth measurements, to provide a definitive test of the consistency of the two techniques. The elastic cross section was measured by detecting the struck proton, rather than the scattered electron. This has several important advantages: (1) no ε -dependence to the momentum of the detected proton at fixed Q^2 , (2) much smaller ε -dependence to the measured cross section, (3) larger cross sections at low ε values, and (4) reduced size and ε -dependence of the radiative corrections.

The experiment ran at JLab in May 2002, and the extraction of the form factors is complete.¹ Figure IV-1 shows the extracted values of $\mu_p G_E/G_M$ compared to previous Rosenbluth and polarization transfer results. The new results disagree with the polarization transfer measurements, but are in excellent agreement with the previous Rosenbluth extraction. This rules out most possible explanations of the discrepancy in terms of experimental systematic errors, and also sets significant constraints on any possible error in the radiative corrections related to the scattered electron (which is not detected in this experiment). At this point, it would appear that the discrepancy between these two techniques must be a result of either a systematic error in the polarization transfer measurements, which have all been performed with the same spectrometer and polarimeter, or the result of an unknown physics correction to one or both techniques.

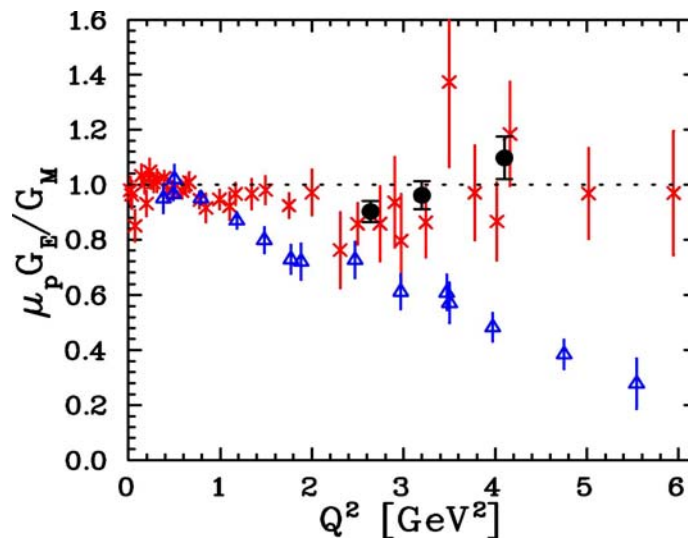


Fig. IV-1. Extracted values of $\mu_p G_E/G_M$ from E01-001¹ (solid circles), a global analysis of previous cross section measurements⁹ (red crosses), and JLab polarization transfer measurements (blue triangles).¹⁰

It is presently believed that two-photon exchange corrections are probably responsible for the discrepancy. While present efforts to calculate effect of two-photon exchange are not yet able to resolve the discrepancy, they do indicate that the effects are large enough to have a significant effect on the Rosenbluth extractions of the form factors. We are

involved in several experiments designed to test the hypothesis that two-photon exchange is responsible for the discrepancy, and if so, to extract the ε and Q^2 dependence of these corrections on both the cross section and polarization data. First, there are experiments that will test the systematic uncertainties of the polarization transfer data by making measurements with a different

spectrometer and polarimeter² or using a polarized target rather than a recoil polarimeter.³ A more direct test will be the comparison of positron-proton to electron-proton scattering, which is sensitive to two-photon exchange corrections. There is some evidence for two-photon corrections at large scattering angle from previous measurements,⁴ and

we have experiments planned to make improved positron-electron comparisons.^{5,6} Finally, there are experiments at JLab that will make precise measurements of the ϵ dependence of the polarization transfer⁷ and unpolarized cross section⁸ with enough sensitivity to measure or strongly constrain the effects of two-photon exchange.

¹I. A. Qattan *et al.*, Phys. Rev. Lett. **94**, 142301 (2005).

²JLab experiment E04-108, "Measurement of G_{Ep}/G_{Mp} to $Q^2 = 9 \text{ GeV}^2$ Via Recoil Polarization", C. F. Perdrisat, V. Punjabi, M. K. Jones, and E. Brash, spokespersons.

³JLab proposal PR04-111, "Measurements of G_{Ep}/G_{Mp} Using Elastic Polarized $\bar{p}(\bar{e}, e')p$ Up to $Q^2 = 5.6 \text{ (GeV/c)}^2$ ", X. Zheng, J. R. Calarco, and O. A. Rondan, spokespersons.

⁴J. Arrington, Phys. Rev. C **69**, 032201(R) (2004).

⁵VEPP-3 experiment, "Two-Photon Exchange and Elastic Scattering of Electrons/Positrons On the Proton", J. Arrington and D. M. Nikolenko, spokespersons.

⁶JLab experiment E06-116, "Beyond the Born Approximation: A Precise Comparison of Positron-Proton and Electron-Proton Elastic Scattering in CLAS", A. Afanasev, J. Arrington, W. K. Brooks, K. Joo, B. A. Raue, and L. B. Weinstein, spokespersons.

⁷JLab experiment E04-019, "Measurement of the Two-Photon Exchange Contribution in ep Elastic Scattering Using Recoil Polarization", R. Suleiman, L. Pentchev, C. F. Perdrisat, and R. Gilman, spokespersons.

⁸JLab experiment E05-017, "A Measurement of Two-Photon Exchange in Unpolarized Elastic Electron-Proton Scattering", J. Arrington, spokesperson.

⁹J. Arrington *et al.*, Phys. Rev. C **71**, 015202 (2005).

¹⁰M. K. Jones *et al.*, Phys. Rev. Lett. **84**, 1398 (2000); O. Gayou *et al.*, Phys. Rev. Lett. **88**, 092301 (2002).

a.2. High-Resolution Search for the Θ^+ Pentaquark at Jlab (P. E. Reimer, J. Arrington, K. Hafidi, R. J. Holt, D. H. Potterveld, E. C. Schulte, X. Zheng, and the E05-009 Collaboration)

Quantum Chromodynamics (QCD) governs the way in which quarks and gluons are bound into hadrons. Until recently, only two different configurations of quarks and antiquarks have been observed: mesons ($\bar{q}q$) and baryons (qqq). These are not the only configurations which can satisfy the basic QCD requirement that hadronic matter is color-neutral—many other configurations exist that also satisfy this condition. One example is the pentaquark ($qqqq\bar{q}$) configuration. Recently, experimental evidence and theoretical work have strongly suggested the existence of a pentaquark state, known as the Θ^+ with a mass near 1540 MeV. Experiment 05-009¹ at JLab will definitively establish or dismiss the existence of the Θ^+ pentaquark. If the Θ^+ exists, the experiment will determine its mass and measure its width.

The experiment will observe the decay products of the Θ^+ in the reactions ${}^2\text{H}(e, K^+K^+n)e'$ and ${}^2\text{H}(e, e'K^+n)K^-$. The K^+ and the neutron will be detected in the BigBite spectrometer and a large, high

resolution neutron detector, respectively. The invariant mass of the K^+n system will be reconstructed to search for the Θ^+ . The remaining kaon or electron will be detected in the HRS spectrometer as a tag on the event. Because of space limitations between the detectors and the beamline, both BigBite and the neutron array will be located out-of-plane. The expected instrumental resolution on the invariant mass is 2.1 MeV (FWHM) and the mass will be established with an absolute accuracy of 0.5 MeV. Based on existing data from Spring-8, the photoproduction cross-section of the Θ^+ is expected to be at least 1.6 nb. Even for a cross-section this small, the Θ^+ could be observed in this experiment with a signal that is seven times that of the statistical fluctuations.

This experiment was approved in early 2005 and current efforts are focused on optimizing the design and constructing the BigBite spectrometer detector package. The experiment could be ready to collect data in late 2007.

¹J. P. Chen *et al.*, "High Resolution Study of the Resonance in nK^+ System", proposal 05-009 to the JLab PAC, G. Cates, P. E. Reimer, B. Wojtsekhowski, spokespersons, December 6, 2004.

a.3. Search for Additional Pentaquark States at Jlab (P. E. Reimer, J. Arrington, K. Hafidi, E. C. Schulte, X. Zheng, and the E04-012 Collaboration)

All observed hadrons have fallen into two categories, mesons made of a quark-antiquark pair mesons ($\bar{q}q$) and baryons composed of three quarks (qqq). These are, however, not the only configurations of quarks and antiquarks allowed by the underlying theory, Quantum Chromodynamics. Configurations not fitting into the meson and baryon framework are known as "exotics". A possible exotic configuration is a pentaquark state with four quarks and an antiquark ($qqqq\bar{q}$). Recently, experimental evidence and theoretical work have suggested the existence of a pentaquark state, known as the Θ^+ with a mass near 1540 MeV. Within the Chiral Soliton model, this state is a member of a set of 10 pentaquark states known as an antidecuplet. Using Hall A at JLab, E04-012¹ was able to search for several antidecuplet-partner states to the Θ^+ . Specifically, the experiment searched for the Σ^0 member of the antidecuplet in the reaction $H(e,e'K^+)X$ and the N^0 in the reaction $H(e,e'\pi^+)X$, by reconstructing the missing mass of the

system. Although these states are not explicitly exotic, the discovery of a narrow state would be a valuable confirmation of the existence of an antidecuplet of states. In addition, the experiment searched for the exotic isospin partner state, Θ^{++} , in the $H(e,e'K^-)X$ reaction. Assuming the mass of the Θ^+ to be around 1540 MeV, the antidecuplet structure limits the possible masses of the partners. In addition, the reported narrowness of the Θ^+ leads implies the partner states are also likely to be narrow. The experiment used collected data in May and June, 2004, using the HRS spectrometers to detect the scattered electron and the K^+ , π^+ and K^- respectively. The mass ranges accessible to the experiment were $1530 < M(\Sigma^0) < 1820$ MeV, $1600 < M(N^0) < 1830$ MeV and $1500 < M(\Theta^{++}) < 1600$ MeV. Preliminary results show no evidence for any narrow resonances within the candidate regions. Ongoing efficiencies studies and better understanding of the background will allow for strict upper limits to be placed on the existence of these states.

¹J. P. Chen *et al.*, "High Resolution Study of the 1540 Exotic State," proposal 04012 to the JLab PAC, P. E. Reimer and B. Wojtsekhowski, spokespersons, December 2, 2003.

a.4. $N \rightarrow \Delta$ Transition Form Factors (J. Arrington, K. Hafidi, R. J. Holt, P. E. Reimer, E. C. Schulte, X. Zheng, and the JLab E01-002 Collaboration)

Measurements of the nucleon transition form factors provide additional information on the structure of the nucleon and nucleon excitations, which complement the measurements of the nucleon elastic form factors. Experiment E01-002 was performed in the spring of 2003 and measured electroproduction of the $\Delta(1232)$ and $S_{11}(1535)$ baryon resonances. The experiment is an extension of previous, lower energy electroproduction experiments¹ at JLab, and at the higher momentum transfers achieved in this experiment we can probe the transition to the high-energy region where perturbative QCD is expected to describe the reaction. Data were taken to separate

out the magnetic dipole (M1), electric dipole (E2), and Coulomb (C2) contributions to the $N \rightarrow \Delta$ transition. The data are currently under analysis.

These measurements will provide a stringent test of recent calculations.²⁻⁴ T.-S. H. Lee has done extensive work on a dynamical model for pion electroproduction in the Δ region.² A. Krassnigg and C. D. Roberts are exploring the effects of axial-vector diquark and pion cloud contributions to the nucleon elastic and $N \rightarrow \Delta$ transition form factors,³ while F. Coester has performed similar explorations of relativistic effects in the elastic and transition form factors.⁴

¹V. Frolov *et al.*, Phys. Rev. Lett **82**, 45 (1999); C. S. Armstrong *et al.*, Phys. Rev. D **60**, 052004 (1999).

²T. Sato and T.-S. H. Lee, Phys. Rev. C **63**, 055201 (2001); T. Sato, T.-S. H. Lee, and T. Nakamura, nucl-th/041182 (2004).

³R. Alkofer *et al.*, nucl-th/0412045 (2004).

⁴B. Julia-Diaz *et al.*, Phys. Rev. C **69**, 035212 (2004).

a.5. The Charged Pion Form Factor (J. Arrington, K. Hafidi, R. J. Holt, P. E. Reimer, E. C. Schulte, X. Zheng, and the JLab E01-004 Collaboration)

A complete understanding the structure of the nucleon is the defining problem in QCD. However, while experiments on the proton are relatively easy, the complicated structure of a three light-quark system makes modeling of the proton in realistic, QCD-based models, is difficult. The pion structure is simpler, and can in some cases provide a better meeting ground between theory and experiment in the study of QCD. Experiment E01-004 is an extension to the previous JLab measurement¹ of the pion form factor, and will improve measurements of

the form factor at 1.6 GeV^2 , the highest value at which the form factor has been measured, as well as extend measurements to 2.5 GeV^2 . These measurements can be used to test models of hadron structure in a simpler system than the nucleon, where more advanced calculations can be performed. The form factor provides information on spatial distribution of the pion constituents, complementary to the information on the quark momentum distributions from the pion structure function measurements. The experiment ran in the summer of 2003, and the analysis is underway.

¹J. Volmer *et al.*, Phys. Rev. Lett. **86**, 1713 (2001).

a.6. Separated and Unseparated Structure Functions in the Nucleon Resonance

Region (J. Arrington, D. Gaskell, D. F. Geesaman, K. Hafidi, R. J. Holt, B. A. Mueller, T. G. O'Neill, D. H. Potterveld, P. E. Reimer, E. C. Schulte, X. Zheng, and the E94-110, E00-002, E00-108, and E00-116 Collaborations)

At high energies, inclusive electron scattering provides a clean and direct probe of the quark distributions in nucleons. At low energies, this simple picture of electron-quark scattering is not valid and the scattering is better understood in terms of resonance excitations and pion production. Measurements of the unpolarized F_2 structure function show a smooth transition between the deep inelastic regime of quasifree quark scattering to the resonance excitation regions, and on average, the resonance region structure function reproduces the deep inelastic limit¹ when taken as a function of ξ . At large momentum transfer, ξ is equivalent to Bjorken- x and represents the momentum fraction of the struck quark. At lower momentum transfers, ξ takes into account scaling violations due to the finite target mass.

Additional measurements of the F_2 structure function of the proton and deuteron in the transition region were made at JLab to better study the phenomenon¹ of Local Duality. While the structure function does change at low Q^2 values, and resonance structure was

clearly visible, the total strength in the region of any of the prominent resonances is identical to the strength in the DIS region to better than 10% down to $Q^2 = 0.5 \text{ GeV}^2$. Furthermore, for very low ξ values, the structure function shows a valence-like behavior, becoming very small as ξ decreases. A more recent experiment, E94-110, extended these measurements by making a Rosenbluth separation of both F_1 and F_2 . These data provided the first observation of duality in both the longitudinal and transverse channels for the proton. They also provided the first indication of significant longitudinal contributions to resonance electroproduction. Final results have been obtained for the L-T separation of both the resonance region structure function³ (Fig. IV-2) and the elastic electron-proton cross sections.⁴ In 2003, three additional measurements were performed in Hall C to further investigate the nature of duality: E00-116, E02-002, and E00-108. Measurements of F_2 for both the proton and deuteron were extended to higher Q^2 values than in the initial investigations. Measurements of the separated structure functions, F_1 and F_2 , were performed at very low x and Q^2 , to investigate in more detail the valence-like nature of the resonance region structure

functions. Finally, these measurements were extended beyond inclusive scattering, to determine if a similar duality is observed in semi-inclusive scattering, where a single high-momentum pion is

tagged in the final state. These experiments were completed in the summer of 2003, and are the data are currently under analysis.

¹E. D. Bloom and F. J. Gilman, Phys. Rev. Lett. **25**, 1140 (1970).

²I. Niculescu *et al.*, Phys. Rev. Lett. **85**, 1182 (2000); *ibid.*, **85**, 1186 (2000).

³M. E. Christy *et al.*, Phys. Rev. C **70**, 015206 (2004).

⁴Y. Liang *et al.*, nucl-ex/0410027 (2004).

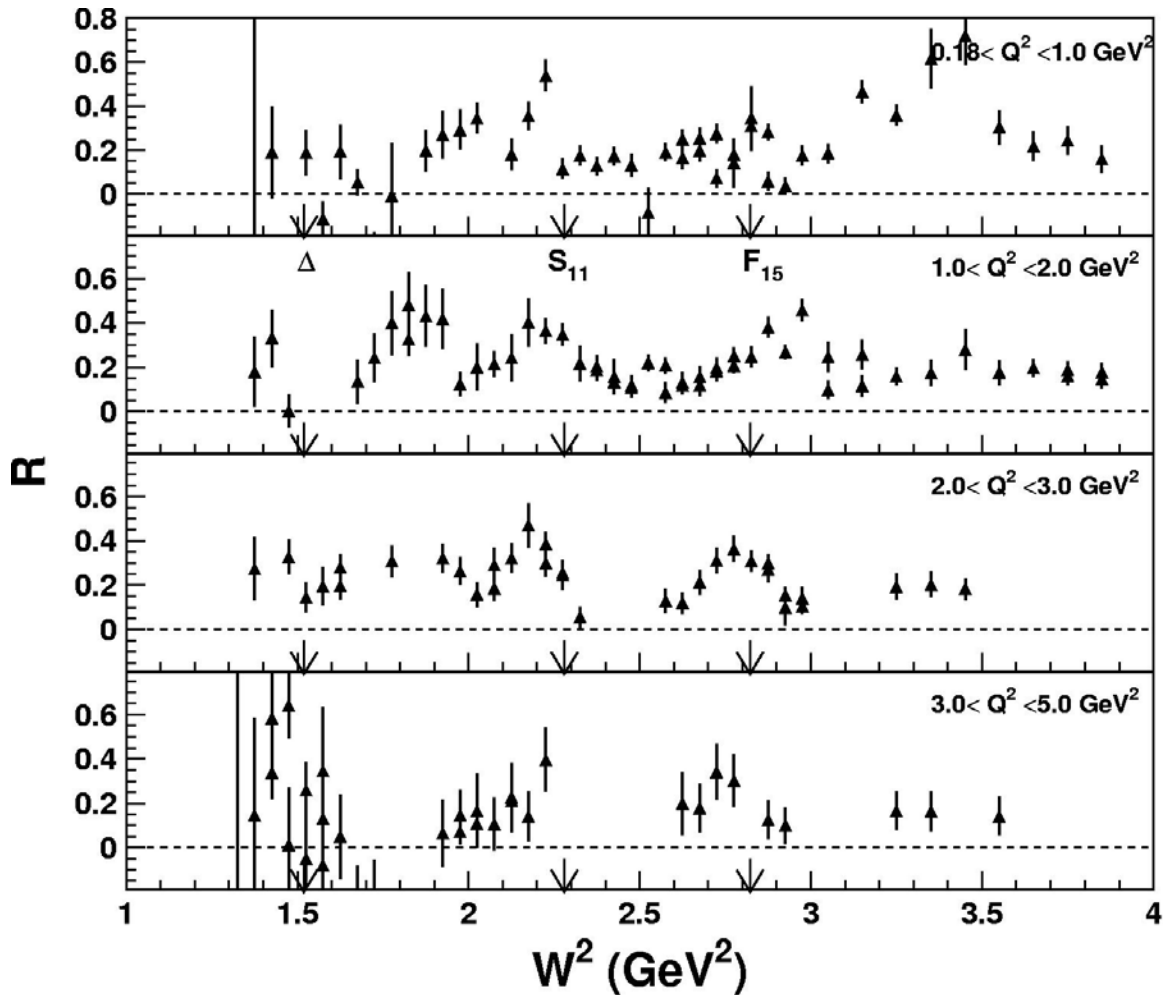


Fig. IV-2. Extracted value of $R = \sigma_L / \sigma_R$ as a function of W^2 for four different ranges in Q^2 . The arrows indicate the positions of the Δ , S_{11} , and F_{15} resonance regions.

B. HADRONS IN THE NUCLEAR MEDIUM

b.1. Search for the Onset of Color Transparency: JLab E02-110 Experiment

(K. Hafidi, B. Mustapha, J. Arrington, A. El Alaoui, L. El Fassi, D. F. Geesaman, R. J. Holt, D. H. Potterveld, P. E. Reimer, E. C. Schulte, X. Zheng, and Hall B Collaboration)

According to QCD, pointlike colorless systems, such as those produced in exclusive processes at high Q^2 have quite small transverse sizes. Therefore, they are expected to travel through nuclear matter experiencing very little attenuation. This phenomenon is known as color transparency (CT). An analogous mechanism is well known in QED: the interaction cross section of an electric dipole is proportional to its square size. As a result the cross section vanishes for objects with very small electric dipole moments. Since color is the charge of QCD, and by analogy to QED, the cross section of a color-neutral dipole, as formed by a pair of oppositely colored quarks for instance, is also predicted to vanish for small sized hadrons. Color transparency cannot be explained by Glauber theory and calls upon quark degrees of freedom. Earlier measurements were mainly focused on quasi-elastic hadronic (p,2p)¹ and leptonic (e,e'p)² scattering from nuclear targets. None of these experiments were able to produce evidence for CT up to $Q^2 \sim 8 \text{ GeV}^2$. The strongest evidence for CT so far comes from Fermilab experiment E791 on the A-dependence of coherent diffractive dissociation of 500 GeV/c pions into di-jets.³ A recent measurement performed by the HERMES collaboration using exclusive ρ^0 electroproduction from nitrogen adds further evidence for the existence of CT.⁴

The main goal of E02-110 experiment⁵ is to search for the onset of CT in the incoherent diffractive ρ^0 electro and photoproduction on deuterium, carbon

and copper. In this process (see Fig. IV-3), the virtual photon fluctuates into $q\bar{q}$ pair which travels through the nuclear medium evolving from its small initial state with a transverse size proportional to $1/Q$, to a "normal size" vector meson detected in the final state. Therefore, by increasing the value of Q^2 one can squeeze the size of the produced $q\bar{q}$ wave packet. The photon fluctuation can propagate over a distance which is known as the coherence length l_c . The coherence length can be estimated relying on the uncertainty principle and Lorentz time dilation as $l_c = 2\nu / (Q^2 + M_{q\bar{q}}^2)$, where ν is the energy of the virtual photon and $M_{q\bar{q}}$ is the mass of the $q\bar{q}$ pair dominated by the ρ^0 mass in the case of exclusive ρ^0 electroproduction. What is measured in the reaction is how transparent the nucleus appears to "small size" ρ^0 by taking the ratio of the nuclear per-nucleon (σ_A/A) to the free nucleon (σ_N) cross-sections, which is called nuclear transparency $T_A = \sigma_A/A\sigma_N$. Consequently, the signature of CT is an increase in the nuclear transparency T_A with increasing hardness (Q^2) of the reaction. Recent theoretical calculations by Kopeliovich *et al.*⁶ predicted an increase of more than 40% at $Q^2 \sim 4 \text{ GeV}^2$. However, one should be careful about other effects that can imitate this signal. Indeed, measurements by HERMES have shown that T_A increases when l_c varies from long to short compared to the size of the nucleus. This so-called coherence length effect can mock the signal of CT and should be under control to avoid confusing it with the CT effect. Therefore, experiment E02-110 intends to measure the Q^2 dependence of the transparency T_A at fixed coherence length l_c .

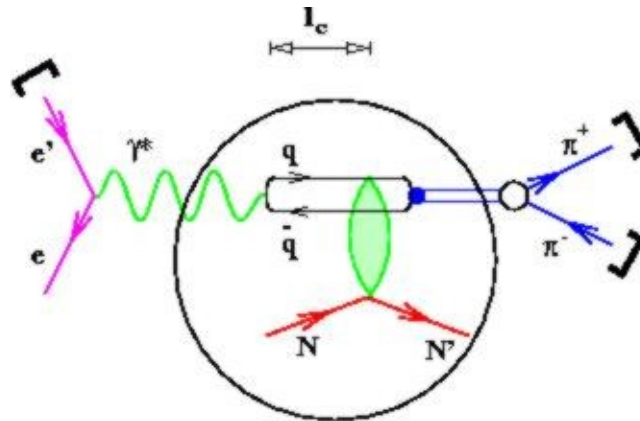


Fig. IV-3. Exclusive leptoproduction of the ρ^0 meson.

The experiment was performed using the CEBAF Large Acceptance Spectrometer (CLAS)⁷ in Hall B of the JLab. The data were taken with both 4 and 5 GeV electron beams incident on 4 cm liquid deuterium target and a solid target (0.4 mm thick ^{56}Fe and 1.72 mm thick ^{12}C) simultaneously. The run period was from December 2003 to March 2004. The data were recorded at an instantaneous luminosity of $2 \times 10^{34} \text{ cm}^{-2} \text{ s}^{-1}$. Figure IV-4 shows the projected uncertainties for complementary I_c

values to map the whole Q^2 region up to 4 GeV^2 using a 6 GeV electron beam and a 2 GeV photon beam on ^{56}Fe versus deuterium. Because the experiment was allocated only 70% of the approved beam time and the highest beam energy available was 5 GeV instead of 6 GeV, the photoproduction measurements will be performed later and the highest Q^2 the measurements will be 3 GeV^2 with a statistical error comparable to that proposed for 4 GeV^2 . The data analysis is in progress.

¹A. S. Carroll *et al.*, Phys. Rev. Lett. **61** 1698 (1988); Y. Mardor *et al.*, Phys. Rev. Lett. **81** 5085 (1998); A. Leksanov *et al.*, Phys. Rev. Lett. **87**, 212301 (2001).

²N. C. R. Makins *et al.*, Phys. Rev. Lett. **72**, 1986 (1994); T. G. O'Neill *et al.*, Phys. Lett. **B351**, 87 (1995); D. Abbott *et al.*, Phys. Rev. Lett. **80**, 5072 (1998); K. Garrow *et al.*, Phys. Rev. C **66**, 044613 (2002).

³E. M. Aitala *et al.*, Phys. Rev. Lett. **86**, 4773 (2001).

⁴A. Airapetian *et al.*, Phys. Rev. Lett. **90**, 052501 (2003).

⁵JLab experiment E02-110, " Q^2 Dependence of Nuclear Transparency for Incoherent ρ^0 Electroproduction", K. Hafidi, B. Mustapha, and M. Holtrop, spokespersons.

⁶B. Kopeliovich *et al.*, Phys. Rev. C **65**, 035201 (2002).

⁷B. Mecking *et al.*, Nucl. Instrum. Methods **A503/3**, 513 (2003).

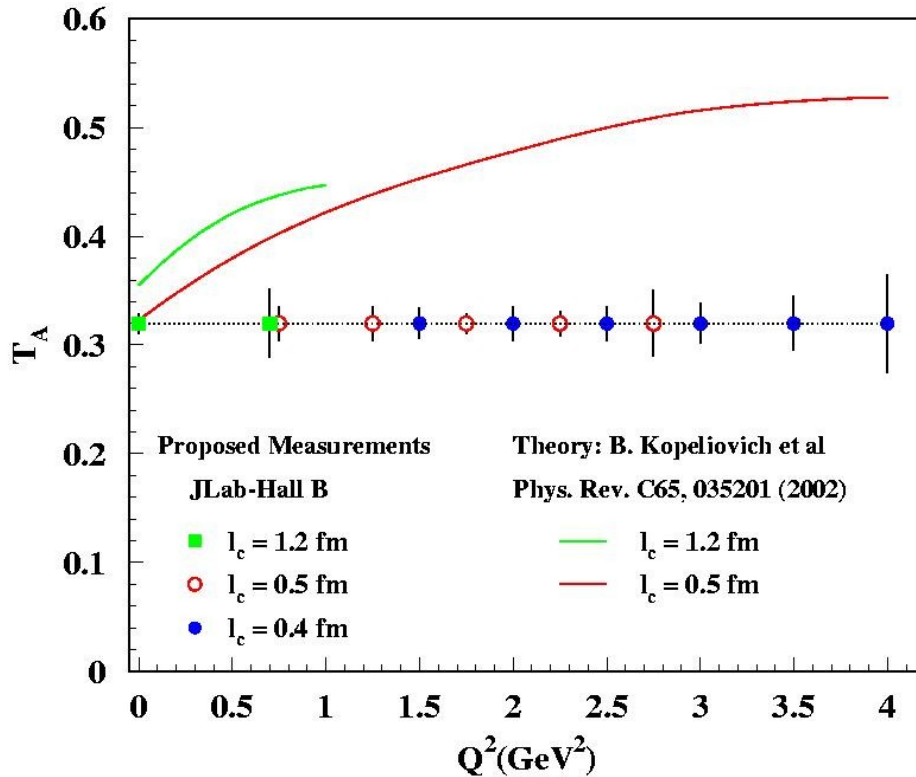


Fig. IV-4. Theoretical predictions and expected statistical accuracy.

b.2. Measurement of High Momentum Nucleons in Nuclei and Short Range Correlations

(J. Arrington, D. F. Geesaman, K. Hafidi, R. J. Holt, H. E. Jackson, P. E. Reimer, E. C. Schulte, X. Zheng, and the E02-019 Collaboration)

Inclusive scattering from nuclei at low energy transfer (corresponding to $x > 1$) is dominated by quasielastic scattering from nucleons in the nucleus. As the energy transfer decreases, the scattering probes nucleons of increasing momentum allowing us to map out the distribution of high momentum nucleons. These data can be used to constrain the high momentum components of nuclear spectral functions.¹ In addition, as the high momentum nucleons are dominantly generated by short-range correlations (SRCs), these data allow us to examine the strength of two-nucleon correlations in heavy nuclei.

Experiment E02-019² ran in late 2004 and measured inclusive scattering at large Q^2 over a broad range in x (up to $x = 3$). The high Q^2 values in this experiment should simplify the extraction of the high momentum components, as effects such as final state interactions are reduced at large Q^2 . The measurement focused on

^2H , ^3He , and ^4He , but data were also taken on several heavier nuclei. Measurements with few-body nuclei allow contact with theoretical calculations *via* essentially "exact" calculations for few-body systems. This can be used to study in detail contributions to the interaction beyond the impulse approximation (*e.g.*, final state interactions for scattering from correlated nucleons). Data on heavy nuclei can then be used to constrain the high momentum components of their spectral functions, as well as allowing an extrapolation to infinite nuclear matter.

These data provide sensitivity to the extremely high momentum components of the nuclear wave function, probing nucleons with momenta in excess of 1000 MeV/c. This will improve our ability to study the structure of nucleon correlations in nuclei. Direct comparisons of heavy nuclei to deuterium at large x will allow us to map out the strength of two-nucleon

correlations in both light and heavy nuclei. These data are expected to be significantly more sensitive to the presence of multi-nucleon correlations. Just as the ratio of heavy nuclei to deuterium at $x \gtrsim 1.5$ shows that the distribution in heavy nuclei is dominated by two-nucleon correlations, a similar ratio of heavy nuclei to ^3He at $x \gtrsim 2.5$ may provide the first experimental signature of three-nucleon correlations. Figure IV-5 shows the yield from ^3He at 18° .

In addition to probing nucleon distributions and short-range correlations, these data fill in a significant void in

our knowledge of the nuclear structure function. Little data exist for nuclei at large x , yet such data are important in the study of scaling and duality in nuclei,³ higher twist effects,^{4,5} and nuclear dependence of the structure function.⁶ In addition the $x > 1$ structure function must be included in studies of the energy-momentum sum rule and analysis of the QCD moments.⁵ While E02-019 emphasized the study of the high momentum nucleons in nuclei, it also provides the data necessary for a variety of studies.

¹J. Arrington *et al.*, Phys. Rev. Lett. **82**, 2056 (1999).

²JLab experiment E02-019, "Inclusive Scattering from Nuclei at $x > 1$ and High Q^2 with a 6 GeV Beam", J. Arrington, D. B. Day, A. F. Lung, and B. W. Filippone, spokespersons.

³J. Arrington *et al.*, Phys. Rev. C **64**, 014602 (2001); J. Arrington, R. Ent, C. E. Keppel, J. Mammei, and I. Niculescu, nucl-ex/0307012.

⁴I. Niculescu, C. Keppel, S. Liuti, and G. Niculescu, Phys. Rev. D **60**, 094001 (1999).

⁵J. Arrington, R. Ent, C. E. Keppel, and I. Niculescu, in preparation.

⁶K. Egiyan *et al.*, Phys. Rev. C **68**, 014313 (2003).

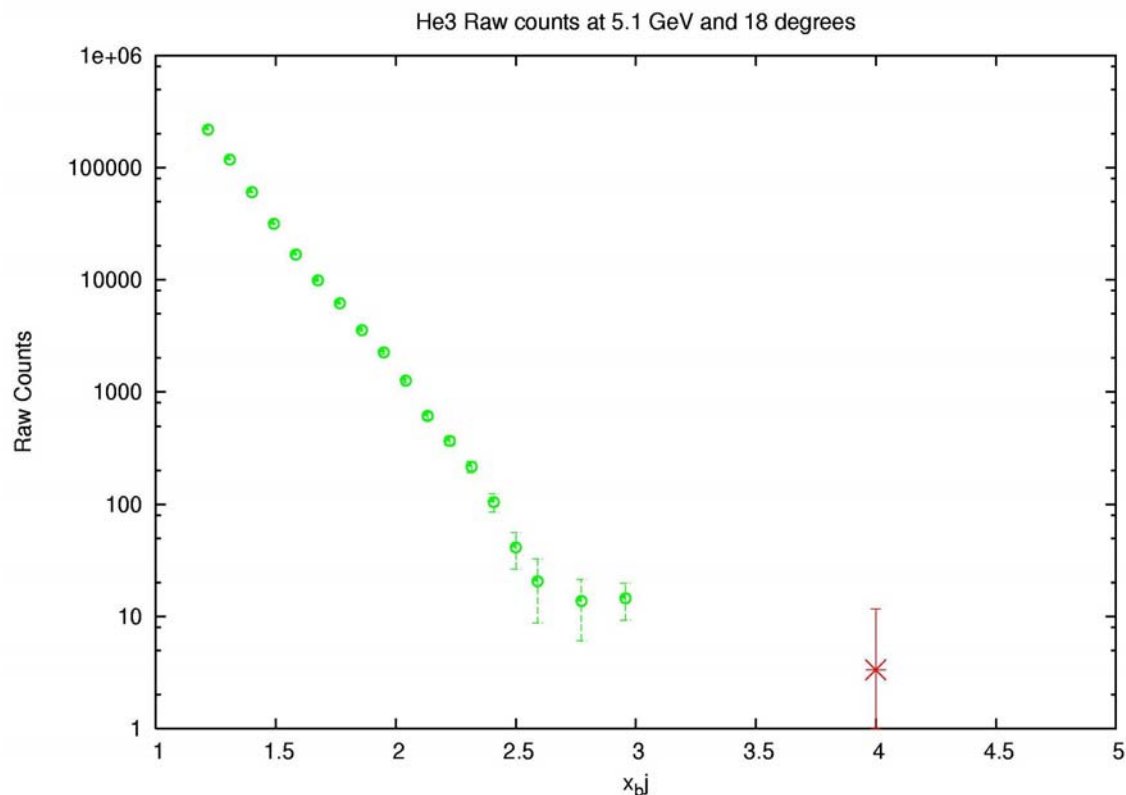


Fig. IV-5. Yield as a function of Bjorken x for the ^3He data at 18° . We have good statistics all the way up to $x = 3$, the kinematic endpoint for scattering from ^3He . The red point shows the sum of counts above $x = 3$.

b.3. Measurement of the EMC Effect in Very Light Nuclei (J. Arrington, D. F. Geesaman, K. Hafidi, R. J. Holt, H. E. Jackson, D. H. Potterveld, P. E. Reimer, E. C. Schulte, X. Zheng, B. Zeidman, and the E03-103 Collaboration)

For more than twenty years, it has been known that the quark momentum distribution of nuclei is not simply the sum of the quark distributions of its constituent protons and neutrons. The structure function is suppressed in heavy nuclei at large values of x (corresponding to large quark momenta), and enhanced at low x values. Measurements to date indicate that the overall form of this modification is the same for all nuclei, but the magnitude of the enhancement and suppression is larger for heavier nuclei. Many attempts have been made to explain the EMC effect, but none of the proposed models can fully reproduce the observed modifications, and there is still no consensus on which effect or combination explain the data.

Experiment E03-103¹ ran in Hall C in late 2004 and measured the EMC effect for ³He, ⁴He, and a series of heavier nuclei. Because ⁴He has an anomalously large density for a light nucleus, it is the most sensitive test to determine if the EMC effect scales with A or with nuclear density. More importantly, these measurements of the EMC effect can be

compared to exact few body calculations. If the EMC effect is caused by few nucleon interactions, the universal shape observed in heavy nuclei may be a result of a saturation of the effect, and the shape may be different in few-body nuclei. While most existing data on heavy nuclei show the same x -dependence, there are hints of an A -dependence at large x values,² and calculations³ predict significantly different dependences for very light nuclei. By making precise measurements in light nuclei, we will be able to distinguish between different models of the EMC effect based on their predictions for few-body nuclei.

Finally, a measurement of $A \leq 4$ nuclei will help constrain models of the EMC effect in deuterium. Models of nuclear effects in deuterium and ³He must be used to extract information on neutron structure, and a high precision measurement including ¹H, ²H, ³He, and ⁴He will give a single set of data that can be used to evaluate these models in several light nuclei. This will help to quantify the model dependence of the neutron structure functions inferred from measurements on ²H and ³He.

¹JLab experiment E03-103, "A Precise Measurement of the Nuclear Dependence of the EMC Effect in Light Nuclei", J. Arrington and D. Gaskell, spokespersons.

²J. Arrington, R. Ent, C. E. Keppel, J. Mammei, and I. Niculescu, nucl-ex/0307012.

³G. I. Smirnov *et al.*, Eur. Phys. J. C **10**, 239 (1999); V. V. Burov *et al.*, Phys. Lett. **B466**, 1 (1999); I. R. Afnan *et al.*, Phys. Rev. C **68**, 035201 (2003); O. Benhar, V. Pandharipande, and I. Sick, Phys. Lett. **B410**, 79 (1997); O. Benhar, private communication.

b.4. Proton Polarization Angular Distribution in Deuteron Photo Disintegration (R. J. Holt, J. Arrington, K. Hafidi, P. E. Reimer, E. C. Schulte, K. Wijesooriya, and JLab E00-007 Collaboration)

The overall goal of experiment¹ E00-007 is to determine the mechanism that governs photoreactions in the GeV energy region. Our previous measurements² of induced polarization in deuteron photodisintegration produced surprising results at photon energies between 1 and 2 GeV. First these results disagreed markedly with previous experiments and secondly there was a remarkable disagreement with the meson-exchange model. The induced polarizations above 1 GeV and at $\theta_{\text{cm}} = 90^\circ$ were near zero, consistent with hadron helicity conservation. The goal of this experiment was to determine the

angular dependence of the polarization. Data were taken for a photon energy of 2 GeV and at five center-of-mass angles: 37° , 53° , 70° , 90° and 110° . The induced polarizations as well as polarization transfers were measured. A new polarimeter that contains both a C and a CH₂ scatterer was used for this experiment.

A significant problem arose in the analysis of the data because of the new "G0 delay by eight" helicity bit-reporting mode. Because the intended time markers in the data stream were not recorded with 100% efficiency, the helicity flags had to be reconstructed with great care. The

extracted form factor ratio agrees well with previous results.

¹JLab proposal E00-007, "Proton Polarization Angular Distribution in Deuteron Photodisintegration", R. Gilman, R. J. Holt, and Z.-E. Meziani, spokespersons.

²K. Wijesooriya *et al.*, Phys. Rev. Lett. **86**, 2975 (2001).

b.5. Measurements of the Nuclear Dependence of $R = \sigma_L/\sigma_T$ at Low Q^2 (J. Arrington, D. F. Geesaman, T. G. O'Neill, D. Potterveld, and the E99-118 Collaboration)

Inclusive electron scattering is a well-understood probe of the partonic structure of nucleons and nuclei. Deep inelastic scattering has been used to make precise measurements of nuclear structure functions over a wide range in x and Q^2 . The ratio $R = \sigma_L/\sigma_T$ has been measured reasonably well in deep inelastic scattering at moderate and high Q^2 using hydrogen and deuterium targets. However, R is still one of the most poorly understood quantities measured in deep inelastic scattering and few measurements exist at low Q^2 or for nuclear targets. Existing data rule out significant nuclear effects in R only at moderate to large values of Q^2 .

JLab experiment E99-119 is a direct measurement of R at low x and low Q^2 . The experiment was performed in July of 2000 and data were taken for hydrogen, deuterium, and heavier nuclei. The data are largely analyzed, but the cross section extraction at extremely small values of x and Q^2 involve large radiative corrections. While the radiative corrections will limit the region for which R can be extracted, these data are ideal for testing the radiative correction procedures in these extreme kinematics, and in particular the corrections coming from the nuclear elastic contributions. The final results for hydrogen and deuterium will be available soon and the analysis of the nuclear targets, with the larger radiative corrections, will be available shortly thereafter.

b.6. Electroproduction of Kaons and Light Hypernuclei (J. Arrington, K. Bailey, F. Dohrmann, D. F. Geesaman, K. Hafidi, B. Mueller, T. G. O'Neill, D. H. Potterveld, P. E. Reimer, B. Zeidman, and the E91-016 Collaboration)

JLab experiment E91-016 "*Electroproduction of Kaons and Light Hypernuclei*" is a study of the production of kaons on targets of H, D, ³He, and ⁴He at an incident electron energy of 3.245 GeV and $Q^2 \approx 0.37$ GeV². For H and D targets, additional data were obtained at an energy of 2.445 GeV and $Q^2 \approx 0.5$ GeV². The scattered electrons and emergent kaons were detected in coincidence with the use of the HMS and SOS spectrometers in Hall C. In addition to obtaining spectra, angular distributions were measured at forward angles with respect to the virtual photons.

The fundamental interaction being studied is the $N(e,e'K^+)Y$ where Y is either Λ or Σ and N is a nucleon, either free or bound in a nucleus. For H, the final state can only be a Λ or Σ^0 , with a missing mass spectrum consisting of two sharp peaks. For heavier targets, however, not only can Σ^- be produced on the neutron, but the relative motion of the bound nucleons results in quasi-free broadening of the peaks. Since there is no known bound state in the

mass 2 hyper-nuclear system, only quasi-free production is observed. For the heavier targets, ^{3,4}He, both Fermi broadening and a rapidly increasing number of final state configurations makes it more difficult to separate the various contributions. Because of the small mass difference between Σ^0 and Σ^- , distinguishing between these contributions is not possible without assuming that the Λ/Σ^0 ratio is the same as that for the free proton. Subtraction of the normalized Σ^0 contribution yields the first accurate value for Σ^- production on the neutron. In the above cases, the final state consists of the kaon, the hyperon, and the spectator nucleons from the target nucleus. For the ³He and ⁴He targets, one can also have final states consisting of only the kaon and a hypernucleus, where the produced hyperon is bound in the strangeness = 1 hypernucleus. Finally, the excellent particle identification and large phase space acceptance allowed an ancillary study of the electroproduction of ω mesons on the proton.

The kaon and ω electroproduction measurements from this experiment have formed the basis of five Ph.D.

theses. In 2004, the angular distributions of kaon electroproduction from ${}^3\text{He}$ and ${}^4\text{He}$ yielding bound hypernuclei¹ (Fig. IV-6) and measurements of ω electroproduction² were published. The results of the

measurements of Λ and Σ production from the proton as well as Λ , Σ and Σ^0 production from light nuclei are being prepared for publication.

¹F. Dohrmann *et al.*, Phys. Rev. Lett. **93**, 242501 (2004).

²P. Ambrozewicz *et al.*, Phys. Rev. C **70**, 035203 (2004).

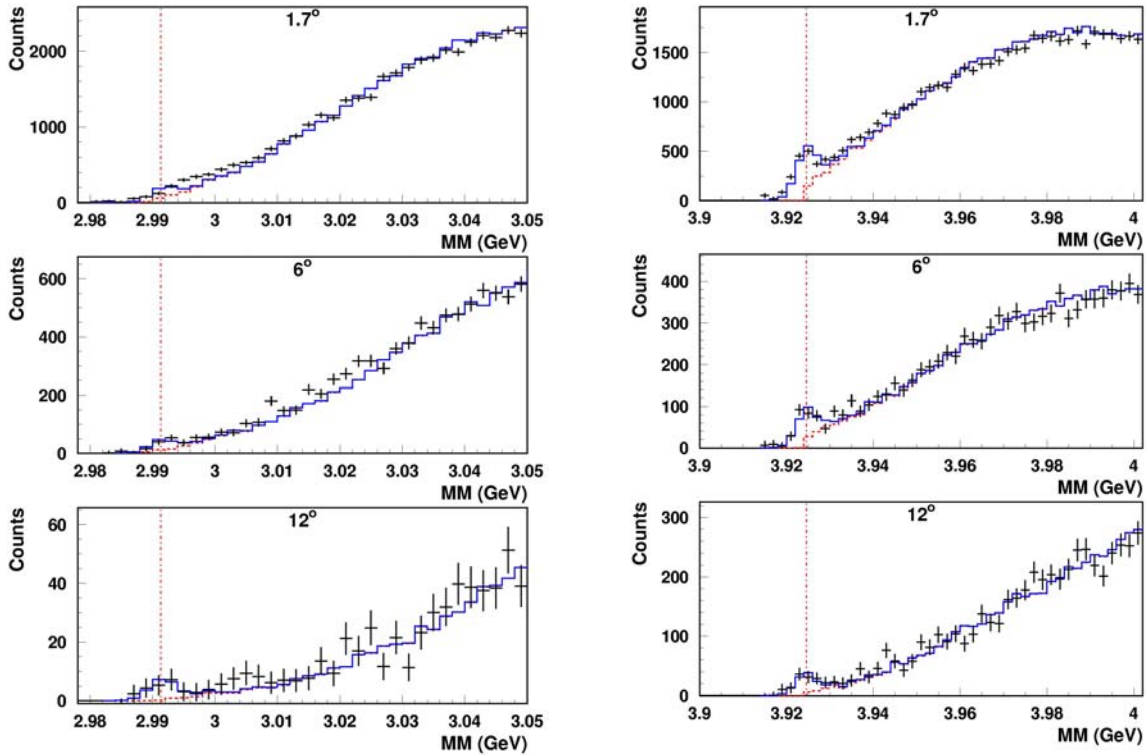


Fig. IV-6. Reconstructed missing mass spectra for ${}^3\text{He}$ (left) and ${}^4\text{He}$ (right) in the region of quasifree Λ production. The dashed lines are the simulations of the quasifree reactions ${}^{3,4}\text{He}(e,e'K^+)$, while the solid lines include the bound state reaction ${}^{3,4}\text{He}(e,e'K^+) {}_{\Lambda}^{3,4}\text{H}$. The thresholds for quasifree production are denoted by vertical lines.

C. QUARK STRUCTURE OF MATTER

c.1. The Structure of the Pion (P. E. Reimer, R. J. Holt, and K. Wijesooriya)

The light mesons have a central role in nucleon and in nuclear structure. The masses of the lightest hadrons, the mesons, are believed to arise from chiral symmetry breaking. The pion, being the lightest meson, is particularly interesting not only because of its importance in effective theories, but also because of its importance in explaining the quark sea in the nucleon and the nuclear force in nuclei. Most of our information about the pion structure in the valence region originates from pion-induced Drell-Yan reactions on a W target.¹ A long-standing mystery is the marked deviation of the high- x pion structure from perturbative QCD. At a Q^2 of 16 GeV² where Drell-Yan measurements are performed, one might expect perturbative QCD to be valid. In addition, the high- x behavior of the pion structure was questioned² recently on more fundamental grounds. We have re-analyzed the Drell-Yan data and made the following

improvements: Next-to-leading order analysis, modern nucleon parton distributions, modern nuclear effects in W and a less-restrictive parameterization of the pion structure function. While the results of this re-analysis indicate that the pion's valence parton distributions at high- x deviates significantly from the earlier leading-order analysis and is in better agreement with Dyson-Schwinger calculations as well as perturbative QCD, there remains substantial disagreement with these calculations.

Unfortunately, existing pion-nucleon Drell-Yan scattering data have limited x -resolution in the high- x region, and this may skew the interpretation of these data. Studies are being made to determine the feasibility of new measurements of the pion-nucleon Drell-Yan process using the E906 apparatus at Fermilab to determine if better x -resolution is achievable.

¹J. S. Conway *et al.*, Phys. Rev. D **39**, 92 (1989).

²M. B. Hecht *et al.*, Phys. Rev. C **63** 025213 (2001).

c.2. Studies of Nucleon Spin Structure and Related Measurements of Deep-Inelastic Scattering at HERA (H. E. Jackson, A. El Alaoui, K. G. Bailey, T. P. O'Connor, K. Hafidi, D. H. Potterveld, P. E. Reimer, Y. Sanjiev, and the HERMES Collaboration)

HERMES, HERA measurement of spin, is an international collaboration of 30 institutions formed to address a basic question of hadron structure. How do the spins of its constituent quarks combine with the spin of the glue and the angular momentum of the partons to give the proton its spin of 1/2? The HERMES experiment uses polarized internal targets in the HERA 30 GeV e^+e^- storage ring at the DESY Laboratory. By emphasizing semi-inclusive deep-inelastic scattering (DIS) in which an identified hadron is observed in coincidence with the scattered lepton, HERMES has brought a new dimension to studies of nucleon spin structure. HERMES achieved a new milestone recently with the completion and publication¹ of a quark-flavor decomposition of the spin of the proton based on measurements of semi-inclusive double spin asymmetries which avoids the need for use of data from hyperon decay and the assumption of SU(3) symmetry. This is the first such measurement using target double-spin asymmetries

for charged pions and kaons. In contrast to previous results based solely on inclusive measurements, all extracted sea quark polarizations are consistent with zero, and within experimental errors the light quark sea helicity densities are flavor symmetric. The measurement was one of the principal objectives of the HERMES program as originally conceived.

Current activities, which are scheduled to continue through October of 2005, are focused on measurements with a transversely polarized target which probes the effects of transverse motion of the quarks. The single-spin asymmetries under study are related to the third structure function, transversity, required to describe nucleon spin structure in leading order. Results of the first phase of this study which have just appeared² have been used for the first time to extract the signal for the quark transversity as generated by the Collins fragmentation process. From the same data a signal has been extracted for a correlation between transverse target

polarization and intrinsic transverse momentum of quarks as represented by the previously unmeasured Sivers distribution function. In an analysis to be reported shortly, these data have been combined with previously reported results for longitudinally polarized proton targets to evaluate the subleading-twist contributions to the longitudinal case.

In 2006 the focus of the HERMES program will change with the installation of a large acceptance recoil detector which will enhance the solid angle acceptance and missing mass resolution in measurements of hard exclusive processes such as electroproduction of mesons and real photons (deeply virtual Compton scattering). HERMES already has studied several exclusive reactions, including exclusive production of charged and neutral pions, and of ρ mesons. Recent measurements of deeply virtual Compton scattering include the first measurements of a beam-charge asymmetry. The intense interest in these processes stems from their description in terms of Generalized Parton Distributions (GPDs) which are expected to provide access to the quark total angular momentum content of the nucleon. With the new detector, the exclusivity of events will be established by positive identification of the recoil proton and measurement of its recoil momentum. The enhanced selectivity of

these measurements will provide a unique opportunity to assess the promise of GPDs as the next step in understanding the spin structure of the nucleon.

A very productive program of measurements of unpolarized DIS continues with the use of high-luminosity dedicated running exclusively for HERMES during the last hour of each fill of the HERA e^+/e^- storage ring. Attempts to isolate and confirm a previously reported signal for the existence of a 5-quark exotic baryon state at 1540 MeV³ continue with the installation of an event trigger designed to select events with the expected pentaquark decay topology. Studies of quark propagation in nuclear matter are continuing with measurements of the ratio of hadron multiplicities in heavy targets to those in deuterium. Data on the kinematic dependences of these ratios as measured for different hadron types provide new insights into the propagation process. Data on the multiplicities measured for proton and deuteron targets currently under analysis will shortly provide accurate measurements of quark fragmentation functions specifically at HERMES kinematics, and provide a rigorous test of factorization. The HERA accelerator will continue operations through the summer of 2007. Every effort is being made to maximize the impact of the beam time that remains. Highlights of recent results are presented below.

¹A. Airapetian *et al.*, Phys. Rev. D **71**, 012003 (2005).

²A. Airapetian *et al.*, Phys. Rev. Lett. **94**, 012002 (2005).

³A. Airapetian *et al.*, Phys. Lett. **B585**, 213 (2004).

c.2.1. Polarization of the Strange Quark Sea in the Proton from Semi-Inclusive Deep-Inelastic Scattering on the Deuteron (H. E. Jackson, A. El Alaoui, K. G. Bailey, T. P. O'Connor, K. Hafidi, D. H. Potterveld, P. E. Reimer, Y. Sanjiev, and the HERMES Collaboration)

The polarization of the strange quarks in the proton is of particular interest, because an explanation of the small net contribution to the nucleon spin from the quark spins under the assumption of SU(3) symmetry implies a significant negative value for this quantity. Such a value would explain the violation of the Ellis-Jaffe sum rule in inclusive deep-inelastic scattering (DIS). However, recent results from HERMES for a flavor decomposition of quark helicity distributions based on semi-inclusive DIS suggest that the polarization of the strange sea is zero or slightly positive. The data are shown in Fig. IV-7. The total strange quark helicity density $\Delta S(x) \equiv \Delta s(x) + \Delta \bar{s}(x)$ carries no isospin. It can be extracted from

measurements of scattering from deuterium alone, which is isoscalar. Effectively, measurements of the inclusive spin asymmetries provide an estimate of the helicity density of the non-strange sea. Using the spin asymmetries measured for charged kaons as the second experimental data set, it is possible to extract directly $\Delta S(x)$. Furthermore, by measuring directly the charged kaon multiplicities at HERMES kinematics, the fragmentation functions relevant to the extraction procedure can be obtained without resort to other experiments. A direct leading-order extraction of $\Delta S(x)$ using this approach is in progress. Because, in contrast to the published data, only the more recently acquired deuterium database is used, the analysis can be carried out

with less stringent data restrictions and attendant higher statistics than that used in the analysis of Fig. IV-7. In parallel, with this effort, a similar analysis chain is being pursued with neutral kaons. With the combined treatment of the spin-asymmetries for

charged and neutral kaons a more accurate measure of $\Delta S(x)$ will be possible. The only assumption made in this analysis is charge-conjugation invariance, and no Monte-Carlo simulations of the fragmentation process are required.

¹A. Airapetian *et al.*, Phys. Rev. D **71**, 012003 (2005).

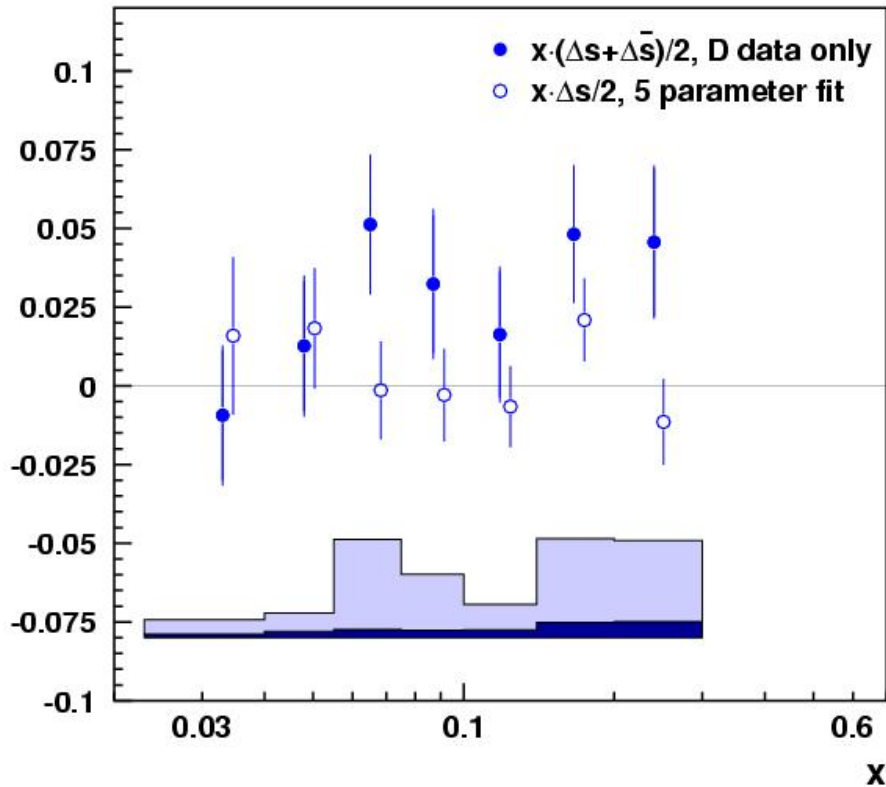


Fig. IV-7. The average strange quark helicity density $x \cdot [\Delta s(x) + \Delta \bar{s}(x)]/2$ from the isoscalar extraction method (full points). For comparison the open symbols denote the results from a five parameter fit, which are offset horizontally for presentation. Both data sets are taken from Ref. 1. The band in the bottom part gives the total systematic uncertainty on the results from the isoscalar extraction. The dark shaded area corresponds to the uncertainty from the input asymmetries, and the open part relates to the uncertainty in fragmentation functions.

c.2.2. Azimuthal Asymmetries and Transversity (H. E. Jackson, A. El Alaoui, K. G. Bailey, T. P. O'Connor, K. Hafidi, D. H. Potterveld, P. Reimer, Y. Sanjiev, and the HERMES Collaboration)

Single-spin asymmetries in the distribution of lepto-produced hadrons in the azimuthal angle around the virtual photon direction are a valuable tool for the exploration of transverse spin and momentum degrees of freedom in nucleon structure. Such asymmetries have been observed in semi-inclusive DIS with unpolarized beams and with targets polarized both longitudinally and transversely with

respect to the incident beam direction. Asymmetries have also been observed with polarized beams and unpolarized nucleons. The asymmetry for a transversely polarized target can be interpreted in terms of the Sivers and the transversity distribution functions, convoluted with the ordinary unpolarized and Collins fragmentation functions, respectively. HERMES recently published the first decomposition of these effects¹ using a transversely

polarized proton target. In the case of targets that are longitudinally polarized, the interpretation is more complex. The HERMES measured lepton asymmetries on a transverse target cited above have been used to eliminate the contribution due to the transverse spin component as seen by the virtual photon, from the measured asymmetries on a longitudinal polarized target, thereby allowing for the

first time, the extraction of the purely subleading twist contribution to the measured lepton asymmetries. This contribution is significantly positive for π^+ mesons and dominates the asymmetries on a longitudinally polarized target previously measured by HERMES. The subleading-twist contribution for π^- mesons is found to be small.

¹A. Airapetian *et al.*, Phys. Rev. Lett. **94**, 012002 (2005).

c.2.3. New Results for Collins and Sivers Asymmetries with a Transversely Polarized Target (H. E. Jackson, A. El Alaoui, K. G. Bailey, T. P. O'Connor, K. Hafidi, D. H. Potterveld, P. E. Reimer, Y. Sanjiev, and the HERMES Collaboration)

The first global evidence for both Collins and Sivers asymmetries was published by the HERMES collaboration in 2005.¹ These results were based on data recorded during the 2002-2003 running period. Running with a transversely polarized target has continued and nearly five times the statistics as was used in the first publication have been accumulated. Results for the unweighted Collins and Sivers moments have been extracted from the data using the same analysis procedures as in the earlier treatment. The Collins moment is generated by a $\sin(\Phi + \Phi_s)$

dependence on the angle Φ between the lepton scattering plane and the hadron production plane and on the target angle Φ_s between the target polarization and the lepton scattering plane. The corresponding dependence for the Sivers moment is $\sin(\Phi - \Phi_s)$. Non-zero values for these azimuthal moments are signatures for significant contributions from the Collins and Sivers effects. The new data shown in Figs. IV-8 and IV-9 confirm with much improved precision the trends observed in earlier measurements. Of particular note is the unexpectedly large Collins moment for negative pions.

¹A. Airapetian *et al.*, Phys. Rev. Lett. **94**, 012002 (2005).

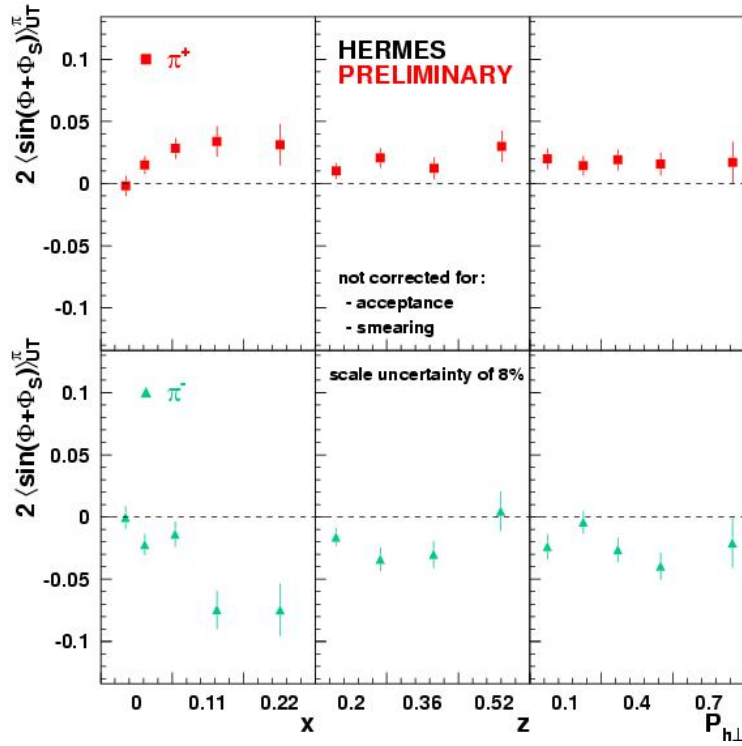


Fig. IV-8. Measured Collins moments for charged pions as a function of x , z , and $P_{h\perp}$. The error bars represent the statistical uncertainties.

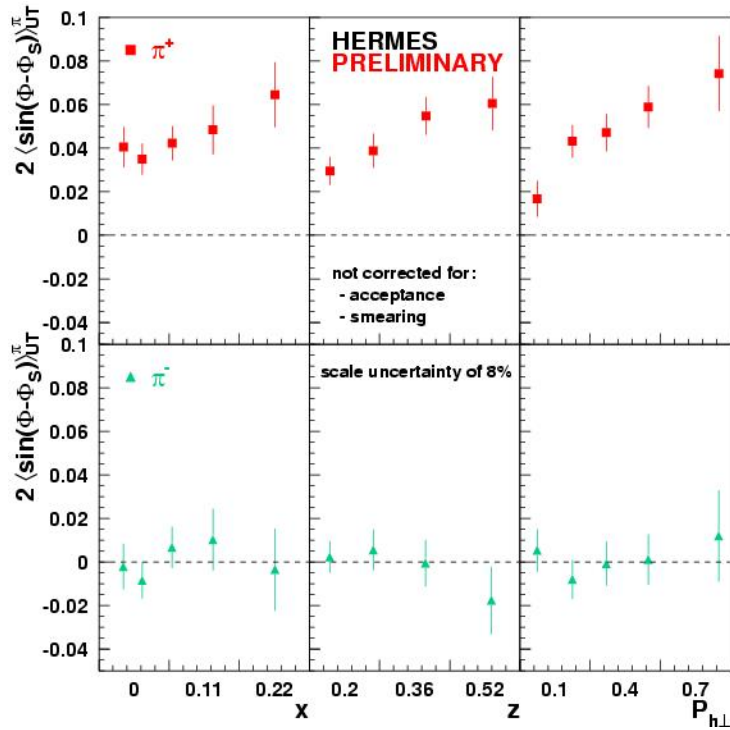


Fig. IV-9. Measured Sivers moments for charged pions as a function of x , z , and $P_{h\perp}$. The error bars represent the statistical uncertainties.

c.2.4. The Deuteron Tensor Polarized Structure Function b_1 (H. E. Jackson, A. El Alaoui, K. G. Bailey, T. P. O'Connor, K. Hafidi, D. H. Potterveld, P. E. Reimer, Y. Sanjiev, and the HERMES Collaboration)

The deep-inelastic scattering (DIS) of leptons by nucleons is characterized by four fundamental structure functions, F_1 , F_2 , g_1 , and g_2 . Polarized beams are required to measure the latter two, and the study of g_1 has been the primary focus of many experiments over the years. When a deuteron is the scatterer, there are four additional fundamental structure functions,¹ b_{1-4} , that arise because the deuteron has spin 1. They have not been measured to date. The first, b_1 , is of considerable interest. It is sensitive to differences in the quark momentum distributions between the 0 helicity (q_0) and the spin-averaged ± 1 helicity ($q^+ + q^-$) states of the hadron. Of leading twist, b_1 should be identically zero for a simple composition of nucleons in an s state. However, a non-zero value is possible through nuclear effects such as binding, the d state of the deuteron, and shadowing effects such as coherent double scattering.^{2,3} If non-zero, it should be taken

into account when extracting the neutron structure functions from deuterium data (hitherto it has been ignored). Moreover, a non-zero value could indicate that the quark sea becomes tensor polarized in the deuteron, which is unexpected in the naive quark model. The HERMES experiment has investigated the tensor spin structure of the deuteron using the 27.6 GeV positron beam of HERA. The use of a tensor polarized deuteron gas target with only a 0.01 residual vector polarization enabled the first measurement of the tensor asymmetry A_{zz}^d and the tensor structure function b_1^d in the kinematic range of the Bjorken variable $0.002 < x < 0.85$ and the squared four-momentum transfer $0.1 < Q^2 < 20 \text{ GeV}^2$. The results are presented in Fig. IV-10. The rise of b_1^d for decreasing values of x can be interpreted either as a significant tensor polarization of the quark sea in the deuteron, or as a shadowing effect in the context of coherent double-scattering models.

¹H. P. Hoodbhoy *et al.*, Nucl. Phys. **B312**, 571(1989).

²J. Edelmann *et al.*, Phys. Rev C **57**, 3392 (1998).

³K. Bora and R. L. Jaffe, Phys. Rev. D **57**, 6906 (1998).

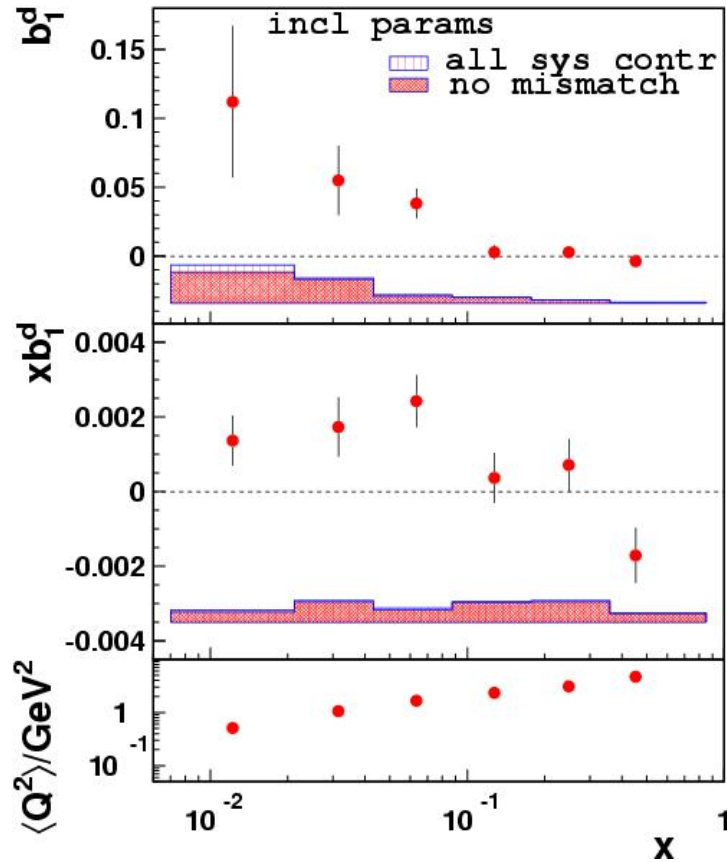


Fig. IV-10. The tensor structure function b_1^d . The error bars are statistical and the shaded bands show the systematic uncertainty, with and without the contribution from possible instrumental asymmetries. The middle panel shows the xb_1^d distribution and the bottom panel shows the average value of Q^2 in each x -bin.

c.2.5. Measurements of Deeply-Virtual Compton Scattering at HERMES (H. E. Jackson, A. El Alaoui, K. G. Bailey, T. P. O'Connor, K. Hafidi, D. H. Potterveld, P. Reimer, Y. Sanjiev, and the HERMES Collaboration)

The concept of Generalized Parton Distributions (GPDs) has recently emerged and generated great interest as a means of studying the dynamics of quarks and gluons in a very general framework. The cleanest way to access GPDs is Deeply Virtual Compton Scattering (DVCS), the production of a real photon in hard exclusive electron scattering. In HERMES experiments the signature for DVCS is an azimuthal asymmetry in the angle ϕ , the azimuthal angle around the virtual photon direction between the lepton scattering plane and the production plane. It is attributed to the interference of the Bethe-Heitler and

DVCS processes. HERMES has already reported substantial beam-spin, target-spin, and beam-charge asymmetries in scattering from proton and deuteron targets. For the first time, DVCS has been measured for nuclear targets. DVCS off nuclei probes GPDs of nuclei, *i.e.*, measures quark properties in nuclei. At small $|t|$, where t is the usual Mandelstam variable, the interference term for heavy nuclei grows with the nuclear charge Z due to the growing Bethe-Heitler amplitude for coherent scattering. A comparison of the asymmetries for deuterium and neon targets is presented in Fig. IV-11. A significantly larger $\sin(\phi)$ moment is observed for neon.

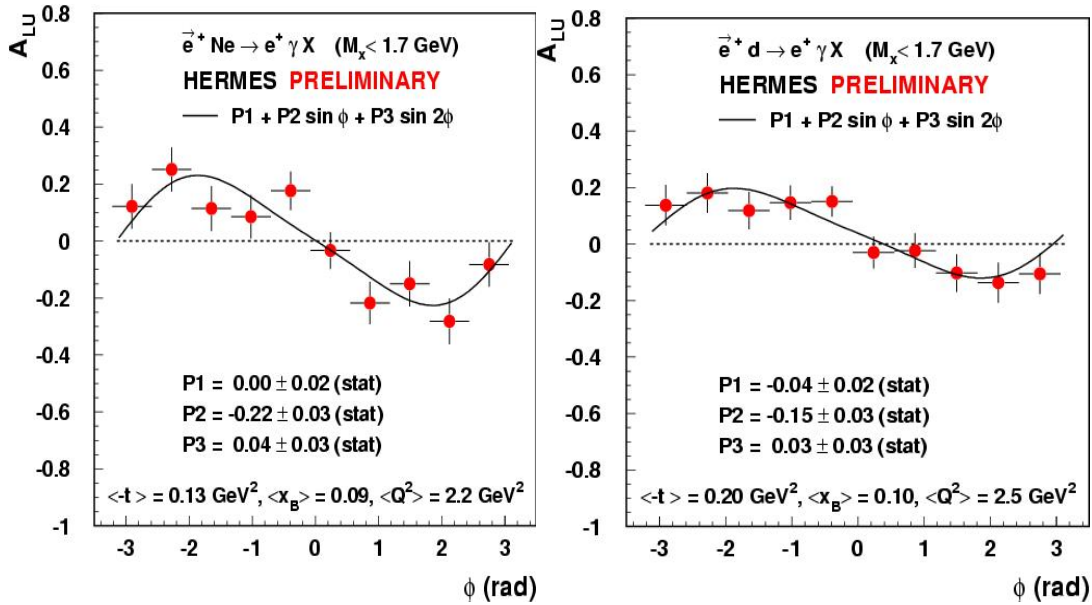


Fig. IV-11. Azimuthal beam charge asymmetries measured for deuterium and neon targets. The $\sin(\phi)$ contribution of the asymmetry for neon (left) is significantly larger than for a deuterium target (right).

c.2.6. Quark Fragmentation to Pions, Kaons, and Nucleons in the Nuclear Environment

(H. E. Jackson, A. El Alaoui, K. G. Bailey, T. P. O'Connor, K. Hafidi, D. H. Potterveld, P. E. Reimer, Y. Sanjiev, and the HERMES Collaboration)

HERMES continues to study the hadronization of quarks into identified hadron types by measuring the nuclear dependence of pion, kaon, and proton multiplicities in targets of krypton, neon, nitrogen, and helium relative to that of a deuterium target. The kinematic and mass dependences of the ratio of multiplicities for heavier targets to deuterium can provide useful constraints on models for the hadronization process. Recently, HERMES published the first data of this type for various identified hadrons, both charged and neutral. The data indicate different formation times for nucleons compared to those of pions and kaons. The data are consistent with an $A^{2/3}$ -dependence predicted by theoretical models which also predict an L^2

dependence on the energy loss of quarks traversing a path length L . HERMES continues to take data in an effort to test this prediction. As part of that effort, measurements have been made of multiplicity ratios for π^0 as a function of the virtual photon energy ν and the relative hadron energy z , and for charged pions, kaons, and (anti)protons as a function of transverse momentum. The 27 GeV data on ${}^4\text{He}$, ${}^{20}\text{Ne}$, and ${}^{84}\text{Kr}$ nuclear targets have been used and the results measured in terms of the ratio of the number of hadrons produced per DIS event for a nuclear target to that on a deuterium target. Figure IV-12 shows the dependence of this ratio on the transverse momentum. The results obtained are sensitive to the production length in the hadronization process on nuclei.

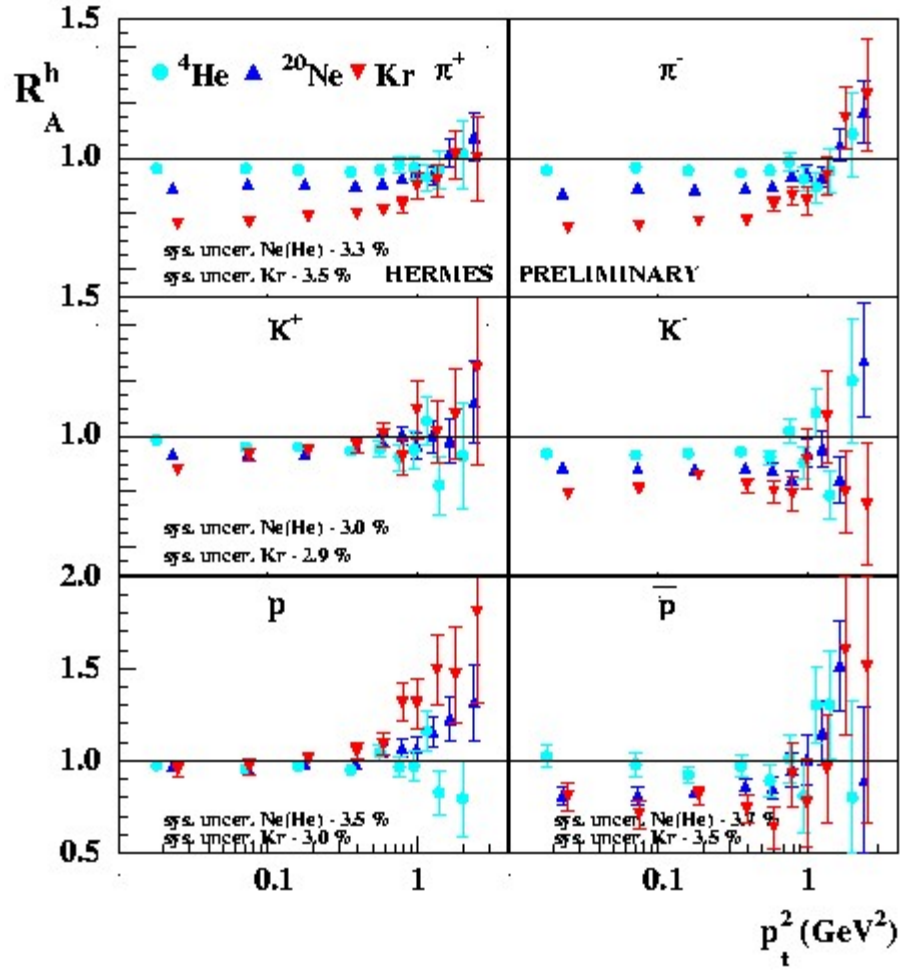


Fig. IV-12. R^h as a function of p_t^2 for π^\pm , K^\pm , and (anti)protons for different nuclei.

c.2.7. Extraction of Hadron Multiplicities from Deep-Inelastic Scattering Data

(H. E. Jackson, A. El Alaoui, K. G. Bailey, T. P. O'Connor, K. Hafidi, D. H. Potterveld, P. E. Reimer, Y. Sanjiev, and the HERMES Collaboration)

The semi-inclusive production of pseudoscalar mesons in deep-inelastic scattering (DIS) provides an excellent test of the accuracy of the quark-parton

model and QCD as a description of DIS at HERMES kinematics. In the QCD improved quark-parton model, the hadron multiplicities are given by the expression

$$\frac{1}{N_{DIS}(Q^2)} \frac{dN^h(z, Q^2)}{dz} = \frac{\sum_f e_f^2 \int_0^1 dx q_f(x, Q^2) D_f^h(z, q^2)}{\sum_f e_f^2 \int_0^1 dx q_f(x, Q^2)}$$

The fragmentation function D_f^h is a measure of the probability that a quark of flavor f fragments into a hadron h of energy E_h . The dependence of the multiplicities on x , z and Q^2 provide direct tests of scaling as well as measures of isospin invariance. They also provide an excellent constraint on Monte

Carlo simulations of the DIS process. HERMES is carrying out a careful determination of the multiplicities for charged hadrons individually identified as pions, kaons, or nucleons using the HERMES RICH particle identification system. The final multiplicities for both charges of pions and kaons are presented in Fig. IV-13.

These data resulted from a special mode of end of fill running at the HERA accelerator in which unpolarized targets of high density provide strongly

enhanced specific luminosities compared to normal polarized operation.

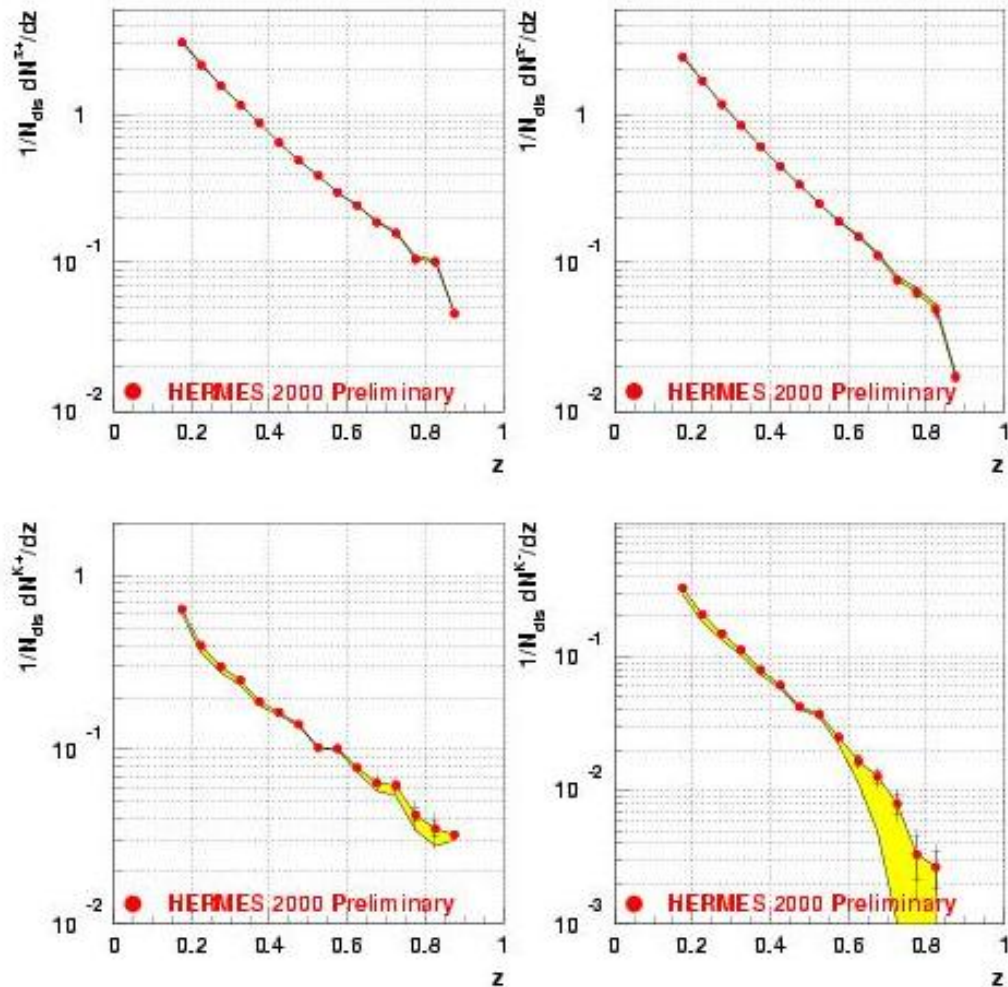


Fig. IV-13. The multiplicities versus z , including all corrections and evolved to $Q_0^2 = 2.5 \text{ GeV}^2$. The yellow band depicts the systematic error due to RICH PID unfolding.

c.2.8. Search for an Exotic $S = -2, Q = -2$ Baryon Resonance with Mass Near 1862 MeV
 (H. E. Jackson, A. El Alaoui, K. G. Bailey, T. P. O'Connor, K. Hafidi, D. H. Potterveld, P. E. Reimer, Y. Sanjiev, and the HERMES Collaboration)

The prediction of narrow exotic baryon resonances based on the chiral solution model has triggered an intensive search for the exotic members of an antidecuplet with spin 1/2. In this antidecuplet, all three vertices are manifestly exotic. The lightest exotic member lying at its apex, named the Θ^+ , is predicted to have a mass near 1530 MeV and a

narrow width. Its existence is currently the subject of considerable controversy. Experimental evidence for a second exotic member of the antidecuplet came from the reported observation of a $S = -2, Q = -2$ baryon resonance in proton-proton collisions at $\sqrt{s} = 17.2 \text{ GeV}$ at the CERN SPS.¹ HERMES has searched for an exotic baryon resonance with $S = -2, Q = -2$ in quasideal

photoproduction on a deuterium target by looking for the decay through the channel $\Xi^- \pi^- \rightarrow p \pi^- \pi^- \pi^-$. No evidence for a previously reported $\Xi^-(1860)$ resonance is found in the $\Xi^- \pi^-$ invariant mass

spectrum. An upper limit for the photoproduction cross section of 2.1 nb is found at the 90% confidence level. The photoproduction cross section for the $\Xi^0(1530)$ is found to be between 9 and 24 nb.

¹C. Alt *et al.* (NA49 Collaboration), Phys. Rev. Lett. **91**, 232003 (2003).

c.2.9. Study of Factorization and Flavor Content of the Nucleon in Unpolarized Semi Inclusive Deep Inelastic Scattering at HERMES (K. Hafidi, A. El Alaoui, K. G. Bailey, T. P. O'Connor, H. E. Jackson, D. Potterveld, P. E. Reimer, and the HERMES Collaboration)

Semi Inclusive Deep Inelastic Scattering (SIDIS) has been used extensively in recent years as an important testing ground for QCD. Indeed, SIDIS offers a great opportunity for studying the spin and the flavor content of the nucleon. However, using SIDIS relies on the factorization assumption between the hard scattering process and the hadronization of the struck quark. Although at high energy the scattering and production mechanisms factorize, it remains unclear to what extent factorization applies at lower energies. HERMES has shown that within the experimental precision which was dominated by the statistical error, factorization works reasonably well at the HERMES kinematics conditions.¹ By accumulating an order of magnitude more statistics, it is now

possible to perform a more precise test of factorization.

In this analysis, all HERMES unpolarized and averaged polarized hydrogen and deuterium data have been used. Four independent yields have been determined; $Y_p^{\pi^+}(x,z)$, $Y_p^{\pi^-}(x,z)$, $Y_n^{\pi^+}(x,z)$ and $Y_n^{\pi^-}(x,z)$ for fixed x -bins as a function of z , where z is the fraction of photon energy carried by the detected hadron. The neutron yield can be obtained from the deuteron yield via $Y_d^{\pi^-} = (Y_p^{\pi^-} + Y_n^{\pi^-})/2$. Assuming isospin symmetry between protons and neutrons $u_p(x) = d_n(x)$, $d_p(x) = u_n(x)$ as well as charge conjugation invariance $\bar{u}_p(x) = \bar{d}_n(x)$, $\bar{d}_p(x) = \bar{u}_n(x)$, one can form two ratios in which the fragmentation functions cancel out:

$$R_1(x) = \frac{Y_p^{\pi^+} + Y_p^{\pi^-}}{Y_d^{\pi^+} + Y_d^{\pi^-}} = \frac{2}{5} \frac{4u(x) + d(x) + 4\bar{u}(x) + \bar{d}(x)}{u(x) + d(x) + \bar{u}(x) + \bar{d}(x)}$$

$$R_2(x) = \frac{Y_p^{\pi^+} - Y_p^{\pi^-}}{Y_d^{\pi^+} - Y_d^{\pi^-}} = \frac{1}{3} \frac{4u(x) - d(x) - 4\bar{u}(x) + \bar{d}(x)}{u(x) + d(x) - \bar{u}(x) - \bar{d}(x)}$$

Defining the valence quark distribution as: $q_v(x) = q(x) - \bar{q}(x)$ the sea contribution cancels exactly in the difference of charge multiplicities and

one obtains the following expression for the valence $d_v(x)/u_v(x)$ ratio:

$$\frac{d_v(x)}{u_v(x)} = \frac{4 - 3R_2(x)}{1 + 3R_2(x)}$$

The observation of the z -scaling behavior of $R_1(x)$ and $R_2(x)$ would be a test of factorization. In such case, the yield ratios R_1 and R_2 will be a direct measurement of the quark distributions and not related to the fragmentation functions. The kinematic range is $0.02 < x < 0.6$ at the average Q^2 of 2.5 GeV^2 . The expected statistical precision of the ongoing analysis represents a considerable

improvement of our ability to check factorization. In addition, measuring d_v/u_v will provide an additional test of factorization by comparing HERMES result with QCD fit of other high energy data.

In conclusion, with the ongoing analysis, we will be able to quantify with high precision the validity of the factorization assumption. We will also extract the

valence quark distribution ratio of the nucleon d_v/u_v using π^+/π^- yield ratios on hydrogen and deuterium.

¹K. Ackerstaff *et al.*, Phys. Rev. Lett. **81**, 5519 (1998).

²EMC Collaboration and J. Ashman *et al.*, Z. Phys. C **52**, 361 (1991).

³G. T. Jones *et al.*, Z. Phys. C **62**, 601 (1994).

c.3. Measurement of the Absolute Drell-Yan Cross Section on Hydrogen and Deuterium
(P. E. Reimer, D. F. Geesaman, S. B. Kaufman, N. C. R. Makins, B. A. Mueller and the FNAL E866/NuSea Collaboration)

Very little is known about the regime in which only one parton carries much of proton's momentum – different theoretical treatments prescribe different behaviors as $x \rightarrow 1$ (where x represents the fraction of the proton's momentum carried by the interacting parton) and there is very little data available to serve as a guide. In the fixed target environment, the Drell-Yan process is sensitive to the high- x behavior of the beam's quarks and the low- and intermediate- x behavior of the target antiquarks. E866 has measured the absolute cross sections for *proton-proton* and *proton-deuterium* Drell-Yan.¹ As $x \rightarrow 1$, these data

are dominated by the beam proton's quark distribution of $4u(x)+d(x)$. The measured absolute cross sections, relative to a next-to-leading order (NLO) calculation are shown in Fig. V-14. Recent work has focused on calculating the effect of radiative corrections to the Drell-Yan cross section. These corrections appear to account for approximately 3-5% of the effect at large- x , and intermediate- x . As can be seen in Fig. V-14, the quark distributions used in the calculation *over predict* the measured cross sections at large- x by a significant amount.

¹J. C. Webb *et al.* (Fermilab E866/NuSea Collaboration), "Absolute Drell-Yan Dimuon Cross Sections in 800 GeV/c pp and pd Collisions", submitted to Phys. Rev. Lett., hep-ex/0302019.

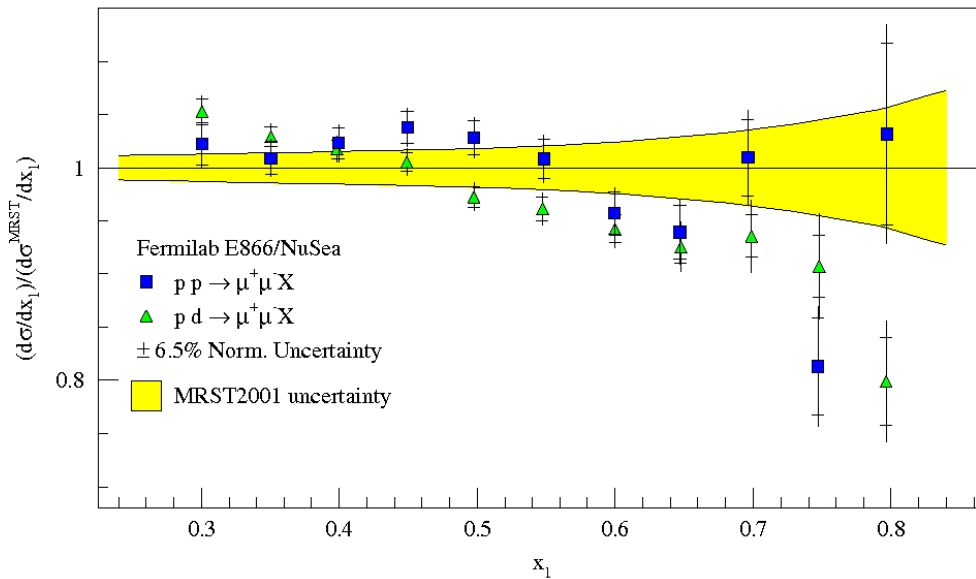


Fig. V-14. The ratio of Drell-Yan cross section (including radiative corrections) measured by Fermilab E866/NuSea for proton-deuterium (triangles) and proton-proton (squares) to calculated NLO cross section based on the MRST2001 parton distributions. The yellow band represents the uncertainty given by MRST2001 on $4u(x) + d(x)$.

c.4. Drell-Yan Measurements with 120 GeV Protons, FNAL E906 (P. E. Reimer, D. F. Geesaman, J. Arrington, K. Hafidi, R. J. Holt, D. H. Potterveld and the FNAL E906 Collaboration)

The proton and the neutron are composite objects, made of quarks, antiquarks and gluons, collectively known as partons. While many of the properties of the proton may be attributed to its three valence quarks, it is, in fact, much more complicated, with over 50% of its momentum being carried by the its non-valence (sea) quarks and gluons. To understand the structure of the proton, it is necessary to understand the sea quarks, their origins and their interactions with the gluons that bind the proton together. E906 is specifically designed to use Drell-Yan scattering to probe the sea quarks of the proton.¹

The Drell-Yan mechanism provides a powerful tool to study the structure of the proton at the quark level. In Drell-Yan scattering a quark (or antiquark) in the proton beam annihilates with an antiquark (or quark) in the target. The resulting annihilation produces a virtual photon that decays into a pair of leptons, which are seen in the detector. The kinematics of the detected leptons can be used to select interactions between beam valence quarks and target antiquarks. This was successfully exploited by Fermilab E866/NuSea using an 800 GeV/c proton beam provided new insight into the antiquark sea in the proton^{2,3} and nuclear dependence phenomena.⁴ FNAL E906 has been approved by Fermilab to extend Drell-Yan measurements to larger values of x (the fraction of the proton's momenta carried by the struck quark) using the new 120 GeV Main Injector at Fermilab. The new data obtained by this experiment will address several outstanding questions.

Vacuum polarization accounts for the creation of a flavor symmetric sea. Previous E866 Drell-Yan data, however, exhibit a large asymmetry between \bar{d} and \bar{u} for $x < 0.25$ (where x represents the fraction of the protons momentum carried by the interacting quark) clearly indicating a non-perturbative origin to the sea. Above $x > 0.28$ these data, albeit with poor statistical uncertainty, indicate the ratio \bar{d}/\bar{u} returns to unity. This result dramatically changed the sea quark parton distribution fits and was completely unpredicted by meson cloud and other non-perturbative models. The return of \bar{d}/\bar{u} to unity clearly signals a change in the mechanism by which the sea is generated.^{2,3,5} Fermilab E906 will determine \bar{d}/\bar{u} and $\bar{d} - \bar{u}$ for $0.1 \leq x \leq 0.45$, encompassing the non-perturbative region and extending well into the region where the sea appears to

return to symmetry, allowing for the study of the relative importance of the perturbative and non-perturbative sea. The current parton distributions now reproduce the previous Drell-Yan data for $0.28 < x < 0.3$, but allow $\bar{d}/\bar{u} < 1$ as x increases above 0.3. This is not expected by *any* models of the proton, either meson or perturbative, and is simply indicative of the complete lack of data. E906 will provide this data, as shown in Fig. V-15.

Very little is known about the regime in which only one parton carries much of proton's momentum – different theoretical treatments prescribe different behaviors as $x \rightarrow 1$ and very little data is available to serve as a guide. Through the partons in the beam proton, Fermilab E906 will access these distributions. The Drell-Yan cross section is dominated by the distribution of $4u(x) + d(x)$ as $x \rightarrow 1$. E906 will extend the data provided by Fermilab E866 to higher x and provide much more precise *proton* data than is currently available.

Models based on the hypothesis that nuclear binding is governed by the exchange of mesons have been used to quite successfully describe the nuclear force. Given the success of these models, it is natural to look for direct experimental evidence for the presence of these mesons in nuclei. Thus far, however, no direct evidence has been found.⁶ If present, these mesons will lead to an enhancement of antiquarks in the nucleus, and Drell-Yan is ideally suited to measure this enhancement. Fermilab E906 will collect data using nuclear targets, in addition to hydrogen and deuterium to look for these effects.

From deep inelastic scattering (DIS) experiments, we know that the quark level structure of a nucleon with in a nucleus is different from that of a free nucleon. In the range $0.10 < x < 0.25$, a surplus of quarks (approximately 2-4%) in nuclei, known as antishadowing, is clearly observed in DIS data. To understand these phenomena, it is important to determine if it is a general property of the quark and antiquark distributions, or just a property of the valence or sea quarks. Drell-Yan, with its ability to measure sea-only quark effects, is the ideal reaction in which to measure this. Early Drell-Yan data indicate that this surplus might not be present,⁶ but with poor statistical uncertainty (3-5%). Fermilab E906's measurements

will clearly determine if there is antishadowing in the sea, with statistical uncertainties of less than 1% throughout this region (see Fig. V-15).

Using the same nuclear target data, Fermilab E906 will also study the propagation of colored partons in strongly interacting, cold nuclear matter. By comparing the Drell-Yan yields from different nuclear targets and looking for apparent shifts in the beam parton's momentum distributions between nuclei, E906 will be able to measure the beam parton's energy loss. Previous Drell-Yan studies have placed upper limits on parton energy loss.⁷ With increased sensitivity from the 120 GeV beam and better statistical accuracy, Fermilab E906 will turn these upper limits into measurements. These measurements will aid in the understanding of jet suppression data from RHIC.

FNAL E906 is able to make these improvements over previous measurements because of the lower beam energy available at the Fermilab Main Injector. For

fixed x_{beam} and x_{target} the cross section scales as the inverse of the beam energy. Thus a factor of seven more events for the same integrated luminosity can be achieved. At the same time, the primary background to the measurement, muons from J/ψ decays, decreases with decreasing beam energy, allowing for an increase in instantaneous luminosity by another factor of seven. These two factors combine to provide roughly 50 times more events for the same beam time.

FNAL E906 has been approved by the Fermilab PAC and will begin collecting data in 2009. Much of the new spectrometer will come from detector elements recycled from the E866 Drell-Yan spectrometer. To increase the rate and triggering capabilities of the spectrometer, some new detectors will be fabricated. In addition, because of the significantly different kinematics of the 120 GeV experiment, the new spectrometer will require a new, large dipole magnet to focus the Drell-Yan muons.

¹L. D. Isenhower *et al.* (Fermilab E906 Collaboration), "Proposal for Drell-Yan Measurements of Nucleon and Nuclear Structure with the FNAL Main Injector", April 1, 2001.

²E. A. Hawker *et al.* (Fermilab E866/NuSea Collaboration), Phys. Rev. Lett. **80**, 3715 (1998).

³R. S. Towell *et al.* (Fermilab E866/NuSea Collaboration), Phys. Rev. D **64**, 05202 (2001).

⁴M. J. Leitch *et al.* (Fermilab E866/NuSea Collaboration), Phys. Rev. Lett. **84**, 3256 (2000).

⁵J. C. Peng *et al.* (Fermilab E866/NuSea Collaboration), Phys. Rev. D **58**, 092004 (1998).

⁶D. M. Alde *et al.* Phys. Rev. Lett. **64**, 2479 (1990).

⁷M. A. Vasiliev *et al.* (Fermilab E866/NuSea Collaboration), Phys. Rev. Lett. **83**, 2304 (1999).

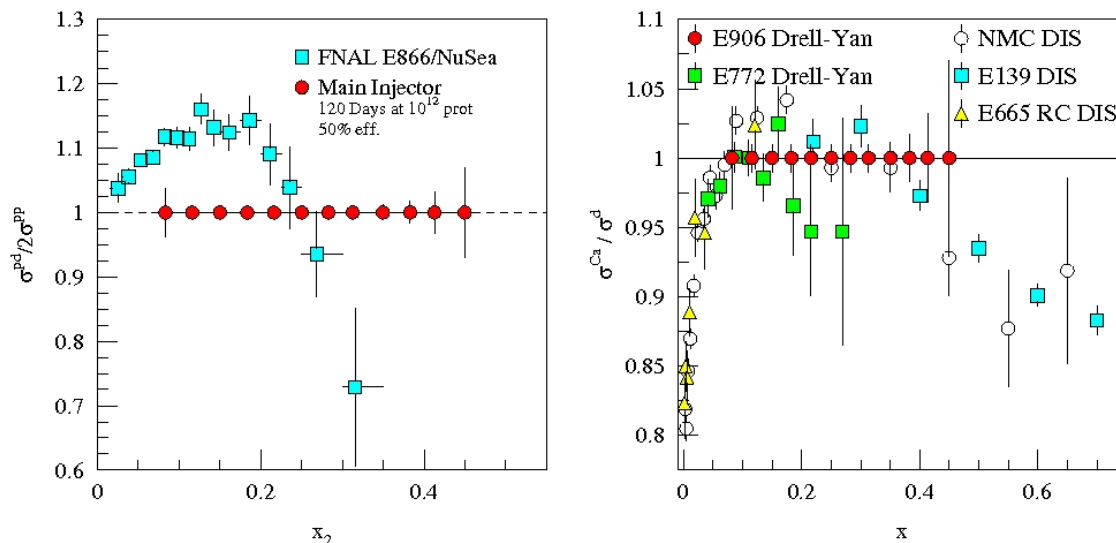


Fig. V-15. The statistical uncertainty of the proposed E906 measurement of the ratio of hydrogen to deuterium cross sections (arbitrarily plotted at 1) compared with the E866 measurements of the same quantity (left). The statistical uncertainty of E906's measurement of the ratio of deuterium to Calcium cross sections (arbitrarily plotted at 1) compared with previous Drell-Yan and deep inelastic scattering (DIS) measurements (right).

D. ATOM TRAP TRACE ANALYSIS

d.1. Laser Spectroscopic Determination^{1,2} of the Nuclear Charge Radius of ⁶He (L.-B. Wang,* P. Mueller, K. Bailey, J. P. Greene, D. Henderson, R. J. Holt, R. V. F. Janssens, C. L. Jiang, Z.-T. Lu, T. P. O'Connor, R. C. Pardo, K. E. Rehm, J. P. Schiffer, X. D. Tang, and G. W. F. Drake†)

The nucleus ⁶He, with 2 protons and 4 neutrons, has been intriguing for quite some time. Measurements in the eighties and nineties have indicated that, when used as a beam, the probability for it to induce a nuclear reaction on any target is much larger than that for ⁴He. This observation was interpreted as a strong indication that ⁶He is a three-body "halo" nucleus, *i.e.*, it can be best viewed as a tightly bound ⁴He core and two neutrons orbiting this core at large distances. Moreover, while these three constituents of ⁶He form a bound system, the nuclear potential is not strong enough to bind any two of them separately. For this reason, ⁶He is often referred to as "Borromean" (the name derives from the heraldic emblem of the medieval princes of Borromeo, three rings interlocked in such a way that the removal of any of the rings will cause the remaining two to fall apart).

Because of its intriguing properties, ⁶He has the potential to teach us about the fundamental forces among the constituent nucleons. Indeed, the halo character can be revealed by an accurate determination of the nuclear charge radius, since the motion of the core with regard to the center of mass reflects both the radial extent of the neutrons and the correlations between these particles. The result can in turn be compared with the most modern theories as recent advances in computational methods have made it possible to calculate the structure of few-nucleon systems from the basic interactions between the constituents.

The charge radius of ⁶He has been determined for the first time by measuring the atomic isotope shift between ⁶He and ⁴He using laser spectroscopy. For this work, ⁶He atoms were produced at the ATLAS accelerator facility at Argonne National Laboratory, and quickly captured and cooled by an on-line laser trap. By applying laser spectroscopy on the trapped ⁶He atoms as well as on their ⁴He isotopic partner atoms, the charge radius of the ⁶He nucleus was determined to be 2.054 ± 0.014 fm. The measurement is of such accuracy that it distinguishes between the available theoretical predictions. The data offer new insight into the dependence of three-body interactions on neutron number, which in turn is essential to the understanding of the structure of all neutron-rich systems, including neutron stars.

In this work, ⁶He nuclei were produced via the ¹²C(⁷Li, ⁶He)¹³N reaction with a 100 pnA, 60 MeV beam of ⁷Li from the ATLAS accelerator at Argonne National Laboratory. Neutral ⁶He atoms diffused out of the hot graphite target and were transferred in vacuum to the nearby atomic beam assembly at a rate of approximately 1×10^6 s⁻¹. Trapping helium atoms in the 2³S₁ metastable level was accomplished by exciting the 2³S₁ – 2³P₂ transition using laser light with a wavelength of 1083 nm. ⁶He atoms were mixed with a krypton carrier gas and sent through a discharge to be excited to the 2³S₁ level. The metastable ⁶He atoms were transversely cooled, decelerated with the Zeeman slowing technique, and then captured in a magneto-optical trap at a rate of approximately one atom per minute.

*University of Illinois-Urbana, †University of Windsor, Ontario.

¹Project homepage: <http://www-mep.phy.anl.gov/atta/>.

²L.-B. Wang *et al.*, Phys. Rev. Lett. **93**, 142501 (2004).

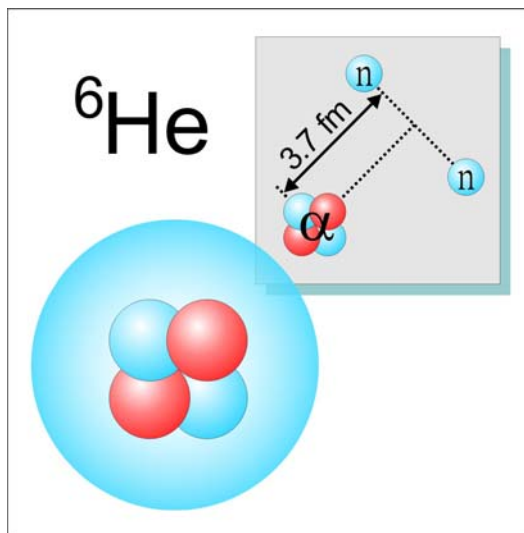


Fig. IV-16. Halo nucleus ${}^6\text{He}$. The nucleus can be viewed as a three-body cluster consisting of a particle core and two loosely bound neutrons.

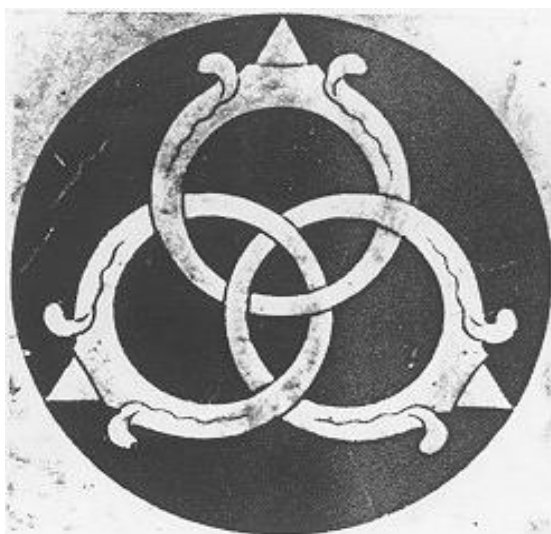


Fig. IV-17. Borromean rings.

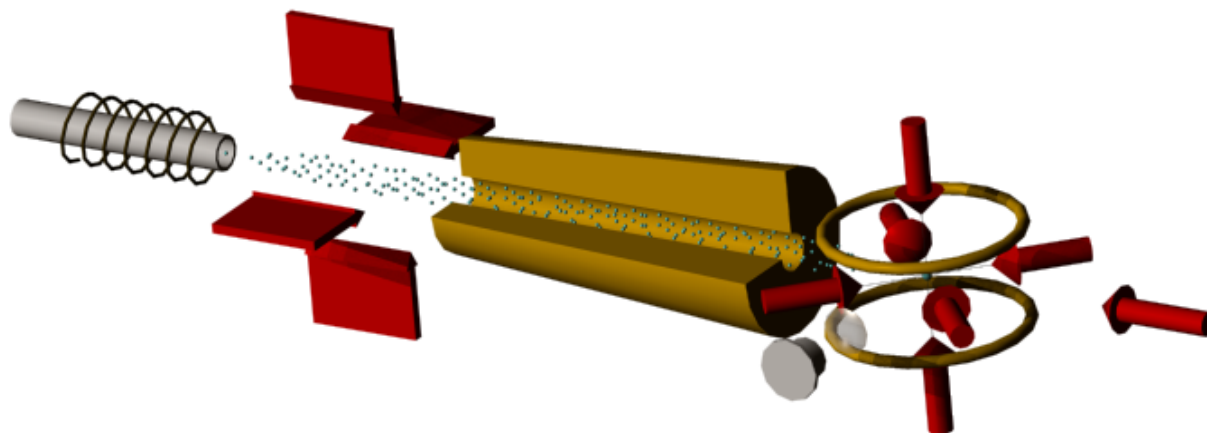


Fig. IV-18. Atomic beam apparatus for the laser trapping and laser spectroscopy of ${}^6\text{He}$ atoms.

d.2. Fine Structure of the $1s3p\ ^3P_J$ Level in Atomic ^4He : Theory and Experiment (P. Mueller, L.-B. Wang,* K. Bailey, Z.-T. Lu, T. P. O'Connor, and G. W. F. Drake†)

The fine structure intervals in helium have attracted a great deal of interest in recent years because of the possibility of using a comparison between theory and experiment to better determine the fine structure constant α . We report on a theoretical calculation and a new experimental determination of the $1s3p\ ^3P_J$ fine structure intervals in atomic ^4He . The values from the theoretical calculation of 8113.730(6) MHz and 658.801(6) MHz for the ν_{01} and ν_{12} intervals, respectively, disagree significantly with the previous most precise experimental results. However, the new

laser spectroscopic measurement¹ reported here yields values of 8113.714(28) MHz and 658.810(18) MHz for these intervals. These results² show an excellent agreement with the theoretical values and resolve the apparent discrepancy between theory and experiment.

This measurement was performed using the apparatus of the ^6He project. In addition to the aforementioned motivation, the measurement also serves as an important test and calibration of the apparatus for the ^6He project.

*University of Illinois-Urbana, †University of Windsor, Ontario.

¹Project homepage: <http://www-mep.phy.anl.gov/atta/>.

²P. Mueller *et al.*, Phys. Rev. Lett. **94**, 133001 (2005).

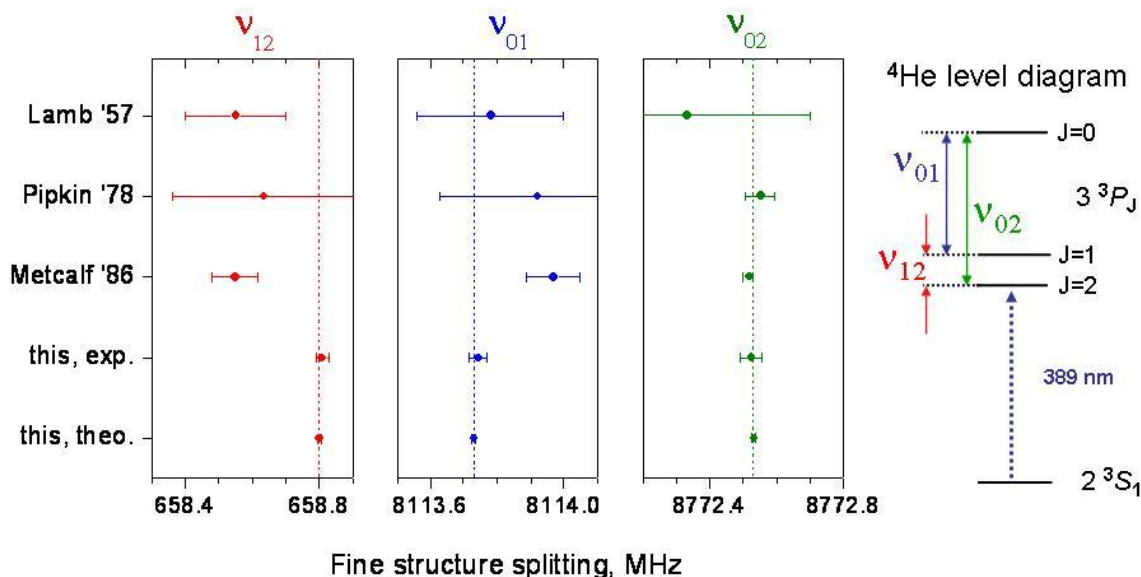


Fig. IV-19. Comparison of results for the three fine structure intervals of the $1s3p\ ^3P_J$ levels.

d.3. Atmospheric ^{81}Kr as an Integrator of Cosmic Ray Flux Over the Past $\sim 3 \times 10^5$ Years¹ (Z.-T. Lu, P. Mueller, T. P. O'Connor, L.-B. Wang, R. Purtschert,* J. Elsig,* B. M. Kennedy,† N. C. Sturchio,‡ and G. Wolber§)

The variability of the cosmic ray flux over time can be studied based on the measurements of a variety of radionuclides. The flux is known to correlate with the short-term (~ 10 year) solar cycles and with the long-term ($\sim 10^4$ year) variations of geomagnetic fields. The atmospheric ^{81}Kr is an ideal integrator of the cosmic ray flux over the ^{81}Kr lifetime of 3.3×10^5 years. ^{81}Kr is

produced by cosmic-ray induced spallation and nuclear reaction of stable Kr nuclei in the atmosphere. Once produced, over 98% of ^{81}Kr remain in the atmosphere with its radioactive decay as its only sink. Based on the abundance of ^{81}Kr in the atmosphere, the cosmic ray flux integrated over the past 3×10^5 years can be

calculated with models that simulate the production of cosmogenic radionuclides.

This collaboration aims to accurately determine the isotopic abundance of ^{81}Kr in the atmosphere. Enriched samples of ^{81}Kr and ^{85}Kr are analyzed with Mass Spectrometry (MS), Low-Level Counting (LLC), and

Atom Trap Trace Analysis (ATTA). Once ATTA is calibrated against MS for $^{81}\text{Kr}/^{85}\text{Kr}$ ratios, ATTA can be used to measure the absolute isotopic abundance of ^{81}Kr in the Earth's atmosphere. At present, calibration measurements and investigation of various systematic effects are in progress.

*University of Bern, Switzerland, †Lawrence Berkeley National Laboratory, ‡University of Illinois-Chicago,

§Deutsches Krebsforschungszentrum Heidelberg, Germany.

¹Project homepage: <http://www-mep.phy.anl.gov/atta/>.

E. FUNDAMENTAL SYMMETRIES IN NUCLEI

e.1. Probing the Intercombination Transition $7s^2\ ^1S_0 - 7p\ ^3P_1$ in ^{225}Ra Atoms for an EDM Measurement (N. D. Scielzo, J. R. Guest, E. C. Schulte, I. Ahmad, K. Bailey, J. P. Greene, R. J. Holt, Z.-T. Lu, T. P. O'Connor, and D. H. Potterveld)

The goal of this project is to measure the electric dipole moment (EDM) of the ^{225}Ra atom. ^{225}Ra is an especially good case because it has a relatively long lifetime, has spin $\frac{1}{2}$ that eliminates systematic effects due to electric quadrupole moments, is available in relatively large quantities from the decay of ^{229}Th , can be trapped with readily available lasers, and has a well-established octupole nature. The octupole deformation enhances the signal from an atomic EDM by increasing the Schiff moment collectively and by the parity doubling of the energy levels. The overall scheme is to collect ^{225}Ra atoms in a magneto-optical trap and transfer the sample to an optical dipole trap. In this second trap, the atoms will be polarized by optical pumping and the EDM measurement will be performed.

We have recently characterized the intercombination transition $7s^2\ ^1S_0 - 7p\ ^3P_1$ on which laser manipulation

of neutral ^{225}Ra atoms will be developed. We obtained 10^8 ^{225}Ra atoms/sec from the oven at temperatures of ~ 700 C by adding barium metal to the existing oven setup to aid in the chemical reduction. By performing laser induced fluorescence measurements on this atomic beam of ^{225}Ra , we have determined the frequency of the transition to the $F = 3/2$ excited state to be $13999.27\ \text{cm}^{-1}$. This frequency is ≈ 710 MHz from a transition in molecular iodine (line number 692 of the I_2 atlas), which we use to control the laser frequency. We have also determined the lifetime of the $7p\ ^3P_1$ state to be 422 ± 20 ns, and derived the strength of the intercombination line. Therefore, the maximum acceleration that can be applied by photon scattering using this transition is $2.9\ \text{km/s}^2$. A magneto-optical trap for ^{225}Ra atoms based on this transition is under development.

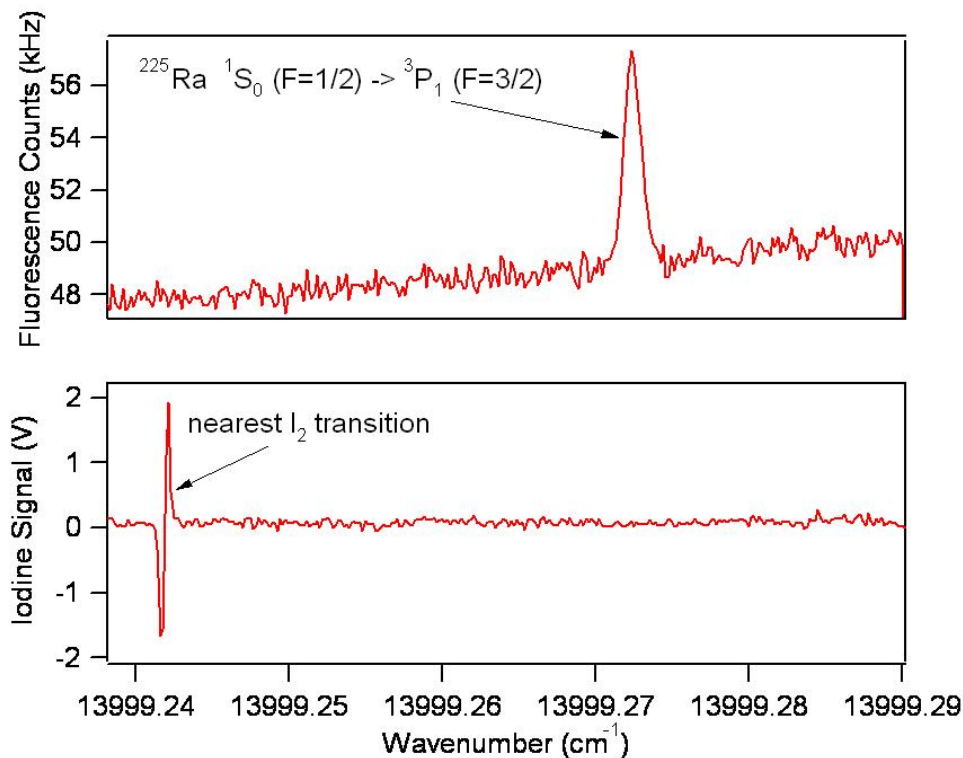


Fig. IV-20. Laser induced fluorescence signal of neutral ^{225}Ra atoms. The laser frequency is scanned across the intercombination transition $7s^2\ ^1S_0 - 7p\ ^3P_1$. The iodine transition shown is used to control the laser frequency.

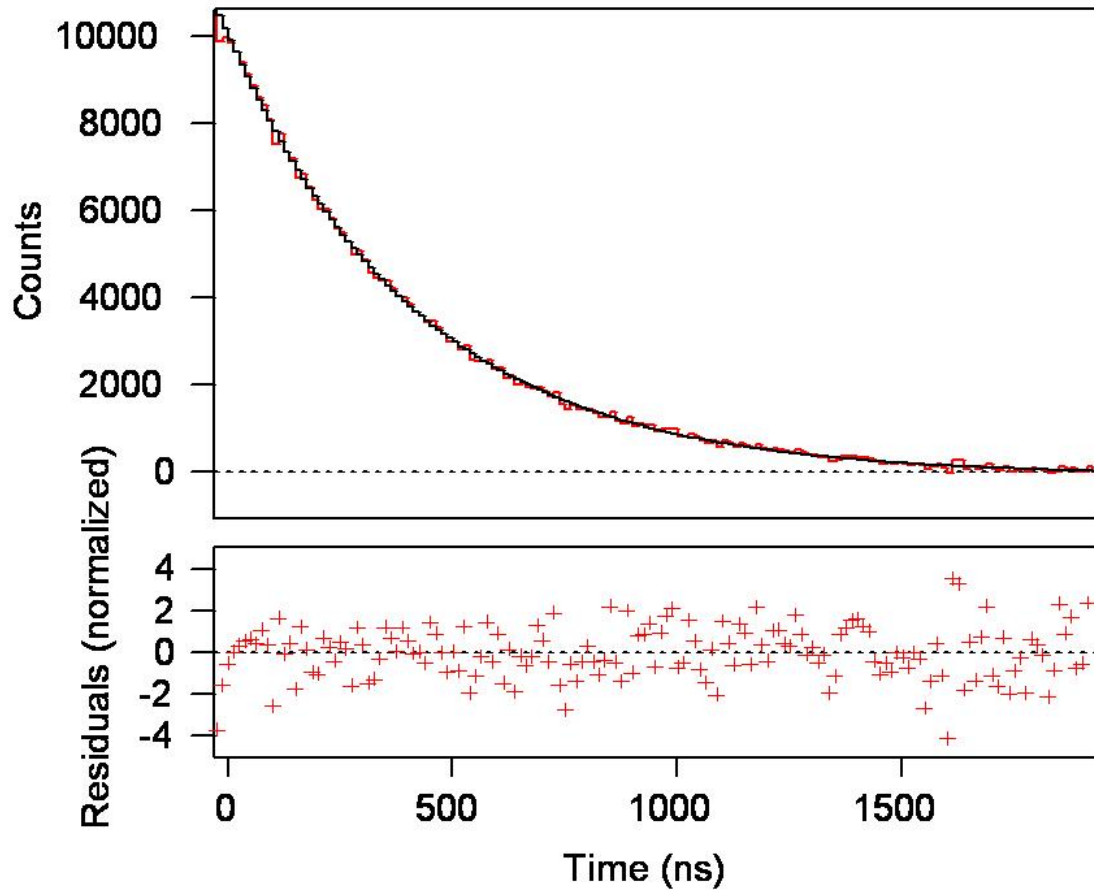


Fig. IV-21. The decay of the fluorescence signal of neutral ^{225}Ra atoms after turning off of the excitation laser pulse at time = 0. Lifetime of the $7p\ ^3P_1$ state is 422 ± 20 ns.

e.2. Measurement of $\sin^2 \theta_W$ Through Parity Violation in Deep Inelastic Scattering (PV DIS) on Deuterium (P. E. Reimer, X. Zheng, J. Arrington, K. Hafidi, R. J. Holt, H. E. Jackson, and D. H. Potterveld)

One of the basic parameters of the Standard Model is $\sin^2 \theta_W$, which represents the relative coupling strength of the weak and electromagnetic forces. The Standard Model predicts that the value $\sin^2 \theta_W$ will vary (or run) as a function of Q^2 , the energy squared at which it is probed. Measurement of this “running” provides a strict test of the Standard Model. At an energy equivalent to the mass of the Z-boson ($Q^2 = M_Z^2$), $\sin^2 \theta_W$ is well measured; but at $Q^2 < M_Z^2$, only a few measurements exist. The asymmetry from parity violation in polarized electron-deuterium deep inelastic scattering (DIS) is linearly dependent on $\sin^2 \theta_W$ and relatively large ($A_d \approx 10^{-4} Q^2$), making it experimentally quite accessible. The sensitivity to $\sin^2 \theta_W$ is through the product of the axial Z-electron

and vector Z-quark couplings (C_{1q}) and the product of the vector Z-electron and axial Z-quark couplings (C_{2q}). Historically, DIS parity violation from a deuterium target was first observed by Prescott *et al.* at SLAC in the mid-1970 and was used to establish the Weinberg-Salam model. Investigations are underway to repeat this experiment with much better precision, focusing on facilities at an upgraded 12 GeV JLab.¹

A preliminary measurement at JLab with a 6 GeV beam has been approved (E05-007).² The 6 GeV measurement will, when combined with other data, provide a measurement of $(2C_{2u} - C_{2d})$. Current experimental knowledge of this quantity has an uncertainty of 300%. The complete measurement at 6 GeV will reduce this

uncertainty by a factor of eight as shown in Fig. IV-22. In addition, the 6 GeV experiment will explore the contribution of higher-twist effects to the

asymmetry, providing crucial guidance to interpreting this data and future PV-DIS measurement with the 12 GeV upgrade to JLab.

¹Conceptual Design Report for the 12 GeV Upgrade of CEBAF, J. Arrington *et al.*, eds., JLab, February 2005.

²J. Arrington *et al.*, " \bar{e} - ^2H Parity Violating Deep Inelastic Scattering at CEBAF 6 GeV", proposal 05007 to the JLab PAC, P. E. Reimer and X. Zheng, spokespersons, December 6, 2004.

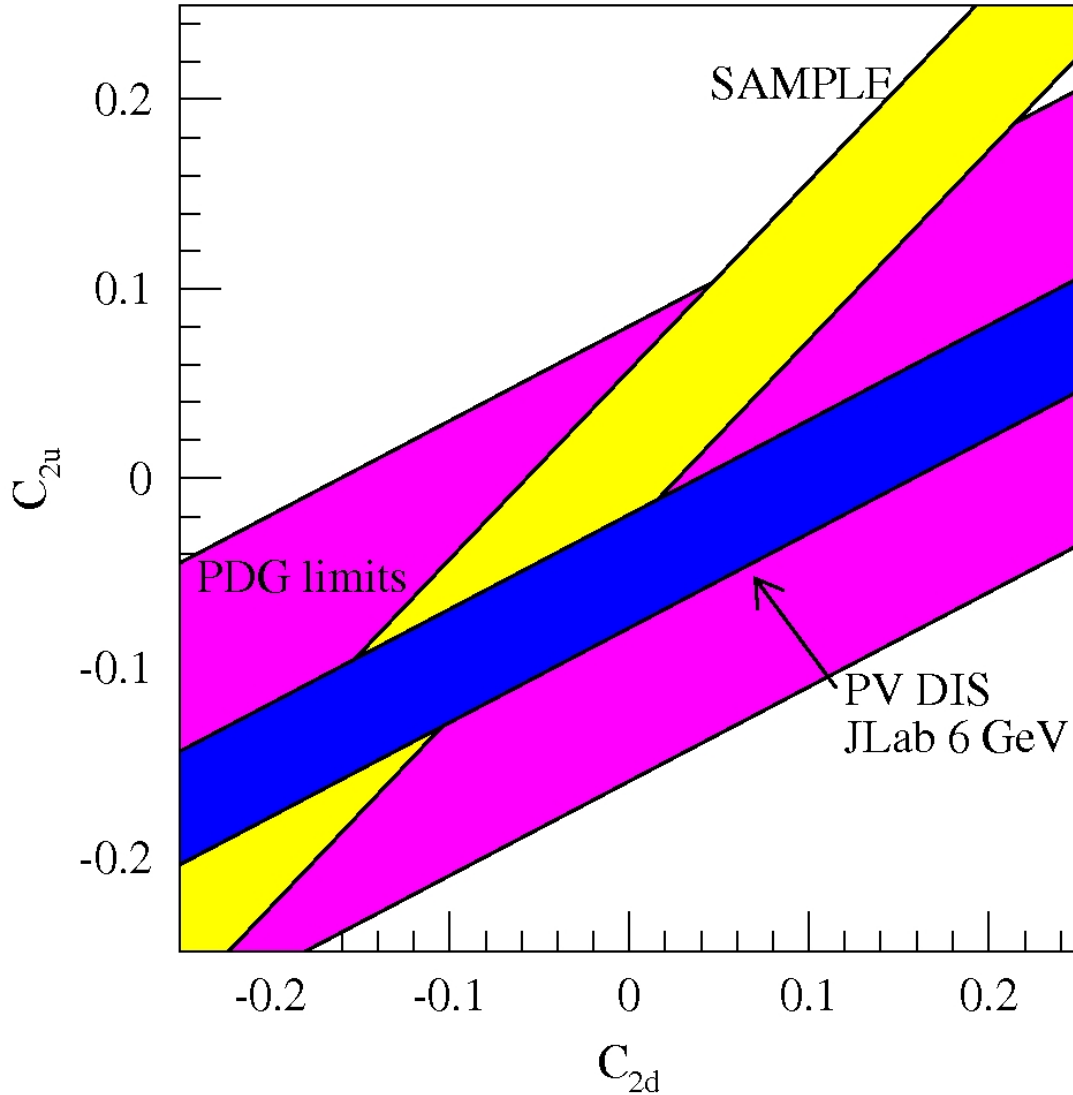


Fig. IV-22. Plot of C_{2u} vs. C_{2d} showing the current Particle Data Group (PDG) limits. The blue band shows the improvement which will be achieved by the 6 GeV JLab experiment. The yellow band represents constraints on C_{2u} and C_{2d} from the SAMPLE experiment.

e.3. Feasibility Study for a Charge Symmetry Violating Quark Distribution

Measurement (K. Hafidi, J. Arrington, A. El Alaoui, L. El Fassi, D. F. Geesaman, R. J. Holt, H. E. Jackson, B. Mustapha, D. Potterveld, P. E. Reimer, E. C. Schulte, and X. Zheng)

Symmetries are the key to understanding and classifying the structure of matter and the fundamental forces and their study leads to better understanding of the underlying physics. Therefore, it is important to test fundamental symmetries, even the approximate ones such as Isospin (IS) and Charge (CS) symmetries. IS requires invariance under all rotations in isospin space such that the Hamiltonian of the system commutes with the isospin operator while CS is related to only one rotation. It requires invariance with respect to rotations of 180° about the T_2 axis, where the charge corresponds to the third axis. If CS is a valid symmetry the Hamiltonian has to commute with the charge symmetry operator.

At the quark level, CS implies the invariance of a system under the interchange of up and down quarks while simultaneously interchanging protons and neutrons, *i.e.*,

$$u^p(x, Q^2) = d^n(x, Q^2) \text{ and } d^p(x, Q^2) = u^n(x, Q^2)$$

Quantum Chromo-Dynamics (QCD) provides a clear formulation of the origin of Charge Symmetry Violation (CSV). In QCD, the only sources of CSV are electromagnetic interactions and the mass difference $\delta m = m_d - m_u$ between down and up quarks. Electromagnetic interactions should play a minor role at high energies. Thus the light quark mass difference is the interesting feature of the QCD view of CSV.¹ CS is a more restricted symmetry than IS; therefore it is generally conserved in strong interactions to a greater degree than IS.² In fact, while in many nuclear reactions IS is violated at the few percent level, in most cases CS is obeyed to better than one percent: the proton and neutron masses are equal to about 1%; the binding energies of tritium and ^3He are equal to 1%, after Coulomb corrections. By comparing energy levels in mirror nuclei, one generally finds agreement to better than 1%, correcting for electromagnetic interactions. At the parton level, one would naively expect CSV to be of the order of up-down current mass difference divided by some average mass expectation value of the strong Hamiltonian which has a value roughly 0.5-1.0 GeV. This would put CSV effects at a level of 1% or smaller.³ From our experience with CS in nuclear systems, and because of the order of

magnitudes estimates of CSV in parton systems, CS has been universally assumed in quark distribution functions. CS reduces by a factor of two the number of independent quark distributions necessary to describe high-energy data, and until recently there has been no compelling reason to suggest CSV. On the other hand, there were no precise tests of charge symmetry in parton distributions. Recently much attention has been focused on the apparent violation of what is called SU(2) flavor symmetry in the nucleon. This was suggested by New Muon Collaboration (NMC)⁴ and later supported by results from NA51 group at CERN⁵ and E866 Drell-Yan experiment⁶ at FNAL. Experimental results from these collaborations seem to show a large flavor symmetry violation in the proton sea distributions. However this could also in principle be explained even if flavor symmetry were conserved, if we assume very large CSV in the nucleon sea. The valence quark CSV is also very important issue because it makes a substantially larger contribution than the sea quark CSV to the extraction of the Weinberg angle from neutrino Deep Inelastic Scattering (DIS). The three standard deviation result from the Standard Model prediction reported by NuTeV collaboration⁷ or the so-called “NuTeV anomaly” could be completely removed by assuming valence quark CSV without being in conflict with high energy data.⁸

At present, there are no direct measurements that reveal the presence of CSV in parton distribution functions. We have only upper limits on its magnitude. These limits arise from comparing the structure function measured in neutrino induced charged current reactions, and the one for charged lepton DIS, both measurements on isoscalar targets. In the region of $0.1 \leq x \leq 0.4$, an upper limit of 9% was set for CSV effects.

Semi-inclusive pion production from lepton DIS on nuclear targets was suggested³ as a sensitive probe of CSV effects in nucleon valence distributions. The authors proposed measuring the quantity $R_{\text{meas}}(x, z)$ defined by:

$$R_{\text{meas}}(x, z) = \frac{4N^{D\pi^-}(x, z) N^{D\pi^+}(x, z)}{N^{D\pi^+}(x, z) N^{D\pi^-}(x, z)}$$

Where $N^{D\pi^+}$ ($N^{D\pi^-}$) is the yield of π^+ (π^-) produced in coincidence with the scattered electron from deuterium.

In the quark-parton formalism, the yield of hadron h per scattering from nucleon N can be written as

$$N^{Nh} = \sum_i e_i^2 q_i^N(x) D_i^h(z).$$

The quantity $q_i^N(x)$ is the distribution functions for quarks of flavor i , and charge e_i , in the nucleon N as a function of Bjorken x . $D_i^h(z)$ is the fragmentation function for a quark of flavor i into hadron h . It

$$R(x, z) = \frac{1 - \Delta(z)}{1 + \Delta(z)} R_{\text{meas}}(x, z), \text{ and } \Delta(z) = \frac{D_u^{\pi^-}(z)}{D_u^{\pi^+}(z)}$$

$$R_f(z) = \frac{5\Delta(z)}{1 + \Delta(z)} - \frac{[4 + \Delta(z)]\delta D(z)}{3[1 - \Delta^2(z)]}, \text{ and } \delta D(z) = \frac{D_u^{\pi^+}(z) - D_d^{\pi^-}(z)}{D_u^{\pi^+}(z)}$$

$$R_{\text{CSV}}(x) = \frac{4[\delta d(x) - \delta u(x)]}{3[u_V^p(x) + d_V^p(x)]}, \delta d(x) = d^p(x) - u^n(x), \delta u(x) = u^p(x) - d^n(x)$$

$$R_{\text{sea}}(x, z) = \frac{5[u_V^{-p}(x) + d_V^{-p}(x)] + \Delta_S(z)[s(x) + \bar{s}(x)]/[1 + \Delta(z)]}{[u_V^p(x) + d_V^p(x)]}, \text{ and } \Delta_S(z) = \frac{D_S^{\pi^+}(z) + D_S^{\pi^-}(z)}{D_u^{\pi^+}(z)}$$

Experimentally, one needs to measure accurately the x dependence of $R(x, z)$ for fixed z values. The sea quark distribution $R_{\text{sea}}(x, z)$ should fall off monotonically and rapidly with x . Therefore by going to sufficiently large x region, the sea contribution will be negligible relative to the CSV term. The CSV contribution of the fragmentation function to the z -dependent term $R_f(x, z)$ was estimated⁹ to be 1%. Therefore it can also be neglected. Because of the low DIS cross sections at high x , these measurements would not be possible

depends on the quark longitudinal momentum fraction $z = E_h/\nu$, where E_h is the energy of the hadron and ν is the energy of the virtual photon. Assuming the validity of the impulse approximation and multiplying R_{meas} by a z -dependent factor, one obtains the following expression;

$$R(x, z) = R_f(z) + R_{\text{CSV}}(x) + R_{\text{sea}}(x, z)$$

where

without the high luminosity available at JLab. Studies have shown that Hall C would be the best place to perform these measurements. Figure IV-23 shows the projected uncertainties of $[\delta d(x) - \delta u(x)]$ with 30 days of data taking using Hall C spectrometers HMS and SOS, 4 cm LH₂ target and 50 μ A electron beam at 6 GeV. Systematic errors related to the detectors efficiencies and particle identification are taken into account. More studies concerning the validity of factorization and contributions from high mass resonances to the pion yield are underway.

¹G. A. Miller, Nucl. Phys. **A518**, 345 (1990); I. Slaus, B. M. K. Nefkens, and G. A. Miller, Nucl. Instrum. Methods **B56/57**, 489 (1991).

²E. M. Henley and G. A. Miller in *Mesons in Nuclei*, eds., M. Rho and D. H. Wilkinson (North-Holland, Amsterdam 1979).

³J. T. Londergan and A. W. Thomas, Prog. Part. Nucl. Phys. **41**, 49 (1998).

⁴P. Amaudruz *et al.*, (NMC Collaboration), Phys. Rev. Lett. **66**, 2712 (1991), Phys. Lett. **B295**, 159 (1992).

⁵A. Baldit *et al.* (NA51 Collaboration), Phys. Lett. **B332**, 244 (1994).

⁶E. A. Hawker *et al.* (E866 Collaboration), Phys. Rev. Lett. **80**, 3715 (1998), R. S. Towell *et al.*, Phys. Rev. D **64**, 052002 (2001).

⁷G. P. Zeller *et al.* (NuTeV Collaboration), Phys. Rev. Lett. **88**, 091802 (2002).

⁸A. D. Martin, R. G. Roberts, W. J. Stirling, and R. S. Thome, hep-ph/0308087.

⁹J. T. Londergan, A. Pang, and A. W. Thomas, Phys. Rev. D **54**, 3154 (1996).

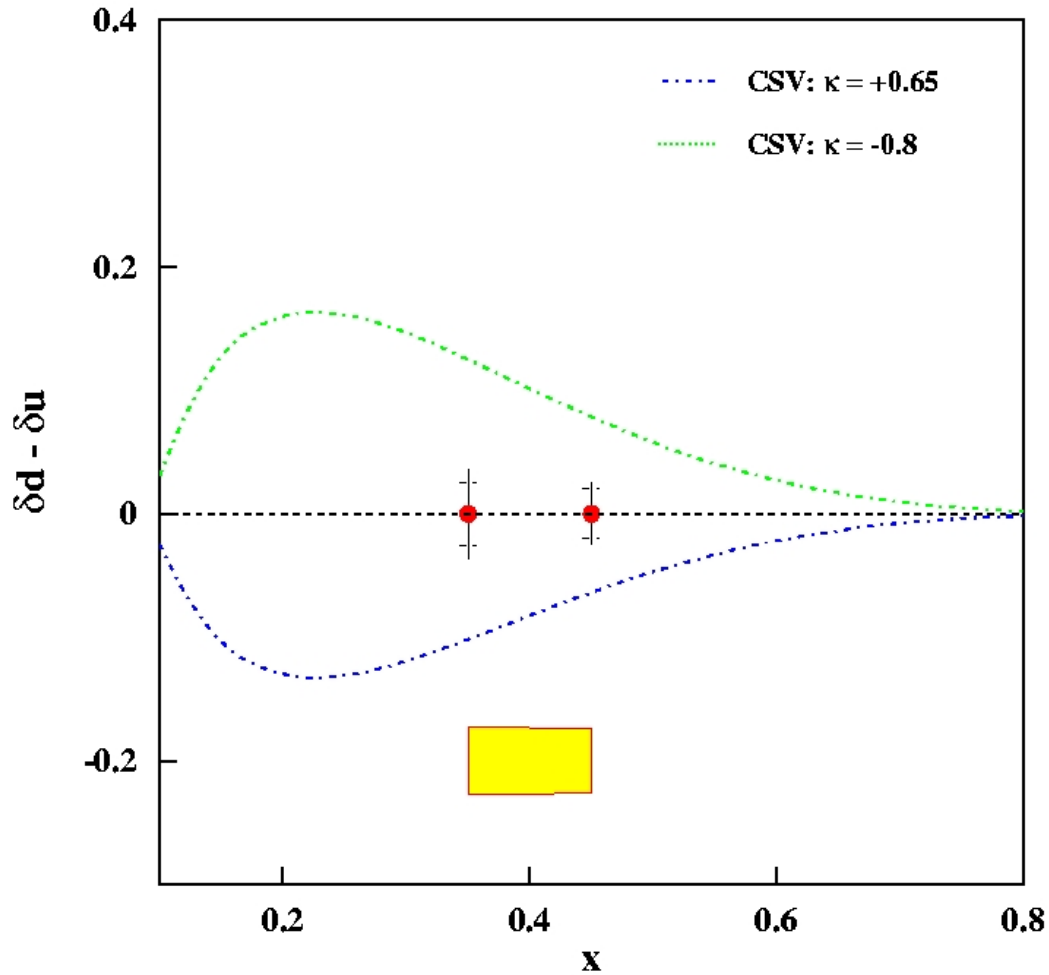


Fig. IV-23. The two curves are the upper and lower limit of CSV contribution given by MRST parameterization. Both statistical and systematical errors are included. The yellow band corresponds to the systematic error related to our present knowledge of PDFs.

V. THEORETICAL PHYSICS

OVERVIEW

Our research addresses the five key questions that comprise the Nation's scientific agenda. We place heavy emphasis on the prediction of phenomena accessible at Argonne's ATLAS facility, at JLab, and at other laboratories around the world; and particularly on anticipating and planning for RIA. One focus is the application of quantum chromodynamics (QCD) to the structure of light- and heavy-hadrons: in vacuum, as relevant to programs such as those pursued at JLab; and in-medium, as appropriate to the early universe, compact astrophysical objects, and the RHIC program. The interactions between light hadrons are studied through the development of reaction theories that exploit modern ideas of hadron structure and which are then used to predict the outcomes of experiments at, *e.g.*, JLab, MIT-Bates and Mainz. The structure and stability of atomic nuclei are explored in *ab-initio* many-body calculations based on the realistic two- and three-nucleon potentials we have constructed. These potentials give excellent fits to nucleon-nucleon elastic scattering data and the properties of light nuclei. In addition, quantum Monte-Carlo methods are being used to compute scattering phase shifts, transition amplitudes, and a variety of electroweak reactions important to astrophysics. Our nuclear structure and reaction program includes: coupled-channels calculations of heavy-ion reactions near the Coulomb barrier; calculations of observables in breakup reactions of nuclei far from stability, the determination of radiative capture rates from Coulomb dissociation experiments, and studies of high-spin deformation and the structure of the heaviest elements. Our programs provide much of the scientific basis for the drive to physics with rare isotopes. Additional research in the Group focuses on atomic physics, neutron physics, fundamental quantum mechanics and quantum computing. The pioneering development and use of massively parallel numerical simulations using hardware at Argonne and elsewhere is a major component of the Group's research.

A. NUCLEAR DYNAMICS WITH SUBNUCLEONIC DEGREES OF FREEDOM

The objective of this research program is to investigate the role of: quark-gluon degrees of freedom in hadron structure and interactions, and in nuclear dynamics; the development and application of reaction theories for use in exploring hadron structure using the data from meson and nucleon-resonance production experiments at modern experimental facilities; and to investigate relations of Poincaré covariant dynamics specified by mass operators to complementary dynamics specified by Green functions.

At the level of quark-gluon degrees of freedom, the Dyson-Schwinger equations (DSEs) provide a Poincaré covariant, nonperturbative method for studying QCD in the continuum. A hallmark of present-day DSE applications in hadron physics is the existence of a symmetry preserving truncation that enables the simultaneous exploration of phenomena such as: confinement, dynamical chiral symmetry breaking, and bound state structure and interactions. In addition the DSEs provide a generating tool for perturbation theory and hence yield model-independent results for the ultraviolet behavior of strong interaction observables. This means that model studies facilitate the use of physical processes to constrain the long-range behavior of the interaction between light-quarks in QCD, which is poorly understood and whose elucidation is a key goal of modern experimental programs. The last year saw numerous successful applications. For example, we demonstrated that the leading-order (rainbow-ladder) term in the DSE truncation scheme, when consistently implemented, is necessary and sufficient to express the Abelian anomaly. We capitalized on this to show that even though excited state pseudoscalar mesons decouple from the axial-vector current in the chiral limit, they nevertheless couple to two photons. It follows that the Primakov process may be used as a tool for their production and study. Furthermore, we employed a Poincaré covariant Faddeev equation to obtain masses and amplitudes for the nucleon and Δ . We subsequently formulated a nucleon-photon vertex, which automatically ensures the vector Ward-Takahashi identity is fulfilled for on-shell nucleons described by the calculated Faddeev amplitudes. This guarantees current conservation. These elements are sufficient for a calculation of the quark contribution to the nucleons' electromagnetic form factors. Our results provide a straightforward explanation of contemporary JLab data on the ratio of the proton's electric and magnetic form factors. Poincaré covariance and pion cloud effects are keystones of this understanding.

At the level of meson and baryon degrees of freedom, we are continuing our effort to develop dynamical models for use in the study of few-GeV electromagnetic meson production reactions. Our objective is an interpretation of the extensive data from JLab in terms of the quark-gluon substructure of nucleon resonances (N^*) as predicted by QCD-based hadron models and simulations of lattice-QCD. In the past year, we have extended our model for pion electroproduction in the Δ region to include neutral current contributions so as to examine local Quark-Hadron Duality in neutrino-induced reactions and determine how the axial $N\text{-}\Delta$ form factor may be determined from a parity violating asymmetry in inclusive $N(\bar{e}, e')$ reactions. We have completed the development of a coupled-channel dynamical model and started to analyze JLab data on two-pion and kaon production. We have completed our study of production mechanisms for the recently observed, narrow-width Θ^+ resonance and found that JLab's data can be fitted by a model consisting of the so-called Drell diagrams ($K\bar{K}$ production through

intermediate vector and tensor meson photoproduction) and mechanisms involving nucleon resonances. An Eikonal model was developed for investigating ρ -meson photoproduction on nuclei. We aim here to analyze JLab data obtained by Argonne's Medium Energy Group to explore Color Transparency issues and address a long-standing question regarding medium effects on di-lepton production in relativistic heavy-ion reactions.

Relativistic quantum dynamics requires a unitary representation of space-time symmetries (Poincaré group) and localization of states, such that states localized in relatively space-like regions are causally independent. We have recently focused on the application and elucidation of complementary mathematical representations of hadron phenomena.

a.1. Aspects and Consequences of a Dressed-Quark-Gluon Vertex (M. S. Bhagwat,* A. Höll, A. Krassnigg, C. D. Roberts, and P. C. Tandy*)

This dressed-quark-gluon vertex is a Schwinger function whose properties are a key to unlocking the nature of light-quark confinement. We explored features of this vertex and their role in the gap and Bethe-Salpeter equations. It became apparent that quenched lattice data indicate the existence of net attraction in the color-octet projection of the quark-antiquark scattering kernel. We saw that this attraction affects the uniformity with which solutions of truncated equations converge pointwise to solutions of the complete gap and vertex equations. We observed that for current-quark masses less than the scale set by dynamical chiral symmetry breaking, the dependence of the dressed-quark-gluon vertex on the current-quark mass is weak and, using a chiral susceptibility, argued that a linear extrapolation to the chiral limit of the results of lattice-QCD simulations of the dressed-quark propagator is inaccurate.

Our analysis employed a vertex model whose diagrammatic content is explicitly enumerable. That enabled the systematic construction of a vertex-

consistent Bethe-Salpeter kernel and thereby an exploration of the consequences for the strong interaction spectrum of attraction in the color-octet channel. We found that with rising current-quark mass the rainbow-ladder truncation provides an increasingly accurate estimate of a bound state's mass. Moreover, the calculated splitting between vector and pseudoscalar meson masses vanishes as the current-quark mass increases, which argues for the mass of the pseudoscalar partner of the $Y(1S)$ to be above 9.4 GeV.

Moreover, our calculations showed that the absence of color-antitriplet diquarks from the strong interaction spectrum is contingent upon the net amount of attraction in the octet projected quark-antiquark scattering kernel. While there is a window within which diquarks appear, the amount of attraction suggested by lattice results is outside this domain.

An article describing this work was published¹ and another submitted.²

*Kent State University.

¹M. S. Bhagwat, A. Höll, A. Krassnigg, C. D. Roberts, and P. C. Tandy, Phys. Rev. C **70**, 035205 (2004).

²A. Höll, A. Krassnigg, and C. D. Roberts, Nucl. Phys. **B141**, 47 (2005).

a.2. Pseudoscalar Meson Radial Excitations (A. Höll, A. Krassnigg, and C. D. Roberts)

The known meson spectrum contains three pseudoscalars [$I^G(J^{PC}) = 1^-(0^{++})$], all with masses below 2 GeV: $\pi(140)$; $\pi(1300)$; and $\pi(1800)$. The lightest of these, the pion [$\pi(140)$], is much studied and well understood as QCD's Goldstone mode. It is the key degree of freedom in chiral effective theories,

and a veracious explanation of its properties requires an approach to possess a valid realization of chiral symmetry and its dynamical breaking. The $\pi(1300)$ is likely the first radial excitation of $\pi(140)$ and while the $\pi(1800)$ may be the second radial excitation, it could also be a hybrid; *i.e.*, a state with nontrivial constituent-gluon-like content. A

hallmark in the contemporary use of Dyson-Schwinger equations is the existence of a nonperturbative, symmetry preserving truncation scheme. We used this scheme to prove that of all pseudoscalar mesons supported by QCD, only the Goldstone modes possess a nonzero leptonic decay constant in the chiral limit when chiral symmetry is dynamically broken. The decay constants of all other pseudoscalar mesons vanish, whether they are radial excitations or hybrids; viz., $f(\pi_n) = 0$ for all $n \geq 1$. This means that in the chiral limit every pseudoscalar meson is blind to the weak interaction except the $\pi(140)$. This exact result places a very tight constraint on all models and nonperturbative methods in their application to hadron spectroscopy and interactions, particularly in connection with the search for exotic and hybrid states in the 1-2 GeV range.

We illustrated these features and aspects of their impact on the meson spectrum using a model of the kernels in the gap and Bethe-Salpeter equations. This work provides the first Poincaré covariant and

symmetry preserving analysis of meson excited states. Moreover, it shows that at realistic current-quark masses the leptonic decay constant of the first radial excitation is two orders of magnitude smaller than that of the $\pi(140)$; and gives the first direct indication that when the current-quark mass is nonzero the leptonic decay constants of mesons on the pseudoscalar trajectory alternate in sign; viz., the decay constants of the ground state and the 2nd, 4th, etc. heaviest states are positive, while those of the 1st, 3rd, etc. are negative. *A posteriori* it is apparent that this outcome is necessary to ensure that the spectral density in the I^{++} channel is non-negative. Nevertheless, the result was not anticipated nor reported previously.

The model was also used to predict: $f(\eta_c) = 0.233\text{GeV}$ and $m(\eta_c) = 3.42\text{GeV}$. In addition, studies were made within this framework that provide support for an interpretation of $\eta(1295)$ and $\dot{\eta}(1470)$ as radial excitations of $\eta(548)$ and $\dot{\eta}(958)$, respectively; and $K(1460)$ as the first radial excitation of the kaon.

Articles describing this work were published.^{1,2}

¹A. Höll, A. Krassnigg, and C. D. Roberts, Phys. Rev. C **70**, 042203(R) (2004).

²A. Höll, A. Krassnigg, C. D. Roberts, and S. V. Wright, Int. J. Mod. Phys. A **20**, 1778 (2005).

a.3. Nucleon Electromagnetic Form Factors (R. Alkofer,* A. Höll, M. Kloker,* A. Krassnigg, C. D. Roberts, and S. V. Wright)

Modern, high-luminosity experimental facilities that employ large momentum transfer reactions are providing remarkable and intriguing new information on nucleon structure. At values of momentum transfer, $Q^2 > M^2$, where M is the nucleon's mass, a veracious understanding of these data requires a Poincaré covariant description of the nucleon. We employed a Poincaré covariant Faddeev equation that describes baryons as composites of confined-quarks and -diquarks, and solved this equation to obtain masses and amplitudes for the nucleon and Delta. Two parameters appear in the model Faddeev equation: masses of the scalar and axial-vector diquark correlations. They were fixed by fitting stipulated masses of the baryons. We interpreted the masses and Faddeev amplitudes thus obtained as representing properties of the baryons' *quark core* and argued that this should be augmented in a consistent fashion by chiral-loop corrections.

We described the formulation of a nucleon-photon vertex, which automatically ensures the vector Ward-

Takahashi identity is fulfilled for on-shell nucleons described by the calculated Faddeev amplitudes. This guarantees current conservation. The vertex *Ansatz* involves three parameters. Two of these specify electromagnetic properties of axial-vector diquarks and a third measures the strength of electromagnetically induced axial-vector \leftrightarrow scalar-diquark transitions. These quantities are also properties of the nucleons' quark core.

These elements are sufficient for a calculation of the quark contribution to the nucleons' electromagnetic form factors. We explored a reasonable range of nucleon-photon-vertex parameter values and found that an accurate description of the nucleons' static properties was not possible with the core components alone. However, this mismatch with experiment was greatly reduced by the inclusion of chiral corrections. Since true pseudoscalar mesons are not pointlike their contribution to baryon form factors diminishes with increasing momentum transfer. Hence, experiments on nucleons involving $Q^2 > 2\text{GeV}^2$ probe properties of the Poincaré covariant quark core.

We calculated ratios of the proton's form factors. On the whole domain of nucleon-photon-vertex parameter values explored, the calculated behavior of $G_{Ep}(Q^2)/G_{Mp}(Q^2)$ for $Q^2 > 2\text{GeV}^2$ agrees with that inferred from contemporary polarization transfer data, and this ratio exhibits a zero at $Q^2 \approx 6.5\text{GeV}^2$. These features are evident in Fig. V-1. Moreover, there is evidence that

$$F_2(Q^2)/F_1(Q^2) \approx (\ln [Q^2/M^2])^2/Q^2 \text{ for } Q^2 > 6\text{GeV}^2.$$

Since the parameters in the nucleon-photon vertex do not influence these outcomes, we judge they are manifestations of features intrinsic to the nucleon's Faddeev amplitude. In the nucleon's rest frame, this amplitude corresponds to a relativistic wave function

with s -, p - and even d -wave quark orbital angular momentum components.

Our study supports a view that baryons can realistically be seen as a dominant Poincaré covariant quark core, augmented by pseudoscalar meson cloud contributions that, *e.g.*, make a noticeable contribution to form factors for $Q^2 < 2\text{GeV}^2$. Since meson compositeness ensures that such contributions diminish with increasing Q^2 , experiments at larger Q^2 serve as an instructive probe of correlations in baryon wave functions; *i.e.*, their Faddeev amplitudes. A good understanding of QCD's long-range dynamics is required in order to obtain a reliable quark-core wave function.

An article describing this work was published² and another submitted.¹

*University of Tübingen, Germany.

¹R. Alkofer, A. Höll, M. Kloker, A. Krassnigg, and C. D. Roberts, to appear in *Few Body Systems*.

²A. Höll, R. Alkofer, M. Kloker, A. Krassnigg, C. D. Roberts, and S. V. Wright, *Nucl. Phys.* **A755**, 298 (2005).

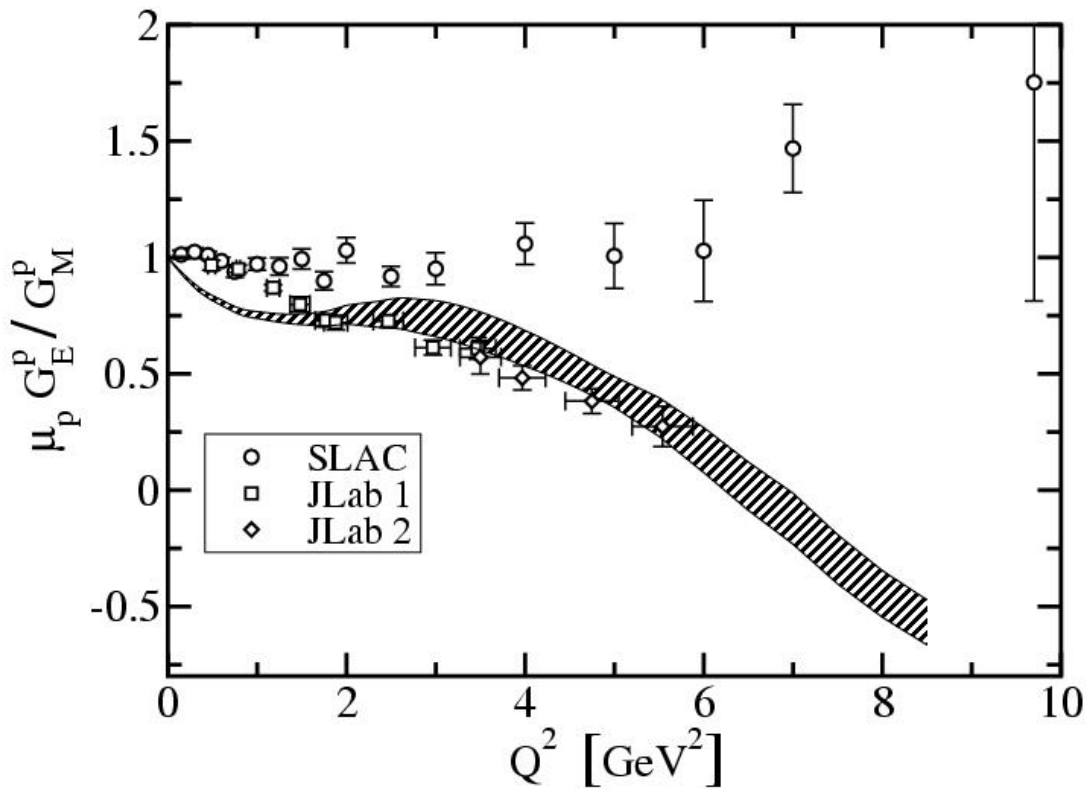


Fig. V-1. This result for the form factor ratios is taken from Ref. 2. Our calculation is the shaded band, whose extent marks the range of sensitivity to the three parameters that characterize our nucleon-photon current. The data are: SLAC – R. C. Walker et al., *Phys. Rev. D* **49**, 5671 (1994); JLAB1 – M. K. Jones et al., *Phys. Rev. Lett.* **84**, 1398 (2000); and JLAB2 – O. Gayou et al., *Phys. Rev. Lett.* **88**, 092301 (2002).

a.4. Electromagnetic Properties of Ground and Excited State Pseudoscalar Mesons (A. Höll, A. Krassnigg, P. Maris,* C. D. Roberts, and S. V. Wright)

The strong interaction spectrum exhibits trajectories of mesons with the same spin+parity, J^P . One may distinguish between the states on these trajectories by introducing an integer label n , with $n=0$ denoting the lowest-mass state, $n=1$ the next-lightest state, etc. The Bethe-Salpeter equation (BSE) yields the mass and amplitude of every bound state in a given channel specified by J^P . Hence it provides a practical tool for the Poincaré covariant study of mesons on these trajectories. A significant feature of such applications is the fact that at least one nonperturbative and symmetry preserving Dyson-Schwinger equation (DSE) truncation scheme exists. This supports the proof of exact results such as, e.g., in the chiral limit excited state 0^- mesons do not

couple to the axial-vector current; viz., $f(\pi_n) \equiv 0$ for all $n \geq 1$.

We demonstrated that the leading-order (rainbow-ladder) term in the DSE truncation scheme, when consistently implemented, is necessary and sufficient to express the Abelian anomaly. It can therefore be used to illustrate the anomaly's observable consequences. We capitalized on this to show that even though excited state pseudoscalar mesons decouple from the axial-vector current in the chiral limit, they nevertheless couple to two photons. It follows that the Primakov process, as employed for example in *PrimEx* at JLab, may be used as a tool for their production and study. We established in addition that the strength of the two-photon coupling is materially

affected by the continuum contribution to the Abelian anomaly.

A renormalization-group-improved rainbow-ladder truncation is guaranteed to express the one-loop renormalization group properties of QCD. We exploited this and thereby determined the leading power-law behavior of the $\gamma^* \pi_n \gamma^*$ transition form factor. When the current-quark mass is nonzero then this form factor behaves as $(4\pi^2/3) (f(\pi_n)/Q^2)$ at deep spacelike momenta. For all but the Goldstone mode this leading order contribution vanishes in the chiral limit. In that case, however, the form factor remains nonzero and the ultraviolet behaviour is $\approx (4\pi^2/3) (-\langle \bar{q} q \rangle / Q^4)$. These results are illustrated in Fig. V-2. Although only exposed starkly in the chiral limit for excited states, this subleading power-law contribution to the transition form factor is always present and in general its coefficient is not simply related to $f(\pi_n)$.

As one might rationally expect, the properties of excited ($n \geq 1$) states are sensitive to the pointwise behavior of what might be called the confinement potential between light-quarks. We illustrated this by

laying out the evolution of the charge radii of the $n = 0, 1$ pseudoscalar mesons. As it is shielded by Goldstone's theorem, the ground state's radius can be insensitive to details of the long-range part of the interaction. However, that is not true of $r(\pi_1)$, the radius of the first excited state, which is orthogonal to the vacuum. An increase in the length-scale that characterizes the range of the confining potential reduces $r(\pi_1)$. This result states that increasing the confinement force compresses the excited state: indeed, it is possible to obtain $r(\pi_1) < r(\pi_0)$. However, our current best estimate is $r(\pi_1) \approx 1.4 r(\pi_0)$.

A detailed exploration of the properties of collections of mesons on particular J^P trajectories offers the hope of exposing features of the long-range part of the interaction between light-quarks. In principle, this interaction can be quite different to that between heavy-quarks. The pseudoscalar trajectory is of particular interest because its lowest mass entry is QCD's Goldstone mode. Chiral current conservation places constraints on some properties of every member of this trajectory, whose study may therefore provide information about the interplay between confinement and dynamical chiral symmetry breaking.

An article describing this work was published.¹

*University of Pittsburgh.

¹A. Höll, A. Krassnigg, P. Maris, C. D. Roberts, and S. V. Wright, Phys. Rev. C **71**, 065204 (2005).

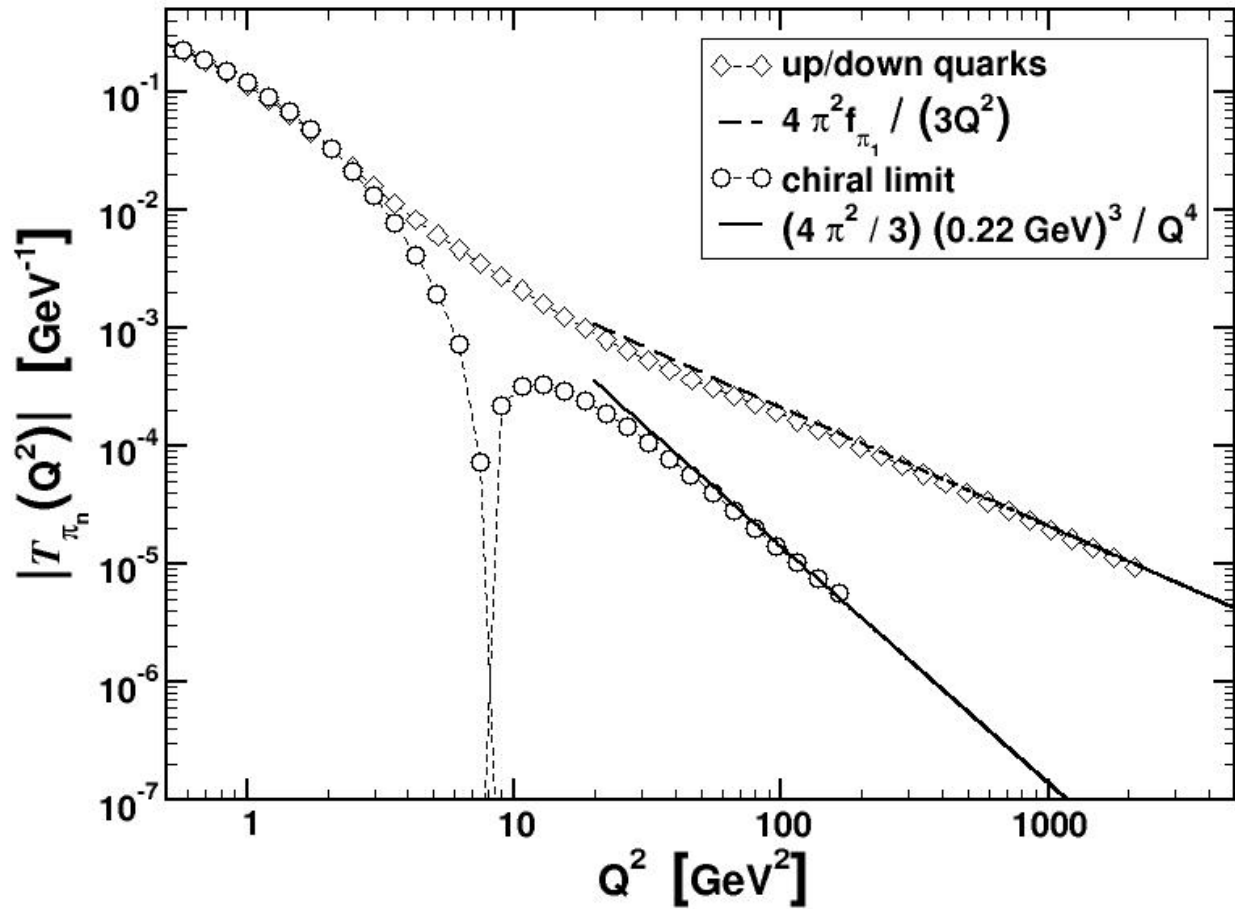


Fig. V-2. Large- Q^2 behavior of the $\gamma^* \pi_n \gamma^*$ transition form factor: Diamonds – result obtained with the physical current-quark mass value of 5.5 MeV; Circles – our chiral limit calculation; Solid line – the curve $(4\pi^2/3) (\langle \bar{q} q \rangle / Q^4)$.

a.5. Charge Form Factors of Quark-Model Pions¹ (F. Coester and W. N. Polyzou*)

Experimental data on the pion charge form factor are well represented by Poincaré invariant constituent-quark phenomenology depending on two parameters, a confinement scale and an effective quark mass. Pion states are represented by eigenfunctions of mass and spin operators, and of the light-front momenta. An effective current density is generated by the dynamics from a null-plane impulse current density. A simple shape of the wave function depending only on the confinement scale is sufficient. The range of

quark-masses and confinement scales consistent with both low and high Q^2 data depends on the shape of the wave function. Such minimal phenomenological models of confined quark dynamics with quark masses between 200 and 300 MeV can easily accommodate existing experimental values of pion form factors, as well as QCD based predictions for Q^2 in the range of several GeV^2 . Sufficiently precise data for larger values of Q^2 will limit acceptable shapes of the wave functions and associated mass scales of the impulse currents.

*University of Iowa.

¹F. Coester and W. N. Polyzou, Phys. Rev. C **71**, 028202 (2005).

a.6. Axial Transition Form Factors and Pion Decay of Baryon Resonances¹ (F. Coester, B. Juliá-Díaz,* and D. O. Riska*)

The pion decay constants of the lowest orbitally excited states of the nucleon and the $\Delta(1232)$ along with the corresponding axial transition form factors are calculated with Poincaré covariant constituent-quark models with instant, point and front forms of relativistic kinematics. The model wave functions are chosen such that the calculated electromagnetic and axial form factors of the nucleon represent the

empirical values in all three forms of kinematics, when calculated with single-constituent currents. The closest description of the empirical values for the axial coupling of the nucleon and the $\Delta(1232)$ - N axial transition coupling obtains with front form kinematics. The pion decay widths calculated in instant and point form are significantly smaller than in front-form kinematics.

*University of Helsinki, Finland.

¹B. Juliá-Díaz, D. O. Riska, and F. Coester, Phys. Rev. C **70**, 045204 (2004).

a.7. Quark-Hadron Duality and Parity Violating Asymmetry of Electroweak Reactions in the Δ Region (T.-S. H. Lee, K. Matsui,* and T. Sato*)

A dynamical model of electroweak pion production reactions in the $\Delta(1232)$ region, developed by Sato and Lee, was extended to include neutral current contributions in order to examine local Quark-Hadron Duality in neutrino-induced reactions and to investigate how the axial N - Δ form factor can better be determined from the parity violating asymmetry in $N(\bar{e}, e')$ reactions. We showed that recent (e, e') data on the structure functions F_1 and F_2 , which exhibit Quark-Hadron Duality, are in good agreement with our predictions. For possible future experimental tests, we then predicted that the structure functions F_1 , F_2 , and F_3 for (ν, e) and (ν, ν') processes should also show a similar Quark-Hadron Duality. These results are shown in Fig. V-3. The spin dependent

structure functions g_1 and g_2 in (e, e') were also calculated in our model. It was found that local Quark-Hadron Duality is not seen in the calculated g_1 and g_2 , while our results for g_1 and some polarization observables associated with the exclusive $p(\bar{e}, e'\pi)$ and $\bar{p}(\bar{e}, e'\pi)$ reactions are in good agreement with recent data. This is shown in Fig. V-4. In an investigation of the parity violating asymmetry A of $N(\bar{e}, e')$ reactions, it was found that the non-resonant contribution is small at the Δ peak and a measurement of A with an accuracy of 20% or better is needed to distinguish two previously determined axial N - Δ transition form factors. This is shown in Fig. V-5. The predicted asymmetry A is also compared with Parton Model predictions for future experimental investigations of Quark-Hadron Duality.

*Osaka University, Japan.

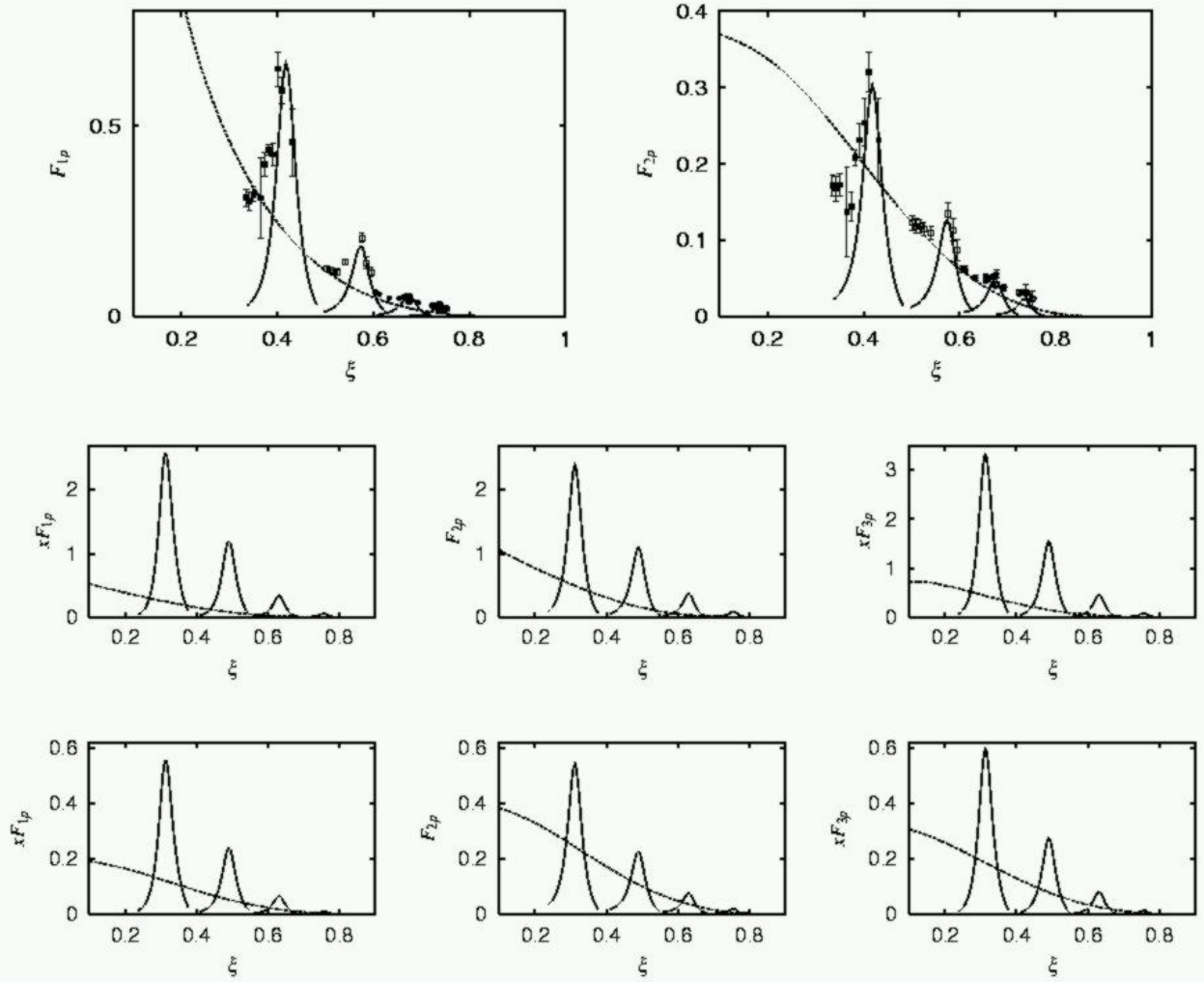


Fig. V-3. Structure functions F_1 (left) and F_2 (right) of $p(e,e')$ (top), and F_1 (left), F_2 (center), and F_3 (right) for $p(\nu,e)$ (middle) and $p(\nu,\nu')$ (bottom) processes. The dashed curves are calculated using the CETQ6 parton distribution functions at $Q^2 = 10 \text{ (GeV/c)}^2$. The solid curves are the results at $Q^2 = 0.7, 1.5, 2.3, 3.5 \text{ (GeV/c)}^2$ (from left to right) calculated with the SL model.

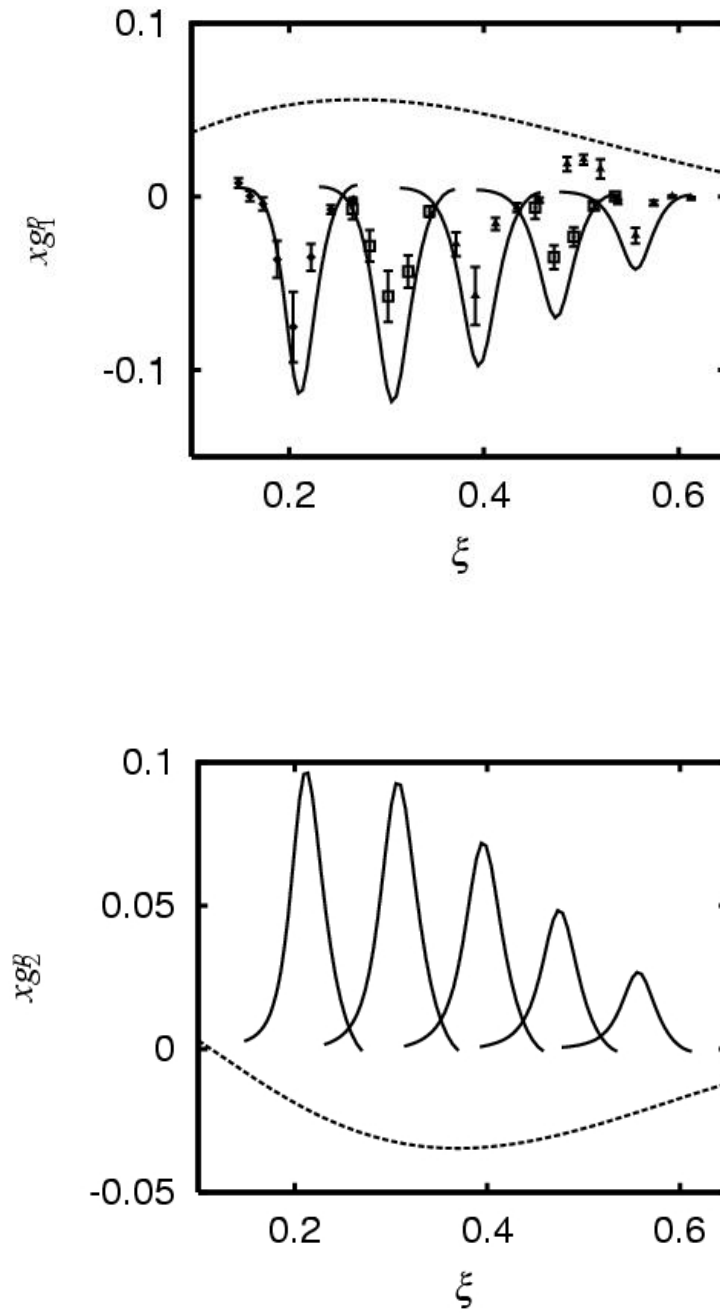


Fig. V-4. Spin dependent structure functions g_1 (top) and g_2 (bottom). The dashed curves are from the fits to deep inelastic scattering data. The solid curves are the results at $Q^2 = 0.21, 0.35, 0.62, 0.92, 1.37$ $(\text{GeV}/c)^2$ (from left to right) calculated with the SL model.

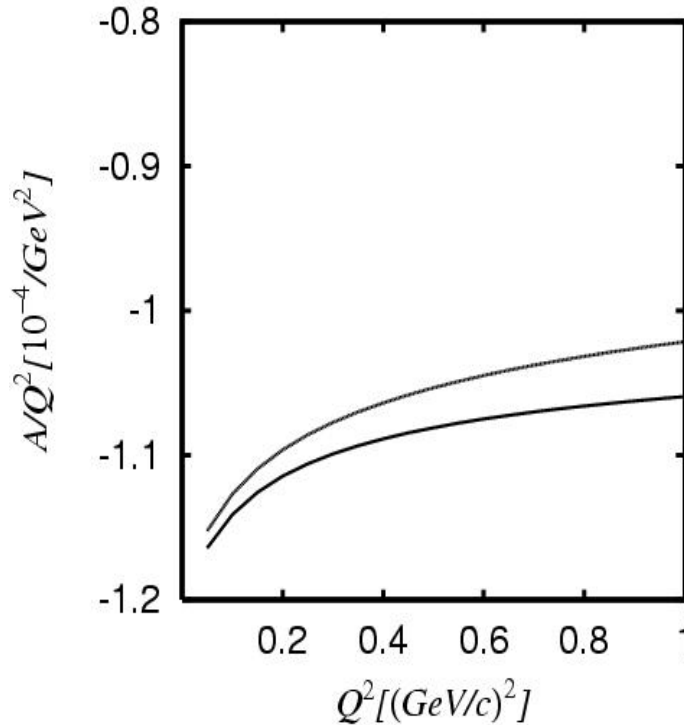


Fig. V-5. The Q^2 -dependence of the parity violating asymmetry (A/Q^2) of $\bar{p}(e,e')$ calculated with the SL model. The solid (dashed) curve is obtained using the axial N - Δ form factor $G_{N,\Delta}^A$ of the SL model [Kitagaki et al., Phys. Rev. D **42**, 1331 (1990)]. The results are for invariant mass $W = 1.232$ GeV and electron scattering angle $\theta = 110^\circ$.

a.8. Dynamical Coupled-Channel Model of Electromagnetic Meson Production Reactions (T.-S. H. Lee, A. Matsuyama,* and T. Sato†)

We have developed a dynamical coupled-channel model for investigating the structure of the nucleon resonances (N^*) using the very extensive data from Jefferson Laboratory. The model Hamiltonian includes interactions between γN , πN , ηN , ωN , and the three-body $\pi\pi N$ ($\pi\Delta$, ρN , σN) channels. Meson cloud effects on the N^* excitations are treated exactly, consistent with the $\pi\pi N$ unitarity condition. The non-resonant parts of the model Hamiltonian are derived from effective Lagrangians by using the unitary transformation method. The N^* parameters are identified with current hadron structure calculations. The resulting Faddeev-type coupled-

channel scattering equations are solved by using a Spline-Function method such that the $\pi\pi N$ cut effects can be included exactly in calculating the meson production cross sections. This crucial numerical advance overcame the main difficulty of all of the previous work using the method of contour rotation. We are now applying the method to analyze the JLab data on $\gamma p \rightarrow \pi\pi N$. One sample result from our calculations at $W = 1.7$ GeV is shown in Fig. V-6. We see that the model can reproduce the main features of the data. We are in the process of exploring whether the remaining discrepancies with data can be interpreted as the contributions from 'missing' N^* resonances.

*Shizuoka University, Japan; †Osaka University, Japan.

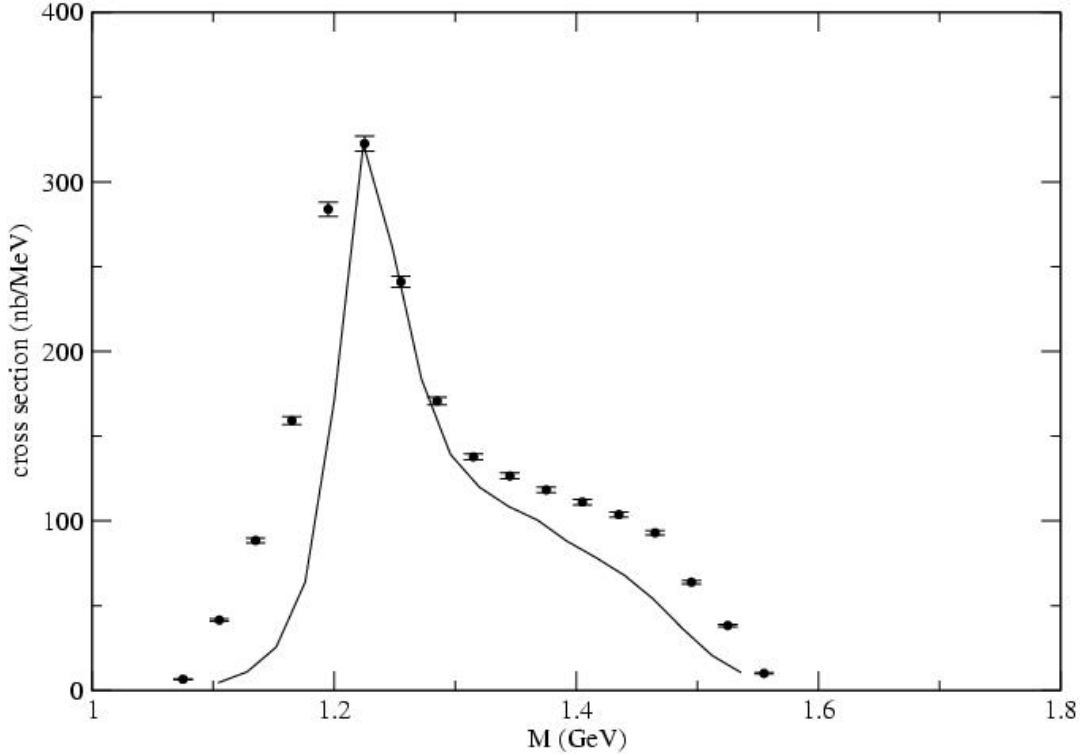


Fig. V-6. The calculated $\gamma p \rightarrow \pi^- \pi^+ p$ cross section as a function of the invariant mass of the final $\pi^+ p$ system (solid line) is compared with the JLab data at $W = 1.7$ GeV.

a.9. Study of N^* Resonances with Kaon Photoproduction Reactions (T.-S. H. Lee, B. Julia-Diaz,*† B. Saghai,* and F. Tabakin†)

We are performing coupled-channel calculations in order to investigate N^* effects in kaon photoproduction reactions. The model consists of γN , πN , KY ($K\Lambda$ and $K\Sigma$) channels. The effects due to other channels, such as the $\pi\pi N$, are treated phenomenologically by using a subtraction method and empirical γN and πN amplitudes. On the other hand, the crucial final state interactions owing to $\pi N \rightarrow KY$ and $KY \rightarrow K'Y'$ are generated from a coupled-channel model, which is derived from an

$SU(3)$ effective Lagrangian and describes well the available $\pi N \rightarrow KY$ data. In Fig. V-7, we show a sample result from our calculations. It is seen that: the coupled-channel effect owing to the πN channel is important; and the N^* excitations play an important role in strangeness production reactions. We are now in the process of analyzing all $\gamma N \rightarrow K\Lambda, K\Sigma$ data from Jefferson Laboratory, aiming at testing the N^* parameters predicted by chiral constituent quark models.

*CEA/Saclay, France, †University of Pittsburgh.

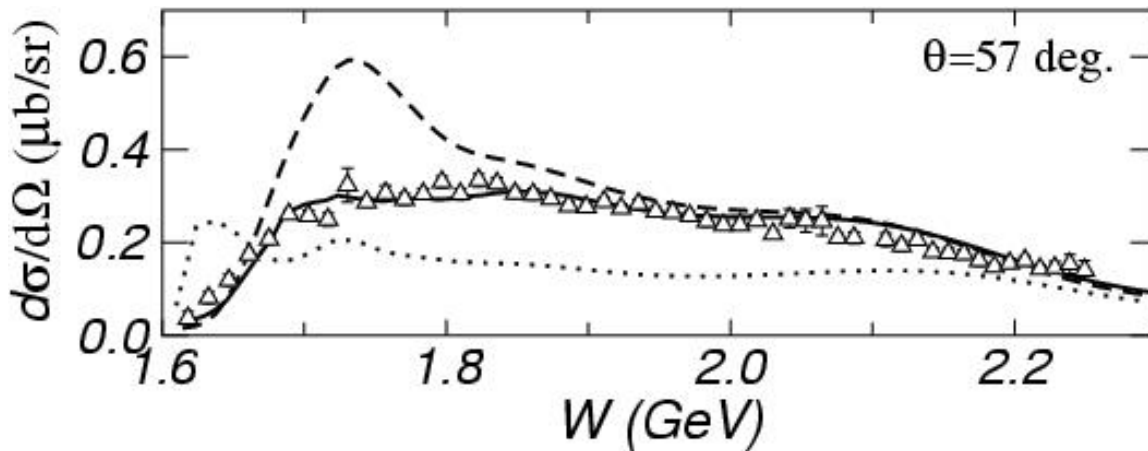


Fig. V-7. Total cross sections for $\gamma p \rightarrow K^+ \Lambda$. The solid curve is our full coupled-channel calculation. The dashed curve is obtained when the coupling with the πN channel is turned off. The dotted curve is from keeping only the N^* effects.

a.10. Medium Effects on the Electromagnetic ρ Meson Production on Nuclei (T.-S. H. Lee, Y. Oh,* and R. Rapp†)

It is recognized that in-medium effects on vector meson propagation are crucial in understanding dilepton production in relativistic heavy-ion collisions. In particular, the effects predicted by Rapp and Wambach have provided a quantitative explanation of the di-lepton production data without invoking the assumption that a quark-gluon plasma was created during the collision. On the other hand, the predicted in-medium effects must be verified in other reactions that do not have the complexities of relativistic

heavy-ion collisions. We are conducting such an investigation by considering the photoproduction of ρ meson on nuclei. The ρ photoproduction amplitude is generated from the model of Oh and Lee, and the ρ propagation in finite nuclei is calculated from the model of Rapp and Wambach by applying the Eikonal formulation of Gottfried and Julius. We are in the process of developing a computation code for analyzing the recent JLab data obtained by Argonne's Medium Energy Group.

*University of Georgia; †Texas A&M University.

a.11. Pentaquark $\Theta^+(1540)$ Production in $\gamma N \rightarrow K \bar{K} N$ Reactions (T.-S. H. Lee, K. Nakayama,* and Y. Oh*)

We investigate how the exotic pentaquark $\Theta(1540)$ baryon can be identified in the $\gamma N \rightarrow K \bar{K} N$ reactions, focusing on the influence of the background (non- Θ production) mechanisms. By imposing the $SU(3)$ symmetry and using various quark model predictions, we are able to fix the coupling constants for evaluating the so-called Drell diagrams, the $K \bar{K}$ production through the intermediate vector meson and tensor meson photoproduction, and the mechanisms involving intermediate $\Lambda(1116)$, $\Lambda(1405)$, $\Lambda(1520)$, $\Sigma(1193)$, $\Sigma(1385)$, and $\Lambda(1232)$ states. The vector meson photoproduction part is calculated from a

phenomenological model which describes well the experimental data at low energies. The charged tensor meson production is calculated from a one-pion-exchange model which describes well the total cross section data of $\gamma p \rightarrow a_2^+(1320) n$. We point out that the neutral tensor meson production cannot be due to π^0 -exchange [as done by Dzierba *et al.*, *Phys. Rev. D* **69**, 051901 (2004)] because of C -parity. Neutral tensor meson production is estimated by considering vector meson exchange and found to be too weak to generate any peak at the position near $\Theta(1540)$. For $\Theta(1540)$ production, we assume that it is an isoscalar and hence can only be produced in $\gamma n \rightarrow K^+ K n$ and $\gamma p \rightarrow K^0 \bar{K}^0 p$ reactions, not in $\gamma p \rightarrow K^+ K p$ and

$\gamma n \rightarrow K^0 \bar{K}^0 n$. The total cross section data for $\gamma p \rightarrow K^+ K^- p$ is thus used to fix the form factors which regularize the background amplitudes so that the signal of $\Theta(1540)$ in $\gamma n \rightarrow K^+ K^- n$ and $\gamma p \rightarrow K^0 \bar{K}^0 p$ cross sections can be predicted. We find that the predicted $K^+ K^-$ and $K^+ n$ invariant mass distributions

in the $\gamma n \rightarrow K^+ K^- n$ reaction can qualitatively reproduce the shapes of the JLab data. However, the predicted $\Theta(1540)$ peak cannot be unambiguously identified in the data. This is shown in Fig. V-8. Our results suggest strongly that high statistics experiments are needed to resolve the problem.

*University of Georgia.

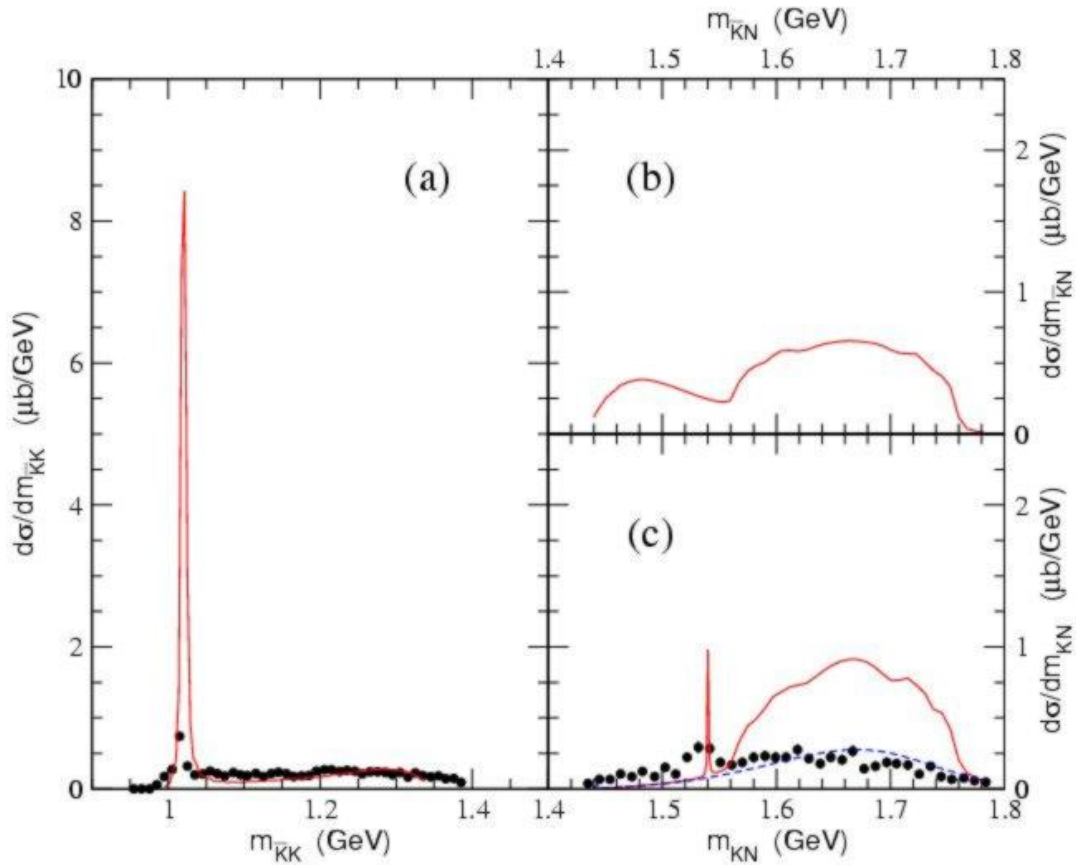


Fig. V-8. (a) $K^+ K^-$, (b) $K^- n$, and (c) $K^+ n$ invariant mass distributions for $\gamma n \rightarrow K^+ K^- n$ at $E_\gamma = 2.3$ GeV. The experimental data are from JLab. The dashed line in (c) is obtained without the ϕ meson background and the Θ contributions. Here we assume that the $\Theta(1540)$ has even parity.

B. NUCLEAR FORCES AND NUCLEAR SYSTEMS

The goal of this program is to achieve a description of nuclear systems ranging in size from deuterium and tritium to nuclear matter and neutron stars using a single parametrization of the nuclear forces. Aspects of our program include both the construction of two- and three-nucleon potentials and the development of many-body techniques for computing nuclear structure and reactions with these interactions. Detailed quantitative, computationally-intensive studies are essential parts of this program.

Quantum Monte Carlo (QMC) calculations of light ($A \leq 12$) nuclei with realistic interactions have been the main focus of our recent efforts. Our nonrelativistic Hamiltonian contains the accurate Argonne $v18$ two-nucleon (NN) potential, which includes charge-independence breaking terms, and either the Urbana IX three-nucleon (NNN) potential, or one of several Illinois NNN models. The QMC calculations include both variational (VMC) and Green function (GFMC) methods. We begin with the construction of variational trial functions based on sums of single-particle determinants with the correct total quantum numbers, and then act on them with products of two- and three-body correlation operators. Energy expectation values are evaluated with Metropolis Monte Carlo integration and parameters in the trial functions are varied to minimize the energy. These optimized variational wave functions can then be used to study other nuclear properties. They also serve as a starting point for the GFMC calculations, which systematically remove higher excited-state components from the trial wave functions by propagation in imaginary time.

We are currently studying all $A \leq 10$ nuclei, including more than 100 ground or excited states, as well as ^{12}C . These are the first calculations to treat $A \geq 6$ nuclei directly with realistic NN and NNN interactions. In GFMC calculations, with our best Hamiltonian, we can reproduce most of the experimental ground- and excited-state energies to within 0.6 MeV .

This year we reported a study of higher excited states in $A = 6-8$ nuclei, based on the discovery that GFMC propagation, when started with orthogonalized VMC wave functions for multiple states of the same spin and parity, preserves the orthogonality to a very good approximation. This has enabled the calculation of many more states in the last few years, and these studies are now being extended to $A \geq 9$ nuclei.

Many excited states in the light nuclei are not particle stable and should be treated as scattering states, though our efforts prior to this year treated all of them as bound. A major effort began this year to extend our GFMC program to nucleon-nucleus scattering, and substantial progress was made on ^5He , or $n-\alpha$ scattering. The results are promising, indicating an ability to calculate *ab-initio* the low-energy scattering cross section, and extract resonance energies and widths. A major long term goal of this effort is to use GFMC wave functions to predict reaction cross sections for astrophysics as part of the Theory Group's nuclear astrophysics effort.

We also began a systematic survey of cluster form factors and spectroscopic factors in the light p -shell nuclei using VMC wave functions. The correlations in these wave functions can provide significant quenching of spectroscopic factors compared to traditional shell-model calculations. Specific applications were made for two (d,p) experiments performed at ATLAS using rare-

isotope beams in inverse kinematics. The calculated cluster form factors were used as input to the distorted-wave Born approximation (DWBA) program PTOLEMY, developed here many years ago, to provide the theoretical analysis of the experiments.

b.1. Quantum Monte Carlo Calculations of Light Nuclei Energies (S. C. Pieper, R. B. Wiringa, K. M. Nollett, and J. Carlson*)

We have been studying the ground states and excitation spectra of light nuclei as A -body problems with realistic nucleon-nucleon (NN) and three-nucleon (NNN) interactions using advanced quantum Monte Carlo (QMC) many-body methods. Our preferred Hamiltonian contains the Argonne v_{18} NN potential (AV18), which gives an excellent fit to elastic NN scattering data and deuteron properties, and the Illinois-2 NNN potential (IL2), which we have fit to binding energies of $A \leq 8$ nuclei. The QMC methods include both variational Monte Carlo (VMC), which gives an initial approximate solution to the many-body Schrodinger equation, and Green function Monte Carlo (GFMC), which systematically improves on the VMC starting solution. The GFMC method produces absolute binding energies that are accurate at the 1-2% level.

The VMC calculations begin with the construction of an antisymmetric Jastrow trial wave function that includes single-particle orbits coupled to the desired JM values of the state of interest as well as pair and triplet correlations. A symmetrized product of two- and three-body spin, isospin, and tensor correlation operators (induced by the NN and NNN potentials) is applied to the Jastrow product to produce the full trial function. The wave function is diagonalized in the small basis of different spatial symmetry components to project out multiple states with the same quantum numbers.

In GFMC calculations an imaginary-time propagator, $\exp[-(H-E_0)\tau]$, where H is the Hamiltonian, E_0 is an estimate of the eigenvalue, and τ is the imaginary time, is applied to the VMC trial function. The excited-state components of the trial function are damped out for large τ , leaving the exact lowest eigenfunction with the quantum numbers of the input VMC trial function. The expectation value of H is computed for a sequence of increasing values of τ to determine the convergence.

Two years ago we found that GFMC can be used to compute higher excited states with the same quantum numbers as lower states if the propagation is started with a trial function that is orthogonal to the starting wave functions for the lower states. This past year we systematically computed all the p -shell states in the $A = 6, 7, 8$ nuclei, doubling the number of states we had been able to study previously. The excited state spectrum is shown in Fig. V-9. With our best Hamiltonian, AV18+IL2, we reproduce 36 experimental energies with an rms deviation of 0.60 MeV.¹ This work is being extended to additional excited states in the $A = 9, 10$ nuclei.

Recently we began studying p -shell nuclei with incomplete s -shell cores, such as ${}^4\text{H}$, negative-parity excited states in ${}^4\text{He}$, ${}^5\text{H}$, ${}^7\text{H}$, etc., with the VMC method. In the $A = 4$ cases, we get reasonable qualitative agreement with R -matrix analyses of experimental data, although ultimately these systems should be studied as $(A-1) + N$ scattering states, as discussed below for ${}^5\text{He}$. However for the heavier hydrogen isotopes, which are not well known but are the subject of experimental searches, we may have to settle for pseudo-bound-state calculations for some time. GFMC results have also been obtained for the ground states of ${}^{4,5}\text{H}$.

We are also working on unnatural-parity states caused by the excitation of one p -shell nucleon to the sd -shell. These states can appear fairly low in the excitation spectrum of $A \geq 7$ nuclei, and particle-stable states occur in ${}^{10}\text{Be}$ and ${}^{10}\text{B}$. First calculations of such states a few years ago found them to be several MeV higher than observed experimentally. Recently we revisited the ${}^9\text{Be}$ positive-parity states and obtained much better results. We also studied ${}^7\text{He}$ positive-parity states for the first time in support of an ATLAS experiment, discussed below in connection with spectroscopic factors. We plan to revisit the $A = 10$ states in the coming year.

*Los Alamos National Laboratory.

¹S. C. Pieper, R. B. Wiringa, and J. Carlson, Phys. Rev. C **70**, 054325 (2004).

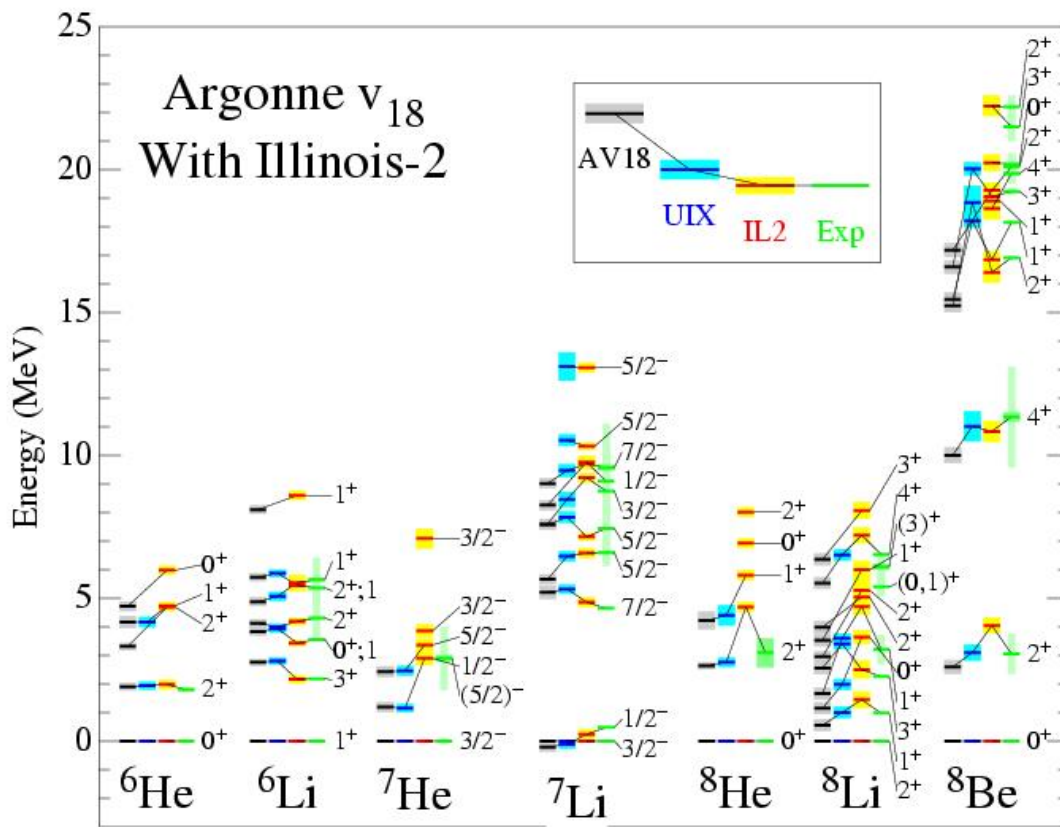


Fig. V-9. GPMC excitation energies computed for the Hamiltonians AV18, AV18 + UIX, and AV18 + IL2, compared with experimental values. The shaded bands show the Monte Carlo statistical (or experimental) errors. The narrow shaded bars on the experimental values show the experimental widths.

b.2. Scattering Methods for Quantum Monte Carlo Calculations (K. M. Nollett, S. C. Pieper, R. B. Wiringa, and J. Carlson*)

Our calculations of properties of light nuclei have concentrated on computing energies, particularly since the development of the methods has until recently required that unbound states be treated as bound states. We have therefore been restricted to bound or narrow states, and unable to compute the widths of resonances. A smaller amount of effort has gone into computing transition probabilities and radiative-capture cross sections using VMC wave functions, along with calculations of a few static nuclear properties like RMS radii.

It is desirable to expand the range of the QMC methods to include unbound states treated as such and the computation of phase shifts and reaction cross sections. This will greatly expand the number of observables against which the potentials can be

tested. It will also open the door to accurate quantitative predictions of reaction cross sections for astrophysics, at least in the light systems important for solar neutrinos, big-bang nucleosynthesis, and seeding the r -process in neutron-rich freezeout.

We are developing methods to compute unbound states, using an R -matrix-like boundary condition to specify the state being computed. As a first application, we have computed low-energy phase shifts in the first three partial waves in ${}^4\text{He}$ - n scattering. In VMC, the boundary condition is set as a condition on the correlation between the ${}^4\text{He}$ nucleus and the last neutron. In GPMC, the boundary condition is enforced through a method of images that enforces a specified logarithmic derivative in the wave function at a specified surface (a fixed ${}^4\text{He}$ - n separation, usually 7 or 8 fm in our calculations).

Preliminary results are in good agreement with R -matrix fits to the laboratory data. These are shown in Fig. V-10 b for the Argonne- v_{18} + Illinois-2 potential. This potential reproduces the experimental energies for the given boundary conditions to within 0.2 MeV for ${}^5\text{He}$ states with $J = 3/2$ and 0.5 MeV for states with $J = 1/2$. This compares favorably with its

performance for the 17 narrow or bound states to which it was fitted.

This work opens the door to several additional calculations in light nuclei, particularly neutron resonances, states in ${}^4\text{H}$, and the ${}^7\text{Be}(p,\gamma){}^8\text{B}$ radiative capture reaction.

*Los Alamos National Laboratory.

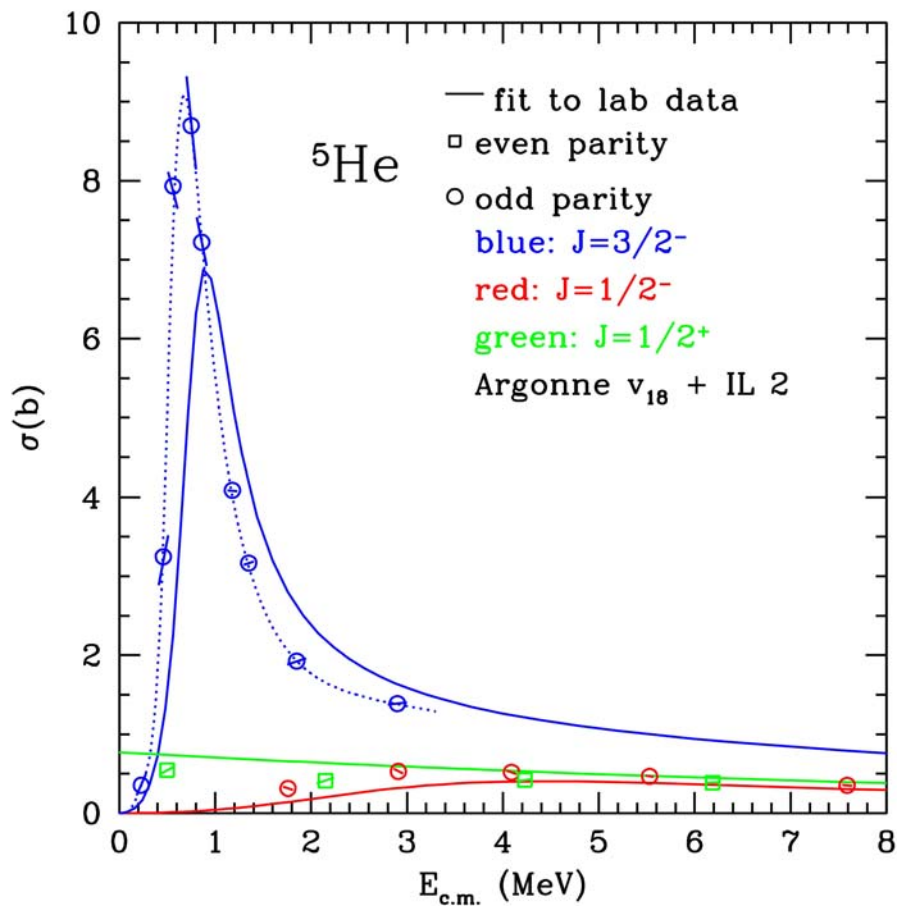


Fig. V-10. Cross sections for ${}^4\text{He}$ -neutron scattering, broken down by partial wave. Solid curves are an R -matrix fit to the measured cross sections. Points with Monte Carlo error bars are results of GFMC calculations. The blue dotted curve connecting the $J^\pi = 3/2^-$ results is a guide to the eye.

b.3. Spectroscopic Factors and Cluster Form Factors of Light Nuclei (R. B. Wiringa, S. C. Pieper, D. Kurath, and D. J. Millener*)

The cluster form factor is defined as the overlap between A -body and $(A-1)$ -body nuclear states, either in configuration or momentum space, $\langle (A-1)_j | a_j(r,p) | A_j \rangle$, where a_j is a nucleon annihilation operator. It is a very useful quantity in

analyzing pickup reactions such as (p,d) , where A_j' is a ground state, or stripping reactions such as (d,p) , where $(A-1)_j$ is a ground state, or nucleon-knockout reactions such as $(e,e'p)$. The cluster form factor can be folded into a DWBA calculation to help extract experimental

information. The spectroscopic factor S is just the normalization of this wave function overlap, and provides a simple characterization of nuclear structure aspects of such reactions.

We have been calculating the cluster form factors and spectroscopic factors for all $A \leq 10$ nuclei using VMC wave functions from the AV18+UIX Hamiltonian. The spectroscopic factors are being compared to predictions from the Cohen-Kurath (CK) shell model. The CK spectroscopic factors for transitions between stable nuclei were first published in 1967, but many additional transitions are now experimentally accessible with the advent of rare-isotope beams at Argonne, MSU, and other facilities.

The main difference between the CK and VMC spectroscopic factors is that the latter can show significant reductions due to the correlations in the VMC wave functions. An example is the ${}^7\text{Li}(e,e'p){}^6\text{He}(J)$ reaction where $J = 0, 2$ for the ground state or first excited state of the residual ${}^6\text{He}$ nucleus. The CK values for these two states are 0.59 and 0.40, while the VMC calculation gives 0.36 and 0.25, respectively, or just 2/3 the strength. This kind of reduction in strength is consistent with electron-scattering experiments. However, the VMC spectroscopic factors are not always significantly

reduced compared to CK, indicating considerable dependence on details of the nuclear structure.

As part of this work, the effect of translational invariance on spectroscopic factors was studied. We find that for light p -shell nuclei described by realistic wave functions, the effect of translational invariance is much smaller than the standard shell-model correction of $A/(A-1)$. We are continuing to study this.

Two specific applications were made this year in conjunction with experiments carried out at ATLAS with rare-isotope beams. These were studies of the experimental spectrum of ${}^9\text{Li}$ using the ${}^8\text{Li}(d,p){}^9\text{Li}$ reaction, and a search for excited states in ${}^7\text{He}$ using the ${}^6\text{He}(d,p){}^7\text{He}$ reaction, both in inverse kinematics. We computed excited state spectra for ${}^9\text{Li}$ and ${}^7\text{He}$, including positive-parity states in the latter case. We then evaluated the cluster form factors for transitions to the different states and fed them into the DWBA program PTOLEMY to compare theoretical predictions with experimental differential cross sections. For ${}^9\text{Li}$ the DWBA results are generally in good agreement with experiment, both for the magnitude and shape of the angular distributions.¹ For ${}^7\text{He}$ the ground-state distribution is well described, but a large, broad, peak around 2.5 MeV excitation energy can only be partially accounted for.

*Brookhaven National Laboratory.

¹A. H. Wuosmaa *et al.*, Phys. Rev. Lett. **94**, 082502 (2005).

C. NUCLEAR ASTROPHYSICS

The objective of this research program is to investigate nuclear processes that take place in stars, in the big bang, and in interstellar and intergalactic space. Nuclear phenomena are ubiquitous in the universe. The stars shine by nuclear energy, and the chemical compositions observed in the solar system and elsewhere are the results of nuclear processes that occurred in the big bang and inside the several generations of stars that have formed since then. Many astrophysical phenomena may only be understood by a combination of nuclear physics with methods more familiar to astrophysicists.

A particularly important problem is to determine rates for the nuclear reactions that occur in astrophysical environments. There are many applications (for example, the rapid neutron capture process) where large contributions from theoretical nuclear physics – particularly masses and cross sections - will always be necessary as input, and we maintain research interests in these areas. We have applied advances in the theoretical descriptions of light nuclei to compute cross sections important for big-bang nucleosynthesis, the solar neutrino flux, and seeding of the r -process. This work continues in close connection with our other work on light nuclei, and the main goals at present are to improve the wave functions and computational methods as described in section **b.2**. In the last year, we have participated in work to improve the computational methods used to compute weak-interaction rates important for the collapse and subsequent supernova explosions of massive stars.

Understanding nucleosynthesis and energy generation in a particular astrophysical environment requires calculations of nuclear reaction networks. Even for cases in which the detailed astrophysical phenomena can only be understood from difficult calculations coupling a reaction network and hydrodynamics, simpler network calculations can identify the crucial reactions and other nuclear properties to be determined by more detailed theoretical and experimental work. Ongoing work in this area involves big-bang nucleosynthesis, nuclear burning in low-mass stars, and photon-nucleus reactions in high-energy cosmic rays.

A major goal of nucleosynthesis studies is to determine the specific physical conditions that gave rise to abundance patterns seen in nature: what mix of different kinds of stellar environments gave rise to observed chemical compositions? Large amounts of important new data on abundance patterns are now being collected, with important evidence arising from low-metallicity stars in our own galaxy, absorption-line systems backlit by distant quasars, and primitive inclusions and pre-solar grains embedded in meteorites. These data contain important clues about the nucleosynthetic history of the universe, both locally and globally, and the effort to disentangle the clues into information on stellar sources and galactic chemical evolution is necessarily coupled to our work on nucleosynthesis.

In addition, studies are underway of electroweak reaction rates relevant to astrophysical processes in dense nuclear matter. These are a part of our attempt to predict observable features of quark matter in compact astrophysical objects.

c.1. Moments Methods for Response Functions with Momentum Transfer Dependence (K. M. Nollett, W. Haxton,* and K. Zurek*)

Models of the pre-supernova evolution of massive stars are very sensitive to the neutrino transport properties of the stellar core, which in turn have large contributions from inelastic neutrino scattering on nuclei in the mass range near iron. Much of the scattering response of these nuclei is dominated by the Gamow-Teller resonance. In a shell-model approach, this contribution to the cross section can be separated into an energy-dependent factor and a separate response function that is independent of momentum transfer q . The response function is found by the Lanczos algorithm, an iterative procedure that casts the Hamiltonian into a tridiagonal form given a suitably-chosen initial basis vector. To find a response function, one applies the operator of interest (in this case, the Gamow-Teller operator) to the initial state, and uses the resulting state as the starting point in a Lanczos tridiagonalization. The eigenvectors of the tridiagonal matrix are then easily related to the response function of the operator.

To determine Gamow-Teller rates averaged over a neutrino energy distribution, one need only apply this procedure once. However, there may be significant contributions from forbidden transitions, introducing more complicated q dependence into the operator, so that the response function has to be recomputed completely for each q . In the usual shell model approach for nuclei of mass comparable to iron, this is computationally prohibitive. Hence, groups who

found Gamow-Teller strengths from the Lanczos procedure have switched to the random-phase approximation in order to incorporate forbidden transitions in their calculations.

We have taken a different approach and sought ways of breaking up the Lanczos algorithm into first a computationally-expensive setup phase that is performed only once and then a much smaller set of steps that take information computed in the first phase and produce the response function at a given value of q . With this in mind, we have produced four new variations on the Lanczos algorithm, and tested them by application to the problem of inelastic electron scattering on ^{28}Si – a problem that contains many of the same kinds of operators as the calculation of weak responses. Each algorithm has distinct strengths and weaknesses that will determine in what cases it is applicable, and all the algorithms are very similar in how they scale with the number of values of q at which the response is to be computed and the size of the shell-model basis. Each method also may be computed to reproduce the true strength function to some specified degree of precision, as shown in Figs. V-11 and V-12.

All of the methods are faster than the traditional Lanczos algorithm by a factor of the ratio of the dimension of the Hamiltonian to the number of values of q at which the response is to be computed. This will always be a large number (several orders of magnitude) for the astrophysical applications that we have in mind.

*University of Washington.

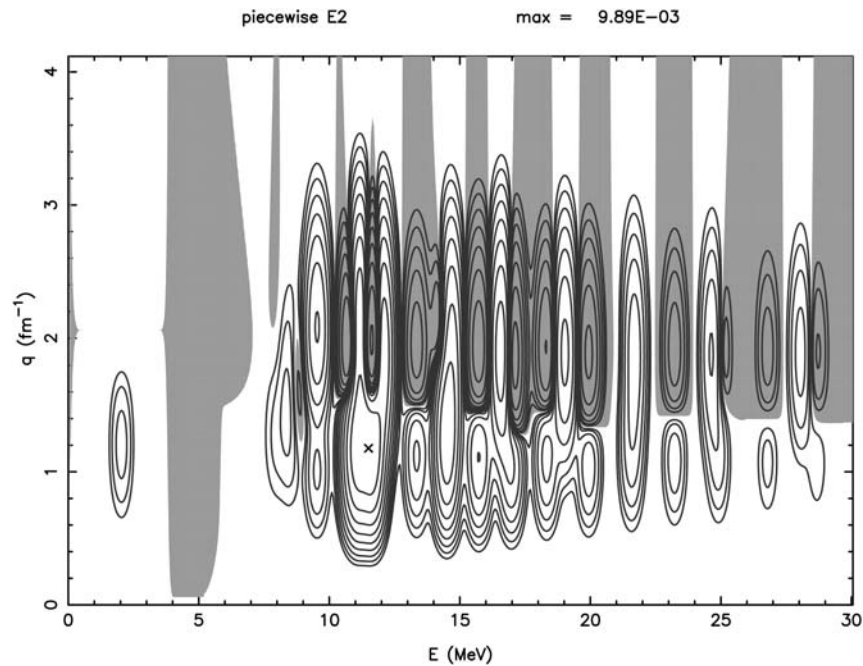


Fig. V-11. Contour plot of the E2 response function of ^{28}Si , computed by one of our new algorithms, the "piecewise Lanczos algorithm." The result has been computed to reproduce 60 moments of the function at a given energy exactly, then smoothed along the E direction by convolution with a Gaussian of full width 0.25 MeV. Shaded areas are regions of negative response, and contours are spaced logarithmically by factors of two.

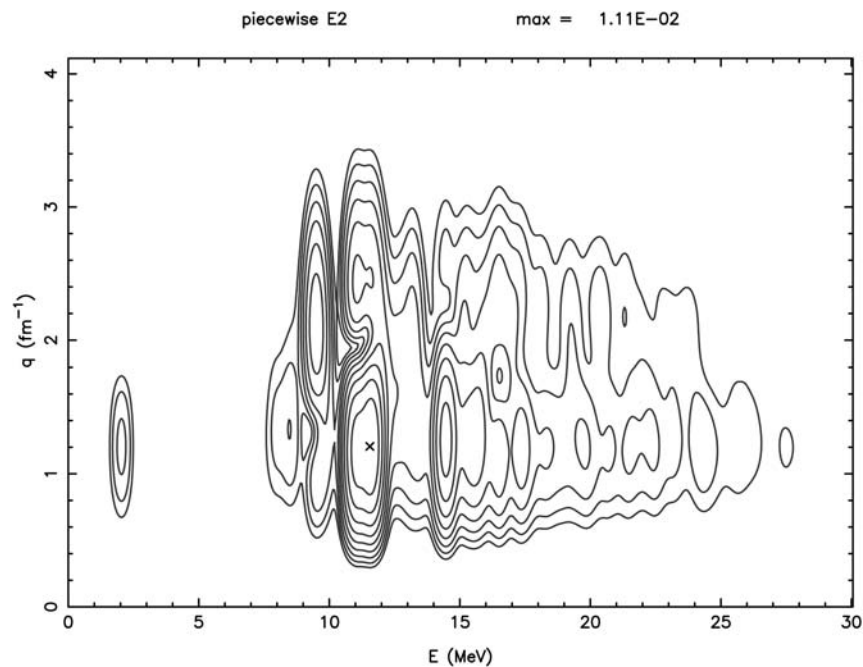


Fig. V-12. Same as Fig. V-11, but with 480 moments exact. Note the disappearance of (gray) regions of negative strength in the improved approximation to the positive-definite true response.

c.2. Short-Lived Nuclei in the Early Solar System and AGB Stars (K. M. Nollett, G. J. Wasserburg*, M. Busso†, and R. Gallino‡)

Sun-like stars, with masses below $3M_{\odot}$, are important sources of nuclei. They produced about half the nuclei heavier than iron in the solar system, a large fraction of the carbon, and possibly most of the nitrogen. In addition, the most numerous type of pre-solar grains recovered from meteorites, the "mainstream" grains, almost certainly formed in the ejecta from such stars.

Composition data from the meteorite grains and from astronomical observations suggest that there are mixing processes inside low-mass stars during the final red giant branch and asymptotic giant branch (AGB) stages, in addition to those processes present in standard one-dimensional stellar evolution models. We previously computed the effects of slow mixing of composition between the convective envelope of a $1.5M_{\odot}$ star and the hotter layers below, during the final few million years of the star's existence on the AGB. This process is referred to as "extra mixing" or "cool bottom processing" (CBP). The calculations showed that without severely disrupting the star's energy budget, composition patterns in the oxygen isotopes found in pre-solar oxide grains may be explained. If mixing is sufficiently deep, the abundances of the short-lived ^{26}Al incorporated into oxide grains may be explained. The characteristic results of this extra mixing now define what are called the "Group 2" oxide grains. New calculations that we have carried out for stars of $2M_{\odot}$ and $3M_{\odot}$ and a range of metallicities, indicate that the

qualitative results are almost independent of stellar parameters.

Since the radioactive ^{26}Al may be produced by CBP, there are also important consequences for the sources of the several radionuclides known to have been present in meteorites that formed when the solar system first condensed. There has long been a puzzle as to how much of the early solar system inventory of radionuclides came from various sources. Possible sources for radionuclides include input from a nearby supernova or AGB star just before the solar system condensed, production from ions accelerated by the magnetic field of the sun during its formation, or simply from accumulated nucleosynthesis by many generations of stars. It is desirable to find a consistent picture involving one or more of these sources that accounts for the origins of the radionuclides, particularly those with lifetimes of 1-100 Myr. AGB-star models for the origins of radionuclides were previously constrained partly by their ^{26}Al production. However, the possibility of substantial ^{26}Al from CBP removes this constraint on the model. At the same time, the number of measured early-solar-system radioactivities has expanded, and it appears that a more diverse range of sources is needed than previously thought. In particular, ^{10}Be can only be made outside stars, and ^{53}Mn cannot come from AGB stars. Divergent results for abundances of ^{129}I , ^{182}Hf , and ^{247}Cm require at least three distinct sources of r -process nuclei that made their last contributions to the protosolar nebula at different times prior to formation of solids in the solar system.

*California Institute of Technology, †University of Perugia, Italy, ‡University of Torino, Italy.

D. NUCLEAR STRUCTURE AND HEAVY-ION REACTIONS

This research focuses on nuclear structure in unusual regimes: nuclei far from stability, and superdeformed nuclei at high spin. We also study heavy-ion reactions near the Coulomb barrier. Much of this work is closely tied to experiments performed at ATLAS and at radioactive beam facilities.

Our studies of heavy-ion reactions include coupled-channels calculations of fusion reactions, elastic and inelastic scattering. The calculated fusion cross sections are usually quite sensitive to the structure and the radii of the reacting nuclei, and it is often possible to reproduce the measurements quite well. However, the calculations can be challenging for very heavy systems because the couplings are strong and the calculations become sensitive to higher-lying states. Another difficulty occurs at energies far below the Coulomb barrier, where the measured cross sections start to fall off steeply compared to calculations.

The hindrance of heavy-ion fusion at low energy is a general phenomenon which has now been observed in many systems, ranging from medium-heavy to heavy systems. The hindrance can be seen clearly by plotting the S factor for fusion. The S factor develops a maximum at low energy, and the energy where that occurs is a good way to characterize the phenomenon. The fusion hindrance is expected to be an entrance channel effect because it occurs at a rather high value of the excitation energy of the compound nucleus, but it has so far not been possible to explain it by conventional coupled-channels calculations.

As part of our continued interest in extracting the rate of radiative capture reactions from experiments, we have focused on proton capture on ${}^7\text{Be}$, which is relevant to the production of ${}^8\text{B}$ in the sun. We have completed a study of the constraints one can obtain on the capture rate from charge symmetry and from the experimental information about the ${}^7\text{Li}(n,\gamma){}^8\text{Li}$ reaction. The result of the study is not unreasonable in comparison to most measurements but it is smaller than the most accurate direct capture measurements.

Many measurements of the ${}^7\text{Be} + p$ capture rate have been performed in recent years, using both direct and indirect methods. One indirect method is to measure the Coulomb dissociation of ${}^8\text{B}$ on a high- Z target and from the data analysis to extract the ${}^7\text{Be} + p$ capture rate. The results obtained are often smaller than the results of direct capture measurements, and it is of interest to understand what causes the discrepancy. We have therefore tested the validity of the first-order approximation that is commonly used in the analysis of Coulomb dissociation experiments by comparing it to more complete dynamical calculations, which include the excitation of ${}^8\text{B}$ to all orders in the Coulomb and nuclear fields from the target. We find that it is necessary to go beyond the conventional first-order analysis if accuracies of 10% or better are required in the extracted capture rate.

We are continuing the development of a program for calculating many-body variational wave functions. This approach puts pairing and particle-hole interactions on an equal footing. These wave functions strictly conserve particle-number and parity. Particle number and parity are projected before variation. In studies of nuclides near the $N = Z$ line, we also project states of good Q , the number parity of $T = 0$ pairs, before variation.

Our treatment of n - p pairing explains many features of nuclear structure for nuclei having almost equal numbers of protons and neutrons. These wave functions explain the Wigner energy anomaly in a simple way. This treatment also explains why the $T = 0$ I^+ state is highly excited in $N = Z$ even-even nuclei and close to ground in odd-odd $N = Z$ nuclides.

We have developed a code for configuration mixing of the wave functions used to describe n - p pairing. We have applied these wave functions to explore n - p pair transfer probabilities in $N = Z$ nuclides. We find that this quantity is very sensitive to $T = 0$ and $T = 1$ correlations in the many-body wave function. Experimental measurements of the pair transfer probability, now under way, will establish the magnitude of $T = 0$ pairing interaction correlations in nuclei near the $N = Z$ line.

The low-lying states of odd mass nuclei provide a good test of the parametrizations of single particle potentials. Study of the spectroscopy of the heavy elements is particularly valuable, as it gives insights into the structure of super-heavy elements. In a collaborative effort with the experimental spectroscopy group at Argonne, we have analyzed low-lying neutron and proton single particle states in the mass 250 region. We have studied neutron single-particle states in ^{247}Cm and proton single particle states in ^{249}Bk , and determined single-particle potentials that are consistent with these analyses.

We also worked toward the development of a universal model for the systematic description of heavy nuclei by configuration mixing of symmetry-restored self-consistent mean-field states using modern effective-energy functionals. The tool developed was employed in large-scale calculations of nuclear properties; *e.g.*, the interpretation and prediction of properties of exotic nuclei.

d.1. Coupled-Channels Calculations of Heavy-Ion Fusion Reactions (H. Esbensen and C. L. Jiang)

We have continued our analysis of heavy-ion fusion cross sections using the coupled-channels technique. This approach works fairly well at energies in the vicinity of the Coulomb barrier and it is often possible to reproduce measurements by including in the calculations the couplings to the low-lying 2^+ and 3^- states, and the mutual and two-phonon excitations of these states. It is also necessary to include one- and two-nucleon transfer channels when the isospin asymmetry of projectile and target are very different.

There are limitations to the coupled-channels method. One example is heavy-ion fusion at energies far below the Coulomb barrier, where the measured cross sections are hindered compared to coupled-channels calculations. A very good example is the fusion of $^{64}\text{Ni} + ^{64}\text{Ni}$ which was measured at ATLAS.¹ It is possible to fit the data above 0.1 mb but the data below 0.1 mb fall off much steeper with decreasing

energy than do the calculations. The hindrance of fusion at low energy is a general phenomenon, which has now been established for many heavy-ion systems.²

Coupled-channels calculations are also challenging for very heavy systems because the couplings are strong and it becomes necessary to include higher multi-phonon excitations in order to make the calculations converge. An example where this might happen is the fusion of $^{64}\text{Ni} + ^{100}\text{Mo}$ which was recently measured at ATLAS.³ The quadrupole mode of ^{100}Mo is very soft and it is almost vibrational, as discussed in section d.2. The calculations that were presented in Ref. 3 included up to three-phonon excitations of the soft quadrupole mode, in addition to the mutual and two-phonon excitations of other low-lying surface modes. We have improved these calculations by including up to six-phonon excitations of the soft quadrupole mode. The surprising result is that the calculated fusion cross section does not change much.

This is illustrated in the top part of Fig. V-13, where the six-phonon calculation (PH6) essentially falls on top of the three-phonon (PH3) calculation.

The effect of couplings to higher multi-phonon states can be seen in the barrier distribution, which is shown in the bottom part of Fig. V-13. The blue dashed curve is the barrier distribution for the three-phonon calculation (PH3) and the red solid curve is the distribution for the six-phonon calculation (PH6). They are very broad, almost 20 MeV, and some of the structures that appear in the three-phonon calculation disappear in the six-phonon calculation. There is a tendency for the calculated distribution to

split into two, one above and one below the barrier obtained in the no-coupling limit (NOC). The data, on the other hand, seem to favor a single, slightly asymmetric, broad barrier distribution.

It appears that the calculated cross sections have essentially converged with respect to multi-phonon excitations of the soft quadrupole mode in ^{100}Mo . The discrepancy with the data around 130 MeV could be due to transfer reactions or incomplete fusion. The discrepancy at the lowest energy is evidence of the fusion hindrance mentioned above. In fact, the S factor obtained from the data exhibits a maximum at about 121 MeV.³

¹C. L. Jiang *et al.*, Phys. Rev. Lett. **93**, 012701 (2004).

²C. L. Jiang *et al.*, Phys. Rev. C **69**, 014604 (2004).

³C. L. Jiang *et al.*, Phys. Rev. C **71**, 044613 (2005).

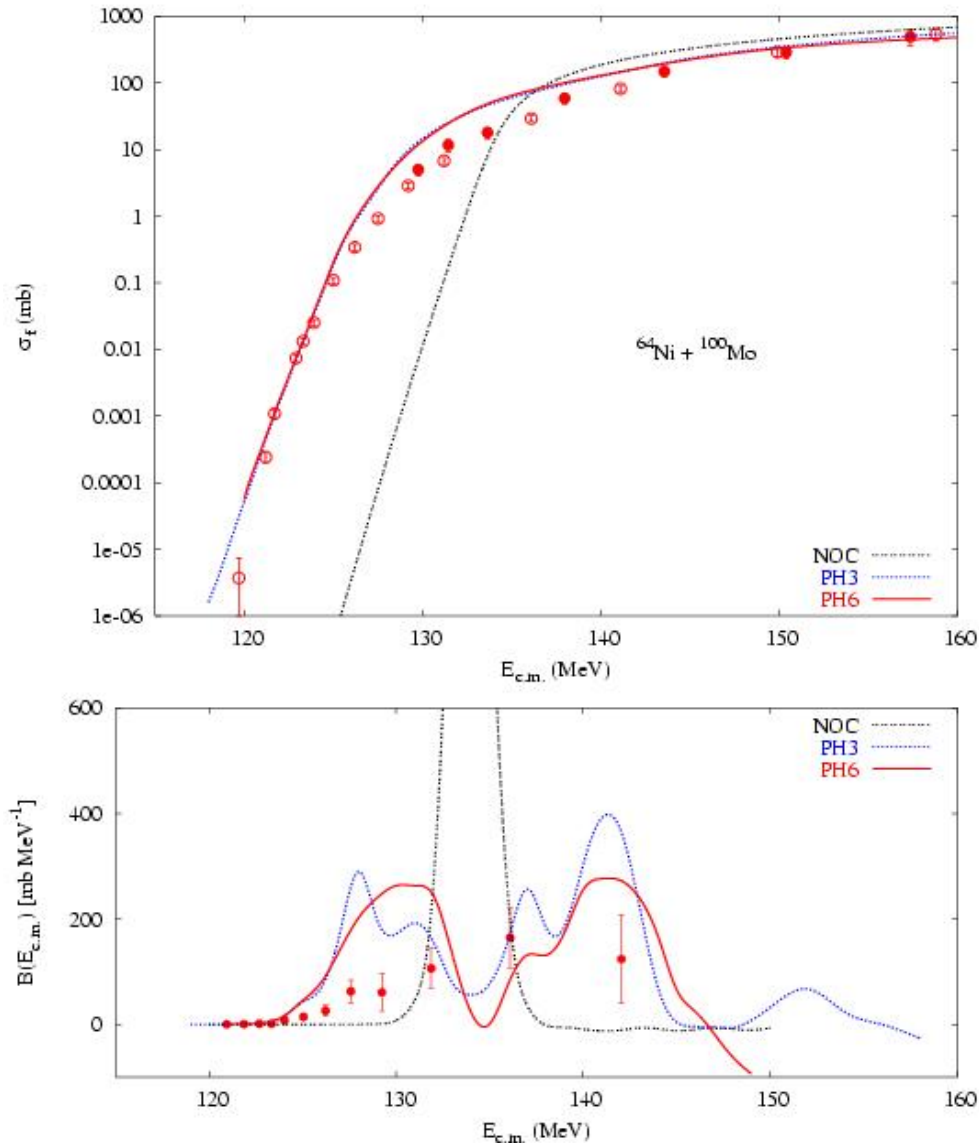


Fig. V-13. Fusion cross section for $^{64}\text{Ni} + ^{100}\text{Mo}$ (top) and the associated barrier distribution (bottom). The data are from Ref. 3. The curves show the no-coupling limit (NOC), the three-phonon (PH3) and six-phonon (PH6) calculations described in the text.

d.2. Modeling the Quadrupole Mode in ^{100}Mo (H. Esbensen)

A problem in the application of the coupled-channels technique to heavy-ion fusion reactions is that the nuclear structure of the reacting nuclei is sometimes poorly known at or above the two-phonon level. It is therefore necessary to make model assumptions about the structure of higher lying states, in order to see their effect on fusion. The rotor and vibrator (harmonic oscillator) models are commonly used, but it would be very useful to have more flexible models that could be used to interpolate between these two

extremes. One such model is the Bohr Hamiltonian, which in general depends on the deformation parameters (β, γ) . This Hamiltonian is particularly easy to apply for γ -unstable nuclei, *i.e.*, when the potential of the Hamiltonian is independent of γ .

To illustrate the application of the Bohr Hamiltonian let us consider the ground state bands of three molybdenum isotopes. They are shown in the top part of Fig. V-14, where they have been normalized to one for the lowest 2^+

state. The red curves are the extreme rotor and vibrator models. The two black dashed curves are the spectra for the $E(5)$ and $X(5)$ dynamical symmetry models developed by Iachello.¹ The green curves are results for γ -unstable nuclei, which have been obtained numerically for the potential

$$V(\beta) = \frac{1}{2}(1-\eta)\beta^2 + \frac{\eta}{4}(1-\beta^2)^2$$

for the three values of the parameter η indicated in the figure. It is noted that the potential for $\eta = 0$ is the harmonic β^2 potential. The spectrum for ^{100}Mo is almost vibrational and it is reproduced quite well for $\eta = 1$.

The $B(E2)$ values (normalized to one for the lowest transition) are shown in the bottom part of Fig. V-14. It is seen that the values for ^{100}Mo are only slightly above the green curve with $\eta = 1$. Thus it appears that the soft quadrupole mode in ^{100}Mo is described fairly well as a γ -unstable, slightly anharmonic vibration. Another feature that can be seen in the two figures is the good agreement between the model with $\eta = 5$ and the $E(5)$ dynamical symmetry model. The reason for this is that the $\eta = 5$ potential resembles the square well potential that was used in the $E(5)$ model.¹

The model described above will be applied to calculate the matrix elements that are needed in coupled-channels calculations of heavy-ion fusion reactions of γ -unstable nuclei. The γ -stable nuclei, with $\gamma \approx 0$, is another simple limit that will be considered.

¹F. Iachello, Phys. Rev. Lett. **85**, 3580 (2000); F. Iachello, Phys. Rev. Lett. **87**, 052502 (2001).

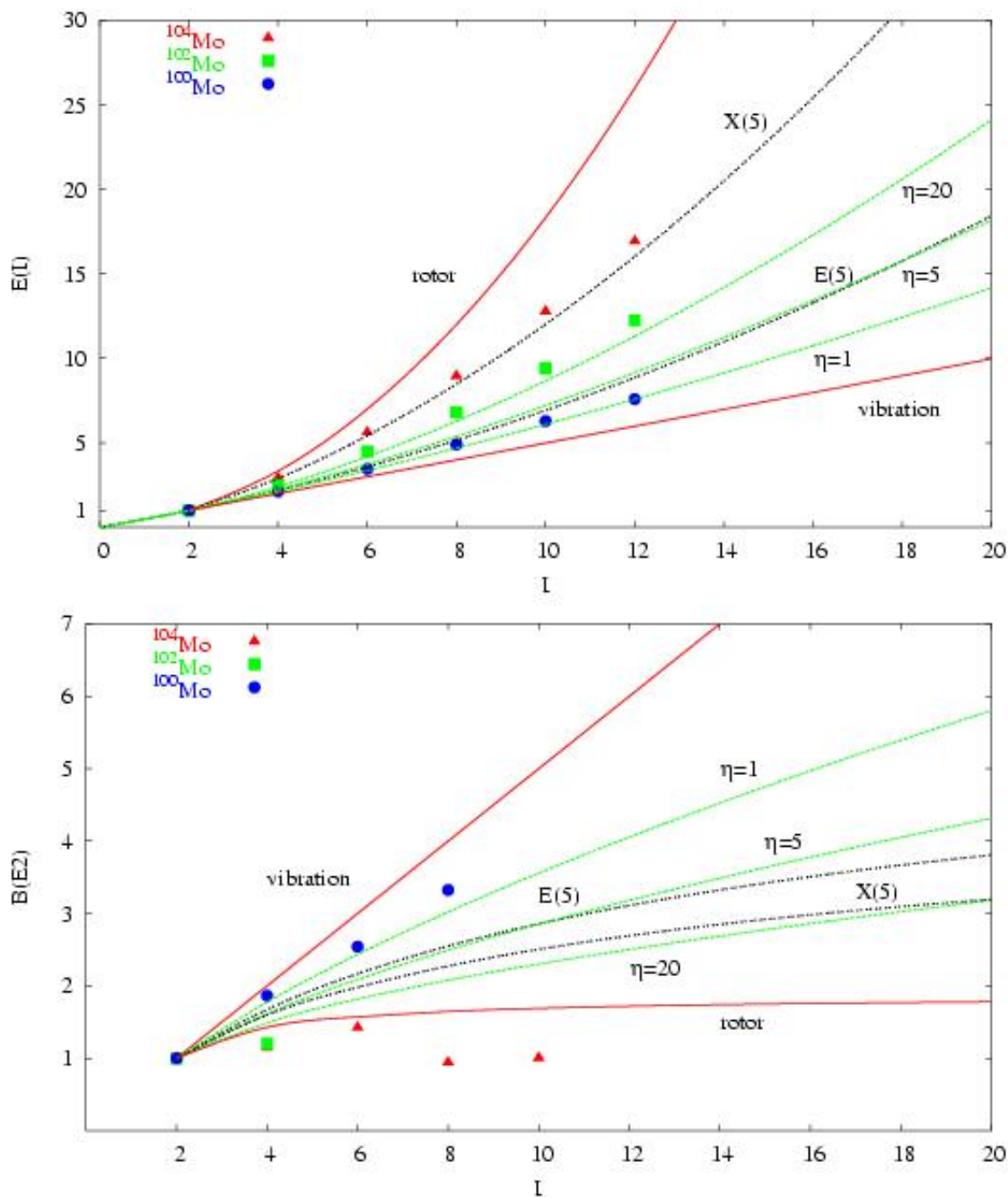


Fig. V-14. Ground state rotational bands of molybdenum isotopes (top part) and the associated $B(E2)$ values (bottom part) are compared to different limits of the Bohr Hamiltonian.

d.3. Constraints on the $^7\text{Be}(p,\gamma)^8\text{B}$ Reaction from Charge Symmetry (H. Esbensen)

The cross section for the radiative proton capture on ^7Be is usually expressed in terms of the S factor at zero relative energy, $S_{17}(0)$. The recommended value¹ in 1998 was $S_{17}(0) = 19 \pm 4 eV b$, and a large

experimental effort has since gone into reducing the uncertainty. Unfortunately, the overlap between more recent results obtained with different techniques (radiative capture, Coulomb dissociation, transfer reactions) is still

marginal. It is therefore of interest to find other ways to put constraints on the 8B S factor.

In a recent work² I assumed charge symmetry between 8B and 8Li and used the measured capture rate of thermal neutrons on 7Li to predict the value of $S_{17}(0)$ for 8B . The analysis was based on a simple two-body model of the valence proton (neutron) interacting with the 7Be (7Li) core. Calculations of the radiative capture rates were repeated for a wide range of the radius (2.1-2.9 fm) and the diffuseness (0.52-0.65 fm) of the nucleon-core nuclear potential, which was parametrized as a Woods-Saxon well. The depth for $p_{3/2}$ orbits was adjusted to give the correct separation energy. The depths for the s -waves (with total $J = I^-$ and 2^-) were adjusted to reproduce the measured neutron scattering lengths on 7Li .

The calculations were analyzed in terms of the asymptotic normalization constant ANC , which relates the asymptotic behavior of the ground state wave function $\varphi(r)$ to the Whittaker function, *i.e.*,

$$\varphi(r) = \frac{ANC}{r} W_{-\eta, l+1/2}(2\kappa r),$$

for large values of r . Here η is the Sommerfeld

$$S_{\text{eff}}(0) \approx N_{\text{nc}} \times S_{17}(0) = [18.4 \pm 1.0 \pm 1.4 (\text{eV b})] \left| \frac{ANC({}^8B)}{ANC({}^8Li)} \right|^2.$$

The ratio of the squares of the two ANC's is found to be 1.03 ± 0.02 . The overall estimate is therefore $S_{\text{eff}}(0) \approx 18.9 \pm 1.8 \text{ eV b}$, which is in very good agreement with the recommended value.¹

It is noted that the conventional shell model approach cannot reproduce the 8Li and 8B capture data simultaneously. The main reason is that the shell

parameter, l is the orbital angular momentum, and κ is the wave number. The calculations showed a strong correlation between the capture rate and the ANC . For the proton capture one obtains

$$S_{17}(0) = 38.7 [\text{eV b fm}] \left| ANC({}^8B) \right|^2,$$

which is essentially independent of the radius and diffuseness of the nuclear potential. For the radiative neutron capture on 7Li to the ground state of 8Li one obtains the following relation between the measured³ and calculated cross sections at thermal energy

$$N_{\text{nc}} = \frac{\sigma_{\text{expt}}}{\sigma_{\text{calc}}} = \frac{0.475 \pm 0.025 \pm 0.036 (\text{fm}^{-1})}{\left| ANC({}^8Li) \right|^2}.$$

The first part of the uncertainty is due to the sensitivity to the parameters of the nuclear potential; the second part reflects the uncertainty in the measured neutron capture rate.³

One can interpret the quantity N_{nc} as a model-dependent spectroscopic factor. Assuming charge symmetry one can then apply the same spectroscopic factor to predict the S factor for 8B . From the above relations one obtains the effective S factor,

model ground state of 8Li (or 8B) has at least two components, namely, a $p_{1/2}$ and a $p_{3/2}$ orbit of the valence nucleon, whereas the ground state is a pure $p_{3/2}$ orbit in the two-body model discussed above. This difference does not affect the 8B capture rate but it causes the neutron capture rate on 7Li to be about 25% higher in the shell model approach than in the two-body model, as explained in the publication.²

¹E. G. Adelberger *et al.*, Rev. Mod. Phys. **70**, 1265 (1998).

²H. Esbensen, Phys. Rev. C **70**, 047603 (2004).

³J. E. Lynn, E. T. Jurney, and S. Raman, Phys. Rev. C **44**, 764 (1991).

d.4. Model Dependence of the ${}^7Be(p, \gamma){}^8B$ Reaction Rate (H. Esbensen)

Measurements of the ${}^7Be(p, \gamma){}^8B$ radiative capture cross sections are performed at relative energies of the proton and 7Be , E_{rel} , that are much higher than the conditions inside the sun. In order to predict the capture rate at stellar conditions it is therefore

necessary to extrapolate the measurements to low energy. This is done in terms of the S factor, $S_{17}(E_{\text{rel}})$, which has a rather modest energy dependence, but to make the extrapolation accurately it is necessary to rely on a good theoretical model for the energy dependence of the

S factor. A model that is sometimes preferred is a three-body model by Descouvemont and Baye from 1994, whereas two-body models are considered less reliable. Since a two-body model is much easier to use in reaction studies, it is of interest to see exactly where the two- and three-body models differ and by how much.

The energy dependence of the S factor for 8B obtained in a two-body model¹ and in Descouvemont's most recent three-body model² are compared in Fig. V-15 with the recent capture data from Seattle.³ Both calculations have been scaled so

they agree with the data below 0.5 MeV. The dashed curves are the two-body results, which have been scaled by the factor 0.98; they show the contributions from s -wave and d -wave capture, and the sum. The nuclear radius and diffuseness of the two-body potential were set to 2.5 fm and 0.58 fm, respectively, and the depths were adjusted for each spin channel as described in Ref. 1. The solid red curves show the three-body results, which were obtained by multiplying Descouvemont's calculation² by a factor of 0.871. It is seen that the d -wave capture rates are essentially identical in the two models. The s -wave capture rates, on the other hand, start to differ at energies above 0.5 MeV.

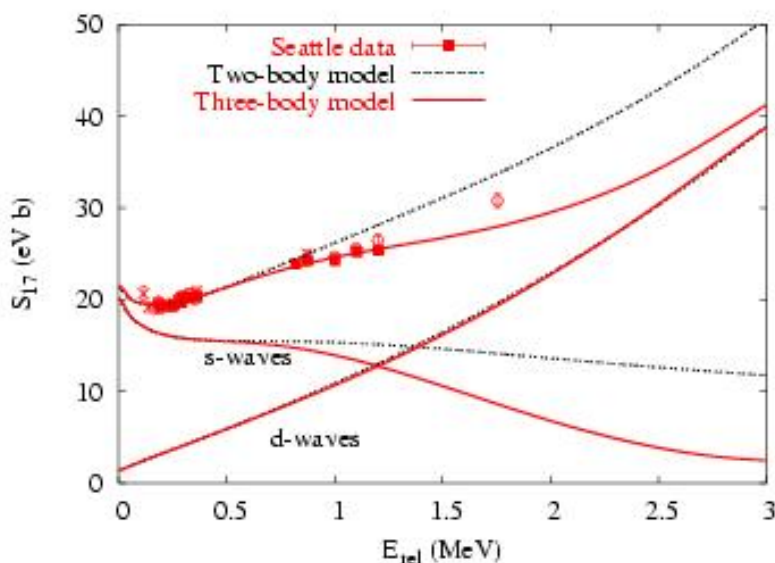


Fig. V-15. Measured³ S factors for 8B are compared to calculations based on a two-body¹ and a three-body model.² The separate contributions from s - and d -wave capture are also shown.

If the extrapolation of the measured S factors to zero relative energy is restricted to energies below the $M1$ resonance, then the two- and three-body models should give the same value of $S_{17}(0)$, according to

Fig. V-15. In fact, they both give $S_{17}(0) = 21.5$ eV b. The difference between the two models shows up at 1 MeV and higher energies, and it is seen that the three-body model is indeed favored by the Seattle data.³

¹H. Esbensen, Phys. Rev. C **70**, 047603 (2004).

²P. Descouvemont, Phys. Rev. C **70**, 065802 (2004).

³A. R. Junghans *et al.*, Phys. Rev. C **68**, 065803 (2003).

d.5. Reconciling Coulomb Dissociation and Radiative Capture Measurements (H. Esbensen, G. F. Bertsch,* and K. A. Snover*)

There is a significant discrepancy between the recent ${}^7Be(p, \gamma){}^8B$ radiative capture measurement¹ and the results extracted from measurements of the Coulomb dissociation (CD) of 8B . The S factors extracted from

the CD experiments are usually smaller, typically by 10-20% at low relative energies (E_{rel}) of the ${}^7Be + p$ final state, and the slope of the S factor is often steeper than obtained in the direct capture measurement. These

differences were identified and analyzed in detail in Ref. 1. They can also be seen in Fig. V-16 by comparing the results of two CD experiments^{2,3} to the prediction of the three-body model (solid curve), which was calibrated in the previous section (see Fig. V-15) to reproduce the direct capture measurement.

In order to understand what causes the discrepancy between the direct and indirect measurements of the S factor for 8B , we have examined the validity of the approximations that are commonly made in the

analysis of CD experiments. The analysis is usually based on first-order perturbation theory and uses the so-called far-field (FF) approximations for the multipole expansion of the Coulomb field. Moreover, the analysis is often restricted to $E1$ transitions. The FF approximation is based on the assumption that projectile and target do not overlap during the collision. We find that both the FF approximation and the first-order theory are inaccurate because of the weak binding and the extended density of the valence proton in 8B .

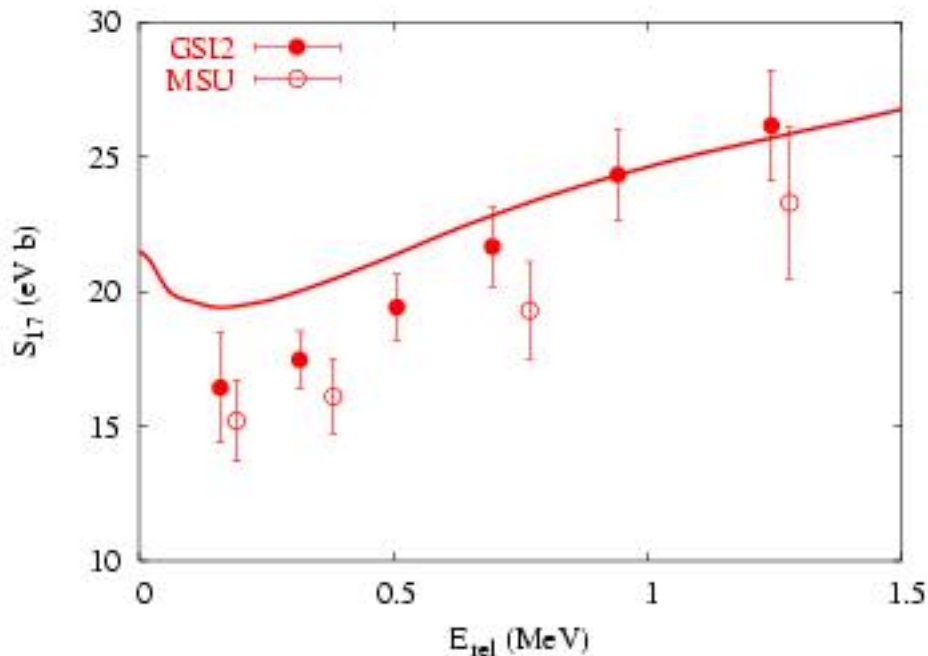


Fig. V-16. S factors for 8B extracted from two Coulomb dissociation experiments^{2,3} are compared to the result of the calibrated three-body model (solid curve), which reproduces the capture data in Fig. V-15.

We have used a semiclassical method to calculate the two-body breakup of 8B into a proton and a 7Be fragment.⁴ This was done numerically by solving the time-dependent Schrödinger equation for the relative motion of the proton and the 7Be core. The breakup is induced by the Coulomb and nuclear fields from a target nucleus, and the time-dependence is generated by the relative motion of projectile and target, which is assumed to follow a classical Coulomb trajectory.

The calculated decay energy spectra we obtain at 52 MeV/n and an impact parameter of 20 fm with a Pb target are shown in Fig. V-17. The top curve shows the result of first-order $E1 + E2$ transitions in the FF approximation, whereas the $E1$ FF approximation is indicated separately by the solid points. The other curves show in decreasing order the effect of using

the correct multipole form factors for the Coulomb field (instead of the FF approximation), of calculating the Coulomb dissociation to all orders (dynamic CD), and finally, the effect of also including the nuclear field from the target (dynamic CN). From the comparison of these calculations it is seen that $E2$ transitions do have a significant strength in the first-order calculation, but their effect is accidentally compensated to some extent by the correct treatment of the Coulomb multipole fields and higher-order processes.

By comparing the solid points and the solid curve in Fig. V-17 it is seen that some discrepancy does remain between the conventional first-order $E1$ calculation (solid points) and the full calculation (lowest solid curve). The full calculation is suppressed at low relative energies but it exceeds the conventional first-order $E1$ calculation at

higher energies. These features provide a qualitative explanation of the observation that the S factors extracted from CD experiments are usually smaller at

low relative energies and their slope is steeper than that obtained in the direct capture measurement. This work has been submitted for publication.⁴

*University of Washington.

¹A. R. Junghans *et al.*, Phys. Rev. C **68**, 065803 (2003).

²F. Schüman *et al.*, Phys. Rev. Lett. **90**, 232501 (2003).

³B. Davids *et al.*, Phys. Rev. C **63**, 065806 (2001).

⁴H. Esbensen, G. F. Bertsch, and K. A. Snover, Phys. Rev. Lett. **94**, 0432502 (2005).

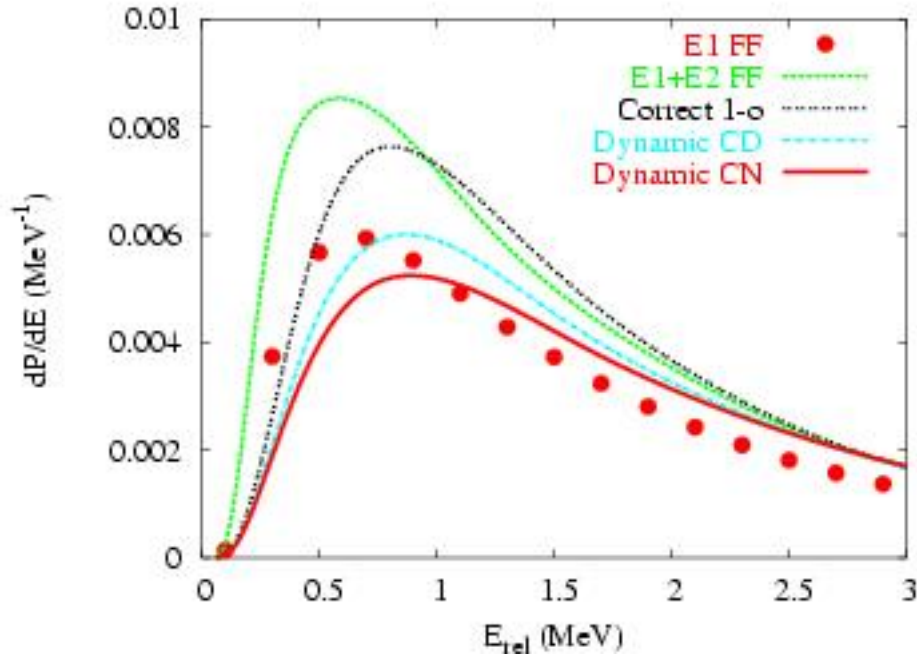


Fig. V-17. Decay energy spectrum for the dissociation of ${}^8\text{B}$ on Pb at 52 MeV/n and an impact parameter of 20 fm. The top curve shows the E1 + E2 FF approximation, and the solid points represent the commonly used E1 FF approximation. The other curves show in decreasing order the effect of using the correct Coulomb form factors to first order (Correct 1-o), of higher-order Coulomb processes (dynamic CD), and finally, the complete calculation which also includes nuclear couplings (dynamic CN).

d.6. Mean Field and Many Body Wave Functions (R. R. Chasman)

We are continuing the development of a program for calculating many-body variational wave functions that puts pairing and particle-hole two-body interactions on an equal footing. The complexity of the wave functions depends only on the number of levels included in the valence space. In these wave functions, we strictly conserve particle number and parity; projecting states of good particle number and parity before carrying out the variational calculations. We have extended the program to improve the treatment of neutron-proton pairing and have applied it to explain several features of nuclides near the

$N = Z$ line. We have also improved the procedure for optimizing variational wave functions.

By using residual interaction strengths (*e.g.*, the quadrupole interaction strength or pairing interaction strength) as generator coordinates, one gets many different wave functions; each having a different expectation value for the relevant interaction mode. Such wave functions are particularly useful when one is dealing with a situation in which a configuration interaction treatment is needed. Because the same basis states are used in the construction of all the many-body wave

functions, it is possible to easily calculate overlaps and interaction matrix elements for the many-body wave functions obtained from different values of the generator coordinates (which are not in general orthogonal). The valence space can contain a very large number of single-particle basis states, when there are constants of motion that can be used to break the levels up into sub-groups. To increase the

manageable size of the valence space, we have parallelized our code to run on the jazz computer system, and we are modifying the code to deal with octupole correlations in heavy nuclei. We have used the generator coordinate method to calculate configuration interaction admixtures for the n - p pairing wave functions. This is important for calculating pair transfer transition probabilities.

d.7. Neutron-Proton Pairing (R. R. Chasman)

We have developed¹⁻³ a treatment of neutron-proton pairing that explains many features of nuclear structure seen near the $N = Z$ line. Our many-body treatment includes n - p pairing, as well as like particle pairing, with full projection of neutron and proton particle number before doing a variational calculation. We also found that there is a new quantum number that holds exactly for collective states; *i.e.*, those states in which no levels are blocked. This new quantum number (Q) is the number parity of the $T = 0$ and $T = 1$ n - p pairs. Fixing the number parity of one n - p mode fixes the other, because we conserve proton number and neutron number exactly. This number parity is closely related to the isospin quantum number. These collective states are the ground states for $N = Z$ nuclides. We project Q before doing a variational calculation. The form of our variational wave function includes an explicit amplitude for “alpha like” correlations in each level as well as the usual amplitudes for n - n , p - p and n - p pairs. We have added terms to the n - p pairing interaction that allow pairs of particles in the same orbitals, giving states with maximum angular momentum. Because of the exclusion principle, these must be n - p pairs and $T = 0$.

In odd-odd $N = Z$ nuclei, the ground state is a degenerate doublet, consisting of a $Q = 0$ and $Q = 1$ state, when the $T = 0$ and $T = 1$ pairing strengths are equal. The splitting of this ground state doublet affords some information about the relative strengths of the $T = 0$ and $T = 1$ pairing strengths. In even-even nuclei, there is a large splitting between the 0^+ $T = 1$ ground state and the 1^+ $T = 0$ excited state. Our model explains this feature in a transparent way.

Most of the excitation energy owes to the breaking of a quartet and the single particle excitation energy involved in making a $T = 0$ pair. In the odd-odd $N = Z$ nuclei case, neither of these effects applies for the $T = 0$ state.

The Wigner energy is the extra binding energy of $N = Z$ even-even nuclei relative to neighboring nuclei. Our approach explains the magnitude of the Wigner energy very well. It owes to the extra pairing energy involved in creating a quartet of nucleons in the same orbital.

Our detailed calculations of the dependence of the binding energies on the relative strengths of the $T = 0$ and $T = 1$ pairing strengths shows that the differences are small as a function of the variation of the relative strengths. Other observables are needed to establish the magnitude of $T = 0$ correlations in nuclei. To that end, we have carried out a calculation of the n - p pair transfer spectroscopic factor. In our calculation, the initial state is an even-even $N = Z$ nuclide and the final states are the lowest $T = 1$ and $T = 0$ states in the neighboring odd-odd ($Z+1, N+1$) nucleus. The relative spectroscopic factors show a considerable sensitivity to the relative strengths of the $T = 0$ and $T = 1$ pairing strengths. A 20% reduction of the $T = 0$ pairing strength gives a 40% reduction in the ratios of $T = 0/T = 1$ pair transfer probabilities. In Fig. V-18, we show single particle levels that are appropriate for the ^{56}Ni region. The blue levels are taken from a Woods-Saxon calculation and the red levels have been shifted to give level spacings in agreement with experimental data. In Fig. V-19, we show the pair transfer probability to the lowest lying $T = 0$ and $T = 1$ states in ^{58}Cu , as a function of $T = 0$ pairing strength, keeping the $T = 1$ pairing strength fixed. The interaction is semi-realistic in this calculation, as we use constant matrix elements for each of the pairing modes.

¹R. R. Chasman, Phys. Lett. **B524**, 81 (2002).

²R. R. Chasman, Phys. Lett. **B553**, 204 (2003).

³R. R. Chasman, Phys. Lett. **B577**, 47 (2003).

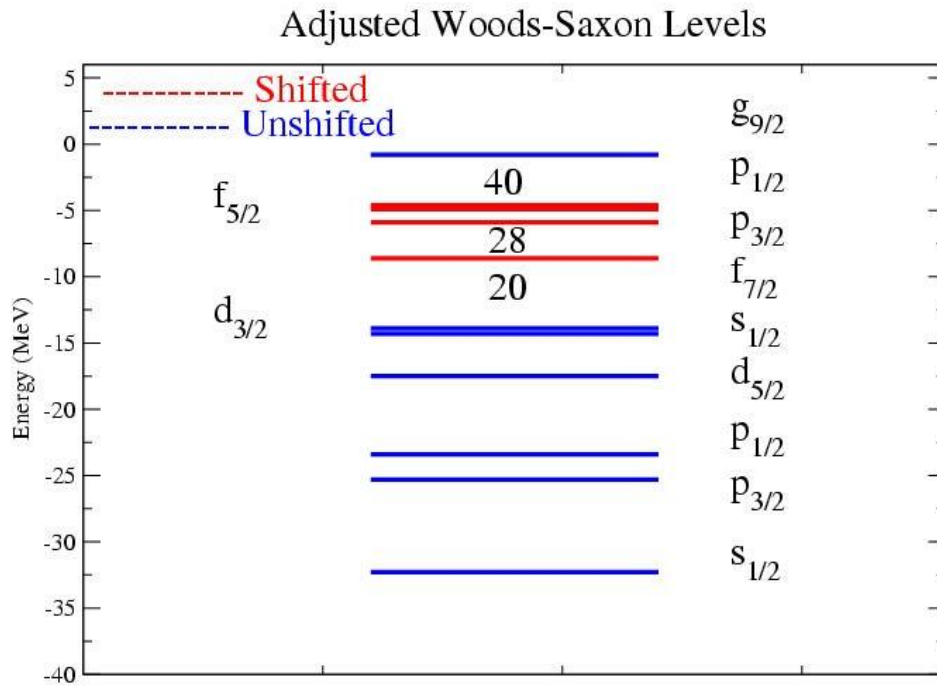


Fig. V-18. Single-Particle States of ^{56}Ni used in calculating pair transfer probability. The states shown in blue are taken directly from a Woods-Saxon calculation. The states shown in red are adjusted to get agreement with level spacings that have been determined experimentally.

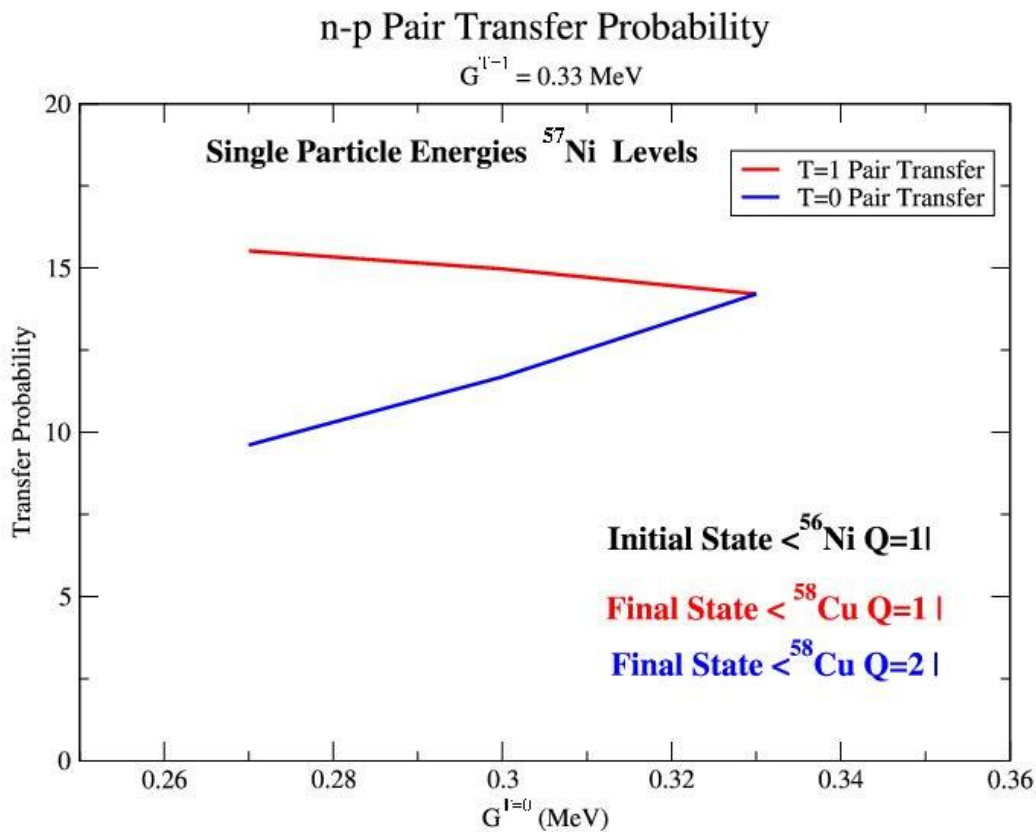


Fig. V-19. Pair Transfer Spectroscopic Factors. The spectroscopic factors are shown for N-P pair transfer to levels in ^{58}Cu from the ground state of ^{56}Ni , as a function of $T = 0$ pairing interaction strength. The $T = 1$ pairing strength is held constant. Semi-realistic matrix elements were used in this calculation.

d.8. Energy Levels of the Heavy Elements (I. Ahmad, and R. R. Chasman)

The study of single-particle states in the heavy elements is a long-term collaborative project. The low-lying states in odd-mass nuclides provide a good test of the parametrizations of single particle models. Vibrational admixtures are usually small for these states. The single-particle energy level spacings in the heavy elements provide useful guidance for single-particle potentials that are appropriate for super-heavy elements. Seven single-particle states have been identified¹ in ^{247}Cm , so this nuclide provides a particularly good test of neutron single particle potentials. Eight single-particle levels have

been identified² in ^{249}Bk . This provides a very good test of proton single-particle potentials in the very heavy elements. When pairing effects are extracted from the observed levels in ^{247}Cm and ^{249}Bk , the orderings and spacings of levels are in good agreement with the levels obtained from our parametrization of a deformed Woods-Saxon potential. These analyses will provide useful constraints on other parametrizations of superheavy potentials. In Fig. V-20, we display the comparison of single-particle levels of ^{249}Bk extracted from experiment with a density-dependent-delta interaction³ and single-particle spacings obtained from a Woods-Saxon potential.

¹I. Ahmad *et al.*, Phys. Rev. C **68**, 044306 (2003).

²I. Ahmad *et al.*, Phys. Rev. C **71**, 054305 (2005).

³R. R. Chasman, Phys. Rev. C **14**, 1935 (1976).

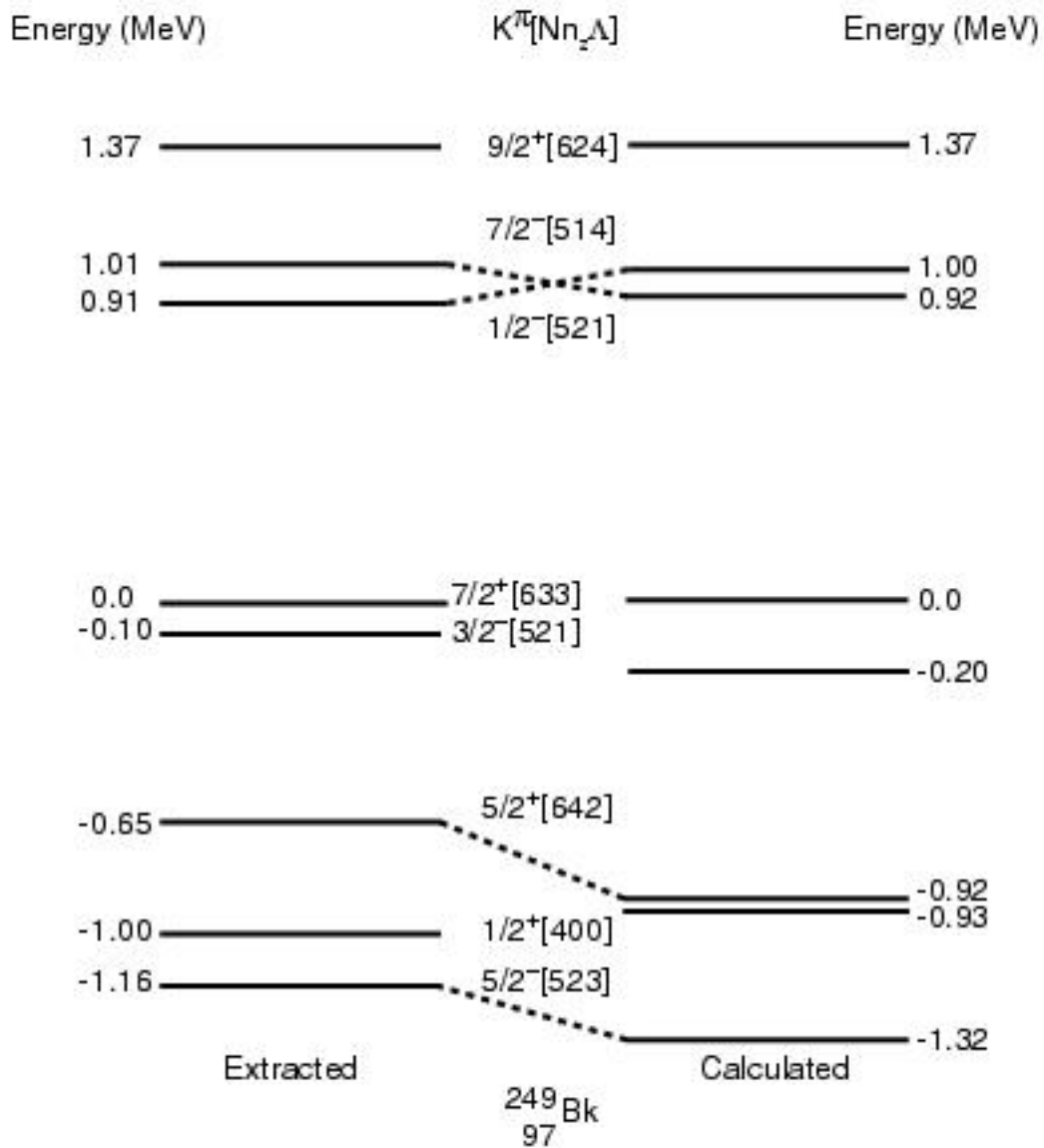


Fig. V-20. Comparison of calculated and observed energy single particle level spacings in ^{249}Bk . The extracted levels are obtained from experimental data by removing pairing effects from experiment. The calculated levels were obtained from a Woods-Saxon potential having deformation parameters $v_2 = 0.255$, $v_4 = 0.01$ and $v_6 = 0.015$.

d.9. Self-Consistent Beyond-Mean-Field Calculations in Exotic Heavy Nuclei

(T. Duguet, M. Bender,* P.-H. Heenen,† and P. Bonche‡)

We studied the low-lying collective excitation spectra of the neutron-deficient lead isotopes ^{182}Pb - ^{194}Pb by performing a configuration mixing of angular-momentum and particle-number projected self-consistent mean-field states. This study supported the interpretation of spectra made on the grounds of more schematic models in terms of coexisting

spherical, oblate, prolate and superdeformed prolate structures. Theoretical spectra and transition probabilities ($E0$ and $E2$) are in relatively good agreement with experimental data. We predicted the presence of superdeformed bands at low excitation energy in the most neutron-deficient isotopes. A paper describing this work was published.¹

*University of Washington, †Universite Libre de Bruxelles, Belgium, ‡Commissariat a L'Energie Atomique, Saclay, France.

¹M. Bender, P. Bonche, T. Duguet, and P.-H. Heenen, Phys. Rev. C **69**, 064303 (2004).

d.10. A New Microscopic Pairing Force for Self-Consistent Mean-Field Calculations (T. Duguet)

We derived a microscopic finite-range effective pairing force from the bare nucleon-nucleon interaction. It reproduces exactly the pairing provided in infinite matter by the AV18 NN interaction. By going from the bare to a well-defined effective force explicitly, we disentangled the effects of the range and of the density dependence of the effective pairing interaction. In particular, the relative success of existing phenomenological finite-range/density-independent and zero-range/density-

dependent forces could be explained on a more fundamental basis. The interaction was made simple enough to be used in self-consistent mean-field calculations of finite nuclei. The first three-dimensional HFB calculations using this new microscopic interaction were carried out and led to a conference proceedings publication.¹ These first calculations confirmed the crucial isovector and low density character of the force when predicting properties of neutron rich nuclei.

¹T. Duguet and P. Bonche, AIP Conference Proceedings **764**, 277 (2005).

d.11. Configuration Mixing of Particle-Number and Angular-Momentum Projected Cranked HFB States (M. Bender and P.-H. Heenen*)

Self-consistent mean-field models are one of the standard approaches in nuclear structure theory. For heavy nuclei, they are the only fully microscopic method that can be systematically applied on a large scale. Despite its many successes, the mean-field approach has several shortcomings and limitations. Including correlations associated with fluctuations of collective degrees of freedom into the modeling via the framework of the projected Generator Coordinate Method removes many of these deficiencies, and simultaneously gives access to shape mixing and collective excitation modes.

Our existing method for configuration mixing of particle-number and angular-momentum projected

axially symmetric and time-reversal invariant mean-field states, which has successfully been applied to nuclei throughout the chart of nuclei¹ was generalized to use cranked triaxial HFB states as the starting point. This allows an extension of the calculations to the whole β - γ plane of quadrupole deformations, and to incorporate effects from the alignment of single-particle states. Several theoretical problems regarding the use of the remaining symmetries, relative phases, and the transformations between various bases of HFB theory were solved to obtain a numerically efficient code. From the generalized model we expect an improvement of the excitation energies, which were systematically slightly too high in the existing model. First results from test calculations for light nuclei are encouraging.

*Universite Libre de Bruxelles, Belgium.

¹M. Bender and P.-H. Heenen, Eur. Phys. J. A **25**, 519 (2005).

d.12. Collective States in the $20 < Z < 28$ and $28 < N < 40$ Region (M. Bender and P.-H. Heenen*)

A systematic study of the collective quadrupole excitations of the nuclei with $20 < Z < 28$ and $28 < N < 40$ was performed in the framework of configuration mixing of particle-number and angular-

momentum projected self-consistent axial mean-field states. This region of the chart of nuclei is of current interest as the excitation spectra around ^{54}Ti and ^{56}Ti show anomalies, which are often associated with enhanced

(sub-)shell closures at $N = 32$ and $N = 34$.^{1,2} With our method we obtain fair agreement between calculations and the available experimental data for

excitation energies and transition moments without having strong $N = 32$ and $N = 34$ sub-shell closures. Further analysis is underway.

*Universite Libre de Bruxelles, Belgium.

¹S. N. Liddick *et al.*, Phys. Rev. C **70**, 064303 (2004).

²B. Fornal *et al.*, Phys. Rev. C **70**, 064304 (2004).

d.13. Systematics of Ground-State Correlations in Even-Even Nuclei (M. Bender, G. F. Bertsch,* and P.-H. Heenen†)

Ground-state correlations beyond the mean-field are a key element of successful microscopic mass formulae. We studied the correlation energies associated with the quadrupole shape degrees of freedom with a view to improving the self-consistent mean-field theory of nuclear binding energies. Systematic calculations were performed for more than 600 even-even nuclei from mass number 16 up to superheavy ones,¹ using the Skyrme interaction SLy4 in connection with a density-dependent pairing

interaction and the angular-momentum projected generator coordinate method. The quadrupole correlation energies range from 0.5 to 6.0 MeV, and their inclusion improves two qualitative deficiencies of the mean-field theory; namely, the exaggerated shell effect at neutron magic numbers and the failure of mean-field theory to describe mutually enhanced magicity. For the mass table as a whole, the quadrupolar correlations improve binding energies, separation energies, and separation energy differences by 20%-30%.

*University of Washington, †Universite Libre de Bruxelles, Belgium.

¹M. Bender and P.-H. Heenen, Eur. Phys. J. A **25**, 519 (2005).

d.14. QRPA of Spherical Nuclei with Skyrme Interactions (M. Bender, J. Terasaki,* J. Engel,* J. Dobaczewski,† W. Nazarewicz,† and M. Stoitsov†)

We developed¹ the first fully self-consistent implementation of a quasiparticle random-phase approximation (QRPA) for arbitrary Skyrme energy density functionals and density-dependent pairing functionals. We use the canonical Hartree-Fock-Bogoliubov basis for the numerical representation of the QRPA equations. The goal of the approach is to accurately describe multipole strength functions in spherical even-even nuclei, including weakly bound

drip-line systems. The accuracy of the method was carefully tested, particularly in handling spurious modes. We also investigated the consequences of neglecting the spin-orbit or Coulomb residual interactions in the QRPA, a common practice in the literature so far. First calculations were performed for isoscalar and isovector monopole, dipole, and quadrupole strength functions in several S_n isotopes, both in the stable region and at the drip lines.

*University of North Carolina, †Oak Ridge National Laboratory and University of Tennessee.

¹J. Terasaki, J. Engel, M. Bender, J. Dobaczewski, W. Nazarewicz, and M. Stoitsov, Phys. Rev. C **71**, 034310 (2005).

E. ATOMIC THEORY AND FUNDAMENTAL QUANTUM MECHANICS

In addition to research on hadronic and nuclear physics, and nuclear astrophysics, we also conduct research in atomic physics, neutron physics, and quantum computing.

Work in atomic physics includes the studies of interactions of electrons or high-energy photons with matter, in support of experiments performed at Argonne's Advanced Photon Source (APS). Theoretical studies are being conducted on the physics of the photoeffect and Compton scattering by bound electrons, focusing on topics selected in view of basic importance, timeliness, and potential in applications. Comprehensive surveys of photo-interaction data for silicon and graphite are underway.

Theoretical work in support of a new experiment to measure the neutron electric-dipole moment continues. This experiment will be conducted at NIST. A proof-of-principle experiment to measure the neutron magnetic-dipole moment in the same way has been approved for the Missouri University Research Reactor. Most of the needed equipment has been built. In addition, work continues to extend the spin-statistics theorem in nonrelativistic quantum mechanics to particles with non-zero spins.

Work continued toward the development of a coherent theory of physics and mathematics. One approach aims to replace the complex number field C , used as the base for the mathematical structures of a physical theory, by the numbers in $C_n = (R_n, I_n)$. The positive real number component R_n corresponds to the infinite discrete hierarchy of binary numbers $\underline{s} \times 2^{n(2e-1)}$ where \underline{s} is a length n 0-1 sequence and e is any integer. R_n is based on the properties of outputs from an infinite hierarchy of binary measurement outputs of length n for any continuous variable with an infinite range. This work emphasized the properties of a discrete space, S_n , based on these numbers. The exponential scale independence of S_n showed the presence of singularities or accumulation points at any coordinate system origin and on coordinate axes. The possible usefulness of S_n to describe inflationary cosmology was developed. The big bang, inflation, and recovery of a discrete space time that is empirically indistinguishable from a continuum space time is obtained by making $n = n(t)$ and $e = e(t)$ depend on cosmological time t . The Hubble expansion is also included. While no physical model was developed to justify the time dependence, it was made apparent that these aspects of cosmological dynamics can easily be accommodated in S_n .

e.1. Interactions of Photons with Matter (M. Inokuti and D. Y. Smith*)

In support of experiments in atomic and condensed-matter physics with the use of synchrotron radiation, theoretical studies are being conducted on the physics of photo-absorption and Compton scattering, focusing on topics selected in view of basic importance, timeliness, and potential applications.

One theme of long-term studies has been the use of dispersion relations and sum rules for indices of

response of matter over the entire range of photon energies. A comprehensive analysis of optical data on silicon is nearly complete. As an application, the data permit us to evaluate the mean excitation energy I in the Bethe stopping-power formula. The best set of data in our present judgment gives $I = 163.5 \pm 2$ eV, appreciably lower than the current standard value, 173 ± 3 eV.

An analysis of reflectivity and absorption of silicate glasses has led to good understanding of the role of

disorder and modifier ions in determining the refractive index for visible light.¹

*University of Vermont.

¹D. Y. Smith, E. Shiles, and M. Inokuti, Phys. Stat. Sol. (c) **2**, 310 (2005).

e.2. Interactions of Charged Particles with Matter (M. Inokuti)

Stopping power, the total yield of ionization, and its statistical fluctuations are examples of quantities describing the penetration of charged particles through matter and are important to applications such as the detection of particles and the analysis of their charges and kinetic energies. The understanding of those quantities in terms of individual collisions and associated cross sections remains a major challenge and is the goal of our continuing effort. Current work is the evaluation of the mean excitation energies,

namely, the I values, in the Bethe stopping-power formula from the oscillator-strength spectra for nine atoms and 23 molecules that are treated by Berkowitz.¹ Results were reported at an international meeting.²

Extensive work for the International Commission on Radiation Units and Measurements (ICRU) continues on the editing of its reports and on physical data such as stopping powers and various interaction cross sections.

¹J. Berkowitz, Atomic and Molecular Photoabsorption. Absolute Total Cross Sections (Academic Press 2002).

²S. Kamakura, N. Sakamoto, H. Ogawa, H. Tsuchida, and M. Inokuti, in Program and Abstracts, "Fourth International Conference on Atomic and Molecular Data and Their Applications," October 5-8, 2004, Toki, Japan (National Institute for Fusion Science, 2004), p. 64.

e.3. Photon Beam Polarization and Non-Dipolar Angular Distributions (N. K. Meshkov and M. Peshkin)

We are updating earlier work, some unpublished, on the consequences of spatial symmetries for the angular distributions of photons scattered by, and of electrons ejected from, atoms and molecules irradiated by polarized photon beams. The purpose of this analysis is to identify the dynamical parameters that can be extracted from measured

angular distributions under conditions where the polarization is accurately known and controlled and also under conditions where the polarization is not known. Because the earlier results have proved to be useful to experimenters in the design of experiments and in the analysis of experimental data, we are now extending them and preparing them for publication.

e.4. The Theory Experiment Connection: R_n Space and Inflationary Cosmology¹ (P. Benioff)

Earlier work^{2,3} on the theory-experiment connection and R_n space was continued with emphasis on the properties of R_n space and its use to describe the big bang and inflation in cosmology. The basic idea starts with the observation that all physical theories are mathematical structures over R and C , the real and complex numbers where R is part of C . Also space and time inherit the continuum properties of R . Here R is replaced with R_n which is the set of numbers of the binary form $s.t \times 2^{2ne}$ where s and t are functions from the interval $1,2,\dots,n$ to $\{0,1\}$ and e is any integer. This form is based on the

observation that all measurements of quantities with an infinite range (*e.g.*, distance) have this form as the number of significant figures is almost independent of the magnitude of the measurement.

R_n space is based on these numbers. Each dimension is discrete and consists of an infinite number of regions separated by exponential jumps. Each region contains $2^{2n}-1$ points with adjacent points separated by a distance $0_{[1,n]}.0_{[1,n-1]}I \times 2^{2ne}$. Adjacent regions are separated by exponential jumps with e going to $e + 1$. The origin of

any coordinate system is a point of accumulation or space singularity.

R_n space was shown to be a natural arena to describe the big bang and inflation. The idea is to make n and e depend on cosmological time τ as $n = n(\tau)$ and $e = e(\tau)$. At $\tau = 0$ e is required to be $\leq e_0$, a negative integer, and $n(0)$ small, around 10. This crams all of space into a ball of radius $2^{n(0)(2^{e_0+1})}$. As τ increases $R_n(\tau)$ space expands at a constant rate of one step per time interval Δ . The expansion velocity is constant at $2^{n(2^{e-1})}/\Delta$ for $2^{2^n}-1$ steps followed by an exponential jump to a higher velocity of $2^{n(2^{(e+1)-1})}/\Delta$, for another $2^{2^n}-1$ steps, etc. This expansion increases

spatial distances at an exponential rate when averaged over 2^n steps. This gives an inflation. When the outer regions of R_n space are expanding at velocities $> c$, inflation is stopped at some time τ' by having $n(\tau)$ increase from some value around 10 to a value of 100 or more. The resulting space region for $e = 0$ is experimentally indistinguishable from ordinary continuum space as the points are separated by at most the Planck length and the region diameter is greater than the size of the observable universe. Hubble expansion is also easily included. This shows that R_n space is not implausible, even though no physical derivation of the time dependence of n and e is provided.

¹P. Benioff, in "Proceedings of SPIE, Vol. 5833: Quantum Informatics 2004", ed. Yu. I. Ozhigov (SPIE, Bellingham, WA, 2005) 1.

²P. Benioff, Foundations of Physics **35**, 1825 (2005).

³P. Benioff, in "Proceedings of SPIE, Vol. 5833: Quantum Informatics 2004", ed. Yu. I. Ozhigov (SPIE, Bellingham, WA, 2005) 1.

F. OTHER ACTIVITIES

f.1. **Hadron Physics: Modern Methods for Modern Challenges** (A. Höll, A. Krassnigg, and C. D. Roberts)

We secured funding from the Argonne Theory Institute (<http://www.anl.gov/ati/>) to run a Theory visitor program, which brought together experts focused on the modern tools of hadron physics: Dyson-Schwinger equations (DSEs); lattice-regularized quantum chromodynamics (LQCD); light-front quantum field theory; QCD modeling; and relativistic quantum mechanics, to identify promising methods for meeting the theoretical challenges that a 12 GeV upgrade of the CEBAF at JLab will provide. Visitors were invited to ANL to speak, and discuss the merits of their chosen research tools. Results were compared and opportunities for constructive feedback explored. The discussions led to significant improvements in our understanding of the role played by the quark-gluon vertex in QCD's gap equation. In

addition, a connection was built between JLab's lattice group and DSE practitioners in Ohio and Pennsylvania, with the latter undertaking to study the current-quark mass dependence of hadron observables that is not accessible to current lattice simulations; and lattice-QCD practitioners were challenged to verify numerically new and exact results in QCD proved by DSE methods. Discussions were also held on the role and nature of diquark correlations in exotic baryons. One particular success was the identification of a means by which a useful model of the dressed-quark-gluon vertex could be constructed from a Slavnov-Taylor identity. This simple model was later employed to explore the validity of lattice data on this Schwinger function, with the result that the lattice-inferred form of one subdominant amplitude is very likely erroneous.

f.2. **17th Annual Midwest Theory Get-Together** (C. D. Roberts)

The Theory Group hosted the seventeenth Annual Midwest Theory Get-Together on September 24-25, 2004. Nuclear theorists from eight Midwest universities and ANL met to learn about the research goals and foci of different individuals and groups throughout the region. While the organizational duties rotate amongst the participants, Argonne is the regular host site because of its meeting facilities and central location. The organizers for 2004 were William Klink and Wayne Polyzoou from the University of Iowa in Iowa City. The meeting provides a good chance for students to broaden their outlook and get some practical

speaking experience in a friendly atmosphere. The format is informal, with an agenda of talks being volunteered at the beginning of the meeting. In 2004 we had thirty registered participants: faculty, postdocs and students. Over the Friday afternoon and Saturday morning approximately twenty-five presentations were made, covering topics such as: effective field theories; hadron physics and QCD; the nuclear shell model, nuclear pairing and nucleon matter; quantum Monte-Carlo methods; relativistic heavy ion collisions; and relativistic quantum mechanics for few body systems. It was a successful event.

VI. OTHER EDUCATIONAL AND COMMUNITY OUTREACH ACTIVITIES

OVERVIEW

Education remains a key part of our mission, especially training young nuclear physicists for the next generation of research, stewardship and homeland security. We are involved in many programs, including education at undergraduate, graduate, and post-doctoral level. We are also involved in using our expertise and capabilities to support programs in local Universities and in our community.

a. **Minority Program** (B. Zeidman)

The primary aim of the minority program is increasing the number and quality of minority participants in physics and other sciences. This involves ongoing interactions with minority students and faculty during visits to colleges and universities with substantial minority populations and a number of other activities. Among these efforts is inclusion of qualified scientists and students from minority institutions in research being performed by ANL scientists; e.g., collaborations on experiments, short-term appointments, and internships, such as SRP and SULI. In addition, attendance at meetings of minority organizations and visits to educational institutions provide chances for individual interactions and discussion of a wide variety of topics, e.g., research opportunities at ANL and other DOE laboratories, graduate education, internships, employment possibilities, etc., that influence choices of major field and career development.

The strongest interactions with minority students result from visits to minority institutions where it is possible to have discussions in depth with individual students. During the academic year, the program involves recruiting trips to minority schools, having been visited in prior years. Included in these visits

were seminars that discussed research performed by the Physics Division, particularly in the Medium Energy and Heavy Ion programs. Since ANL experiments at JLab include collaborators (both faculty and student) from some of these universities, (e.g., Florida International University, Hampton University, North Carolina A&T University, Southern University, New Orleans, UTEP) some members of the audience are often active participants in the research being discussed. Inasmuch as many students from these colleges may also have been at ANL as participants in the SRP and SULI (ERULF) programs, it is possible to make direct connections between the research being discussed and persons present or known to the audience. SRP and SULI students recruited under the programs performed research in several ANL divisions other than PHY during the past year. Institutions recently visited include: Clark-Atlanta University; Morehouse; Spelman; North Carolina A&T; North Carolina Central; Hampton; Norfolk State; Howard University; Morgan State; Fisk; and Vanderbilt. Southern University, Xavier University, and Dillard University are visited annually. A FAST (Faculty And Student Team) team from Southern-Baton Rouge worked with the RIA group during the summer.

The detailed discussions with students that occur during visits to their home institutions are often followed by discussions during meetings of minority organizations. Frequently, students will introduce me to other students who share common interests and attempt to recruit them to apply to ANL as well. One major area of overlap is that between PHY and HEP where the common interest in particle physics is particularly attractive. Another benefit of these interactions is an opportunity to outline features of the DOE labs and describe the complementary nature of their programs. Indeed, sometimes they effect other activities which include: serving on the Advisory Board of the COSM center at Hampton University and on the Advisory Committee of the ITSSTEM program at North Carolina Central

University; attending meetings of the National Conference of Black Physics Students; participation in meetings of the National Society of Black Physicists and of the National Society of Hispanic Physicists.

Another activity involves serving as Distinguished Adjunct Professor in the Physics Department at Hampton University and thesis advisor or committee member for PhD students. A number of Hampton PhDs have received degrees based upon data from ANL experiments, one of who is currently an Asst. Prof. at Norfolk State University. A number of former undergraduate interns have returned to perform their thesis research at ANL under the supervision of ANL scientists. Some of the interns who have received their Ph.D. degrees have been named in previous reports.

b. Third RIA Summer School (R. V. F. Janssens, E. F. Moore, C. Davids, D. Seweryniak, A. Hecht, K. Sharma, J. Clark, Y. Wang, M. P. Carpenter, T. L. Khoo, S. Zhu, C. J. Lister, F. G. Kondev, S. Fischer, I. Ahmad, B. Back, D. Peterson, and J. P. Greene)

The RIA Summer School, held within the Physics Division (PHY) and the Division of Educational Programs (DEP) at Argonne National Laboratory from August 8 to 14, 2004, was the third of a series of summer programs aimed at educating young researchers about the challenges of radioactive ion beam physics. Through these annual schools the research community continues to educate young scientists so that they will be able to exploit fully the opportunities created by the Rare Isotope Accelerator (RIA). All the schools held thus far have been jointly organized by the 88-Inch Cyclotron (I. Y. Lee), ATLAS (R. Janssens), HRIBF (W. Nazarewicz), and MSU/NSCL (B. Sherrill). This annual event will continue to rotate among these laboratories, with the next school scheduled to take place at Berkeley from July 31 to August 6, 2005.

Fifty two graduate and postdoctoral students attended the school. The participants came predominantly from 25 U.S. universities and national laboratories, with an additional small participation by students from Canada (1), Europe (4) and Israel (1). The Local Organizing Committee consisted of A. Bernstein (budget, PHY), S. Fischer (hands-on program, DePaul Univ. and PHY), E. F. Moore (secretary, PHY), H. Myron (coordination, DEP), C. Reynolds (administration, DEP), F. Vivio (budget, DEP), and R. V. F. Janssens (coordination, school director, PHY).

The summer school had four main components. The mornings were devoted to lectures on major breakthroughs in RIA science. The lectures covered topics in both the experimental and theoretical physics of nuclei far from stability. The main topics of the third RIA Summer School lectures were:

- Nuclear Reactions with Exotic Beams - K. Kemper (FSU)
- Nuclear Astrophysics and the Origin of the Elements - G. Fuller (UCSD)
- Nuclear Structure Theory of Rare Isotopes- J. Dobaczewski (UT/ORNL and Warsaw University)
- Excitations in Neutron-Rich Nuclei with γ -Ray Spectroscopy Techniques - Th. Glasmacher (NSCL, MSU)

Shorter lectures focused on various aspects of exotic beam physics and on techniques and developments specific to RIA itself. These were:

- Accelerator Mass Spectrometry - P. Collon (ND)
- Exotic Beams at ATLAS – R. Pardo (ANL)
- Ion Trapping – Z.-T. Lu (ANL & UC)
- The RIA Concept – G. Savard (ANL & UC)

The afternoons provided opportunities for "hands-on" demonstrations of experimental equipment and techniques useful in RIA research. The hands-on part of the program was held at the ATLAS facility, was coordinated by S. Fischer (DePaul Univ. & ANL) and involved the participation of a large number of scientists from the ANL Physics Division staff, and

of some of the lecturers and organizers of the Summer School. A safety lecture by T. Mullen (ANL, Physics Division) was part of the school's program and was a prerequisite for participation in the "hands-on" activities. Every student participated in 5 of 7 of the following activities:

- In-Beam Measurement at the Fragment Mass Analyzer
Cary Davids, Darek Seweryniak and Adam Hecht
- Mass Measurement Using the Canadian Penning Trap
Kumar Sharma, Jason Clark and Yuyan Wang
- Compton Suppression of a Ge detector + $\gamma\gamma$ Coincidences with Gammasphere
Mike Carpenter, Teng Lek Khoo and Shaofei Zhu
- Ge Double-Sided Strip Detectors and an Introduction to γ -Ray Tracking
Kim Lister, Filip Kondev, and Susan Fischer
- X-Ray Fluorescence and γ -Ray Absorption
Irshad Ahmad and Frank Moore
- "Heads-On" Theory Session
Jacek Dobaczewski and Witek Nazarewicz
- α -Particle Measurements Using Si Detectors
Birger Back and Don Peterson
- An Introduction to Target Making
John Greene and Janelle Neubauer

Participants had the opportunity to present 10-minute talks on their research projects at their home institution. This last part of the program also included a questions-answers session with the morning lecturers about the lectures of that day. On one evening a special session was devoted to RIA R&D activities. It gave the students an overview of

the many development activities going on in U.S. laboratories and was also an opportunity to see some of the RIA hardware currently under development. During the entire duration of the school, there were also numerous opportunities for open discussions between students and lecturers in an informal setting.

c. **Homeland Security Activities - Scientific Support of the Radiological Assistance Program** (E. F. Moore)

The Radiological Assistance Program (RAP) is a nation-wide Department of Energy emergency response asset which provides support to the Department of Homeland Security and other Federal, State, Tribal, and local agencies in the event of a radiological accident or incident. RAP is implemented on a regional basis and has eight Regional Coordinating Offices (RCO's) in the U.S. The Region 5 RCO is based at Argonne and serves the states of Illinois, Indiana, Iowa, Michigan, Minnesota, Nebraska, North and South Dakota, Ohio, and Wisconsin. RAP teams from one region can integrate into and assist RAP teams from other regions as well as other national DOE assets.

The RAP mission is to provide a flexible, around-the-clock response capability for radiological emergencies. The RAP teams consist of a small core of full-time personnel supplemented by volunteers from the DOE facilities in which they are based. The team members have extensive experience in various aspects of health physics, nuclear physics, and radiation safety.

Frank Moore of the Physics Division serves as a RAP team captain on a volunteer basis with the region 5 team. Among his RAP related activities are the testing and evaluation of radiation detection equipment, the training of other team members in the use of some of the specialized detection equipment, the analysis of measurements obtained in the field, and deployment on

RAP responses and exercises. Frank has also participated in outreach and training activities with the Chicago Fire Department and members of the Illinois National Guard.

Frank serves as a member of the RAP Equipment Advisory Team, which has the responsibility to evaluate new equipment and advise DOE Headquarters and the RAP regions on issues related to the purchase and use of radiological detection equipment.

d. Repair and Refurbishment of Germanium Detectors (C. J. Lister, R. V. F. Janssens, P. Wilt, M. P. Carpenter, E. F. Moore, and S. Zhu)

The infrastructure for keeping Gammasphere operational at a high level of performance is deep. For routine maintenance, and especially for times when Gammasphere is moved, our annealing laboratory, the “in-cryostat” repair capability, our mechanical and electronic engineering experience, and our testing and diagnosis capability are essential.

When Gammasphere is running smoothly some excess capability is available. During these times of lower activity we have used our capabilities to evaluate and perform minor repairs on detectors from around the nation, but especially from local

universities, RAP teams, and laboratories. Often, minor problems can be repaired immediately. For more serious problems, a detailed diagnosis can be made which helps expedite factory repairs at the detector manufacturer. Our annual turnover of repairs is 6-10/yr.

This outreach effort is beneficial to all concerned: it exercises our capabilities and keeps our facilities in top condition, it helps train young people in detector maintenance, and it supports research in local facilities. We continue to explore expansion of this program and finding effective cost-recovery mechanisms.

STAFF MEMBERS OF THE PHYSICS DIVISION

Listed below is the staff of the Physics Division for the year ending December 31, 2004.
The program headings indicate only the individual's current primary activity.

SCIENTIFIC STAFF EXPERIMENTAL NUCLEAR PHYSICS STAFF

Regular Staff

- ¶ Irshad Ahmad, Ph.D., University of California-Berkeley, 1966
 - John R. Arrington Ph.D., California Institute of Technology, 1998
 - Birger B. Back, Ph.D., University of Copenhagen, Denmark 1974
 - Michael P. Carpenter, Ph.D., University of Tennessee-Knoxville, 1988
 - ‡ Cary N. Davids, Ph.D., California Institute of Technology, 1967
 - § Bela Erdelyi, Ph.D., Michigan State University, 2001
 - * Susan M. Fischer, Ph.D., University of Notre Dame, 1994
 - Donald F. Geesaman, Ph.D., State University of New York-Stony Brook, 1976
 - Kawtar Hafidi, Ph.D., University of Paris South XI, France, 1999
 - ‡‡ Walter F. Henning, Ph.D., Technical University of Munich, Germany, 1968
 - §§ Roy J. Holt, Ph.D., Yale University, 1972
 - ** Robert V. F. Janssens, Ph.D., Université Catholique de Louvain, Belgium, 1978
 - Cheng-lie Jiang, Ph.D., China Institute of Atomic Energy, China 1960
 - Michael P. Kelly, Ph.D., University of Washington, 1999
 - Teng Lek Khoo, Ph.D., McMaster University, Canada, 1972
 - Torben Lauritsen, Ph.D., State University of New York-Stony Brook, 1990
 - Eliane S. Lessner, Ph.D., Syracuse University, 1975
 - Christopher J. Lister, Ph.D., University of Liverpool, England, 1977
 - ⊕ Zheng-tian Lu, Ph.D., University of California-Berkeley, 1994
 - Eugene F. Moore, Ph.D., Florida State University, 1988
 - ⊗ Brahim Mustapha, Ph.D., University of Paris, France, 1999
 - Jerry A. Nolen, Jr., Ph.D., Princeton University, 1965
 - Peter N. Ostroumov, Ph.D., Moscow Engineering and Physical Institute, Russia, 1982
 - Richard C. Pardo, Ph.D., University of Texas, 1976
 - David H. Potterveld, Ph.D., California Institute of Technology, 1988
 - K. Ernst Rehm, Ph.D., Technical University, Munich, Germany, 1973
 - Paul E. Reimer, Ph.D., University of Illinois at Urbana-Champaign, 1996
 - ⊕⊕ Guy Savard, Ph.D., McGill University, Canada, 1988
 - ⊗ John P. Schiffer, Ph.D., Yale University, 1954
 - Dariusz Seweryniak, Ph.D., Uppsala University, Sweden, 1994
 - Kenneth W. Shepard, Ph.D., Stanford University, 1970
 - Kenneth M. Teh, Ph.D., Vanderbilt University, 1988
-
- ¶ Retired November 2004
 - ‡ Adjunct Professor, Vanderbilt University
 - § Joint appointment with Northern Illinois University
 - * Joint appointment with DePaul University
 - ‡‡ On leave of absence at GSI, Darmstadt, Germany
 - §§ Adjunct Professor, University of Illinois at Urbana-Champaign
 - ** Associate Director of the Physics Division. Adjunct Professor, Michigan State University, Vanderbilt University, and University of Notre Dame
 - ⊕ Professor Coterminous, University of Chicago
 - ⊗ Term Appointment
 - Director of the ATLAS Facility. Adjunct Professor, Michigan State University
 - ⊕⊕ Professor Coterminous, University of Chicago and Adjunct Professor, University of Manitoba, Canada
 - ⊗ Professor Emeritus, University of Chicago

Special Appointments

- Irshad Ahmad, Ph.D., University of California-Berkeley, 1966
- Lowell M. Bollinger, Ph.D., Cornell University, 1951
- William J. Childs, Ph.D., University of Michigan, 1956
- Donald S. Gemmell, Ph.D., Australian National University, Australia 1960
- Harold E. Jackson, Jr., Ph.D., Cornell University, 1959
- * Michael Paul, Ph.D., Hebrew University of Jerusalem, Israel, 1973
- ⌘ Ben Zeidman, Ph.D., Washington University, 1957

THEORETICAL NUCLEAR PHYSICS STAFF

Regular Staff

- Henning Esbensen, Ph.D., University of Århus, Denmark, 1977
- Tsung-Shung Harry Lee, Ph.D., University of Pittsburgh, 1973
- Kenneth Nollet, Ph.D., University of Chicago, 2000
- Steven C. Pieper, Ph.D., University of Illinois at Urbana-Champaign, 1970
- Craig D. Roberts, Ph.D., Flinders University of South Australia, 1989
- ‡ James W. Truran, Ph.D., Yale University, 1965
- Robert B. Wiringa, Ph.D., University of Illinois at Urbana-Champaign, 1978

Special Appointments

- Paul Benioff, Ph.D., University of California-Berkeley, 1959
- Richard R. Chasman, Ph.D., University of California-Berkeley, 1959
- Fritz Coester, Ph.D., University of Zurich, Switzerland, 1944
- Mitio Inokuti, Ph.D., University of Tokyo, Japan, 1962
- Dieter Kurath, Ph.D., University of Chicago, 1951
- Malcolm H. Macfarlane, Ph.D., University of Rochester, 1955
- § Vijay Pandharipande, Ph.D., University of Bombay, India, 1969
- Murray Peshkin, Ph.D., Cornell University, 1951

* Special Term Appointee from the Hebrew University of Jerusalem, India
⌘ Special Term Appointee. Adjunct Professor, Hampton University
‡ Joint appointment with the University of Chicago
§ Special Term Appointee from the University of Illinois at Urbana-Champaign

TEMPORARY APPOINTMENTS

Michael Bender (from University of Washington)
Theoretical studies
(June 2004 - November 2004)

Thomas Duguet (from CEA, Saclay, France)
Theoretical studies
(November 2002 - November 2004)

* Jeffrey R. Guest (from University of Michigan)
Medium-energy physics studies
(August 2004 -)

Neil J. Hammond (from University of Liverpool, England)
Research at ATLAS
(July 2002 - June 2004)

Arne Hoell (from University of Rostock, Germany)
Theoretical studies
(October 2003 -)

Prashanth Jaikumar (from McGill University, Canada)
Theoretical physics studies
(September 2004 -)

Peter Mueller (from Johannes Gutenberg-University, Germany)
Medium-energy physics studies
(Jully 2003 -)

† Brahim Mustapha (from University of Paris, France)
ATLAS operations and development
(May 2000 - May 2004)

Donald A. Peterson (from Oregon State University)
Research at ATLAS
(January 2004 -)

Elaine C. Schulte (from University of Illinois at Urbana-Champaign)
Medium-energy physics studies
(February 2002 -)

Nicholas D. Scielzo (from University of California-Berkeley)
Medium-energy physics
(July 2003 -)

Shrabani Sinha (from India Institute of Technology, Bombay, India)
Research at ATLAS
(June 2002 - December 2004)

* Argonne Scholar-AHCPF (Arthur Holly Compton Postdoctoral Fellowship)

† Term appointment in May 2004

Nikolai Vinogradov (from Moscow Engineering Physical Institute, Russia)
ATLAS operation and development
(November 2001 -)

Hariprakash Sharma (from University of Manitoba, Canada)
Research at ATLAS
(July 2004 -)

Xiaodong Tang (from Texas A&M University)
Research at ATLAS
(May 2003 -)

Stewart V. Wright (from University of Liverpool, England)
Theoretical physics studies
(September 2004 -)

Xiaochao Zheng (from Massachusetts Institute of Technology)
Medium-energy physics
(January 2003 -)

Zhen Zhou (from University of Giessen, Germany)
Research at ATLAS
(February 2002 – June 2004)

Shaofei Zhu (from University of Notre Dame)
Research at ATLAS
(January 2004 -)

TECHNICAL AND ENGINEERING STAFF
(and areas of activity)

Kevin G. Bailey (B.S., University of Nebraska, 1989)
Technical assistance, medium-energy physics

Donald Barnett
ATLAS operations

John M. Bogaty (A.A.S., DeVry University, 1961)
Electrical systems, ATLAS operation and development

L. Kevin Carlquist (A.S., College of DuPage, 1986)
ATLAS operations

* Benny E. Clifft (A.S.E.E., DeVry University, 1959)
Electrical systems, ATLAS operation and development

† Donald Cyborski
Computer operations

* Special Term Appointee

† Retired April 2004, Special Term Appointee

Alex Deriy (B.S., University of Illinois-Chicago, 1988)
ATLAS operations

Gregory Devane
ATLAS operations

* Joseph Falout (B.S.M.E., University of Illinois-Chicago, 1970)
Experimental equipment design

Joel Fuerst (M.S.M.E., Northwestern University, 1990)
Cryogenic development at ATLAS

Scott M. Gerbick (B.S., Purdue University, 2003)
ATLAS experimental equipment maintenance, technical assistance, heavy-ion physics

John P. Greene (M.S., DePaul University, 1982)
Target preparation

Gerald Gribbon (A.A., DeVry University, 1992)
ATLAS operations

* Ray E. Harden (A.A.S., Milwaukee School of Engineering, 1957)
ATLAS operator

* Dale J. Henderson (B.S., Elmhurst College, 1951)
Detector development, technical assistance, heavy-ion physics

Robert Jenkins
ATLAS operations

Mark Kedzie
ATLAS experimental equipment development

* Raymond B. Kickert
ATLAS experimental equipment maintenance, technical assistance, heavy-ion physics

* David Kurth
Graphic specialist

Anthony Krupa (A.A.S.-E.E.T., Purdue University, 1987)
ATLAS operations

Anthony Levand (B.S.M.E., University of Illinois at Urbana-Champaign, 1986)
Experimental equipment design at ATLAS

Eric Lindert (B.S., University of Wisconsin-Milwaukee, 1992)
ATLAS operations

Britt Lundgren (B.A., University of Chicago, 2003)
Heavy-ion research at ATLAS

* Special Term Appointee

- * Paul Markovich (B.S., Purdue University, 1972)
Surface chemistry, ATLAS development and operation

- Thomas P. Mullen (B.S., Marquette University, 1966)
Division ESH/QA engineer

- Floyd Munson, Jr. (A.A.S., DeVry University, 1966; B.S., Lewis University, 1993)
Control system for ATLAS

- Bruce G. Nardi (A.A.S., Morton Jr. College, 1967; A.A.S., DeVry University, 1969)
Electronics design and maintenance

- Tom O'Connor (M.S., DePaul University, 1995)
Technical assistance, medium-energy physics

- Tad Pennington (M.S. University of Missouri, 1989; M.S. University of Alabama, 1998)
Detector development, technical assistance, heavy-ion physics

- Donald Phillips (A.S., DeVry University, 1974)
ATLAS operations

- * John Phillips (M.S., University of Illinois-Chicago, 1986)
Consulting ESH/QA engineer

- Maria Power (M.S., Illinois Institute of Technology, 1993)
Technical assistance, ATLAS control system

- John Rohrer
Experimental equipment support, heavy-ion physics

- Robert Scott (B.S., University of Illinois-Chicago, 1995)
ATLAS operations

- Sergey Sharamentov (M.S., Moscow Engineering Physical Institute, Russia, 1976)
Electrical systems, ATLAS operation and development

- Brent R. Shumard (B.S., University of Valparaiso, 2002).
Detector development, technical assistance, heavy-ion physics.

- * James R. Specht (A.A.S., DeVry University, 1964)
Cryogenics engineer. ATLAS development and operation

- Philip Strickhorn (B.S., DeVry University, 1990)
Electrical and technical assistance with ATLAS operations

- Cory Stuart (B.S., Lewis University, 2002)
Computer operations

- Seetha Sundaram (B.S., University of Madras, India, 1989)
ATLAS operations

*Special Term Appointee

Richard Vondrasek (B.S., University of Chicago, 1990)
ATLAS ECR source

- * Loren Weber (M.S., Northern Illinois University, 1974)
ATLAS operations

Philip R. Wilt (Johnstown Technical School, 1973)
Electronics design and maintenance

Bruce J. Zabransky (M.S., University of Illinois, Chicago, 1973)
Mechanical engineer

Gary P. Zinkann (B.S., DeVry University, 1975)
ATLAS operations supervisor

-
- * Special Term Appointee

ADMINISTRATIVE STAFF

- * Allan Bernstein, M.B.A., Rosary College, 1986
- * James E. Nelson, B.A., University of Illinois-Chicago, 1975
- † Karen J. Thayer
- ‡ Barbara Fletcher (B.A., DePaul University, 1998)
- Janet Bergman (Administrative Secretary)
- Jeannie Glover (Administrative Secretary)
- Jessica Herrera (Secretary)
- Debra Morrison (Administrative Secretary)
- Katherine Peters (Administrative Secretary)
- Elizabeth Rizzo (Administrative Assistant)
- Colleen Tobolic (Administrative Secretary)
- Barbara Weller (Administrative Secretary)

-
- * Assistant Director of the Physics Division
 - † Special Term Appointee
 - ‡ Executive Secretary

VISITORS AND STUDENTS

Long-Term Visitors (at Argonne more than 4 months)

Vladislav Asseev (from Institute for Nuclear Research of Russian Academy of Sciences, Russia)
Accelerator development
(October 2003 -)

Philip Caligiuri (from University of Chicago)
Research at ATLAS
(April 2003 - April 2004)

Partha Chowdhury (from University of Massachusetts-Lowell)
Research at ATLAS
(October 2003 - June 2004)

Jason Clark (from University of Manitoba, Canada)
Heavy-ion research at ATLAS
(May 1999 -)

Moulay El Alaoui Ahmed (from Laboratory for Theoretical Physics, Morocco)
Medium-energy physics
(February 2001 -)

William Karstens (from Saint Michaels College)
Theoretical physics studies
(July 2003 -)

Andrei Kolomiets (from Institute of Theoretical and Experimental Physics, Moscow, Russia)
Research at ATLAS
(April 2004 -)

Andreas Krassnigg (from University of Graz, Austria)
Theoretical physics studies
(January 2003 -)

Masahiro Notani (from Michigan State University)
Heavy-ion research at ATLAS
(January 2004 - May 2005)

Iouri Sanjiev (from St. Petersburg Nuclear Physics Institute, Gatchina, Leningrad, Russia)
Medium energy studies
(November 2000 -)

Hariprakash Sharma (from University of Manitoba, Canada)
Heavy-ion research at ATLAS
(July 2004 -)

Kumar Sharma (from University of Manitoba, Canada)
Heavy-ion research at ATLAS
(July 2004 -)

* Eugene Shiles (from University of Vermont-Burlington)
Theoretical physics studies
(August 2002 -)

* David Smith (from University of Vermont-Burlington)
Theoretical physics studies.
(February 2002 -)

Isao Tanihata (from RIKEN the Institute of Physical and Chemical Research, Japan)
Heavy-ion research at ATLAS
(March 2004 -)

Antonio Villari (from GANIL, Caen, France)
Heavy-ion research at ATLAS
(August 2004 -)

Jicheng Wang (from University of Manitoba, Canada)
Heavy-ion research at ATLAS
(January 2001 - July 2004)

Short-Term Visitors (at Argonne less than 4 months)

* Nour-eddi Berrah (from Western Michigan University)
Atomic physics research
(October 1991 -)

* Christopher Fasano (from Monmouth College)
Theoretical studies
(February 1999 -)

* Michael Kroupa (from Monmouth College)
Theoretical physics studies
(July 2002 -)

Arlene Larabee (from Greenville College)
Heavy-ion research at ATLAS
(June 2004 - August 2004)

Rachid Nouicer (from University of Chicago)
Heavy-ion research at ATLAS
(April 1998 -)

Achim Richter (from Darmstadt University of Technology, Germany)
Heavy-ion research at ATLAS
(February 2004 - March 2004)

Alan Wuosmaa (from Western Michigan University)
Research at ATLAS
(May - June 2004)

Resident Graduate Students

Zachary Conway (from University of Illinois at Urbana-Champaign)
Research at ATLAS
(June 2003 -)

Jason Shergur (from University of Maryland)
Research at ATLAS
(January 2002 -)

* Guest Faculty Research Participant

Peter Simko (from Illinois Institute of Technology)
Computer operations
(October 2003 -)

Guest Graduate Students

Lamiaa El Fassi (from Mohammed V University, Rabat, Morocco):
Medium-energy physics
(September 2003 -)

Nathan Hoteling (from University of Maryland)
Research at ATLAS
(February 2003 -)

Louis Jisonna (from Northwestern University)
Heavy-ion research at ATLAS
(June 2000 -)

Issam Qattan (from Northwestern University, Evanston, IL):
Medium-energy physics studies
(September 2001 -)

Li-Bang Wang (from University of Illinois, Urbana, IL):
Medium-energy studies
(September 2001 -)

Yu Yan Wang (from University of Manitoba, Canada):
Research at ATLAS
(September 2003 -)

Undergraduate Students

Ryan Blinstrup (Monmouth University)
Andrew Bump (DeVry University)
Robyn Brewer (DeVry University)
Kevin Broadnax (North Carolina AT&T State University)
Robert Carrier (St. Xavier University)
David Cipriano (DeVry University)
Samuel Clapp (Williams College)
Mark Durante (North Central College)
Jennifer Fallis (University of Manitoba, Canada)
Andrew Giagnacova (Lincoln University)
Mark Gieras (DeVry University)
Michael Kern (DeVry University)
Michael King (Purdue University)
Jesse London (University of Chicago)
Benjamin Mitchell (North Central College)
Chad Muir (University of Illinois at Urbana-Champaign)
Roman Mongado (DeVry University)

* Guest Faculty Research Participant

Janelle Neubauer (North Central College)
Ilana Percher (Oberlin College)
Peter Probst (University of Illinois-Chicago)
Nathan Rassi (University of Illinois at Urbana-Champaign)
Peter Probst (University of Illinois-Chicago)
Stuart Russell (University of Manitoba, Canada)
Matthew Scholte-van de Vorst (University of Manitoba, Canada)
Matthew Sternberg (University of Oregon)
William Trimble (University of Washington)
Onome Ugbeme (University of New Orleans)
Gregory Waligorski (DeVry University)

HEAVY-ION NUCLEAR PHYSICS RESEARCH

- Reevaluation of the $^{22}\text{Na}(p,\gamma)$ Reaction Rate: Implications for the Detection of ^{22}Na Gamma Rays from Novae
D. G. Jenkins, C. J. Lister, R. V. F. Janssens, T. L. Khoo, E. F. Moore, K. E. Rehm, B. Truett, A. H. Wuosmaa, M. Freer, B. R. Fulton, and J. José
Phys. Rev. Lett. **92**, 031101/1-4 (2004)
- Lowest Excitations in ^{56}Ti and the Predicted $N = 34$ Shell Closure
S. N. Liddick, P. F. Mantica, R. V. F. Janssens, R. Broda, B. A. Brown, M. P. Carpenter, B. Fornal, M. Honma, T. Mizusaki, A. C. Morton, W. F. Mueller, T. Otsuka, J. Pavan, A. Stolz, S. L. Tabor, B. E. Tomlin, and M. Wiedeking
Phys. Rev. Lett. **92**, 072502/1-4 (2004)
- Is the Nuclear Spin-Orbit Interaction Changing with Neutron Excess?
J. P. Schiffer, S. J. Freeman, J. A. Caggiano, C. Deibel, A. Heinz, C.-L. Jiang, R. Lewis, A. Parikh, P. D. Parker, K. E. Rehm, S. Sinha, and J. S. Thomas
Phys. Rev. Lett. **92**, 162501/1-4 (2004)
- Precise Mass Measurement of ^{68}Se , a Waiting-Point Nuclide Along the rp Process
J. A. Clark, G. Savard, K. S. Sharma, J. Vaz, J. C. Wang, Z. Zhou, A. Heinz, B. Blank, F. Buchinger, J. E. Crawford, S. Gulick, J. K. P. Lee, A. F. Levand, D. Seweryniak, G. D. Sprouse, and W. Trimble
Phys. Rev. Lett. **92**, 192501/1-4 (2004)
- Influence of Nuclear Structure on Sub-Barrier Hindrance in $\text{Ni} + \text{Ni}$ Fusion
C. L. Jiang, K. E. Rehm, R. V. F. Janssens, H. Esbensen, I. Ahmad, B. B. Back, P. Collon, C. N. Davids, J. P. Greene, D. J. Henderson, G. Mukherjee, R. C. Pardo, M. Paul, T. O. Pennington, D. Seweryniak, S. Sinha, and Z. Zhou
Phys. Rev. Lett. **93**, 012701/1-4 (2004)
- Pseudorapidity Distribution of Charged Particles in $d + \text{Au}$ Collisions at $\sqrt{s_{NN}} = 200$ GeV
B. B. Back *et al.* (PHOBOS Collaboration)
Phys. Rev. Lett. **93**, 082301/1-5 (2004)
- New Half-Life Measurement of ^{182}Hf : Improved Chronometer for the Early Solar System
C. Vockenhuber, F. Oberli, M. Bichler, I. Ahmad, G. Quitté, M. Meier, A. N. Halliday, D.-C. Lee, W. Kutschera, P. Steier, R. J. Gehrke, and R. G. Helmer
Phys. Rev. Lett. **93**, 172501/1-4 (2004)
- Charged Hadron Transverse Momentum Distributions in $\text{Au} + \text{Au}$ Collisions at $\sqrt{s_{NN}} = 200$ GeV
B. B. Back *et al.* (PHOBOS Collaboration)
Phys. Lett. **B578**, 297-303 (2004)
- Identification of Yrast High- K Isomers in ^{177}Lu and Characterisation of ^{177m}Lu
G. D. Dracoulis, F. G. Kondev, G. J. Lane, A. P. Byrne, T. Kibédi, I. Ahmad, M. P. Carpenter, S. J. Freeman, R. V. F. Janssens, N. J. Hammond, T. Lauritsen, C. J. Lister, G. Mukherjee, D. Seweryniak, P. Chowdhury, S. K. Tandel, and R. Gramer
Phys. Lett. **B584**, 22-30 (2004)
- Complete Structure Determination of the Astrophysically Important Nucleus ^{20}Ne Below the Proton Threshold
D. Seweryniak, P. J. Woods, B. Blank, M. P. Carpenter, T. Davinson, S. J. Freeman, J. Görres, A. Heinz, R. V. F. Janssens, H. Mahmud, T. L. Khoo, Z. Liu, G. Mukherjee, E. Rehm, F. Sarazin, J. Shergur, M. Shawcross, S. Sinha, and A. Woehr
Phys. Lett. **B590**, 170-175 (2004)

- The Influence of $\nu h_{11/2}$ Occupancy on the Magnetic Moments of Collective 2^+ States in $A \sim 100$ Fission Fragments
A. G. Smith, D. Patel, G. S. Simpson, R. M. Wall, J. F. Smith, O. J. Onakanmi, I. Ahmad, J. P. Greene, M. P. Carpenter, T. Lauritsen, C. J. Lister, R. V. F. Janssens, F. G. Kondev, D. Seweryniak, B. J. P. Gall, O. Dorvaux, and B. Roux
Phys. Lett. **B591**, 55-60 (2004)
- Proton Decay of the Highly Deformed Odd-Odd Nucleus ^{130}Eu
C. N. Davids, P. J. Woods, H. Mahmud, T. Davinson, A. Heinz, J. J. Ressler, K. Schmidt, D. Seweryniak, J. Shergur, A. A. Sonzogni, and W. B. Walters
Phys. Rev. C **69**, 011302(R)/1-3 (2004)
- Proton Decay of the Highly Deformed Nucleus ^{135}Tb
P. J. Woods, P. Munro, D. Seweryniak, C. N. Davids, T. Davinson, A. Heinz, H. Mahmud, F. Sarazin, J. Shergur, W. B. Walters, and A. Woehr
Phys. Rev. C **69**, 051302(R)/1-3 (2004)
- Analysis of Heavy-Ion Fusion Reactions at Extreme Sub-Barrier Energies
C. L. Jiang, H. Esbensen, B. B. Back, R. V. F. Janssens, and K. E. Rehm
Phys. Rev. C **69**, 014604/1-6 (2004)
- High-Precision Measurement of the Half-Life of ^{62}Ga
B. Blank, G. Savard, J. Döring, A. Blazhev, G. Canchel, M. Chartier, D. Henderson, Z. Janas, R. Kirchner, I. Mukha, E. Roeckl, K. Schmidt, and J. Żylicz
Phys. Rev. C **69**, 015502/1-7 (2004)
- Observation of Octupole Excitations in ^{141}Cs and ^{143}Cs Nuclei
W. Urban, T. Rzača-Urban, J. L. Durell, W. R. Phillips, A. G. Smith, B. J. Varley, N. Schulz, and I. Ahmad
Phys. Rev. C **69**, 017305/1-4 (2004)
- Low-Lying Levels in ^{15}F and the Shell Model Potential for Drip-Line Nuclei
V. Z. Goldberg, G. G. Chubarian, G. Tabacaru, L. Trache, R. E. Tribble, A. Aprahamian, G. V. Rogachev, B. B. Skorodumov, and X. D. Tang
Phys. Rev. C **69**, 031302/1-5 (2004)
- Decay Rate of Triaxially Deformed Proton Emitters
Cary N. Davids and Henning Esbensen
Phys. Rev. C **69**, 034314/1-9 (2004)
- High-Spin Study of Rotational Structures in ^{72}Br
C. D. O'Leary, R. Wadsworth, P. Fallon, C. E. Svensson, I. Ragnarsson, D. E. Appelbe, R. A. E. Austin, G. C. Ball, J. A. Cameron, M. P. Carpenter, R. M. Clark, M. Cromaz, M. A. Deleplanque, R. M. Diamond, D. F. Hodgson, R. V. F. Janssens, D. G. Jenkins, N. S. Kelsall, G. L. Lane, C. J. Lister, A. O. Macchiavelli, D. Sarantites, F. S. Stephens, D. Seweryniak, K. Vetter, J. C. Waddington, and D. Ward
Phys. Rev. C **69**, 034316/1-10 (2004)
- High-Angular-Momentum Structures in ^{64}Zn
D. Karlgren, R. M. Clark, I. Ragnarsson, C. E. Svensson, D. Ward, R. Wyss, C. Andreoiu, R. A. E. Austin, M. P. Carpenter, M. Cromaz, M. A. Deleplanque, R. M. Diamond, P. Fallon, A. Görgen, R. V. F. Janssens, T. L. Khoo, F. Kondev, G. J. Lane, T. Lauritsen, I. Y. Lee, A. O. Macchiavelli, T. Roderger, D. Rudolph, D. G. Sarantites, D. Seweryniak, T. Steinhardt, F. S. Stephens, O. Thelen, K. Vetter, and J. C. Waddington
Phys. Rev. C **69**, 034330/1-13 (2004)

High-Spin Spectroscopy and Quasiparticle Alignments in $^{124,125}\text{Ce}$

J. F. Smith, V. Medina-Chico, C. J. Chiara, M. P. Carpenter, C. N. Davids, M. Devlin, J. L. Durell, D. B. Fossan, S. J. Freeman, R. V. F. Janssens, D. R. LaFosse, M. J. Leddy, P. Reiter, D. G. Sarantites, D. Seweryniak, K. Starosta, R. Wadsworth, A. N. Wilson, and J. N. Wilson
Phys. Rev. C **69**, 034339/1-20 (2004)

Production of ϕ Mesons in Au + Au Collisions at 11.7 A GeV/c

B. B. Back *et al.* (E917 Collaboration)
Phys. Rev. C **69**, 054901/1-13 (2004)

Determination of the Direct Capture Contribution for $^{13}\text{N} (p,\gamma)^{14}\text{O}$ from the $^{14}\text{Q} \rightarrow ^{13}\text{N} + p$ Asymptotic Normalization Coefficient

Xiaodong Tang, A. Azhari, Changbo Fu, C. A. Gagliardi, A. M. Mukhamedzhanov, F. Pirlepesov, L. Trache, R. E. Tribble, V. Burjan, V. Kroha, F. Carstoiu, and B. F. Irgaziev
Phys. Rev. C **69**, 055807/1-9 (2004)

Low-Lying Levels in ^{59}Cr : Inadequacy of the fp Model Space and Onset of Deformation

S. J. Freeman, R. V. F. Janssens, B. A. Brown, M. P. Carpenter, S. M. Fischer, N. J. Hammond, M. Honma, T. Lauritsen, C. J. Lister, T. L. Khoo, G. Mukherjee, D. Seweryniak, J. F. Smith, B. J. Varley, M. Whitehead, and S. Zhu
Phys. Rev. C **69**, 064301/1-7 (2004)

High-Spin States in ^{179}Au : Spectroscopy of Shape-Driving Orbitals Beyond the Neutron Midshell

W. F. Mueller, W. Reviol, M. P. Carpenter, R. V. F. Janssens, F. G. Kondev, K. Abu Saleem, I. Ahmad, H. Amro, C. R. Bingham, J. Caggiano, C. N. Davids, D. Hartley, A. Heinz, B. Herskind, D. Jenkins, T. L. Khoo, T. Lauritsen, W. C. Ma, J. Ressler, L. L. Riedinger, D. G. Sarantites, D. Seweryniak, S. Siem, A. A. Sonzogni, J. Uusitalo, P. G. Varmette, I. Wiedenhöver, and R. Wadsworth
Phys. Rev. C **69**, 064315/1-10 (2004)

In-Beam Electron Spectroscopy of ^{226}U and ^{254}No

R. D. Humphreys, P. A. Butler, J. E. Bastin, P. T. Greenlees, N. J. Hammond, R.-D. Herzberg, D. G. Jenkins, G. D. Jones, H. Kankaanpää, A. Keenan, H. Kettunen, T. Page, P. Rahkila, C. Scholey, J. Uusitalo, N. Amzal, P. M. T. Brew, K. Eskola, J. Gerl, K. Hauschild, K. Helariutta, F.-P. Heßberger, A. Hürstel, P. M. Jones, R. Julin, S. Juutinen, T.-L. Khoo, W. Korten, P. Kuusiniemi, Y. Le Coz, M. Leino, A.-P. Leppänen, M. Muikku, P. Nieminen, S. W. Ødegard, J. Pakarinen, P. Reiter, G. Sletten, Ch. Theisen, and H.-J. Wollersheim
Phys. Rev. C **69**, 064324/1-6 (2004)

Measurements of ^{17}F Scattering by ^{208}Pb with a New Type of Large Solid Angle Detector Array

M. Romoli, E. Vardaci, M. Di Pietro, A. De Francesco, A. De Rosa, G. Inghima, M. La Commara, B. Martin, D. Pierrousakou, M. Sandoli, M. Mazzocco, T. Glodariu, P. Scopel, C. Signorini, R. Bonetti, A. Guglielmetti, F. Soramel, L. Stroe, J. Greene, A. Heinz, D. Henderson, C. L. Jiang, E. F. Moore, R. C. Pardo, E. E. Rehm, A. Wuosmaa, and J. F. Liang
Phys. Rev. C **69**, 064614/1-8 (2004)

Centrality Dependence of Charged Antiparticle to Particle Ratios Near Midrapidity in $d + \text{Au}$ Collisions at $\sqrt{s_{NN}} = 200 \text{ GeV}$

B. B. Back *et al.* (The PHOBOS Collaboration)
Phys. Rev. C **70**, 011901(R)/1-5 (2004)

 Q Value of the Superallowed Decay of ^{22}Mg and the Calibration of the $^{21}\text{Na}(p,\gamma)$ Experiment

G. Savard, J. A. Clark, F. Buchinger, J. E. Crawford, S. Gulick, J. C. Hardy, A. A. Hecht, V. E. Jacob, J. K. P. Lee, A. F. Levand, B. F. Lungren, N. D. Scielzo, K. S. Sharma, I. Tanihata, I. S. Towner, W. Trimble, J. C. Wang, Y. Wang, and Z. Zhou
Phys. Rev. C **70**, 042501(R)/1-4 (2004)

Particle Production at Very Low Transverse Momenta in Au + Au Collisions at $\sqrt{s_{NN}} = 200$ GeV

B. B. Back, M. D. Baker, M. Ballintijn, D. S. Barton, R. R. Betts, A. A. Bickley, R. Bindel, A. Budzanowski, W. Busza, A. Carroll, M. P. Decowski, E. Garcia, N. George, K. Gulbrandsen, S. Gushue, C. Halliwell, J. Hamblen, G. A. Heintzelman, C. Henderson, D. J. Hofman, R. S. Hollis, R. Holyński, B. Holzman, A. Iordanova, E. Johnson, J. L. Kane, J. Katzy, N. Khan, W. Kucewicz, P. Kulinich, C. M. Kuo, W. T. Lin, S. Manly, D. McLeod, A. C. Mignerey, R. Nouicer, A. Olszewski, R. Pak, I. C. Park, H. Pernegger, C. Reed, L. P. Remsberg, M. Reuter, C. Roland, G. Roland, L. Rosenberg, J. Sagerer, P. Sarin, P. Sawicki, W. Skulski, S. G. Steadman, P. Steinberg, G. S. F. Stephans, A. Sukhanov, J.-L. Tang, A. Trzupek, C. Vale, G. J. van Nieuwenhuizen, R. Verrier, F. L. H. Wolfs, B. Wosiek, K. Woźniak, A. H. Wousmaa, and B. Wyslouch

Phys. Rev. C **70**, 051901(R)/1-4 (2004)

Pseudorapidity Dependence of Charged Hadron Transverse Momentum Spectra in $d + Au$ Collisions at $\sqrt{s_{NN}} = 200$ GeV

B. B. Back *et al.* (PHOBOS Collaboration)

Phys. Rev. C **70**, 061901(R)/1-3 (2004)

Excitation Energies and Spins of the Yrast Superdeformed Band in ^{191}Hg

S. Siem, P. Reiter, T. L. Khoo, T. Lauritsen, P.-H. Heenen, M. P. Carpenter, I. Ahmad, H. Amro, I. Calderin, T. Døssing, T. Duguet, S. M. Fischer, U. Garg, D. Gassmann, G. Hackman, F. Hannachi, K. Hauschild, R. V. F. Janssens, B. Kharraja, A. Korchi, I.-Y. Lee, A. Lopez-Martens, A. O. Macchiavelli, E. F. Moore, D. Nisius, and C. Schück

Phys. Rev. C **70**, 014303/1-10 (2004)

 γ -Spectroscopy of Core-Excited States in ^{51}Mn

J. Ekman, D. Rudolph, C. Andreoiu, C. Fahlander, M. N. Mineeva, M. A. Bentley, S. J. Williams, R. Charity, E. Ideguchi, W. Reviol, D. G. Sarantites, V. Tomov, R. M. Clark, M. Cromaz, P. Fallon, A. O. Macchiavelli, M. P. Carpenter, and D. Seweryniak

Phys. Rev. C **70**, 014306/1-14 (2004)

Shape Coexistence and Band Crossings in ^{174}Pt

J. T. M. Goon, D. J. Hartley, L. L. Riedinger, M. P. Carpenter, F. G. Kondev, R. V. F. Janssens, K. H. Abu Saleem, I. Ahmad, H. Amro, J. A. Cizewski, C. N. Davids, M. Danchev, T. L. Khoo, A. Heinz, C. J. Lister, T. Lauritsen, W. C. Ma, G. L. Poli, J. Ressler, D. Seweryniak, I. Wiedenhöver, W. Reviol, M. Smith, and Jing-ye Zhang

Phys. Rev. C **70**, 014309/1-6 (2004)

Rotational Bands in Neutron-Rich $^{169,171,172}\text{Er}$

C. Y. Wu, D. Cline, M. W. Simon, R. Teng, K. Vetter, M. P. Carpenter, R. V. F. Janssens, and I. Wiedenhöver

Phys. Rev. C **70**, 014313/1-7 (2004)

Collision Geometry Scaling of Au + Au Pseudorapidity Density from $\sqrt{s_{NN}} = 19.6$ to 200 GeV

B. B. Back *et al.* (PHOBOS Collaboration)

Phys. Rev. C **70**, 021902/1-5 (2004)

Alignments in the Odd-Proton Actinides ^{237}Np and ^{241}Am

K. Abu Saleem, R. V. F. Janssens, M. P. Carpenter, F. G. Kondev, I. Wiedenhöver, I. Ahmad, J. Caggiano, P. Chowdhury, J. A. Cizewski, D. Cline, M. Devlin, N. Fotiades, J. P. Greene, G. Hackman, A. Heinz, T. L. Khoo, T. Lauritsen, C. J. Lister, A. O. Macchiavelli, E. H. Seabury, D. Seweryniak, A. Sonzogni, and C. Y. Wu

Phys. Rev. C **70**, 024310/1-15 (2004)

Probing the Sustainability of the $N = 82$ and $Z = 50$ Shell Closures for Neutron-Rich Nuclides: Decay of $^{120}\text{Rh}_{75}$ to Levels of $^{120}\text{Pd}_{74}$

W. B. Walters, B. E. Tomlin, P. F. Mantica, B. A. Brown, J. Rikovska Stone, A. D. Davies, A. Estrade, P. T. Hosmer, N. Hoteling, S. N. Liddick, T. J. Mertzimekis, F. Montes, A. C. Morton, W. F. Mueller, M. Ouellette, E. Pellegrini, P. Santi, D. Seweryniak, H. Schatz, J. Shergur, and A. Stolz
Phys. Rev. C **70**, 034314/1-5 (2004)

Absolute Intensities of γ Rays in ^{182}Hf Decay

I. Ahmad, J. P. Greene, E. F. Moore, W. Kutschera, and C. Vockenhuber
Phys. Rev. C **70**, 047301/1-3 (2004)

Highly-Deformed Bands in ^{175}Hf

D. T. Scholes, D. M. Cullen, F. G. Kondev, R. V. F. Janssens, M. P. Carpenter, D. J. Hartley, M. K. Djongolov, G. Sletten, G. Hagemann, C. Wheldon, P. M. Walker, K. Abu Saleem, I. Ahmad, D. L. Balabanski, P. Chowdhury, M. Danchev, G. D. Dracoulis, H. M. El-Masri, J. Goon, A. Heinz, R. A. Kaye, T. L. Khoo, T. Lauritsen, C. J. Lister, E. F. Moore, L. L. Riedinger, M. A. Riley, D. Seweryniak, I. Shestakova, I. Wiedenhöver, O. Zeidan, and Jing-ye Zhang
Phys. Rev. C **70**, 054314/1-8 (2004)

Core Excited States in the $A = 51$ Mirror Nuclei

J. Ekman, C. Andreoiu, C. Fahlander, M. N. Mineeva, D. Rudolph, M. A. Bentley, S. J. Williams, R. J. Charity, E. Ideguchi, W. Reviol, D. G. Sarantites, V. Tomov, R. M. Clark, M. Cromaz, P. Fallon, A. O. Macchiavelli, M. P. Carpenter, and D. Seweryniak
Phys. Rev. C **70**, 057305/1-4 (2004)

Near-Yrast, Medium-Spin Structure of the ^{107}Tc Nucleus

W. Urban, T. Rzača-Urban, J. L. Durell, A. G. Smith, and I. Ahmad
Phys. Rev. C **70**, 057308/1-4 (2004)

Development of Shell Closures at $N = 32, 34$. I. β Decay of Neutron-Rich Sc Isotopes

S. N. Liddick, P. F. Mantica, R. Broda, B. A. Brown, M. P. Carpenter, A. D. Davies, B. Fornal, T. Glasmacher, D. E. Groh, M. Honma, M. Horoi, R. V. F. Janssens, T. Mizusakik, D. J. Morrissey, A. C. Morton, W. F. Mueller, T. Otsuka, J. Pavan, H. Schatz, A. Stolz, S. L. Tabor, B. E. Tomlin, and M. Wiedeking
Phys. Rev. C **70**, 064303/1-9 (2004)

Development of Shell Closures at $N = 32, 34$. II: Lowest Yrast Excitations in Even-Even Ti Isotopes from Deep Inelastic Heavy-Ion Collisions

B. Fornal, S. Zhu, R. V. F. Janssens, M. Honma, R. Broda, P. F. Mantica, B. A. Brown, M. P. Carpenter, P. J. Daly, S. J. Freeman, Z. W. Grabowski, N. J. Hammond, F. G. Kondev, W. Królas, T. Lauritsen, S. N. Liddick, C. J. Lister, E. F. Moore, T. Otsuka, T. Pawlat, D. Seweryniak, B. E. Tomlin, and J. Wrzesinski
Phys. Rev. C **70**, 064304/1-6 (2004)

Erratum: Low-Lying Levels in ^{59}Cr : Inadequacy of the fp Model Space and Onset of Deformation [Phys. Rev. C **59**, 064301 (2004)]

S. J. Freeman, R. V. F. Janssens, B. A. Brown, M. P. Carpenter, S. M. Fischer, N. J. Hammond, M. Honma, T. Lauritsen, C. J. Lister, T. L. Khoo, G. Mukherjee, D. Seweryniak, J. F. Smith, B. J. Varley, M. Whitehead, and S. Zhu
Phys. Rev. C **70**, 029901(E) (2004)

Erratum to: "Recent Results from PHOBOS at RHIC" [Nucl. Phys. **A721**, 227c (2003)]

B. B. Back *et al.* (PHOBOS Collaboration)
Nucl. Phys. **A733**, 352-354 (2004)

The $N = Z$ rp-Process Waiting-Point Nucleus ^{68}Se and Its Astrophysical Implications

A. Wöhr, A. Aparahamian, P. Boutachkov, J. L. Galache, J. Görres, M. Shawcross, A. Teymurazyan, M. C. Wiescher, D. S. Brenner, C. N. Davids, S. M. Fischer, A. M. Heinz, R. V. F. Janssens, and D. Seweryniak
Nucl. Phys. **A742**, 349-362 (2004)

High-Spin Structure of $N \simeq Z$ Nuclei Around the $A = 72$ Region

N. S. Kelsall, C. E. Svensson, S. Fischer, D. E. Appelbe, R. A. E. Austin, D. P. Balamuth, G. C. Ball, J. A. Cameron, M. P. Carpenter, R. M. Clark, M. Cromaz, M. A. Deleplanque, R. M. Diamond, P. Fallon, D. F. Hodgson, R. V. F. Janssens, D. G. Jenkins, G. J. Lane, C. J. Lister, A. O. Macchiavelli, C. D. O'Leary, D. G. Sarantites, F. S. Stephens, D. C. Schmidt, D. Seweryniak, K. Vetter, J. C. Waddington, R. Wadsworth, D. Ward, A. N. Wilson, A. V. Afanasjev, S. Frauendorf, and I. Ragnarsson
Eur. Phys. J. A **20**, 131-132 (2004)

First Observation of Excited States in the ^{110}Mo Nucleus

W. Urban, T. Rzaça-Urban, J. L. Durell, W. R. Phillips, A. G. Smith, B. J. Varley, I. Ahmad, and N. Schulz
Eur. Phys. J. A **20**, 381-384 (2004)

Isospectral Superdeformed Bands in the $N = 46$ Nuclei ^{88}Mo and ^{89}Tc

K. Lagergren, B. Cederwall, R. M. Clark, P. Fallon, A. Görgen, T. Issa, R. V. F. Janssens, A. Johnson, A. O. Macchiavelli, L. Milechina, D. G. Sarantites, and R. Wyss
Eur. Phys. J. A **21**, 375-381 (2004)

K-Mixing and Fast Decay of a Seven-Quasiparticle Isomer in ^{179}Ta

F. G. Kondev, G. D. Dracoulis, G. J. Lane, I. Ahmad, A. P. Byrne, M. P. Carpenter, P. Chowdhury, S. J. Freeman, N. J. Hammond, R. V. F. Janssens, T. Kibédi, T. Lauritsen, C. J. Lister, G. Mukherjee, D. Seweryniak, and S. K. Tandel
Eur. Phys. J. A **22**, 23-27 (2004)

New Spins for Ground States and Isomers in ^{115}Pd and ^{117}Pd

W. Urban, A. Zlomaniec, G. Simpson, J. A. Pinston, J. Kurpeta, T. Rzaça-Urban, J. L. Durell, A. G. Smith, B. J. Varley, N. Schulz, and I. Ahmad
Eur. Phys. J. A **22**, 157-161 (2004)

New Bands and Spin-Parity Assignments in ^{111}Ru

W. Urban, T. Rzaça-Urban, Ch. Droste, S. G. Rohoziński, J. L. Durell, W. R. Phillips, A. G. Smith, B. J. Varley, N. Schulz, I. Ahmad, and J. A. Pinston
Eur. Phys. J. A **22**, 231-239 (2004)

The $\nu 9/2[404]$ Orbital and the Deformation in the $A \sim 100$ Region

W. Urban, J. A. Pinston, J. Genevey, T. Rzaça-Urban, A. Zlomaniec, G. Simpson, J. L. Durell, W. R. Phillips, A. G. Smith, B. J. Varley, I. Ahmad, and N. Schulz
Eur. Phys. J. A **22**, 241-252 (2004)

The Frank Karasek Memorial Scholarship Fund Revisited

John P. Greene
Int. Nucl. Target Dev. Society Newsletter **31**, 9 (2004)

Highly Selective Studies of GDR in ^{164}Er

V. Nanal, T. L. Khoo, D. J. Hofman, B. B. Back, M. P. Carpenter, I. Dioszegi, K. Eisenman, M. L. Halbert, P. Heckman, A. M. Heinz, D. Henderson, D. Jenkins, M. P. Kelly, F. G. Kondev, T. Lauritsen, C. J. Lister, B. McClintock, S. Mitsuoka, T. Pennington, J. Seitz, R. H. Siemssen, M. Thoennessen, R. J. van Swol, R. L. Varner, P. Wilt, and Y. Alhassid
Proceedings of the International Conference on Collective Motion in Nuclei Under Extreme Conditions (COMEX 1), Paris, France, June 10-13, 2003; Nucl. Phys. **A731**, 153-159 (2004)

Results from the PHOBOS Experiment at RHIC

Marguerite Belt Tonjes, for the PHOBOS Collaboration

Proceedings of the 8th International Conference on Nucleus-Nucleus Collisions (NN2003), Moscow, Russia, June 17-21, 2003; Nucl. Phys. **A734**, 61-64 (2004)

Nuclear Astrophysics Experiments with Stable and Unstable Beams

K. E. Rehm

Proceedings of the 8th International Conference on Nucleus-Nucleus Collisions (NN2003), Moscow, Russia, June 17-21, 2003; Nucl. Phys. **A734**, 615-622 (2004)Tracking the Monopole Migration of the $\nu 1f_{5/2}$ State Near the $N = 32$ Subshell Closure in Neutron-Rich Nuclei Above ^{48}Ca

S. N. Liddick, P. F. Mantica, R. V. F. Janssens, R. Broda, B. A. Brown, M. P. Carpenter, B. Fornal, A. C. Morton, W. F. Mueller, J. Pavan, A. Stolz, S. L. Tabor, B. E. Tomlin, and M. Wiedeking

Proceedings of the 6th International Conference on Radioactive Nuclear Beams (RNB6), Argonne, IL, September 22-26, 2003; Nucl. Phys. **A746**, 140c-144c (2004)

A Solenoidal Transport Device for Transfer Reactions in Inverse Kinematics

A. H. Wuosmaa, T. Al Tahtamouni, and J. P. Schiffer

Proceedings of the 6th International Conference on Radioactive Nuclear Beams (RNB6), Argonne, IL, September 22-26, 2003; Nucl. Phys. **A746**, 267c-271c (2004)Determination of the ^8B Neutrino Spectrum

W. T. Winter, K. E. Rehm, C. L. Jiang, I. Ahmad, S. J. Freedman, J. Greene, A. Heinz, D. Henderson, R. V. F. Janssens, E. F. Moore, C. Mukherjee, R. C. Pardo, M. Paul, T. Pennington, G. Savard, J. P. Schiffer, D. Seweryniak, and G. Zinkann

Proceedings of the 6th International Conference on Radioactive Nuclear Beams (RNB6), Argonne, IL, September 22-26, 2003; Nucl. Phys. **A746**, 311c-315c (2004)

Precise Mass Measurements of Astrophysical Interest Made with the Canadian Penning Trap Mass Spectrometer

J. A. Clark, R. C. Barber, B. Blank, C. Boudreau, F. Buchinger, J. E. Crawford, S. Gulick, J. C. Hardy, A. Heinz, J. K. P. Lee, A. F. Levand, R. B. Moore, C. Savard, D. Seweryniak, K. S. Sharma, C. D. Sprouse, W. Trimble, J. Vaz, J. C. Wang, and Z. Zhou

Proceedings of the 6th International Conference on Radioactive Nuclear Beams (RNB6), Argonne, IL, September 22-26, 2003; Nucl. Phys. **A746**, 342c-346c (2004)First Studies of the $^8\text{B}(\alpha, p)^{11}\text{C}$ Reaction

K. E. Rehm, C. L. Jiang, J. P. Greene, D. Henderson, R. V. F. Janssens, E. F. Moore, G. Mukherjee, R. C. Pardo, T. Pennington, J. P. Schiffer, S. Sinha, X. D. Tang, R. H. Siemssen, L. Jisonna, R. E. Segel, and A. H. Wuosmaa

Proceedings of the 6th International Conference on Radioactive Nuclear Beams (RNB6), Argonne, IL, September 22-26, 2003; Nucl. Phys. **A746**, 354c-358c (2004)Elastic Scattering of ^{17}F on ^{208}Pb and ^{17}F Breakup Cross Section at Coulomb Barrier Energies

M. Romoli, M. Mazzocco, E. Vardaci, M. Di Pietro, R. Bonetti, A. De Francesco, A. De Rosa, T. Glodariu, A. Guglielmetti, G. Inglima, M. La Commara, B. Martin, D. Pierroutsakou, M. Sandoli, P. Scopel, C. Signorini, F. Soramel, L. Stroe, J. Greene, A. Heinz, D. Henderson, C. L. Jiang, J. F. Liang, E. F. Moore, R. C. Pardo, K. E. Rehm, and A. Wuosmaa

Proceedings of the 6th International Conference on Radioactive Nuclear Beams (RNB6), Argonne, IL, September 22-26, 2003; Nucl. Phys. **A746**, 522c-525c (2004)

Production and Isobaric Separation of ^{63}Ni Ions for Determination of the $^{62}\text{Ni}(n,\gamma)^{63}\text{Ni}$ Reaction Cross Section at Stellar Temperatures

H. Nassar, S. Ghelberg, M. Paul, S. Dababneh, M. Heil, F. Käppeler, R. Plag, I. Ahmad, J. P. Greene, D. J. Henderson, C. L. Jiang, R. C. Pardo, T. Pennington, K. E. Rehm, R. Scott, S. Sinha, X. Tang, R. Vondrasek, H. Koivisto, D. Berkovits, M. Bettan, R. Reifarth, P. Collon, S. O'Brien, and N. Patronis
 Proceedings of the 6th International Conference on Radioactive Nuclear Beams (RNB6), Argonne, IL, September 22-26, 2003; Nucl. Phys. **A746**, 613c-616c (2004)

The Canadian Penning Trap Mass Spectrometer

J. C. Wang, G. Savard, K. S. Sharma, J. A. Clark, Z. Zhou, A. F. Levand, C. Boudreau, F. Buchinger, J. E. Crawford, J. P. Greene, S. Gulick, J. K. P. Lee, G. D. Sprouse, W. Trimble, J. Vaz, and B. J. Zabransky
 Proceedings of the 6th International Conference on Radioactive Nuclear Beams (RNB6), Argonne, IL, September 22-26, 2003; Nucl. Phys. **A746**, 651c-654c (2004)

Using a Wide-Beam Ion Source to Produce Large Area Sputtered Films for Low-Energy Laboratory Studies of Alpha Capture Cross-Sections

John P. Greene, Michael C. Wiescher, and Michael Paul
 Proceedings of the 21st World Conference of the International Nuclear Target Development Society, Argonne, IL, November 4-8, 2002; Nucl. Instrum. Methods **A521**, 12-16 (2004)

Developing a Detection Method of Environmental ^{244}Pu

S. Winkler, I. Ahmad, R. Golser, W. Kutschera, K. A. Orlandini, M. Paul, A. Priller, P. Steier, A. Valenta, and C. Vockenhuber
 Proceedings of the 9th International Conference on Accelerator Mass Spectrometry, Nagoya, Japan, September 9-13, 2002; Nucl. Instrum. Methods **B223-224**, 817-822 (2004)

Oceans Circulation and Electron Cyclotron Resonance Sources: Measurement of the AR-39 Isotopic Ratio in Seawater

M. Gaelens, M. Loiselet, G. Ryckewaert, R. C. Pardo, R. H. Scott, R. Vondrasek, Ph. Collon, and W. Kutschera
 Proceedings of the 10th International Conference on Ion Sources (ICIS2003), Dubna, Russia, September 8-13, 2003; Rev. Sci. Instrum. **75**, 1916-1918 (2004)

The Landscape of Particle Production: Results from PHOBOS

Peter Steinberg (for the PHOBOS Collaboration)
 Proceedings of the 17th International Conference on Ultra Relativistic Nucleus-Nucleus Collisions (Quark Matter 2004), Oakland, CA, January 11-17, 2004; J. Phys. G **30**, S683-S691 (2004)

Rapidity and k_T Dependence of HBT Correlations in Au + Au Collisions at 200 GeV with PHOBOS

Burt Holzman (for the PHOBOS Collaboration)
 Proceedings of the 17th International Conference on Ultra Relativistic Nucleus-Nucleus Collisions (Quark Matter 2004), Oakland, CA, January 11-17, 2004; J. Phys. G **30**, S1049-S1052 (2004)

Pseudorapidity Distributions of Charged Particles in d + Au and p + p Collisions at $\sqrt{s_{NN}} = 200$ GeV

Rachid Nouicer (for the PHOBOS Collaboration)
 Proceedings of the 17th International Conference on Ultra Relativistic Nucleus-Nucleus Collisions (Quark Matter 2004), Oakland, CA, January 11-17, 2004; J. Phys. G **30**, S1133-S1137 (2004)

Identified Hadron Spectra from PHOBOS

Gábor I. Veres (for the PHOBOS Collaboration)
 Proceedings of the 17th International Conference on Ultra Relativistic Nucleus-Nucleus Collisions (Quark Matter 2004), Oakland, CA, January 11-17, 2004; J. Phys. G **30**, S1143-S1147 (2004)

Flow in Au + Au Collisions at RHIC

Marguerite Belt Tonjes (for the PHOBOS Collaboration)

Proceedings of the 17th International Conference on Ultra Relativistic Nucleus-Nucleus Collisions (Quark Matter 2004), Oakland, CA, January 11-17, 2004; J. Phys. G **30**, S1243-S1246 (2004)Charged Particle Multiplicity Fluctuations in Au + Au Collisions $\sqrt{s_{NN}} = 200$ GeV

Krzysztof Wóznik (for the PHOBOS Collaboration)

Proceedings of the 17th International Conference on Ultra Relativistic Nucleus-Nucleus Collisions (Quark Matter 2004), Oakland, CA, January 11-17, 2004; J. Phys. G **30**, S1377-S1380 (2004)

Strip Interpolation in Silicon and Germanium Strip Detectors

Eric A. Wulf, Bernard F. Philips, W. Neil Johnson, James D. Kurfess, C. J. Lister, and Filip Kondev

Proceedings of the IEEE Nuclear Science Symposium and Medical Imaging Conference (NSS-MIC2004), Rome, Italy, October 16-22, 2004, (IEEE Publishing 2004) **2**, 925-929

Systematics of Heavy-Ion Fusion Reactions at Extreme Sub-Barrier Energies

C. L. Jiang, H. Esbensen, K. E. Rehm, B. B. Back, R. V. F. Janssens, C. N. Davids, J. P. Greene, D. J. Henderson, G. Mukherjee, R. C. Pardo, T. O. Pennington, D. Seweryniak, S. Sinha, Z. Zhou, M. Paul, P. Collon, J. A. Caggiano, A. M. Heinz, and I. Nishinaka

Proceedings of the International Conference FUSION03: From a Tunneling Nuclear Microscope to Nuclear Processes in Matter, Matsushima, Miyagi, Japan, November 12-15, 2003; Progress of Theoretical Physics Supplement **154**, 61-68 (2004)

Nuclear Structure at the Limits: Continued Exploration with Gammasphere

R. V. F. Janssens

22nd International Nuclear Physics Conference (INPC2004), Göteborg, Sweden, June 27-July 2, 2004, Book of Abstracts, p. 21 (2004)

Some Aspects of Charged Particle Multiplicity in Ultrarelativistic Au + Au Collisions

B. B. Back *et al.*

22nd International Nuclear Physics Conference (INPC2004), Göteborg, Sweden, June 27-July 2, 2004, Book of Abstracts, p. 164 (2004)

Setting Limits on Nuclear Structure Properties of the Low-Lying 3.5-eV Isomeric State in ^{229}Th

I. Ahmad, K. Bailey, D. L. Bowers, Z.-T. Lu, I. D. Moore, and T. P. O'Connor

22nd International Nuclear Physics Conference (INPC2004), Göteborg, Sweden, June 27-July 2, 2004, Book of Abstracts, p. 342 (2004)

In-Beam Gamma-Ray Spectroscopy of ^{254}No

S. Eckhauudt, N. Amzal, J. E. Bastin, E. Bouchez, P. A. Butler, A. Chatillon, K. Eskola, J. Gerl, T. Grahn, A. Gørgen, P. T. Greenlees, R. D. Herzberg, F. P. Hessberger, A. Hürstel, P. J. C. Ikin, G. D. Jones, P. Jones, R. Julin, S. Juutinen, H. Kettunen, T. L. Khoo, W. Korten, P. Kuusiniemi, Y. Le Coz, M. Leino, A. P. Leppänen, P. Nieminen, J. Pakarinen, J. Perkowski, A. Pritchard, P. Reiter, P. Rahkila, C. Scholey, C. Theisen, J. Uusitalo, K. Van de Vel, J. Wilson, and H. J. Wollersheim

22nd International Nuclear Physics Conference (INPC2004), Göteborg, Sweden, June 27-July 2, 2004, Book of Abstracts, p. 353 (2004)

Strength Distributions for Coupling to Ordered or Chaotic Spectra

T. Døssing, T.-L. Khoo, T. Lauritsen, A. P. Lopez-Martens, and S. Åberg

22nd International Nuclear Physics Conference (INPC2004), Göteborg, Sweden, June 27-July 2, 2004, Book of Abstracts, p. 361 (2004)

Influence of Nuclear Structure on Sub-Barrier Hindrance in Ni + Ni Fusion

C. L. Jiang, K. B. Rehm, R. V. F. Janssens, H. Esbensen, I. Ahmad, B. B. Back, P. Collon, C. N. Davids, J. P. Greene, D. J. Henderson, G. Mukherjee, R. C. Pardo, M. Paul, T. O. Pennington, D. Seweryniak, S. Sinha, and Z. Zhou
22nd International Nuclear Physics Conference (INPC2004), Göteborg, Sweden, June 27-July 2, 2004, Book of Abstracts, p. 456 (2004)

Proton Single-Particle States in the Heaviest Actinide Nuclei

I. Ahmad, F. G. Kondev, E. F. Moore, R. R. Chasman, J. P. Greene, M. P. Carpenter, C. J. Lister, R. V. F. Janssens, T. Lauritsen, D. Seweryniak, R. W. Hoff, J. E. Evans, R. W. Loughheed, C. E. Porter, L. K. Felker
Conference on "Nuclei at the Limits", Argonne, IL, July 26-30, 2004, Book of Abstracts, p. 4 (2004)

Spherical and Deformed Structures in ^{189}Pb

A. M. Baxter, G. D. Dracoulis, A. P. Byrne, T. Kibédi, P. M. Davidson, R. V. F. Janssens, M. P. Carpenter, C. N. Davids, T. L. Khoo, and T. Lauritsen
Conference on "Nuclei at the Limits", Argonne, IL, July 26-30, 2004, Book of Abstracts, p. 10 (2004)

First Measurement of Excited States in ^{181}Tl

M. P. Carpenter, F. G. Kondev, R. V. F. Janssens, D. Seweryniak, G. Mukherjee, I. Ahmad, C. N. Davids, S. Freeman, G. Jones, N. Hammond, D. G. Jenkins, T. L. Khoo, A. J. Larabee, T. Lauritsen, N. Liechty, C. J. Lister, E. F. Moore, P. Raddon, S. Sinha, and R. Wadsworth
Conference on "Nuclei at the Limits", Argonne, IL, July 26-30, 2004, Book of Abstracts, p. 22 (2004)

First Observation of Excited States in the $T = -1$, Odd-Odd Nucleus ^{48}Mn

C. Chandler, M. A. Bentley, M. P. Carpenter, C. N. Davids, R. Du Rietz, J. Ekman, S. J. Freeman, P. E. Garrett, G. Hammond, R. V. F. Janssens, and D. Seweryniak
Conference on "Nuclei at the Limits", Argonne, IL, July 26-30, 2004, Book of Abstracts, p. 25 (2004)

Decay Rate of Triaxially Deformed Proton Emitters

Cary N. Davids and Henning Esbensen
Conference on "Nuclei at the Limits", Argonne, IL, July 26-30, 2004, Book of Abstracts, p. 36 (2004)

Recoil-Decay Tagging Study of ^{146}Tm

C. N. Davids, A. Robinson, D. Seweryniak, P. J. Woods, B. Blank, M. P. Carpenter, T. Davinson, S. J. Freeman, N. Hammond, N. Hoteling, R. F. V. Janssens, Z. Liu, G. Mukherjee, J. Shergur, S. Sinha, A. A. Sonzogni, W. B. Walters, and A. Woehr
Conference on "Nuclei at the Limits", Argonne, IL, July 26-30, 2004, Book of Abstracts, p. 37 (2004)

Reduced Transition Probabilities to the First 2^+ State in $^{52,54,56}\text{Ti}$

D.-C. Dinca, R. V. F. Janssens, A. Gade, D. Bazin, R. Broda, C. M. Campbell, M. P. Carpenter, P. Chowdhury, J. M. Cook, A. Deacon, B. Fornal, S. J. Freeman, T. Glasmacher, F. G. Kondev, J.-L. Lecouey, S. N. Liddick, P. F. Mantica, W. F. Mueller, H. Olliver, K. Starosta, J. R. Terry, B. A. Tomlin, and K. Yoneda
Conference on "Nuclei at the Limits", Argonne, IL, July 26-30, 2004, Book of Abstracts, p. 43 (2004)

Decay-Out of Superdeformed Bands by Coupling to Ordered or Chaotic Spectra

T. Døssing, T. L. Khoo, T. Lauritsen, A. P. Lopez-Martens, and S. Åberg
Conference on "Nuclei at the Limits", Argonne, IL, July 26-30, 2004, Book of Abstracts, p. 46 (2004)

Structure of Multi-Quasiparticle Isomers in the Region of ^{177}Lu

G. D. Dracoulis, F. G. Kondev, G. J. Lane, A. P. Byrne, T. Kibédi, I. Ahmad, M. P. Carpenter, S. J. Freeman, R. V. F. Janssens, N. J. Hammond, T. Lauritsen, C. J. Lister, G. Mukherjee, D. Seweryniak, P. Chowdhury, and S. K. Tandel

Conference on “Nuclei at the Limits”, Argonne, IL, July 26-30, 2004, Book of Abstracts, p. 47 (2004)

Level Structure of ^{56}Ti and the Possible Shell Gap at $N = 34$

B. Fornal, R. V. F. Janssens, R. Broda, S. Zhu, M. P. Carpenter, P. J. Daly, S. Freeman, Z. W. Grabowski, N. Hammond, F. G. Kondev, W. Krolas, T. Lauritsen, S. Liddick, C. J. Lister, P. Mantica, E. F. Moore, T. Pawlat, B. Tomlin, D. Seweryniak, and J. Wrzesinski

Conference on “Nuclei at the Limits”, Argonne, IL, July 26-30, 2004, Book of Abstracts, p. 53 (2004)

Structure of Neutron-Rich Cr Isotopes: Inadequacy of the fp Model Space and the Onset of Deformation

S. J. Freeman, R. V. F. Janssens, B. A. Brown, I. V. Calderin, M. P. Carpenter, P. Chowdhury, A. N. Deacon, S. M. Fischer, N. J. Hammond, M. Honma, T. Lauritsen, C. J. Lister, T. L. Khoo, G. Mukherjee, D. Seweryniak, J. F. Smith, S. L. Tabor, B. J. Varley, M. Whitehead, and S. Zhu

Conference on “Nuclei at the Limits”, Argonne, IL, July 26-30, 2004, Book of Abstracts, p. 54 (2004)

Heavy-Element Spectroscopy at JYFL

P. T. Greenlees, S. Eeckhaudt, T. Grahn, P. Jones, R. Julin, S. Juutinen, H. Kettunen, M. Leino, A.-P. Leppänen, P. Nieminen, M. Nyman, J. Pakarinen, P. Rahkila, C. Scholey, J. Uusitalo, P. A. Butler, J. E. Bastin, R.-D. Herzberg, R. D. Humphreys, P. J. C. Ikin, G. D. Jones, T. Page, A. Pritchard, A. Chatillon, A. Gørgen, W. Korten, Ch. Theisen, J. Gerl, F. P. Heßberger, P. Kuusiniemi, T. L. Khoo, P. Reiter, and K. Eskola

Conference on “Nuclei at the Limits”, Argonne, IL, July 26-30, 2004, Book of Abstracts, p. 59 (2004)

Linear Polarization Measurements of Gamma Rays Following Alpha Decay

N. J. Hammond, C. J. Lister, K. Teh, E. F. Moore, and G. D. Jones

Conference on “Nuclei at the Limits”, Argonne, IL, July 26-30, 2004, Book of Abstracts, p. 63 (2004)

Search for Hyperdeformation in Xe Nuclei

C. Rønn Hansen, C. B. Hagemann, B. Herskind, D. R. Jensen, G. Sletten, J. N. Wilson, S. W. Ødegård, P. Bringel, C. Engelhardt, H. Hübel, A. Neusser, A. K. Singh, G. Benzoni, A. Bracco, F. Camera, S. Leoni, A. Maj, P. Bednarczyk, T. Byrski, D. Curien, A. Korichi, J. Roccoz, J. Lisle, T. Steinhardt, O. Thelen, M. P. Carpenter, R. V. F. Janssens, T. L. Khoo, T. Lauritsen, R. M. Clark, and P. Fallon

Conference on “Nuclei at the Limits”, Argonne, IL, July 26-30, 2004, Book of Abstracts, p. 64 (2004)

Search for Wobbling Excitations in Hf Nuclei: Are the TSD Bands Triaxial?

D. J. Hartley, M. K. Djongolov, F. G. Kondev, M. P. Carpenter, G. Hagemann, R. V. F. Janssens, E. F. Moore, L. L. Riedinger, M. A. Riley, G. Sletten, A. Aguilar, C. R. Bingham, D. Campbell, P. Chowdhury, M. Cromaz, D. Cullen, M. Danchev, G. Dracoulis, P. Fallon, J. Goon, R. A. Kaye, R. W. Laird, T. Lauritsen, A. O. Macchiavelli, B. McClain, G. Mukherjee, E. Ngijoi-Yogo, S. K. Tandel, Jing-ye Zhang

Conference on “Nuclei at the Limits”, Argonne, IL, July 26-30, 2004, Book of Abstracts, p. 65 (2004)

Mapping the Limits of Chiral Structure in the Mass $A \sim 130$ Region

A. A. Hecht, C. W. Beausang, H. Amro, D. L. Balabanski, C. J. Barton, Z. Berant, M. A. Caprio, F. R. Casten, J. R. Cooper, F. Donau, D. J. Hartley, R. Krucken, D. A. Meyer, H. Newman, J. R. Novak, E. S. Paul, N. Pietralla, J. J. Ressler, A. Wolf, N. V. Zamfir, Jing-Ye Zhang, and K. E. Zyromski

Conference on “Nuclei at the Limits”, Argonne, IL, July 26-30, 2004, Book of Abstracts, p. 67 (2004)

Confirmation of a Doorway Mechanism as the Principal Decay Mode in the Heavy Ion Radiative Capture Reaction $^{12}\text{C}(^{12}\text{C},\gamma)^{24}\text{Mg}$

D. G. Jenkins, B. R. Fulton, R. Glover, J. Pearson, R. Wadsworth, D. Watson, C. J. Lister, M. P. Carpenter, P. Chowdhury, S. Freeman, R. V. F. Janssens, D. Seweryniak, The DRAGON E947 Collaboration, F. Haas, C. Beck, P. Papka, M. Rousseau, A. Sánchez i Zafra, C. Andreoiu, J. Dobon, P. Fallon, A. Gørgen, A. O. Macchiavelli, and M. McMahan

Conference on “Nuclei at the Limits”, Argonne, IL, July 26-30, 2004, Book of Abstracts, p. 73 (2004)

Influence of Nuclear Structure on Sub-Barrier Hindrance in Ni + Ni Fusion

C. L. Jiang, K. E. Rehm, R. V. F. Janssens, H. Esbensen, I. Ahmad, B. B. Back, P. Collon, C. N. Davids, J. P. Greene, D. J. Henderson, G. Mukherjee, R. C. Pardo, M. Paul, T. O. Pennington, D. Seweryniak, S. Sinha, and Z. Zhou

Conference on “Nuclei at the Limits”, Argonne, IL, July 26-30, 2004, Book of Abstracts, p. 74 (2004)

Rotational Damping, Ridges and the Quasicontinuum of γ Rays in ^{152}Dy

T. Lauritsen, I. Ahmad, M. P. Carpenter, A. M. Heinz, R. V. F. Janssens, D. G. Jenkins, T. L. Khoo, F. G. Kondev, A. J. Larabee, C. J. Lister, D. Seweryniak, P. Fallon, A. O. Macchiavelli, D. Ward, R. M. Clark, M. Cromaz, G. Lane, A. Lopez-Martens, A. Korichi, S. Siem, B. Herskind, and T. Dossing

Conference on “Nuclei at the Limits”, Argonne, IL, July 26-30, 2004, Book of Abstracts, p. 82 (2004)

Search for Triaxial Superdeformation and Wobbling Mode in $^{172,171}\text{Hf}$

W. C. Ma, M. P. Carpenter, P. Chowdhury, D. Cullen, M. K. Djongolov, N. Hammond, D. J. Hartley, R. V. F. Janssens, T. L. Khoo, F. G. Kondev, T. Lauritsen, C. J. Lister, E. F. Moore, S. Odegard, S. V. Rigby, D. G. Roux, D. T. Scholes, J. A. Winger, R. Yadav, J. Y. Zhang, Y. Zhang, and S. Zhu

Conference on “Nuclei at the Limits”, Argonne, IL, July 26-30, 2004, Book of Abstracts, p. 89 (2004)

Electrons from A 0.3s Isomer in ^{254}No

G. Mukherjee, T. L. Khoo, R. Blinstrup, D. Seweryniak, I. Ahmad, P. A. Butler, M. P. Carpenter, P. Chowdhury, J. A. Cizewski, C. N. Davids, S. Freeman, R. Gramer, J. Greene, N. Hammond, R. D. Herzberg, A. Heinz, P. Ikin, R. V. F. Janssens, M. Johnson, G. D. Jones, F. G. Kondev, T. Lauritsen, C. J. Lister, E. Ngijoi-Yogo, and P. Reiter

Conference on “Nuclei at the Limits”, Argonne, IL, July 26-30, 2004, Book of Abstracts, p. 103 (2004)

Triaxial Superdeformed Bands in ^{175}Hf

D. T. Scholes, D. M. Cullen, F. G. Kondev, R. V. F. Janssens, M. P. Carpenter, D. J. Hartley, M. K. Djongolov, G. Sletten, G. Hagemann, W. Sheldon, P. M. Walker, K. Abu Saleem, I. Ahmad, D. L. Balabanski, P. Chowdhury, M. Danchev, G. D. Dracoulis, H. M. El-Masri, J. Goon, A. Heinz, R. A. Kaye, T. L. Khoo, T. Lauritsen, C. J. Lister, E. F. Moore, L. L. Riedinger, M. A. Riley, D. Seweryniak, I. Shestakova, I. Wiedenhöver, O. Zeidan, and Jing-ye Zhang

Conference on “Nuclei at the Limits”, Argonne, IL, July 26-30, 2004, Book of Abstracts, p. 132 (2004)

Ground-State Bands in the Transitional Proton Emitters $^{145,147}\text{Tm}$

D. Seweryniak, C. N. Davids, A. Robinson, P. J. Woods, B. Blank, M. P. Carpenter, T. Davinson, S. J. Freeman, N. Hammond, N. Hoteling, R. V. F. Janssens, Z. Liu, G. Mukherjee, J. Shergur, S. Sinha, A. A. Sonzogni, W. B. Walters, and A. Woehr

Conference on “Nuclei at the Limits”, Argonne, IL, July 26-30, 2004, Book of Abstracts, p. 134 (2004)

In-Beam Studies of the Astrophysically Important $T_z = -1$ Nuclei

D. Seweryniak, P. J. Woods, B. Blank, M. P. Carpenter, T. Davinson, S. J. Freeman, J. Goerres, N. Hammond, A. Heinz, N. Hoteling, R. V. F. Janssens, D. G. Jenkins, H. Mahmud, T. L. Khoo, C. J. Lister, Z. Liu, G. Mukherjee, E. Rehm, F. Sarazin, J. Shergur, M. Shawcross, S. Sinha, and A. Woehr

Conference on “Nuclei at the Limits”, Argonne, IL, July 26-30, 2004, Book of Abstracts, p. 135 (2004)

Low. Energy Levels in $^{111,113}\text{Sb}$ Populated Via β -Decay of $^{111,113}\text{Te}$

J. Shergur, D. Seweryniak, W. B. Walters, A. Woehr, P. Boutachkov, C. N. Davids, I. Dillmann, G. Mukherjee, S. Sinha, A. Teymurazyan, and I. Zartova

Conference on "Nuclei at the Limits", Argonne, IL, July 26-30, 2004, Book of Abstracts, p. 138 (2004)

High-K Isomers and Rotational Structures in ^{174}W

S. K. Tandel, P. Chowdhury, E. H. Seabury, I. Ahmad, M. P. Carpenter, S. Fischer, R. V. F. Janssens, T. L. Khoo, T. Lauritsen, C. J. Lister, and D. Seweryniak

Conference on "Nuclei at the Limits", Argonne, IL, July 26-30, 2004, Book of Abstracts, p. 147 (2004)

Determination of the Direct Capture Contribution for $^{13}\text{N}(p,\gamma)^{14}\text{O}$ from the $^{14}\text{O} \rightarrow ^{13}\text{N} + p$ Asymptotic Normalization Coefficient

Xiaodong Tang, A. Azhari, Changbo Fu, C. A. Gagliardi, A. M. Mukhamedzhanov, F. Pirlpesov, L. Trache, R. E. Tribble, V. Burjan, V. Kroha, and B. F. Irgaziev

Conference on "Nuclei at the Limits", Argonne, IL, July 26-30, 2004, Book of Abstracts, p. 148 (2004)

Isomeric Transitions in Neutron-Rich Nuclides Observed Following Projectile Fragmentation of a ^{136}Xe Beam at 120 MeV/A

B. E. Tomlin, W. B. Walters, P. F. Mantica, B. A. Brown, A. D. Davies, A. Estrade, P. Hosmer, N. Hoteling, S. N. Liddick, T. J. Mertzimekis, F. Montes, A. C. Morton, W. F. Mueller, M. S. Ouellette, E. Pellegrini, J. Rikovska Stone, P. Santi, D. Seweryniak, H. Schatz, and J. Shergur

Conference on "Nuclei at the Limits", Argonne, IL, July 26-30, 2004, Book of Abstracts, p. 151 (2004)

Triaxial Superdeformed Bands and Wobbling in $^{163}_{69}\text{Tm}$

X. Wang, N. S. Pattabiraman, U. Garg, A. A. Afanasjev, M. P. Carpenter, R. S. Chakrawarthy, S. S. Ghugre, N. J. Hammond, R. V. F. Janssens, T. Li, A. O. Macchiavelli, E. F. Moore, G. Mukherjee, B. K. Nayak, D. Seweryniak, M. Whitehead, and S. Zhu

Conference on "Nuclei at the Limits", Argonne, IL, July 26-30, 2004, Book of Abstracts, p. 159 (2004)

Study of ^7He Using the $d(^6\text{He},p)^7\text{He}$ Reaction

A. H. Wuosmaa, K. E. Rehm, J. P. Greene, D. J. Henderson, R. V. F. Janssens, C. L. Jiang, L. Jisonna, E. F. Moore, R. C. Pardo, M. Paul, D. Peterson, S. C. Pieper, G. Savard, J. P. Schiffer, R. E. Segel, S. Sinha, X. Tang, and R. B. Wiringa

Conference on "Nuclei at the Limits", Argonne, IL, July 26-30, 2004, Book of Abstracts, p. 165 (2004)

Investigation of Anti-Magnetic Rotation in ^{101}Pd

S. Zhu, U. Garg, A. V. Afanasjev, S. Frauendorf, B. Kharraja, S. S. Ghugre, S. N. Chintalapudi, N. S. Pattabiraman, R. V. F. Janssens, M. P. Carpenter, F. G. Kondev, and T. Lauritsen

Conference on "Nuclei at the Limits", Argonne, IL, July 26-30, 2004, Book of Abstracts, p. 171 (2004)

Level Structure of ^{104}Ag

S. Zhu, U. Garg, A. V. Afanasjev, S. Frauendorf, B. Kharraja, S. S. Ghugre, S. N. Chintalapudi, N. S. Pattabiraman, R. V. F. Janssens, M. P. Carpenter, F. G. Kondev, and T. Lauritsen

Conference on "Nuclei at the Limits", Argonne, IL, July 26-30, 2004, Book of Abstracts, p. 172 (2004)

Nuclear Pairing and Coriolis Effects in Proton Emitters

A. S. Volya and C. N. Davids

4th International Conference on Exotic Nuclei and Atomic Masses (ENAM'04), Pine Mountain, GA, September 12-16, 2004, Book of Abstracts, p. 24 (2004)

Understanding the rp-Processes with the Canadian Penning Trap Mass Spectrometer

J. A. Clark, R. C. Barber, B. Blank, C. Boudreau, F. Buchinger, J. E. Crawford, J. P. Greene, S. Gulick, J. C. Hardy, A. A. Hecht, A. Heinz, J. K. P. Lee, A. F. Levand, B. F. Lundgren, R. B. Moore, G. Savard, N. D. Scielzo, D. Seweryniak, K. S. Sharma, G. D. Sprouse, W. Trimble, J. Vaz, J. C. Wang, Y. Wang, B. J. Zabransky, and Z. Zhou

4th International Conference on Exotic Nuclei and Atomic Masses (ENAM'04), Pine Mountain, GA, September 12-16, 2004, Book of Abstracts, p. 59 (2004)

Filling in the Gaps for Odd-A Sb Isotopes from Shell to Shell: A Systematic Perspective of Low-Energy Excitations
Nathan Hotelling, Jason Shergur, and William Walters

4th International Conference on Exotic Nuclei and Atomic Masses (ENAM'04), Pine Mountain, GA, September 12-16, 2004, Book of Abstracts, p. 66 (2004)

In-Beam and Decay Spectroscopy of Transfermium Elements

P. T. Greenlees, D. Ackermann, J. E. Bastin, P. A. Butler, A. Chatillon, S. Eeckhaudt, K. Eskola, J. Gerl, T. Grahn, A. Gorgen, R.-D. Herzberg, F. P. Hesberger, R. D. Humphreys, P. J. C. Ikin, G. D. Jones, P. Jones, R. Julin, S. Juutinen, H. Kettunen, T. L. Khoo, W. Korten, P. Kuusiniemi, M. Leino, A.-P. Leppanen, P. Nieminen, M. Nyman, T. Page, J. Pakarinen, A. Pritchard, P. Rahkila, P. Reiter, C. Scholey, Ch. Theisen, and J. Uusitalo

4th International Conference on Exotic Nuclei and Atomic Masses (ENAM'04), Pine Mountain, GA, September 12-16, 2004, Book of Abstracts, p. 72 (2004)

In-Beam Gamma-Ray Spectroscopy of ²⁵⁴No

S. Eeckhaudt, N. Amzal, J. E. Bastin, E. Bouchez, P. A. Butler, A. Chatillon, K. Eskola, J. Gerl, T. Grahn, A. Gorgen, P. T. Greenlees, R.-D. Herzberg, F. P. Hessberger, A. Hurstel, P. J. C. Ikin, G. D. Jones, P. Jones, R. Julin, S. Juutinen, H. Kettunen, T. L. Khoo, W. Korten, P. Kuusiniemi, Y. Le Coz, M. Leino, A.-P. Leppannen, P. Nieminen, J. Pakarinen, J. Perkowski, A. Pritchard, P. Reiter, P. Rahkila, C. Scholey, Ch. Theisen, J. Uusitalo, K. Van de Vel, J. Wilson, and H. J. Wollersheim

4th International Conference on Exotic Nuclei and Atomic Masses (ENAM'04), Pine Mountain, GA, September 12-16, 2004, Book of Abstracts, p. 75 (2004)

Ion Manipulation with Cooled and Bunched Beams

G. Savard

4th International Conference on Exotic Nuclei and Atomic Masses (ENAM'04), Pine Mountain, GA, September 12-16, 2004, Book of Abstracts, p. 128 (2004)

Recoil-Decay Tagging Study of ¹⁴⁶Tm

A. P. Robinson, C. N. Davids, D. Seweryniak, P. J. Woods, B. Blank, M. P. Carpenter, T. Davinson, S. J. Freeman, N. Hammond, N. Hotelling, R. V. F. Janssens, Z. Liu, G. Mukherjee, J. Shergur, S. Sinha, A. A. Sonzogni, W. B. Walters, and A. Woehr

4th International Conference on Exotic Nuclei and Atomic Masses (ENAM'04), Pine Mountain, GA, September 12-16, 2004, Book of Abstracts, p. 164 (2004)

Atomic Mass Ratios for Some Stable Isotopes of Platinum Relative to ¹⁹⁷Au

K. S. Sharma, J. Vaz, R. C. Barber, F. Buchinger, J. A. Clark, J. E. Crawford, H. Fukutani, J. P. Greene, S. Gulick, A. Heinz, J. K. P. Lee, G. Savard, Z. Zhou, and J. C. Wang

4th International Conference on Exotic Nuclei and Atomic Masses (ENAM'04), Pine Mountain, GA, September 12-16, 2004, Book of Abstracts, p. 199 (2004)

Precise Mass Measurements of ^{252}Cf Fission Fragments with The Canadian Penning Trap Mass Spectrometer

Y. Wang, C. Boudreau, F. Buchinger, J. A. Clark, J. E. Crawford, J. P. Greene, S. Gulick, J. C. Hardy, A. A. Hecht, A. Heinz, J. K. P. Lee, A. F. Levand, B. F. Lundgren, G. Savard, N. Scielzo, K. S. Sharma, G. D. Sprouse, W. Trimble, J. Vaz, J. C. Wang, B. J. Zabransky, and Z. Zhou
4th International Conference on Exotic Nuclei and Atomic Masses (ENAM'04), Pine Mountain, GA, September 12-16, 2004, Book of Abstracts, p. 201 (2004)

The $N = Z$ rp-Process Waiting-Point Nucleus ^{68}Se and its Astrophysical Implication

A. Wöhr, A. Aprahamian, P. Boutachkov, J. L. Galache, J. Görres, M. Shawcross, A. Teymurazyan, M. C. Wiescher, D. S. Brenner, C. N. Davids, S. M. Fischer, A. M. Heinz, R. V. F. Janssens, and D. Seweryniak
4th International Conference on Exotic Nuclei and Atomic Masses (ENAM'04), Pine Mountain, GA, September 12-16, 2004, Book of Abstracts, p. 203 (2004)

EMMA: A Recoil Mass Spectrometer for ISAC II at TRIUMF

B. Davids and C. N. Davids
4th International Conference on Exotic Nuclei and Atomic Masses (ENAM'04), Pine Mountain, GA, September 12-16, 2004, Book of Abstracts, p. 212 (2004)

Decay Rate of Triaxially Deformed Proton Emitters

Cary N. Davids and Henning Esbensen
4th International Conference on Exotic Nuclei and Atomic Masses (ENAM'04), Pine Mountain, GA, September 12-16, 2004, Book of Abstracts, p. 245 (2004)

Study of Multi-Quasiparticle Isomers in Deformed $A \sim 180$ Nuclei Near and Beyond the Valley of Stability

F. G. Kondev, G. D. Dracoulis, G. J. Lane, I. Ahmd, A. P. Byrne, M. P. Carpenter, S. J. Freeman, N. J. Hammond, R. V. F. Janssens, T. Kibedi, T. Lauritsen, C. J. Lister, G. Mukherjee, D. Seweryniak, P. Chowdhury, and S. K. Tandel
4th International Conference on Exotic Nuclei and Atomic Masses (ENAM'04), Pine Mountain, GA, September 12-16, 2004, Book of Abstracts, p. 292 (2004)

Particle-Core Coupling in the Transitional Proton Emitters $^{145,146,147}\text{Tm}$

D. Seweryniak, C. N. Davids, A. Robinson, P. J. Woods, B. Blank, M. P. Carpenter, T. Davinson, S. J. Freeman, N. Hammond, N. Hoteling, R. V. F. Janssens, Z. Liu, G. Mukherjee, J. Shergur, S. Sinha, A. A. Sonzogni, W. B. Walters, and A. Woehr
4th International Conference on Exotic Nuclei and Atomic Masses (ENAM'04), Pine Mountain, GA, September 12-16, 2004, Book of Abstracts, p. 312 (2004)

Neutron-Proton Correlations in $N = Z$ Nuclei Above ^{56}Ni

C. J. (Kim) Lister
2004 Annual April Meeting of the American Physical Society, Denver, CO, May 1-4, 2004; Bull. Am. Phys. Soc. **49**, 45 (2004)

Determination of Low-Spin Levels in $^{134,135}\text{Sb}$ via Decay of ^{135}Sn

Jason Shergur, Andreas Woehr, William B. Walters, Karl-Ludwig Kratz, Oliver Arndt, Iris Dillmann, Per Hoff, Ulli Koster, and Bernd Pfeiffer
2004 Annual April Meeting of the American Physical Society, Denver, CO, May 1-4, 2004; Bull. Am. Phys. Soc. **49**, 106 (2004)

Loading ^{225}Ra Atoms in a Magneto-Optical Trap as the First Step to an Electric Dipole Moment Measurement

N. D. Scielzo, I. Ahmad, K. Bailey, R. J. Holt, Z.-T. Lu, T. O'Conner, D. H. Potterveld, and E. C. Schulte
2004 Annual April Meeting of the American Physical Society, Denver, CO, May 1-4, 2004; Bull. Am. Phys. Soc. **49**, 113 (2004)

Hadron Spectra from PHOBOS in d + Au Collisions

Gabor Veres (PHOBOS Collaboration)

2004 Annual April Meeting of the American Physical Society, Denver, CO, May 1-4, 2004; Bull. Am. Phys. Soc. **49**, 167 (2004)

Multiplicity Fluctuations in 200 GeV Au - Au Collisions

Zhengwei Chai (PHOBOS Collaboration)

2004 Annual April Meeting of the American Physical Society, Denver, CO, May 1-4, 2004; Bull. Am. Phys. Soc. **49**, 168 (2004)

Early Days and the Beginnings of the Iron Age

John P. Schiffer

2004 Annual April Meeting of the American Physical Society, Denver, CO, May 1-4, 2004; Bull. Am. Phys. Soc. **49**, 173 (2004)

Alpha-Gamma Angular Correlations Using Position-Sensitive Detectors

P. Chowdhury, C. M. Wilson, R. Gramer, S. K. Tandel, N. J. Hammond, C. J. Lister, S. M. Fischer, E. F. Moore, K. M. Teh, M. McClish, K. S. Shah, and R. Farrell

2004 Annual April Meeting of the American Physical Society, Denver, CO, May 1-4, 2004; Bull. Am. Phys. Soc. **49**, 181 (2004)

Linear Polarization Measurements of Gamma Rays Following Alpha Decay

N. J. Hammond, C. J. Lister, K. Teh, E. F. Moore, and G. D. Jones

2004 Annual April Meeting of the American Physical Society, Denver, CO, May 1-4, 2004; Bull. Am. Phys. Soc. **49**, 183 (2004)

Germanium Double Sided Strip Detectors

C. J. (Kim) Lister

2004 Fall Meeting of the Division of Nuclear Physics of the American Physical Society, Chicago, IL, October 27-30, 2004; Bull. Am. Phys. Soc. **49**, 9 (2004)

Experiments in Nuclear Astrophysics

K. Ernst Rehm

2004 Fall Meeting of the Division of Nuclear Physics of the American Physical Society, Chicago, IL, October 27-30, 2004; Bull. Am. Phys. Soc. **49**, 11 (2004)

A Linear Polarimeter with Exceptional "Figure of Merit"

C. J. (Kim) Lister, N. J. Hammond, K. Teh, E. F. Moore, S. J. Freeman, and G. D. Jones

2004 Fall Meeting of the Division of Nuclear Physics of the American Physical Society, Chicago, IL, October 27-30, 2004; Bull. Am. Phys. Soc. **49**, 19 (2004)

Study of the $d(^6\text{He},p)^7\text{He}$ Reaction

A. H. Wuosmaa, K. E. Rehm, J. P. Greene, R. V. F. Janssens, C. L. Jiang, E. F. Moore, R. C. Pardo, D. Peterson, S. C. Pieper, G. Savard, J. P. Schiffer, S. Sinha, X. Tang, R. B. Wiringa, L. Jisonna, R. E. Segel, and M. Paul

2004 Fall Meeting of the Division of Nuclear Physics of the American Physical Society, Chicago, IL, October 27-30, 2004; Bull. Am. Phys. Soc. **49**, 21(2004)

The ^{16}N Experiment at ATLAS - A Target Preparation *Tour de Force*

John Greene, Janelle Neubauer, Dale Henderson, Bruce Zabransky, Bruce Nardi, Xiaodong Tang, Richard Pardo, and Ernst Rehm

2004 Fall Meeting of the Division of Nuclear Physics of the American Physical Society, Chicago, IL, October 27-30, 2004; Bull. Am. Phys. Soc. **49**, 21 (2004)

Excited States in ${}^9\text{Li}$ from $d({}^8\text{Li},p){}^9\text{Li}$

K. E. Rehm, J. P. Greene, D. J. Henderson, R. V. F. Janssens, C. L. Jiang, E. F. Moore, R. C. Pardo, D. Peterson, S. C. Pieper, G. Savard, J. P. Schiffer, S. Sinha, X. Tang, R. B. Wiringa, A. H. Wuosmaa, L. Jisonna, R. E. Segel, and M. Paul

2004 Fall Meeting of the Division of Nuclear Physics of the American Physical Society, Chicago, IL, October 27-30, 2004; Bull. Am. Phys. Soc. **49**, 22 (2004)

Sub-Barrier Fusion Hindrance in ${}^{64}\text{Ni} + {}^{100}\text{Mo}$

C. L. Jiang, B. B. Back, C. N. Davids, H. Esbensen, R. V. F. Janssens, J. P. Greene, D. J. Henderson, C. J. Lister, R. Pardo, D. Peterson, K. B. Rehm, D. Seweryniak, B. Shumard, S. Sinha, X. D. Tang, I. Tanihata, S. Zhu, P. Collon, and S. Kurtz

2004 Fall Meeting of the Division of Nuclear Physics of the American Physical Society, Chicago, IL, October 27-30, 2004; Bull. Am. Phys. Soc. **49**, 23 (2004)

Characterization of States in the $N = Z + 1$ Nucleus ${}^{71}\text{Br}$

S. M. Fischer, C. J. Lister, T. Anderson, P. Kerns, G. Mesoloras, D. Svelnys, D. P. Balamuth, P. A. Hausladen, and D. G. Sarantites

2004 Fall Meeting of the Division of Nuclear Physics of the American Physical Society, Chicago, IL, October 27-30, 2004; Bull. Am. Phys. Soc. **49**, 25 (2004)

Probing Explosive Stellar Environments with Gammasphere

Dariusz Seweryniak

2004 Fall Meeting of the Division of Nuclear Physics of the American Physical Society, Chicago, IL, October 27-30, 2004; Bull. Am. Phys. Soc. **49**, 25 (2004)

 $T = 0$ Pairing in the Even-Even $N = Z$ Nucleus ${}^{92}\text{Pd}$

O. L. Pechenaya, C. J. Chiara, D. G. Sarantites, W. Reviol, L.-L. Andersson, E. K. Johansson, D. Rudolph, M. P. Carpenter, R. V. F. Janssens, D. Seweryniak, and S. Zhu

2004 Fall Meeting of the Division of Nuclear Physics of the American Physical Society, Chicago, IL, October 27-30, 2004; Bull. Am. Phys. Soc. **49**, 25 (2004)

Evidence for Anti-Magnetic Rotation in ${}^{101}\text{Pd}$

S. Zhu, U. Garg, A. V. Afanasjev, S. Frauendorf, B. Kharraja, S. S. Ghugre, S. N. Chintalapudi, R. V. F. Janssens, M. P. Carpenter, F. G. Kondev, and T. Lauritsen

2004 Fall Meeting of the Division of Nuclear Physics of the American Physical Society, Chicago, IL, October 27-30, 2004; Bull. Am. Phys. Soc. **49**, 26 (2004)

Quadrupole Moments of Wobbling Bands in ${}^{167}\text{Lu}$

H. Amro, G. B. Hagemann, G. B. Beausang, D. A. Meyer, R. F. Casten, H. Herskind, G. Sletten, W. C. Ma, D. G. Roux, M. P. Carpenter, D. J. Hartley, E. F. Moore, P. Pringle, and A. Neusser

2004 Fall Meeting of the Division of Nuclear Physics of the American Physical Society, Chicago, IL, October 27-30, 2004; Bull. Am. Phys. Soc. **49**, 26 (2004)

Search for Triaxial Superdeformation and Wobbling Mode in ${}^{172,171}\text{Hf}$

Y. Zhang, W. C. Ma, D. G. Roux, J. A. Winger, R. B. Yadav, M. P. Carpenter, N. Hammond, R. V. F. Janssens, T. L. Khoo, F. G. Kondev, T. Lauritsen, C. J. Lister, E. F. Moore, S. Zhu, D. J. Hartley, D. Cullen, S. V. Rigby, D. T. Scholes, P. Chowdhury, S. Odegard, M. K. Djongolov, and J. Y. Zhang

2004 Fall Meeting of the Division of Nuclear Physics of the American Physical Society, Chicago, IL, October 27-30, 2004; Bull. Am. Phys. Soc. **49**, 26 (2004)

Multiple Band Structures in $^{237,239}\text{U}$ from “Unsafe” Coulomb Excitation

S. Zhu, R. V. F. Janssens, M. P. Carpenter, N. Hammond, S. J. Freeman, T. L. Khoo, F. G. Kondev, C. J. Lister, E. F. Moore, T. Lauritsen, D. Seweryniak, P. Chowdhury, A. Deacon, J. F. Smith, and G. D. Jones
 2004 Fall Meeting of the Division of Nuclear Physics of the American Physical Society, Chicago, IL, October 27-30, 2004; Bull. Am. Phys. Soc. **49**, 27 (2004)

Search for Wobbling Excitations in Superdeformed Hf Nuclei

D. J. Hartley, M. K. Djongolov, L. L. Riedinger, C. R. Bingham, M. Danchev, J. Goon, J. Y. Zhang, M. P. Carpenter, R. V. F. Janssens, T. L. Khoo, F. G. Kondev, T. Lauritsen, E. F. Moore, G. Hagemann, G. Sletten, A. Aguilar, D. B. Campbell, M. A. Riley, P. Chowdhury, C. Mukherjee, E. Ngijoi-Yogo, S. K. Tandel, D. M. Cullen, C. D. Dracoulis, R. A. Kaye, and R. W. Laird
 2004 Fall Meeting of the Division of Nuclear Physics of the American Physical Society, Chicago, IL, October 27-30, 2004; Bull. Am. Phys. Soc. **49**, 27 (2004)

Sub-Microsecond Isomers in Neutron-Rich Hf Isotopes

S. K. Tandel, U. S. Tandel, C. Parnell-Lampen, P. Chowdhury, M. P. Carpenter, N. J. Hammond, R. V. F. Janssens, T. L. Khoo, F. G. Kondev, T. Lauritsen, C. J. Lister, E. F. Moore, D. Seweryniak, S. Zhu, G. D. Jones, A. Deacon, S. J. Freeman, and J. F. Smith
 2004 Fall Meeting of the Division of Nuclear Physics of the American Physical Society, Chicago, IL, October 27-30, 2004; Bull. Am. Phys. Soc. **49**, 27 (2004)

Asymptotic Normalization Coefficient and Interference of the Resonance and Direct Capture Terms in the Astrophysical Factor for the Hot CNO Process $^{13}\text{N}(p,\gamma)^{14}\text{O}$

A. M. Mukhamedzhanov, A. Azhari, C. Fu, C. A. Gagliardi, F. Pirlepesov, X. D. Tang, L. Trache, R. E. Tribble, V. Burjan., V. Kroha, F. Carstoiu, and B. F. Irgaziev
 2004 Fall Meeting of the Division of Nuclear Physics of the American Physical Society, Chicago, IL, October 27-30, 2004; Bull. Am. Phys. Soc. **49**, 38 (2004)

Collision Geometry Scaling of Midrapidity Charged Particle Multiplicity at RHIC from $\sqrt{s_{NN}} = 19.6$ to 200 GeV
Aneta Iordanova and the PHOBOS Collaboration

2004 Fall Meeting of the Division of Nuclear Physics of the American Physical Society, Chicago, IL, October 27-30, 2004; Bull. Am. Phys. Soc. **49**, 38 (2004)

Pseudorapidity Dependence of Anisotropic Flow in Au + Au Collisions at 62.4 GeV Using the PHOBOS Experiment at RHIC

Joshua Hamblen and the PHOBOS Collaboration

2004 Fall Meeting of the Division of Nuclear Physics of the American Physical Society, Chicago, IL, October 27-30, 2004; Bull. Am. Phys. Soc. **49**, 38 (2004)

Measurement of the β -Delayed α Spectrum of ^{16}N with a New Technique

X. Tang, K. E. Rehm, I. Ahmad, J. Greene, A. A. Hecht, D. Henderson, C. L. Jiang, E. F. Moore, R. C. Pardo, R. V. F. Janssens, G. Savard, J. P. Schiffer, B. Shumard, S. Sinha, A. Wuosmaa, L. J. Jisonna, R. E. Segel, M. Paul, and C. Brune
 2004 Fall Meeting of the Division of Nuclear Physics of the American Physical Society, Chicago, IL, October 27-30, 2004; Bull. Am. Phys. Soc. **49**, 40 (2004)

Remeasurement of $^{14}\text{N} + ^7\text{Be}$ for Astrophysical S_{17} Factor

G. Tabacaru., A. Azhari, C. Fu, C. A. Gagliardi, X. Tang, L. Trache, R. E. Tribble, and V. Burjan
 2004 Fall Meeting of the Division of Nuclear Physics of the American Physical Society, Chicago, IL, October 27-30, 2004; Bull. Am. Phys. Soc. **49**, 40 (2004)

Measurement of the Excitation Function for the $^{21}\text{Na}(p,\alpha)^{18}\text{Ne}$ Reaction

S. Sinha, J. Greene, D. Henderson, R. V. F. Janssens, C. L. Jiang, E. F. Moore, R. C. Pardo, D. Peterson, K. E. Rehm, J. P. Schiffer, X. Tang, A. Chen, L. Jisonna, R. Segel, and A. H. Wuosmaa
2004 Fall Meeting of the Division of Nuclear Physics of the American Physical Society, Chicago, IL, October 27-30, 2004; Bull. Am. Phys. Soc. **49**, 41(2004)

Single-Particle States in the Heaviest Actinide Nuclei

I. Ahmad, F. G. Kondev, E. F. Moore, M. P. Carpenter, R. R. Chasman, J. P. Greene, R. V. F. Janssens, T. Lauritsen, C. J. Lister, and D. Seweryniak
2004 Fall Meeting of the Division of Nuclear Physics of the American Physical Society, Chicago, IL, October 27-30, 2004; Bull. Am. Phys. Soc. **49**, 43 (2004)

Measurement of Neutron Reflectivity in Bragg Reflection from a Perfect Silicon Crystal

Helmut Kaiser, Thomas Dombek, Donald Koetke, Robert Smither, Roy Ringo, Kerry Schoen, Samuel Werner, and Daniel Dombek
2004 Fall Meeting of the Division of Nuclear Physics of the American Physical Society, Chicago, IL, October 27-30, 2004; Bull. Am. Phys. Soc. **49**, 46 (2004)

The ^8B Neutrino Spectrum

W. T. Winter, S. J. Freedman, J. P. Schiffer, and K. E. Rehm
2004 Fall Meeting of the Division of Nuclear Physics of the American Physical Society, Chicago, IL, October 27-30, 2004; Bull. Am. Phys. Soc. **49**, 47 (2004)

Gamma-Ray Spectroscopy of ^{83}Nb

J. Carney, S. M. Fischer, C. J. Lister, M. P. Carpenter, N. J. Hammond, R. V. F. Janssens, E. F. Moore, D. Seweryniak, S. Sinha, and D. P. Balamuth
2004 Fall Meeting of the Division of Nuclear Physics of the American Physical Society, Chicago, IL, October 27-30, 2004; Bull. Am. Phys. Soc. **49**, 53 (2004)

Centrality Dependence and Species Composition of Charged Hadron p_T Spectra in Au + Au Collisions at 62.4 and 200 GeV

Conor Henderson and the PHOBOS Collaboration
2004 Fall Meeting of the Division of Nuclear Physics of the American Physical Society, Chicago, IL, October 27-30, 2004; Bull. Am. Phys. Soc. **49**, 71 (2004)

Charged Particle Multiplicity Distributions for Au + Au and d + Au Collisions at RHIC

Richard Hollis and the PHOBOS Collaboration
2004 Fall Meeting of the Division of Nuclear Physics of the American Physical Society, Chicago, IL, October 27-30, 2004; Bull. Am. Phys. Soc. **49**, 71 (2004)

Half-Life of ^{44}Ti from a 12-Year Decay Measurement

I. Ahmad, F. F. Moore, J. P. Greene, W. Kutschera, and M. Paul
2004 Fall Meeting of the Division of Nuclear Physics of the American Physical Society, Chicago, IL, October 27-30, 2004; Bull. Am. Phys. Soc. **49**, 72 (2004)

Measurement of Charged Particle Distributions in 200 GeV p + p Interactions Using the PHOBOS Detector

Joseph Sagerer and the PHOBOS Collaboration
2004 Fall Meeting of the Division of Nuclear Physics of the American Physical Society, Chicago, IL, October 27-30, 2004; Bull. Am. Phys. Soc. **49**, 82 (2004)

Precise Mass Measurements Along the rp-Process Path

Jason Clark
2004 Fall Meeting of the Division of Nuclear Physics of the American Physical Society, Chicago, IL, October 27-30, 2004; Bull. Am. Phys. Soc. **49**, 85 (2004)

N_{coll} Scaling and High p_T

Birger Back

2004 Fall Meeting of the Division of Nuclear Physics of the American Physical Society, Chicago, IL, October 27-30, 2004; Bull. Am. Phys. Soc. **49**, 87 (2004)

Level Structure of ^{56}Ti and the Possible Shell Gap at $N = 34$

B. Fornal, S. Zhu, R. V. F. Janssens, R. Broda, M. P. Carpenter, P. J. Daly, S. Freeman, Z. W. Grabowski, N. Hammond, F. G. Kondev, W. Krolas, T. Lauritsen, S. Liddick, C. J. Lister, P. Mantica, F. F. Moore, T. Pawlat, B. Tomlin, D. Seweryniak, and J. Wrzesinski

2004 Fall Meeting of the Division of Nuclear Physics of the American Physical Society, Chicago, IL, October 27-30, 2004; Bull. Am. Phys. Soc. **49**, 93 (2004)

Nuclear Structure of Neutron-Rich Nuclides Following Projectile Fragmentation of a Xe-136 Beam at 120 MeV/A

B. E. Tomlin, W. B. Walters, P. F. Mantica, B. A. Brown, A. D. Davies, A. Estrade, P. Hosmer, S. N. Liddick, T. J. Mertzimekis, F. Montes, A. C. Morton, W. F. Mueller, M. S. Ouellette, E. Pellegrini, P. Santi, H. Schatz, N. Hoteling, J. Shergur, D. Seweryniak, and J. Rikowska

2004 Fall Meeting of the Division of Nuclear Physics of the American Physical Society, Chicago, IL, October 27-30, 2004; Bull. Am. Phys. Soc. **49**, 93 (2004)

Ion Trap for Precision β -Decay Studies

N. D. Scielzo, A. Levand, B. F. Lundgren, C. Savard, B. J. Zabransky, Z. Zhou, J. Clark, K. S. Sharma, J. Wang, and Y. Wang

2004 Fall Meeting of the Division of Nuclear Physics of the American Physical Society, Chicago, IL, October 27-30, 2004; Bull. Am. Phys. Soc. **49**, 111 (2004)

**OPERATION AND DEVELOPMENT OF ATLAS
and
R & D RELATED TO A FUTURE RARE ISOTOPE ACCELERATOR
FACILITY**

Beam Loss Studies in High-Intensity Heavy-Ion Linacs

P. N. Ostroumov, V. N. Aseev, and B. Mustapha
Phys. Rev. ST Accel. Beams **7**, 090101/1-18 (2004)

A Detector of Bunch Time Structure for CW Heavy-Ion Beams

N. E. Vinogradov, P. N. Ostroumov, R. C. Pardo, S. I. Sharamentov, and G. P. Zinkann
Nucl. Instrum. Methods **A526**, 206-214 (2004)

Overview of the U.S. Rare Isotope Accelerator Proposal

J. A. Nolen
Proceedings of the 8th International Conference on Nucleus-Nucleus Collisions (NN2003), Moscow, Russia, June 17-21, 2003; Nucl. Phys. **A734**, 661-668 (2004)

Radioactive Beam Facilities of North America

J. A. Nolen
Proceedings of the 6th International Conference on Radioactive Nuclear Beams (RNB6), Argonne, IL, September 22-26, 2003; Nucl. Phys. **A746**, 9c-16c (2004)

A 20 kw Beam-on-Target Test of a High-Power Liquid Lithium Target for RIA

Claude B. Reed, Jerry A. Nolen, James R. Specht, Vincent J. Novick, and Perry Plotkin
Proceedings of the 6th International Conference on Radioactive Nuclear Beams (RNB6), Argonne, IL, September 22-26, 2003; Nucl. Phys. **A746**, 161c-165c (2004)

The Influence of Secondary Reactions in the Wedge of a Magnetic Separator at RIA

C. L. Jiang, B. B. Back, J. Nolen, K. E. Rehm, and G. Savard
Proceedings of the 6th International Conference on Radioactive Nuclear Beams (RNB6), Argonne, IL, September 22-26, 2003; Nucl. Phys. **A746**, 403c-406c (2004)

Development and First On-Line Tests of the RIA Gas Catcher Prototype

W. Trimble, G. Savard, B. Blank, J. A. Clark, F. Buchinger, T. Cocolios, J. E. Crawford, A. Frankel
J. P. Greene, S. Gulick, J. K. P. Lee, A. Levand, M. Portillo, K. S. Sharma, J. C. Wang, B. J. Zabransky,
Z. Zhou and the S258 Collaboration
Proceedings of the 6th International Conference on Radioactive Nuclear Beams (RNB6), Argonne, IL, September 22-26, 2003; Nucl. Phys. **A746**, 415c-418c (2004)

Uranium Carbide Fission Target R&D for RIA - An Update

J. P. Greene, A. Levand, J. Nolen, and T. Burtseva
Proceedings of the 6th International Conference on Radioactive Nuclear Beams (RNB6), Argonne, IL, September 22-26, 2003; Nucl. Phys. **A746**, 425c-428c (2004)

Simulation of Effusion from Targets of Tilted Foils

B. Mustapha, J. A. Nolen, and I. C. Gomes
Proceedings of the 6th International Conference on Radioactive Nuclear Beams (RNB6), Argonne, IL, September 22-26, 2003; Nucl. Phys. **A746**, 437c-440c (2004)

Development of a Low Charge-to-Mass Ratio Injector for a RIB Linac

N. Y. Vinogradov, J. A. Nolen, P. N. Ostroumov, and K. W. Shepard

Proceedings of the 6th International Conference on Radioactive Nuclear Beams (RNB6), Argonne, IL, September 22-26, 2003; Nucl. Phys. **A746**, 445c-448c (2004)

The Use of Electron Beam in RIA R&D

Itacil C. Gomes, Jerry Nolen, and Claude Reed

Proceedings of the 6th International Conference on Radioactive Nuclear Beams (RNB6), Argonne, IL, September 22-26, 2003; Nucl. Phys. **A746**, 453c-456c (2004)

Superconducting Linac Beam Dynamics with High-Order Maps for RF Resonators

Andrew A. Geraci, Jerry A. Nolen, and Richard C. Pardo

Proceedings of the 6th International Conference on Charged Particle Optics (CPO-6), Greenbelt, MD, October 22-25, 2002; Nucl. Instrum. Methods **A519**, 388-395 (2004)

Heavy-Ion Beam Dynamics in the RIA Accelerators

P. N. Ostroumov

Proceedings of the 6th International Conference on Charged Particle Optics (CPO-6), Greenbelt, MD, October 22-25, 2002; Nucl. Instrum. Methods **A519**, 412-424 (2004)

Simulations of Effusion from ISOL Target/Ion Source Systems

B. Mustapha and J. A. Nolen

Proceedings of the 21st World Conference of the International Nuclear Target Development Society, Argonne, IL, November 4-8, 2002; Nucl. Instrum. Methods **A521**, 59-64 (2004)

Rotating Target Wheel System for Super-Heavy Element Production at ATLAS

John P. Greene, Andreas Heinz, Joe Falout, and Robert V. F. Janssens

Proceedings of the 21st World Conference of the International Nuclear Target Development Society, Argonne, IL, November 4-8, 2002; Nucl. Instrum. Methods **A521**, 214-221 (2004)

Calculated Intensity of High-Energy Neutron Beams

B. Mustapha, J. A. Nolen, and B. B. Back

Proceedings of the 21st World Conference of the International Nuclear Target Development Society, Argonne, IL, November 4-8, 2002; Nucl. Instrum. Methods **A521**, 247-253 (2004)

Heavy-Ion Beams Required for the RIA Accelerator

R. C. Pardo, C. L. Jiang, J. A. Nolen, K. E. Rehm, and G. Savard

Proceedings of the 10th International Conference on Ion Sources (ICIS2003), Dubna, Russia, September 8-13, 2003; Rev. Sci. Instrum. **75**, 1427-1430 (2004)

Magnetic Field Upgrade of Argonne National Laboratory 14 GHz ECR Ion Source

R. C. Vondrasek, R. Scott, and R. C. Pardo

Proceedings of the 10th International Conference on Ion Sources (ICIS2003), Dubna, Russia, September 8-13, 2003; Rev. Sci. Instrum. **75**, 1532-1534 (2004)

Electron-Ion Collider at CEBAF: New Insights and Conceptual Progress

Ya. Derbenev, A. Afanasev, K. Beard, A. Bogacz, P. Degtiarenko, J. Delayen, A. Hutton, G. A. Krafft, R. Li, L. Merminga, M. Poelker, B. Yunn, Y. Zhang, and P. Ostroumov

Proceedings of the 9th European Particle Accelerator Conference (EPAC04), Lucerne, Switzerland, July 5-9, 2004, pp. 893-895 (2004)

RF Focusing of Low-Charge-to-Mass-Ratio Heavy-Ions in Superconducting Linac

E. S. Masunov, D. A. Efimov, and P. N. Ostroumov

Proceedings of the 9th European Particle Accelerator Conference (EPAC04), Lucerne, Switzerland, July 5-9, 2004, pp. 1405-1407 (2004)

Multiple-Charge-State Beam Steering in High-Intensity Heavy-Ion Linacs

E. S. Lessner and P. N. Ostroumov

Proceedings of the 9th European Particle Accelerator Conference (EPAC04), Lucerne, Switzerland, July 5-9, 2004, pp. 1476-1478 (2004)

Beam Loss Studies in High-Intensity Heavy-Ion Linacs

P. N. Ostroumov, V. N. Aseev, E. S. Lessner, and B. Mustapha

Proceedings of the 9th European Particle Accelerator Conference (EPAC04), Lucerne, Switzerland, July 5-9, 2004, pp. 2176-2178 (2004)

A Novel Device for Non-Intersecting Bunch Shape Measurement at the High Current GSI-Linac

P. Forck, Ch. Dorn, M. Herty, P. Strehl, V. Peplov, and S. Sharamentov

Proceedings of the 9th European Particle Accelerator Conference (EPAC04), Lucerne, Switzerland, July 5-9, 2004, pp. 2541-2543 (2004)

Electron-Ion Collider at CEBAF: New Insights and Conceptual Progress

Ya. Derbenev, A. Afanasev, K. Beard, A. Bogacz, P. Degtiarenko, J. Delayen, A. Hutton, G. A. Krafft, R. Li,

L. Merminga, M. Poelker, B. Yunn, Y. Zhang, and P. Ostroumov

9th European Particle Accelerator Conference (EPAC04), Lucerne, Switzerland, July 5-9, 2004, Abstract No. MOPLT153 (2004)

RF Focusing of Low-Charge-to-Mass Ratio Heavy-Ions in a Superconducting Linac

E. S. Masunov, D. A. Efimov, and P. N. Ostroumov

9th European Particle Accelerator Conference (EPAC04), Lucerne, Switzerland, July 5-9, 2004, Abstract No. TUPLT111 (2004)

Multiple-Charge-State Beam Steering in High-Intensity Heavy-Ion Linacs

E. S. Lessner and P. N. Ostroumov

9th European Particle Accelerator Conference (EPAC04), Lucerne, Switzerland, July 5-9, 2004, Abstract No. TUPLT147 (2004)

Beam Loss Studies in High-Intensity Heavy-Ion Linacs

P. N. Ostroumov, V. N. Aseev, E. S. Lessner, and B. Mustapha

9th European Particle Accelerator Conference (EPAC04), Lucerne, Switzerland, July 5-9, 2004, Abstract No. WEPLT145 (2004)

A Novel Device for Non-Intersecting Bunch Shape Measurement at the High Current GSI-Linac

P. Forck, Ch. Dorn, M. Herty, P. Strehl, V. Peplov, and S. Sharamentov

9th European Particle Accelerator Conference (EPAC04), Lucerne, Switzerland, July 5-9, 2004, Abstract No. THPLT030 (2004)

Beam Intensity Adjustment in the RIA Driver Linac

P. N. Ostroumov, J. A. Nolen, S. I. Sharamentov, and A. V. Novikov-Borodin

XXII International Linear Accelerator Conference (LINAC2004), Lübeck, Germany, August 16-20, 2004, Abstract No. MOP01 (2004)

Advanced Beam-Dynamics Simulation Tools for RIA

T. P. Wangler, R. Garnett, N. Aseev, P. N. Ostroumov, R. Crandall, D. Gorelov, R. C. York, J. Qiang, and R. Ryne

XXII International Linear Accelerator Conference (LINAC2004), Lübeck, Germany, August 16-20, 2004, Abstract No. MOP71 (2004)

Alternating Phase Focusing in Low-Velocity Heavy-Ion Superconducting Linac

P. N. Ostroumov, A. A. Kolomiets, and E. S. Masunov

XXII International Linear Accelerator Conference (LINAC2004), Lübeck, Germany, August 16-20, 2004, Abstract No. TUP26 (2004)

End-to-End Beam Dynamics Simulations for the ANL RIA Driver Linac

P. N. Ostroumov

XXII International Linear Accelerator Conference (LINAC2004), Lübeck, Germany, August 16-20, 2004, Abstract No. TH204 (2004)

Superconducting $\beta = 0.15$ Quarter-Wave Cavity for RIA

J. D. Fuerst, M. Kedzie, M. P. Kelly, and K. W. Shepard

XXII International Linear Accelerator Conference (LINAC2004), Lübeck, Germany, August 16-20, 2004, Abstract No. THP05 (2004)

Cold Tests of a Superconducting Co-Axial Half-Wave Cavity for RIA

J. D. Fuerst, M. Kedzie, M. P. Kelly, and K. W. Shepard

XXII International Linear Accelerator Conference (LINAC2004), Lübeck, Germany, August 16-20, 2004, Abstract No. THP06 (2004)

Penning Traps at RIA

Jason Clark

2004 Fall Meeting of the Division of Nuclear Physics of the American Physical Society, Chicago, IL, October 27-30, 2004; Bull. Am. Phys. Soc. **49**, 9 (2004)

Research with In-Flight Beams from Fragment Separators

Isao Tanihata

2004 Fall Meeting of the Division of Nuclear Physics of the American Physical Society, Chicago, IL, October 27-30, 2004; Bull. Am. Phys. Soc. **49**, 15 (2004)

Modeling Radiation Effects Near High Power Production Targets at Heavy Ion Facilities

I. C. Gomes, I. Baek, J. A. Nolen, S. G. Mashnik, and K. K. Gudima

2004 Fall Meeting of the Division of Nuclear Physics of the American Physical Society, Chicago, IL, October 27-30, 2004; Bull. Am. Phys. Soc. **49**, 44 (2004)

Beam Stripping Solutions for RIA

E. Simmons, K. Chipps, U. Greife, J. Livesay, J. Nolen, and M. Portillo

2004 Fall Meeting of the Division of Nuclear Physics of the American Physical Society, Chicago, IL, October 27-30, 2004; Bull. Am. Phys. Soc. **49**, 45 (2004)

MEDIUM-ENERGY NUCLEAR PHYSICS RESEARCH

Flavor Decomposition of the Sea-Quark Helicity Distributions in the Nucleon from Semiinclusive Deep Inelastic Scattering

A. Airapetian *et al.* (HERMES Collaboration)
Phys. Rev. Lett. **92**, 012005/1-5 (2004)

Search for Anomalously Heavy Isotopes of Helium in the Earth's Atmosphere

P. Mueller, L.-B. Wang, R. J. Holt, Z.-T. Lu, T. P. O'Connor, and J. P. Schiffer
Phys. Rev. Lett. **92**, 022501/1-4 (2004)

Parity-Violating Electron Deuteron Scattering and the Proton's Neutral Weak Axial Vector Form Factor

T. M. Ito *et al.* (SAMPLE Collaboration)
Phys. Rev. Lett. **92**, 102003/1-4 (2004)

Counting Individual ^{41}Ca Atoms with a Magneto-Optical Trap

I. D. Moore, K. Bailey, J. Greene, Z.-T. Lu, P. Müller, T. P. O'Connor, Ch. Geppert, K. D.A. Wendt, and L. Young
Phys. Rev. Lett. **92**, 153002/1-4 (2004)

Laser Spectroscopic Determination of the ^6He Nuclear Charge Radius

L.-B. Wang, P. Mueller, K. Bailey, G. W. F. Drake, J. P. Greene, D. Henderson, R. J. Holt, R. V. F. Janssens, C. L. Jiang, Z.-T. Lu, T. P. O'Connor, R. C. Pardo, M. Paul, K. E. Rehm, J. P. Schiffer, and X. D. Tang
Phys. Rev. Lett. **93**, 142501/1-4 (2004)

Angular Distributions of Λ H Bound States in $^{3,4}\text{He}(e, e'K^+)$ Reaction

F. Dohrmann *et al.*
Phys. Rev. Lett. **93**, 242501/1-4 (2004)

Evidence for a Narrow $|S| = 1$ Baryon State at a Mass of 1528 MeV in Quasi-Real Photoproduction

A. Airapetian *et al.* (HERMES Collaboration)
Phys. Lett. **B585**, 213-222 (2004)

Hard Exclusive Electroproduction of $\pi^+\pi^-$ Pairs

A. Airapetian *et al.* for the HERMES Collaboration
Phys. Lett. **B599**, 212-222 (2004)

Implications of the Discrepancy Between Proton Form Factor Measurements

J. Arrington
Phys. Rev. C **69**, 022201(R)/1-5 (2004)

Evidence for Two-Photon Exchange Contributions in Electron-Proton and Positron-Proton Elastic Scattering

J. Arrington
Phys. Rev. C **69**, 032201/1-5 (2004)

Measurements of Electron-Proton Elastic Cross Sections for $0.4 < Q^2 < 5.5$ (GeV/c) 2

M. E. Christy *et al.*
Phys. Rev. C **70**, 015206/1-15 (2004)

Coulomb Distortion in High- Q^2 Elastic e - p Scattering

John Arrington and Ingo Sick
Phys. Rev. C **70**, 028203/1-3 (2004)

Near Threshold Electroproduction of the ω Meson at $Q^2 \approx 0.5 \text{ GeV}^2$ P. Ambrozewicz *et al.*Phys. Rev. C **70**, 035203/1-9 (2004)

Basic Instrumentation for Hall A at Jefferson Lab

J. Alcorn *et al.*Nucl. Instrum. Methods **A522**, 294-346 (2004)

Nuclear Polarization of Molecular Hydrogen Recombined on a Non-Metallic Surface

A. Airapetian *et al.* (for the HERMES Collaboration)Eur. Phys. J. D **29**, 21-26 (2004)

One Million Year Old Groundwater in the Sahara Revealed by Krypton-81 and Chlorine-36

N. C. Sturchio, X. Du, R. Purtschert, M. Sultan, L. J. Patterson, Z.-T. Lu, P. Mueller, T. Bigler, K. Bailey, T. P. O'Connor, L. Young, R. Lorenzo, R. Becker, Z. El Alfy, B. El Kaliouby, Y. Dawood, and A. M. A. Abdallah

Geophys. Res. Lett. **31**, L05503/1-4 (2004)A First Measurement of the Tensor Structure Function b_1^d

M. Contalbrigo (on behalf of the HERMES Collaboration)

Proceedings of the International Conference on the Structure and Interactions of the Photon, including the 15th International Workshop on Photon-Photon Collisions, Frascati, Italy, April 7-11, 2003; Nucl. Phys. **B126**, 41-45 (2004)Diffractive Exclusive Electroproduction of ρ^0 Mesons at HERMES

A. Airapetian (on behalf of the HERMES Collaboration)

Proceedings of the International Conference on the Structure and Interactions of the Photon, including the 15th International Workshop on Photon-Photon Collisions, Frascati, Italy, April 7-11, 2003; Nucl. Phys. **B126**, 232-236 (2004)

Modeling Neutrino Quasielastic Cross Sections on Nucleons and Nuclei

A. Bodek, H. Budd, and J. Arrington

Proceedings of the 8th Conference on Intersections of Particle and Nuclear Physics (CIPANP2003), ed. Zohreh Parsa, AIP Conference Proceedings **698**, 148-152 (2004)

Hadron Suppression in DIS at HERMES

Pasquale Di Nezza (on behalf of the HERMES Collaboration)

Proceedings of the 17th International Conference on Ultra Relativistic Nucleus-Nucleus Collisions (Quark Matter 2004), Oakland, CA, January 11-17, 2004; J. Phys. G **30**, S783-S790 (2004)Charge Radius Measurement of ^6He in an Atom Trap

P. Mueller, L.-B. Wang, K. Bailey, J. Greene, R. J. Holt, D. Henderson, R. V. F. Janssens, C. L. Jiang, Z.-T. Lu, T. P. O'Connor, R. C. Pardo, K. E. Rehm, J. P. Schiffer, X. Tang, M. Paul, and G. W. F. Drake

Conference on "Nuclei at the Limits", Argonne, IL, July 26-30, 2004, Book of Abstracts, p. 102 (2004)

Laser Spectroscopic Determination of the ^6He Charge Radius

P. Mueller, L.-B. Wang, K. Bailey, G. W. F. Drake, J. Greene, R. J. Holt, D. Henderson, R. V. F. Janssens, C. L. Jiang, Z.-T. Lu, T. P. O'Connor, R. C. Pardo, M. Paul, K. E. Rehm, J. P. Schiffer, and X. Tang

4th International Conference on Exotic Nuclei and Atomic Masses (ENAM'04), Pine Mountain, GA, September 12-16, 2004, Book of Abstracts, p. 31(2004)

Counting Individual Ca41 Atoms with a MOT for Biomedical Applications

I. D. Moore, K. Bailey, P. Mueller, Z.-T. Lu, T. P. O'Connor, L. Young, Ch. Geppert, and K. D. A. Wendt
2004 Meeting of the Division of Atomic, Molecular, and Optical Physics of the American Physical Society (DAMOP04), Tucson, AZ, May 25-29, 2004; Bull. Am. Phys. Soc. **49**, 35 (2004)

One Million Years of Groundwater History Revealed by Atom Trap Trace Analysis of Krypton-81

Peter Mueller for the Sahara Groundwater Age Collaboration
2004 Meeting of the Division of Atomic, Molecular, and Optical Physics of the American Physical Society (DAMOP04), Tucson, AZ, May 25-29, 2004; Bull. Am. Phys. Soc. **49**, 52 (2004)

Experimental Program to Measure the Electric Dipole Moment of Radium-225

E. Schulte, I. Ahmad, K. Bailey, D. Bowers, R. Holt, Z.-T. Lu, T. O'Connor, D. Potterveld, and N. Scielzo
2004 Meeting of the Division of Atomic, Molecular, and Optical Physics of the American Physical Society (DAMOP04), Tucson, AZ, May 25-29, 2004; Bull. Am. Phys. Soc. **49**, 60 (2004)

Measuring the Nuclear Charge Radius of ${}^6\text{He}$

L.-B. Wang, P. Mueller, K. Bailey, J. Greene, D. Henderson, R. J. Holt, R. V. F. Janssens, C. L. Jiang, Z.-T. Lu, T. P. O'Connor, R. C. Pardo, K. E. Rehm, J. P. Schiffer, X.-D. Tang, G. W. F. Drake, and M. Paul
2004 Meeting of the Division of Atomic, Molecular, and Optical Physics of the American Physical Society (DAMOP04), Tucson, AZ, May 25-29, 2004; Bull. Am. Phys. Soc. **49**, 76 (2004)

Neutron Spin Structure in the Resonance Region and Quark-Hadron Duality

Patricia Solvignon and the Jefferson Lab Hall A Collaboration
2004 Fall Meeting of the Division of Nuclear Physics of the American Physical Society, Chicago, IL, October 27-30, 2004; Bull. Am. Phys. Soc. **49**, 29 (2004)

Two-Photon Exchange Corrections to the Proton Elastic Form Factors

John Arrington
2004 Fall Meeting of the Division of Nuclear Physics of the American Physical Society, Chicago, IL, October 27-30, 2004; Bull. Am. Phys. Soc. **49**, 33 (2004)

Constraints on Two-Photon Exchange Effects from High-Precision Rosenbluth Measurements

Issam Qattan and the JLAB E-01-001 Collaboration
2004 Fall Meeting of the Division of Nuclear Physics of the American Physical Society, Chicago, IL, October 27-30, 2004; Bull. Am. Phys. Soc. **49**, 34 (2004)

Measurements of G_E^p / G_M^p Using a Polarized Target

Xiaochao Zheng
2004 Fall Meeting of the Division of Nuclear Physics of the American Physical Society, Chicago, IL, October 27-30, 2004; Bull. Am. Phys. Soc. **49**, 34 (2004)

Search for Anomalously Heavy Helium Isotopes in the Earth's Atmosphere

L.-T. Wang, P. Mueller, R. J. Holt, Z.-T. Lu, T. P. O'Connor, and J. P. Schiffer
2004 Fall Meeting of the Division of Nuclear Physics of the American Physical Society, Chicago, IL, October 27-30, 2004; Bull. Am. Phys. Soc. **49**, 39 (2004)

Search for the Σ^0 and Θ^{++} Partners of the Pentaquark

Paul E. Reimer (JLAB E04-012 Collaboration)
2004 Fall Meeting of the Division of Nuclear Physics of the American Physical Society, Chicago, IL, October 27-30, 2004; Bull. Am. Phys. Soc. **49**, 80 (2004)

High Resolution Search for Pentaquark Partners in Jefferson Lab Hall A

Yi Qiang and the Jefferson Lab E04-012 and Hall A Collaborations

2004 Fall Meeting of the Division of Nuclear Physics of the American Physical Society, Chicago, IL,
October 27-30, 2004; Bull. Am. Phys. Soc. **49**, 81 (2004)

Measurement of the Double Polarization Asymmetry of Θ^+ Production on the Neutron

Xiaochao Zheng

2004 Fall Meeting of the Division of Nuclear Physics of the American Physical Society, Chicago, IL,
October 27-30, 2004; Bull. Am. Phys. Soc. **49**, 81(2004)

Laser Spectroscopic Determination of the ^6He Nuclear Charge Radius

P. Mueller, L.-B. Wang, K. Bailey, J. P. Greene, D. Henderson, R. J. Holt, R. V. F. Janssens, C. L. Jiang,
Z.-T. Lu, T. P. O'Connor, R. C. Pardo, K. E. Rehm, J. P. Schiffer, X. D. Tang, G. W. F. Drake, and M. Paul

2004 Fall Meeting of the Division of Nuclear Physics of the American Physical Society, Chicago, IL,
October 27-30, 2004; Bull. Am. Phys. Soc. **49**, 91 (2004)

Omega Electroproduction in Hall C at Jefferson Lab

Pawel Ambrozewicz and the Jefferson Lab E91-016 Collaboration

2004 Fall Meeting of the Division of Nuclear Physics of the American Physical Society, Chicago, IL,
October 27-30, 2004; Bull. Am. Phys. Soc. **49**, 96 (2004)

New Measurement of G_E/G_M for the Proton

Ralph Segel and the JLAB E-01-001 Collaboration

2004 Fall Meeting of the Division of Nuclear Physics of the American Physical Society, Chicago, IL,
October 27-30, 2004; Bull. Am. Phys. Soc. **49**, 97 (2004)

Hyperon Nucleon Interaction and Hypernuclear Structure in the $(e,e'K)$ Reaction on Light Targets

Joerg Reinhold and the Jefferson Lab E91-016 Collaboration

2004 Fall Meeting of the Division of Nuclear Physics of the American Physical Society, Chicago, IL,
October 27-30, 2004; Bull. Am. Phys. Soc. **49**, 98 (2004)

THEORETICAL PHYSICS ρ Meson Photoproduction at Low Energies

Yongseok Oh and T.-S. H. Lee

Phys. Rev. C **69**, 025201/1-14 (2004)

Baryon Form Factors of Relativistic Constituent-Quark Models

B. Juliá-Díaz, D. O. Riska, and F. Coester

Phys. Rev. C **69**, 035212/1-18 (2004)

Bare vs Effective Pairing Forces: A Microscopic Finite-Range Interaction for Hartree-Fock-Bogolyubov Calculations in Coordinate Space

T. Duguet

Phys. Rev. C **69**, 054317/1-18 (2004)

Configuration Mixing of Angular Momentum Projected Self-Consistent Mean-Field States for Neutron-Deficient Pb Isotopes

M. Bender, P. Bonche, T. Duguet, and P.-H. Heenen

Phys. Rev. C **69**, 064303/1-13 (2004)

Dynamical Coupled-Channel Model of Kaon-Hyperon Interactions

Wen-Tai Chiang, B. Saghai, F. Tabakin, and T.-S. H. Lee

Phys. Rev. C **69**, 065208/1-13 (2004)

Pseudoscalar Meson Radial Excitations

A. Höll, A. Krassnigg, and C. D. Roberts

Phys. Rev. C **70**, 042203(R)/1-5 (2004)

Aspects and Consequences of a Dressed-Quark-Gluon Vertex

M. S. Bhagwat, A. Höll, A. Krassnigg, C. D. Roberts, and P. C. Tandy

Phys. Rev. C **70**, 035205/1-15 (2004)

In-Medium Vector Meson Masses in a Chiral SU(3) Model

D. Zschesche, A. Mishra, S. Schramm, H. Stöcker, and W. Greiner

Phys. Rev. C **70**, 045202/1-13 (2004)

Axial Transition Form Factors and Pion Decay of Baryon Resonances

B. Juliá-Díaz, D. O. Riska, and F. Coester

Phys. Rev. C **70**, 045204/1-8 (2004)Constraints on the ${}^7\text{Be}(p,\gamma){}^8\text{B}$ Radiative Capture Rate from Charge Symmetry

Henning Esbensen

Phys. Rev. C **70**, 047603/1-4 (2004)Quantum Monte Carlo Calculations of Excited States in $A = 6 - 8$ Nuclei

Steven C. Pieper, R. B. Wiringa, and J. Carlson

Phys. Rev. C **70**, 054325/1-11 (2004)

Order Generated by Random Many-Body Dynamics

Alexander Volya and Vladimir Zelevinsky

Acta Phys. Hungarica **19**, 221-225 (2004)

Electromagnetic Meson Production in the Nucleon Resonance Region

V. D. Burkert and T.-S. H. Lee

Int. J. Mod. Phys. E **13**, 1035-1112 (2004)

Pairing Correlations in Nuclei: Old Knowledge and New Ideas

Vladimir Zelevinsky and Alexander Volya

Proceedings of the International Conference on Collective Motion in Nuclei Under Extreme Conditions (COMEX 1), Paris, France, June 10-13, 2003; Nucl. Phys. **A731**, 299-310 (2004)

Dyson-Schwinger Equations: An Instrument for Hadron Physics

A. Krassnigg and C. D. Roberts

Proceedings of the 17th International IUPAP Conference on Few-Body Problems in Physics (Few-Body 17), Durham, NC, June 5-10, 2003; Nucl. Phys. **A737**, 7-15 (2004)

A Replay of Few-Body Reactions in Particle Cosmology

W.-Y. P. Hwang, T.-S. H. Lee, and Bo-Qiang Ma

Proceedings of the 17th International IUPAP Conference on Few-Body Problems in Physics (Few-Body 17), Durham, NC, June 5-10, 2003; Nucl. Phys. **A737**, 294-297 (2004)

Neutron Matter: A Superfluid Gas

S.-Y. Chang, J. Morales, Jr., V. R. Pandharipande, D. G. Ravenhall, J. Carlson, Steven C. Pieper, R. B. Wiringa, and K. E. Schmidt

Proceedings of the 6th International Conference on Radioactive Nuclear Beams (RNB6), Argonne, IL, September 22-26, 2003; Nucl. Phys. **A746**, 215c-221c (2004)

Refraction and Dispersion in Optical Glass

D. Y. Smith, E. Shiles, and Mitio Inokuti

Proceedings of the 12th International Conference on Radiation Effects in Insulators, Gramado, Brazil, August 31-September 5, 2003; Nucl. Instrum. Methods **B218**, 170-175 (2004)

DSEs, The Pion, and Related Matters

A. Krassnigg and C. D. Roberts

Proceedings of the 2nd International Conference on Nuclear and Particle Physics with CEBAF at JLab, Dubrovnik, Croatia, May 26-31, 2003; Fizika **B13**, 143-152 (2004)

Unifying Aspects of Light- and Heavy-Systems

C. D. Roberts

Proceedings of the International School on Heavy Quark Physics, Dubna, Moscow Region, Russia, May 27-June 1, 2002; Lect. Notes Phys. **647**, 149-188 (2004)

Challenges in Coupled-Channels Calculations of Heavy-Ion Fusion Reactions

Henning Esbensen

Proceedings of the International Conference FUSION03: From a Tunneling Nuclear Microscope to Nuclear Processes in Matter, Matsushima, Miyagi, Japan, November 12-15, 2003; Progress of Theoretical Physics Supplement **154**, 11-20 (2004)

DSE's and Pseudoscalar Mesons: An Aperçu

A. Höll, A. Krassnigg, and C. D. Roberts

Proceedings of the International Workshop on Light Cone Physics: Hadrons and Beyond (LC03), Durham, UK, August 5-9, 2003, ed. S. Dalley, Report IPPP/03/71, pp. 158-165 (2004)

Models of Meson-Baryon Reactions in the Nucleon Resonance Region

T.-S. H. Lee, A. Matsuyama, and T. Sato

Proceedings of the 9th International Workshop on the Physics of Excited Nucleons (NSTAR 2004), Grenoble, France, March 24-27, 2004, eds. Jean-Paul Bocquet, Viatcheslav Kuznetsov, and Dominique Rebreyend (World Scientific Pub. Co. 2004) pp. 104-115

Quantum Monte Carlo Calculations of Light Nuclei and Neutron Drops

Steven C. Pieper

22nd International Nuclear Physics Conference (INPC2004), Göteborg, Sweden, June 27-July 2, 2004, Book of Abstracts, p. 36 (2004)

A Microscopic Finite-Range Pairing Interaction for HFB Calculations in Coordinate Space

T. Duguet

Conference on "Nuclei at the Limits", Argonne, IL, July 26-30, 2004, Book of Abstracts, p. 48 (2004)

Constraints on the ${}^7\text{Be}(p,\gamma){}^8\text{B}$ Radiative Capture

H. Esbensen

Conference on "Nuclei at the Limits", Argonne, IL, July 26-30, 2004, Book of Abstracts, p. 50 (2004)

Ab Initio Theory of Light Nuclei

R. B. Wiringa

Conference on "Nuclei at the Limits", Argonne, IL, July 26-30, 2004, Book of Abstracts, p. 164 (2004)

Can Modern Nuclear Hamiltonians Tolerate a Bound Tetraneutron?

Steven C. Pieper

4th International Conference on Exotic Nuclei and Atomic Masses (ENAM'04), Pine Mountain, GA, September 12-16, 2004, Book of Abstracts, p. 46 (2004)

How Fast, Realistically: *Ab initio* Calculations of Low-Energy Astrophysical Reaction Rates

K. M. Nollett

2004 Annual April Meeting of the American Physical Society, Denver, CO, May 1-4, 2004; Bull. Am. Phys. Soc. **49**, 49 (2004)

Correlations in Light Nuclei

Robert B. Wiringa

2004 Annual April Meeting of the American Physical Society, Denver, CO, May 1-4, 2004; Bull. Am. Phys. Soc. **49**, 170 (2004)

Spectroscopic Factors and Particle Widths in Light Nuclei

K. M. Nollett, J. P. Schiffer, K. E. Rehm, and A. H. Wuosmaa

2004 Fall Meeting of the Division of Nuclear Physics of the American Physical Society, Chicago, IL, October 27-30, 2004; Bull. Am. Phys. Soc. **49**, 23 (2004)

A Measurement of the Neutron MDM Interaction in Silicon

Donald Koetke, Thomas Dombeck, Helmut Kaiser, Murray Peshkin, Robert Smither, and Shirvel Stanislaus

2004 Fall Meeting of the Division of Nuclear Physics of the American Physical Society, Chicago, IL, October 27-30, 2004; Bull. Am. Phys. Soc. **49**, 46 (2004)

A Model for Investigating the Parity of Θ Using ${}^3\bar{\text{He}}$ Target

Yongseok Oh, T.-S. H. Lee, and Kanzo Nakayama

2004 Fall Meeting of the Division of Nuclear Physics of the American Physical Society, Chicago, IL, October 27-30, 2004; Bull. Am. Phys. Soc. **49**, 80 (2004)

Microscopic Low-Energy Nuclear Reactions for Astrophysics and Applied Physics

R. B. Wiringa

2004 Fall Meeting of the Division of Nuclear Physics of the American Physical Society, Chicago, IL,
October 27-30, 2004; Bull. Am. Phys. Soc. **49**, 102 (2004)

The ^8B S-Factor Extracted from Coulomb Dissociation Experiments

Henning Esbensen, George F. Bertsch, and Kurt A. Snover

2004 Fall Meeting of the Division of Nuclear Physics of the American Physical Society, Chicago, IL,
October 27-30, 2004; Bull. Am. Phys. Soc. **49**, 103 (2004)



Physics Division

Argonne National Laboratory
9700 South Cass Avenue, Bldg. 203
Argonne, IL 60439-4843

www.anl.gov



THE UNIVERSITY OF
CHICAGO



**Office of
Science**

U.S. DEPARTMENT OF ENERGY

A U.S. Department of Energy laboratory managed by The University of Chicago